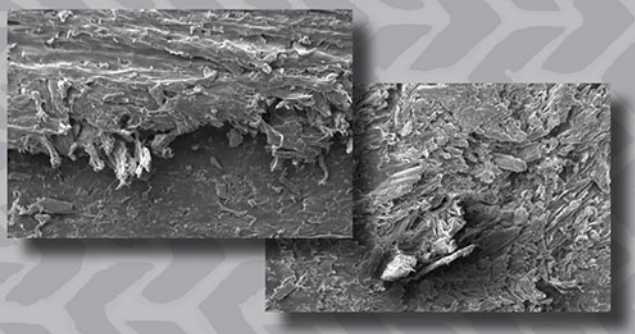
Composite Science and Technology

COMSAT2025

2nd Composite Science and Technology International Conference (COMSAT2025), held virtually from September 24 to 25th, 2025, by The Centre for Advanced Composite Materials (CACM) at Universiti Teknologi Malaysia (UTM)



Edited by
Norhayani binti Othman,
Mohd Nor Faiz Norrrahim,
Munirah binti Onn, P. S. Khoo

MRF

Composite Science and Technology
COMSAT2025

2nd Composite Science and Technology International Conference (COMSAT 2025), held virtually from September 24 to 25th, 2025, by The Centre for Advanced Composite Materials (CACM) at Universiti Teknologi Malaysia (UTM)

Editors

Norhayani binti Othman, Mohd Nor Faiz Norrrahim, Munirah binti Onn, P. S. Khoo

Centre for Advanced Composite Materials (CACM), Universiti Teknologi Malaysia, Johor, Malaysia

Peer review statement

All papers published in this volume of "Materials Research Proceedings" have been peer reviewed. The process of peer review was initiated and overseen by the above proceedings editors. All reviews were conducted by expert referees in accordance to Materials Research Forum LLC high standards.

Copyright © 2026 by authors

Content from this work may be used under the terms of the Creative Commons Attribution 3.0 license. Any further distribution of this work must maintain attribution to the author(s) and the title of the work, journal citation and DOI.

Published under License by **Materials Research Forum LLC**
Millersville, PA 17551, USA

Published as part of the proceedings series
Materials Research Proceedings
Volume 74 (2026)

ISSN 2474-3941 (Print)
ISSN 2474-395X (Online)

ISBN 978-1-64490-446-6 (Print)
ISBN 978-1-64490-447-3 (eBook)

This book contains information obtained from authentic and highly regarded sources. Reasonable efforts have been made to publish reliable data and information, but the author and publisher cannot assume responsibility for the validity of all materials or the consequences of their use. The authors and publishers have attempted to trace the copyright holders of all material reproduced in this publication and apologize to copyright holders if permission to publish in this form has not been obtained. If any copyright material has not been acknowledged please write and let us know so we may rectify in any future reprint.

Distributed worldwide by

Materials Research Forum LLC
105 Springdale Lane
Millersville, PA 17551
USA
https://mrforum.com

Manufactured in the United States of America
10 9 8 7 6 5 4 3 2 1

Table of Contents

Preface
Committees

Effects of Crushing Cycle on The Mechanical Properties and Morphology of Napier Grass Stem Fibre
Siti Syafiqah MAT NOR, Siti Khairunisah GHAZALI, Rohah A. MAJID 1

Insight on Mechanical Properties of Hybrid Graphene/Glass/ABS Nanocomposites
Anahar Nurul Aina, Muhammad Asyraf Muhammad Rizal, Muhamad Fauzi Abd Rased, Rohah A. Majid, Desmond Daniel Chin Vui Sheng, Amer Iskandar Ra'eis, Noryani Muhammad..... 9

Mechanical Characteristics of Virgin/Recycled Polypropylene-Wood Composites with Different Wood Species and Content
Indah WIDIASTUTI, Bagas Ade Emas Saka Putra..... 16

Rainwater Absorption Characteristics and Material Characterisation of Single-Ply Carbon/Epoxy Composite
N.G. Machava, K.J. WONG, A.B. CHAI, K.Y. Tshai, K.W. Gan 24

Structure-Property Relationship of Modified versus Natural Clinoptilolite Powders in Congo Red Removal
Nur Najeehah MOHD NASIR, Fatin Nur Afifi MOHD FADIL, Ashraf AZMI, Muhammad Azan TAMAR JAYA, R.A. ILYAS, Yahaya MUHAMMAD SANI, Iylia IDRIS 32

Simulation-Based Consequence Assessment of Ethylene Leakage from High-Pressure Primary Compressor Feed Line in Low-Density Polyethylene Production
Anis Farina MANSOR, Arina SAUKI, Iylia IDRIS, Dinie MUHAMMAD, Rushdan Ahmad ILYAS, Fakhrony Sholahudin ROHMAN, Abdul Aziz HAIRUDDIN, Ashraf AZMI..... 40

Experimental Investigation of the Acoustical and Mechanical Properties of an Ultrasonic Attenuation Functionally Graded Composite
Majid MOHAMMADI..... 48

Eco-Friendly NiO Nanomaterials Synthesized Using Waste-Derived Cellulose: Tailored Structural, Textural, and Optical Properties
Alvin Lim Teik ZHENG, Azrul Nurfaiz Mohd FAIZAL, Syeed Saifulazry Osman EL-EDRUS, Keeren Sundara RAJOO, Kar Ban TAN, Yoshito ANDOU..... 55

Tailored Electromagnetic Wave Absorption Performance of $Ni_{0.7}Zn_{0.3}Fe_2O_4$/Zeolite/CNT Composites: Influence of Single and Multilayer Structures
Fadzidah MOHD IDRIS, Faisal bin Abdul RAHMAN, Muhammad Aqil Haziq bin Mohd ZAMRI, Ahmad Haziq bin Mohamed SABRI, Hatika KACO, Mohd Shamsul Ezzad SHAFIE..... 63

AI Driven in Composite Material Science
Anis Farina MANSOR, Iylia IDRIS, Dinie MUHAMMAD, Rushdan Ahmad ILYAS, Fakhrony Sholahudin ROHMAN, Ashraf AZMI..... 76

Recent Advances in Green Synthesis of Nanoparticles for Sustainable Applications: A Brief Review
Sarah OMAR, Taib Iskandar MOHAMAD, Kamaruzaman SOPIAN, Merna OMAR 84

Machine Learning in Geopolymer Concrete: A Bibliometric Analysis of Global Trends, Key Contributors, and Emerging Research Directions
Abdullahi MUSA, Mohd Azreen MOHD ARIFFIN, Mohd Nur Asmawisham ALEL, Wan Ikram Wajdee WAN AHMAD KAMAL, Han-Seung LEE, Jitendra Kumar SINGH, Mohammed TIJJANI, Abdullahi Garba MUSA 93

Turmeric (*Curcuma longa*) as a Dual-Function Source of Cellulose Nanofibers and Essential Oil for Mechanical Modulation of PVA Bionanocomposite Films
Akmal AKMAL, Hairul ABRAL, Lovely SON, Syafii SYAFII, Kadriadi KADRIADI 101

Evaluating the Role of Biomass Allocation in Mango (*Mangifera indica L.*) as Predictors of Natural Fiber Yield for Sustainable Composites
Fadhilnor ABDULLAH, Nurul Afidah UMORUDDIN, Mohd Khairul Rabani HASHIM, Zainal Abidin ARSAT, M.N.A. UDA, Muhammad Firdaus ABDUL MUTTALIB 109

Influence of Drying Heat Treatment on Physical and Mechanical Properties of Mycelium Based Composite
Zatty MINAI, M.K.R HASHIM, Noorulnajwa Diyana YAACOB, M.N.A.UDA, Z.A. ARSAT, M. Firdaus A. MUTTALIB, F. ABDULLAH, S.M. SHAHRIL, Nur Khuzaima AZMAN, M.A.M. AKHIR 117

Effects of Stacking Sequence on Mode II Delamination in Hybrid Carbon/Flax Reinforced Epoxy Composites
W.K. SEE, M. JOHAR, K.J. WONG, W.W.F. CHONG, A.B. CHAI 125

Statistical Evaluation of Alkali-treated Bamboo Fibre Reinforced Polyester Composites using Weibull Analysis
K.J. WONG, K.O. LOW, A.B. CHAI 133

Thermal Conductivity of Ceramic Tiles Incorporating Iraqi Porcelanite Waste as a Partial Substitute for Ball Clay
Ishraq Abdalkareem Kalaf ALOGAIDI, Ahmed Hafedh Mohammed MOHAMMED, Khairul Anuar SHARIFF, Hasmaliza MOHAMAD, Muhamed Abdul Fatah Muhamed MUKHTAR 141

Enhancing Recycled Polypropylene Composites with Rice Husk Biochar via Electron Beam Irradiation
Syahirah YUSSOFF, Noor Fauziyah ISHAK, Muhammad Hazim MUHAMMAD SAYUTI .. 148

Preparation and In Vitro Antibacterial Evaluation of Shrimp Shell-Derived Chitosan–Silica Formulations Against *Escherichia coli*
M.N.A. Uda, Chong Siew Hong, Meor Ahmad Faris, M.K.R. Hashim, Tijjani Adam, Z.A. Arsat, Uda Hashim, M.N. Afnan Uda, F. Abdullah, Maisara A.M. Akhir, M. Firdaus A. Muttalib, N.A. Parmin, A.A.A. Halim, N.H. Ibrahim 156

Composite Material in Road Pavement: A Review of Experimental, Numerical and Machine Learning Approaches
Mazlan RAFIDAH, Mohd Khairul Afzan Mohd LAZI, Fauzan Mohd JAKARNI, Yusra Aulia SARI, Mohamad Saifullah SAMSUDIN, Rosmawati MAMAT, Ekarizan SHAFFIE, Dylan Tay WANG AN, Nurul Najihah MAD ROSNI, Ikhwanul IHSAN 165

Examination of the Microstructure and Corrosion Resistance of 6063 Aluminium Alloy Reinforced with Palm Fruit Mesocarp Particles (PP) for Automobile Radiator Applications
Itopa G. AKANDE, Oluwaseun M. DARAMOLA, Ebenezer O. AKANDE, Ezedeen A. OWOO, Abiodun D. OLORUNFEMI, Kunle M. OLUWASEGUN, Daniel O. NASAMU 173

Fresh, Mechanical, and Drying Shrinkage Properties of Sustainable Self-Consolidating Lightweight Foamed Concrete Incorporating Recycled Concrete Aggregate and Waste Glass Fibre Powder
Mohd Afiq Mohd FAUZI, Muhd Norhasri Muhd SIDEK, Nor Adlina AZWAN, Nurliza JASMI, Siti Zaidah OTHMAN, Kishen Jubli RINJA, Khafidho ZAENAL 180

Compressive and Flexural Strength of Mortar with Ceramic Tile Waste Powder as Partial Cement Replacement
Samia BOUZOUAID 188

Effect of Sulfuric Acid Attack on the Properties of Fiber Reinforced Geopolymer Concrete
Muhammad Affiq ABDUL JAMIL, Meor Ahmad Faris MEOR AHMAD TAJUDIN, Warid Wazien AHMAD ZAILANI, Mohammad Firdaus ABU HASHIM, Muhammad Fahem MOHD TAHIR, Mohd Ikram RAMLI, Mohammed Izzuddeen MOHD YAZID, M.N.A. UDA 197

Effect of Sintering on the Structural, Dielectric, and Acetone Gas-Sensing Properties of Yttria-Stabilized Zirconia
Lara A. SHALAL, Wafaa K. KHALEF, Shihab A. ZAIDAN 205

Crashworthiness Assessment of AL6061-T4 / Composite Hybrid Tubes Subjected to Axial Loading
Ali FAROKHI NEJAD, Amir Abbas REZVANFAR, Mohamad Yusuf BIN SALIM, Saleh A ALI ELHOATI, Didik NURHADIYANTO, M.Y. YAHYA 213

Concrete Incorporating Palm Oil Fuel Ash and Polyethylene Terephthalate for Gamma-Ray Shielding
Nurain Najwa RAMLI, Siti Amira OTHMAN 222

Polymer Graphene Nanocomposites: A Historical Preliminary Review
Zaid G. MOHAMMADSALIH 231

Cadmium Oxide Nanostructures Prepared by Oblique Angle Physical Vapour Deposition
Wafaa K. KHALEF, Nibras S. HAMEED, Raghad H. HILAL, Rafah A. NASSIF, Dhufigar S. MUTASHAR, Zinah S. SHAKIR, Sura R. MOHAMMED 241

Keyword Index

About the Editors

Preface

Composite materials are increasingly important in the aerospace, marine, transportation, civil engineering, and industrial sectors because of their high strength-to-weight ratio, corrosion resistance, energy-absorption capacity, durability, and relatively low maintenance requirements compared with conventional metallic structures. The 2nd Composite Sciences and Technology International Conference (COMSAT 2025), themed "Sustainable and Digitalized Advanced Composite Solutions to Global Challenges," provided an international platform for exchanging knowledge and presenting recent advances in composite science and technology.

This triennial conference brought together academics, researchers, policymakers, and industry professionals from around the world to discuss advances in the manufacturing, testing, characterization, and application of composite materials. The conference covered a broad range of topics, including natural-fiber composites, polymer-matrix and metal-matrix composites, hybrid materials, recycling technologies, artificial intelligence, digital twins, and digitalized approaches to sustainability.

We gratefully acknowledge the support of our sponsors, committee members, co-organizing institutions, and volunteers, whose dedication made this event possible. We also thank all participants, students, researchers, speakers, and industry professionals for sharing their research, expertise, and perspectives. Their contributions made COMSAT 2025 a meaningful platform for advancing composite technologies toward a more sustainable and digitalized future.

Committees

Steering and Scientific Advisory Committee

1. Prof. Dr. Sanjay Mavinkere Rangappa
King Mongkut's University of Technology North Bangkok (KMUTNB), Thailand

2. Prof. Dr. Olga Klinkova
ISAE-Institut Supérieur de Mécanique de Paris (ISAE-SUPMECA), France

3. Dr. Melbi Mahardika
National Research and Innovation Agency (BRIN), Indonesia

4. Dr. Senthil Muthu Kumar Thiagamani
Kalasalingam Academy of Research and Education, India

5. Prof. Dr. Tomasz Kozior
Kielce University of Technology, Poland

6. Dr. Mubarak Ali M
TKM College of Engineering, APJAK Technological University, Kerala, India

7. Dr. Quanjin Ma
Southern University of Science and Technology, China

8. Dr. Mohd Shahneel Saharudin
Robert Gordon University, United Kingdom

9. Dr. Mohammad Fikry Mohammad Jelani
Hiroshima University, Japan

10. Prof. Dr. Cyrille Boyer
University of New South Wales, Australia

11. Dr. Kuzmin Anton
National Research Mordovia State University, Russia

12. Dr. Khubab Shaker
National Textile University, Pakistan

13. Prof. Dr. Tay Tong Earn
National University of Singapore, Singapore

14. Prof. Emeritus Dr. Salim Hiziroglu
Oklahoma State University, USA

15. Prof. Dr. Fares Mohammed Laid Rekbi
Research Center in Industrial Technologies (CRTI), Algeria

16. Prof. Dr. -Ing. Ir Hairul Abral
Andalas University, Indonesia
Institut Teknologi Batam (ITEBA)

17. Assoc. Prof. Dr. Michal Petrů
Technical University of Liberec, Czech Republic

18. Ir. Dr. Ashraf Azmi
Universiti Teknologi MARA, Malaysia

Organizing Committee

Patron	Prof. Dr. Mohd Shafry bin Mohd Rahim
Advisor 1	Prof. Dr. Rosli bin Md Illias
Advisor 2	Prof. Ts. Dr. Mohd Hafiz Dzarfan bin Othman
Advisor 3	Prof. Dr. Mohd Yazid bin Yahya
Advisor 4	Prof. Dr. Mat Uzir bin Wahit
Chairman	Ts. Dr. Ahmad Ilyas bin Rushdan
Co-Chairman	Ts. Dr. Muhammad Asyraf bin Muhammad Rizal
Secretary	Dr. Mohd Haziq bin Dzulkifli
Co-Secretary 1	Dr. Muhamad Fauzi bin Abd Rased
Co-Secretary 2	Ms. Hafizah binti Ithnin
Treasurer	Assoc. Prof. Dr. Tuty Asma binti Abu Bakar
Co-Treasurer 1	Ms. Hafizah binti Ithnin
Co-Treasurer 2	Mr. Mohammad Nabil bin Jainal
Co-Treasurer 3	Ms. Nurul Aina binti Anahar
Co-Treasurer 4	Ms. Nur Diyana Nadhah binti Norhasrul Hadi
UNITS	
Registration	Assoc. Prof. Dr. Rohah binti A. Majid (H)
	Mr. Wong Chang Koon
	Ms. Siti Khairunisah binti Ghazali
	Ms. Azriena Haninah binti Abd Aziz
Publicity, Media, Promotion	Dr. Dinie bin Muhammad (H)
	Ms. Siti Nor Hawanis binti Husain
	Ms. Najwa Wajihah binti Mohd Rusli
	Ms. Fatin Amirah binti Razmi
	Eur Ing Dr. Mohd Shahneel Saharudin
	Dr. Melbi Mahardika, S.T.
	Dr. Mohammad Fikry bin Mohammad Jelani
	Ir. Dr. Ashraf Azmi
	Ir. Dr. Iylia bin Idris
	Mr. Ahmad Arsyad bin Muhammad Gani
Technical & Logistic	Dr. Mohd Ayub bin Sulong (H)
	Ms. Nurul Aina binti Anahar
	Ms. Devita Amelia
	Mr. Amer Iskandar bin Ra'eis
Publication & Proceedings	Dr. Norhayani Bt Othman (H)
	Dr. Khoo Pui San
	Dr. Ng Lin Feng
	Dr. Munirah binti Onn
	Dr. Mohd. Nurazzi bin Norizan
	Dr. Mohd Nor Faiz Norrrahim
	Dr. Zaid Mohammadsalih
Protocol, Program & Speaker	Dr. Nur Hafizah binti Abd Khalid (H)
	Ir. Dr. Izni Mariah binti Ibrahim
	Dr. Muhamed Yusuf bin Shahul Hameed
	Ms. Rafidah binti Mazlan
	Ms. Elvaara Windra Madyarati
	Ts. ChM. Dr. Azrul Nurfaiz bin Mohd Faizal
Sponsorship, Awards & Certificates	Dr. Norfarhana binti Abdul Samad (H)
	Ms. Azzumawardhani Almi
	Mr. Leong Kok Seng
	Ms. Zuraidah binti Muhammad

Note: (H) indicates the Head of the respective unit.

Materials Research Proceedings 74 (2026) 1-8 https://doi.org/10.21741/9781644904473-1

Effects of Crushing Cycle on The Mechanical Properties and Morphology of Napier Grass Stem Fibre

Siti Syafiqah MAT NOR[1,a], Siti Khairunisah GHAZALI[1,b] and Rohah A. MAJID[1,c *]

[1]Department of Bioprocess and Polymer Engineering, Faculty of Chemical and Energy Engineering, Universiti Teknologi Malaysia, 81310 Johor Bahru, Johor, Malaysia

[a]syafiqah.matnor@gmail.com, [b]skhairunisah2@graduate.utm.my, [c]r-rohah@utm.my

Keywords: Napier Grass, Alkali Treatment, Cellulose, Mechanical-Chemical Treatment

Abstract. *Pennisetum purpureum*, commonly known as Napier grass, a cellulose-rich perennial, is a promising source for the composite and pulp/paper industries. While alkaline sodium hydroxide (NaOH) treatment effectively extracts cellulose, excessive NaOH can damage fibres. This study combined mechanical stem crushing (1-5 cycles) with a fixed 3% (w/v) NaOH treatment. Optimal 3-cycle crushing yielded the highest tear index (99.0 mN/g.m^{-2}) and tensile strength (0.0247 MPa), as splitting the fibre facilitated non-cellulosic removal and enhanced the interface adhesion between the fibres. However, 5-cycle crushing excessively split the fibre, leading NaOH to damage the cellulose, consequently reducing its tear index and tensile strength.

Introduction

The environmental impact of deforestation caused by the extraction of wood for wood-based industries is considerable. Alternative fibres derived from non-wood sources provide an effective solution to the ecological damage associated with tree harvesting. Soft plant fibres such as ramie, kenaf, and Napier grass are rich in cellulose, making them suitable for composite reinforcement and pulp and paper production [1]. Napier grass (*Pennisetum purpureum*), an abundant agro-waste material with rapid growth, offers particular advantages as a sustainable non-wood source for papermaking. Mercerisation, also known as alkali treatment, is a widely adopted technique for producing high-quality fibres [2]. This treatment removes non-structural components such as fats, ash, and waxes, while roughening the fibre surface and exposing more cellulose, thereby enhancing adhesion between hydrophilic fibres and hydrophobic matrices [3]. Alkali treatment also modifies the chemical composition of fibres, influencing their mechanical properties, surface roughness, crystallinity, and thermal behaviour [4].

Previous studies have demonstrated that alkalization can improve the mechanical performance of natural fibres under varying soaking times and concentrations. Reddy et al. reported that treatment of Napier grass fibres with up to 5 % NaOH reduced their thermal stability and tensile properties [5]. Similarly, Murali Mohan Rao et al. examined the tensile properties of Indian-grown Napier grass fibres extracted through chemical and water retting methods [6]. However, higher alkali concentrations and prolonged soaking times were shown to weaken fibres due to structural damage [7]. In contrast, Haameem et al. observed that treatment with 10 % NaOH produced optimal strength compared to untreated fibres [8]. More recent work has expanded to Napier grass fibre/polyester composites, with results suggesting strong potential for composite applications [9–11].

In papermaking applications, studies on Napier grass leaves and stems revealed that fibres treated with 4 % NaOH exhibited reduced moisture uptake, improved shear strength, enhanced tensile stress, and uniform fibre distribution, making them effective replacements for wood-based fibres [12]. Nevertheless, excessive NaOH concentrations can damage cellulose surfaces and compromise fibre strength [13]. To address this issue, combined mechanical or physical methods

Content from this work may be used under the terms of the Creative Commons Attribution 3.0 license. Any further distribution of this work must maintain attribution to the author(s) and the title of the work, journal citation and DOI. Published under license by Materials Research Forum LLC.

with chemical treatments have been employed to yield fibres with high cellulose content, typically at NaOH concentrations up to 15 % (w/v) [14].

In this study, Napier grass stems were subjected to mechanical crushing at varying cycles prior to alkali treatment. The NaOH concentration was intentionally kept low to minimise fibre degradation during hydrolysis and paper production. Scanning electron microscopy revealed that crushed and chemically treated Napier fibres exhibited a compact and condensed structure. Complementary chemical composition analysis confirmed the high cellulose content and relatively low lignin levels of Napier grass, which contribute to fibre quality suitable for pulp and paper applications [15]. However, removal of non-cellulosic components such as lignin and hemicellulose is necessary to ensure good interfacial adhesion with the matrix [16]. This can be achieved by pulping fibres with alkaline solutions, often accelerated by heat. In this work, the treated fibres were moulded into sheets, and the effects of mechanical crushing cycles on their mechanical and morphological properties were systematically investigated.

Materials and Methods

Napier grass stems were collected from the Universiti Teknologi Malaysia campus grounds. Sodium hydroxide (NaOH) pellet was procured from Merck Sdn. Bhd., Malaysia. Napier fibres were extracted using a mechanical-co-chemical approach to assess the effects of the NaOH concentrations and crushing cycles.

First, the Napier stems were subjected to a standardised single crushing cycle using a mechanical crusher, followed by alkaline pulping using NaOH solution of various concentrations (1-10 % w/v). The pulping process was carried out for 90 minutes at 80 °C under constant agitation to ensure uniform treatment. The resulting pulp was thoroughly washed with water and subsequently blended to obtain a uniform slurry. The fibre slurry was then moulded into a paper sheet and dried. The paper sheet was heat-pressed to enhance surface smoothness prior to further characterisation.

To elucidate the effect of mechanical refining on fiber morphology and paper performance, Napier stems were mechanically refined for 1–5 cycles before chemical pulping. In this study, the concentration of NaOH was 3% (w/v). The treatment gave the highest tear index and tensile strength based on the preliminary mechanical testing. The alkali treatment at 3% NaOH significantly improved the mechanical properties compared to the untreated fibers, indicating improved fiber fibrillation and inter-fiber bonding. In contrast, a further increase of NaOH concentration to 5% leads to a significant decrease in tear and tensile performance, indicating excessive removal of structural components and partial degradation of the cellulose network. Thus 3% NaOH was selected as the optimum alkali concentration for further crushing-cycle experiments.

Tear test

Tear index is used to measure the internal tearing resistance of paper. The testing was carried out according to ASTM D686 by using an HT-8181 Elmendorf Tearing Strength Tester. The testing sample replicate for 10 pieces per samples. A test piece of superimposed sheets with a specified pre-cut slit was torn through a fixed distance using a pendulum with a capacity of 3.2 kg, which applies the tearing force by moving in a plane perpendicular to the initial plane of the test piece. The tear index was calculated using Eq. 1-3.

$$\text{Average tearing force, mN} = \frac{16 \times 9.81 \times \text{Average scale reading}}{\text{Number of plies}} \quad \text{Eq. 1}$$

$$\text{Average grammage, gm}^{-2} = \frac{\text{Weight}}{\text{Area}}\text{, where area is } 3.1856 \times 10^{-3} \quad \text{Eq. 2}$$

$$\text{Tear index} = \frac{\text{Average training force (mN)}}{\text{Average grammage (g.m}^{-2})} \quad \text{Eq. 3}$$

Tensile test

Tensile strength of Napier fibre was measured in accordance with TAPPI T494 Standard Method. Rectangular test specimens (25 mm × 150 mm) were clamped and stretched to rupture under a constant rate of elongation. Tensile strength values were obtained from the average of ten replicates. All tests were performed at room temperature using a crosshead speed of 25 mm/min and a maximum load capacity of 20 kN. The testing sample replicate for 10 pieces per samples.

Scanning Electron Microscopy

Morphological investigations were carried out on both untreated and treated Napier fibres using a Scanning Electron Microscope (SEM) JEOL JSM-IT300LV model to examine the fibre surface. Prior to imaging, the samples were sputter-coated with a thin layer of gold to enhance electrical conductivity and improve image resolution.

Result and Discussion

Mechanical properties

Tear strength, also referred to as tear resistance, describes the ability of paper to resist propagation of an initiated tear [17], whereas tensile strength represents the maximum stress that paper can withstand under uniaxial stretching before rupture or permanent deformation [18]. Fig. 1 compares the tear index and tensile strength of Napier paper sheets subjected to a single crushing cycle and treated with varying NaOH concentrations. The highest tear index (88.3 mN/g·m^{-2}) and tensile strength (0.0249 MPa) were obtained at 3% NaOH treatment. This can be attributed to the enhanced fibre fibrillation and improved fibre–fibre bonding [19]. However, at higher NaOH concentrations, a decline in both properties was observed. This reduction is attributed to excessive alkaline attack on cellulose fibres, which disrupts the crystalline structure and compromises the fibre core, ultimately weakening the overall mechanical performance [20]. Given the superior performance achieved at 3 % NaOH treatment, this concentration was selected for subsequent experiments investigating the influence of mechanical crushing cycles.

Fig. 2 reveals the effects of mechanical crushing on the fibre properties. The tear index reaches its maximum value of 99.0 mN·m^2/g at 3 cycles, representing 18 % improvement over single-cycle treatment, while tensile strength peaks at 0.0247 MPa, showing a 31 % enhancement. The initial improvement in mechanical properties correlates with enhanced fibre defibrillation and surface area exposure[21]. Nevertheless, both properties declined significantly at 5 cycles, with the tear index dropping to 83.2 mN·m^2/g and the tensile strength to 0.018 MPa, which represents 16 % and 27 % reduction from the peak values, respectively. It can be postulated that the excessive crushing cycles can cause structural damage, reducing both fibre length and strength [13,22].

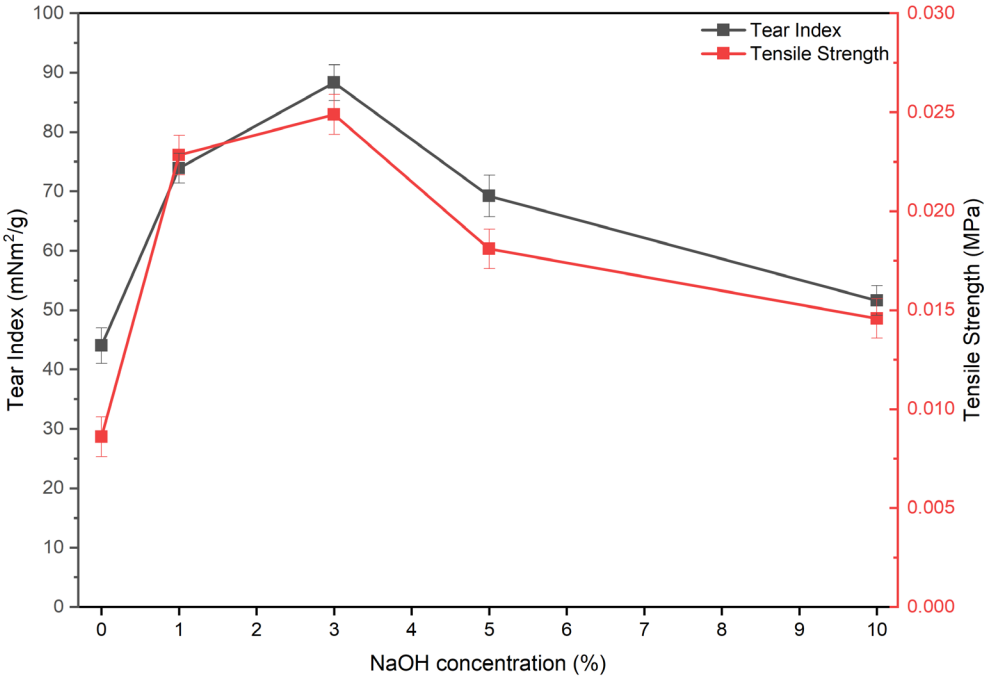


Fig. 1. Tear index and tensile strength of the Napier stem fibres subjected to different concentrations of NaOH.

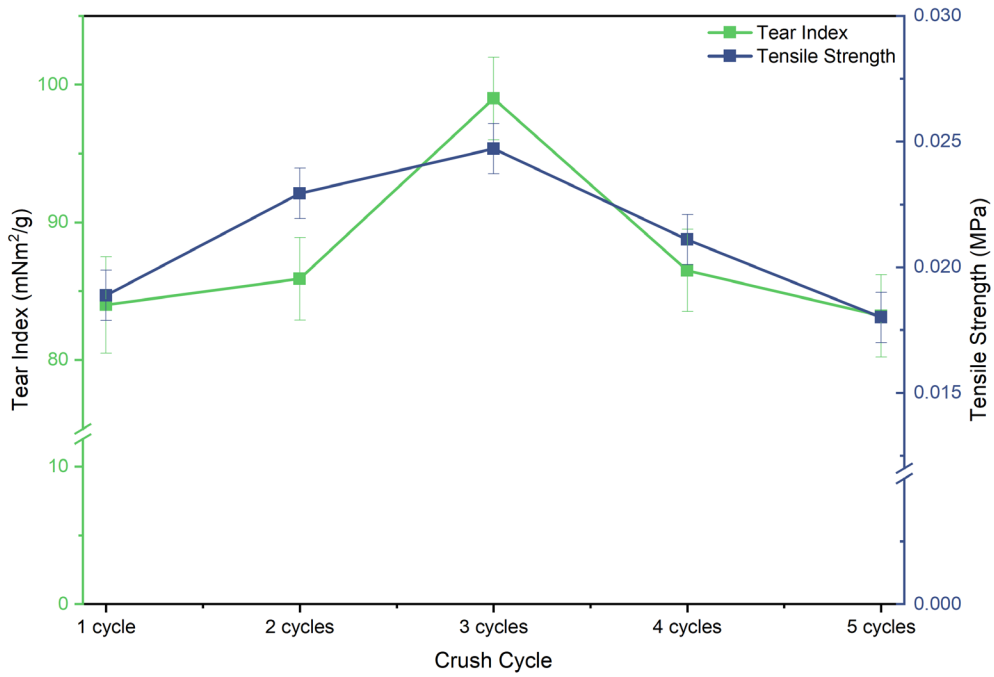


Fig. 2. Tear index and tensile strength of the Napier stem fibres at various crushing cycles.

Scanning Electron Microscopy

Fig. 3 reveals distinct morphological changes in the Napier fibres under different extraction conditions. The untreated fibre (Fig. 3a) exhibited intact and compact structures with minimal surface disruption. Further increased the NaOH concentration to 3 % (Fig. 3b) resulted in more pronounced fibrillar structures and cleaner fibre surfaces with minimal residue of non-cellulosic components. The SEM image shows a well-fibrillated surface without any significant structural damage. This observation suggests that the treatment intensity was sufficient to improve the fibre flexibility and bonding, while preserving the integrity of the cellulose framework. Recent studies have demonstrated that moderate alkali concentrations provide the best compromise between impurity removal and cellulose preservation, thus achieving maximum mechanical performance[23][24]. In contrast, at 5% NaOH concentration (Fig. 3c), notable fibre degradation with visible damage to the fibre integrity (wall thinning and worn surface) was observed. These morphological changes are consistent with the observed deterioration in the mechanical properties, i.e., tear index and tensile strength of the Napier fibres. SEM observations (Fig. 3c) revealed localized surface erosion and structural deterioration, which indicate over-delignification and partial degradation of cellulose microfibrils. Excessive alkali exposure can destroy the hierarchical fibre structure, shorten the fibre length, and introduce surface defects that can weaken fibre bonding. Similar results were reported in recent investigations where excessive NaOH concentrations caused damage to fibrils, swelling of cellulose and degradation of mechanical performance despite improved surface cleanliness[25].

Similarly, when subjected to different crushing cycles, i.e., 1, 3 and 5 cycles, induced mechanical damage to the Napier fibres as portrayed in Fig. 3d-f. With increasing cycles, the fibres became flatter and thinner, thereby increasing their contact surface area with the NaOH solution and facilitating the delignification process. However, excessive exposure to the alkaline environment, combined with repeated mechanical stress, led to fibre degradation. In particular, five crushing cycles caused substantial structural damage, resulting in shorter fibre fragments and a marked loss in mechanical performance [26]. SEM observations verify the tear index and tensile results by showing increased fibrillation and improved fibre dispersion after repeated crushing. At three cycles (Fig. 3e) the fibres showed extensive fibrillar development and tight fibre entanglement, indicating the formation of a dense and highly interconnected fibre network[23,27]. The fibrillation improvement contributes to the hydrogen-bond formation and stress distribution throughout the paper matrix, giving rise to the superior mechanical performance. Such behaviour has been widely reported in cellulose-based materials where moderate refining enhances fibre flexibility and bonding efficiency.

The optimum processing condition of the developed hybrid paper system was the synergistic use of 3% NaOH treatment and three crushing cycles. The mild alkali treatment was effective in removal of lignin, hemicellulose and other non-cellulosic components, and thus in promoting the fibre fibrillation and inter-fibre bonding, while maintaining the integrity of the cellulose structure[24]. At the same time, three crushing cycles were sufficient to provide adequate fibrillation and fibre flexibility to optimize fibre entanglement and bonding area without excessive fibre shortening or fragmentation. SEM observations revealed a highly fibrillated and interconnected fibre network, which strongly supported the higher tear index and tensile strength achieved under these conditions[23]. The results underlined the importance of balancing chemical modification and mechanical refining for optimizing the microstructure and mechanical performance of sustainable lignocellulosic paper materials.

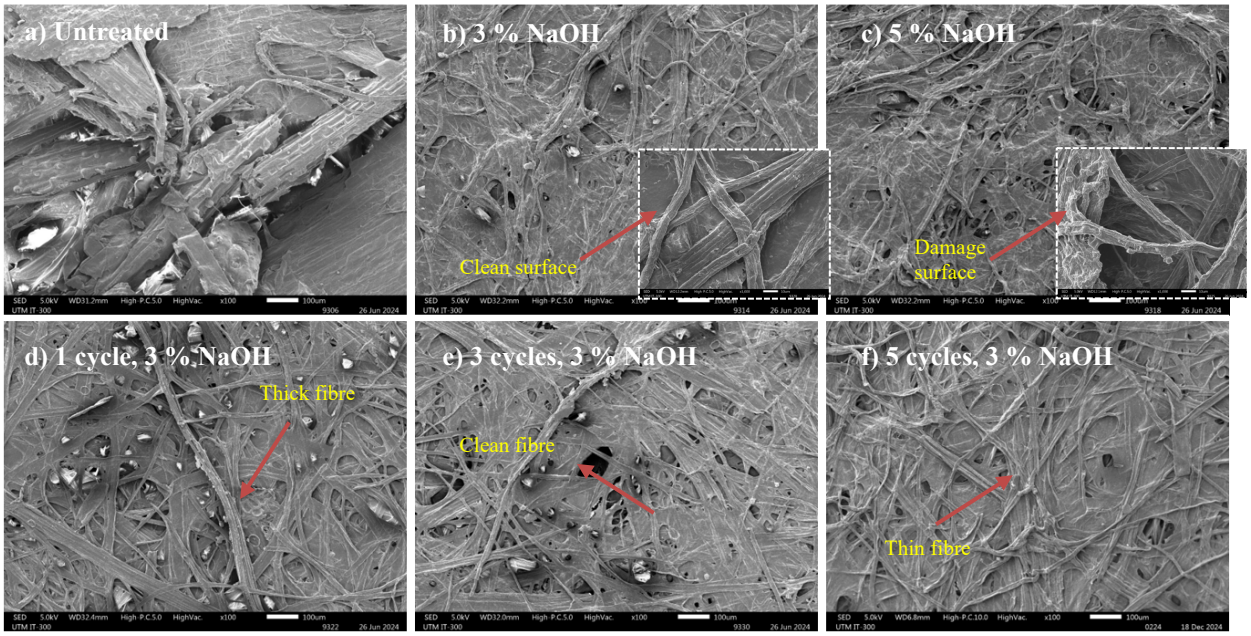


Fig. 3. SEM images of the Napier fibres at various concentrations of NaOH (a-c) and different crushing cycles (d-f).

Conclusions

Napier stem fibres were successfully extracted by implementing the mechanical-chemical method at a low concentration of NaOH solution. Alkaline treatment facilitated removal of non-cellulosic components, yielding cleaner fibre surfaces and improved fibrillation, as reflected in the increment of tear index (100.7 %) and tensile strength (189.5 %) compared to untreated fibre. In contrast, higher alkali concentrations led to fibre wall thinning, structural degradation, and deterioration of mechanical strength, consistent with SEM observations of over-extracted and damaged fibre surfaces. Similarly, the crushing process enhanced fibre accessibility to the alkaline solution, thereby promoting delignification. However, increasing the crushing cycles (up to 5 cycles) damaged the cellulose, consequently reducing its tear and tensile strengths. These findings highlight that mechanical pretreatment (3 crushing cycles) in synergy with mild chemical pulping (3 % w/v) offers a more effective strategy for Napier stem fibre extraction than solely increasing the chemical concentration. This mechanical-chemical method allows the production of fibres with superior mechanical properties and morphology, suitable for pulp and paper-based applications.

Acknowledgment

This work was funded by the Ministry of Higher Education Malaysia under the Fundamental Research Grant Scheme (FRGS/1/2019/STG07/UTM/02/5).

References

[1] L.A. Worku, A. Bachheti, R.K. Bachheti, C.E. Rodrigues Reis, A.K. Chandel, Agricultural Residues as Raw Materials for Pulp and Paper Production: Overview and Applications on Membrane Fabrication, Membranes (Basel) 13 (2023) 228. https://doi.org/10.3390/membranes13020228

[2] K. Obi Reddy, C. Uma Maheswari, M. Shukla, E. Muzenda, Preparation, Chemical Composition, Characterization, and Properties of Napier Grass Paper Sheets, Separation Science and Technology (Philadelphia) 49 (2014) 1527–1534. https://doi.org/10.1080/01496395.2014.893358

[3] P.S. Rai, S. Unnikrishnan, A. Chandrashekar, Influence of alkali treatment on physiochemical and morphological properties of palmyra fibers, Ind. Crops Prod. 224 (2025) 120298. https://doi.org/10.1016/j.indcrop.2024.120298

[4] A.A.N. Anuwar, A.H.A. Rashid, S.S. Jikan, M.N. Roslan, A.A.H.M. Tahir, N.H. Zolkifflee, F.A.M. Razal, The Effect of Alkaline Treatment On the *Schizostachyum grande* Fibre for Textile Applications, International Journal of Integrated Engineering 14 (2022) 37–49. https://doi.org/10.30880/ijie.2022.14.08.006

[5] K.O. Reddy, C.U. Maheswari, D.J.P. Reddy, A.V. Rajulu, Thermal properties of Napier grass fibers, Mater. Lett. 63 (2009) 2390–2392. https://doi.org/10.1016/j.matlet.2009.08.035

[6] K.M.M. Rao, A.V.R. Prasad, M.N.V.R. Babu, K.M. Rao, A.V.S.S.K.S. Gupta, Tensile properties of elephant grass fiber reinforced polyester composites, J. Mater. Sci. 42 (2007) 3266–3272. https://doi.org/10.1007/s10853-006-0657-8

[7] M.J.M. Ridzuan, M.S.A. Majid, M. Afendi, K. Azduwin, S.N.A. Kanafiah, Y. Dan-mallam, The Effects of the Alkaline Treatment's Soaking Exposure on the Tensile Strength of Napier Fibre, in: Procedia Manuf., Elsevier B.V., 2015: pp. 353–358. https://doi.org/10.1016/j.promfg.2015.07.062

[8] J.A. M. Haameem, M.S. Abdul Majid, M. Haslan, M. Afendi, E.A. Helmi, F. Idris, Effects of Alkaline Treatments on the Tensile Strength of Napier Grass Fibres, Applied Mechanics and Materials 695 (2014) 340–343. https://doi.org/10.4028/www.scientific.net/amm.695.340

[9] M.J.A. Haameem, M.S. Abdul Majid, E.A.H.E. Ubaidillah, M. Afendi, R. Daud, N.A.M. Amin, Tensile strength of untreated napier grass fibre reinforced unsaturated polyester composites, in: Applied Mechanics and Materials, Trans Tech Publications Ltd, 2014: pp. 189–193. https://doi.org/10.4028/www.scientific.net/AMM.554.189

[10] N. Abu Bakar, M. Thariq, H. Sultan, M.E. Azni, H. Hazwan, A.H. Ariffin, Extraction and surface characterization of novel bast fibers extracted from the *Pennisetum purpureum* plant for composite application, Materials Today: Proceedings 5 (2018) 21926-21935. https://doi.org/10.1016/j.matpr.2018.07.052

[11] S. Karthi, K.S.K. Sasikumar, R.K. Sangeetha, N. Saravanan, Effect of relative content on mechanical properties of coir and napier grass fibers reinforced hybrid polyester composites, in: Materials Today: Proceedings 33 (2020) 2929–2933. https://doi.org/10.1016/j.matpr.2020.02.891

[12] H.P. Lim, W.A. Wan Abdul Rahman, J.H. Low, Properties Characterization of Napier Grass (*Pennisetum purpureum*) as the Non-wood Substitution for Natural Fiber Papermaking, Journal of Advanced Mechanical Engineering Applications 1 (2020) 27-35. https://doi.org/10.30880/jamea.2020.01.01.004

[13] R. Hajizadeh, A. Montazeri, M. Esnaasharieh, M.H. Beheshti, Z. Garavand, Determination of the effect of alkaline chemical modification using sodium hydroxide on the acoustic and thermal properties of bagasse fibers, Sci. Rep. 15 (2025) 17515. https://doi.org/10.1038/s41598-025-02385-1

[14] N. Kumar, A. Singh, S. Singh, J.I.P. Singh, S. Kumar, Napier natural fibre used as reinforcement polymer composite: As asbestos free brake friction material, Mater. Today Proc. 56 (2022) 2532–2536. https://doi.org/10.1016/j.matpr.2021.09.006

[15] Z. Daud, M.Z.M. Hatta, A.S.M. Kassim, A.M. Aripin, H. Awang, Analysis of Napier grass (*Pennisetum purpureum*) as a potential alternative fibre in paper industry, Materials Research Innovations 18 (2014) S6-18-S6-20. https://doi.org/10.1179/1432891714Z.000000000925

[16] P. Rattanawongkun, N. Kerddonfag, N. Tawichai, U. Intatha, N. Soykeabkaew, Improving agricultural waste pulps via self-blending concept with potential use in moulded pulp packaging, J. Environ. Chem. Eng. 8 (2020) 104320. https://doi.org/10.1016/j.jece.2020.104320

[17] T. Yamauchi, A. Tanaka, Tearing test for paper using a tensile tester, 2002.

[18] M.J.M. Ridzuan, M.S. Abdul Majid, M. Afendi, S.N. Aqmariah Kanafiah, J.M. Zahri, A.G. Gibson, Characterisation of natural cellulosic fibre from *Pennisetum purpureum* stem as potential reinforcement of polymer composites, Mater. Des. 89 (2016) 839–847. https://doi.org/10.1016/j.matdes.2015.10.052

[19] L. Ma, Y. Hou, R. Jiang, Y. Ren, Y. Wang, C. Liu, C. Shen, M. Jing, Defibrillation and functionalization of cellulose fibers from different sources in one-step via a mechanochemical method, Cellulose 31 (2024) 6173–6192. https://doi.org/10.1007/s10570-024-06000-w

[20] D.M. Krishnudu, P.V. Reddy, R.V.S. Reddy, R.M. Reddy, Synthesis, characterization and mechanical properties evaluation of *muntingia calabura* fibre reinforced epoxy composites: Fibre treatment comparison with NaOH and KOH, Green Technologies and Sustainability 3 (2025) 100155. https://doi.org/10.1016/j.grets.2024.100155

[21] E. Xu, D. Wang, L. Lin, Chemical structure and mechanical properties of wood cell walls treated with acid and alkali solution, Forests 11 (2020) 87. https://doi.org/10.3390/f11010087

[22] J. Chen, X. Ma, M. Liang, Z. Guo, Y. Cai, C. Zhu, Z. Wang, S. Wang, J. Xu, H. Ying, Physical–Chemical–Biological Pretreatment for Biomass Degradation and Industrial Applications: A Review, Waste 2 (2024) 451–473. https://doi.org/10.3390/waste2040024

[23] T. Eleutério, M.J. Trota, M.G. Meirelles, H.C. Vasconcelos, A Review of Natural Fibers: Classification, Composition, Extraction, Treatments, and Applications, Fibers 13 (2025) 119. https://doi.org/10.3390/fib13090119

[24] H. Berhanu Lemma, F. Steffen, A. Yimam Ali, B. Saake, Production of Long-Fiber Pulp from Enset Plant Residues by Soda Pulping, Molecules 20 (2024) 4874. https://doi.org/10.3390/molecules29204874

[25] Z. Zhang, Y. Kong, J. Gao, X. Han, Z. Lian, J. Liu, W.J. Wang, X. Yang, Engineering strong man-made cellulosic fibers: a review of the wet spinning process based on cellulose nanofibrils, Nanoscale 16 (2024) 6383–6401. https://doi.org/10.1039/d3nr06126d

[26] W.S. Samsudin, H. Abu Bakar, T. Hussein, O. Malaysia, Study on the Effect of Sodium Hydroxide Treatment on Surface Morphology and Tensile Properties of Oil Palm Empty Fruit Bunch, Recent Trends in Civil Engineering and Built Environment 4 (2023) 144–152. https://doi.org/10.30880/rtcebe.2023.04.03.016

[27] T.M. Loganathan, M.T.H. Sultan, Q. Ahsan, M. Jawaid, A.U.M. Shah, Comparative Study of Mechanical Properties of Chemically Treated and Untreated *Cyrtostachys Renda* Fibers, Journal of Natural Fibers 19 (2022) 5940–5955. https://doi.org/10.1080/15440478.2021.1902900

Materials Research Proceedings 74 (2026) 9-15 https://doi.org/10.21741/9781644904473-2

Insight on Mechanical Properties of Hybrid Graphene/Glass/ABS Nanocomposites

Anahar Nurul Aina[1,2], Muhammad Asyraf Muhammad Rizal[1,2,a *], Muhamad Fauzi Abd Rased[1,2], Rohah A. Majid[2,3], Desmond Daniel Chin Vui Sheng[1,2], Amer Iskandar Ra'eis[1,2] and Noryani Muhammad[4]

[1]Faculty of Mechanical Engineering, Universiti Teknologi Malaysia, 81310 Johor Bahru, Johor, Malaysia

[2]Centre for Advanced Composite Materials (CACM), Universiti Teknologi Malaysia, 81310 Johor Bahru, Johor, Malaysia

[3]Faculty of Chemical and Energy Engineering, Universiti Teknologi Malaysia, 81310 Johor Bahru, Johor, Malaysia

[4]Fakulti Teknologi dan Kejuruteraan Mekanikal, Universiti Teknikal Malaysia Melaka, Hang Tuah Jaya, 76100, Durian Tunggal, Melaka, Malaysia

[a]muhammadasyraf.mr@utm.my

Keywords: Mesh, Woven, Glass Fibre, Acrylonitrile Butadiene Styrene, Graphene

Abstract. Glass fibre-reinforced acrylonitrile butadiene styrene (ABS) composites modified with graphene nanoplatelets (GNPs) have gained attention as a potential alternative to conventional thermoset-based glass fibre composites, particularly for applications requiring impact resistance, repairability, and sustainability. This review discusses the mechanical performance of hybrid graphene/glass/ABS nanocomposites by focusing on the roles of ABS as the thermoplastic matrix, woven glass fibre and glass fibre mesh as reinforcement phases, and GNPs as nano-scale additives. Reported preparation routes commonly involve melt blending or extrusion of ABS with GNPs, followed by laminate fabrication using glass fibre reinforcement through hot compression moulding or related thermoplastic processing techniques. Previous studies have shown that graphene-based reinforcement can increase tensile strength by 16–28% and improve flexural modulus by up to 42%, depending on filler type, loading, dispersion quality, and fibre–matrix interaction. For ABS/GNP composites, GNP loadings of 0.1–2.0 wt.% have been investigated, with 0.2-0.5 wt.% reported as an effective loading for improving fatigue-related performance. Studies on mesh-reinforced composite systems have also reported strength improvement from 86 MPa to 110 MPa, while fibreglass mesh sizes of 1 mm², 3 mm², and 5 mm² have been considered for thermoplastic ABS-based composites. Overall, the reviewed literature indicates that the combined use of ABS, glass fibre reinforcement, glass fibre mesh, and GNPs can improve stiffness, strength, impact resistance, stress transfer, and damage tolerance in hybrid thermoplastic composite systems for aerospace-related applications.

Introduction

Among the various types of composites, glass fibre reinforced acrylonitrile butadiene styrene (ABS) composites embedded with glass fibre mesh have attracted significance owing to their superior mechanical characteristics and adaptability. To improve the mechanical performance of these composites, hybridization techniques incorporating advanced reinforcements, such as graphene, have been explored. Graphene, known for its remarkable strength, elevated stiffness, and superior thermal and electrical conductivity, significantly enhances the overall characteristics of glass fibre reinforced ABS composites integrated with glass fibre mesh. Adding graphene to the

Content from this work may be used under the terms of the Creative Commons Attribution 3.0 license. Any further distribution of this work must maintain attribution to the author(s) and the title of the work, journal citation and DOI. Published under license by Materials Research Forum LLC.

matrix improves load transfer within the composite. As a result, the tensile strength of the epoxy composites increased by 16% and 19% [1]. Graphene reinforcement also improved impact resistance [2], and fatigue life [1]. The synergistic effect of hybridization strengthens the composite and maintains its lightweight characteristics, making it highly suitable for aerospace and other high-performance applications [3]. Comparative studies between conventional glass fibre reinforced ABS composites and graphene-enhanced hybrid systems show a substantial increase in mechanical performance, making hybridized composites a promising material for robust and lightweight structures. Malik et al. [4] evaluated in their studies that graphene nanoplatelets significantly enhance the mechanical characteristics of glass fibre reinforced polymer (GFRP) composites hence the incorporation of graphene nanoplatelets elevates tensile strength by 27.62%, improving load distribution within the composite. It enhances flexural characteristics, exhibiting a 41.26% increase in flexural modulus, essential for automotive and structural components applications. These improvements position graphene-reinforced woven and wire mesh glass fibre ABS composites as ideal candidates for next-generation aerospace and structural applications requiring superior durability, impact resistance, and weight reduction. In Hassanifard et al. [5] studies have shown that adding graphene nanoplatelets (GNPs) with weight fractions (0.1–2.0 wt%), the research indicates that the ideal GNP weight fraction for improving ABS composites is 0.5 wt%, essential for attaining excellent performance attributes where the filaments with 0.5% GNPs exhibited the greatest fatigue life due to their superior static strength, Young's modulus, and ductility. Along with material hybridisation, the structural configuration of the composite significantly influences its mechanical performance.

Despite the demonstrated benefits of hybrid woven/mesh glass fibre reinforced thermoplastic in enhancing composite performance, research on their hybridization with advanced reinforcements such as graphene remains limited. While previous studies have extensively explored woven glass fibre composites, wire mesh reinforcements, and quasi-isotropic stacking sequence-based laminates, the combined effect of these elements within ABS composites remains an underexplored area [6,7]. However, these studies often focus on conventional fibre-reinforced polymers, with limited attention given to hybridized graphene reinforcement in ABS-based composites. To address this gap, this study integrates graphene hybridization and glass fibre mesh reinforcements within a glass fibre reinforced ABS composite system. This research seeks to improve mechanical performance by examining the synergistic impacts of various reinforcements, specifically regarding energy absorption, impact resistance, and structural integrity.

Hybrid FRP Composites in Aircraft-Related Applications

Hybrid composites have recently gained attention for their enhanced mechanical properties, such as increased strength, stiffness, and impact resistance. By combining different types of fibres, such as glass, basalt, or natural fibres, these materials benefit from the unique advantages of each component, resulting in better overall performance compared to single-fibre composites. Hybrid composites are produced by incorporating multiple reinforcing fibres within a single polymer matrix to enhance the qualities of the composite. The combination of various reinforcing materials might yield either a synergistic or negative impact. In this case, hybrid fibres may be organised into three primary configurations: (1) interlayer, (2) yarn-by-yarn, and (3) fibre-by-fibre, as illustrated in Fig. 1.

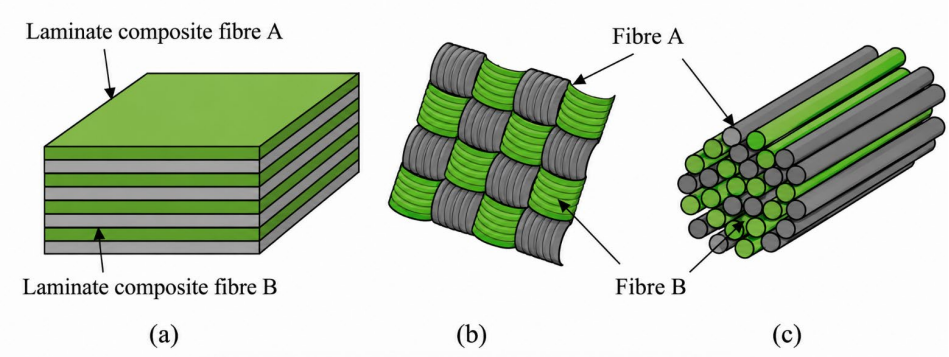


Fig. 1. Hybrid fibre configurations: (a) interlayer; (b) yarn-by-yarn; and (c) fibre by-fibre [8].

Hybrid materials and composites theories are a set of concepts and models for explaining the behaviour, properties, and uses of goods made up of two or more different constituents. Coupling constituents of dissimilar materials to gain synergistic benefits, like improved mechanical, thermal, or electrical properties [9], over individual constituents is one of the key features. Theories pertaining to hybrid materials and composites encompass material selection, interface engineering, microstructural design, and performance forecasting. They are increasingly utilised in engineering applications owing to their enhanced features and advantages compared to conventional composite materials [10]. The distinctive characteristics of the hybrid composite can be utilised in various structures, and structural components without compromising their structural performance and durability [11]. Glass fibres are seldom utilised independently in the fabrication of hybrid composites; rather, they are typically combined with a matrix, conventional fillers, and micro fillers to create hybrid composites. They can provide a synergistic impact by integrating several types of reinforcements inside a single matrix [12]. Hybrid composites offer enhanced flexibility in customising their functional qualities, achieving an improved equilibrium between the benefits and drawbacks of the reinforcements.

ABS as Thermoplastic Matrix

As the matrix, the ABS binds the reinforcement phases together, protects the fibres from environmental exposure, supports stress transfer between the fibres, and contributes to the impact resistance of the composite. Compared with thermosetting matrices, thermoplastics generally offer higher fracture toughness, shorter processing cycles, and better recyclability [13,14]. These advantages make the ABS suitable for composite fabrication methods such as film stacking, hot compression moulding, and fibre impregnation [15,16]. However, the quality of ABS-based composites still depends strongly on processing temperature, pressure, fibre wetting, and interfacial contact [17]. In thermoplastic polymer composite processing, sufficient temperature and pressure are needed to improve fibre–matrix contact and reduce defects such as poor consolidation, shrinkage, and fibre relaxation.

Glass Fibre: Woven and Mesh Form

Woven glass fibre is one of the most important materials utilised in the creation of composites, especially hybrid composites. Its composition facilitates superior tensile strength and flexibility, hence enabling its use across several domains. When combined with basalt fibre, it improves the mechanical properties of composites, especially elasticity and viscous flow [18]. The incorporation of woven glass fibre enhances thermal stability by limiting the mobility of polymer chains. While hybridisation enhances damping performance marginally compared to single glass fibre-reinforced composites, all hybrid composites exhibit superior damping behaviour relative to the unmodified polyester matrix. Woven glass fibre composites are materials composed of glass fibres interlaced in a fabric form [19]. They are employed primarily because of their mechanical properties and adaptability. The research indicated that woven flax composites exhibit markedly superior

interlaminar fracture toughness in comparison to glass fibre composites. Hybrid composites using glass and flax fibres were observed to improve interlaminar fracture characteristics.

The fundamental importance of mesh material, orientation, and surface treatment in enhancing the structural efficiency of wire mesh-reinforced composite systems was emphasised. This study utilized two varieties of wire mesh as structural reinforcements in hybrid natural fibre composites [21]. The aluminium wire mesh (AWM) was integrated at angles of 45º and 90º, demonstrating improved mechanical characteristics. The copper wire mesh (CWM) was integrated at angles of 45º and 90º, demonstrating improved performance. The wire meshes were cleansed with deionised water to ensure optimal bonding and performance. The wire mesh's orientation significantly influenced the composite's mechanical properties, with a 45º alignment improving stiffness, strength, and ductility. Chemical treatment was utilised to improve adhesion between the wire mesh and fibre interface. Fig. 2 illustrates the orientations of jute fibre and the configurations of aluminium/copper wire mesh.

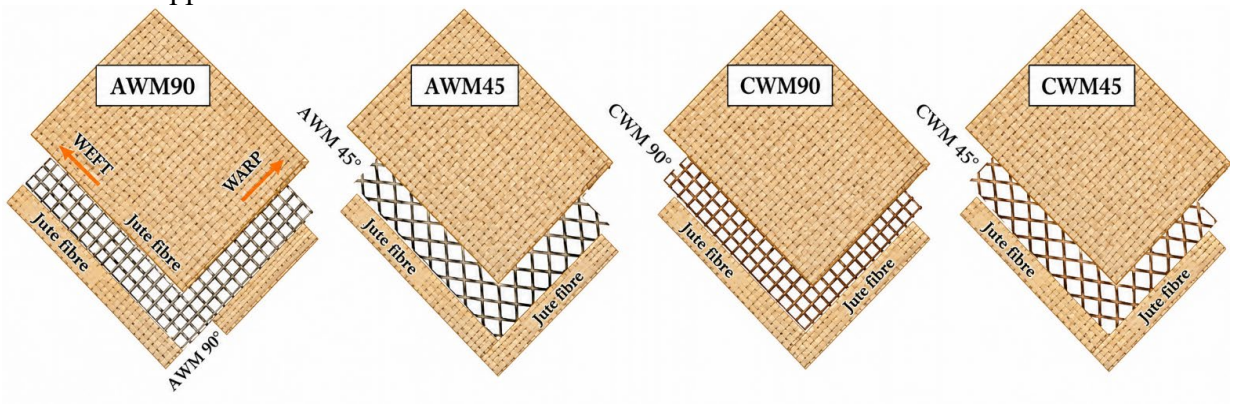


Fig. 2. Schematic diagram of AWM and CWM composites [21].

Liu et al. [22], their study investigates the application of steel wire mesh (SWM) as a reinforcing technique in 3D concrete printing and its material properties. The wire mesh employed is 304 stainless steels with a tensile strength of 800 MPa, available in dimensions of 400 mm × 100 mm and 100 mm × 100 mm, tensile strength improvement from 86 MPa to 110 MPa, mesh sizes of 1 mm², 3 mm², and 5 mm², and flexural strength of 76.1 MPa. The reinforcement is accomplished by incorporating numerous layers of mesh into the printed concrete, so assuring optimal contact and minimising the danger of delamination. The investigation demonstrated a notable enhancement in mechanical characteristics, maximum loads, and deflection capacity, surpassing random steel fibres regarding shear capacity and structural efficiency. Consequently, SWM serves as an ideal reinforcement technique for 3D-printed concrete buildings.

Hence, the use of glass fibre together with glass fibre mesh as a hybrid reinforcement in polymer composites has demonstrated significant potential to improve structural performance and damage resistance. Glass fibre mesh, characterised by its high tensile strength, low density, and economical nature, is extensively utilised in composite applications. The material's fragility and susceptibility to impact and delamination pose issues in extreme structural conditions. To mitigate these deficiencies, glass fibre meshes are expected to be used to provide improved toughness, crack-arresting capacity, and energy absorption [20].

GNPs as Additives in Hybrid Composites

GNPs can improve resin–fibre interfacial adhesion, promote more efficient load transfer, and increase resistance to crack initiation and growth. Iqbal et al. [23] reported that graphene can delay the formation of critical cracks and extend the fatigue life of composites, particularly in structural applications. This suggests that GNPs do not only improve static mechanical performance but may also support damage tolerance under repeated or severe loading conditions. Their contribution to

crack deflection, crack bridging, and heat dissipation is especially relevant for aircraft structures, which are commonly exposed to cyclic stress, impact loading, vibration, and temperature variation. Beyond mechanical performance, the electrical conductivity of GNPs can also provide additional benefits, including electromagnetic interference shielding and lightning protection. However, these improvements depend strongly on dispersion quality and compatibility with the matrix. Recent studies have shown that functionalised GNPs can improve dispersion and matrix interaction [24], which is important because poor dispersion or excessive filler loading may lead to agglomeration, local stress concentration, and reduced reinforcing efficiency.

Topkaya et al. [25] studied GNP additions of 0.1–0.3 wt.% in GFRP, CFRP, and AFRP composites using GNPs with a diameter of 5 μm and thickness of 5–8 nm. The optimum loading was 0.2 wt.%, which increased the tensile strength of GFRP from 348.28 to 359.84 MPa (3.33%) and CFRP from 852.50 to 921.25 MPa (8.05%). Young's modulus also improved in all composites. However, AFRP tensile strength decreased from 773.28 to 747.81 MPa, indicating that the effectiveness of GNP reinforcement depends on fibre type and dispersion quality. However, the same loading did not produce a similar improvement in AFRP composites, indicating that the effect of GNPs depends strongly on the fibre type, matrix chemistry, dispersion behaviour, and interfacial bonding. This comparison is useful because it shows that the performance of GNP-modified composites cannot be generalised across different fibre systems. In hybrid graphene/glass/ABS nanocomposites, GNPs are expected to strengthen the ABS matrix while complementing the load-bearing function of the glass fibre reinforcement. Therefore, the mechanical performance of this system depends not only on the presence of GNPs, but also on how effectively the GNP loading, dispersion, fibre–matrix adhesion, and processing route are controlled.

Conclusions

Initiatives by industry and government aimed at sustainability have prompted a transition from thermoset to thermoplastic systems, with ABS emerging as a likely matrix. To achieve ideal thermal performance, the incorporation of GNPs should be confined to a specific range of 0.2–0.5 wt.%, as this ensures superior dispersion, reduces agglomeration and enhances thermal conductivity while preserving structural integrity. Furthermore, quasi-isotropic stacking sequences are favoured due to their multi-directional strength and damage resistance, making them ideal for components subjected to diverse stress situations. Their fibre orientations in symmetry improve stress distribution and cracking resistance, making them ideally suited for future structural applications that demand reliability, weight reduction, and energy absorption. high-strength composites.

Acknowledgements

The authors gratefully acknowledge Universiti Teknologi Malaysia for financial support through ASCEND Reseach Prominence Grant 2026 and the Ministry of Higher Education, Malaysia, for funding under the Fundamental Research Grant Scheme (FRGS/1/2024/TK04/UTM/02/1). The authors also thank Universiti Teknikal Malaysia Melaka for its support through the UTeM Research Fellowship.

References

[1] A. kordi, S. Adibnazari, A. Imam, M. Najafi, Effects of two- and three-dimensional graphene-based nanomaterials on the fatigue behavior of epoxy nanocomposites, Mater. Today Commun. 24 (2020) 101194. https://doi.org/10.1016/j.mtcomm.2020.101194

[2] M. Song, X. Li, S. Kitipornchai, Q. Bi, J. Yang, Low-velocity impact response of geometrically nonlinear functionally graded graphene platelet-reinforced nanocomposite plates, Nonlinear Dyn. 95 (2019) 2333–2352. https://doi.org/10.1007/s11071-018-4695-y

[3] F. Zaccardi, E. Toto, F. Marra, M.G. Santonicola, S. Laurenzi, Hybrid Carbon Nanocomposites Made of Aerospace-Grade Epoxy Showing Synergistic Effects in Electrical Properties and High Processability, Polymers (Basel). 15 (2023) 1163. https://doi.org/10.3390/polym15051163

[4] K. Malik, F. Ahmad, N.A. Yunus, P.S.M.M. Yusoff, B. Guan, N. Nosbi, S. Ali, T. Nakato, E. Mouri, The effects of graphene hybridization on mechanical properties of GFRP composites, in: 2021: p. 020023. https://doi.org/10.1063/5.0072598

[5] S. Hassanifard, K. Behdinan, Fatigue response of multiscale extrusion-based additively manufactured acrylonitrile butadiene styrene-graphene nanoplatelets composites, Compos. Part B Eng. 279 (2024) 111464. https://doi.org/10.1016/j.compositesb.2024.111464

[6] A.N. Aina, M.A.M. Rizal, M.F.A. Rased, S.A. Hassan, L.F. Ng, L. Rajeshkumar, R.A. Ilyas, H.A. Israr, Fiber-Reinforced Thermoplastic Composites for Future Use in Aircraft Radomes: Biomimetic Design Approaches and Its Performances, Fibers Polym. (2024). https://doi.org/10.1007/s12221-024-00776-1

[7] A.I. Ra'eis, M.A.M. Rizal, A.P.M. Saad, A. Syamsir, M.S.R.M. Saufi, Performance and lifespan prediction of pultruded glass fibre reinforced polymer composite cross-arms in transmission towers: A review of machine learning approaches, Structures 90 (2026) 112212. https://doi.org/10.1016/j.istruc.2026.112212

[8] Y. Swolfs, L. Gorbatikh, I. Verpoest, Fibre hybridisation in polymer composites: A review, Compos. Part A Appl. Sci. Manuf. 67 (2014) 181–200. https://doi.org/10.1016/j.compositesa.2014.08.027

[9] P. Kaliappan, R. Kesavan, B. Vijaya Ramnath, Investigation on effect of fibre hybridization and orientation on mechanical behaviour of natural fibre epoxy composite, Bull. Mater. Sci. 40 (2017) 773–782. https://doi.org/10.1007/s12034-017-1420-2

[10] N. Bouhfid, M. Raji, R. Boujmal, H. Essabir, M.-O. Bensalah, R. Bouhfid, A. el kacem Qaiss, Numerical modeling of hybrid composite materials, in: Model. Damage Process. Biocomposites, Fibre-Reinforced Compos. Hybrid Compos., Elsevier, 2019: pp. 57–101. https://doi.org/10.1016/B978-0-08-102289-4.00005-9

[11] A. Karakoti, P. Tripathy, V.R. Kar, K. Jayakrishnan, M. Rajesh, M. Manikandan, Finite element modeling of natural fiber-based hybrid composites, in: Model. Damage Process. Biocomposites, Fibre-Reinforced Compos. Hybrid Compos., Elsevier, 2019: pp. 1–18. https://doi.org/10.1016/B978-0-08-102289-4.00001-1

[12] A. Shahzad, Investigation into fatigue strength of natural/synthetic fiber-based composite materials, in: Mech. Phys. Test. Biocomposites, Fibre-Reinforced Compos. Hybrid Compos., Elsevier, 2019: pp. 215–239. https://doi.org/10.1016/B978-0-08-102292-4.00012-6

[13] M.Y. Salim, M.F.M. Fitri, M.A.M. Rizal, A.B.M. Supian, M.H. Dzulkifli, R.A. Ilyas, S.A. Hassan, Layering Sequences of Fibreglass Meshes: Effects on the Quasi-static Indentation and Flexural Properties of Kenaf/Acrylonitrile Butadiene Styrene Composites, Fibers Polym. 26 (2025) 2057–2068. https://doi.org/10.1007/s12221-025-00941-0

[14] M.F.M. Fauzi, M.R.M. Asyraf, S.A. Hassan, R.A. Ilyas, T. Khan, Hybrid Kenaf Fibre/Fibreglass Meshes Reinforced Thermoplastic ABS Composites based on Quasi-Isotropic Mechanism: A Brief Review, J. Nat. Fibre Polym. Compos. 2 (2023) 1–9

[15] A.N. Aina, M.A.M. Rizal, M.F.A. Rased, R.A. Majid, D.D. Chin Vui Sheng, S.A. Hassan, Experimental investigations on performance and failure mechanisms of glass fiber-reinforced

acrylonitrile butadiene styrene composites considering mesh density effect, Polym. Compos. (2025). https://doi.org/10.1002/pc.29744

[16] A.N. Aina, M.A.M. Rizal, M.F.A. Rased, R.A. Majid, D.D.C.V. Sheng, Silane-Coupling Effect on Mechanical and Functional Properties of Glass Fiber-Reinforced Acrylonitrile Butadiene Styrene Composites, Polym. Compos. 47 (2026) S120–S134. https://doi.org/10.1002/pc.70920

[17] M.R.M. Asyraf, M. Rafidah, S. Ebadi, A. Azrina, M.R. Razman, Mechanical properties of sugar palm lignocellulosic fibre reinforced polymer composites: a review, Cellulose 29 (2022) 6493–6516. https://doi.org/10.1007/s10570-022-04695-3

[18] N.I.N. Haris, R.A. Ilyas, M.Z. Hassan, S.M. Sapuan, A. Afdzaluddin, K.R. Jamaludin, S.A. Zaki, F. Ramlie, Dynamic Mechanical Properties and Thermal Properties of Longitudinal Basalt/Woven Glass Fiber Reinforced Unsaturated Polyester Hybrid Composites, Polymers (Basel). 13 (2021) 3343. https://doi.org/10.3390/polym13193343

[19] E.H. Saidane, D. Scida, M.-J. Pac, R. Ayad, Mode-I interlaminar fracture toughness of flax, glass and hybrid flax-glass fibre woven composites: Failure mechanism evaluation using acoustic emission analysis, Polym. Test. 75 (2019) 246–253. https://doi.org/10.1016/j.polymertesting.2019.02.022

[20] A.A. Megahed, F. Abd El-Wadoud, A. Wagih, A.M. Kabeel, Effect of incorporating aluminum wire mesh on the notched and un-notched strengths of glass fiber/epoxy composites, Compos. Struct. 263 (2021) 113695. https://doi.org/10.1016/j.compstruct.2021.113695

[21] P. Krishnasamy, G. Rajamurugan, M. Thirumurugan, Performance of fiber metal laminate composites embedded with AL and CU wire mesh, J. Ind. Text. (2020) 152808372093557. https://doi.org/10.1177/1528083720935570

[22] M. Liu, Q. Zhang, Z. Tan, L. Wang, Z. Li, G. Ma, Investigation of steel wire mesh reinforcement method for 3D concrete printing, Arch. Civ. Mech. Eng. 21 (2021) 24. https://doi.org/10.1007/s43452-021-00183-w

[23] A. Asif Iqbal, A.K.M. Parvez Iqbal, D.M. Nuruzzaman, A review on fatigue fracture characteristics in graphene reinforced nanocomposites, Ain Shams Eng. J. 15 (2024) 102730. https://doi.org/10.1016/j.asej.2024.102730

[24] F.S. da Luz, F.D.C. Garcia Filho, M.T.G. Del-Rio, L.F.C. Nascimento, W.A. Pinheiro, S.N. Monteiro, Graphene-incorporated natural fiber polymer composites: A first overview, Polymers (Basel). 12 (2020) 1601

[25] T. Topkaya, Y.H. Çelik, E. Kilickap, Mechanical properties of fiber/graphene epoxy hybrid composites, J. Mech. Sci. Technol. 34 (2020) 4589–4595. https://doi.org/10.1007/s12206-020-1016-4

Materials Research Proceedings 74 (2026) 16-23 https://doi.org/10.21741/9781644904473-3

Mechanical Characteristics of Virgin/Recycled Polypropylene-Wood Composites with Different Wood Species and Content

Indah WIDIASTUTI[1,a *] and Bagas Ade Emas Saka Putra[1,b]

[1]Mechanical Engineering Education Department, Universitas Sebelas Maret, Jl. Ir. Sutami No 36A Kentingan, Surakarta, Indonesia

[a]indahwidiastuti@staff.uns.ac.id, [b]bagasadeesp@students.uns.ac.id

Keywords: Wood Plastic Composite, Hardness, Morphological Characteristics, Recycled Polypropylene

Abstract. This study investigates the effects of wood fibre type (hardwood/teakwood and softwood/*albizia*), polymer matrix type (virgin polypropylene/v-PP and recycled polypropylene/ r-PP), and fibre-to-matrix mass fraction on the hardness characteristics of wood–plastic composites (WPCs). A full-factorial experimental design with three factors at two levels was employed. Composite specimens were fabricated via a two-step process involving extrusion followed by injection moulding. Hardness measurements were conducted in accordance with ASTM D2240 (Shore D), and morphological analysis was performed using scanning electron microscopy (SEM). The results indicate that the combination of softwood *Albizia* fibres with virgin polypropylene at a composition of 60 % fibre to 40 % matrix achieved the highest hardness value of 80.1 Shore D. Analysis of variance (ANOVA) confirmed that all three independent variables exerted statistically significant effects on WPC hardness. Furthermore, SEM micrographs revealed that strong interfacial bonding between the fibres and the matrix was a key factor contributing to improved hardness performance. This study offers valuable insights for optimizing WPC formulations and supports the development of sustainable composite materials utilizing wood wastes and recycled plastics to achieve superior mechanical properties while promoting environmental sustainability.

Introduction

Wood–plastic composites (WPCs) have attracted significant research interest due to their growing demand across multiple industrial sectors and the abundant availability of their raw materials. WPCs utilize wood waste and discarded plastics, which are commonly found in large quantities in landfills [1]. Their recyclability, light weight, cost-effectiveness, ease of maintenance, favourable mechanical properties, and low environmental impact have made WPCs an increasingly popular choice of material for a wide range of applications [2]. The adaptability of WPCs for both structural and aesthetic purposes has further contributed to their rising market demand [3].

Polypropylene (PP) is one of the most widely used polymers as a matrix material in WPC production due to its ease of processing, relatively low cost compared to conventional polymers, wide availability, and high thermal stability, making it suitable for WPC applications [4]. In addition, polypropylene offers excellent chemical resistance, flexibility, and recyclability, making it a preferred matrix material for WPCs [5]. Wood waste also has great potential as a reinforcement material for WPC production. The abundant availability of wood residues and furniture industry waste provides a sustainable source of raw materials [6].

The proportion of wood fibre in the polymer matrix plays a crucial role in determining mechanical properties such as strength, stiffness, and weather resistance. Sidik [7] reported that the optimal composition for achieving desirable mechanical properties in WPCs is 30 % teak wood fibre and 70 % LDPE, producing a composite with a density of 1.081 g/cm³, very low water absorption (0.01 %), flexural strength of 11 MPa, Shore D hardness of 40.33, and compressive

Content from this work may be used under the terms of the Creative Commons Attribution 3.0 license. Any further distribution of this work must maintain attribution to the author(s) and the title of the work, journal citation and DOI. Published under license by Materials Research Forum LLC.

strength of 10.8 MPa. Increasing the wood fibre content up to 70 % results in a stiffer material; however, this may compromise tensile strength and impact resistance due to non-uniform fibre distribution and weak fibre–matrix interfacial bonding [8]. Therefore, selecting an appropriate fibre fraction is essential for enhancing the mechanical performance of WPCs [9].

Hardness, as one of the key mechanical properties, has become a primary focus in WPC research. In general, the mechanical performance of WPCs is strongly influenced by both the wood species and the matrix type. Yadav & Srivastava [10] reported that composites produced using teak wood fibres and polypropylene showed improved mechanical properties, particularly hardness, making them well-suited for outdoor applications. *Albizia* wood (commonly known as "*sengon"*) also has potential as a reinforcement material for WPC production. Although research on *Albizia*-based WPCs remains limited, studies suggest that softer woods often yield composites with higher hardness compared to those reinforced with hardwoods such as teak [11].

The type of polymer matrix also plays a crucial role in determining WPC mechanical properties, such as hardness. Nukala [12] found that incorporating recycled polypropylene (r-PP) can enhance the mechanical properties of WPCs when combined with a higher fibre content. Composites fabricated with virgin polypropylene (v-PP) typically exhibit superior mechanical properties compared to those made with r-PP; however, r-PP is widely used to address plastic waste accumulation [13]. Despite extensive research on WPCs, relatively few studies have examined the combined effects of wood species and matrix type on WPC hardness.

Given this background, further investigation is warranted to determine the influence of wood species and polymer matrix type on WPC hardness. The present study employs teak (a hardwood) and *Albizia* (a softwood) fibres as reinforcement, with r-PP and v-PP as matrix materials. Two fibre-to-matrix ratios (30:70 and 60:40) were selected for evaluation. This study aims to determine the optimal combination of wood species, matrix type, and composition to maximise hardness performance. The findings are expected to serve as a reference for producing high-quality WPC products with superior hardness, offering valuable insights for industrial applications and future research.

Materials and Methods

Experimental design

A full factorial experimental design with three factors at two levels was employed, resulting in eight experimental runs (Table 1). The three factors were: wood species (Factor A: *Albizia* = −1, Teakwood = +1), fibre-to-matrix mass fraction (Factor B: 30:70 = −1, 60:40 = +1), and polymer matrix type (Factor C: recycled polypropylene, r-PP = −1, virgin polypropylene, v-PP = +1). Each condition was replicated with five specimens, resulting in a total of 40 specimens for testing. The response variable was Shore D hardness.

Materials

The polymer matrices used were virgin polypropylene (v-PP) and recycled polypropylene (r-PP). The r-PP was washed, sun-dried to remove moisture, and shredded to an approximate 5-mesh size, following the procedure described by Tan and Pahlevi [4]. *Albizia* (softwood) and teak (hardwood) fibres were obtained from furniture industry waste in *Jepara*, Central Java, sieved to 80–100 mesh as reported by Desiasni [14], and subjected to 2 % NaOH treatment for 24 h. After treatment, the fibres were rinsed to neutral pH and oven-dried at 90 °C for 24 h [6]. Maleic anhydride-grafted polypropylene (MAPP) was used at 3 wt.% as a compatibiliser to enhance fibre–matrix interfacial bonding [15].

Table 1. Full factorial design with three factors and two levels.

Exp.	A	B	C
1	−1	−1	−1
2	+1	−1	−1
3	−1	+1	−1
4	+1	+1	−1
5	−1	−1	+1
6	+1	−1	+1
7	−1	+1	+1
8	+1	+1	+1

Composite preparation

The fibres, polypropylene matrix (v-PP or r-PP), and MAPP were mixed in specified proportions (30 % or 60 % fibre content) and compounded in a twin-screw extruder to produce homogeneous pellets. The formulations were 30 % fibre + 3 % MAPP + 67 % matrix and 60 % fibre + 3 % MAPP + 37 % matrix. The compounded material was processed by injection moulding at 170 °C for 25 min, with the mould temperature maintained at 100 °C, and cooled to 40 °C before demolding (Akbar and Hermawan, 2014). Specimens were then cut using CNC equipment and a hand saw to conform to the dimensions specified in ASTM D2240 [16].

Hardness testing

Shore D hardness was measured in accordance with ASTM D2240. A durometer was pressed against each specimen, and the indentation depth was recorded. Higher Shore D values correspond to greater resistance to penetration, indicating higher hardness [10].

Morphological analysis

SEM was used to examine fibre dispersion and interfacial bonding between the matrix and the reinforcement. Prior to imaging, specimens were sputter-coated with a gold–palladium (Au–Pd) layer to improve conductivity, then placed under vacuum to remove air and dust particles for clear imaging. SEM micrographs were taken at 100× magnification to evaluate fibre distribution and at 500× magnification to identify agglomeration and inspect fibre–matrix adhesion [11].

Results and Discussion

This study evaluated the influence of wood fibre type, fibre-to-matrix mass fraction, and polymer matrix type on the hardness properties of wood–plastic composites (WPCs) produced using injection moulding. Hardness was measured using the Shore D standard (ASTM D2240), and SEM analysis was conducted to examine fibre morphology within the composite. The collected data were analysed using three-way ANOVA to determine the significance of each factor.

The Shore D hardness values for all eight experimental conditions ranged from 74.4 to 80.1. The lowest value was obtained for composition N2 (*Albizia*/r-PP, 30:70), while the highest value was observed for composition N8 (*Albizia*/v-PP, 60:40). Fig. 1 shows the trend of hardness values across all compositions, indicating that higher fibre content (60 %) generally led to increased hardness, with *Albizi*a-based composites consistently exhibiting higher hardness compared to teakwood-based composites.



Fig. 1. Hardness of all WPC specimens.

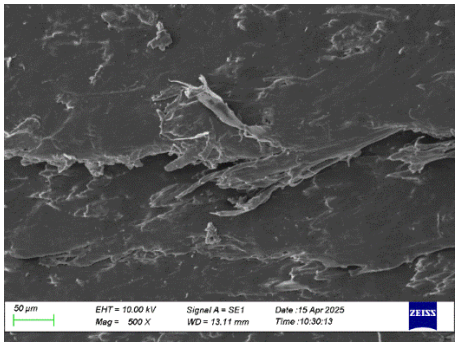
Table 2. Results of ANOVA.

Source	Type III Sum of Squares	df	Mean Square	F	Sig.
Corrected Model	133.602[a]	7	19.086	5.122	.001
Intercept	239027.060	1	239027.060	64142.509	.000
Wood	15.500	1	15.500	4.159	.050
Matrix	70.490	1	70.490	18.916	.000
%wt	21.170	1	21.170	5.681	.023
Wood * Matrix	2.450	1	2.450	.658	.423
Wood * %wt	11.990	1	11.990	3.218	.082
Matrix * %wt	.870	1	.870	.234	.632
Wood * Matrix * %wt	11.130	1	11.130	2.987	.094
Error	119.248	32	3.727		
Total	239279.910	40			
Corrected Total	252.850	39			

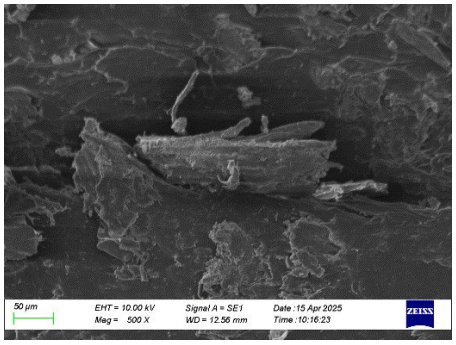
a. R Squared = .528 (Adjusted R Squared = .425)

Before performing a three-way ANOVA, a normality test was conducted as a prerequisite. The results indicated that the data were normally distributed, with a significance value of 0.788 > 0.05, thus accepting H_0 and confirming normal distribution. A homogeneity of variance test was also performed to verify that the variances among the eight groups were equal. The test yielded a p-value of 0.712 > 0.05, indicating no significant differences in variance and fulfilling the assumption of homogeneity.

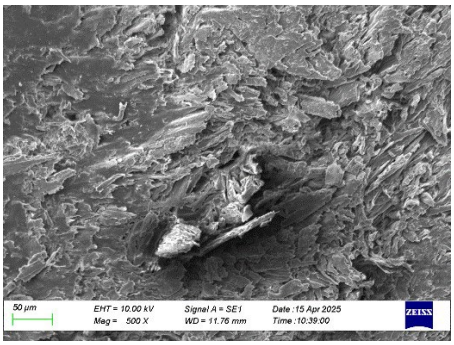
The three-way ANOVA results, as shown in Table 2, confirmed that all three factors—wood species ($p = 0.050$), polymer matrix type ($p = 0.000$), and fibre content ($p = 0.023$)—had statistically significant effects on the hardness of WPCs ($p \leq 0.05$). Interaction effects between wood species and matrix type, as well as between matrix type and fibre content, were statistically insignificant ($p > 0.05$), indicating that these factors largely act independently.



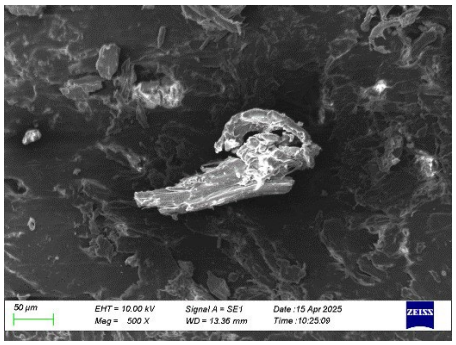
(a) Teakwood/r-PP 30/70 (N1)



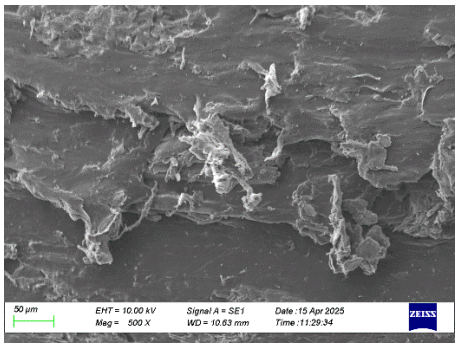
(b) Albizia/r-PP 30/70 (N2)



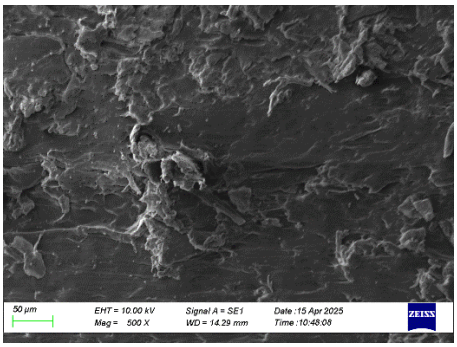
(c) Teakwood/r-PP 60/40 (N3)



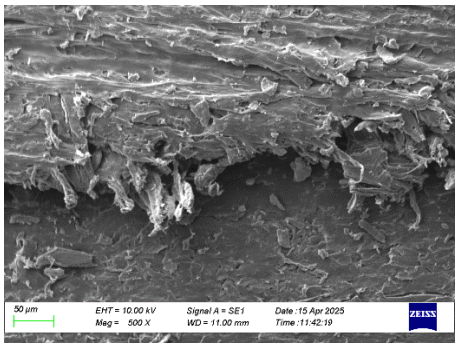
(d) Albizia/r-PP 60/40 (N4)



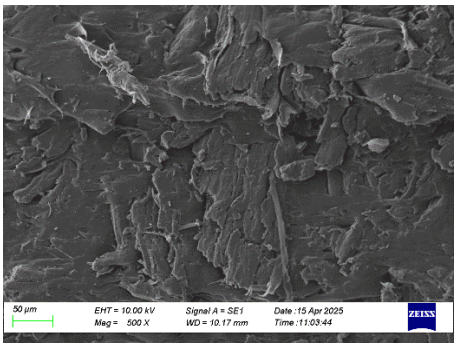
(e) Teakwood/v-PP 30/70 (N5)



(f) Albizia/v-PP 30/70 (N6)



(g) Teakwood/v-PP 60/40 (N7)



(h) Albizia/v-PP 60/40 (N8)

Fig. 2. Images of SEM 500× for all composite specimens.

SEM analysis was carried out using a Zeiss Evo 10 to observe fibre distribution and the fibre–matrix interface. The SEM micrographs (Fig. 2) revealed clear differences in fibre–matrix interaction influenced by wood species, fibre content, and matrix type. At a lower fibre content (30 %), teakwood/r-PP composites (N1) showed uneven fibre distribution, visible agglomeration,

and several voids at the interface, indicating poor interfacial bonding that can lead to clustering and the formation of aggregates [17]. In contrast, *Albizia*/r-PP composites (N2) displayed more uniform fibre dispersion, improved matrix embedding, and fewer voids, suggesting stronger adhesion between the fibre and the matrix. Similar patterns were observed in v-PP composites: teakwood/v-PP (N5) exhibited weak bonding and incomplete fibre wetting, whereas *Albizia*/v-PP (N6) demonstrated better compatibility, fewer voids, and a more homogeneous microstructure. At higher fibre loading (60 %), fibre agglomeration became more pronounced for both species, but the effect was more severe in teakwood composites, which exhibited dense fibre bundles and larger voids. *Albizia* composites maintained relatively better fibre distribution even at 60 % loading, with fewer large agglomerates. This is likely due to the softer structure of *Albizia* fibres, which allows better integration with the polymer matrix. Comparing the matrix types, composites produced with virgin polypropylene (v-PP) generally exhibited smoother surfaces and fewer voids than those produced with recycled polypropylene (r-PP), a result attributed to the higher purity and consistency of v-PP, which improves fibre wetting.

These results emphasise that uniform fibre dispersion and strong interfacial bonding are critical for enhancing the mechanical performance of WPCs. A well-distributed fibre–matrix interface enhances compatibility and stress-transfer efficiency, leading to improved mechanical properties [18]. In contrast, fibre agglomeration and entrapped voids act as stress concentrators, degrading mechanical performance [19]. Taken together, the results show that *Albizia*-based composites exhibit superior microstructural quality, whereas teakwood-based composites tend to suffer from fibre clustering and poor dispersion, which likely reduces their hardness performance.

Conclusion

This study employed three-way ANOVA to evaluate the effects of wood species, fibre-to-matrix mass fraction, and polymer matrix type on the hardness properties of wood–plastic composites (WPCs) produced via two-step extrusion and injection moulding. The results confirmed that wood species, polymer matrix type, and fibre-to-matrix ratio each had a statistically significant effect on composite hardness. *Albizia*-based composites consistently outperformed teakwood-based composites, and virgin polypropylene (v-PP) provided higher hardness than recycled polypropylene (r-PP), reflecting its superior fibre wetting and compatibility. Increasing the fibre content from 30 % to 60 % generally enhanced hardness but also promoted fibre agglomeration, particularly in teakwood composites. The optimal configuration was identified as *Albizia*/v-PP with a 60:40 fibre-to-matrix ratio, achieving the highest hardness value of 80.1 Shore D. These results emphasise that uniform fibre distribution and strong interfacial bonding are critical to improving WPC mechanical performance. Overall, this study contributes to the optimisation of WPC formulations and provides a reference for manufacturing high-performance, environmentally friendly composites with superior hardness characteristics for industrial applications.

Acknowledgement

The authors gratefully acknowledge the financial support provided by the Institute of Research and Community Service, Universitas Sebelas Maret, through the research grant on Penguatan Kapasitas Grup Riset (PKGR-UNS) B under Contract No. 371/UN27.22/PT.01.03/2025.

References

[1] M.B. Waluyo, S.T. Kismanti, Sanudin, Pemanfaatan Limbah Plastik Sebagai Penguat pada Material Komposit Bermatriks Epoxy, Al Jazari: Jurnal Ilmiah Teknik Mesin 8 (2023) 94–98. https://doi.org/10.31602/al-jazari.v8i2.12764

[2] A. Yousaf, A. Al Rashid, R. Polat, M. Koç, Potential and challenges of recycled polymer plastics and natural waste materials for additive manufacturing, Sustainable Materials and Technologies 41 (2024) e01103. https://doi.org/10.1016/j.susmat.2024.e01103

[3] T. Boonsri, S. Rukchonlatee, I. Jangchud, Wood plastic composites (WPCs) from multilayer packaging wastes and rHDPE as pallets for green industry, IOP Conf Ser Mater Sci Eng. 1234 (2022) 012022. https://doi.org/10.1088/1757-899x/1234/1/012022

[4] T.L. Ing, W.R. Pahlevi, Studi Penggunaan Plastik Polypropylene pada Campuran Asphalt Concrete-Wearing Course, Cantilever: Jurnal Penelitian dan Kajian Bidang Teknik Sipil 8 (2019) 65–71. https://doi.org/10.35139/cantilever.v8i2.13

[5] I.O. Ohijeagbon, A.A. Adeleke, V.T. Mustapha, J.A. Olorunmaiye, I.P. Okokpujie, P.P. Ikubanni, Development and characterization of wood-polypropylene plastic-cement composite board, Case Studies in Construction Materials 13 (2020) e00365. https://doi.org/10.1016/j.cscm.2020.e00365

[6] D. Holzer, M. Popowicz, R. Rauter, K. Silberschneider, T. Stern, Parallel universes, one circular goal: An empirical study comparing Austrian wood- and plastic-based industries, Sustain Prod Consum. 43 (2023) 46–61. https://doi.org/10.1016/j.spc.2023.10.014

[7] R. Sidik, Studi Pengaruh Penambahan Polypropylene dan Low Density Polyethylene Terhadap Sifat Fisik dan Mekanik Wood Plastic Composite Untuk Aplikasi Genteng Ramah Lingkungan, Institut Teknologi Sepuluh Nopember, pp. 1–112, 2018

[8] K. Alokabel, A. D. Betan, Pengaruh Variasi Serbuk Kayu Terhadap Sifat Mekanis Material Komposit, TAPAK (Teknologi Aplikasi Konstruksi): Jurnal Program Studi Teknik Sipil 8 (2019) 150–154. https://doi.org/10.24127/tp.v8i2.951

[9] D.D. Wacono, S. Sulardjaka, Pengaruh Persentase Berat Serbuk Sic Terhadap Sifat Fisik Dan Sifat Mekanik Komposit Dengan Matrik Alsitib Yang Diperkuat Serbuk Sic, Jurnal Teknik Mesin S-1 2 (2014) 239–248.

[10] A.K. Yadav, R. Srivastava, Selection of teak sawdust polypropylene composite's composition for outdoor applications using TOPSIS analysis, Sadhana - Academy Proceedings in Engineering Sciences 45 (2020) 1–12. https://doi.org/10.1007/s12046-020-01435-w

[11] B. Effah, A. Van Reenen, M. Meincken, Mechanical properties of wood-plastic composites made from various wood species with different compatibilisers, European Journal of Wood and Wood Products 76 (2018) 57–68. https://doi.org/10.1007/s00107-017-1186-7

[12] S.G. Nukala, I. Kong, A.B. Kakarla, K.Y. Tshai, W. Kong, Preparation and Characterisation of Wood Polymer Composites Using Sustainable Raw Materials, Polymers (Basel) 14 (2022) 1–18. https://doi.org/10.3390/polym14153183

[13] Y.M. Lopez, J.B. Paes, F.G. Gonçalves, E.M. Rodríguez, P.N. de M. Neto, Physico-mechanical properties of wood-plastic produced with forest species and thermoplastic materials, Floresta e Ambiente 27 (2020) e20170736. https://doi.org/10.1590/2179-8087.073617

[14] R. Desiasni, N. Azman, F. Widyawati, Sifat fisik dan mekanik komposit papan partikel berdasarkan variasi ukuran serbuk kayu mahoni (Swietenia Macrophylla) sebagai material alternatif: papan komposit, Jurnal Tambora 7 (2023) 78–83. https://doi.org/10.35139/cantilever.v8i2.13

[15] N. Hongsriphan, Polymer Chemistry, *Polymer Chemistry (POL-1165)*, pp.1217–1222, 2016.

[16] A.D. Laksono, Basyaruddin, N. Adlina, Pengaruh Perlakuan Alkalisasi Serat Alam Kayu Bangkirai (Shorea Laevifolia Endert) pada Sifat Mekanik Komposit dengan Matriks Poliester, Jurnal Sains Terapan 5 (2019) 60–66. https://doi.org/10.32487/jst.v5i2.672

[17] M.H.S. Ginting, N.H. Siregar, F. Suwito, B. Tanujaya, “Pengaruh komposisi kulit kerang darah (Anadara granosa) terhadap kerapatan, keteguhan patah komposit partikel poliester, Prosiding Semnastek (2016) 1–7.

[18] N.A.T. Fadhly, I.Hs. Bahruddin, Pengaruh Nisbah Polypropylene/Serat Pelepah Sawit Dan Kadar Maleated Polypropylene (MAPP) Terhadap Sifat Dan Morfologi Wood Plastic Composites (WPC), Riau University, pp. 1–9, 2015.

[19] M.R. Hossain, F. Hossain, M. A. Islam, Effects of Wood Properties on the Behaviors of Wood Particle Reinforced Polymer Matrix Composites, Journal of Scientific Research 6 (2014) 431–443. https://doi.org/10.3329/jsr.v6i3.15811

Rainwater Absorption Characteristics and Material Characterisation of Single-Ply Carbon/Epoxy Composite

N.G. MACHAVA[1,a], K.J. WONG[1,b], A.B. CHAI[1,c *], K.Y. TSHAI[1,d] and K.W. GAN[2,e]

[1]Department of Mechanical, Materials and Manufacturing Engineering, Faculty of Science and Engineering, University of Nottingham Malaysia, Jalan Broga, 43500 Semenyih, Selangor, Malaysia

[2]Smart Manufacturing and Systems Research Group, University of Southampton Malaysia, 79100 Iskandar Puteri, Johor, Malaysia

[a]nakisha.machava@gmail.com, [b]KingJye.Wong@nottingham.edu.my, [c]AiBao.Chai@nottingham.edu.my, [d]Kim-Yeow.Tshai@nottingham.edu.my, [e]K.W.Gan@soton.ac.uk

Keywords: Carbon/epoxy Composite, Rainwater Immersion, Non-Fickian, Field Emission Scanning Electron Micrograph, Dynamic Mechanical Analysis

Abstract. This study investigates the moisture absorption behaviour and thermal response of single-ply carbon/epoxy composites subjected to rainwater immersion under ambient conditions. Over a 74-day period, the composite reached a maximum moisture content of 1.023%, exhibiting non-Fickian diffusion characteristics. Moisture uptake was modelled using both conventional Fickian and thickness-dependent non-Fickian approaches, with the latter providing a better fit to the experimental data. Field emission scanning electron microscopy (FESEM) revealed no significant microstructural changes or fibre-matrix debonding, suggesting that capillary action along the interface is not a contributing factor to the observed non-Fickian behaviour. Dynamic mechanical analysis (DMA) showed a 5.67 °C increase in glass transition temperature (T_g), rising from 146.25 °C to 151.92 °C after immersion. This shift indicates potential post-curing or secondary crosslinking effects induced by moisture exposure, which may enhance the thermal stability of the composite. These findings offer valuable insights into the environmental durability of thin carbon/epoxy laminates and support the development of predictive models for moisture-induced ageing in composite structures, particularly in applications exposed to natural weathering conditions.

Introduction

Owing to their lightweight nature and favourable mechanical efficiency, fibre-reinforced polymer composites are increasingly utilised in structural systems where high specific strength and stiffness are required. Their high strength-to-weight ratio makes them ideal for applications where weight reduction is critical, such as in aerospace and automotive industries. Additionally, composites offer superior corrosion resistance compared to conventional materials like steel and aluminium, particularly in aggressive environments such as marine settings. These advantages contribute to extended service life and reduced maintenance costs.

Nevertheless, prolonged environmental exposure can progressively alter the physical and mechanical characteristics of composite laminates, thereby affecting their long-term service reliability. Long-term exposure to moisture, temperature fluctuations, and other environmental factors can significantly impair their mechanical performance [1-3]. The extent of degradation is often correlated with the duration of ageing [4-6] and the amount of absorbed moisture [7-9]. Moisture uptake behaviour is influenced by several factors, including the type of composite, ambient temperature, and the nature of the ageing medium [10-12]. Therefore, it is essential to

Content from this work may be used under the terms of the Creative Commons Attribution 3.0 license. Any further distribution of this work must maintain attribution to the author(s) and the title of the work, journal citation and DOI. Published under license by Materials Research Forum LLC.

characterise moisture absorption behaviour which reflects the intended service conditions of the material.

Accelerated ageing tests are commonly employed in laboratory settings to simulate long-term environmental exposure. These tests typically involve elevated temperatures and humidity levels to expedite moisture saturation. Alternatively, using thinner specimens can reduce the time required to reach saturation. However, for moisture absorption data to be applicable across different thicknesses, the absorption process must follow Fickian diffusion. If non-Fickian behaviour is observed, a different model such as thickness-dependent model has to be established [13-15].

This study focuses on characterising the rainwater absorption behaviour of single-ply unidirectional carbon/epoxy composites. The moisture uptake was evaluated using both Fickian and non-Fickian models. Additionally, the microstructural changes were examined using field emission scanning electron microscopy (FESEM), and the thermal properties were assessed through dynamic mechanical analysis (DMA). The findings aim to provide foundational insights into the environmental durability of thin composite laminates under natural ageing conditions.

Materials and Methods

Material

Single-ply unidirectional carbon/epoxy composite, with an average thickness of 0.162 mm, areal weight of 150 gsm and average fibre volume fraction of 65.7% ± 6.3% [16-19], was sourced from X-Plas Singapore. The composite was cut into square specimens measuring 5 × 5 cm^2. A total of six specimens were prepared for the rainwater absorption tests.

Pre-immersion Preparation

To eliminate residual moisture from manufacturing, each specimen was weighed three times to determine its average initial mass, then oven-dried at 50°C for 8 hours. Post-drying, the specimens were reweighed to establish their dry mass and stored individually in sealed bags to prevent premature moisture uptake.

Rainwater Absorption Test

Rainwater obtained in Semenyih, Selangor, was employed as the immersion medium. The collected water exhibited a measured pH value of 6.32 using an SI Analytics Lab Meter 845. Ageing was conducted by maintaining complete specimen submersion in the collected rainwater under ambient laboratory conditions averaging 23.1°C for a duration of 74 days. Moisture uptake was monitored by measuring weight gain using a Rasse MH-8028 precision balance (±0.001 g) periodically.

Surface Morphology Analysis

Dry and wet specimens were sectioned to a width of 10 mm and embedded in epoxy resin. Polishing was performed using a Yuzhou YMPZ-1 grinding machine with silicon carbide papers of grit sizes #320, #600, and #1000, followed by diamond suspensions of 9, 6, 3, and 1 micron. Each polishing step lasted 3 minutes. The polished samples were gold-sputtered using a Q150R S Plus coater and examined under a FEI QUANTA 400F field emission scanning electron microscope (FESEM).

Dynamic Mechanical Analysis

Viscoelastic properties of both dry and immersed specimens were characterised using a PerkinElmer DMA 8000. The specimens were cut to a size of 12.5 × 6.3 mm^2. The test was conducted in tension clamp mode. The heating rate was set to 5 °C/min, ranging from room temperature to 200 °C, with a strain amplitude of 20 μm and a frequency of 1 Hz.

Result and Discussion

Rainwater Absorption

Fig. 1 illustrates the moisture uptake profile of the single-ply carbon/epoxy composite, plotted as average moisture content versus the square root of time. Moisture content was calculated using Eq. 1:

$$M\ (\%) = \frac{W_i - W_o}{W_o} \times 100 \qquad \text{Eq. 1}$$

where W_i is the current mass and W_o is the oven-dry mass of the specimen. The data show an initial rapid absorption phase followed by a plateau at approximately 1.023%, indicating saturation. The relatively large standard deviation (represented by the error bars) is attributed to the low initial mass of the specimens, which increases sensitivity to measurement fluctuations.

To model the absorption behaviour, Fickian diffusion [20] was first applied using Eq. 2:

$$M(t) = M_m \left\{1 - exp\left[-7.3\left(\frac{D_z t}{h^2}\right)^{0.75}\right]\right\} \qquad \text{Eq. 2}$$

Here, M is the instantaneous moisture content at time t, M_m is the maximum moisture content, h is the specimen thickness, and D_z is the diffusivity, calculated using Eq. 3:

$$D_z = \pi\left(\frac{h}{4M_m}\right)^2\left(\frac{M_2 - M_1}{\sqrt{t_2} - \sqrt{t_1}}\right)^2 \qquad \text{Eq. 1}$$

The subscripts 1 and 2 refer to any two instances of the moisture absorption process. Using the initial linear region of the absorption curve, the slope $\frac{M_2 - M_1}{\sqrt{t_2} - \sqrt{t_1}}$ was estimated to be 0.9525. With h = 0.162 mm and M_m = 1.023%, D_z was calculated to be 4.45×10^{-3} mm^2/day. Substituting these values into Eq. (2), the Fickian diffusion curve was plotted as a dotted line in *Fig. 1*. However, the Fickian model overpredicts moisture uptake in the shoulder region, deviating from ideal Fickian behaviour. To address this, a thickness-dependent non-Fickian model was employed (Eq. 4):

$$M\ (t) = M_F\ (t) + M_{NF}\ (t) = M_{m,F}G(t) + \left(M_m - M_{m,F}\right)W(t) \qquad \text{Eq. 2}$$

Here, M_F and M_{NF} refer to the Fickian and non-Fickian stage, respectively. $G(t)$ and $W(t)$ indicate the Fickian and non-Fickian moisture absorption function, while $M_{m,F}$ is the maximum moisture content for the Fickian stage. This equation can be expressed as:

$$M\ (t) = M_{m,F}\left\{1 - exp\left[-7.3\left(\frac{D_{z,F}t}{h^2}\right)^{0.75}\right]\right\} + (M_m - M_{m,F})\{1 - exp[-(\alpha(t - t_o))^{0.75}]\} \qquad \text{Eq. 3}$$

In Eq. 5, $D_{z,F}$ is the maximum moisture content and diffusivity for the Fickian stage, while t_o is the initiation time of non-Fickian behaviour and α is the non-Fickian diffusivity per square thickness. The modelling approach considers moisture transport as a two-stage process. The initial stage is governed predominantly by classical diffusion mechanisms, whereas the later stage is associated with delayed polymer-network relaxation phenomena that contribute additional moisture accumulation. Earlier studies demonstrated the applicability of this formulation for epoxy moulding compounds (EMCs) [13] before extending it to woven [14] and unidirectional [15] fibre-reinforced epoxy composites. The schematic diagram of the thickness-dependent moisture

absorption model is illustrated in *Fig. 2*. In this study, $M_{m,F}$ is estimated to be 0.614%, which is 60% of the M_m, in accordance to the guideline reported in an earlier study [15]. Subsequently, $D_{z,F}$ is calculated using Eq. 6, yielding 0.0124 mm^2/day. It is worth noting that the slope $\frac{M_2-M_1}{\sqrt{t_2}-\sqrt{t_1}}$ remains 0.9525 $\sqrt{day}^{-1}$, as the same initial region is used.

$$D_{z,F} = \pi\left(\frac{h}{4M_{m,F}}\right)^2\left(\frac{M_2 - M_1}{\sqrt{t_2} - \sqrt{t_1}}\right)^2 \quad \text{Eq. 4}$$

For the non-Fickian part, t_o is obtained by identifying the point at which the Fickian curve (solid line in Fig. 2) deviates from the experimental data. In this study, it is estimated to be 1/3 day. Subsequently, the experimental *W(t)*, denoted as $W_{exp}(t)$, is calculated using:

$$W_{exp}(t) = \frac{M(t) - M_F(t)}{M_m - M_{m,F}} \quad \text{Eq. 5}$$

By plotting the experimental $W_{exp}(t)$ versus t-t_o and fitting it using $1 - exp[-(\alpha(t - t_o))^{0.75}]$, the best fit α is estimated to be 0.0988 day^{-1} (Fig. 3). The non-Fickian curve is plotted as a dotted line in Fig. 1. Considering the scatter in the data, a comparative well-fitted curve is obtained.

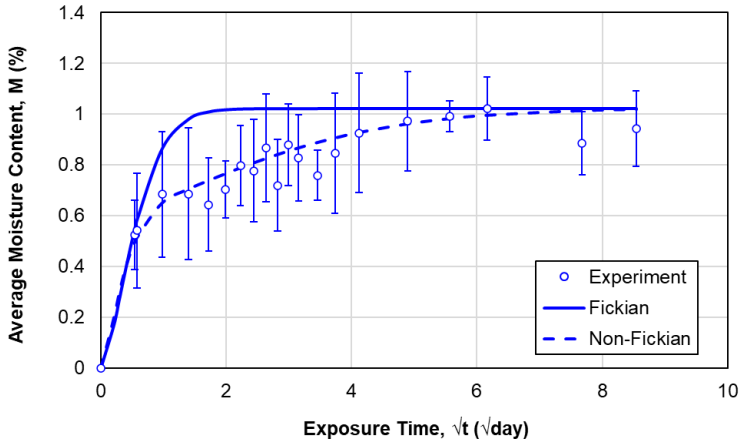


Fig. 1. Comparison of experimental moisture absorption data with fitted Fickian and non-Fickian models for single-ply carbon/epoxy composite.

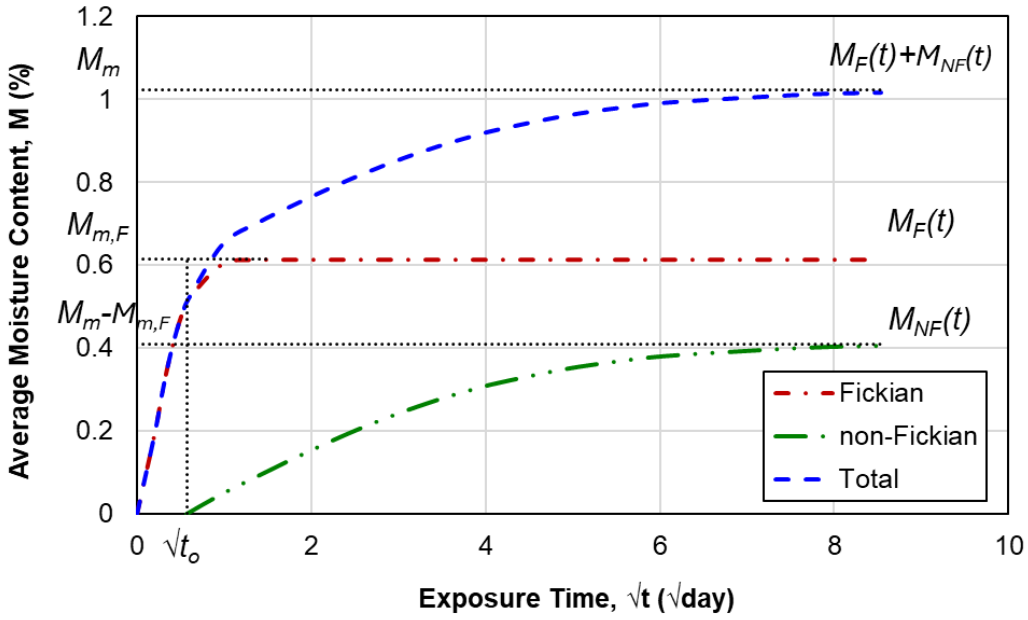


Fig. 2. Conceptual illustration of the thickness-dependent non-Fickian moisture absorption model.

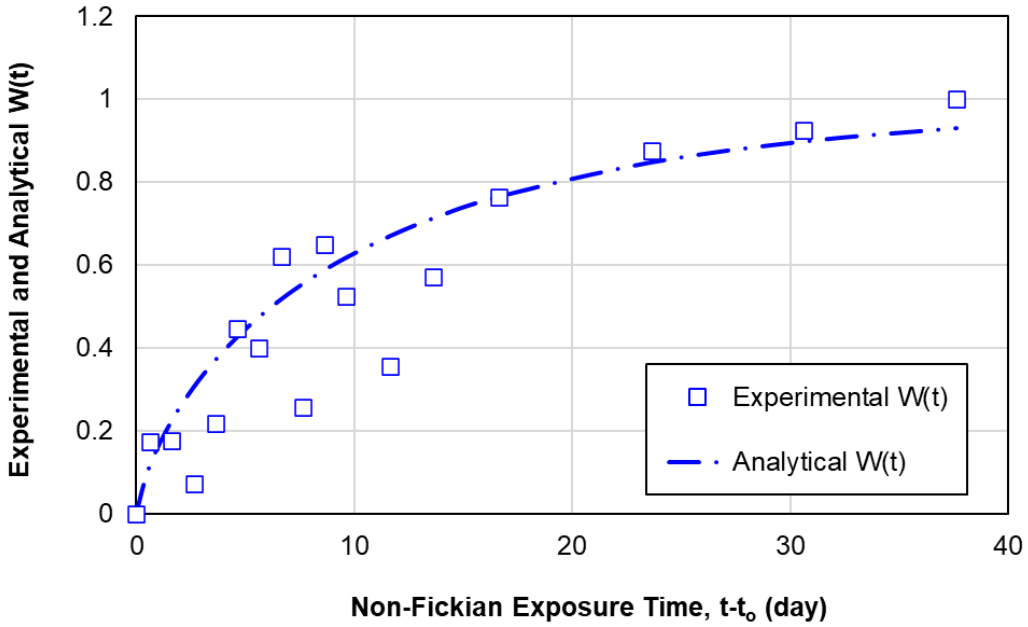
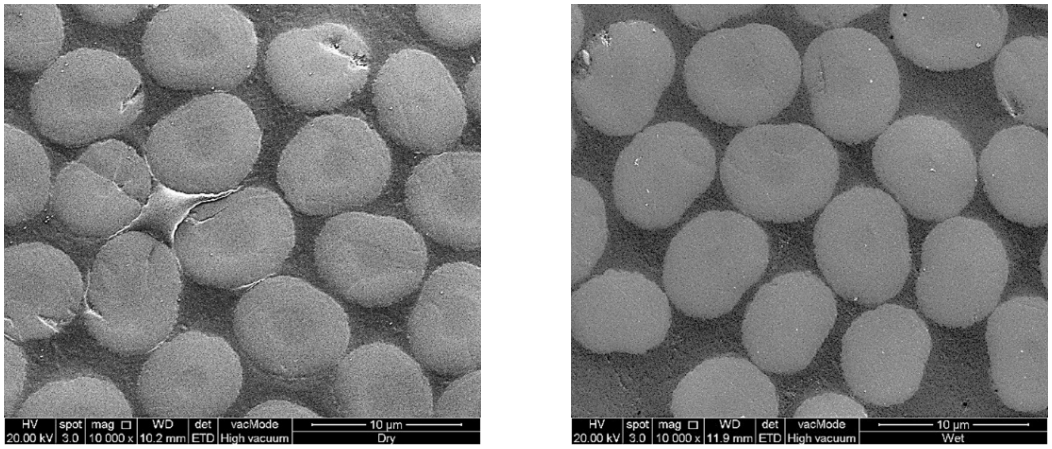


Fig. 3. Comparison of experimental and analytical non-Fickian W(t) for single-ply carbon/epoxy composite.

Field Emission Scanning Electron Microscopy

Fig. 4 presents FESEM micrographs of dry and wet specimens. Comparison of the micrographs obtained before and after immersion revealed no discernible deterioration of the fibre-matrix interface. Furthermore, evidence of interfacial separation or crack initiation was absent within the examined regions. Consequently, moisture ingress through interfacial capillary channels is unlikely to be the dominant mechanism responsible for the observed absorption behaviour.



(a) (b)

Fig. 4. FESEM micrographs of the cross-section of single-ply carbon/epoxy composite under (a) dry and (b) wet conditions.

Dynamic Mechanical Analysis

Fig. 5 shows the damping factor (tan δ) as a function of temperature (T) for both dry and immersed specimens. The glass transition temperature (T_g) increased from 146.25°C to 151.92°C after 74 days of immersion. The observed upward shift in glass transition temperature reflects a marginal improvement in the thermal resistance of the epoxy network. A higher T_g suggests improved resistance to thermal softening and better structural performance at elevated temperatures. One plausible explanation is that prolonged environmental exposure facilitated additional curing reactions, resulting in a more constrained polymer network and reduced molecular mobility [21, 22].

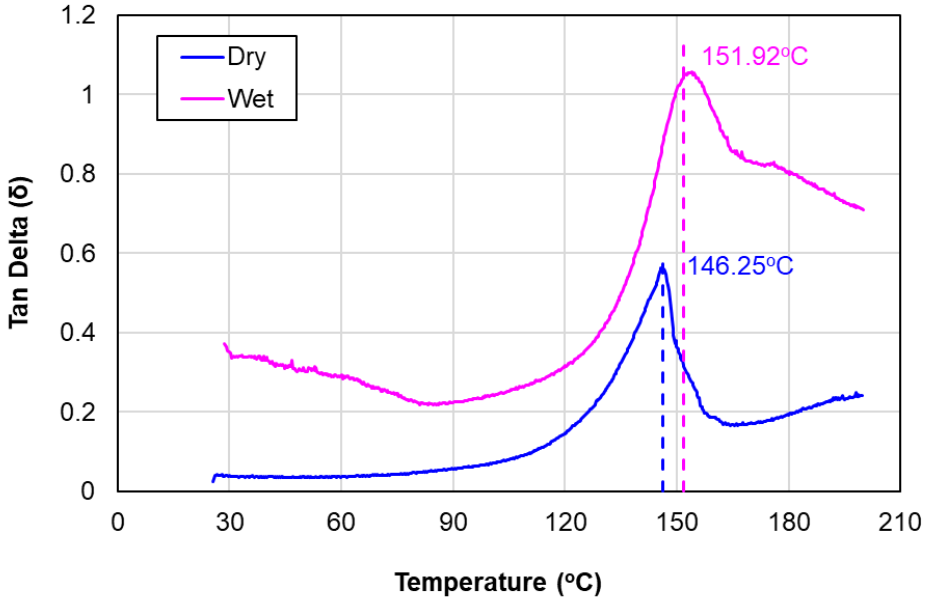


Fig. 5. DMA results showing damping factor (tan δ) versus temperature for dry and rainwater-immersed specimens.

Conclusions

This study investigated the rainwater absorption behaviour and thermal response of single-ply carbon/epoxy composites under ambient conditions. Moisture uptake was modelled using both

Fickian and thickness-dependent non-Fickian diffusion approaches. Microstructural and thermal analyses were conducted using FESEM and DMA, respectively. Key findings include:

a) The composite reached a maximum moisture content of 1.023% after 74 days of immersion.
b) Experimental observations demonstrated that conventional diffusion theory alone could not adequately capture the moisture uptake profile, whereas the thickness-dependent approach provided a more representative description of the measured response.
c) FESEM analysis revealed no visible fibre-matrix debonding, indicating that capillary effects along the interface are not responsible for the non-Fickian behaviour.
d) DMA results showed an increase in glass transition temperature (T_g) from 146.25°C to 151.92°C, suggesting moisture-induced post-curing or secondary crosslinking that enhances thermal stability and resistance to thermal softening.

These results provide foundational insights into the environmental durability of thin carbon/epoxy laminates and support the development of predictive models for moisture-related ageing in composite structures.

Acknowledgements
This work is supported by Ministry of Higher Education Malaysia through Fundamental Research Grant Scheme (FRGS) No. FRGS/1/2021/TK0/UNIM/02/4. N.G. Machava acknowledges Department of Mechanical, Materials and Manufacturing Engineering, Faculty of Science and Engineering, University of Nottingham Malaysia for the financial support during Summer Research Internship 2024.

References

[1] Y. Du, Y. Ma, W. Sun, Z. Wang, Effect of hygrothermal aging on moisture diffusion and tensile behavior of CFRP composite laminates, Chinese Journal of Aeronautics (2023) 36(3) 382-392. https://doi.org/10.1016/j.cja.2022.11.022

[2] M. Johar, W.W.F. Chong, K.J. Wong, Moisture absorption and tensile behaviour of hybrid carbon/flax composites, Fibers Polym. (2023) 24(5) 1799-1810. https://doi.org/10.1007/s12221-023-00157-0

[3] A. Karimzadeh, M.Y. Yahya, M.N. Abdullah, K.J. Wong, Effect of stacking sequence on mechanical properties and moisture absorption characteristic of hybrid PALF/glass fiber composites, Fibers and Polymers (2020) 21(7) 1583-1593. 10.1007/s12221-020-9640-2

[4] M. Massou, N. Babu, G. Xian, Experimental study on the mechanical properties of CFRP/epoxy composite plates under seawater immersion, Structures (2023) 54 48-57. https://doi.org/10.1016/j.istruc.2023.05.042

[5] E.O. Ogunsona, M. Misra, A.K. Mohanty, Accelerated hydrothermal aging of biocarbon reinforced nylon biocomposites, Polymer Degradation and Stability (2017) 139 76-88. https://doi.org/10.1016/j.polymdegradstab.2017.03.013

[6] Q. Xu, F. Li, W. Mu, J. Na, W. Tan, G. Wang, Effect of hygrothermal and alternating load coupled aging on CFRP/Al bonded joints, International Journal of Adhesion and Adhesives (2021) 109 102912. https://doi.org/10.1016/j.ijadhadh.2021.102912

[7] S.F. Mad Asasaari, K.J. Wong, M.N. Tamin, M. Johar, Moisture absorption effects on the mechanical properties of carbon/epoxy composites, International Journal of Structural Integrity (2020) 11(4) 605-614. https://doi.org/10.1108/IJSI-12-2019-0136

[8] K.J. Wong, H.A. Israr, M.N. Tamin, Characterisation of moisture absorption effects on the strength of composite materials, Advanced Materials Research (2015) 1125 69-73. 10.4028/www.scientific.net/AMR.1125.69

[9] E. Pérez-Pacheco, J.I. Cauich-Cupul, A. Valadez-González, P.J. Herrera-Franco, Effect of moisture absorption on the mechanical behavior of carbon fiber/epoxy matrix composites, J. Mater. Sci. (2013) 48 1873-1882. https://doi.org/10.1007/s10853-012-6947-4

[10] C.-H. Shen, G.S. Springer, Moisture absorption and desorption of composite materials, Journal of Composite Materials (1976) 10(1) 2-20. https://doi.org/10.1177/002199837601000101.

[11] C.-H. Shen, G.S. Springer, Effects of moisture and temperature on the tensile strength of composite materials, Journal of Composite Materials (1977) 11(1) 2-16. https://doi.org/10.1177/002199837701100102.

[12] C.-H. Shen, G.S. Springer, Environmental effects on the elastic moduli of composite materials, Journal of Composite Materials (1977) 11(3) 250-264. https://doi.org/10.1177/002199837701100301.

[13] K.J. Wong, K.O. Low, H.A. Israr, M.N. Tamin, Thickness-dependent non-Fickian moisture absorption in epoxy molding compounds, Microelectronics Reliability (2016) 65 160-166. https://doi.org/10.1016/j.microrel.2016.08.014

[14] M. Johar, H.S. Kang, W.W.F. Chong, K.J. Wong, A further generalized thickness-dependent non-Fickian moisture absorption model using plain woven epoxy composites, Polymer Testing (2018) 69 522-527. https://doi.org/10.1016/j.polymertesting.2018.06.013

[15] A. Azizan, M. Johar, S.S. Karam Singh, S. Abdullah, S.S. Koloor, M. Petrů, K.J. Wong, M.N. Tamin, An Extended Thickness-Dependent Moisture Absorption Model for Unidirectional Carbon/Epoxy Composites, Polymers (2021) 13(3) 440. 10.3390/polym13030440

[16] K.O. Low, S.M. Teng, M. Johar, H.A. Israr, K.J. Wong, Mode I delamination behaviour of carbon/epoxy composite at different displacement rates, Compos. Part B-Eng. (2019) 176 107293. https://doi.org/10.1016/j.compositesb.2019.107293

[17] K.O. Low, M. Johar, H.A. Israr, K.W. Gan, S.S. Rahimian Koloor, M. Petrů, K.J. Wong, Displacement rate effects on the mode II shear delamination behavior of carbon fiber/epoxy composites, Polymers (2021) 13(11) 1881. 10.3390/polym13111881

[18] K.O. Low, M. Johar, A.N. Sung, M.N. Mohd Nasir, S.S. Rahimian Koloor, M. Petrů, H.A. Israr, K.J. Wong, Displacement rate effects on mixed-mode I/II delamination of laminated carbon/epoxy composites, Polym. Test. (2022) 108 107512. https://doi.org/10.1016/j.polymertesting.2022.107512

[19] K.J. Wong, M. Johar, S.S. Koloor, M. Petrů, M.N. Tamin, Moisture absorption effects on mode II delamination of carbon/epoxy composites, Polymers (2020) 12(9) 2162. https://doi.org/10.3390/polym12092162

[20] A. Fick, Über diffusion, Poggendorff's Annalen der Physik und Chemie (1855) 94 59-86. https://doi.org/10.1002/andp.18551700105.

[21] B. Hassanpour, V.M. Karbhari, Moisture and Glass Transition Temperature Kinetics of Ambient-Cured Carbon/Epoxy Composites, J. Compos. Sci. (2023) 7(11) 447. https://doi.org/10.3390/jcs7110447

[22] P. Ghabezi, N.M. Harrison, Hygrothermal deterioration in carbon/epoxy and glass/epoxy composite laminates aged in marine-based environment (degradation mechanism, mechanical and physicochemical properties), J. Mater. Sci. (2022) 57(6) 4239-4254. 10.1007/s10853-022-06917-2

Materials Research Proceedings 74 (2026) 32-39 https://doi.org/10.21741/9781644904473-5

Structure-Property Relationship of Modified versus Natural Clinoptilolite Powders in Congo Red Removal

Nur Najeehah MOHD NASIR[1,a], Fatin Nur Afifi MOHD FADIL[1,b], Ashraf AZMI[1,2,c], Muhammad Azan TAMAR JAYA[3,d], R.A. ILYAS[4,e], Yahaya MUHAMMAD SANI[5,f], and Iylia IDRIS[1,2,d *]

[1]Faculty of Chemical Engineering, Universiti Teknologi MARA, 40450 Shah Alam, Selangor, Malaysia

[2]Integrated Separation Technology Research Group (i-STRonG), Faculty of Chemical Engineering, Universiti Teknologi MARA, 40450 Shah Alam, Selangor, Malaysia

[3]PERMATA Insan College, Universiti Sains Islam Malaysia, 71800 Nilai, Negeri Sembilan, Malaysia

[4]Faculty of Chemical and Energy Engineering, Universiti Teknologi Malaysia, 81310 Johor Bahru, Johor Malaysia

[5]Department of Chemical Engineering, Faculty of Engineering, Ahmadu Bello University, 810211 Zaria, Nigeria

[a]najeehah30@gmail.com, [b]fatinafify83@gmail.com, [c]ashraf.azmi@uitm.edu.my, [d]azan@usim.edu.my, [e]ahmadilyas@utm.my, [f]ymsani@abu.edu.ng, [g]iyliaidris@uitm.edu.my

Keywords: Adsorption, Clinoptilolite, Congo Red, Cetyltrimethylammonium Bromide, Modification

Abstract. The increasing volume of wastewater generated from growing industrial activities has raised serious environmental concerns. Among the hazardous components present in wastewater, synthetic dyes such as Congo Red (CR) are particularly harmful to the environment. This research assessed the adsorption efficacy of Cetyltrimethylammonium Bromide (CTAB)-modified powdered clinoptilolite for removing CR. Among the various treatment methods, adsorption is widely recognized as one of the most effective techniques for dye removal. Powdered clinoptilolite was selected over other zeolite forms due to its higher surface area and better dispersion in aqueous solutions. However, its adsorption performance can be further enhanced through CTAB modification, which increases surface functionality and improves affinity toward target pollutants. This study aims to improve the adsorption capacity of natural clinoptilolite through surface modification and to evaluate its performance under different parameters. Characterization using Fourier Transform Infrared Spectroscopy (FTIR) and Scanning Electron Microscopy (SEM) confirmed the presence of functional groups and the surface morphology of the clinoptilolite powder. The optimal CR concentration was found to be 40 mg/L for both modified and natural clinoptilolite, achieving maximum adsorption capacities of 50.60 mg/g and 17.17 mg/g, respectively. The findings confirm the enhanced performance of CTAB-modified powdered clinoptilolite as a promising adsorbent for effective dye removal in wastewater treatment.

Introduction

Global environmental contamination by coloured, acidic, and metalliferous effluents has been an increasing concern [1]. Organic compounds are frequently used for colouring items in several industries, including plastics, textiles, cosmetics, rubber, and paper. The chemical structures of waste products and dyes emitted by these industries exhibit resistance to degradation and pose challenges for treatment using conventional approaches. Consequently, discharging such effluents

Content from this work may be used under the terms of the Creative Commons Attribution 3.0 license. Any further distribution of this work must maintain attribution to the author(s) and the title of the work, journal citation and DOI. Published under license by Materials Research Forum LLC.

into aquatic environments is highly dangerous [2]. Their discharge into the hydrosphere presents considerable environmental hazards, imparting undesirable colouration to the receiving water bodies and blocking sunlight penetration, which restricts photosynthetic processes and elevates organic matter levels in the water, consequently disrupting aquatic ecosystems [3].

CR is a commonly utilised industrial azo dye. Discovered by Paul Bottinger in 1884, it possesses two azo (–N=N–) chromophores and acidic auxochromes ($–SO_3H$) attached to benzene moieties [4]. Upon cleavage of the azo groups, the dye colourant may decompose into benzidine. Table 1 shows physiochemical properties of CR and Fig.1 illustrate CR's molecular structure.

Table 1. Physicochemical properties of CR [5].

Properties	Values/Parameters
Molecular formula	$C_{32}H_{22}N_6Na_2O_6S_2$
Molecular Weight	696.68 g/mol
pH	6.7
λ_{max}	497 nm

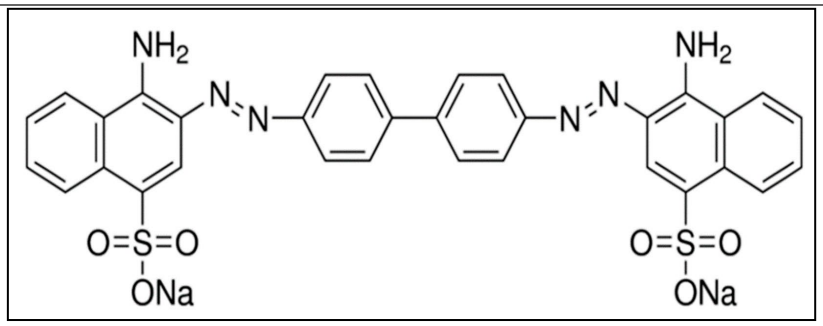


Fig. 1. Molecular structure of CR [6].

Currently, several conventional and advanced treatment methodologies have been documented in the literature, with several having been industrially adopted for the treatment of this category of effluent, including biodegradation, coagulation-flocculation, electro-coagulation, membrane filtration, ion-exchange resin, fenton oxidation, ozonation, photocatalysis, and adsorption [7]. However, certain methods exhibit constraints regarding bacterial growth suppression, sludge generation, applicability to various colours, limited operational lifespan, elevated costs, sluggish kinetics, and byproduct formation [3].

Clinoptilolite is among the most common natural varieties of zeolites. Key characteristics of clinoptilolite include its comparatively inexpensive cost and porous structure. Clinoptilolite can be modified by several approaches to establish or enhance new conditions, including enhancing adsorption capacity [8]. Powdered clinoptilolite was used in this study rather than granules or pellets due to its high surface area to volume ratio, increased dispersion in solution and surface availability of active adsorption sites, which enhances adsorption capacity [9]. To improve its efficiency even more, clinoptilolite was functionalized with CTAB a quaternary ammonium cationic surfactant. The cationic surfactant CTAB modification creates a surface with hydrophobic and electrostatic binding sites with the clinoptilolite that enhance its binding to anionic dyes like CR adsorbent [10]. This paper discussed the modification of clinoptilolite and its effect on adsorption performance such as initial dye concentration. Powdered modified clinoptilolite using CTAB was characterized using various characterization tools such as FTIR and SEM. The adsorption capacity,(q_e) and percentage removal efficiency of CR (%), were determined to identify the efficiency of adsorbent.

Materials and Methods

Natural clinoptilolite in its granular form was processed into a fine powder supplied from ACME Chemicals Pte Ltd. CR was purchased from Chemiz (M) Sdn. Bhd. and CTAB was supplied by R&M Chemicals. 1000 mL stock solution of CR was prepared by dissolving 0.1 g of CR in distilled water.

Preparation of Clinoptilolite Powder

The granular clinoptilolite was washed with distilled water to remove impurities and then dried in an oven at 110°C for 24 h. The dried material was ground into a fine powder using a Fritsch Pulverisette 6 ball mill. The milling process was carried out at 550 rpm for 20 minutes to achieve uniform particle size. The resulting powder exhibited an average particle size of approximately ±0.42 μm, as measured using a Zetasizer Nano ZS90.

Preparation of Powdered Modified Clinoptilolite

A CTAB solution was prepared at a specific between 0.05 mM and 5.0 mM. 2 grams of powdered clinoptilolite was added to the CTAB solution and stirred continuously using a rotary shaker for 24 hours at 120 rpm at room temperature to allow surface modification via cation exchange. Afterward, the modified clinoptilolite was separated by filtration, washed several times with distilled water to remove unbound CTAB, and dried at 100°C for 24 hours. The resulting CTAB-modified powdered clinoptilolite was stored in airtight containers for subsequent characterization and adsorption experiments.

Preparation of Calibration Curve

A calibration curve for CR was prepared to determine its concentration in solution using UV-Vis's spectrophotometry. A stock solution of Congo Red dye at 100 mg/L was first prepared by dissolving an accurately weighed amount of the dye in distilled water. From this stock solution, serial dilutions were performed to obtain standard concentrations of 10-50 mg/L. Each diluted solution was analyzed for absorbance at the maximum wavelength (λ_{max}) of Congo Red, determined to be 495 nm, using a UV-Vis spectrophotometer (Agilent Cary 60). The spectrophotometer was calibrated with distilled water as a blank before measurements. The absorbance values obtained for each concentration were plotted to generate a standard curve, which was linear within the tested range. This curve was subsequently used to quantify the concentration of CR in experimental solutions by interpolating the absorbance values.

Characterization of Clinoptilolite Powder

The powdered clinoptilolite was characterized using a FTIR spectrophotometer to investigate the functional group of natural clinoptilolite by using an Agilent Cary 630 spectrometer equipped with a diamond ATR (Attenuated Total Reflectance) crystal, covering a frequency range of 650–4000 cm^{-1}. Surface morphology, including porosity and particle aggregation before and after modification, was observed using a JEOL scanning electron microscope (SEM, Model JSM-5910). The SEM was operated at an accelerating voltage of 15–20 kV and a current of 10–20 μA, enabling high-resolution imaging of surface features.

Adsorption Studies

A batch experiments were carried out in a 250 mL Erlenmeyer flask, and the sample was placed in a shaker with a constant speed of 120 rpm at room temperature (25°C± 1°C). To evaluate the effect of initial dye concentration on adsorption, CR solutions of 10, 20, 30, 40, and 50 mg/L were prepared and agitated with 0.5 g of powdered clinoptilolite in 100 mL of solution. The flasks were shaken in an orbital incubator at 25°C and 120 rpm for 60 minutes. After filtration, the residual dye concentrations were measured using a UV-Vis spectrophotometer (Agilent Cary 60) at 495 nm, and the percentage removal and adsorption capacity, (q_e) were calculated by Eq. 1 and Eq. 2, respectively.

$$\mathbf{R}\ (\%) = \frac{\mathbf{C_O - C_e}}{\mathbf{C_o}} \times \mathbf{100} \quad (1)$$

$$q_e(\%) = \frac{C_O - C_e}{m} \times V \quad (2)$$

where C_o and C_e are the initial and final equilibrium concentrations of CR (mg/L) respectively, m is the weight of the adsorbent (mg) and V is the volume of the CR (L) [11].

Results and Discussion

Preparation of Calibration Curve

Calibration curve for CR was established using UV-Vis spectrophotometry to quantify dye concentration in adsorption samples. Known concentrations of Congo red were prepared in the range of 10 to 50 mg/L, and their absorbance at 495 nm (λ_{max}) was recorded. Standard concentration and absorbance outcomes were related linearly, as expected in the Beer-Lambert Law, and a linear regression equation was determined using plotted data in Fig. 2. The high correlation coefficient ($R^2 > 0.99$) confirmed the accuracy of the curve, which was then used to determine unknown concentrations in treated samples and evaluate the removal efficiency of the modified clinoptilolite powder.

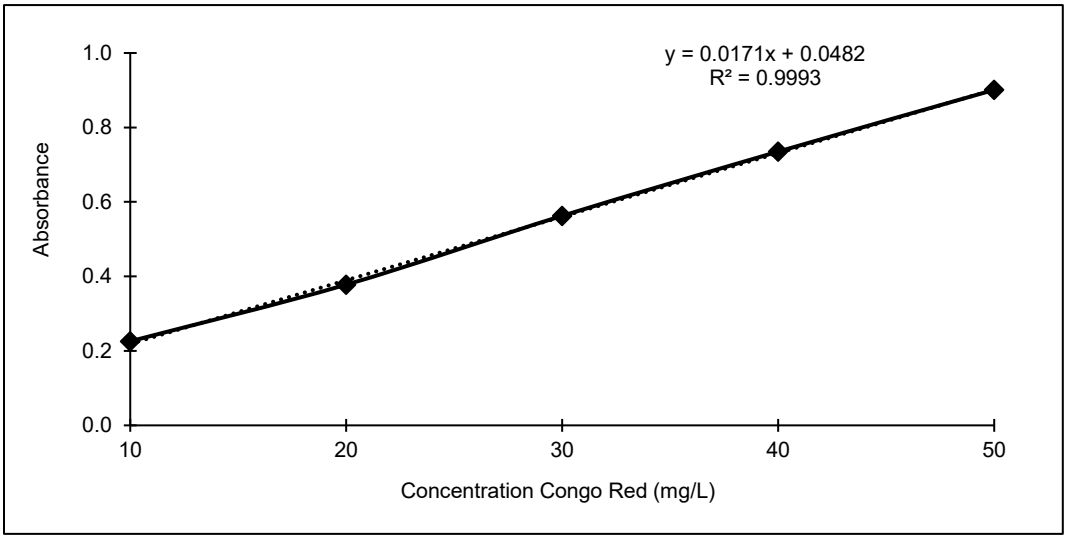


Fig. 2. Standard curve.

Characterizations

The FTIR spectrum in Fig. 3 displays several characteristic peaks for both modified and natural clinoptilolite respectively, which correspond to the stretching and bending vibrations of chemical bonds within the zeolite framework and surfactant modification. A broad band around 3410–3586 cm^{-1} in both samples corresponds to O–H stretching vibrations from adsorbed water and internal hydroxyl groups [12]. The peak around 1626-1627cm^{-1} is attributed to H–O–H bending vibrations of molecular water [13]. A strong peak near 998–1002 cm^{-1}confirms the presence of Si–O and Al–O asymmetric stretching vibrations within the tetrahedral framework, indicating the preservation of the clinoptilolite structure. Additional peaks around 798, 778, and 694 cm^{-1} represent symmetric Si–O/Al–O stretching and bending vibrations, while the band at 424 cm^{-1} and 427 cm^{-1} for modified and natural clinoptilolite respectively corresponds to asymmetric T–O vibrations (T = Fe, Ti, Mg), further validating the presence of the aluminosilicate network [14]. The similarity in both spectra suggests that CTAB modification primarily altered surface properties without disrupting the core structure of the clinoptilolite.

SEM images illustating the surface morphology of modified and natural clinoptilolite are presented in Fig.4. Fig.4a reveals porous networks and intergranular voids, and these are instrumental in increasing dye diffusion within the interior channels. Fig. 4b shows finer textural

features, such as microchannels and fissures, becoming more apparent. These structures contribute to an increased number of active sites for both physical adsorption and ion-exchange processes.

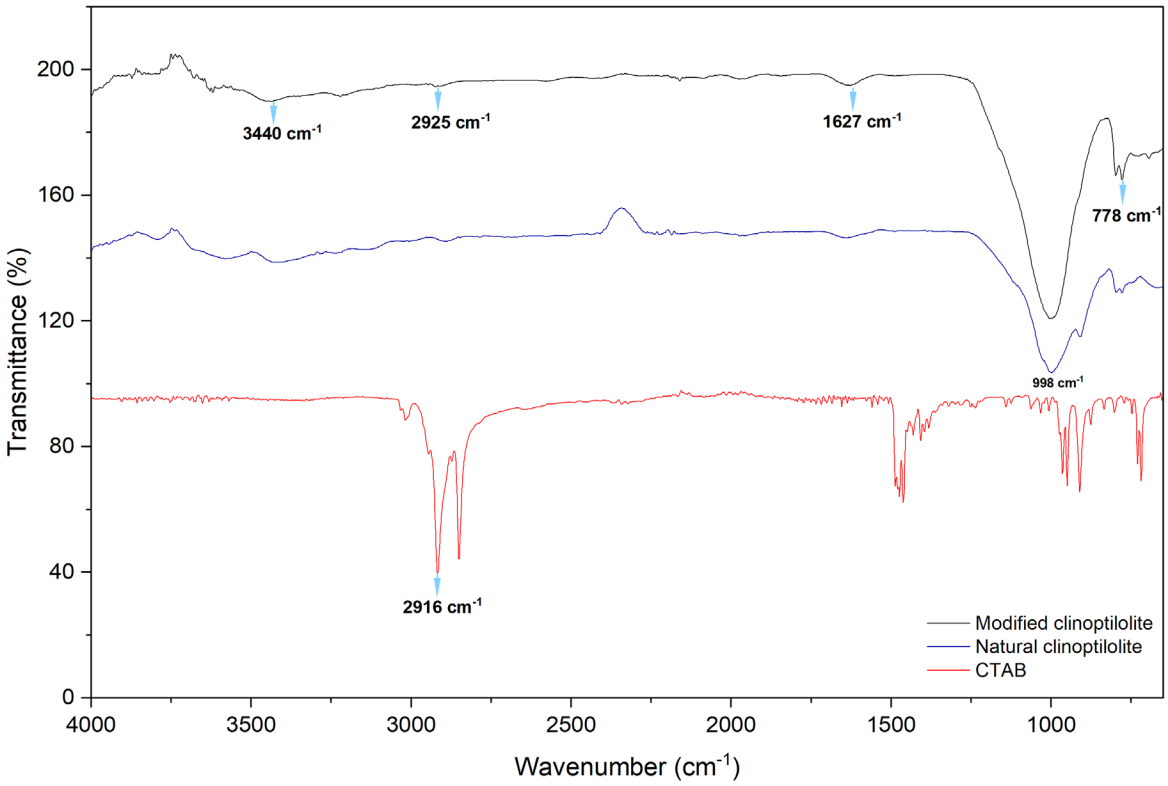


Fig. 3. FTIR spectra of CTAB, natural and modified clinoptilolite.

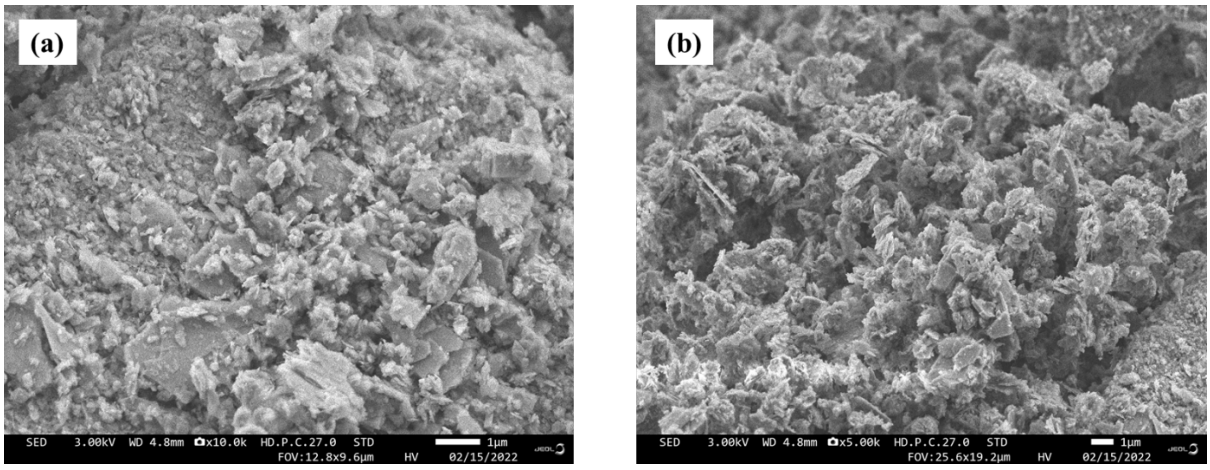


Fig. 4. SEM images of (a) modified clinoptilolite and (b) natural clinoptilolite.

Adsorption Studies

Fig. 5a shows the percentage removal of CR at different initial concentrations of the dye (10-50 mg/L). The modified clinoptilolite consistently exhibited significantly higher removal efficiency compared to the natural form. When the concentration of the dye was 10 mg/L-40 mg/L, the modified clinoptilolite improved the removal of about 78.89 to 94.20% due to the increase of the mass transfer driving force and the CR molecules to interact with the active sites of the modified adsorbent [15]. Conversely, natural clinoptilolite increased the removal efficiency by a small percentage, approximately 20.45% to 31.98%, showing its low adsorption ability without facing any modification. However, when the initial dye concentration was further increased to 50

mg/L, the percentage removal decreased slightly to 74.48% for the modified clinoptilolite and 23.63% for the natural clinoptilolite. This decline can be attributed to the progressive saturation of available adsorption sites, whereby the number of CR molecules exceeds the accessible active sites on the adsorbent surface, thereby reducing adsorption efficiency. Similar behavior has been reported in previous CR adsorption studies [6],[16]. Compared to other studies, the CTAB-modified clinoptilolite in this work demonstrates higher removal performance. For example, [17] reported a maximum CR removal of only 84.05% using activated carbon derived from *Spathodea campanulata* flowers at an initial concentration of 20 mg/L, and [18] achieved a removal of just 81.3% using modified bagasse fly ash at 100mg/L. These values are noticeably lower than the 94.20% of percentage removal achieved at 40mg/L, indicating the stronger affinity and better surface accessibility of the CTAB-modified powder used in this study.

The results of the adsorption capacity (q_e) of the CTAB-modified clinoptilolite are also displayed in Fig. 5b. After 10 mg/L initial CR concentration, there was a significant increase in q_e values of from 11.04 mg/g to 50.60 mg/g at 40 mg/L, indicating greater availability of CR molecules for interaction with the adsorbent surface and a stronger concentration gradient that enhanced mass transfer and utilization of active sites. Similar trends have been reported for CR adsorption onto various modified adsorbents [19], [20]. The very small decrease in q_e at 50 mg/L (49.90 mg/g) is probably due to the active sites on the surface being saturated and no more dye can be loaded onto the active site [5] Meanwhile, the natural clinoptilolite has significantly lower adsorption capacities, ranging from 2.86 to 17.17 mg/g. The slight decrease in adsorption capacity at concentrations above 40 mg/L for both adsorbents can be attributed to site saturation when the ratio of dye molecules to available adsorption sites reaches the maximum, thus plateauing or decreasing q_e values slightly [19].

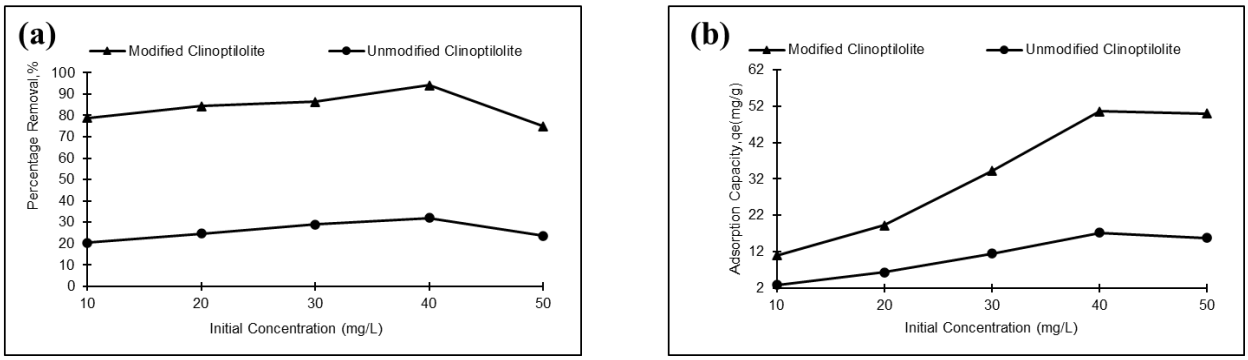


Fig. 5. Effect of initial CR concentration for modified and natural clinoptilolite (a) CR percentage removal and (b) adsorption capacity.

Conclusion

This study successfully demonstrated that CTAB modified powdered clinoptilolite exhibits significantly enhanced adsorption performance for the removal of CR dye from aqueous solutions due to the increased surface area, pore structure, and electrostatic affinity introduced by CTAB functionalization. Characterization with FTIR and SEM revealed the successful surface modification. Adsorption studies demonstrated that the most effective removal efficiency (94.20%) and adsorption capacity (50.60 mg/g) were achieved at a concentration of 40 mg/L for modified clinoptilolite. The study also found that the modified clinoptilolite outperformed the natural form in all investigated parameters, particularly in terms of equilibrium time, dye uptake, and resistance to site saturation. These findings support the use of CTAB modified clinoptilolite as a highly efficient, low-cost, and environmentally friendly adsorbent for wastewater treatment applications.

Acknowledgement
The authors gratefully acknowledge the financial support received from the Strategic International Research Grant SRP) under the Universiti Teknologi MARA through project UiTM.800-3/1 SRP INT (005/2025). This funding was essential in facilitating the successful completion of this research. The authors also wish to express their sincere appreciation to the Faculty of Chemical Engineering, Universiti Teknologi MARA (UiTM) and the Halal Laboratory, Kolej Permata Insan (KPI), Universiti Sains Islam Malaysia (USIM) for providing the necessary research facilities, technical assistance, and continuous institutional support throughout the project's duration.

References

[1] V. Masindi, S. Foteinis, and E. Chatzisymeon, Co-treatment of acid mine drainage and municipal wastewater effluents: Emphasis on the fate and partitioning of chemical contaminants, J. Hazard. Mater. 421 (2022). 126677. https://doi.org/10.1016/j.jhazmat.2021.126677

[2] T. Al-dahri, A. A. AbdulRazak, and S. Rohani, Preparation and characterization of Linde-type A zeolite (LTA) from coal fly ash by microwave-assisted synthesis method: Its application as adsorbent for removal of anionic dyes, Int. J. Coal Prep.Util. 42 (2022), 2064–2077. https://doi.org/10.1080/19392699.2020.1792456

[3] A. Imessaoudene et al., Adsorption performance of zeolite for the removal of Congo Red dye: Factorial design experiments, kinetic, and equilibrium studies," Separations 10 (2023) 57. https://doi.org/10.3390/separations10010057

[4] O. T. S. Altaie, H. Zeidan, N. Karakaya, M. Karakaya, and M. E. Marti, Removal of Congo Red from aqueous solutions by adsorption onto illite clay, Desalin. *Water Treat.* 310 (2023) 226–237. https://doi.org/10.5004/dwt.2023.29941

[5] M. M. Abou Alsoaud, M. A. Taher, A. M. Hamed, M. S. Elnouby, and A. M. Omer, Reusable kaolin impregnated aminated chitosan composite beads for efficient removal of Congo Red dye: Isotherms, kinetics and thermodynamics studies, Sci. Rep. 12 (2022) 12972. https://doi.org/10.1038/s41598-022-17305-w

[6] M. Harja, G. Buema, and D. Bucur, Recent advances in removal of Congo Red dye by adsorption using an industrial waste, Sci. Rep. 12 (2022) 6087. https://doi.org/10.1038/s41598-022-10093-3

[7] A. Hadadi, A. Imessaoudene, J. C. Bollinger, A. A. Assadi, A. Amrane, and L. Mouni, Comparison of four plant-based bio-coagulants performances against alum and ferric chloride in the turbidity improvement of bentonite synthetic water, Water 14 (2022) 3324. https://doi.org/10.3390/w14203324

[8] A. Badeenezhad, A. Azhdarpoor, S. Bahrami, and S. Yousefinejad, Removal of methylene blue dye from aqueous solutions by natural clinoptilolite and clinoptilolite modified by iron oxide nanoparticles, Mol. Simul. 45 (2019) 564–571. https://doi.org/10.1080/08927022.2018.1564077

[9] L. Velarde, M. S. Nabavi, E. Escalera, M. L. Antti, and F. Akhtar, Adsorption of heavy metals on natural zeolites: A review, Chemosphere 338 (2023) 138508. https://doi.org/10.1016/j.chemosphere.2023.138508

[10] M. M. Trojeni, A. Samadi-Maybodi, and H. Shafiei, Investigating the adsorption of volatile organic compounds from kerosene using clinoptilolite (natural zeolite) modified by cationic surfactant cetyltrimethylammonium bromide, MethodsX 14 (2025) 103354. https://doi.org/10.1016/j.mex.2025.103354

[11] M. A. Tamar Jaya et al., Recent advances in methylene blue adsorption using clinoptilolite: Mechanisms, modifications, and future perspectives, IOP Conf. Ser.: Earth Environ. Sci. 1516 (2025) 012014. https://doi.org/10.1088/1755-1315/1516/1/012014

[12] H. Cao et al., High-efficiency adsorption removal of CR and MG dyes using AlOOH fibers embedded with porous CoFe2O4 nanoparticles, Environ. Res. 216 (2023) 114730. https://doi.org/10.1016/j.envres.2022.114730

[13] A. Grouli, A. Chraka, Y. Bachra, M. Elkouali, S. Chtita, and M. Berrada, An investigation of the adsorption of Congo Red dye on two naturally occurring adsorbents hydroxyapatite and bentonite: An experimental analysis, DFT calculations, and Monte Carlo simulation, Heliyon, 10 (2024) e39884. https://doi.org/10.1016/j.heliyon.2024.e39884

[14] R. Nodehi, H. Shayesteh, and A. R. Kelishami, Enhanced adsorption of Congo Red using cationic surfactant functionalized zeolite particles, Microchem. J. 153 (2020) 104281. https://doi.org/10.1016/j.microc.2019.104281

[15] I. H. Khalaf, F. T. Al-Sudani, A. A. AbdulRazak, T. Aldahri, and S. Rohani, Optimization of Congo Red dye adsorption from wastewater by a modified commercial zeolite catalyst using response surface modeling approach, Water Sci. and Technol. 83 (2021) 1369–1383. https://doi.org/10.2166/wst.2021.078

[16] M. A. Adebayo, J. M. Jabar, J. S. Amoko, E. O. Openiyi, and O. O. Shodiya, Coconut husk-raw clay-Fe composite: preparation, characteristics and mechanisms of Congo red adsorption, Sci. Rep.12 (2022) 14370. https://doi.org/10.1038/s41598-022-18763-y

[17] S. Sudarsan, G. Murugesan, T. Varadavenkatesan, R. Vinayagam, and R. Selvaraj, Efficient adsorptive removal of Congo Red dye using activated carbon derived from *Spathodea campanulata* flowers, Sci. Rep. 15 (2025) 86032. https://doi.org/10.1038/s41598-025-86032-9

[18] A. Gebre Meskel, M. M. Kwikima, B. T. Meshesha, N. G. Habtu, S. V. C. S. Naik, and B. P. Vellanki, Malachite green and methylene blue dye removal using modified bagasse fly ash: Adsorption optimization studies, Environ. Chall. 14 (2024) 100829. https://doi.org/10.1016/j.envc.2023.100829

[19] N. Semwal, D. Mahar, M. Chatti, A. Dandapat, and M. Chandra Arya, Adsorptive removal of Congo Red dye from its aqueous solution by Ag–Cu–CeO2 nanocomposites: Adsorption kinetics, isotherms, and thermodynamics, Heliyo 9 (2023) e22027. https://doi.org/10.1016/j.heliyon.2023.e22027

[20] M. M. Jegede, O. S. Durowoju, and J. N. Edokpayi, Sequestration of Congo Red from aqueous solution using raw and citric acid-modified Dicerocaryum eriocarpum biomass: isotherm, kinetics and thermodynamics, Appl. Water Sci. 14 (2024) 59. https://doi.org/0.1007/s13201-024-02114-5

Materials Research Proceedings 74 (2026) 40-47 https://doi.org/10.21741/9781644904473-6

Simulation-Based Consequence Assessment of Ethylene Leakage from High-Pressure Primary Compressor Feed Line in Low-Density Polyethylene Production

Anis Farina MANSOR[1], Arina SAUKI[1], Iylia IDRIS[1], Dinie MUHAMMAD[2], Rushdan Ahmad ILYAS[2], Fakhrony Sholahudin ROHMAN[3], Abdul Aziz HAIRUDDIN[4] and Ashraf AZMI[1,a *]

[1]Faculty of Chemical Engineering, Universiti Teknologi MARA, 40450, Shah Alam Selangor, Malaysia

[2]School of Chemical and Energy Engineering, Faculty of Engineering, Universiti Teknologi Malaysia (UTM), Johor Bahru, Johor 81310, Malaysia

[3]Faculty of Engineering, Universiti Malaysia Sabah, Jalan UMS, 88450, Kota Kinabalu, Sabah, Malaysia

[4]Department of Mechanical and Manufacturing Engineering, Faculty of Engineering, Universiti Putra Malaysia, 43400 UPM Serdang, Selangor, Malaysia

[a]ashraf.azmi@uitm.edu.my

Keywords: Ethylene Leakage, Primary Compressor Feed Line, High-Pressure Tubular Reactor, ALOHA Modeling, consequence assessment

Abstract. Ethylene is a highly flammable feedstock used in low-density polyethylene (LDPE) production, and pressurized transfer systems present important safety concerns. This study evaluates accidental ethylene release from the primary compressor feed line in an LDPE process using Areal Locations of Hazardous Atmospheres (ALOHA) to estimate dispersion, flammable cloud extent, overpressure, and thermal radiation under representative operating scenarios. Leak diameters of 10 mm and 25 mm were analyzed at 200, 250, and 300 bar to represent small-to-moderate loss-of-containment cases in the compressor feed line. The results show that increasing pressure generally enlarges the hazardous zones, with the 10 mm leak at 300 bar producing a flammable threat distance of 117 m downwind. Although ALOHA is a consequence-modeling tool rather than a full risk model, the analysis provides a practical screening-level assessment of hazard severity for compressor feed-line releases in LDPE service.

Introduction

Ethylene is one of the most important industrial olefins and a key raw material in LDPE production. Ethylene is a colourless, flammable gas with a faintly sweet odour that is present at ambient temperature [1]. The production of LDPE involves several key steps: compressing ethylene gas, carrying out high-pressure polymerization, separating unused gas, shaping the melted polymer, and finally storing and packaging the product [2]. Before polymerization, ethylene is compressed to very high pressures. The reaction then takes place under strict conditions, with high temperatures and pressures, while initiators are added continuously to keep the process going [3]. Ethylene is compressed to extremely high pressures to help form LDPE's branched structure [4]. In high-pressure LDPE plants, ethylene must be compressed before entering the polymerization section, and any loss of containment in the pressurized transfer system can create serious fire and explosion hazards. As ethylene is highly flammable and can disperse rapidly after release, consequence modeling is useful for supporting safety screening and emergency planning.

The LDPE process commonly uses a two-stage compression arrangement consisting of a primary compressor and a hyper compressor [2]. The primary compressor raises the fresh and

Content from this work may be used under the terms of the Creative Commons Attribution 3.0 license. Any further distribution of this work must maintain attribution to the author(s) and the title of the work, journal citation and DOI. Published under license by Materials Research Forum LLC.

recycle ethylene stream to an intermediate pressure range of about 200-300 bar, while the hyper compressor provides the much higher pressure ranging from 2,000 to 3,000 bar required for polymerization [3],[4],[5]. In order to provide effective downstream compression by the hyper compressor and create ideal conditions for the polymerization process, the primary compressor plays a crucial role in raising the ethylene supply pressure to an intermediate level. Therefore, the effectiveness, stability, and continuity of the LDPE production process depend heavily on the performance and dependability of the primary compressor [6].

This paper presents a consequence-based assessment of accidental ethylene release from the primary compressor feed line in an LDPE facility. The objective is to estimate hazard distances associated with dispersion, flammable vapor cloud formation, overpressure, and thermal radiation under representative operating conditions. Leak sizes of 10 mm and 25 mm were selected to represent small-to-moderate loss-of-containment scenarios, and operating pressures of 200, 250, and 300 bar were examined to evaluate how consequence severity changes with pressure. The results are intended to support early-stage hazard screening, not full quantitative risk assessment.

This study addresses that gap by evaluating ethylene release from the primary compressor feed line of an LDPE plant rather than from the downstream polymerization section. The main novelty is not the use of ALOHA itself, but the application of a consequence-based screening framework to a specific high-pressure ethylene transfer line that is operationally important, relatively underreported in the literature, and directly relevant to early-stage hazard identification in LDPE production. In addition, the study compares two leak sizes across multiple operating pressures to identify which scenario governs different hazard types, and it links the modeled consequence envelopes to practical emergency-planning implications for on-site and near-boundary areas.

ALOHA, developed by NOAA and EPA, is widely used to estimate the extent of hazardous atmospheres resulting from accidental chemical releases. It is particularly useful for rapid consequence analysis of toxic dispersion, flammable cloud spread, thermal radiation, and vapor cloud explosion effects [7]. In this study, ALOHA was selected because it provides a practical way to examine the consequences of ethylene releases using available process and meteorological data. However, it should be emphasized that this work evaluates consequence severity only; it does not include event frequency, ignition probability, or complete risk quantification.

The scientific contribution of this study lies in applying a standard consequence model to a specific LDPE compressor feed-line scenario and showing how leak size and operating pressure influence the resulting hazard distances. Although ALOHA has been applied widely to natural gas and other hydrocarbon releases, fewer studies have addressed ethylene in the context of LDPE production. This makes the present work useful as a screening-level reference for process safety analysis in high-pressure ethylene systems.

Previous Studies Using ALOHA for Consequence Assessment

ALOHA is widely recognized in chemical process safety due to its reliability, ease of use, and practical application. It is commonly used in quantitative risk assessments (QRA) for hazardous gas dispersion in both academic research and industrial practice [8]. Multiple studies have confirmed ALOHA's efficacy in predicting the impact zones of accidental chemical releases, thereby endorsing its incorporation into emergency response planning and land-use policy decisions. The application encompasses a range of chemicals across various release scenarios [9], [10], [11], [12], [13],[14]. The ability of ALOHA to integrate real-time meteorological and chemical input data significantly increases its utility as a decision-support tool in risk assessment and emergency management in industrial settings.

So far, no published studies have specifically examined ethylene gas leaks in LDPE production using ALOHA. However, studies on similar chemicals show that ALOHA is a reliable tool for modeling gas dispersion. Although direct research on ethylene is limited, existing studies and technical references support the use of ALOHA for this type of analysis.

Shao and Duan [15] analyzed accident scenarios involving natural gas leaks from pipelines at a power plant using the ALOHA model to evaluate risks to nearby residents. They simulated three leak sizes 100 mm, 200 mm, and 1200 mm to assess both individual and societal risks. The results showed that in all scenarios, the risk levels exceeded acceptable safety limits, indicating that such incidents would be considered unsafe without additional mitigation measures.

Zhu et al. [13] studied hazard distances from natural gas pipeline incidents using the ALOHA model, focusing on four main risks: suffocation, flammable vapor clouds, overpressure, and thermal radiation. The study also examined how environmental conditions and pipeline characteristics affect the spread of these hazards. The results showed that flammable vapor clouds posed the greatest risk, reaching distances of about 530 meters. This was followed by overpressure effects at 417 meters and suffocation risks at 135 meters. These findings highlight the need to consider multiple hazard types, with flammable gas dispersion playing a major role in determining the overall danger zone.

Khalid et al. [11] combined the ALOHA modeling tool with a quantitative risk assessment (QRA) methodology to analyze the potential effects of jet fires resulting from natural gas leaks in pipeline systems at a natural gas power plant. The analysis indicated that increases in both leak size and operating pressure significantly heightened the severity of fire-related consequences. In contrast, increased pipeline temperatures correlated with a decrease in the intensity of the outcomes. Variations in wind speed demonstrated a negligible impact on the intensity of jet fire incidents. The insights provided improve the comprehension of essential parameters that influence fire hazards within pressurized pipeline infrastructure.

Besiktas et al. [10] used the ALOHA model to study how pipeline characteristics and weather conditions affect thermal radiation distances from jet fire incidents. The research focused on a natural gas pipeline release scenario in Istanbul, Türkiye. The results showed that pipeline geometry, especially its length and diameter, strongly influences the size of thermal hazard zones. In addition, environmental factors such as wind speed, temperature, and humidity were found to significantly affect gas dispersion and the resulting threat distances. The findings collectively support ALOHA's credibility in ethylene dispersion modeling, even with the limited volume of ethylene-specific empirical research available.

Materials and Methods

This study assessed the consequence severity of ethylene release from the primary compressor feed line in an LDPE facility. ALOHA was used to model gas dispersion, flammable vapor cloud extent, overpressure from a potential vapor cloud explosion, and thermal radiation from a possible jet fire. The analysis considered two leak diameters, 10 mm and 25 mm, at three operating pressures: 200, 250, and 300 bar.

The selected leak diameters represent screening-level loss-of-containment openings in the compressor feed line rather than a specific flange, gasket, or rupture failure. The 10 mm leak was treated as a small release case, while the 25 mm leak represented a moderate opening consistent with a more severe but still credible incident scenario. The selection of these diameters is guided by internationally recognized risk assessment frameworks, API Recommended Practice 581 (API RP 581). API RP 581 classifies standard leak sizes for pipelines and pressure vessels to reflect the range of potential incident scenarios. It categorizes "small" leaks as approximately 6.4 mm (¼ inch), "medium" leaks as roughly 25.4 mm (1 inch), and "large" leaks as 101.6 mm (4 inches) in diameter [18]. These cases were selected to compare how release size influences hazardous distances under high-pressure ethylene service.

The simulated source was the ethylene transfer pipeline connected to the primary compressor. The line was modeled with an internal diameter of 7 cm and a length of 160 m, representing the actual feed line used in the process layout. The release was modeled as a single leak point on the line, with the remaining system treated as sealed for consequence calculation purposes. Because

the study was designed for consequence screening, the pressure range analyzed was limited to the primary compressor operating conditions rather than the much higher pressure of the hyper compressor.

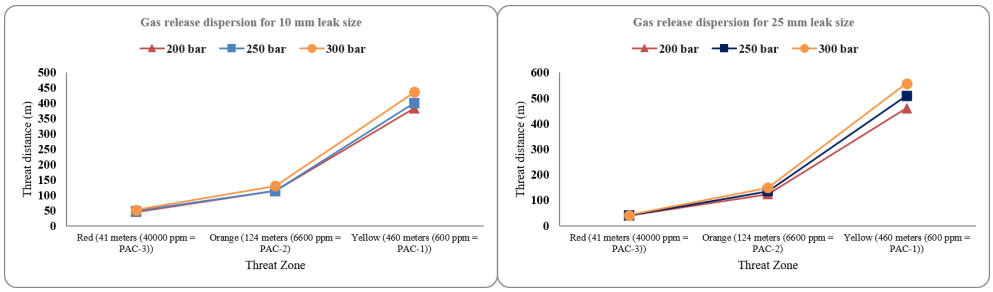
Ethylene was specified as the released chemical, with an operating temperature of 90 °C. The meteorological case was based on conditions representative of the Kerteh industrial area, namely wind speed 3.58 m/s, ambient temperature 26 °C, atmospheric stability class E, no inversion, and 50% relative humidity. These conditions were selected as a representative stable scenario for dispersion screening, while recognizing that hazard distances may vary under different weather conditions.

To improve reliability, the model inputs were based on the actual process layout, operating pressure range, ethylene properties, and representative meteorological conditions at the study site. The release scenarios were also cross-checked against standard loss-of-containment categories and literature-reported ALOHA applications for pressurized hydrocarbon releases. However, this work is a consequence simulation rather than an experimentally validated model, so the results should be interpreted as screening-level estimates of hazard extent. The selected pressures of 200–300 bar fall within the primary compressor operating range used in this study, but ALOHA is not intended for detailed modeling of hyper-compressor conditions at much higher pressures.

Results and Discussion

Consequence analysis

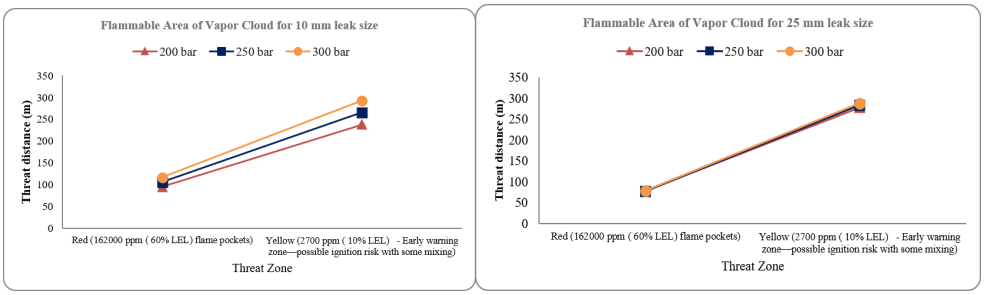
Figs. 1(a) and (b) show gas dispersion distances for 10 mm and 25 mm ethylene leaks at pressures of 200, 250, and 300 bar. The results indicate that dispersion distances increase with pressure for all hazard zones (red, orange, and yellow). The yellow zone (PAC-1) shows the largest extent, with an increase of about 53 m from 200 bar to 300 bar, indicating that low-concentration gas can travel significant distances under high pressure. Overall, the results confirm that higher operating pressure leads to wider and more severe dispersion hazards.



(a) (b)

Fig. 1. Gas dispersion distances at (a) 10 mm and (b) 25 mm leak sizes under three operating pressures: 200 bar, 250 bar, and 300 bar.

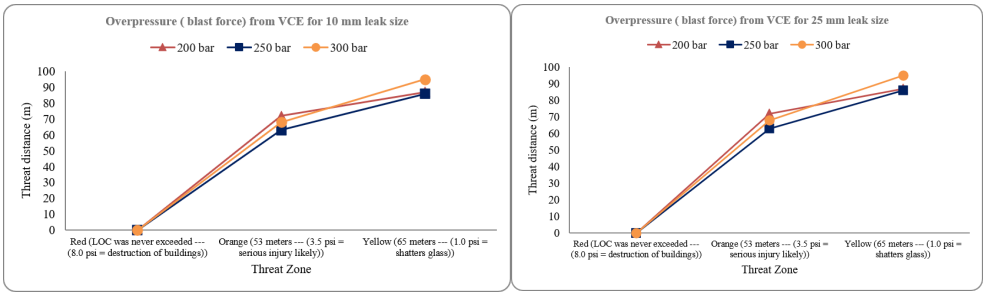
Figs 2(a) and (b) show different dispersion patterns for flammable vapor clouds from 10 mm and 25 mm leaks, highlighting the effect of leak size and pressure. For the 10 mm leak, the flammable area increases with pressure, with the red zone expanding from 95 m to 117 m. This indicates that higher pressure leads to greater dispersion distances and larger hazard zones due to sustained gas release and mixing. In contrast, the 25 mm leak shows minimal change with pressure, with the red zone remaining around 77–79 m. Despite the larger opening, the hazard distance is shorter than in the 10 mm case. Overall, the results show that dispersion behavior depends on both leak size and pressure, and different leak scenarios must be considered in high-pressure ethylene risk assessment.



(a) (b)

Fig. 2. Dispersion patterns for flammable areas of cloud vapor for (a) 10 mm and (b) 25 mm leak size.

Figs 3(a) and (b) show overpressure hazard distances for VCE scenarios at 10 mm and 25 mm leak sizes under pressures of 200, 250, and 300 bar. The zones are classified as Red (≥8.0 psi), Orange (≥3.5 psi), and Yellow (≥1.0 psi). The results show that the red zone was not reached in all cases, indicating no structural failure. The orange zone varies slightly with pressure but shows no clear trend, suggesting the influence of dispersion and gas concentration. In contrast, the yellow zone increases with pressure, indicating a wider impact area at higher pressures. Overall, blast effects are more significant in the lower overpressure range, with the largest impact observed in the yellow zone at 300 bar.



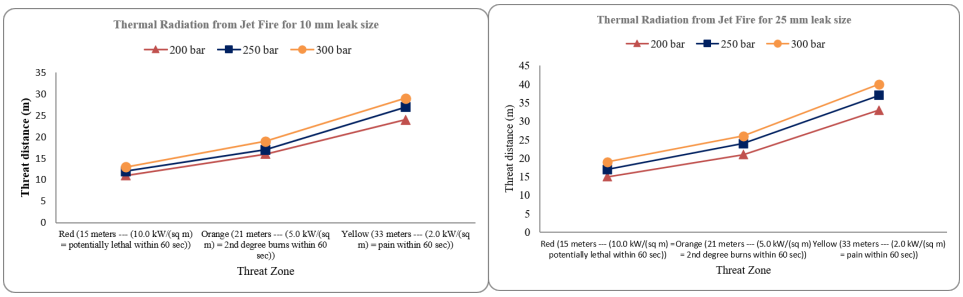
(a) (b)

Fig. 3. Overpressure threat distances associated with a vapor cloud explosion (VCE) scenario for a (a) 10 mm and (b) 25 mm leak.

Figs 4(a) and (b) show the thermal radiation hazard distances from jet fire events for ethylene leaks with sizes of 10 mm and 25 mm, at pressures of 200, 250, and 300 bar. The hazard zones are classified as: Red Zone (≥10.0 kW/m², potentially fatal within 60 seconds), Orange Zone (≥5.0 kW/m², causing second-degree burns), and Yellow Zone (≥2.0 kW/m², causing pain). For the 10 mm leak, thermal radiation distances increase with pressure, especially in the orange and yellow zones. This shows that even small leaks at high pressure can pose significant risks to nearby personnel. For the 25 mm leak, all hazard distances are larger compared to the 10 mm case due to higher flame intensity and longer flame length. This highlights the combined effect of larger leak size and higher pressure. Overall, increasing pressure leads to a larger hazard area for both leak sizes, with the most noticeable expansion in the yellow zone. This confirms that thermal radiation hazards increase with both leak size and pressure.

Figs 5(a) and (b) show ALOHA simulation results of flammable threat zones at 300 bar for 10 mm and 25 mm leaks, overlaid on a Google Earth image of the Kerteh industrial area. The red zone represents 60% of the Lower Explosive Limit (LEL), indicating potential flash fire risk, while the yellow zone defines the outer flammable boundary. For both leak sizes, the yellow zone extends beyond the facility boundary, crossing AH18 (Route 3) and approaching nearby off-site

areas. The dispersion pattern is elongated due to wind direction. The 10 mm leak produces a narrower but longer red zone, whereas the 25 mm leak shows a slightly larger and more concentrated red zone near the source. This indicates faster gas accumulation and higher ignition potential for the larger leak.



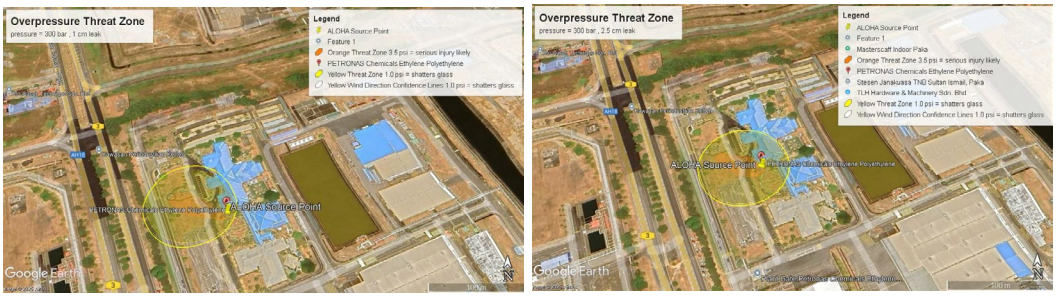
(a) (b)

Fig. 4. Thermal radiation threat distances associated with jet fire at (a) 10 mm and (b) 25 mm leak sizes.



(a) (b)

Fig. 5. Flammable threat zone for operating pressure (a) 300 bar, 10 mm leak (b) 300 bar, 25 mm leak.



(a) (b)

Fig. 6. Overpressure threat zone for operating pressure (a) 300 bar, 10 mm leak; (b) 300 bar, 25 mm leak.

Figs 6(a) and (b) show ALOHA simulation results of overpressure (blast) effects at 300 bar for 10 mm and 25 mm leaks. The orange zone (3.5 psi), associated with serious injury and structural damage, is concentrated near the release point, indicating that the highest risk is limited to areas close to the leak. The yellow zone (1.0 psi), which may cause minor damage such as glass breakage, extends over a wider area and may affect nearby structures and off-site locations. Both leak sizes show similar extents for the orange zone, largely confined within the plant boundary. However, the 10 mm leak produces a slightly larger yellow zone compared to the 25 mm leak. This is likely due to a longer release duration, allowing greater gas dispersion despite the smaller leak size.

Conclusions

The findings indicate that both leak size and operating pressure significantly influence the hazards of high-pressure ethylene releases. For 10 mm leaks, all hazard zones (red, orange, and yellow) increased consistently with pressure, showing a clear linear trend. In contrast, for 25 mm leaks, the red zone was less sensitive to pressure and remained shorter than in the 10 mm case due to rapid gas expansion and improved atmospheric mixing. Overpressure results showed that the red zone (8.0 psi) was not reached for either leak size. However, the orange (3.5 psi) and yellow (1.0 psi) zones expanded moderately as pressure increased. For instance, the yellow zone for a 10 mm leak grew from 87 to 95 meters between 200 and 300 bar, indicating a rising blast risk even for smaller leaks. In jet fire scenarios, thermal radiation distances increased with both pressure and leak size. The 25 mm leaks consistently produced larger hazard zones than the 10 mm leaks, with the yellow zone extending up to 40 meters at 300 bar. Overall, the yellow zones representing lower-intensity but more widespread hazards were the most sensitive to pressure changes. ALOHA is well suited for simulating accidental releases under typical industrial pressures, its validated operational pressure range is limited to approximately 600 atm. Consequently, it is not capable of analyzing gas leaks from hyper compressors operating at more than 2000 bar. For future studies, it is recommended to adopt Computational Fluid Dynamics (CFD) tools such as Ansys Fluent, OpenFOAM or PHAST which support detailed simulation under extremely high-pressure conditions. Overall, the results underscore the importance of controlling operating pressure, detecting leaks promptly, and establishing sufficient safety buffer zones to minimize the consequences of accidental releases in high-pressure ethylene systems.

Acknowledgement

The financial support received from the Faculty of Chemical Engineering, Universiti Teknologi MARA (UiTM) and Universiti Teknologi MARA (UiTM), through research grant no. 600-RMC/GIP 5/3 (025/2024) are greatly acknowledged.

References

[1] K.M. Sundaram, M.M. Shreehan, E.F. Olszewski, Ethylene, Kirk-Othmer Encyclopedia of Chemical Technology (2010) pp. 1–39.

[2] P.M.M.V. Erdeghem, F. Logist, M. Heughebaert, C. Dittrich, J.F. Van Impe, Conceptual modelling and optimization of jacketed tubular reactors for the production of LDPE, Proc. 9th Int. Symp. Dynamics and Control of Process Systems (DYCOPS 2010) (2010) 419–424.

[3] N.M. Supion, I. Idris, A.M. Som, F.S. Rahman, R.A. Ilyas, A. Azmi, Low-density polyethylene simulated production in high pressure tubular reactor, Materials Today Proceedings (2023). https://doi.org/10.1016/j.matpr.2022.12.155

[4] D. Stoiljkovic, B. Damjanovic, J. Djordjevic, D. Spehar, S. Jovanovic, Compressed ethylene phase states and their importance for the production of low-density polyethylene, Hem. Ind. 60 (2006) 283–286.

[5] A. Azmi, S.A. Sata, F.S. Rohman, N. Aziz, Dynamic Optimization of Low-Density Polyethylene Production in Tubular Reactor Under Thermal Safety Constraint, Chemical Industry and Chemical Engineering Quarterly 27 (2021) 85-97. https://doi.org/10.2298/CICEQ190108027A

[6] LDPE Production from Ethylene (High-Pressure Tubular Process) Report LDPE E11A. (2021). https://cdn.intratec.us/docs/reports/previews/ldpe-e11a-b.pdf. Intratec.

[7] NOAA (1999) and EPA. ALOHA 5.2.3 Online Help, Office of Response and Restoration of the National Oceanic and Atmospheric Administration (NOAA) and Chemical Emergency Preparedness and Prevention Office (CEPPO) of the U.S. Environmental (EPA), Seattle, WA.

[8] U.S. Department of Energy Office of Environment, Safety and Health. (2004). ALOHA Computer Code Application Guidance for Documented Safety Analysis (DOE-EH-4.2.1.3-ALOHA Code Guidance).

[9] A.J. Da Silva Rodrigues, M.H.L.F. Da Silva, D.O. De Farias, M.M. Teixeira, M.F. De Brito Rocha, G.B. Lins, R.A. D'Emery, J.F. Da Silva, J. Da Silva Correia Neto, Risk reliability analysis, resulting from explosions in petrochemical industries: A case study using Aloha software, 2022 17th Iberian Conference on Information Systems and Technologies (CISTI) (2017) 1–6. https://doi.org/10.23919/cisti.2017.7975733

[10] R. Besiktas, H. Baltaci, B.O. Akkoyunlu, Simulation of the jet fire using Atmospheric Dispersion Modeling (ALOHA): a case study of natural gas pipeline in Istanbul, Türkiye. Atmosphere 15 (2024) 456. https://doi.org/10.3390/atmos15040456

[11] N.A. Khalid, M.Z.M. Tohir, M.S.M. Said, Consequence Simulation of Jet Fire Due to Leakage of Pipelines in a Natural Gas Power Plant in Malaysia, Perintis Ejournal 9 (2019) 15–29.

[12] Y. Zhou, G. Hu, J. Li, C. Diao, Risk assessment along the gas pipelines and its application in urban planning, Land Use Policy 38 (2013) 233–238. https://doi.org/10.1016/j.landusepol.2013.11.011

[13] H. Zhu, Z. Mao, Q. Wang, J. Sun, The Influences of Key Factors on the Consequences Following the Natural Gas Leakage from Pipeline, Procedia Engineering 62 (2013) 592–601. https://doi.org/10.1016/j.proeng.2013.08.104

[14] R. Jones, W. Lehr, D. Simecek-Beatty, M. Reynolds, ALOHA® (Areal Locations of Hazardous Atmospheres) 5.4.4: Technical Documentation Volume 43 of NOAA Technical Memorandum NOS-OR&R (Vol. 43). U.S. Department of Commerce, National Oceanic and Atmospheric Administration, National Ocean Service, Office of Response and Restoration (2013)

[15] H. Shao, G. Duan, Risk quantitative calculation and ALOHA simulation on the leakage accident of natural gas power plant. Procedia Engineering 45 (2012) 352–359. https://doi.org/10.1016/j.proeng.2012.08.170

[16] N.M. Hanafiah, L. Zardasti, N. Yahaya, N.M. Noor, N. Hassan, A. Valipour, Comparison Study on human health and safety loss for rural and urban areas in monetary value subjected to gas pipeline failure, Journal of Environmental Science and Technology 8 (2015) 300–309. https://doi.org/10.3923/jest.2015.300.309

[17] S. Çetinyokuş, Determination of explosion, fire and toxic emission physical effect areas, Pamukkale University Journal of Engineering Sciences 23 (2017) 845–853. https://doi.org/10.5505/pajes.2016.90093

[18] S. Trahmawan, E.S. Siradj, J.F. Fatriansyah, Analysis Risk Based Inspection API 581 on LPG Spherical Tank at PT. XYZ, Journal of Materials Exploration and Findings 3 (2024) 172–180. https://doi.org/10.7454/jmef.v3i2.1069

Materials Research Proceedings 74 (2026) 48-54 https://doi.org/10.21741/9781644904473-7

Experimental Investigation of the Acoustical and Mechanical Properties of an Ultrasonic Attenuation Functionally Graded Composite

Majid MOHAMMADI

Department of Aerospace Engineering, Universiti Putra Malaysia, Serdang 43400, Selangor, Malaysia

majidmohammadi.us@gmail.com

Keywords: Ultrasonic Attenuation, Functionally Graded Structure (FGMs), Polymer Reinforced Composite, Ultrasonic Transducer

Abstract. In this study, epoxy-alumina based composites were fabricated and tested to be used as ultrasonic attenuation back layers, with graded materials produced by varying alumina sizes (50, 100, 200 m) and volume fractions, in order to improve both the acoustic and mechanical properties. Significantly, the functionally graded materials (FGMs) possess much better ultrasonic attenuation %, showing an increase of up to 30% than uniform composites, attributed to the arrangement of graded layers which can well absorb acoustic energy, with improvement on particle-matrix adhesion as well as the modulus control inside the resin. By using scan electron microscopy (SEM), well-dispersed alumina particles were obtained within optimum content levels; thus, the agglomeration of particles inside the composites and the flaws within can be prevented. While mechanical testing demonstrated improvements in hardness and elastic modulus at less than 19% and 15% alumina content, respectively, performance decreased more than the above percentage due to the agglomerates formation of particles, as well as introduction of voids and pores inside the composites, but acoustic testing result indicated that up to 98% ultrasonic energy absorption can be found from the FGMs due to variety in impedance (sound waves and resin matrix with various densities), in comparison with other materials due to the interaction between particles and matrix in FGMs, as well as energy convert phenomena.

Introduction

Ultrasonic transducers, known for their versatility and high efficiency, have become essential components in a wide range of applications [1]. They were first widely acknowledged for their crucial role in medical imaging, where they allow accurate visualization of internal body structures with minimal invasiveness [2]. Over time, however, their use has expanded far beyond this initial field into many other areas. In energy harvesting, ultrasonic transducers play an important role by converting ambient vibrations into electrical energy, providing sustainable power solutions for different devices and systems. In addition, they are extensively used in non-destructive testing, where they enable detailed inspection and evaluation of materials and structures without causing any harm [3]. By transmitting high-frequency sound waves and interpreting the reflected signals, these devices can accurately identify defects, cracks, and irregularities in various materials, thereby enhancing safety and reliability in industries such as aerospace and automotive.

Ultrasonic transducers designed for non-destructive testing feature a sophisticated structure composed of several key components responsible for generating and transmitting ultrasonic waves [4]. At the heart of the system lies the piezoelectric element, which converts electrical energy into mechanical vibrations and produces sound waves. This core component functions as the main source of ultrasonic waves, responding to electrical inputs by vibrating at high frequencies and emitting sound into the surrounding medium. Another important component is the matching layer,

Content from this work may be used under the terms of the Creative Commons Attribution 3.0 license. Any further distribution of this work must maintain attribution to the author(s) and the title of the work, journal citation and DOI. Published under license by Materials Research Forum LLC.

which is placed between the piezoelectric element and the target medium. Its role is to match acoustic impedance, allowing efficient transfer of ultrasonic waves into the material while reducing reflections and energy loss. In addition, a backing layer is commonly included to improve the acoustic performance and stability of the transducer. This layer absorbs unwanted sound waves and reduces internal reflections within the transducer structure. By minimizing effects such as ringing and reverberation, the backing layer helps produce clearer and more accurate ultrasonic signals, which are critical for precise imaging and reliable non-destructive evaluation. Fig. 1 shows the components of a non-destructive ultrasonic transducer.

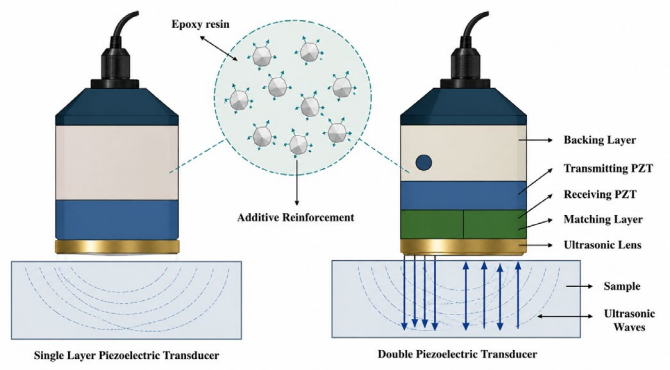


Fig. 1. A schematic of components of single and double piezoelectric ultrasonic transducer.

The backing layer in ultrasonic transducers is essential for performance, acting as a damper for vibrations from the piezoelectric element and ensuring efficient energy transfer. Positioned behind the active component, it reduces echoes and provides acoustic impedance matching, often using metal-polymer composites such as heavy metal particles in epoxy or rubber. Fabrication challenges include controlling layer thickness, preventing particle sedimentation, and balancing wave absorption with sensitivity. Selecting appropriate backing materials requires careful consideration of acoustic and mechanical properties. Metals like tungsten, copper, and silver, as well as alumina, have been studied for their sound absorption and compatibility with piezoelectric elements. Alumina, in particular, offers effective damping and impedance matching, improving signal clarity. Studies with Al_2O_3-polyurethane composites show enhanced low-frequency sound absorption, and proper particle dispersion is critical to avoid agglomeration. Natural fiber/epoxy composites also provide sustainable sound absorption solutions [5-7]. While single-layer polymer-metal composites dominate research, they often face limitations in absorption and uniformity. Functionally graded alumina-epoxy composites offer a promising alternative, allowing optimization of acoustic and mechanical properties by varying particle size and volume fraction [8]. Shi et al. [9] showed that an FGM acoustic structure improves sound absorption in mid-high frequencies and offers good hydrostatic pressure resistance compared to conventional cavity structures. Li et al. [10] studied FGM acoustic windows and reported that optimization of FRP-rubber functionally graded structures significantly improves both sound transmission performance and self-noise suppression, confirming the effectiveness of the proposed optimization approach. This study introduces a functionally graded material backing layer as a novel approach to reduce wave reflections, enhance energy dissipation, and improve signal stability, thereby offering improved performance and reliability in ultrasonic testing and imaging applications.

Material and Method

In this study, composite materials for sound-absorbing structures in ultrasonic transducers were prepared using epoxy resin (LR620) with a density of 1.17 g/cm³ and acoustic impedance of 3×10^5 kg·cm^{-2}·s^{-1}, hardener Eponate 520 (99% purity, Iran Composite Company), and alumina powder (>99% purity, Merck) with a density of 3.86 g/cm³ and acoustic impedance of 35×10^5

$kg \cdot cm^{-2} \cdot s^{-1}$. Composites were fabricated in both single-layer and FGM structures. A series of samples was produced to study the effects of alumina particle size and volume fraction. Three particle sizes (50, 100, and 200 μm) were used, and for each size, nine volume fractions were tested. Nine groups of samples were fabricated, with five specimens prepared for each group. The dimensions of all specimens were 20 mm × 10 mm × 10 mm. The FGM samples consisted of three layers, whose compositions were selected based on the optimum performance of the corresponding non-FGM composites. The graded structures were fabricated using a sequential slip-casting process. Single-layer composites without alumina served as control samples. The fabrication followed a two-step process. First, backing specimens were prepared to optimize particle size and volume fraction. Then, using the best-performing results from this step, FGM backings were produced. Alumina powders were sieved to the desired sizes and mixed with epoxy using a mechanical mixer (RQ-40 Plus, REMI Group, India) at 50, 70, and 90 rpm for 30 minutes to ensure uniform dispersion. To reduce bubbles and ensure proper mixing, the raw materials were initially combined at room temperature for 15 minutes, then stirred at 90 rpm in a 70 °C water bath for 20 minutes, followed by cooling at -4 °C with stirring at 50 rpm. Finally, the mixture was hand-cast into molds. Fig. 2 schematically illustrates the fabrication process.

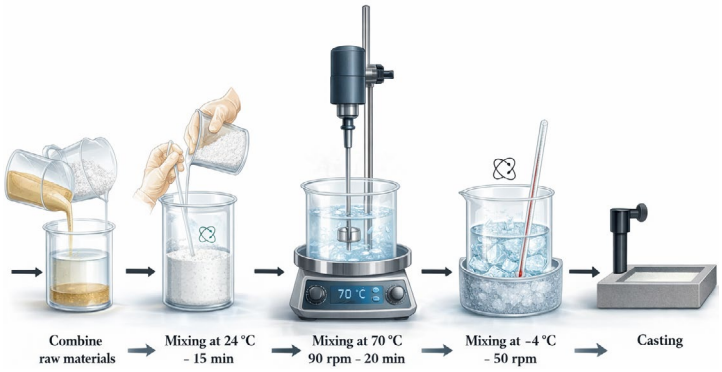


Fig. 2. The fabrication process of FGM composites.

To observe the uniformity of alumina powder spread, the appearance of cavities and bubbles, and the ability to wet additives on the substrate in the uniform single and FGM samples, the VEGA/TESCAN Scanning Electron Microscope (SEM) (Czech Republic) was utilized. A KOOPA UV1device (KOOPA Company, Iran) was used to measure the hardness of the composite samples at a load of 1kg for 10s. The elastic module was measured at an 18N load using a ZWICK/ROELL Z100 testing machine (ZwickRoell GmbH & Co. KG, Germany) according to ASTM D790 standards. Since a suitable impedance tube was not available for measuring the coefficient of sound absorption at high frequencies, an alternative was used.A 2.25 MHz ultrasonic transducer (HUATEC Company, China) serving as both transmitter and receiver, along with a Masterscan D-70 detector (HUATEC Company, China), was used for this purpose. In this method, a double piezoelectric transducer configuration was used, where the transmitting and receiving elements were arranged to improve signal stability and measurement reliability during ultrasonic testing. The amplitude of the ultrasonic signal transmitted through the sample was compared with the reference amplitude obtained without the sample. The ultrasonic attenuation percentage was calculated according to Eq. 1.

$$Attenuation\ (\%) = \left[\frac{(A_0 - A)}{A_0}\right] \times 100\% \quad \text{Eq. 1}$$

where A_0 is the reference signal amplitude and A is the transmitted signal amplitude after passing through the specimen. Therefore, the reported values represent ultrasonic wave attenuation (energy

loss) at 2.25 MHz rather than the conventional normal-incidence ultrasonic attenuation percentage measured using an impedance tube.

Results and Discussion

As shown in Fig. 3, samples with well-dispersed alumina particles exhibit a homogeneous microstructure, indicating strong particle-matrix interaction. In contrast, samples with 100 µm particles form localized clusters, typical of agglomeration, which can act as stress concentrators and acoustic scattering sites, reducing mechanical and ultrasonic performance. The proposed fabrication method effectively minimizes agglomeration and ensures uniform particle distribution, highlighting the importance of controlling processing parameters mixing force, speed, and duration especially at higher alumina loadings. At elevated filler contents, increased viscosity can restrict particle mobility, promoting agglomeration and void formation.

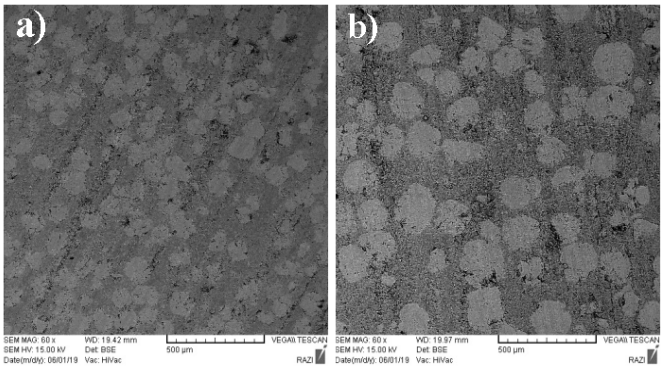


Fig. 3. Uniform distribution of alumina particles within the epoxy resin matrix of single-layer samples (a) 100 µm and (b) 200 µm.

Fig. 4 shows the hardness of composites reinforced with 50, 100, and 200 µm alumina powders at different volume fractions. Hardness increases with alumina content, rising from 16.1 kPa (0.0161 MPa) for the unreinforced epoxy to a maximum of 60 kPa (0.06 MPa), due to the rigid alumina particles acting as reinforcements and the strong particle-matrix bonding that resists deformation. However, at volume fractions above 19%, hardness decreases for all particle sizes. SEM images (Fig. 5) reveal that higher alumina content leads to bubble and cavity formation, which creates voids, disrupts interfacial bonding, and concentrates stress, reducing the effective reinforcement and overall hardness. Thus, 19% alumina represents the optimal loading for maximizing composite hardness.

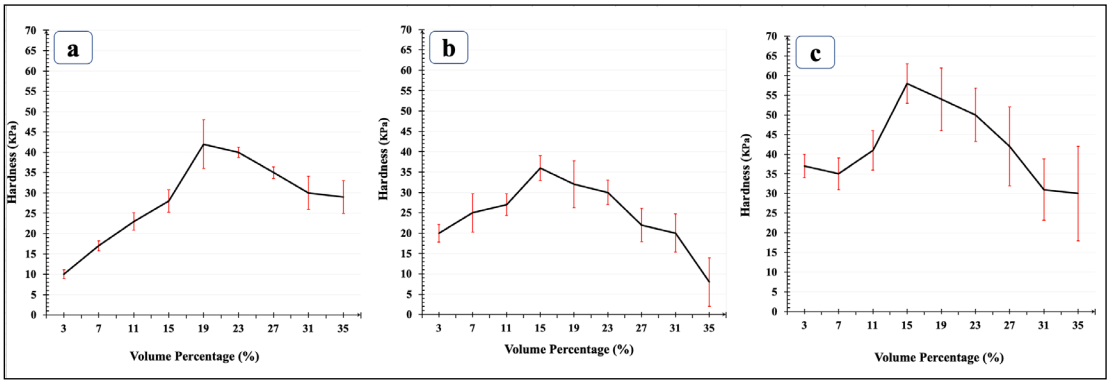


Fig. 4. Variation in composite hardness with different average alumina particle sizes, (a) 50 µm, (b) 100 µm, and (c) 200 µm.

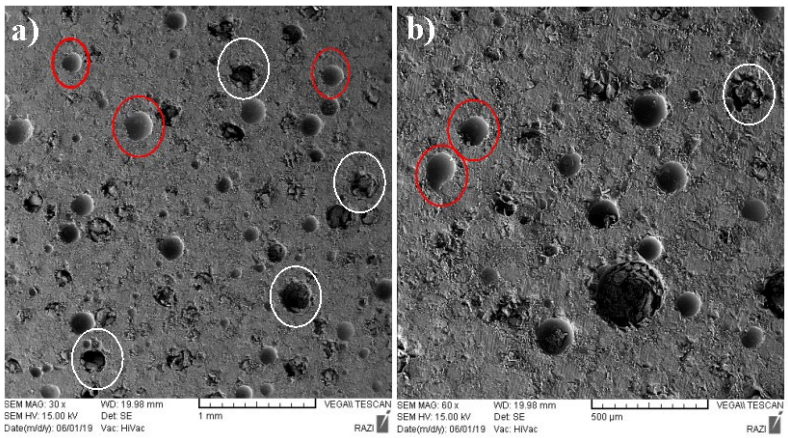


Fig. 5. SEM images showing bubbles (red) and cavities (white) in (a) 23 Al 200 and (b) 31 Al 200 samples.

Table 1 indicates that the elastic modulus of the composites increases with increasing alumina content up to 15 vol%, where the maximum value of 160 kPa is achieved. This improvement is mainly attributed to enhanced stiffness of the composite, restricted mobility of epoxy chains, improved load transfer, and effective dispersion and interaction between alumina particles and the polymer matrix. The rigid Al_2O_3 particles act as reinforcing agents, increasing the overall resistance of the material to deformation. However, at reinforcement levels above 15 vol%, the elastic modulus decreases. This reduction is associated with particle agglomeration, which leads to an inhomogeneous microstructure, increased porosity, weak interfacial bonding, and reduced stress transfer efficiency between the filler and matrix. These microstructural defects collectively diminish the reinforcing effect of alumina particles. Based on these results, 15 vol% is identified as the optimum reinforcement content for particle sizes of 50, 100, and 200 µm, providing the best balance between reinforcement efficiency and microstructural integrity.

Fig. 6 illustrates the ultrasonic wave attenuation behavior of epoxy composites reinforced with alumina particles of different sizes. The results show that ultrasonic attenuation increases with increasing alumina content, rising from approximately 25% at low loading (3%) to about 95% at higher concentrations. This trend is mainly attributed to the viscoelastic nature of the epoxy matrix, which promotes energy dissipation, as well as the presence of rigid alumina particles that enhance scattering within the composite. At higher alumina volume fractions (above ~23%), the increase in attenuation becomes more pronounced. This is associated not only with enhanced particle interactions but also with the formation of micro-voids and trapped air pockets during processing. However, it should be noted that the presence of such voids may also indicate a compromise in microstructural integrity and can potentially degrade mechanical performance and long-term reliability. Therefore, their influence should be considered as part of a trade-off between improved ultrasonic attenuation and reduced structural quality. Fig. 7 shows that functionally graded composites exhibit even higher ultrasonic attenuation, reaching up to 98%. This improvement is attributed to the optimized distribution of particle size and volume fraction across the graded structure, as well as the increased effective thickness of the backing layer (6 mm). Overall, these results confirm that both filler content and functionally graded architecture significantly influence ultrasonic attenuation, while also highlighting the importance of balancing acoustic performance with microstructural integrity.

Table 1. Elastic modulus of the composite specimens at different volume fractions [Vol%]. The reported values represent the mean of three independent measurements and are expressed as mean ± standard deviation (σ).

Volume percentages (%)									
Particle size, μm	3	7	11	15	19	23	27	31	35
Modulus of elasticity									
50	50.0 ± 2.0	56 ± 2.62	53 ± 2.01	160 ± 4.32	81 ± 2.68	94 ± 2.47	63 ± 0.25	43 ± 1.21	46 ± 0.12
100	33 ± 3.0	59 ± 0.47	67 ± 0.94	132 ± 2.49	101 ± 1.25	65 ± 2.95	67 ± 1.23	60 ± 2.22	43 ± 1.00
200	55 ± 1.25	66 ± 1.70	65 ± 0.82	68 ± 0.47	50 ± 0.47	52 ± 3.01	59 ± 0.34	44 ± 1.92	45 ± 0.23

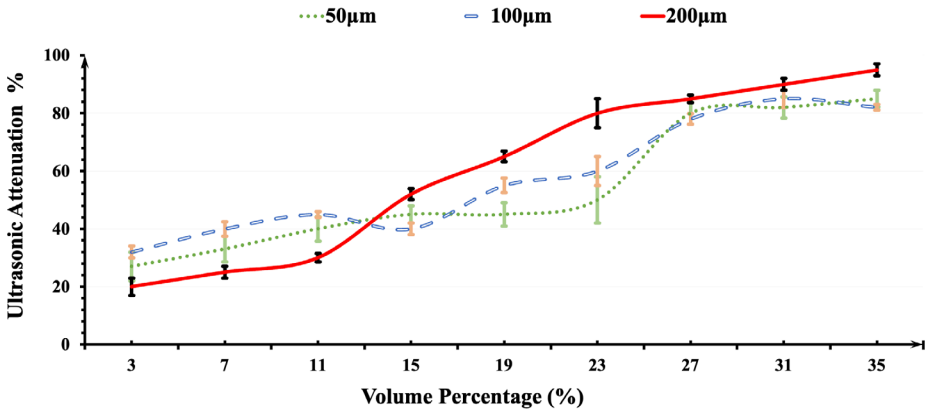


Fig. 6. Ultrasonic attenuation of composite samples containing alumina particles with different average particle sizes.

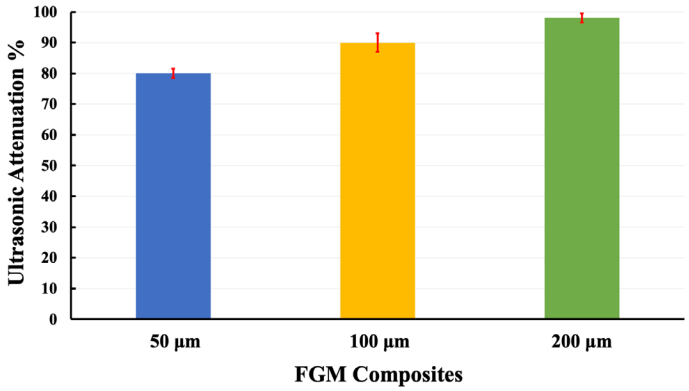


Fig. 7. Percentage of ultrasonic attenuation in composite samples with a functionally graded material (FGM) structure. The FGM samples consist of three layers with gradually increasing alumina volume fractions of 15%, 19%, and 23%, respectively.

Conclusion

Epoxy-Al_2O_3-FGMs were successfully fabricated and evaluated as backing materials for ultrasonic transducers. The results showed that increasing alumina content improved both mechanical and acoustic properties up to an optimum level. The hardness increased from 16.1 kPa to 60 kPa, while the elastic modulus reached a maximum value of 160 kPa at 15 vol.% Al_2O_3. Higher filler contents led to bubble formation, cavities, and particle agglomeration, resulting in reduced mechanical performance. Acoustic measurements demonstrated a significant enhancement in ultrasonic attenuation with increasing alumina content. Single-layer composites achieved up to 95% sound absorption, whereas the FGM structure reached approximately 98% ultrasonic wave absorption, corresponding to about 30% higher attenuation than conventional single-layer composites. This improvement is attributed to the graded acoustic impedance, enhanced wave scattering, and

increased energy dissipation throughout the multilayer structure. Overall, the developed epoxy-Al_2O_3-FGM exhibited an effective combination of high hardness, improved elastic modulus, and excellent ultrasonic damping capability, making it a promising backing material for high-performance ultrasonic transducers.

References

[1] V.M. Mastronardi, A. Qualtieri, E. Boni, P. Tortoli, R. De Fazio, P. Visconti, M.T. Todaro, M. De Vittorio, Additive Manufacturing Electronics for Packaging High-Frequency Aluminum Nitride Piezoelectric Micromachined Ultrasonic Transducer Probes, Proceedings 97 (2024) 52. https://doi.org/10.3390/proceedings2024097052

[2] S. Sadeghpour, S.V. Joshi, C. Wang, M. Kraft, Novel phased array piezoelectric micromachined ultrasound transducers (pMUTs) for medical imaging, IEEE Open Journal of Ultrasonics, Ferroelectrics, and Frequency Control 2 (2022) 194-202. https://doi.org/10.1109/OJUFFC.2022.3207128

[3] R. Hampson, D. Zhang, A. Gachagan, G. Dobie, Modelling and characterisation ultrasonic phased array transducers for pipe inspections. International Journal of Pressure Vessels and Piping 200 (2022) 104808. https://doi.org/10.1016/j.ijpvp.2022.104808

[4] C. Hou, Z. Li, C. Fei, X. Wei, Y. Yang, Y. Wang, Y. Quan, Y. Yang, Optimal design of ultrasonic transducer based on multi-layer backing with adjustable impedance, Ceramics International 50 (2024) 51693-51700. https://doi.org/10.1016/j.ceramint.2024.02.006

[5] M. Mohammadi, E. Taban, W.H. Tan, N.B.C. Din, A. Putra, U. Berardi, Recent progress in natural fiber reinforced composite as sound absorber material, Journal of Building Engineering 84 (2024) 108514. https://doi.org/10.1016/j.jobe.2024.108514

[6] M. Mohammadi, M.R. Ishak, M.T.H. Sultan, E.S. Zainudin, A comprehensive review of factors influencing the sound absorption properties of micro-perforated panel structures, Journal of Vibration Engineering & Technologies 13 (2025) 319. https://doi.org/10.1007/s42417-025-01849-y

[7] M. Mohammadi, M.R. Ishak, M.T. Hameed Sultan, E.S. Zainudin, Cutting-edge innovations in sound absorption properties of natural fiber reinforced polylactic acid composites, Journal of Reinforced Plastics and Composites 45 (2025) 2814-2853. https://doi.org/10.1177/07316844251352718

[8] M. Mohammadi, M. Rajabi, M. Ghadiri, Functionally graded materials (FGMs): A review of classifications, fabrication methods and their applications, Processing and Application of Ceramics 15 (2021) 319-343. https://doi.org/10.2298/PAC2104319M

[9] K. Shi, D. Hu, D. Li, G. Jin, Sound absorption behaviors of composite functionally graded acoustic structure under hydrostatic pressure. Applied Acoustics 211 (2023) 109474. https://doi.org/10.1016/j.apacoust.2023.109474

[10] B. Li, F.L. Zhou, J. Fan, B. Wang, L.W. Tan, Research on the Performance Optimization of Turbulent Self-Noise Suppression and Sound Transmission of Acoustic Windows Made from Functionally Graded Material, Archives of Acoustics (2023) 475-495. https://doi.org/10.24425/aoa.2023.146812

Materials Research Proceedings 74 (2026) 55-62 https://doi.org/10.21741/9781644904473-8

Eco-Friendly NiO Nanomaterials Synthesized Using Waste-Derived Cellulose: Tailored Structural, Textural, and Optical Properties

Alvin Lim Teik ZHENG[1,2,a *], Azrul Nurfaiz Mohd FAIZAL[1,b], Syeed Saifulazry Osman EL-EDRUS[1,c], Keeren Sundara RAJOO[1,d], Kar Ban TAN[3,e] and Yoshito ANDOU[4,f]

[1]Institute of Ecoscience Borneo, Universiti Putra Malaysia Sarawak, Bintulu 97008, Sarawak, Malaysia

[2]Department of Science and Technology, Faculty of Humanities, Management and Science, Universiti Putra Malaysia Sarawak, Bintulu 97008, Sarawak, Malaysia

[3]Department of Chemistry, Faculty of Science, Universiti Putra Malaysia, Serdang 43400, Selangor, Malaysia

[4]Graduate School of Life Sciences and Systems Engineering, Kyushu Institute of Technology, Fukuoka 808-0196, Japan

[a]alvinltz@upm.edu.my, [b]azrulnurfaiz@upm.edu.my, [c]saifulazry@upm.edu.my, [d]keeren.rajoo@upm.edu.my, [e]tankarban@upm.edu.my, [f]yando@life.kyutech.ac.jp

Keywords: Dissolved Cellulose, Nickel Oxide, Green Synthesis, Precipitation

Abstract. The sustainable synthesis of nanomaterials using biomass-derived resources offers a practical strategy to address environmental concerns and resource depletion. In this study, dissolved cellulose, typically discarded as waste, was employed as a template and stabilizing agent for nickel oxide (NiO) synthesis via the co-precipitation method. XRD analysis showed that cellulose-assisted NiO exhibited larger crystallite sizes and reduced lattice strain. UV–DRS and Tauc plot measurements revealed a reduced band gap energy for NiO–C (2.10 eV) compared to pure NiO (2.54 eV), indicating enhanced visible-light absorption. BET and DFT pore size analysis demonstrated that NiO–C possessed a lower surface area (64.42 m^2/g) but a more uniform pore structure relative to pure NiO (179.42 m^2/g). SEM micrographs further revealed porous, aggregated features in NiO–C, in contrast to the dense, uniform morphology of pure NiO. Importantly, the synthesis achieved a material cost of approximately RM 4.83 per gram, highlighting its affordability alongside sustainability. These findings highlight the significant role of dissolved cellulose in tailoring structural and functional properties of NiO, while advancing a low-cost and green route for high-performance nanomaterials.

Introduction

The development of sustainable and eco-friendly materials has become a paramount focus in modern materials science, driven by the urgent need to address environmental challenges and resource depletion. Among the various strategies employed, the utilization of biomass-derived materials has garnered significant attention due to their abundance, renewability, and biodegradability [1,2]. Cellulose, the most abundant natural polymer on Earth, stands out as a promising candidate for the synthesis of advanced functional materials [3]. The dissolution of cellulose and its subsequent use in material synthesis presents a novel approach to valorize this abundant biopolymer [4,5]. Dissolved cellulose can act as a structure-directing agent, influencing the nucleation, growth, and assembly of nanoparticles, thereby controlling their final morphology and properties [6,7].

Nickel oxide (NiO), a p-type semiconductor with a wide bandgap, has been extensively studied due to its unique electronic, optical, and catalytic properties [8]. However, the synthesis of NiO

Content from this work may be used under the terms of the Creative Commons Attribution 3.0 license. Any further distribution of this work must maintain attribution to the author(s) and the title of the work, journal citation and DOI. Published under license by Materials Research Forum LLC.

with controlled morphology, size, and porosity remains a challenge, often requiring complex procedures and hazardous chemicals [9]. The integration of biomass-derived materials, such as cellulose, into the synthesis process offers a green and cost-effective alternative, enabling the production of nanomaterials with tailored properties while minimizing environmental impact [10]. Foo and co-workers reported the synthesis of NiO and Ni nanoparticles using nanocrystalline cellulose (NCC) as a bio-template in a glycine-nitrate combustion process, showing that cellulose can significantly influence particle morphology and crystallinity [11]. While cellulose has been investigated in solid or microcrystalline form as a structural modifier, little attention has been given to dissolved cellulose, which is typically discarded as a waste stream from cellulose dissolution processes. Addressing this gap, the present work investigates dissolved cellulose as both template and stabilizer in NiO synthesis, linking its structural and optical modifications to potential performance advantages while demonstrating clear cost savings.

Materials and Method

Materials

Nickel chloride ($NiCl_2$), sodium hydroxide (NaOH), urea, and ethanol were obtained from Wako Pure Chemical Industries Ltd., Japan. All chemicals were used as received without further purification. Deionized water was used throughout the experiments. Bamboo biomass was used as the cellulose precursor.

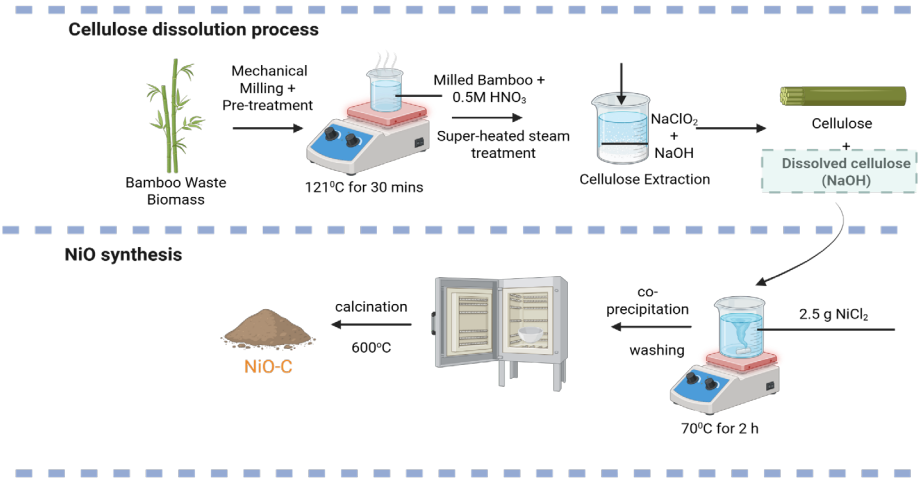


Fig. 1. Waste cellulose extraction procedure for the synthesis of NiO-C.

Extraction and dissolution of cellulose

Bamboo biomass was mechanically milled and pretreated to remove lignin and hemicellulose [12]. The milled bamboo was treated with 0.5 M HNO_3 at 121 °C for 30 min, followed by superheated steam treatment at 265 °C for 5 min. The extracted cellulose, with a degree of polymerization of 312, was subsequently subjected to delignification using sodium chlorite and an 8.8 wt.% NaOH solution. The purified cellulose was separated by filtration, while the cellulose-containing alkaline solution generated during the dissolution process was retained for NiO-C synthesis.

Synthesis of NiO and NiO-C

Pure NiO was prepared by dissolving 2.5 g of $NiCl_2$ in deionized water. A NaOH solution was then added under vigorous stirring at 70 °C [13,14]. For NiO-C synthesis, dissolved cellulose in the alkaline solution was added to the nickel precursor under the same reaction conditions, as shown in Fig. 1. The resulting precipitates were collected by centrifugation at 4500 rpm for 15 min and washed thoroughly with deionized water and absolute ethanol. The samples were dried at 70 °C for 24 h and subsequently calcined at 500 °C for 2 h to obtain NiO and NiO-C.

Material characterization

The morphology and elemental composition of the samples were examined using scanning electron microscopy coupled with energy-dispersive X-ray spectroscopy. Their crystalline structure was analysed using X-ray diffraction. Surface area and pore-size distribution were determined through N_2 adsorption-desorption analysis. Optical absorption and band-gap energy were evaluated using ultraviolet-visible diffuse reflectance spectroscopy.

Results and Discussion

Characterization

The Brunauer–Emmett–Teller surface area analysis was conducted to evaluate the specific surface area of NiO and NiO-C, as shown in Fig. 2(a). The BET surface area of NiO was 179.42 m^2/g, whereas NiO-C recorded a lower surface area of 64.42 m^2/g. The lower surface area of NiO-C corresponds with its larger crystallite size and aggregated morphology, indicating that cellulose-assisted synthesis altered nucleation and particle growth. A related effect was reported for nickel-cellulose nanocomposites, where cellulose controlled nucleation, particle development, and aggregation [15]. The pore-size distribution was analysed using density functional theory, as shown in Fig. 2(b). Both samples exhibited mesopores ranging from 2 to 20 nm. NiO displayed a broad distribution centred near 4 nm, whereas NiO-C showed a narrower distribution with a prominent peak near 6 nm. This result confirms that dissolved cellulose produced a more uniform pore-size distribution despite reducing the total surface area. Mesoporous NiO prepared using mixed surfactant templates also exhibited defined pore-size distributions, although larger pore diameters of approximately 25 and 77 nm were reported [16].

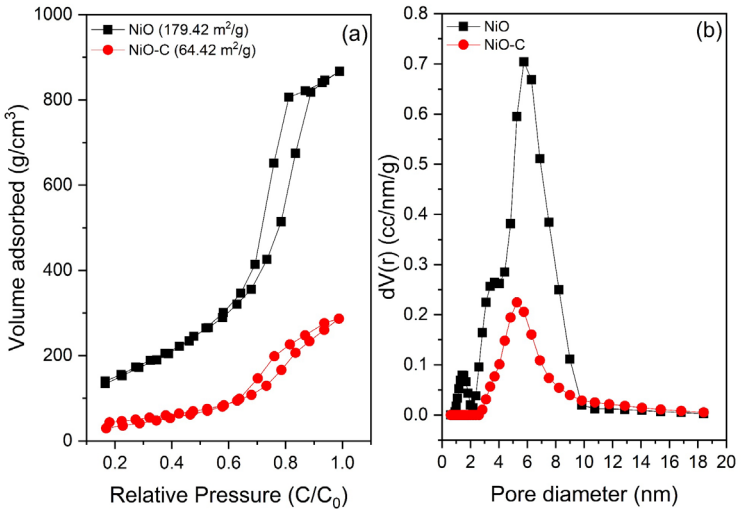


Fig. 2. BET analysis and DFT pore size distribution of NiO and NiO-C.

The optical properties and band-gap energies of NiO and NiO-C were examined using UV–Vis diffuse reflectance spectroscopy, as depicted in Fig. 3(a). NiO exhibited an absorption edge near 350 nm, whereas NiO-C showed broader absorption extending to approximately 400 nm. The corresponding Tauc plots in Fig. 3(b) gave band-gap energies of 2.54 eV for NiO and 2.10 eV for NiO-C. The lower band-gap value confirms that cellulose-assisted synthesis modified the optical absorption of NiO. Similar changes in the optical properties of cellulose-templated metal oxides have been associated with modifications in crystallite structure, particle interfaces, and synthesis-induced defects [11]. The present result supports the use of dissolved cellulose as a structure-directing component for adjusting the optical response of NiO. Further spectroscopic analysis is required to identify the specific defect states responsible for the observed band-gap reduction.

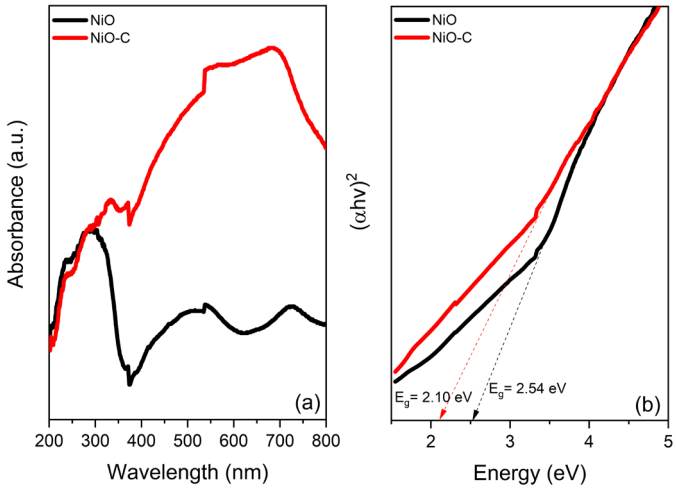


Fig. 3. UV-DRS and Tauc plot of NiO and NiO-C.

The X-ray diffraction patterns of NiO and NiO-C are presented in Fig. 4. Both samples exhibited diffraction peaks indexed to the cubic phase of NiO based on JCPDS card No. 04-0835, confirming the formation of crystalline NiO [17]. The principal peaks at 2θ values of 37.2°, 43.3°, and 62.9° correspond to the (111), (200), and (220) planes, respectively. The crystallite sizes calculated using the Scherrer equation were approximately 4.9 nm for NiO and 10.78 nm for NiO-C. The larger crystallite size of NiO-C demonstrates that dissolved cellulose altered the nucleation and crystal-growth behaviour during synthesis. Similar changes in NiO crystallite development have been reported in template-assisted synthesis, where the organic template affected particle formation and crystal growth [18]. The Williamson-Hall analysis further showed lower lattice strain in NiO-C than in NiO. This lower strain indicates fewer lattice distortions within the NiO-C crystalline domains. The simultaneous increase in crystallite size and reduction in lattice strain agrees with the established relationship between crystal growth and lower grain-boundary density [19,20]. Nevertheless, charge-carrier mobility and recombination behaviour were not directly measured in this study and therefore require confirmation through electrical or photoluminescence analysis.

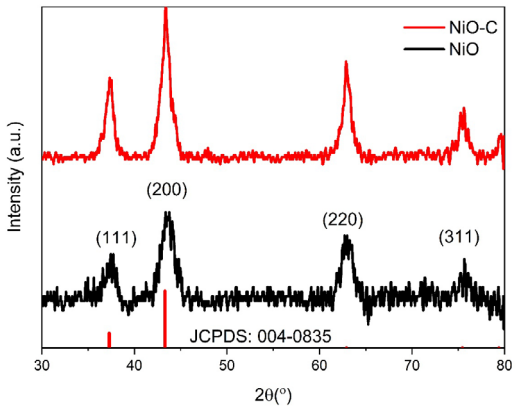


Fig. 4. XRD diffraction of NiO and NiO-C.

The SEM micrograph of NiO shown in Fig. 5(a) displays a relatively dense structure consisting of compact and closely packed spherical particles. The particle surfaces are comparatively smooth, with limited interparticle voids. In contrast, NiO-C in Fig. 5(b) exhibits irregularly shaped aggregates, rougher surfaces, and visible spaces between particle clusters. These morphological differences confirm that dissolved cellulose altered particle assembly during precipitation and

calcination. Similar effects have been reported for cellulose-assisted metal oxide synthesis, where cellulose acted as a structure-directing matrix and disrupted compact particle packing [21]. The interparticle voids observed in NiO-C agree with the mesoporous structure identified through the DFT pore-size analysis in Fig. 2(b). The aggregated morphology also corresponds with the lower BET surface area and larger crystallite size measured for NiO-C. The EDX spectra of NiO and NiO-C are presented in Fig. 5(c) and Fig. 5(d), respectively. After excluding the carbon signal, NiO contained 64.9 at.% oxygen and 35.1 at.% nickel, corresponding to an O atomic ratio of 1.85. The oxygen-rich composition reflects the contribution of surface oxygen species, hydroxyl groups, or adsorbed oxygen. NiO-C contained 6.99 at.% oxygen and 93.01 at.% nickel, producing an O atomic ratio of 0.075. This large difference indicates substantial compositional variation between the two samples. Since EDX provides semi-quantitative elemental information and does not determine oxidation states, the result should not be interpreted as direct evidence of metallic Ni or a specific oxygen-deficient NiO phase. X-ray photoelectron spectroscopy or related surface-sensitive analysis is required to confirm the nickel oxidation state and oxygen-vacancy concentration.

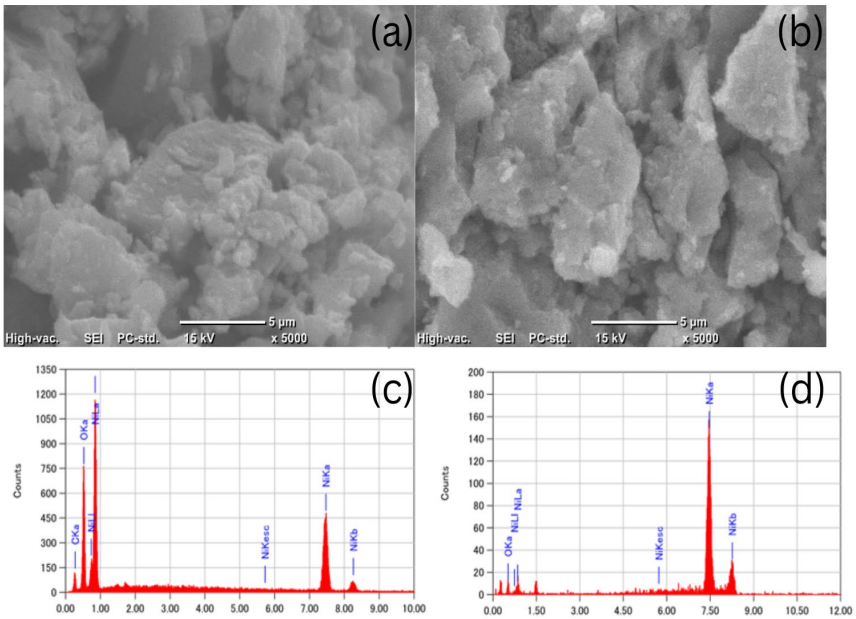


Fig. 5. SEM and EDX images of (a,c) NiO and (b,d) NiO-C.

Cost analysis

The cost analysis presented in Table 1 indicates that the cellulose-templated NiO can be synthesized at approximately RM 4.83 per gram under laboratory-scale conditions. While this value highlights a clear reduction compared to surfactant-assisted or hydrothermal routes, the assumptions underlying this estimate must be critically examined. Future work should include detailed techno-economic modeling that accounts for energy optimization, waste valorization, and scale-up logistics to establish a more robust economic feasibility for industrial adoption.

Table 1. Cost analysis for the synthesis of NiO-C.

Item	Quantity	Unit Cost (RM)	Total Cost (RM)	Remarks
Raw Material				
Nickel chloride ($NiCl_2$)	2.5 g	RM 0.432/g	RM 1.08	NiO precursor
Sodium hydroxide (NaOH)	8.8 g	RM 0.10/g	RM 0.88	Base for reaction
Ethanol (C_2H_5OH)	10 mL	RM 0.30/mL	RM 3.00	Used for washing of NiO and NiO-C
*Waste cellulose from biomass	-	-	RM 0.00	Obtained from dissolution process
Total chemical cost			RM 4.96	
Synthesis cost				
Hotplate stirring (70°C)	0.450 kWh × 2 h	RM 0.39 per kWh**	RM 0.35	Co-precipitation
Oven Drying (70°C)	1.5 kWh × 24 hours = 36 kWh	RM 0.39 per kWh**	RM 14.04	Post-reaction drying
Calcination (500°C)	1.8 kWh × 2 hours = 3.6 kWh	RM 0.39 per kWh**	RM 1.40	High-temperature treatment
Total synthesis cost			RM 15.79	
Total Cost of Goods Sold			**RM 20.75**	Synthesis of 4.3 g of NiO
Estimated cost for 1 g of NiO-C			**RM 4.83**	

*The chemicals required for cellulose extraction and dissolution is omitted.

** refer to the Tenaga Nasional Berhad tariff rate.

Conclusion

In this study, we successfully demonstrated the sustainable synthesis of NiO-C using dissolved cellulose, a typically discarded byproduct, as a template and stabilizing agent. Structural analysis confirmed that dissolved cellulose promoted larger crystallite sizes and reduced lattice strain, as shown by Williamson–Hall (W-H) and Scherrer equation analysis. Optical characterization revealed a narrowed band gap of NiO-C (2.10 eV) compared to pure NiO (2.54 eV), enhancing visible light absorption. Textural analysis highlighted a lower surface area but a more uniform pore distribution, while SEM imaging showed a porous and aggregated morphology distinct from the dense structure of pure NiO. These features collectively enhance the photocatalytic potential of NiO-C for environmental remediation and energy conversion. Importantly, the synthesis achieved an estimated cost of RM 4.83 per gram, demonstrating clear economic viability compared to surfactant-assisted or hydrothermal routes. Overall, this work establishes a sustainable pathway for nanomaterial synthesis that not only tailors functional properties but also valorizes biomass waste, aligning with the principles of green chemistry and circular economy.

Acknowledgment

This work was supported by Universiti Putra Malaysia Grant GPB/9832200. The authors confirm that there are no additional funders. The funder had no role in study design, data collection and analysis, decision to publish, or preparation of the manuscript.

References

[1] N. Choudhary, A. Tomar, S. Bhardwaj, J. Ćwiertnia, D. Just, D. Janas, R. Chandra, P.K. Maji, Advancements in biomass-derived cellulose composite electrodes for supercapacitors: a review, J. Mater. Chem. A (2025). https://doi.org/10.1039/D4TA05470A

[2] R. Wang, Y. Feng, D. Li, K. Li, Y. Yan, Towards the sustainable production of biomass-derived materials with smart functionality: a tutorial review, Green Chem. 26 (2024) 9075-9103. https://doi.org/10.1039/D4GC01771D

[3] C. Fu, X. Han, Y. Zhang, J. Hu, J. Du, H. Wang, Synergistic functionality of metal-organic framework-cellulose composites structures for advanced high-performance energy materials, Chem. Eng. J. 503 (2025) 158384. https://doi.org/10.1016/j.cej.2024.158384

[4] Z.-J. He, K. Chen, Z.-H. Liu, B.-Z. Li, Y.-J. Yuan, Valorizing renewable cellulose from lignocellulosic biomass toward functional products, J. Clean. Prod. 414 (2023) 137708. https://doi.org/10.1016/j.jclepro.2023.137708

[5] M. Moniruzzaman, H. Mahmood, M.F. Ibrahim, S. Yusup, Y. Uemura, Effects of pressure and temperature on the dissolution of cellulose in ionic liquids, Adv. Mater. Res. 1133 (2016) 588-592. https://doi.org/10.4028/www.scientific.net/AMR.1133.588

[6] A. Anžlovar, E. Žagar, Cellulose structures as a support or template for inorganic nanostructures and their assemblies, Nanomaterials 12 (2022) 1837. https://doi.org/10.3390/nano12111837

[7] Q. Lv, C. Xu, D. Wu, Z. Wang, R. Lan, L. Wu, The role of nanocrystalline cellulose during crystallization of poly(ε-caprolactone) composites: Nucleation agent or not?, Compos. Part A Appl. Sci. Manuf. 92 (2017) 17-26. https://doi.org/10.1016/j.compositesa.2016.10.035

[8] B.A. Nail, J.M. Fields, J. Zhao, J. Wang, M.J. Greaney, R.L. Brutchey, F.E. Osterloh, Nickel oxide particles catalyze photochemical hydrogen evolution from water, nanoscaling promotes p-type character and minority carrier extraction, ACS Nano 9 (2015) 5135-5142. https://doi.org/10.1021/acsnano.5b00435

[9] D.Y. Han, H.Y. Yang, C.B. Shen, X. Zhou, F.H. Wang, Synthesis and size control of NiO nanoparticles by water-in-oil microemulsion, Powder Technol. 147 (2004) 113-116. https://doi.org/10.1016/j.powtec.2004.09.024

[10] M. Aslam, A. Rani, B.N. Pant, P. Singh, G. Pandey, Recent development in the production and utilization of plant biomass-based nanomaterials, in: (2023) pp. 331-368. https://doi.org/10.1007/978-981-99-0996-4_12

[11] Y.-T. Foo, J.E.-M. Chan, G.-C. Ngoh, A.Z. Abdullah, B.A. Horri, B. Salamatinia, Synthesis and characterization of NiO and Ni nanoparticles using nanocrystalline cellulose (NCC) as a template, Ceram. Int. 43 (2017) 16331-16339. https://doi.org/10.1016/j.ceramint.2017.09.006

[12] C. Arce, L. Kratky, Mechanical pretreatment of lignocellulosic biomass toward enzymatic/fermentative valorization, iScience 25 (2022) 104610. https://doi.org/10.1016/j.isci.2022.104610

[13] B. Shanmugapriya, G. Sivasankari, K. Kannagi, P. Sankari, R.A. Kiruthika, N. Pavithra, A.A. Al-Zaharani, M. Sarif, Nickel oxide nanoparticles: Synthesis and characterization for optical studies, Mod. Phys. Lett. B 37 (2023). https://doi.org/10.1142/S021798492350046X

[14] N. Srivastava, P.C. Srivastava, Synthesis and characterization of (single- and poly-) crystalline NiO nanorods by a simple chemical route, Phys. E Low-Dimens. Syst. Nanostruct. 42 (2010) 2225-2230. https://doi.org/10.1016/j.physe.2010.04.023

[15] C.H. Gong, X.X. Wang, H.J. Liu, C. Zhao, Y.D. Zhang, Y.S. Jia, H.J. Meng, J.W. Zhang, Z.J. Zhang, Facile in situ synthesis of nickel/cellulose nanocomposites: mechanisms, properties and perspectives, Cellulose 21 (2014) 4359-4368. https://doi.org/10.1007/s10570-014-0453-6

[16] F. Liu, W. Yuan, T. Li, Z. Zhang, Synthesis and electrochemical performance of mesoporous nickel oxide using mixed surfactant template, Mater. Res. Innov. 19 (2015) S2-70-S2-75. https://doi.org/10.1179/1432891714Z.0000000001062

[17] Z.H. Alhashem, Ni-doped ZnO nanoparticles derived by the sol-gel method: structural, optical, and magnetic characteristics, Arab. J. Chem. 17 (2024) 105701. https://doi.org/10.1016/j.arabjc.2024.105701

[18] N. Mironova-Ulmane, A. Kuzmin, I. Sildos, Template-based synthesis of nickel oxide, IOP Conf. Ser. Mater. Sci. Eng. 77 (2015) 012025. https://doi.org/10.1088/1757-899X/77/1/012025

[19] R. Ciesielski, F. Schäfer, N.F. Hartmann, N. Giesbrecht, T. Bein, P. Docampo, A. Hartschuh, Grain boundaries act as solid walls for charge carrier diffusion in large crystal MAPI thin films, ACS Appl. Mater. Interfaces 10 (2018) 7974-7981. https://doi.org/10.1021/acsami.7b17938

[20] Q. Zhao, R. Tang, B. Che, Y. He, T. Wu, X. Peng, J. Yang, S. Sheng, C. Zhu, T. Chen, Grain-boundary elimination via liquid medium annealing toward high-efficiency Sb2Se3 solar cells, Adv. Mater. 37 (2025). https://doi.org/10.1002/adma.202414082

[21] B.W. Hoogendoorn, B.K. Birdsong, A.J. Capezza, V. Ström, Y. Li, X. Xiao, R.T. Olsson, Ultra-low concentration of cellulose nanofibers (CNFs) for enhanced nucleation and yield of ZnO nanoparticles, Langmuir 38 (2022) 12480-12490. https://doi.org/10.1021/acs.langmuir.2c01713

Materials Research Proceedings 74 (2026) 63-75 https://doi.org/10.21741/9781644904473-9

Tailored Electromagnetic Wave Absorption Performance of $Ni_{0.7}Zn_{0.3}Fe_2O_4$/Zeolite/CNT Composites: Influence of Single and Multilayer Structures

Fadzidah MOHD IDRIS[1,a,*], Faisal bin Abdul RAHMAN[2,b], Muhammad Aqil Haziq bin Mohd ZAMRI[3,c], Ahmad Haziq bin Mohamed SABRI[4,d], Hatika KACO[1,e] and Mohd Shamsul Ezzad SHAFIE[5,f]

[1]Education & Advanced Sustainability (EdAS) Unit, Kolej PERMATA Insan, Universiti Sains Islam Malaysia, Bandar Baru Nilai, 71800 Nilai, N.Sembilan, Malaysia

[2]Universiti Pertahanan Malaysia, Kem Sungai Besi, 57000 Kuala Lumpur, Malaysia

[3]Faculty of Medicine, Universiti Sultan Zainal Abidin, Medical Campus, Jalan Sultan Mahmud, 20400 Kuala Terengganu, Terengganu Darul Iman, Malaysia

[4]University of Bristol, Beacon House, Queens Rd, BS8 1QU, United Kingdom

[5]Advanced Technology and Sustainability Unit, Kolej PERMATA Insan, Universiti Sains Islam Malaysia, Bandar Baru Nilai, 71800 Nilai, Malaysia

[a]fadzidahmohdidris@usim.edu.my, [b]faisal.abdrahman.568@gmail.com, [c]aqilhayyii@gmail.com, [d]ahmadhaziq2@gmail.com, [e]hatikakaco@usim.edu.my, [f]seezzad@gmail.com

Keywords: Microwave Absorber, Reflection Loss, Single Layer, Multilayer, Electromagnetic Interference

Abstract. The rapid advancement of wireless communication technologies creates more electromagnetic (EM) wave interference that deteriorates other equipment performance and pose risks to human health. Thus, it attracts researchers' attention in designing and fabricating more EM wave absorber in reducing the unwanted signals. Traditional single-phase absorbers struggle to overcome Snoek's limit to achieve thin and broadband absorption. To address this gap, this study introduces a novel structurally tailored multilayer composite by utilizing a unique combination of fillers of porous dielectric Zeolite to maximize impedance matching, carbon nanotubes synthesized by industrial mill scale waste to drive intense dielectric loss and magnetic $Ni_{0.7}Zn_{0.3}Fe_2O_4$ nanoparticles to provide strong high frequency magnetic dissipation. This research highlights the fabrication and reflection loss (RL) performance in both single-layer and multilayer composite materials. Different materials were used as fillers ($Ni_{0.7}Zn_{0.3}Fe_2O_4$, Zeolite and Carbon Nanotubes) while epoxy resin as polymer matrix. The single layer was fabricated using mixing method at thickness of 1 mm, 2 mm and 3 mm, while the multilayer was fixed at thickness 3 mm (1 mm sub layers) and tailored of different materials as impedance matching layer, absorbing layer and reflective layer. The materials properties and microwave characterization were analysed by using Field Emission Scanning Electron Microscope (FESEM) and Vector Network Analyzer (VNA) across the frequency range of 4 – 18 GHz. The single layer achieved a minimum RL of -14 dB at 10 GHz (thickness=3 mm), while significantly improved RL in multilayer structure. The multilayer structure composed of tailored impedance matching layer (zeolite), absorbing layer (carbon nanotubes) and reflective layer ($Ni_{0.7}Zn_{0.3}Fe_2O_4$) of thickness 3 mm with RL of -32 dB (14 GHz). This is due to enhanced impedance matching and internal multiple reflections within the layered structure. The results obtained demonstrate a highly competitive, green and geometrically optimized approach for advanced electromagnetic interference (EMI) mitigation applications.

Content from this work may be used under the terms of the Creative Commons Attribution 3.0 license. Any further distribution of this work must maintain attribution to the author(s) and the title of the work, journal citation and DOI. Published under license by Materials Research Forum LLC.

Introduction

The proliferation of various wireless communication systems has increased concerns regarding electromagnetic (EM) wave pollution. Moreover, demands increased in improving quality-of-service, thus higher frequency range was used as for 5G and beyond were implemented to upgrade the networks [1]. Thus, it creates more electromagnetic field (EMF) radiation exposure that may contribute to health risk. The simulation revealed that the EMF exposure exceeds the regulatory limits and exposure level remains high [1]. Therefore, the development of wideband, lightweight, thin thickness and strong absorption EM wave absorber is crucial [2,3,4]. Absorbing materials refers to attenuation of electromagnetic waves in the material and efficiently absorbs the energy and transforms it into heat or other types of energy and later dissipates it. The absorbed energy was emitted as a small or nearly unmeasurable quantity of heat. According to microwave absorption theory, the electromagnetic wave signal that passes through the absorbing materials, it can be partially transmitted or reflected. The transmitted signal may also create multiple internal reflection in the sample which the waves emerge out-of-phase by 180°. The multiple internal reflection in the sample may also represent the absorption as also shown in Fig. 1.

Recent research studies have explored various materials to be used as an EM wave absorber, including by exploring multilayer nanocomposite structure to improve the EM wave absorbing properties [5,6]. Moreover, recent research also focuses on the development of EM wave absorbers by utilizing silica from beach sand and mill scale from industrial waste with single and multilayer structure that may improve the performance and increase in sustainability [7]. The ability to absorb the incoming EM waves in the materials can be determined by the impedance matching condition. When the incoming waves completely absorb in the absorbing materials, it shows that no reflection of the sample and it results in ideal impedance matching [8].

Snoek's limit states that materials' permeability value must be less than five at GHz frequency range, where it shows that single dielectric or magnetic materials cannot achieve impedance match and broad frequency wave absorption [9]. Thus, to obtain good EM wave absorber performance, different structures have been introduced: 1) mixture of dielectric and magnetic materials, 2) multilayer structures and 3) core-shell structures. In the case of multilayer structures, the layer consists of three layers that are reflective layers, electromagnetic wave loss layer and impedance matching layer [10]. The function of the reflective layer is to make less quantity of transmission wave back to the wave loss layer, while the impedance matching act as to transmit the EM wave without reflection by modifying the complex permittivity and permeability. It can also be designed by using nanoparticles and disperse it uniformly throughout the EM wave absorber multilayer structure of electric and magnetic materials.

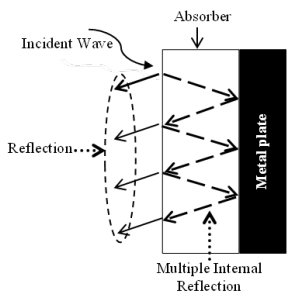


Fig. 1. Normal phenomena of multiple internal reflection.

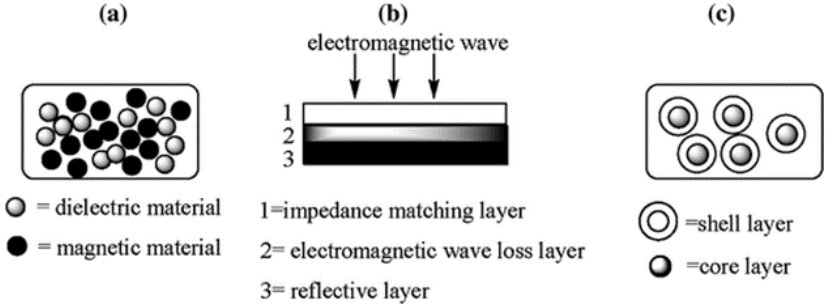


Fig. 2. The Three Positive Structures for Electromagnetic Wave Absorption Material [10].

Among various EM wave absorbers being used, hybrid composites incorporating magnetic, dielectric and conductive components offer promising performance through enhanced internal reflection, impedance matching and multiple scattering in the sample. Nickel Zinc ferrite is well

known for its high permeability and low coercivity, while zeolite provides porous dielectric matrix and carbon nanotubes (CNT) contribute to excellent electrical conductivity and interfacial polarization. While ferrite/conductive carbon multi-structures have been previously studied, the novelty of this research highlights two aspects. The first one is this research introduces a highly sustainable synthesis route by utilizing industrial mill scale waste as a main catalyst to grow carbon nanotubes via chemical vapor deposition (CVD) method. This shows the effectiveness of transforming and industrial byproduct into a usable and functional EM wave attenuating filler. Secondly, this works establishes structurally tailored "impedance loss reflection" gradient framework using sub layers of 1 mm each, unlike the conventional trial and error blending to obtain better EM wave absorption performance. Therefore, the aim of this research is to investigate and compare the EM wave absorption performance of single and multilayer composites that are synthesized based on $Ni_{0.7}Zn_{0.3}Fe_2O_4$, zeolite and CNT incorporated into epoxy matrix. This research also highlighted the tailoring of layer functions to improve the impedance matching and increase the EM wave absorption. This is also to address the current research gaps that is to obtain lower reflection loss value with thinner materials.

Methodology

Preparation of filler materials

The overall main materials to be used as fillers are Nickel Zinc Ferrite, Zeolite and synthesized Carbon Nanotubes (CNT) catalyzed by mill scale waste, while epoxy resins as the polymer matrix. The Nickel Zinc Ferrite was synthesized by using solid state sintering, whereas carbon nanotubes were synthesized by using chemical vapor deposition (CVD) method. On the other hand, Zeolite was commercially purchased. Nickel zinc ferrite was prepared by using solid state sintering according to the chemical equation below:

$$0.7NiO + 0.3ZnO + Fe_2O_3 \rightarrow Ni_{0.7}Zn_{0.3}Fe_2O_4 \quad \text{Eq. 1}$$

The mixture of powder NiO (Nickel (II) Oxide, 99.00%, Alfa Aesar), ZnO (Zinc Oxide 99.90%, Alfa Aesar) and Fe_2O_3 (Iron (III) Oxide, 99.50%, Alfa Aesar) materials were prepared according to the targeted proportion and milled for 10 hours by using High Energy Ball Milling (HEBM) (SPEX8000D mill) to obtain nanoparticle size. The milling process being carried out at room temperature in a hardened steel vial together with grinding steel balls with the Ball to Powder weight Ratio (BPR) was 10:1. The sample was then sintered by using open tube ceramic furnace at 900^0C for 10 hours (holding time) by using heating rate of 4^0C/min to obtain the full phase of $Ni_{0.7}Zn_{0.3}Fe_2O_4$.

On the other hand, industrial mill scale waste was used as catalyst to grow the carbon nanotubes. The flaky shape of mill scale waste was first crush by using Ball Milling and further crushed by using High Energy Ball Milling for 4 hours to obtain nanoparticle size. The powder sample was then used as catalyst to grow carbon nanotubes and further synthesize by using chemical vapor deposition (CVD) method. The starting weight of catalyst being used to grow CNT was 0.1 g. The powder was put in an alumina boat and located at the center of the closed end tube furnace. Argon gas with pressure set to 1- 2 bar and ethanol were used as liquid carrier gas and carbon source respectively in synthesizing the carbon nanotubes. The ethanol was heated and boiled to 80 ^{0}C to get the vapour flow into the tube furnace. The temperature was set at 700^0C with 30 minutes reaction time.

Preparation of single layer

The synthesized powder materials were mixed with epoxy resin as the polymer matrix and hardener as the curing agent. Different filler weight percentages were used, as the weight percentage obtained were the optimized weight percentage based on previous research conducted in the research group. Different weight percentages used were 6 wt% $Ni_{0.7}Zn_{0.3}Fe_2O_4$ (denoted as

sample ‘a’), 10 wt% Zeolite (denoted as sample ‘b’) and 8wt% synthesized carbon nanotubes (denoted as sample ‘c’). as the amount of filler used in the polymer matrix.

All the fillers ‘a’, ‘b’ and ‘c’ were mixed together with epoxy resin where epoxy resin was fixed to 1 to 2 wt%. This insulating polymer was used as the polymer matrix since it was transparent and has almost no absorption. The mixing process was carried out by using mini vortex mixer at 3000 rpm to prevent agglomeration of CNTs. Hardener was then added into the mixture as a curing agent and was continuously mixed. The epoxy resin and hardener were added to ratio 10: 1 respectively for 15 to 20 minutes. The sample was cured for overnight at room temperature.

Preparation of multilayer

Among the broad polymer candidates suitable for embedding fillers for preparing the microwave absorbing materials, epoxy is one of the most attractive polymers due to its commercial availability, resistance to corrosion, and relatively easy for processing. In this study, we focused on the EM wave absorption performance of the polymer composites in a continuous frequency range from 4 GHz to 18 GHz. Thus, EM wave absorbing composite materials were prepared to explore the EM wave absorbing properties in the C-band, X-band and Ku-Band. The shrinkage of epoxy resin was 1 to 2 wt% and this insulating polymer was used as the polymer matrix since it was transparent and has almost no absorption. Hardener was then poured into the mixture as a curing agent and was continually mixed. The ratio of epoxy resin and the hardener that are added into the filler is 5.5:1.5 respectively for 5-10 minutes. Care was taken to reduce the bubbles in the mixture. After mixing, the mixture was poured into the sample holder. All the mixing steps were repeated with different filler materials and were poured into the sample holder to form a multilayer sample. The total thickness of the multilayer sample is 3 mm that consists of three different materials (each layer of materials thickness is 1 mm) placed in the sample holder to form the multilayer sample. The thickness of each layer is controlled by using the equation, V = Ah (V: Volume, A: Area and h: thickness). 6 wt% $Ni_{0.7}Zn_{0.3}Fe_2O_4$ (denoted as sample ‘a’), 10 wt% Zeolite (denoted as sample ‘b’) and 8wt% synthesized carbon nanotubes (denoted as sample ‘c’). For multilayer sample, the EM wave signals start to penetrate through matching layer (layer 1), absorbing layer (layer 2) and the reflective layer (layer 3) as also shown in Fig. 2(b). Therefore, three different layered structures were prepared following the layer arrangement (layer 1, 2 and 3) and the structures are denoted as ‘bca’, ‘cba’ and ‘cab’.

Materials’ characterization

The microstructure micrographs were taken using FE NOVA NanoSEM230 Field emission scanning electron microscope (FeSEM) measurements. The measurement was conducted by placing small amount of dry powder onto a carbon-taped aluminium stub and blowing off the loose particles with compressed gas. The sample was then coated with carbon to prevent charging. On the other hand, Vector Network Analyzer (Agilent N5230A) was used to measure the reflection loss at frequency range of 4 to 18 GHz at different frequency band of C-band (4 – 8 GHz), X-band (8 – 12 GHz) and Ku-band (12 – 18 GHz). This instrument was used to measure S-parameters (S_{11}, S_{22}, S_{12}, S_{21}), in different microwave bands. For perfect reading, special manufacture sample holder was used as shown in Fig. 3. Samples were put into the middle of a rectangular-shaped sample holder and backed by a metal short and were connected with screws and they are not separated from each other. The dimension of the rectangular shape depends on the frequency range needed to be measured (C-band: 34.85 mm x 15.80 mm, X-band: 22.860 mm x 10.160 mm, Ku-band: 15.799 mm x 7.899 mm). Since the measurement was backed by a metal short, the measurements were only taken by using single port measurement with S_{11} parameter.



(a) *(b)* *(c)*

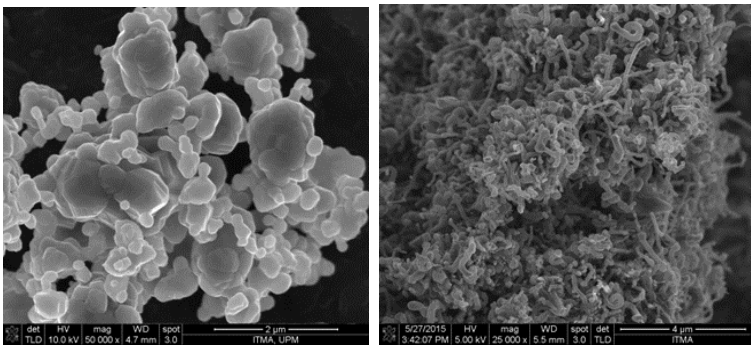
Fig. 3. (a) X-band empty sample holder, (b) metal plate for metal backed absorber, and (c) S-parameters measured by using Vector Network Analyzer.

Results and Discussion

Fig. 4(a) shows the micrograph of $Ni_{0.7}Zn_{0.3}Fe_2O_4$ with the mixture of irregular, roundish and elongated shapes within the range of ~150 nm to ~250 nm and the average particle size is 218 nm. The particles are agglomerated due to the effect of magnetic dipole interactions between particles. Smaller grain size has a magnetic moment that could interact with the neighbouring magnetic moment. Moreover, smaller grain size that consist of single domain or few domains results in higher anisotropy field that rendering the magnetic moment harder to reverse. Thus, the EM wave can be absorbed more effective by having nanoscale particles. The amorphous surface area of a nanoscale crystallite is the source of its surface states. Electrons can absorb energy and move from the ground state to excited states if the surface energy level interval falls within the microwave energy range. This results in increase in the EM wave absorption [11]. Nanomaterials exhibit remarkable EM wave absorber performance in the GHz frequency range due to its small size and shape anisotropy effects [12].

Fig. 4 (b) shows the FESEM image of CNT catalyzed by mill scale reveals the presence of bundles and entanglements that consist of 50 to a few hundred individual CNTs and it is due to the strong Van der Waals forces. In comparison to microparticles, short fibers may also be more effective in absorbing the EM wave due to their higher surface-to-volume ratio, quantum size effects and influence of the network structure [13].

The morphological results obtained showing the macroscopic reflection loss performance of the composites. The average particle size for the ferrite particles is within the single magnetic domain threshold, that suppresses domain wall displacement and forces the magnetic dissipation to rely on the spin natural resonance. The microstructural characteristics results in the peak of magnetic loss contributions shifting towards higher frequency range (X and Ku band). Moreover, the synthesized CNT with entangled and bundle morphology creates a dense and interconnected conductive network within the insulating polymer. This network structure creates thousands of micro capacitor nodes that can amplify interfacial polarization.



(a) (b)

Fig. 4. FeSEM images of a) $Ni_{0.7}Zn_{0.3}Fe_2O_4$ and b) Synthesized Carbon Nanotubes.

The EM wave absorption performance can be obtained mainly by the reflection coefficient data that is represented in decibels. This quantitative value is also known as reflection loss. An EM wave aborber will absorb significant number of signals and minimizing the reflection. The reflection loss value below -10 dB represent 90% of the EM wave attenuated in the sample. Whereas, a value of -20 dB corresponds to 99% of the EM wave energy being absorbed while -30 dB represents 99.9 % of energy is absorbed. Fig. 5 shows the single layer EM wave absorber that consist mixture of 6 wt% $Ni_{0.7}Zn_{0.3}Fe_2O_4$, 10 wt% Zeolite and 8wt% synthesized carbon nanotubes. The sample was measured at the thickness of 1 mm, 2 mm and 3 mm. As can be observed from Fig. 5, for thickness 1 mm, there is no peak can be observed since the reflection loss peak formation is at much higher frequency range. This is the same as observed for thickness 2 mm, where the main reflection loss peak starts to form at frequency of higher than 16 GHz. On the other hand, for thickness 3 mm, the main reflection loss peak present at frequency of 10 GHz. This shows that as thickness increases, the reflection loss peak move towards lower frequency range. This can be explained by the quarter-wavelength cancellation theory that provides an explanation for this situation. More precisely, the matching thickness and matching frequency satisfy the following equation to obtain smallest reflection loss value [14,15,16]:

$$t_m = \frac{n\lambda}{4} = \frac{nc}{4f_m\sqrt{|\varepsilon_r||\mu_r|}} \qquad (n = 1,3,5 \ldots\ldots) \qquad \text{Eq. 2}$$

Where, t_m is matching thickness, λ is wavelength, c is the speed of light, $f_m$is matching frequency, ε_r is relative permittivity and μ_r is relative permeability. Dotted line in the figure shows the reflection loss peak of less than -10 dB showing 90 % of the EM wave being absorbed.

At the matching frequency of (f_m = 10.14 GHz), the measured relative permittivity and relative permeability staisfy equation (2). When the incident wave strikes the metal backed composite, part of the wave reflected from the front air absorber interface and the other part reflected back from the metal plate merge with a phase difference of 180^0. Since the thickness of 3 mm aligns perfectly with the quarter wavelength (λ/4) under the specific values of the ε_r and μ_r, the two vectors destructively cancel each other out that is out of phase. However, at lower thickness of 1 mm and 2 mm, the structural path for the signal transmitted in the sample is too short to fullfill this phase cancellation within the frequency range of 4 to 18 GHz. Thus, shifting the corresponding EM wave absorption peaks to higher GHz frequency range.

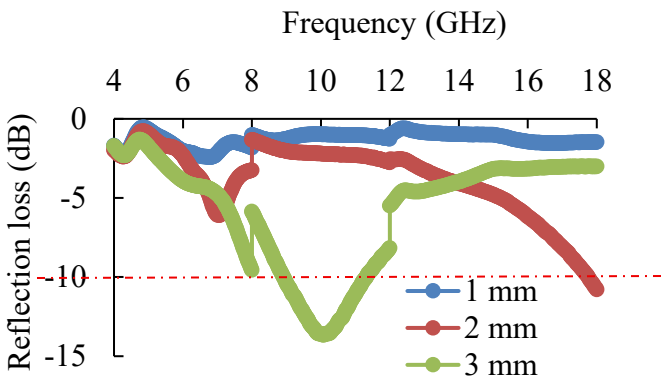


Fig. 5. Reflection loss of single layer samples at 4 to 18 GHz.

Table 1 shows the reflection loss performance of single layer and multilayer sample. 6 wt% $Ni_{0.7}Zn_{0.3}Fe_2O_4$ (denoted as sample 'a'), 10 wt% Zeolite (denoted as sample 'b') and 8wt% synthesized carbon nanotubes (denoted as sample 'c'). For multilayer sample, the EM wave signals start to penetrate through matching layer (layer 1), absorbing layer (layer 2) and the reflective layer (layer 3). Therefore, three different layer structures were prepared following the layer arrangement (layer 1, 2 and 3) and the structure are denoted as 'bca', 'cba' and 'cab'. All samples were measured at frequency of 4 to 18 GHz with fixed thickness of 3 mm.

Table 1. Reflection loss performance of single layer and multilayer.

Layer	List of sample	Thickness	Frequency Band	Reflection loss (dB)	Bandwidth (GHz) (< -10dB)
Single layer	Mixture a, b and c	1 mm	C, X, Ku-band	- 2.42 dB (6.8 GHz)	-
		2 mm	C, X, Ku-band	-6.03 dB (7.38 GHz)	-
		3 mm	C, X, Ku-band	-13.59 dB (10.14 GHz)	2.3 GHz
Multilayer	bca	3 mm (each layer 1mm)	C-band	-3.41 dB (5.42 GHz),	-
				-4.57 dB (7.78 GHz)	-
			X-band	-6.07 dB (8.36 GHz)	-
			Ku-band	-32.36 dB (14.01 GHz)	3.81 GHz
	cba	3 mm (each layer 1mm)	C-band	-6.71 dB (5.96 GHz)	-
			X-band	-5.71 dB (8.48 GHz)	-
			Ku-band	-13.09 dB (14.19 GHz)	4.11 GHz
	cab	3 mm (each layer 1mm)	C-band	-.9.96 dB (6.56 GHz)	-
			X-band	-6.34 dB (9.90 GHz)	-
			Ku-band	-19.15 dB (17.67 GHz)	>3.66 GHz

Fig. 6 shows the reflection loss of three-layer arrangement of multilayer samples at frequency C-band, X-band and Ku-band. Fig. 6(a) shows the most obvious trend of the minimum reflection loss peak formation shift towards higher frequency range starting with 'bca' and followed by 'cba' and finally 'cab'. At frequency of 4 to 8 GHz, the minimum reflection loss peak was obtained by

sample 'cab' where synthesized carbon nanotubes suitable to be used as the matching layer, $Ni_{0.7}Zn_{0.3}Fe_2O_4$ as the absorbing layer and zeolite as the reflective layer. However, the reflection loss peak was only -9.96 dB at 6.56 GHz represent almost 90% of the EM wave absorption being absorbed.

On the other hand, as for Fig. 6(b), the formation of minimum reflection loss peak starts to present at much higher frequency range (>11.5 GHz). As for Fig. 6(c) the minimum reflection loss peak was obtained for sample 'bca' with -32.36 dB (14.01 GHz). However, the highest bandwidth can be obtained for sample 'cab' with bandwidth > 3.66 GHz although with reflection loss around -19.15 dB. Thus, it shows that for multilayer sample, the best performance is depend on the frequency range as the application needed.

The main factors affecting the EM wave absorption performance depends on the minimum reflection loss, the absorption bandwidth and the matching thickness. The reflection loss of the EM wave absorber may be referred to the transmission line theory by calculating using the following equation [17,18,19]:

$$RL\ (dB) = 20 \log \left| \frac{(Z_{in} - Z_0)}{Z_{in} + Z_0} \right| \quad \text{Eq. 3}$$

$$Z_{in} = Z_0 \left(\frac{\mu_r}{\varepsilon_r} \right)^{\frac{1}{2}} tanh \left[j \left(\frac{2\pi f d}{c} \right) (\varepsilon_r \mu_r)^{\frac{1}{2}} \right] \quad \text{Eq. 4}$$

where Z_{in}, Z_0, μ_r, ε_r, f, d and c are the input impedance, free space impedance, relative complex permeability and relative complex permittivity, frequency, thickness of the absorber and speed of light respectively.

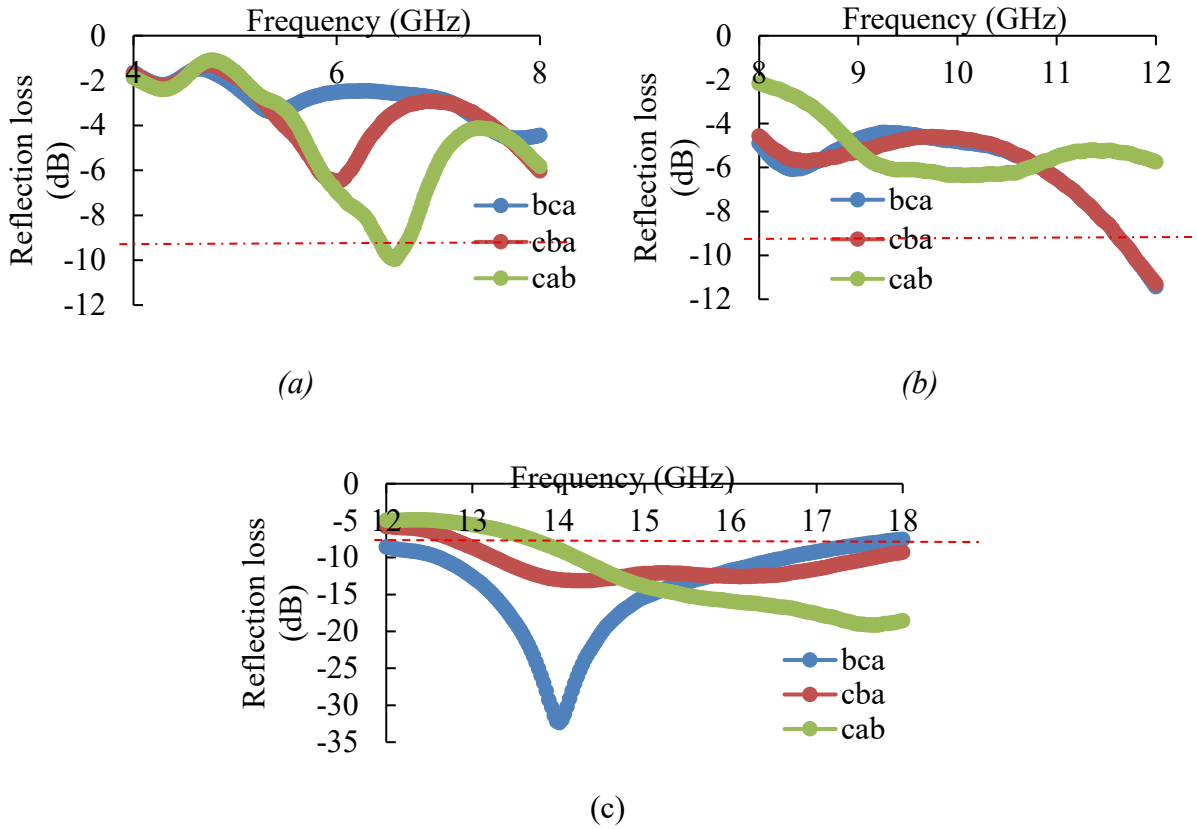


Fig. 6. Reflection loss of multilayer samples at (a) C-band, (b) X-band and (c) Ku-band.

Based on the fundamental concept, the EM wave absorption performance of the 'bca' multilayer structure can be attributed to the synergy between dielectric loss, magnetic loss and impedance

matching behavior. Fig. 7 shows the results of 'bca' structure with the highest EM wave absorption performance indicating an ideal attenuation in the sample. Zeolite is used as the impedance matching layer (layer 1) due to its high porosity and low dielectric properties of dielectric constant ($\varepsilon' \approx 2.5 - 3.5$) [20]. The low intrinsic complex permittivity of zeolite minimizes the primary reflection at the air-absorber interface ($Z_{in} \approx Z_0$). This may result in allowing maximum penetration of the incident EM waves into the polymer composite matrix. Whereas carbon nanotubes are used as main absorbing layer (layer 2) due to its dielectric loss. Although CNT has excellent electrical conductivity to be used as an EM wave absorber, the weight percentages added must be fixed at lower percentage since too high percentage as filler, results in higher reflectivity and bad dispersion in the polymer matrix. Thus, as the wave travels through the second layer, attenuation is driven by the dielectric loss mechanisms. The interconnected network of CNT plays role in contributing to conduction loss via the micro current networks. In fact, the high surface to volume ratio of CNT induces the interfacial polarization at the CNT epoxy boundaries. On the other hand, magnetic properties of $Ni_{0.7}Zn_{0.3}Fe_2O_4$ serve as reflective layers (layer 3) that may enhance the magnetic loss due to spin resonance and trapping the EM waves in the sample. As demonstrated in recent literature on high performance Ni-Zn ferrites, domain wall resonance diminishes at high gigahertz frequencies, thus the magnetic loss tangent explicitly governed by spin natural resonance and exchange resonance within the spinel lattice [21].

The magnetic loss is usually from the hysteresis loss, domain wall resonance, eddy current loss, natural resonance and exchange resonance [22]. However, the magnetic loss from hysteresis loss and domain wall resonance form at lower frequency range (<2 GHz), whereas at higher frequency range, spin resonance will be dominant. According to ref. [22], natural resonance happens at lower frequency whereas, exchange resonance at higher frequency. The equation related to the natural resonance is as follows [23]:

$$f_r = \frac{\gamma H_\alpha}{2\pi} \quad \text{Eq. 5}$$

$$H_\alpha = \frac{4|K_1|}{3\mu_0 M_s} \quad \text{Eq. 6}$$

where $f_r, \gamma, H_\alpha, |K_1|, M_s$ are natural resonance frequency, gyromagnetic ratio, anisotropic energy, anisotropic coefficients and saturation magnetisation respectively. Smaller particle size contributed by surface anisotropic field may also increase the anisotropic energy and results in enhanced EM wave absorption properties. At higher frequency range, exchange resonance takes place in enhancing the EM wave absorption properties. Therefore, the nanoscale dimensions of the ferrite particles (~218 nm) significantly show the role of surface anisotropy field (H_α), shifting the resonance frequencies higher, thus maximizing the magnetic attenuation within the structure.

Fig. 8 shows the reflection loss obtained for single layer and multilayer sample ('bca') of thickness 3 mm with the minimum reflection loss obtained was -13.7 dB (10 GHz) and -32.4 dB (14 GHz) respectively. The quantitative correlation of this data reveals the physical structural arrangement enhance the final reflection loss perfromance. At the overall thickness of 3mm, dispersing the fillers uniformly into a single layer composite yields a moderate minimum reflection loss of -13.59 dB (10.14 GHz) with a narrow absorption bandwidth of only 2.3 GHz (RL < - 10 dB). However, when these materials quantities are geometrically isolated into the tailored 'bca' multilayer strcutures (1 mm/layer), the EM wave absorption performance improves dramatically by having minimum RL is -32.36 dB (14.01 GHz) with bandwidth expands to 3.81 GHz.

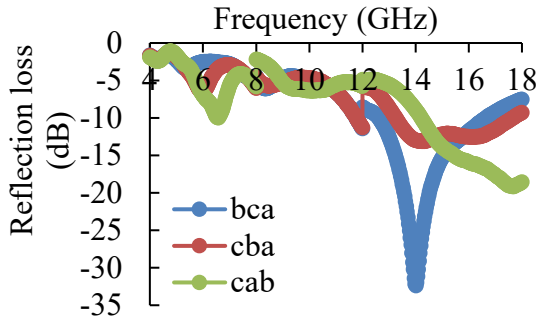


Fig. 7. Reflection loss of multilayer samples at frequency range of 4 to 18 GHz.

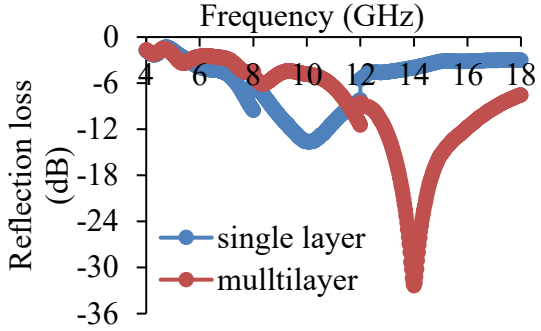


Fig. 8. Comparison reflection loss of single layer and multilayer (bca) EM wave absorber of thickness 3 mm.

The shifting from -13.59 dB to -32.36 dB represents the attenuating from roughly 95% of the incident wave energy to absorbing over 99% of it. This might happen because in single layer blend, conflicting the dielectric and magnetic interfaces can disrupt the phase cancellation that results in degrade the overall impedance matching. When the filler is in single layer, it causes impedance mismatch that limits the reflection loss values. On the other, hand, isolating the phases into functional gradient layers may induces extensive multiple internal reflections at the boundaries between each layer 1, 2 and 3. The structural scattering effects may effectively extend the transmission route so that the wave energy can completely dissipates into heat. Moreover, for 'bca' multilayer, the nanoscale morphology of CNT layer can attenuate the wave via dielectric damping oce the wave transmitted the porous zolite surface.

The EM wave absorption usually considering the surface reflection and multiple reflection in the sample. Multiple reflection from different layers and internal multiple reflection in the material itself results in enhanced EM wave absorption performance. The internal multiple reflection was caused by scattering effects results from inhomogeneity in the material. In addition, by having porous and hollow structures, it helps in extend the transmission route of the EM wave absorber. By having spiral carbon nanotubes, it may also enhance the multiple reflection in the carbon nanotubes itself. Based on these structural formation, it may helps in achieving the impedance matching (Z) characteristics and imrpoving the EM wave absorption performance of the sample. The impedance matching is given as in the equation below:

$$\boldsymbol{Z = \left|\frac{Z_{in}}{Z_0}\right| = \sqrt{\left|\frac{\mu_r}{\varepsilon_r}\right|}\tanh[j(2\pi f dc)\sqrt{\mu_r \varepsilon_r}]} \qquad \textbf{Eq. 7}$$

Table 2 compares the EM absorption of the 'bca' structure against reported absorbers in literature.

Table 2. Comparison of EM wave absorption performance with reported literature.

Absorber Material Structure	Total thickness (mm)	Minimum RL (dB)	Frequency (GHz)/Band	Ref.
Mutiwalled Carbon Nanotubes/$Ni_{0.5}Zn_{0.5}Fe_2O_4$	3.0	-19.34	8.46 GHz	[24]
Nickel Zinc Ferrite/MWCNTs	2.0	-14	16 GHz	[25]
MWCNTs/Fe	4.27	-39	2.68 GHz	[26]
Zeolite/CNT/ $Ni_{0.7}Zn_{0.3}Fe_2O_4$ Multilayer 'bca'	3.0	-32.36	14.01 GHz (Ku band)	[This work]

Conclusion

This study successfully synthesized the composite samples and demonstrates the tunable EM wave absorption performance by manipulating the structural configuration between single layer and multilayer sample. The single layer samples exhibit a minimum reflection loss of -13.7 dB (10 GHz) of thickness 3 mm. The minimum reflection loss obtained shows that more than 90% of the EM wave being absorbed indicating moderate EM attenuation. However, for multilayer structure, 'bca' arrangement shows the minimum reflection loss of -32.4 dB (14 GHz) with zeolite as the impedance matching layer, CNT as the absorbing layer and $Ni_{0.7}Zn_{0.3}Fe_2O_4$ as the reflective layer corresponds to 99.9% EM wave being absorbed. Better performance in the multilayer structure is attributed to improved impedance matching, synergistic dielectric and magnetic losses and enhanced internal multiple reflections. In addition, the multilayer structure allows in tailoring the EM wave absorption properties across different frequency band (C, X and Ku-band). Thus, it indicates the versatility of the structure materials to be used for various EM interference mitigation applications. Therefore, this research demonstrated that the fabricated polymer composites present a novel, eco-friendly approach for designing high performance microwave absorbers by utilizing synthesized CNTs derived directly from industrial mill scale waste. By transitioning from traditional, uniform single layer mixing to a strategically tailored 'bca' multilayer geometric configuration, the composite's sample suitable to be used according to the frequency range needed for specific applications.

Acknowledgements

This research was funded by the Ministry of Higher Education (MOHE) of Malaysia under the Fundamental Research Grant Scheme (FRGS/1/2020/STG05/USIM/02/3) (USIM/FRGS/KGI/KPT/52020). This research acknowledges Kolej PERMATA Insan for the laboratory equipment and apparatus used and Institute of Nanoscience and Nanotechnology, Universiti Putra Malaysia for the microwave measurement using Vector Network Analyzer.

References

[1] M.A. Salem, H.S. Lim, K.S. Diong, K.A. Alaghbari, C.C. Zarakovitis, S.F. Chien, Electromagnetic Field-Aware Radio Resource Management for 5G and Beyond: A Survey, Computers 14 (2025) 1-28. https://doi.org/10.3390/computers14020051

[2] J. Liu, R. Che, H. Chen, F. Zhang, F. Xia, Q. Wu, M. Wang, Microwave absorption enhancement of multifunctional composite microspheres with spinel Fe_3O_4 cores and anatase TiO_2 shells, Small 8 (2012) 1214–21. https://doi.org/10.1002/smll.201102245

[3] C. Zhi, S. Zhang, H. Wu, Y. Ming, S. Shi, W.F. Lo, S. Meng, Y. Si, B. Fei, J. Huo, J. Hu, Perovskite nanocrystals induced core–shell inorganic–organic nanofibers for efficient energy harvesting and self-powered monitoring, ACS Nano 18 (2024) 9365–77. https://doi.org/10.1021/acsnano.3c09935

[4] Y. Yang, J. Cheng, F. Pan, S. Lu, X. Wang, L. Cai, H. Guo, H. Jiang, L. Li, J. Wang, Z. Xiu, H. Yu, W. Lu, Phragmites-derived magnetic carbon fiber with hollow assembly architecture toward fullcovered effective bandwidth at ku band. Carbon 213 (2023) 118228. https://doi.org/10.1016/j.carbon.2023.118228

[5] H. Pang, R. Sahu, J. Liu, Y. Fu, L. Huang, Y. Duan, I. Puri, Facile synthesis of a hierarchical multi-layered CNT-NiFe2O4@MnO2 composite with enhanced microwave absorbing performance, Applications of Surface Science (2021). https://doi.org/10.1016/j.apsusc.2021.152363

[6] M. Amini, M. Kamkar, A. Ghafarkhah, S. Ghaderi, M. Arjmand, Epoxy/CNT$Zn_{0.5}Ni_{0.5}Fe_2O_4$ Multilayer Polymeric Nanocomposites for Electromagnetic Wave Absorption, Italian National Conference on Sensors (2021). https://doi.org/10.1109/SENSORS47087.2021.9639466

[7] F. Mohd Idris, M. I. Ruliza, I. H. K. Shah, N. A. Ashraf, A. I. Mohd Razif, M. S. E. Shafie, Z. M. Idris, Designing 3D Printed Electromagnetic Wave Absorber, Journal of Advanced Research Design 130 (2025) 80–93. https://doi.org/10.37934/ard.130.1.8092

[8] C.K. Lin, Y.J. Chiou, S.J. Tsou, C.Y. Chung, C.C. Chao, R.B. Yang, One pot self-assembling Fe@PANI core–shell nanowires for radar absorption application, Nanomaterials 13 (2023) 1100. https://doi.org/10.3390/nano13061100

[9] V.B. Bregar, Advantages of Ferromagnetic Nanoparticle Composites in Microwave Absorbers, IEEE Transactions On Magnetics 40 (2004) 1679-1684. https://doi.org/ 10.1109/TMAG.2004.826622

[10] J. Huo, L. Wang, H. Yu, Polymeric nanocomposites for electromagnetic wave absorption, Journal of Material Science 44 (2009) 3917-3927. https://doi.org/10.1007/s10853-009-3561-1

[11] J. Qiu, H. Shen, M. Gu, Microwave absorption of nanosized barium ferrite particles prepared using high energy ball milling, Powder Technol. 154 (2005) 116–119. https://doi.org/10.1016/j.powtec.2005.05.003

[12] H. Zheng, Y. Yang, M. Zhou, F. Li, Microwave absorption and Mössbauer studies of Fe_3O_4 nanoparticles, Hyperfine Interactions 189 (2009) 131-136. https://doi.org/10.1007/978-3-642-01370-6_16

[13] S.C. Chiu, H.C. Yu, Y.Y. Li, High electromagnetic wave absorption performance of silicon carbide nanowires in the Gigahertz range, J. Phys. Chem. C 114 (2010) 1947–1952. https://doi.org/10.1021/jp905127t

[14] Q. Zeng, D.W. Xu, P. Chen, Q. Yu, X.H. Xiong, H.R. Chu, Q. Wang, 3D graphene-Ni microspheres with excellent microwave absorption and corrosion resistance properties, J. Mater. Sci. Mater. Electron. 29 (2017) 2421–2433. https://doi.org/10.1007/s10854-017-8161-2

[15] Q. Liao, M. He, Y. Zhou, S. Nie, Y. Wang, S. Hu, H. Yang, H. Li, Y. Tong, Highly cuboid-shaped heterobimetallic metalorganic frameworks derived from porous Co/ZnO/C microrods with improved electromagnetic wave absorption capabilities, ACS Appl. Mater. Interfaces 10 (2018) 29136–29144. https://doi.org/10.1021/acsami.8b09093

[16] R. Shu, Z. Wan, J. Zhang, Y. Wu, Y. Liu, J. Shi, M. Zheng, Facile design of three-dimensional nitrogen-doped reduced graphene oxide/multi-walled carbon nanotube composite foams as lightweight and highly efficient microwave absorbers, ACS Appl. Mater. Interfaces 12 (2020) 4689–4698. https://doi.org/ 10.1021/acsami.9b16134

[17] M. Zhang, X. Fang, Y. Zhang, J. Guo, C. Gong, D. Estevez, F. Qin, J. Zhang, Ultralight reduced graphene oxide aerogels prepared by cation-assisted strategy for excellent electromagnetic wave absorption, Nanotechnology 31 (2020) 275707. https://doi.org/10.1016/j.carbon.2023.118435

[18] H. Wang, H. Ma, Highly enhanced electromagnetic wave absorption bandwidth based on reduced graphene oxide-Fe aerogel composites, Nanotechnology 31 (2020) 095711. https://doi.org/10.1088/1361-6528/ab59b4

[19] B. Wang, Q. Fu, Q. Song, Z. Yu, R. Riedel, In situ growth of B_4C nanowires on activated carbon felt to improve microwave absorption performance, Appl. Phys. Lett. 116 (2020) 203101. https://doi.org/10.1063/5.0007332

[20] C. Ellison, J. Hoffman, D. Shekhawat, Comparison of microwave and conventional heating for CO_2 desorption from zeolite, International Journal of Greenhouse Gas Control (2021) 103311. https://doi.org/10.1016/j.ijggc.2021.103311

[21] D. Mandal, B. Bhandari, S.V. Mullurkara, P.R. Ohodnicki, All-Around Electromagnetic Wave Absorber Based on Ni–Zn Ferrite, ACS Applied Materials & Interfaces 16 (2024) 33846-33854. https://doi.org/10.1021/acsami.4c06498

[22] X. Zhang, X. Zhang, H. Yuan, K. Li, Q. Ouyang, C. Zhu, S. Zhang, Y. Chen, CoNi nanoparticles encapsulated by nitrogendoped carbon nanotube arrays on reduced graphene oxide sheets for electromagnetic wave absorption, Chem. Eng. J. 383 (2020) 216–225. https://doi.org/10.1016/j.cej.2019.123208

[23] X. Jian, B. Wu, Y. Wei, S.X. Dou, X. Wang, W. He, N. Mahmood, Facile synthesis of Fe_3O_4/GCs composites and their enhanced microwave absorption properties, ACS Appl. Mater. Interfaces 8 (2016) 6101–6109. https://doi.org/10.1021/acsami.6b00388

[24] M.S. Mustaffa, R.S. Azis, N.H. Abdullah, I. Ismail, I.R. Ibrahim, An investigation of microstructural, magnetic and microwave absorption properties of multi-walled carbon nanotubes/$Ni_{0.5}Zn_{0.5}Fe_2O_4$, Sci Rep 9 (2019) 15523. https://doi.org/10.1038/s41598-019-52233-2

[25] F.M. Idris, K.A. Matori, I.R. Ibrahim, R. Nazlan, M.S.E. Shafie, Enhancing Microwave Absorbing Properties of Nickel-Zinc-Ferrite with Multi-walled Carbon Nanotubes (MWCNT) Loading at Higher Gigahertz Frequency, Malaysian Journal of Science Health & Technology 7 (2021) 1-7. https://doi.org/10.33102/mjosht.v7i1.151

[26] F. Wen, F. Zhang, Z. Liu, Investigation on Microwave Absorption Properties for Multiwalled Carbon Nanotubes/Fe/Co/Ni Nanopowders as Lightweight Absorbers, J. Phys. Chem. C 115 (2011) 14025–14030. https://doi.org/10.1021/jp202078p

Materials Research Proceedings 74 (2026) 76-83 https://doi.org/10.21741/9781644904473-10

AI Driven in Composite Material Science

Anis Farina MANSOR[1], Iylia IDRIS[1], Dinie MUHAMMAD[2], Rushdan Ahmad ILYAS[2], Fakhrony Sholahudin ROHMAN[3] and Ashraf AZMI[1,a *]

[1]Faculty of Chemical Engineering, Universiti Teknologi MARA, 40450, Shah Alam Selangor, Malaysia

[2]School of Chemical and Energy Engineering, Faculty of Engineering, Universiti Teknologi Malaysia (UTM), Johor Bahru, Johor 81310, Malaysia

[3]Faculty of Engineering, Universiti Malaysia Sabah, Jalan UMS, 88450 , Kota Kinabalu, Sabah, Malaysia

[a]ashraf.azmi@uitm.edu.my

Keywords: Artificial Intelligence, Machine Learning, Deep Learning, Composite Material

Abstract. Artificial intelligence (AI) integrated into composite material science is revolutionizing material design, optimization, and monitoring. Especially Machine Learning (ML) and Deep Learning (DL), artificial intelligence methods improve manufacturing efficiency, fault identification, and material selection. Important artificial intelligence uses like structural health monitoring (SHM), generative design, and predictive modelling are reviewed in this paper. Examining high-impact studies helps the present work to show how artificial intelligence is expediting material discovery, enhancing accuracy, and allowing real-time condition monitoring. Still unresolved, though, are issues like data availability, computing limits, and experimental validation. For next-generation smart materials, future directions stress artificial intelligence integration with quantum computing and Internet of Things (IoT). This paper shows how artificial intelligence is transforming composite materials, therefore offering insightful analysis for academics and business leaders.

Introduction

Composite materials have long been a cornerstone of innovation across aerospace, automotive, construction, and biomedical industries due to their superior strength-to-weight ratio, corrosion resistance, and customizable properties. Traditionally, the design and optimization of composite materials relied heavily on empirical methods and iterative experimental testing, which are often time-consuming, expensive, and limited by human-driven intuition. The emergence of Artificial Intelligence (AI) has revolutionized this process by enabling data-driven insights, predictive modeling, and accelerated material discovery.

AI, particularly machine learning (ML) and deep learning (DL), offers powerful tools for handling the complex, nonlinear, and multi-scale nature of composite materials. Through supervised and unsupervised learning, AI models can predict material properties, optimize manufacturing parameters, and even propose novel composite formulations with targeted performance [1]. Furthermore, AI facilitates real-time monitoring and defect detection in composite production, leading to enhanced quality control and reduced wastage.

Machine learning (ML) is transforming the development and optimization of polymer composites by providing data-driven solutions to address their inherent complexity. Through various ML techniques, researchers can accelerate material discovery, enhance performance, and lower production costs. Table 1 presents a comparative analysis of different ML models along with their corresponding quantitative performance metrics [2].

Content from this work may be used under the terms of the Creative Commons Attribution 3.0 license. Any further distribution of this work must maintain attribution to the author(s) and the title of the work, journal citation and DOI. Published under license by Materials Research Forum LLC.

Table 1. The comparative analysis between different ML techniques and quantitative metrics.

ML Technique	Key applications in polymer composites	Advantages	Limitation
Supervised learning	Property prediction (e.g., tensile strength and elasticity)	High predictive accuracy (85-95%)	Requires large labeled datasets
Artificial Neural Networks (ANNs)	Mechanical property estimation	Can model complex, nonlinear relationship	Prone to overfitting with small datasets
Support Vector Machines (SVM)	Classification of composite types	Effective with small datasets	Computationally expensive for large datasets
Random Forest (RF)	Material selection and property prediction	Robust against overfitting	Requires careful parameter tuning
Unsupervised learning	Clustering materials based on properties	No need for labeled data	Limited for direct property prediction
Principal Component Analysis (PCA)	Feature reduction for composite datasets	Reduces dimensionality and improve efficiency	Can lose critical information
K-Means clustering	Grouping materials based on similarities	Fast and scalable	Requires predefined cluster number
Deep learning	Microstructural analysis and failure prediction	High accuracy with large datasets	Requires significant computational resources
Convolutional Neural Networks (CNNs)	Microstructure and defect detection	Excellent at image-based analysis	Computationally expensive
Recurrent Neural Networks (RNNs)	Time-series prediction for material degradation	Captures sequential dependencies	Difficult to train and prone to vanishing gradient
Reinforcement Learning (RL)	Process optimization (e.g., injection molding and extrusion)	Learns optimal process parameters over time	Requires significant trial-and-error data

Recent years have witnessed a surge in research integrating AI into composite material science. This integration not only shortens development cycles but also unlocks previously unattainable material designs by uncovering hidden patterns in large datasets. As industries push toward sustainable and lightweight solutions, AI's role in accelerating design, manufacture and performance loops become critical. This review provides an overview of AI-driven advancements in composite material science, focusing on key research contributions and future outlooks.

Summaries of Research Work Related to AI-Driven Advancements in Composite Material Science

Several studies have demonstrated the potential of AI in various facets of composite material science, including property prediction, process optimization, defect detection, and material discovery.

Property Prediction

Polymer composites are extensively applied in engineering and industry because of their lightweight nature, high strength, corrosion resistance, and design flexibility. However, conventional experimental and computational approaches for their design and analysis are often

complex and expensive [3]. AI methods, particularly supervised learning and deep neural networks, have been effectively applied to predict mechanical, thermal, and physical properties of fiber-reinforced polymer (FRP) composites with high accuracy. By learning complex, nonlinear relationships from extensive experimental and simulated datasets, AI models enable rapid estimation of composite performance under diverse conditions, reducing reliance on costly and time-consuming physical testing. This capability is critical for tailoring composites to aerospace, automotive, and biomedical applications where precise property control is essential [4].

To assess fatigue damage in Carbon Fiber Reinforced Plastic (CFRP), an entropy-based damage evaluation model was introduced that does not require knowledge of the loading history. However, this model is computationally intensive and impractical for high-cycle analysis. Yoshimori et al. [5] addressed this issue by implementing a multi-timescale analysis, which substitutes cyclic loading with constant displacement loading to reduce computational costs. They optimized characteristic variables using both the LightGBM machine learning model and the response surface method (RSM). LightGBM achieved a 75% reduction in root mean squared error compared to RSM by increasing the number of features from 3 to 21. This approach reduced analysis time by over 90% while preserving predictive accuracy, showing that LightGBM outperforms RSM and that multi-timescale analysis effectively decreases computational demands [5].

Composites are used in many industries because they are strong, lightweight, durable, and resistant to corrosion. However, making and testing reinforced composites can be expensive and time-consuming. Dev et al. [6] employed machine learning (ML) to understand important factors in manufacturing and to predict composite properties, making design easier and more efficient. Their study provides a critical review and comparison of various ML models used to predict mechanical, thermal, tribological, acoustic, and electrical properties of reinforced composites. It also summarizes details such as the ML models used, methods, database sizes and sources, input and output parameters, and statistical measures. Furthermore, the performance of these ML models is evaluated and analyzed based on training and testing results, helping guide the selection of suitable models for predicting composite properties [6].

Carbon fiber reinforced thermoplastic composites (CFRTP) are promising materials for car structural parts. Since CFRTP parts are made of multiple layers, designing and optimizing these layers is important for safety and weight reduction. Hou et al. [7] introduced a new method that combines a simplified load calculation (ESLM) with deep learning to find the best layer designs quickly and efficiently. First, the layers of the composite B-pillar are designed using the equal stiffness principle, similar to traditional steel parts. The study then tests how well the B-pillar performs in crashes, considering the speed of impact. To speed up data collection for the deep learning model, a modified version of ESLM is used to replace complex simulations with simpler calculations, creating 18,000 design samples. Finally, a deep learning model called a conditional generative adversarial network (CGAN) is trained to suggest good layer designs. The results show that this approach can quickly produce many effective design options, helping improve CFRTP parts for vehicles [7].

Process Optimization

AI-driven optimization techniques, including Bayesian optimization and reinforcement learning, have been employed to fine-tune manufacturing parameters such as curing temperature, fiber orientation, and resin composition. These approaches surpass traditional trial-and-error methods by systematically exploring large parameter spaces to identify optimal processing conditions that maximize composite quality and performance. Real-time process control using AI further enhances manufacturing consistency and reduces defects, enabling adaptive adjustments during production.

Manufacturing techniques for polymer composites such as injection molding, extrusion, and additive manufacturing (3D printing) are governed by multiple interdependent variables, including

temperature, pressure, and processing time. Machine learning (ML) has been effectively leveraged to optimize these processes, leading to reduced material waste, enhanced efficiency, and improved consistency in product quality [2]. Similarly, Yin et al. [8] reported that Gradient Boosting Regression (GBR) and ANN models outperformed conventional approaches in estimating interfacial shear strength (IFSS). These findings underscore the efficiency and precision of ML models compared to traditional experimental techniques [8].

Machine learning (ML) has emerged as an effective approach for optimizing composite material manufacturing by enhancing predictive accuracy and process efficiency. Shirolkar et al. [9] investigated ML applications in carbon fiber production, focusing on continuous stabilization and carbonization processes. Using data from 600 trials, the study applied models such as support vector regression (SVR), multilayer perceptron (MLP), gradient boosted regression trees (GBRT), and recurrent neural networks (RNN) to predict tensile strength and modulus based on process parameters. Among these, RNN achieved superior performance, with R^2 values of 0.85 for tensile strength and 0.67 for modulus, demonstrating its capability in capturing processing–structure–property relationships. The findings emphasize the critical influence of stabilization and low-temperature carbonization stages on fiber properties, highlighting ML as a key enabler for accelerating composite material development while reducing experimental costs [9].

Defect Detection and Quality Control

In manufacturing, AI-driven process optimization and quality control significantly improve efficiency while reducing costs. By analyzing sensor data in real time, AI algorithms can identify process anomalies and potential defects, enabling proactive interventions to prevent quality issues [10]. Advanced sensor technologies combined with AI-powered image processing and machine learning algorithms have revolutionized non-destructive evaluation (NDE) of composites. AI models analyze data from ultrasonic, X-ray, and optical imaging to detect defects such as voids, delamination, and fiber misalignment with high sensitivity and speed. This early detection facilitates prompt corrective actions, minimizing material waste and improving reliability. Additionally, AI aids in microstructural characterization, linking defect patterns to mechanical property variations for enhanced quality assurance [11].

Magnesium matrix composites are widely utilized in aerospace, automotive, and engineering applications for their low density and high strength, though their production often involves time-intensive, costly, and complex processes. Huang et al. [12] compared regression models including support vector machines (SVM), random forests (RF), and XGBoost for predicting mechanical properties using a large dataset comprising matrix type, reinforcement type, particle morphology, and process parameters. XGBoost delivered the highest accuracy ($R^2 = 0.94$) and lowest error rates (MAE = 8.19, RMSE = 10.42). Feature importance analysis identified reinforcement particle form as the most influential factor, with findings suggesting that nano-sized particles can enhance performance through higher surface area ratios. This study demonstrates the effectiveness of machine learning in the design and optimization of magnesium matrix composites [12].

Composite materials are extensively applied in engineering due to their superior mechanical and thermal properties; however, accurately predicting these properties remains challenging because of their complex structures. Song et al. [13] introduced a multimodal fusion learning model integrating microstructural data (SEM images) and material composition information. Microstructural features were extracted using convolutional neural networks (CNN), while component features were processed through a multilayer perceptron (MLP), with an adaptive feature fusion module optimizing their combined effect. The model achieved high accuracy (MAPE = 0.009, $R^2 = 0.974$, MSE = 0.078) and significantly outperformed single-modal approaches, offering a robust solution for composite material design and development [13].

Machine learning (ML) and artificial intelligence (AI) are revolutionizing composite materials research by enabling predictive modeling, optimization, and automated analysis, thereby

overcoming the limitations of conventional experimental and computational methods. Okafor et al. [14] demonstrated the effectiveness of techniques such as artificial neural networks (ANN), support vector machines (SVM), and deep learning in predicting mechanical properties such as tensile strength and fracture toughness while optimizing material composition. The integration of ML with finite element analysis (FEA) further improves stress-strain simulations and failure predictions, reducing reliance on costly physical testing. AI-driven approaches, including high-throughput screening and digital twin technologies, accelerate material discovery, whereas ML-based non-destructive testing enhances defect detection and quality control. Despite these advancements, challenges remain in data availability, model interpretability, and experimental integration, highlighting the need for continued research. Overall, AI and ML offer scalable, data-driven solutions that enhance performance and streamline composite material design and manufacturing across sectors such as aerospace, automotive, and structural engineering [14].

Material Discovery and Design

In material design and optimization, artificial intelligence (AI) transforms the traditional trial-and-error and empirically driven processes into a data-centric, predictive methodology [15]. Generative AI models, including generative adversarial networks (GANs) and variational autoencoders (VAEs), have been applied to accelerate the discovery of novel composite materials by generating candidate formulations with targeted properties. These models analyze vast materials databases to propose innovative composite structures that balance strength, weight, and durability. Integration of AI with robotics and cloud computing platforms enables automated experimentation and rapid screening, significantly shortening development cycles. Such AI-driven material design fosters breakthroughs in sustainable and high-performance composites [15].

In the context of generative design, Lee et al. [16] employed AI-driven optimization combined with Bézier curve manipulation and finite element analysis to develop polymer lattice structures with enhanced mechanical performance. Their method iteratively refined lattice beam geometries based on simulated mechanical responses, significantly reducing design cycles and achieving superior modulus and strength compared to conventional human-guided approaches.

Qavi et al. [17] investigated the correlation between rheological properties and printability in multi-material bioinks for extrusion-based bioprinting (EBB). Using a design of experiments combined with response surface methodology, they optimized formulations containing sodium alginate, gelatin, and laponite, focusing on parameters such as zero-shear viscosity and storage modulus. An artificial neural network (ANN) was trained on the experimental data to generalize parameter relationships, achieving a mean absolute error of 6.3% in predicting bioink printability [17].

Lee et al. [16] developed an ML-based approach to design biocompatible, 3D-printable bioinks using collagen, hyaluronic acid, and fibrin. Their study established the relationship between mechanical properties and printability, noting that high elastic modulus improves shape fidelity while extrusion is feasible below a critical yield stress. Through multiple regression analysis, they predicted formulations with optimal properties and successfully fabricated 3D constructs supporting viable and proliferative cells [16].

Modeling the long-term performance of glass fiber-reinforced epoxy (CFRP) composites under humid conditions remains a significant challenge in materials science. Aghabalaei Baghaei et al. [18] proposed a predictive framework integrating micromechanical finite element (FE) simulations with artificial neural networks (ANN). The approach involved automatic generation of two-dimensional representative volume elements (RVEs) and incorporation of fiber–matrix interface effects. Microstructural features were statistically analyzed using two-point correlation functions, with dimensionality reduction achieved via principal component analysis (PCA). Geometric and environmental data were linked to an ANN model, whose hyperparameters were optimized through cross-validation and Bayesian optimization. Results demonstrated that the ANN

accurately predicted the transverse modulus of CFRP under humid conditions, with training dataset size strongly influencing performance. This method surpassed conventional techniques in both computational efficiency and accuracy, offering a robust solution for long-term property prediction of composite materials [18].

Table 2. Summary of AI Techniques, Applications, and Key Findings in Composite Material Science.

Ref.	Study	AI Technique	Composite Material / Application	Objective	Key Findings
[5]	Yoshimori et al. (2024)	LightGBM, RSM	CFRP fatigue damage prediction	Predict fatigue damage with reduced computational cost	LightGBM reduced RMSE by 75% and analysis time by >90%.
[6]	Dev et al. (2024)	Multiple ML models	Reinforced polymer composites	Predict multiple composite properties	Compared ML models and guided model selection.
[7]	Hou et al. (2025)	CGAN + ESLM	CFRTP B-pillar	Layup optimization	Generated ~18,000 optimized designs efficiently.
[8]	Yin et al. (2021)	ANN, GBR	Fiber-reinforced composites	Predict IFSS	Higher accuracy than conventional methods.
[9]	Shirolkar et al. (2020)	SVR, MLP, GBRT, RNN	Carbon fiber manufacturing	Process optimization	RNN achieved R^2=0.85 for tensile strength.
[12]	Huang et al. (2023)	SVM, RF, XGBoost	Magnesium matrix composites	Predict mechanical properties	XGBoost achieved R^2=0.94.
[13]	Song et al. (2023)	CNN + MLP	Composite materials	Mechanical property prediction	R^2=0.974 using multimodal fusion.
[14]	Okafor et al. (2023)	ANN, SVM, DL	Reinforced polymer composites	Prediction & optimization	Improved prediction, NDT and material discovery.
[16]	Lee et al. (2022)	AI generative design + FEA	Polymer lattice structures	Generative design	Improved stiffness and reduced design cycles.
[17]	Qavi et al. (2024)	ANN	Bioink composites	Optimize printability	MAE=6.3%.
[16]	Lee et al. (2022)	Regression + ML	3D printable bioinks	Predict printability	Identified optimal printable formulations.
[18]	Aghabalaei Baghaei et al. (2024)	ANN + PCA + Bayesian Optimization	Glass fiber-reinforced epoxy	Long-term modulus prediction	Improved efficiency and predictive accuracy.

Table 2 summarizes representative studies on AI applications in composite material science. Machine learning techniques such as ANN, LightGBM, XGBoost, and RNN are predominantly employed for property prediction and process optimization, while deep learning approaches including CNN and CGAN demonstrate strong performance in defect detection and material design. Overall, AI-driven methodologies improve prediction accuracy, reduce computational cost, and accelerate material development compared with conventional approaches.

Conclusion

Artificial intelligence (AI) has transformed composite material science by enabling data-driven approaches for material property prediction, process optimization, defect detection, and accelerated material design. The reviewed studies demonstrate that machine learning and deep learning techniques significantly improve prediction accuracy, reduce experimental costs, and shorten material development cycles, making AI a promising tool for next-generation composite engineering. However, several research gaps remain. Many existing studies rely on limited and application-specific datasets, restricting model generalizability and reproducibility. In addition, the lack of standardized databases, limited interpretability of deep learning models, and insufficient experimental and industrial validation continue to hinder large-scale adoption of AI in composite manufacturing. Future research should focus on developing standardized, high-quality datasets, improving explainable and physics-informed AI models, and integrating AI with experimental validation to enhance reliability and industrial applicability. Furthermore, combining multimodal data, digital twins, Internet of Things (IoT), and autonomous experimentation platforms offers significant potential for intelligent material discovery and manufacturing. Addressing these challenges will strengthen the practical implementation of AI and accelerate the development of sustainable, high-performance composite materials.

Acknowledgement

The financial support received from Faculty of Chemical Engineering, Universiti Teknologi MARA (UiTM) and Universiti Teknologi MARA (UiTM), through research grant no. 600-RMC/GIP 5/3 (025/2024) are greatly acknowledged.

References

[1] F. Rohman, S. Wan Alwi, D. Muhammad, A. Azmi, M. Murat, Nonlinear model predictive controller of hydrogenation of dimethyl oxalate for ethylene glycol production, Chemical Product and Process Modeling 19 (2024) 761-774. https://doi.org/10.1515/cppm-2024-0025

[2] M. Karuppusamy, R. Thirumalaisamy, S. Palanisamy, S. Nagamalai, E. El Sayed Massoud, N. Ayrilmis, A review of machine learning applications in polymer composites: Advancements, challenges, and future prospects, Journal of Materials Chemistry A 13 (2025) 16290–16308. https://doi.org/10.1039/D5TA00982K

[3] A.B. Abdulhussein, I.F. Senturk, Machine Learning and Artificial Intelligence in Composite Materials: A Comprehensive Review, SSRN (2025) http://dx.doi.org/10.2139/ssrn.5343332

[4] F. Kibrete, T. Trzepieciński, H.S. Gebremedhen, D.E. Woldemichael, Artificial Intelligence in Predicting Mechanical Properties of Composite Materials, Journal of Composites Science 7 (2023) 364. https://doi.org/10.3390/jcs7090364

[5] S. Yoshimori, J. Koyanagi, R. Matsuzaki, Efficient Prediction of Fatigue Damage Analysis of Carbon Fiber Composites Using Multi-Timescale Analysis and Machine Learning, Polymers 16 (2024) 3448. https://doi.org/10.3390/polym16233448

[6] B. Dev, M.A. Rahman, M.J. Islam, M.Z. Rahman, D. Zhu, Properties prediction of composites based on machine learning models: A focus on statistical index approaches, Materials Today Communications 38 (2024) 107659. https://doi.org/10.1016/j.mtcomm.2023.107659

[7] W. Hou, M. Li, Y. Yang, Z. Liu, L. Sang, Layup optimization of composite B-pillar under side impact, International Journal of Mechanical Sciences 287 (2025) 109927. https://doi.org/10.1016/j.ijmecsci.2025.109927

[8] B.B. Yin, K.M. Liew, Machine learning and materials informatics approaches for evaluating the interfacial properties of fiber-reinforced composites, Composite Structures 273 (2021) 114328. https://doi.org/10.1016/j.compstruct.2021.114328

[9] N. Shirolkar, P. Patwardhan, A. Rahman, A. Spear, S. Kumar, Investigating the efficacy of machine learning tools in modelling the continuous stabilization and carbonization process and predicting carbon fiber properties, Carbon 174 (2021) 605-616. https://doi.org/10.1016/j.carbon.2020.12.044

[10] W. Villegas-Ch, J. García-Ortiz, S. Sánchez-Viteri, Toward intelligent monitoring in IoT: AI applications for real-time analysis and prediction, IEEE access 12 (2024) 40368-40386.

[11] M. Seckin, P. Demircioglu, A.C. Seckin, I. Bogrekci, S. Aksoy, Artificial Intelligence for Non-Destructive Imaging in Composite Materials, Eng. 6 (2025) 46. https://doi.org/10.3390/eng6030046

[12] S.J. Huang, Y. Adityawardhana, J. Sanjaya, Predicting Mechanical Properties of Magnesium Matrix Composites with Regression Models by Machine Learning, Journal of Composites Science 7 (2023) 347. https://doi.org/10.3390/jcs709034

[13] L. Song, D. Wang, X. Liu, A. Yin, Z. Long, Prediction of mechanical properties of composite materials using multimodal fusion learning, Sensors and Actuators A: Physical 358 (2023) 114433. https://doi.org/10.1016/J.SNA.2023.114433

[14] C.E. Okafor, S. Iweriolor, O.I. Ani, S. Ahmad, S. Mehfuz, G.O. Ekwueme, O.E. Chukwumuanya, S.E. Abonyi, I.E. Ekengwu, O.P. Chikelu, Advances in machine learning-aided design of reinforced polymer composite and hybrid material systems, Hybrid Advances 2 (2023) 100026. https://doi.org/10.1016/j.hybadv.2023.100026

[15] I. Papadimitriou, I. Gialampoukidis, S. Vrochidis, I. Kompatsiaris, AI methods in materials design, discovery and manufacturing: A review, Computational Materials Science 235 (2024) 112793. https://doi.org/10.1016/j.commatsci.2024.112793

[16] S. Lee, Z. Zhang, G.X. Gu, Generative machine learning algorithm for lattice structures with superior mechanical properties, Mater Horiz. 9 (2022) 952-960. https://doi.org/10.1039/D1MH01792F

[17] I. Qavi, S. Halder, G. Tan, Optimization of printability of bioinks with multi-response optimization (MRO) and artificial neural networks (ANN), Progress in Additive Manufacturing 10 (2025) 3573-3598. https://doi.org/10.1007/s40964-024-00828-1

[18] K. Aghabalaei Baghaei, S.A. Hadigheh, Artificial neural network prediction of transverse modulus in humid conditions for randomly distributed unidirectional fibre reinforced composites: A micromechanics approach, Composite Structures 337 (2024) 118073. https://doi.org/10.1016/J.COMPSTRUCT.2024.118073

Materials Research Proceedings 74 (2026) 84-92 https://doi.org/10.21741/9781644904473-11

Recent Advances in Green Synthesis of Nanoparticles for Sustainable Applications: A Brief Review

Sarah OMAR[1,a *], Taib Iskandar MOHAMAD[1,b], Kamaruzaman SOPIAN[1,c] and Merna OMAR[1,d]

[1]Department of Mechanical Engineering, Universiti Teknologi PETRONAS (UTP), 32610 Bandar Seri Iskandar, Perak Darul Ridzuan, Malaysia

[a]sarah_24004955@utp.edu.my, [b]taib.mohamad@utp.edu.my, [c]ksopian@utp.edu.my, [d]merna_24004883@utp.edu.my

Keywords: Sustainable Nanomaterials, Nanoparticles, Renewable Resources, Plant Extract Synthesis

Abstract. Growing interest in sustainable nanomaterials has highlighted green nanoparticle synthesis as an eco-friendly alternative to conventional methods. However, challenges related to scalability, stability, and process optimization continue to limit practical implementation. This brief review discusses the main green sources, synthesis approaches, and applications of nanoparticles in environmental, biomedical, and energy sectors. Unlike previous reviews focusing on specific aspects, it provides a concise overview linking green feedstocks, synthesis methods, and sustainable applications while highlighting current challenges and future opportunities.

Introduction

Increasing environmental concerns, the global energy crisis, and the limitations of conventional resources have intensified interest in sustainable materials [1]. Among these, green nanoparticles (NPs) have gained attention due to their unique physicochemical properties and environmentally friendly synthesis routes [2]. Biomass residues, plant extracts, and microorganisms have been widely explored as renewable resources for nanoparticle production, offering lower toxicity and reduced environmental impact than conventional methods [3]. However, chemical and physical synthesis generally provide superior control over particle size, uniformity, reproducibility, and scalability, emphasizing the need for further optimization of green approaches [4]. Green synthesis is influenced by parameters such as temperature, pH, pressure, and solvent conditions, while bioactive compounds in plant extracts act as natural reducing and stabilizing agents, enabling applications in catalysis, environmental remediation, antimicrobial systems, sensing, and biomedicine [5]. Unlike previous reviews that focus on specific biological sources, synthesis routes, or applications, this review integrates green nanoparticle sources, synthesis approaches, and sustainable applications within a single framework Table 1. It further highlights biomass-derived feedstocks, scalability challenges, and emerging energy-related opportunities, providing a concise reference for researchers and practitioners in sustainable nanotechnology and related fields.

Content from this work may be used under the terms of the Creative Commons Attribution 3.0 license. Any further distribution of this work must maintain attribution to the author(s) and the title of the work, journal citation and DOI. Published under license by Materials Research Forum LLC.

Table 1. Comparison of Recent Reviews and the Present Review.

Scientific Contribution	Limitations	Main Focus	Ref
Comprehensive review of biological synthesis, characterization, applications, toxicity, and limitations of metallic NPs.	Limited coverage of energy-related applications.	Biological synthesis, toxicity, characterization, applications	[3]
Integrated green synthesis strategies with biomedical applications, toxicity, and biocompatibility aspects of metal and metal oxide NPs.	Primarily focused on biomedical and tissue engineering applications, with limited discussion of environmental remediation, energy applications, biomass valorization, and sustainability challenges.	A comprehensive review of green synthesis routes for metal and metal oxide nanoparticles, covering synthesis principles, solvent systems, key synthesis parameters, tissue engineering applications, and biomedical aspects including toxicity and biocompatibility.	[6]
Highlighted environmentally friendly NPs synthesis approaches and demonstrated the role of green NPs in wastewater remediation, bioremediation, membrane technologies, advanced oxidation processes, and biosensors.	Primarily focused on environmental and wastewater treatment applications, with limited emphasis on energy-related applications, comparisons of synthesis methods, and biomass-derived nanomaterials.	Green synthesis of NPs using plant extracts and microorganisms, with emphasis on environmental sustainability and wastewater treatment applications.	[7]
Provided a comprehensive analysis of plant-based synthesis mechanisms of Ag NPs, factors influencing synthesis optimization, physicochemical characteristics, and diverse applications while addressing toxicity and future perspectives.	Limited to Ag NPs synthesized via plant extracts, with minimal consideration of other NPs systems, including microbial synthesis approaches, biomass-derived materials, and energy-related applications.	Plant-mediated green synthesis of s Ag NPs, Physicochemical properties of Ag NPs, synthesis mechanisms, optimization parameters, and applications.	[8]
This review links green resources, synthesis methods, and sustainable applications, highlighting scalability challenges and emerging opportunities in renewable energy and nanomaterial development.	Brief review; not intended to provide exhaustive mechanistic or application-specific analysis.	Green NPs sources, eco-friendly synthesis approaches, and sustainable applications in biomedicine, environmental remediation, and renewable energy.	This work

Green Sources for Nanoparticles Synthesis

Among the green sources discussed, plant extracts are generally considered the most practical and widely adopted option for nanoparticle synthesis due to their simplicity, low cost, rapid synthesis, and scalability. Biomass-derived materials offer additional sustainability benefits through waste valorization and resource recovery, making them particularly attractive for environmental applications. In contrast, microbial synthesis provides better control over nanoparticle formation and stability but often requires more complex cultivation and processing conditions [7]. Therefore, the selection of an appropriate green source depends on the desired nanoparticle properties, application requirements, and production scale.

Agricultural Biomass-Based Approaches for the Green Synthesis of Nanoparticles

Biomass waste, particularly lignocellulosic materials such as agricultural residues, has gained increasing attention as a low-cost and renewable resource for green nanoparticle synthesis [9]. Various plant-derived materials, including leaves, stems, roots, seeds, and other components, contain naturally occurring biomolecules that can be used during nanoparticle formation. Utilizing biomass not only supports sustainable nanomaterial production but also helps mitigate environmental issues associated with improper waste disposal. In addition, biomass-derived materials can be transformed into efficient adsorbents for environmental applications, especially in wastewater treatment [10]. These materials exhibit a strong ability to remove organic and inorganic pollutants, including heavy metals and microbial contaminants, due to the presence of functional groups such as hydroxyl, carboxyl, amino, and carbonyl groups that facilitate metal binding [11]. Furthermore, physical and chemical modifications of biomass can enhance its

adsorption capacity and lead to the development of advanced nanostructured materials [12]. Overall, biomass-based approaches offer an eco-friendly, cost-effective, and sustainable route for nanoparticle synthesis and environmental remediation.

Plant Extracts as Green Reducing Agents for Nanoparticle Synthesis

Plant extracts provide a simple and sustainable alternative to conventional nanoparticle synthesis by eliminating hazardous reducing and stabilizing chemicals [13]. Biomolecules such as polyphenols, flavonoids, proteins, sugars, and organic acids act as both reducing and capping agents. These compounds donate electrons to reduce metal ions into metallic nanoparticles, followed by nucleation and particle growth through the accumulation of reduced atoms. Simultaneously, they adsorb onto nanoparticle surfaces, regulating growth, enhancing colloidal stability, and preventing agglomeration, thereby improving size and morphology control [14]. This dual functionality simplifies the synthesis process while reducing toxic by-products and environmental impact. Nanoparticles can be produced either from plant extracts or directly within plant tissues through the reduction of absorbed metal ions. For example, Brassica juncea, Medicago sativa, and Helianthus annuus have been employed for the synthesis of Zn, Cu, Ni, and Co nanoparticles [15]. Plant-mediated synthesis has been widely applied for producing silver and gold nanoparticles for antimicrobial, catalytic, and environmental applications.

Microbial Approaches for the Green Synthesis of Nanoparticles

Microorganisms are efficient biofactories for green nanoparticle synthesis due to their ability to reduce and detoxify metal ions through enzymes and biomolecules [16]. Bacteria, fungi, and yeasts have been widely utilized to produce metal and metal oxide nanoparticles with controlled physicochemical properties. Bacterial genera such as Bacillus, Pseudomonas, Escherichia, and Streptomyces are commonly employed, while fungi often provide higher yields and better particle uniformity because of their rich enzymatic systems and high metal tolerance. Fungi are highly effective agents for green nanoparticle synthesis due to their rich enzymatic systems and high metal tolerance, often producing well-defined nanoparticles with higher yields than bacterial systems. In addition, yeasts, as unicellular eukaryotic microorganisms, have also been successfully utilized for biogenic nanoparticles [12]. Various yeast species, such as Saccharomyces cerevisiae, have been reported to produce metallic NPs, particularly silver and gold, through enzymatic reduction mechanisms. Despite these advantages, microbial synthesis faces several practical challenges that limit up-scale implementation. The process often requires sterile cultivation conditions to prevent contamination and long synthesis times compared to plant-mediated approaches. In addition, nanoparticle recovery and downstream purification can be complex and costly, while variations among microbial strains affect reproducibility and product consistency [14]. Therefore, further optimization is required to improve process scalability and industrial applicability. Overall, microorganisms offer a sustainable platform for synthesizing nanoparticles such as silver, gold, copper, zinc, titanium, palladium, and nickel with controlled physicochemical properties for diverse applications [17].

Synthesis Approaches of Green Nanoparticles

Among the synthesis approaches, microwave-assisted synthesis appears to be one of the most promising routes for sustainable nanoparticle production due to its rapid reaction kinetics, reduced energy consumption, and ability to generate highly uniform nanoparticles within short processing times. Hydrothermal synthesis remains advantageous for obtaining highly crystalline nanostructures with controlled morphology; however, its scalability is constrained by high-pressure operating conditions. The sol-gel method offers excellent compositional homogeneity and process flexibility, whereas CVD is preferred when precise structural control and high-purity nanomaterials are required, despite its relatively high operational cost. Therefore, the selection of an appropriate synthesis route depends on the targeted application, desired nanoparticle characteristics, and economic considerations. In this section, each method is explained and

clarified in detail. Table 2 compares the main synthesis approaches discussed in terms of their key characteristics and practical considerations.

Hydrothermal Treatment

The hydrothermal method is a widely used technique for nanoparticle synthesis due to its ability to produce high-purity materials with controlled morphology and small particle size. It involves chemical reactions in aqueous or solvent systems under high temperature and pressure in a sealed autoclave. Precursors are heated under controlled conditions to promote crystal growth, followed by cooling, washing, and drying to obtain the final product. Particle size and shape can be tuned by adjusting parameters such as temperature, pressure, pH, and precursor concentration [2]. This method is considered relatively eco-friendly and energy-efficient compared to conventional approaches. It has been used to synthesize various nanostructures, including nanorods, nanowires, and nanosheets, for applications in environmental remediation, biomedical fields, and energy storage.

Sol-Gel Method

The sol-gel method is a simple and widely used technique for synthesizing green nanoparticles due to its low processing temperature and ability to produce homogeneous materials with controlled properties [18]. It involves the conversion of a liquid precursor solution into a solid three-dimensional network through hydrolysis and condensation reactions. The process typically starts with dissolving a precursor in a suitable solvent to form a uniform solution, followed by controlled reactions that lead to a colloidal sol and subsequent gel formation [19]. The resulting gel is then washed, dried, and sometimes calcined to enhance crystallinity and stability. The properties of the final nanoparticles can be tuned by adjusting parameters such as precursor concentration, water-to-precursor ratio, catalyst type, solvent, temperature, and pH, which influence particle size, morphology, and reaction kinetics [2]. Overall, the sol-gel method enables the production of high-purity, uniform nanomaterials with tailored properties for applications in catalysis, environmental remediation, and biomedical fields.

Microwave-Assisted Green Synthesis

Microwave-assisted synthesis is an efficient and sustainable approach that uses microwave irradiation to accelerate reaction kinetics through rapid and uniform heating [20]. This enables the production of highly crystalline and uniform nanoparticles within short reaction times, while reducing energy consumption and chemical waste [21]. The process is influenced by factors such as microwave power, irradiation time, temperature, precursor concentration, and pH [2]. Consequently, microwave-assisted synthesis has been widely applied in the fabrication of green nanoparticles for catalysis, environmental remediation, biomedicine, and energy applications.

Chemical Vapor Deposition

Chemical Vapour Deposition (CVD) involves the deposition of nanomaterials from gaseous precursors onto heated substrates under controlled conditions [14]. The technique offers high controllability and reproducibility, making it suitable for the fabrication of advanced nanostructured materials [22]. The properties of CVD-produced nanomaterials can be tailored by controlling parameters such as temperature, pressure, gas flow rate, and precursor composition. This versatility enables the fabrication of nanomaterials with well-defined structures and properties for advanced applications. Although conventional CVD is generally considered an energy-intensive technique, recent developments have improved its sustainability profile through the use of bio-derived precursors, renewable carbon sources, biomass-based substrates, and Plasma-Enhanced Chemical Vapor Deposition (PECVD) systems operating at lower temperatures [23]. These modifications reduce energy consumption and reliance on hazardous chemical feedstocks, making CVD a potentially compatible approach within green nanomaterial fabrication strategies when appropriately designed and implemented.

Table 2. Comparison of green nanoparticle synthesis approaches.

Synthesis approaches	Particle Size Control	Energy Demand	Reproducibility	Main Advantages	Limitations
Hydrothermal	High	Moderate	High	High purity, controlled morphology, tunable particle size and crystallinity	Requires elevated temperature and pressure;long processing time
Sol-Gel	High	Low to moderate	High	Low processing temperature, homogeneous products, excellent compositional control	Drying and calcination steps may increase processing time and cost
Microwave-Assisted	High	Low	High	Rapid heating, short synthesis time, low energy consumption, uniform NPs	Limited reactor volume may restrict large-scale production
CVD	Very High	High	Very High	Excellent control over particle structure and morphology; suitable for high-quality nanomaterials	CVD requires high temperatures, specialized equipment, and significant energy input

Application of Green Synthesized Nanoparticles

Applications of Green Nanoparticles in Biomedicine

Green nanoparticles have gained considerable attention in biomedical applications due to their small size, high surface area, and enhanced reactivity. They exhibit strong antibacterial activity against both Gram-positive and Gram-negative bacteria, including *Escherichia coli* (*E. coli*) and *Staphylococcus aureus* (*S. aureus*), making them promising alternatives to conventional antibiotics in combating antimicrobial resistance [3, 6]. In addition, several green nanoparticles have demonstrated anticancer potential by inhibiting tumor cell proliferation and inducing apoptosis in various cancer cell lines [24]. Their mechanisms include membrane disruption, generation of reactive oxygen species, and interference with cellular components. They also possess antioxidant properties, enabling them to scavenge free radicals and reduce oxidative stress. For instance, TiO_2 nanoparticles have demonstrated significant antioxidant activity through DPPH radical scavenging and were shown to normalize oxidative stress biomarkers, including lipid peroxidation and antioxidant enzyme levels in biological systems [25]. In addition, nanoparticles serve as efficient green drug delivery systems by providing controlled release, improved bioavailability, and targeted delivery [3]. Despite these promising biomedical applications, concerns regarding cytotoxicity, biodistribution, dosage optimization, and long-term safety remain important challenges. Furthermore, many reported outcomes are still based on in vitro studies, while comprehensive in vivo investigations and standardized safety assessments are required before large-scale clinical translation [26]. Overall, green nanoparticles offer versatile biomedical applications, although further studies are required to confirm their clinical safety and effectiveness.

Environmental Applications of Green Nanoparticles

Green nanoparticles have emerged as effective tools in environmental remediation, particularly in wastewater treatment [27]. Due to their small size, large surface area, and high reactivity, they can efficiently remove a wide range of pollutants, including heavy metals, organic dyes, and microbial contaminants [28]. One of the most common approaches is adsorption, where pollutants attach to the nanoparticle surface, enabling their rapid and efficient removal. For example, green-synthesized, rGO, CuO, ZnO and TiO_2 NPs have been widely applied for the organic dyes degradation such as methylene blue and rhodamine B, demonstrating high pollutant removal efficiency under light irradiation [29, 30]. In addition, green nanoparticles are widely used as catalysts, especially in photocatalytic processes, where they help degrade harmful organic compounds into less toxic substances under light irradiation. Furthermore, these nanoparticles are incorporated into filtration systems and membranes to enhance purification efficiency and prevent microbial growth [31]. Some nanomaterials also exhibit magnetic properties, allowing easy

separation from treated water using an external magnetic field [32]. Overall, green nanoparticles offer a cost-effective and sustainable solution for environmental protection, although concerns related to their potential toxicity and long-term impact still require further investigation.

Energy Applications of Green Nanoparticle

Green nanoparticles are increasingly used in energy applications as sustainable alternatives to fossil-based systems due to their high surface area, stability, and catalytic activity. They enhance biofuel production and in bioethanol and biodiesel synthesis they serve as catalysts or enzyme supports, improving efficiency, yield, recyclability, and reducing cost [33]. For example, metal oxide nanoparticles such as MgO, TiO_2, and CaO have been reported to enhance biodiesel production by increasing catalytic activity and improving catalyst reusability during transesterification reactions [9]. Additionally, magnetic nanoparticles enable easy recovery of catalysts and enzymes, improving process sustainability. In biogas and biohydrogen production, nanoparticles enhance microbial activity and increase conversion efficiency in anaerobic digestion and fermentation. For example, TiO_2 , NiO, MoO_3 and ZnO NPs are commonly employed in solar cells due to their photocatalytic properties and ability to enhance light absorption and charge separation [34]. In supercapacitors, Ti, Co, V, Cu, Cr, Mn, Fe, Au, and Ag oxides NPs serve as electrode materials owing to their high surface area and charge-storage capability [35]. Furthermore, ZrFeO and modified carbon materials have been utilized as electrocatalysts and electrode-support materials in fuel cells to enhance reaction kinetics and electron-transfer efficiency [36, 37]. Overall, green nanoparticles provide a promising platform for developing cleaner and more efficient energy technologies, supporting the transition toward renewable and environmentally friendly energy systems.

Summary, Challenges, and Future Perspectives

Recent advances in green nanoparticle research have shifted the field from proof-of-concept synthesis toward applications in environmental remediation, biomedicine, drug delivery, and renewable energy. Increased interest in sustainable materials has promoted the use of plant extracts, microorganisms, and biomass-derived resources, while recent progress has focused on biomass valorization, energy-efficient synthesis, and process optimization to enhance nanoparticle performance [38]. However, large-scale implementation remains limited by the lack of standardized protocols and the variability of biological feedstocks. Differences in plant species, cultivation conditions, seasonal factors, and biomolecule composition can lead to batch-to-batch variations in nanoparticle properties, while controlling precursor concentration, pH, size distribution, and purification processes remains challenging [2]. Additional concerns include long-term environmental impacts, nanoparticle persistence, bioaccumulation, and economic feasibility [3]. Future research should prioritize process standardization, mechanistic understanding of biomolecule-mediated synthesis, optimization of production conditions, techno-economic and environmental assessments, pilot-scale manufacturing, and application-specific performance validation to support commercialization of green nanoparticles.

References

[1] S.V. Kaymaz, H.M. Nobar, H. Sarıgül, C. Soylukan, L. Akyüz, M. Yüce, Nanomaterial surface modification toolkit: Principles, components, recipes, and applications, Advances in Colloid and Interface Science 322 (2023) 103035. https://doi.org/10.1016/j.cis.2023.103035

[2] A. Azad, H. Zafar, F. Raza, M. Sulaiman, Factors influencing the green synthesis of metallic nanoparticles using plant extracts: a comprehensive review, Pharmaceutical Fronts 5 (2023) e117-e131. https://doi.org/10.1055/s-0043-1774289

[3] P.K. Dikshit, J. Kumar, A.K. Das, S. Sadhu, S. Sharma, S. Singh, P.K. Gupta, B.S. Kim, Green synthesis of metallic nanoparticles: applications and limitations, Catalysts 11 (2021) 902. https://doi.org/10.3390/catal11080902

[4] H. Abuzeid, C. Julien, L. Zhu, A. Hashem, Green synthesis of nanoparticles and their energy storage, environmental, and biomedical applications. Crystals 13 (11): 1576, 2023. https://doi.org/10.3390/cryst13111576

[5] K. Jain, A. Takuli, T.K. Gupta, D. Gupta, Rethinking nanoparticle synthesis: a sustainable approach vs. traditional methods, Chemistry–An Asian Journal 19 (2024) e202400701. https://doi.org/10.1002/asia.202400701

[6] H.M. Abuzeid, C.M. Julien, L. Zhu, A.M. Hashem, Green synthesis of nanoparticles and their energy storage, environmental, and biomedical applications, Crystals 13 (2023) 1576. https://doi.org/10.3390/cryst13111576

[7] S. Rathod, S. Preetam, C. Pandey, S.P. Bera, Exploring synthesis and applications of green nanoparticles and the role of nanotechnology in wastewater treatment, Biotechnology Reports 41 (2024) e00830. https://doi.org/10.1016/j.btre.2024.e00830

[8] F. Eker, E. Akdaşçi, H. Duman, M. Bechelany, S. Karav, Green synthesis of silver nanoparticles using plant extracts: A comprehensive review of physicochemical properties and multifunctional applications, International Journal of Molecular Sciences 26 (2025) 6222. https://doi.org/10.3390/ijms26136222

[9] S.J. Chauhan, B. Devliya, B. Patel, J. Nagapara, S. Mevada, H. Solanki, H.D. Patel, Biodiesel production from waste cooking oil using novel heterogenous CaO-MgO-ZnO-TiO2 nanoconjugate catalyst (CMZT-Nano Cat): A green approach towards renewable energy, Biomass and Bioenergy 200 (2025) 107985. https://doi.org/10.1016/j.biombioe.2025.107985

[10] H.N. Hamad, S. Idrus, Recent developments in the application of bio-waste-derived adsorbents for the removal of methylene blue from wastewater: a review, Polymers 14 (2022) 783. https://doi.org/10.3390/polym14040783

[11] K. Wolny-Koładka, D. Malina, A. Suder, K. Pluta, Z. Wzorek, Bio-based synthesis of silver nanoparticles from waste agricultural biomass and its antimicrobial activity, Processes 10 (2022) 389. https://doi.org/10.3390/pr10020389

[12] G. Nagda, N. Rai, Jaya, Shakshi, C. Bhalothia, N.A. Singh, Nanoparticles synthesis using extremophilic microbes and their potential agricultural applications, Extremophiles for sustainable agriculture and soil health improvement, Springer, Cham, 2024, pp. 455-483. https://doi.org/10.1007/978-3-031-70203-7_21

[13] P.K. Sukul, C. Kar, Green conversion methods to prepare nanoparticle, Bioinspired and green synthesis of nanostructures: a sustainable approach, Wiley, United State, 2023, pp. 115-139. https://doi.org/10.1002/9781394174928.ch5

[14] K. Hachem, M.J. Ansari, R.O. Saleh, H.H. Kzar, M.E. Al-Gazally, U.S. Altimari, S.A. Hussein, H.T. Mohammed, A.T. Hammid, E. Kianfar, Methods of chemical synthesis in the synthesis of nanomaterial and nanoparticles by the chemical deposition method: a review, BioNanoScience 12 (2022) 1032-1057. https://doi.org/10.1007/s12668-022-00996-w

[15] H. Ayub, U. Jabeen, I. Ahmad, M. Aamir, A. Ullah, A. Mushtaq, F. Behlil, B. Javaid, A. Syed, A.M. Elgorban, Enhanced anticancer and biological activities of environmentally friendly Ni/Cu-ZnO solid solution nanoparticles, Heliyon 10 (2024) e39912. https://doi.org/10.1016/j.heliyon.2024.e39912

[16] H. Bahrulolum, S. Nooraei, N. Javanshir, H. Tarrahimofrad, V.S. Mirbagheri, A.J. Easton, G. Ahmadian, Green synthesis of metal nanoparticles using microorganisms and their application in the agrifood sector, Journal of nanobiotechnology 19 (2021) 86. https://doi.org/10.1186/s12951-021-00834-3

[17] A. Sandhu, A. Goel, Biosynthesis of Nanoparticles by Micro-organisms and its Applications, Journal of Young Pharmacists 15 (2023) 430. https://doi.org/10.5530/jyp.2023.15.58

[18] R. Perveen, S. Shujaat, Z. Qureshi, S. Nawaz, M. Khan, M. Iqbal, Green versus sol-gel synthesis of ZnO nanoparticles and antimicrobial activity evaluation against panel of pathogens, Journal of Materials Research and Technology 9 (2020) 7817-7827. https://doi.org/10.1016/j.jmrt.2020.05.004

[19] F. Moradnia, S.T. Fardood, A. Ramazani, B.-k. Min, S.W. Joo, R.S. Varma, Magnetic Mg0. 5Zn0. 5FeMnO4 nanoparticles: green sol-gel synthesis, characterization, and photocatalytic applications, Journal of Cleaner Production 288 (2021) 125632. https://doi.org/10.1016/j.jclepro.2020.125632

[20] H. Ashraf, T. Anjum, S. Riaz, S. Naseem, Microwave-assisted green synthesis and characterization of silver nanoparticles using Melia azedarach for the management of Fusarium wilt in tomato, Frontiers in microbiology 11 (2020) 238. https://doi.org/10.3389/fmicb.2020.00238

[21] M. Torabfam, M. Yüce, Microwave-assisted green synthesis of silver nanoparticles using dried extracts of Chlorella vulgaris and antibacterial activity studies, Green Processing and Synthesis 9 (2020) 283-293. https://doi.org/10.1515/gps-2020-0024

[22] A.E. Adeoye, O. Adeaga, K. Ukoba, Chemical vapour deposition (CVD) and physical vapour deposition (PVD) techniques: advances in thin film solar cells, Nigerian Journal of Technology 43 (2024) 479-489. https://doi.org/10.4314/njt.v43i3.10

[23] F. Tabarkhoon, M. Bazmi, N.A. Welchert, T.T. Tsotsis, M. Gupta, One-pot fabrication of silicon carbide thin films via plasma-enhanced chemical vapor deposition (PECVD) followed by in situ pyrolysis, Industrial & Engineering Chemistry Research 64 (2025) 5973-5981. Ind. Eng. Chem. Res. 2025, 64, 11, 5973–5981

[24] A.A. Kajani, A.-K. Bordbar, A. Pouresmaeili, M.A. Mehrgardi, Green and one-step synthesis of fluorescent carbon dots with the significant antibacterial effects, Iranian Journal of Science 49 (2025) 577-584. https://doi.org/10.1007/s40995-024-01755-0

[25] M.M. Venkatappa, C. Udagani, S.M. Hanume Gowda, S. Venkataramaiah, R. Casini, I.M. Moussa, R. Achur, D. Sannaningaiah, H.O. Elansary, Green synthesised TiO2 nanoparticles-mediated Terenna asiatica: evaluation of their role in reducing oxidative stress, inflammation and human breast cancer proliferation, Molecules 28 (2023) 5126. https://doi.org/10.3390/molecules28135126

[26] S. Petrovic, B. Bita, M.-E. Barbinta-Patrascu, Nanoformulations in pharmaceutical and biomedical applications: green perspectives, International Journal of Molecular Sciences 25 (2024) 5842. https://doi.org/10.3390/ijms25115842

[27] S. Bassim, A.K. Mageed, A.A. AbdulRazak, H.S. Majdi, Green synthesis of Fe3O4 nanoparticles and its applications in wastewater treatment, Inorganics 10 (2022) 260. https://doi.org/10.3390/inorganics10120260

[28] K. Neeti, R. Singh, S. Ahmad, The role of green nanomaterials as effective adsorbents and applications in wastewater treatment, Materials Today: Proceedings 77 (2023) 269-276. https://doi.org/10.1016/j.matpr.2022.11.300

[29] O.M. El-Borady, Wastewater treatment using innovative green-synthesized rGO, TiO2NPs, and rGO/TiO2 nanocomposite: structural, morphological, spectroscopic, thermal, and photocatalytic studies, Water, Air, & Soil Pollution 236 (2025) 75. https://doi.org/10.1007/s11270-024-07692-3

[30] S.M. Abegunde, M.A. Adebayo, E.F. Olasehinde, Green synthesis of ZnO nanoparticles and its application for methyl green dye adsorption, Green Energy and Resources 2 (2024) 100073. https://doi.org/10.1016/j.gerr.2024.100073

[31] E.H. Khader, T.J. Mohammed, T.M. Albayati, K.T. Rashid, N.M.C. Saady, S. Zendehboudi, Green nanoparticles blending with polyacrylonitrile ultrafiltration membrane for antifouling oily wastewater treatment, Separation and Purification Technology 353 (2025) 128256. https://doi.org/10.1016/j.seppur.2024.128256

[32] S.A. Mousa, H. Abdallah, S. Khairy, Low-cost photocatalytic membrane modified with green heterojunction TiO2/ZnO nanoparticles prepared from waste, Scientific Reports 13 (2023) 22150. https://doi.org/10.1038/s41598-023-49516-0

[33] U. Demir, M. Keskin, S. Özer, G. Coskun, The effect of adding green synthesized and commercial silver nanoparticles to biodiesel on diesel engine performance and emissions, Case Studies in Thermal Engineering 67 (2025) 105797. https://doi.org/10.1016/j.csite.2025.105797

[34] M. Girtan, B. Negulescu, A review on oxide/metal/oxide thin films on flexible substrates as electrodes for organic and perovskite solar cells, Optical Materials: X 13 (2022) 100122. https://doi.org/10.1016/j.omx.2021.100122

[35] J. Meena, S. shankari Sivasubramaniam, E. David, Green supercapacitors: review and perspectives on sustainable template-free synthesis of metal and metal oxide nanoparticles, RSC Sustainability 2 (2024) 1224-1245. https://doi.org/10.1039/D4SU00009A

[36] U. Habib, M.E.A. Mohsin, Z.I. Khan, Z. Mohamad, N. Othman, S. Mousa, S.S. Hossain, S.S. Ali, Mechanical, Thermal, and Flammability Properties of Eco-Friendly Nanocomposites from Recycled PET/PA-11 Blends Reinforced with Graphene Nanoplatelets, Polymers 17 (2025) 1038. https://doi.org/10.3390/polym17081038

[37] S. Tarhan, A. Ekinci, O. Baytar, A. Akdag, Ö. Şahin, Green-synthesized ZrFeO nanoparticles as efficient cathode materials in PEM fuel cells, International Journal of Hydrogen Energy 142 (2025) 852-863. https://doi.org/10.1016/j.ijhydene.2025.01.046

[38] N.M. Adassooriya, A. Manipura, A. Husen, Industrial Scale-Up Production of Nanoparticles—Challenges and Opportunities, Industrial Scale Production of Nanoparticles, Smart Nanomaterials Technology, Springer, Singapore, 2025. https://doi.org/10.1007/978-981-96-9176-0_1

Materials Research Proceedings 74 (2026) 93-100 https://doi.org/10.21741/9781644904473-12

Machine Learning in Geopolymer Concrete: A Bibliometric Analysis of Global Trends, Key Contributors, and Emerging Research Directions

Abdullahi MUSA[1,2,a *], Mohd Azreen MOHD ARIFFIN[1,b *], Mohd Nur Asmawisham ALEL[1,c], Wan Ikram Wajdee WAN AHMAD KAMAL[1,d], Han-Seung LEE[3,e], Jitendra Kumar SINGH[4,f], Mohammed TIJJANI[5,g] and Abdullahi Garba MUSA[2,h]

[1]Faculty of Civil Engineering, Universiti Teknologi Malaysia, Johor Bahru, Johor, Malaysia

[2]Department of Civil Engineering, Nigerian Army University Biu, PMB, 1500, Borno State, Nigeria

[3]Department of Architectural Engineering, Hanyang University, 1271, sa-3-dong, Sangnok-gu, Ansan, 15588, South Korea

[4]Innovative Durable Building and Infrastructure Research Center, Department of Architectural Engineering, Hanyang University, 1271, sa-3-dong, Sangnok-gu, Ansan, 15588, South Korea

[5]Department of Architecture, Abubakar Tafawa Balewa University, Bauchi, PMB, 0248, Nigeria

[a]musa20@graduate.utm.my, [b]mohdazreen@utm.my, [c]alel@utm.my, [d]wanikramwajdee@utm.my, [e]ercleehs@hanyang.ac.kr, [f]jk200386@hanyang.ac.kr, [g]mtijjani@atbu.edu.ng, [h]abdul4one2003@gmail.com

Keywords: Geopolymer Concrete, Machine Learning, Hybrid Systematic–Bibliometric Review, Durability Prediction, Sustainable Construction Materials, Artificial Neural Networks

Abstract. The application of machine learning (ML) in geopolymer concrete (GPC) research has expanded rapidly, yet no comprehensive bibliometric mapping of this domain exists. This study addresses this gap by conducting a PRISMA-guided bibliometric analysis of 291 peer-reviewed articles published between 2015 and 2024, retrieved from Scopus, Web of Science, and ScienceDirect. The analysis reveals three key findings. First, ML adoption in GPC has entered an acceleration phase, with 75% of all publications (219 out of 291) appearing after 2021, driven predominantly by artificial neural networks (47% of ML models), support vector machines (22%), and genetic algorithms (18%). Second, research is geographically concentrated, with India (93 publications), China (52), and Saudi Arabia (35) accounting for 62% of global output, indicating a critical need for broader regional participation. Third, a significant thematic imbalance exists: compressive strength prediction dominates 89% of ML studies, while durability properties (chloride penetration, carbonation, sulfate attack) remain severely understudied (11%). Based on these findings, this review proposes a five-priority research agenda: (1) establishment of open-access GPC datasets with standardized protocols; (2) expansion into durability prediction models; (3) integration of explainable AI (SHAP, LIME) for model interpretability; (4) exploration of hybrid ML models (ANN-GA, RF-XGBoost); and (5) early-stage investigation of digital twins and 3D printing integration. This study provides the first systematic roadmap for researchers adopting ML in GPC development.

Introduction

Portland cement production accounts for approximately 8% of global anthropogenic CO_2 emissions [1], driving interest in sustainable alternatives. Geopolymer concrete (GPC) synthesized from industrial by-products including fly ash, slag, and metakaolin offers superior durability,

Content from this work may be used under the terms of the Creative Commons Attribution 3.0 license. Any further distribution of this work must maintain attribution to the author(s) and the title of the work, journal citation and DOI. Published under license by Materials Research Forum LLC.

chemical resistance, and a substantially lower carbon footprint compared to conventional cement [2,3]. Despite these advantages, widespread adoption remains limited by challenges in mix design optimization, strength prediction, long-term durability assessment, and quality control [4-6]. Unlike Portland cement concrete, GPC exhibits complex, non-linear relationships between precursor composition, activator chemistry, curing conditions, and performance outcomes that conventional statistical methods struggle to model effectively [7].

Machine learning (ML) provides a powerful solution to these challenges by enabling data-driven analysis without requiring explicit mathematical formulations [8]. Algorithms including artificial neural networks (ANN), support vector machines (SVM), and genetic algorithms (GA) have demonstrated strong potential in predicting material properties and optimizing mix designs [9,10]. Despite growing research at this intersection, no comprehensive bibliometric review has systematically mapped ML applications specifically in GPC. Existing reviews have either focused broadly on GPC without computational emphasis or examined ML in concrete without distinguishing geopolymer systems.

This study addresses this gap through a PRISMA-guided bibliometric analysis of 291 peer-reviewed articles (2015–2024). The review aims to: (i) quantify publication trends and growth trajectories; (ii) identify leading contributors including countries, institutions, authors, and journals; (iii) map ML techniques and their application domains; and (iv) reveal critical research gaps and emerging directions. The findings provide the first systematic roadmap for researchers applying ML to GPC development, clarifying the current state of the field and highlighting priority areas for future investigation.

Methodology

This study employed a systematic bibliometric review approach guided by the PRISMA framework [11]. A comprehensive literature search was conducted on June 15, 2025, across Scopus, Web of Science, and ScienceDirect using the Boolean string: TITLE-ABS-KEY(("machine learning" OR "artificial neural network" OR "support vector machine" OR "genetic algorithm" OR "random forest" OR "deep learning") AND ("geopolymer concrete" OR "alkali-activated" OR "fly ash concrete" OR "slag concrete")). The search was restricted to peer-reviewed journal articles and conference proceedings published between 2015 and 2024 in English. Inclusion criteria were: (i) explicit application of ML techniques to geopolymer or alkali-activated materials; (ii) reporting of quantitative performance metrics or optimization outcomes; (iii) peer-reviewed publications. Exclusion criteria included: (i) non-ML studies; (ii) duplicates; (iii) non-English publications; (iv) editorials or abstracts-only papers; (v) unavailable full-text.

The initial search yielded 623 records. After duplicate removal (n=102), title/abstract screening (n=193 excluded), and full-text assessment (n=37 excluded), 291 studies were included as shown in Table 1. Extracted data included authorship, affiliation, country, publication year, source, citations, ML technique, and target property. Two authors independently extracted data from a random sample of 50 articles (inter-rater agreement = 94%). Bibliometric analysis was performed using VOSviewer (v1.6.20) for network visualization and Bibliometrix (R v4.1.0) for statistical analysis.

Table 1. PRISMA screening summary.

Phase	Action	Records	Description
Identification	Initial stage (Scopus, WoS, ScienceDirect)	623	Search based on Boolean string
Screening	Duplicate removal	102	Manual + Mendeley filtering
Eligibility	Full-text evaluation	328	Evaluated against inclusion/exclusion criteria
Inclusion	Final articles included	291	Studies satisfying all criteria used

Results

Publication Trends

Table 2 presents summary of publication and citation metrics from 2015 to 2024, highlighting research output and impact trends over the last decade. It shows accelerated sharply after 2018, with 75% of publications (219 of 291) appearing after 2021. Annual output grew from 1 publication in 2015 to 100 in 2024 (34.8% of total). The highest citation impact occurred in 2022 (2,788 citations, H-index=34). These indices indicate robust academic and industrial networks, transparency in research performance, supports bibliometric analysis at the forefront of ML applications in geopolymer concrete.

Table 2. Annual publication and citation metrics (2015–2024).

Year	Number of Publications	Number of Publications Cited	Total Citations	H-Index	Percentage [%]	Cumulative [%]
2024	100.0	9.0	71.0	6.0	34.84	34.84
2023	57.0	54.0	1820.0	26.0	19.86	54.7
2022	59.0	58.0	2788.0	34.0	20.56	75.26
2021	36.0	34.0	2497.0	25.0	12.54	87.8
2020	15.0	13.0	745.0	11.0	5.22	93.02
2019	8.0	8.0	575.0	6.0	2.79	95.81
2018	5.0	5.0	258.0	5.0	1.74	97.55
2017	3.0	2.0	168.0	2.0	1.04	98.59
2016	3.0	3.0	137.0	1.0	1.04	99.63
2015	1.0	1.0	41.0	1.0	0.34	100.0

Geographic Distribution

Table 3 presents publication statistics, which show that India (93 publications, 26.6%), China (52, 14.9%), and Saudi Arabia (35, 10.0%) collectively account for 51.4% of global output. In terms of citation impact, India leads with 2,402 citations (H-index=27), followed by Saudi Arabia (2,078 citations, H-index=25) and Pakistan (1,974 citations, H-index=22). These countries, with robust academic and industrial networks, are among the top ML users in geopolymer concrete. Specifically, India emerged as the most prolific country, contributing 93 publications, followed by China with 52, and Saudi Arabia with 35. Strong collaborative networks exist among these countries and Australia, Pakistan, and Iran as shown in Fig. 1.

Table 3. Top contributing countries with percentage publication share.

Country	Number of Publications	Number of Publications Cited	Total Number of Citations	H-Index	Percentage of Publications [%]	Cumulative Percentage [%]
India	93	86	2402	27	26.57	26.57
China	52	52	1918	23	14.86	41.43
Saudi Arabia	35	35	2078	25	10.0	51.43
Australia	32	32	1458	19	9.14	60.57
Pakistan	31	31	1974	22	8.86	69.43
Iran	21	20	763	12	6.0	75.43
Nigeria	17	16	514	11	4.86	80.29
Egypt	16	13	562	10	4.57	84.86
Iraq	14	13	876	11	4.0	88.86
Turkey	13	13	726	11	3.71	92.57
UK	13	12	617	10	3.71	96.28
Vietnam	13	13	1088	11	3.71	100.0

ML Techniques Employed

Fig. 2 provides an overview of the frequency of ML techniques applied in geopolymer concrete studies, highlighting the central role of these algorithms in optimizing mix designs and improving performance predictions. ANN dominates (47% of studies), followed by SVM (22%) and GA (18%). Hybrid models (ANN-GA, RF-XGBoost) gained traction in 2022–2024 (6% of applications). XGBoost and other techniques account for the remaining applications.

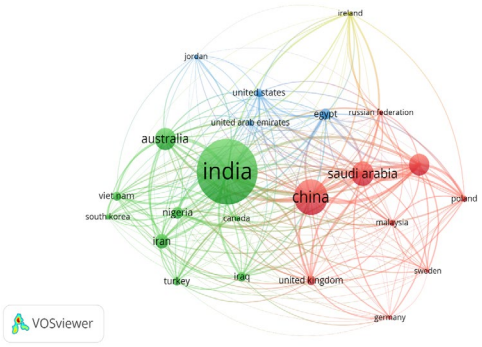


Fig. 1. Visualization of some countries actively involved in research area.

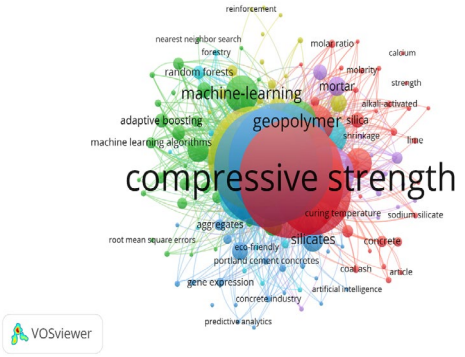


Fig. 2. Visualization overview of the most frequently used ML techniques in the field.

Thematic Focus

Compressive strength prediction dominates 89% of ML studies. Durability properties (chloride penetration, carbonation, sulfate attack) represent only 11% a critical research gap that must be addressed to enable widespread GPC adoption in infrastructure applications.

Leading Sources and Authors

Table 4 presents publication output and citation impact across major sources, highlighting *Construction and Building Materials*, *Materials*, and *Case Studies in Construction Materials* as the leading journals in this field. These outlets have served as the principal platforms for disseminating high-impact research on the integration of machine learning with geopolymer concrete, which account for over 50% of the top tier publication. Their prominence reflects the interdisciplinary character of the domain, linking civil engineering, materials science, and artificial intelligence. In addition to their strong publication records, these journals facilitate broad knowledge exchange through wide readership, supporting collaboration and the diffusion of innovative findings.

Table 4. Leading publication sources contributing to the research field.

Sources	Number of Publications	Number of Publications Cited	Total Citation	H-Index	Percentage Publications (%)	Cumulative Percentage (%)
Construction and Building Materials	31	31	1780	23	30.39	30.39
Materials	12	12	1010	10	11.76	42.15
Case Studies in Construction Materials	11	11	697	9	10.78	52.93
Asian Journal of Civil Engineering	10	10	238	9	9.8	62.73
Buildings	10	10	162	6	9.8	72.53
Journal of Building Engineering	10	10	428	9	9.8	82.33
Computers and Concrete	9	9	141	6	8.82	91.15
Journal of Cleaner Production	9	9	854	9	8.82	100.0

Fig. 3 visually represents the leading journals in production of best quality in terms of impact and popularity in application of machine learning to geopolymer concrete, the leading source is link to the geographical location as well as the funding sponsors.

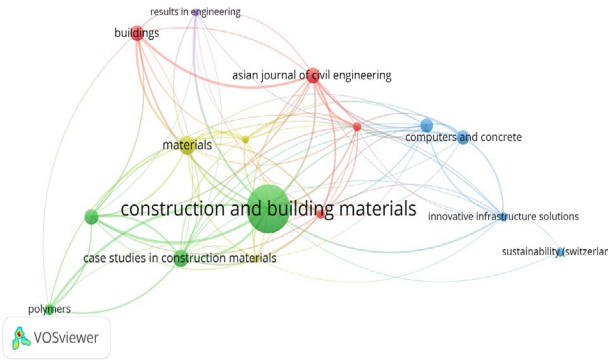


Fig. 3. Visualizations of some of the leading sources of research area.

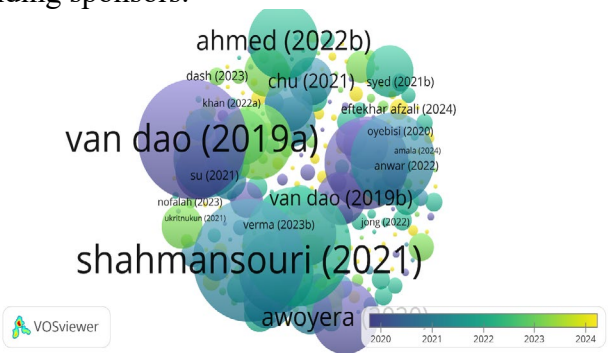


Fig. 4. Visualizations of some of the leading authors of research area.

Table 5 presents the publication output of these leading contributors, highlighting their impact on the development and progression of this research area. Several authors have played a central role in advancing research on machine learning applications in geopolymer concrete. Notably, studies by [12,13] have made significant contributions by demonstrating the predictive capabilities of machine learning models for assessing geopolymer concrete properties. These works have supported the integration of advanced computational approaches into the field and have influenced subsequent research directions.

Table 5. Leading authors contributing to the research field, based on the top contributors.

Author	Number of Publications	Number of Publications Cited	Total Number of Citations	H-Index	Percentage Publications (%)	Cumulative Percentage (%)
Ahmad, A.	10	10	978	9	14.93	14.93
Ahmed, H.U.	9	9	916	9	13.43	28.36
Amin, M.N.	9	9	333	7	13.43	41.79
Ahmad, W.	8	8	720	8	11.94	53.73
Aslam, F.	8	8	1117	8	11.94	65.67
Huang, J.	8	8	89	5	11.94	77.61
Javed, M.F.	8	8	672	7	11.94	89.55
Khan, K.	7	7	291	6	10.45	100.0

Fig. 4 illustrates the co-authorship network of researchers applying machine learning to geopolymer concrete, generated using VOSviewer. The dense interconnections among these researchers indicate a growing level of collaboration, particularly in studies focused on mix design optimization, performance prediction, and sustainability using ML techniques. Overall, the network highlights the expansion of an active and increasingly interdisciplinary research community at the intersection of machine learning and geopolymer concrete.

Subject Area Distribution

Table 6 presents the distribution of machine learning-based geopolymer concrete research across subject areas from 2015 to 2024, highlighting both concentration and disciplinary breadth. Engineering (39.1%) and Materials Science (28.2%) dominate, followed by Environmental Science (8.5%) and Computer Science (6.5%). The highest H-index values are in Materials Science (45) and Engineering (42). Moderate contributions from Physics and Astronomy, Energy, and Chemical Engineering (3.96%–5.58%) point to emerging interests in thermal behavior and energy-related performance. In contrast, Social Sciences, Business, and Mathematics remain

underrepresented. The H-index values confirm that the most influential work is concentrated in Engineering and Materials Science (42 and 45, respectively). Overall, more than 95% of publications are clustered within the leading subject areas, underscoring both the maturity of core disciplines and opportunities for expansion into less explored fields.

Table 6. Distribution of research output across major subject areas, based on the top contributing disciplines.

Subject Area	Number of Publications	Number of Publications Cited	Total Number of Citations	H-Index	Publication Percentage (%)	Cumulative Percentage (%)
Engineering	194	183	5981	42	39.11	39.11
Materials Science	140	136	6300	45	28.23	67.34
Environmental Science	42	38	1497	20	8.47	75.81
Computer Science	32	27	1110	16	6.45	82.26
Physics and Astronomy	31	28	1628	18	6.25	88.51
Energy	22	19	1167	17	4.44	92.95
Earth and Planetary Sciences	18	16	158	7	3.63	96.58
Chemical Engineering	17	17	723	14	3.43	100.0

Discussion

Unlike previous narrative reviews on geopolymer concrete [14] or machine learning in construction materials, this study offers three distinctive contributions. First, The results confirm that ML adoption in GPC research has entered an acceleration phase, with 75% of publications appearing after 2021. This trajectory aligns with broader trends in computational materials science and signals the field's transition from feasibility demonstration to performance optimization. The geographic concentration in India, China, and Saudi Arabia (51.4% of global output) reflects domestic demand for sustainable construction, active research funding, and availability of industrial by-products such as fly ash. Strong collaborative networks among these countries indicate effective international knowledge exchange. Second, it quantitatively reveals a strength-durability prediction imbalance: 89% of ML models target compressive strength, while only 11% address durability properties such as chloride penetration, carbonation resistance, or sulfate attack. This finding, not previously documented, identifies a clear priority for future research. Third, The dominance of ANN (47% of studies) is consistent with its proven effectiveness in modeling complex, non-linear material relationships without requiring explicit mathematical formulations [15-17]. The emergence of hybrid models (ANN-GA, RF-XGBoost) in 2022–2024 publications (6% of applications) represents a methodological maturation toward ensemble and multi-objective approaches that outperform single-model architectures.

Conclusion

This PRISMA-guided bibliometric analysis of 291 articles (2015–2024) provides the first systematic mapping of ML applications in GPC research. Three principal conclusions emerge.

First, ML adoption has accelerated dramatically: 75% of publications appeared after 2021, with annual output growing from 1 to 100 publications. India, China, and Saudi Arabia collectively account for 51.4% of global output. Second, ANN remains the dominant technique (47% of studies), followed by SVM (22%) and GA (18%). Hybrid models are gaining traction in recent publications, indicating methodological maturation. Third, a critical thematic imbalance exists: 89% of ML studies target compressive strength, while durability properties remain severely understudied (11%). This gap must be addressed to enable widespread GPC adoption in infrastructure applications. Based on identified gaps, future research should prioritize: (1) ML

models for durability prediction to address the 89:11 imbalance; (2) explainable AI techniques (SHAP, LIME) for model transparency; (3) multi-objective optimization frameworks considering strength, durability, embodied carbon and cost.

Acknowledgments
The authors express their sincere gratitude to Universiti Teknologi Malaysia (UTM) and the DuraBi Center, Hanyang University (ERICA), South Korea, for providing financial and administrative support that enabled this study (Grant No. Q.J130000.3022.04M92). The authors also thank the anonymous reviewers for their constructive feedback, which significantly improved the quality of this manuscript.

References

[1] Y.S. Wudil, A. Al-Fakih, M.A. Al-Osta, M.A. Gondal, Intelligent optimization for modeling carbon dioxide footprint in fly ash geopolymer concrete: A novel approach for minimizing CO2 emissions, J. Environ. Chem. Eng. 12 (2024) 111835. https://doi.org/10.1016/j.jece.2023.111835

[2] M. Bypour, M. Yekrangnia, M. Kioumarsi, Machine learning-driven optimization for predicting compressive strength in fly ash geopolymer concrete, Clean. Eng. Technol. 25 (2025) 100899. https://doi.org/10.1016/j.clet.2025.100899

[3] H. Hu, M. Jiang, M. Tang, H. Liang, H. Cui, C. Liu, C. Ji, Y. Wang, S. Jian, C. Wei, S. Song, Prediction of compressive strength of fly ash-based geopolymers concrete based on machine learning, Results in Engineering 27 (2025) 106492. https://doi.org/10.1016/j.rineng.2025.106492

[4] M. Katlav, F. Ergen, I. Donmez, AI-driven design for the compressive strength of ultra-high performance geopolymer concrete (UHPGC): From explainable ensemble models to the graphical user interface, Mater. Today Commun. 40 (2024) 109915. https://doi.org/10.1016/j.mtcomm.2024.109915

[5] H. Ji, Y. Lyu, W. Ying, J.C. Liu, H. Ye, Machine learning guided iterative mix design of geopolymer concrete, Journal of Building Engineering 91 (2024) 109710. https://doi.org/10.1016/j.jobe.2024.109710

[6] H. Hao, K. Bi, W. Chen, T.M. Pham, J. Li, Towards next generation design of sustainable, durable, multi-hazard resistant, resilient, and smart civil engineering structures, Engineering Structures 277 (2023) 115477. https://doi.org/10.1016/j.engstruct.2022.115477

[7] S.A. Benameur, H. Siad, M. Lachemi, Y. Houmadi, Development of sustainable self-healing engineered cementitious composites incorporating maximum amounts of natural pozzolan, Constr. Build. Mater. 456 (2024) 139278. https://doi.org/10.1016/j.conbuildmat.2024.139278

[8] S.A. Eftekhar Afzali, M.A. Shayanfar, M. Ghanooni-Bagha, E. Golafshani, T. Ngo, The use of machine learning techniques to investigate the properties of metakaolin-based geopolymer concrete, J. Clean. Prod. 446 (2024) 141305. https://doi.org/10.1016/j.jclepro.2024.141305

[9] S.K. Baduge, S. Thilakarathna, J.S. Perera, M. Arashpour, P. Sharafi, B. Teodosio, A. Shringi, P. Mendis, Artificial intelligence and smart vision for building and construction 4.0: Machine and deep learning methods and applications, Automation in Construction, 141 (2022) 104440. https://doi.org/10.1016/j.autcon.2022.104440

[10] M. Rathnayaka, D. Karunasinghe, C. Gunasekara, K. Wijesundara, W. Lokuge, D.W. Law, Machine learning approaches to predict compressive strength of fly ash-based geopolymer concrete: A comprehensive review, Construction and Building Materials 419 (2024) 135519. https://doi.org/10.1016/j.conbuildmat.2024.135519

[11] M.J. Page, J.E. McKenzie, P.M. Bossuyt, I. Boutron, T.C. Hoffmann, C.D. Mulrow, L. Shamseer, J.M. Tetzlaff, E.A. Akl, S.E. Brennan, R. Chou, J. Glanville, J.M. Grimshaw, A. Hrobjartsson, M.M. Lalu, T. Li, E.W. Loder, E. Mayo-Wilson, S. McDonald, L.A. McGuinness, L.A. Stewart, J. Thomas, A.C. Tricco, V.A. Welch, P. Whiting, D. Moher, The PRISMA 2020 statement: an updated guideline for reporting systematic reviews, BMJ 372 (2021) n71. https://doi.org/10.1136/bmj.n71

[12] R. Kumar, E. Althaqafi, S.G.K. Patro, V. Simic, A. Babbar, D. Pamucar, S.K. Singh, A. Verma, Machine and deep learning methods for concrete strength Prediction: A bibliometric and content analysis review of research trends and future directions, Applied Soft Computing 164 (2024) 111956. https://doi.org/10.1016/j.asoc.2024.111956

[13] M. Abdellatief, Y.M. Hassan, M.T. Elnabwy, L.S. Wong, R.J. Chin, K.H. Mo, Investigation of machine learning models in predicting compressive strength for ultra-high-performance geopolymer concrete: A comparative study, Constr. Build. Mater. 436 (2024) 136884. https://doi.org/10.1016/j.conbuildmat.2024.136884

[14] S. Nazar, M. Iqbal, J. Yang, M. Ashraf, Machine Learning-Driven Evaluation of Carbon Emissions in Geopolymer Concrete, Appl. Soft Comput. 185 (2025) 114017. https://doi.org/10.1016/j.asoc.2025.114017

[15] M.O. Yusuf, Flyash and coffee silverskin binary blended geopolymer, Constr. Build. Mater. 453 (2024) 138983. https://doi.org/10.1016/j.conbuildmat.2024.138983

[16] C. Balasooriya Arachchilage, G. Huang, C. Fan, W.V. Liu, Forecasting unconfined compressive strength of calcium sulfoaluminate cement mixtures using ensemble machine learning techniques integrated with shapely-additive explanations, Constr. Build. Mater. 409 (2023) 134083. https://doi.org/10.1016/j.conbuildmat.2023.134083

[17] N.M.S. Hasan, M.H.R. Sobuz, N.M.N. Shaurdho, M.M. Meraz, S.D. Datta, F.S. Aditto, M.K.I. Kabbo, M.J. Miah, Eco-friendly concrete incorporating palm oil fuel ash: Fresh and mechanical properties with machine learning prediction, and sustainability assessment, Heliyon 9 (2023) e22296. https://doi.org/10.1016/j.heliyon.2023.e22296

Materials Research Proceedings 74 (2026) 101-108 https://doi.org/10.21741/9781644904473-13

Turmeric (*Curcuma longa*) as a Dual-Function Source of Cellulose Nanofibers and Essential Oil for Mechanical Modulation of PVA Bionanocomposite Films

Akmal AKMAL[1,a], Hairul ABRAL[1,2,b *], Lovely SON[1,c], Syafii SYAFII[3,d] and Kadriadi KADRIADI[1,e]

[1]Department of Mechanical Engineering, Universitas Andalas, Padang 25163, Indonesia

[2]Laboratory of Nanoscience and Technology, Department of Mechanical Engineering, Universitas Andalas, Padang 25163, Indonesia

[3]Department of Electrical Engineering, Universitas Andalas, Padang 25163, Indonesia

[a]2430912002_akmal@student.unand.ac.id, [b]habral@yahoo.com, [c]lovelyson@eng.unand.ac.id, [d]syafii@eng.unand.ac.id, [e]2330912002_kadriadi@student.unand.ac.id

Keywords: Turmeric Residue, Composites, Nanocellulose Fiber, Elongation at Break

Abstract. The growing problem of petroleum-derived packaging waste has driven greater interest in biodegradable film materials, where poly(vinyl alcohol) (PVA) stands out as a promising candidate despite having mechanical performance that needs to be adjusted. Cellulose nanofibers and essential oils have been widely used to modify PVA films, this work introduces a dual-source strategy where both the structural reinforcing agent and the plasticizer are extracted from the same plant, namely turmeric rhizome (*Curcuma longa*). Cellulose nanofibers derived from turmeric (TCNF) and turmeric essential oil (TEO) were combined into a PVA matrix to form nanocomposite films, and their respective contributions to tensile properties were evaluated. The introduction of TCNF resulted in an increase in tensile strength (27.3 MPa), elongation at break (157.8%), and tensile modulus (190.4 MPa), confirming its reinforcing role. TEO, on the other hand, disrupted intermolecular polymer associations, reducing tensile strength to 21.6 MPa while simultaneously extending the film's flexibility to 161.9%, in line with classical plasticization behaviour. These results indicate that two different functional fractions derived from turmeric rhizomes can be utilized simultaneously to enable the tuning of the mechanical properties of PVA films.

Introduction

The environmental crisis caused by conventional plastic waste continues to escalate, with global production reaching 413.8 Mt in 2023 and forecast to surpass 1.1 Gt within the next three decades if current trajectories persist [1,2]. Plastics made from petrochemicals, such as polypropylene, polyethylene, polyethylene terephthalate, and polystyrene, are often used in the packaging industry. These plastics are highly resistant to decomposition and can persist in the environment for centuries [3]. Approximately 142 Mt of plastic waste were generated by the packaging sector in 2019, placing a significant burden on global waste management systems [1]. As sustainable substitutes, biodegradable polymers such as starch, cellulose, chitosan, polylactic acid, and polyvinyl alcohol have been developed [4]. Polyvinyl alcohol (PVA) has attracted attention due to its biodegradable properties, excellent film forming ability, transparency, water solubility, biocompatibility, and reported suitability for food-related applications by FAO/WHO and USDA [5–7]. However, neat PVA films exhibit limited mechanical and barrier performance, which restrict their widespread application across various industries, including packaging [8–10]. Reported tensile strengths for neat PVA films vary widely, typically on the order of 14-57 MPa depending on the degree of hydrolysis (DH), molecular weight (MW), and processing conditions

Content from this work may be used under the terms of the Creative Commons Attribution 3.0 license. Any further distribution of this work must maintain attribution to the author(s) and the title of the work, journal citation and DOI. Published under license by Materials Research Forum LLC.

[8,11,12]. In terms of barrier behaviour, the abundant hydrophilic hydroxyl groups of PVA render the films sensitive to humidity and confer a high water-vapor permeability, i.e., a poor moisture barrier, although PVA provides an excellent oxygen barrier under dry conditions, this property deteriorates markedly at high relative humidity owing to water-induced plasticization of the matrix. To overcome these limitations, reinforcement with nano-scale fillers such as cellulose nanofibers has been proposed as an effective approach [13].

Cellulose nanofibers (CNF), derived from abundant lignocellulosic biomass, exhibit a high aspect ratio, excellent mechanical strength, and biocompatibility. Incorporation of CNF into polymer matrices has been shown to improve the tensile strength, flexibility, and thermal stability of biopolymer films [7,14,15]. Turmeric (*Curcuma longa*), a plant widely cultivated and used in the food and health sectors in Asia, particularly in Indonesia, is a valuable source for CNF production, and its processing residues contain cellulose that can be utilized and processed into turmeric cellulose nanofibers (TCNF). Cellulosic fibres from turmeric residues have previously been extracted and characterized, and turmeric residue has been valorised in various other product systems [16]. Building on this prior work, the present study employs the nanofibrillated form (TCNF) as a reinforcing agent in a PVA matrix and, in parallel, incorporates turmeric essential oil obtained from the same plant. Besides reinforcing, the incorporation of essential oils (EO) has been extensively investigated in biodegradable films to impart active functionalities [17,18]. Turmeric essential oil (TEO), extracted from turmeric rhizomes, is rich in ar-turmerone and β-turmerone, compounds noted for their antibacterial and antioxidant characteristics [19]. Essential oils, in addition to their biological activities, can affect the microstructure and mechanical characteristics of polymer films via their plasticizing effects and interactions with the polymer matrix [20,21]. While the mechanical effects of EO from various sources have been reported, the combined use of a reinforcing nanofiber and a plasticizing essential oil obtained from one and the same plant (turmeric rhizome), and its effect on the tensile behaviour of PVA films, has received little dedicated attention. Therefore, this study develops a PVA-based bionanocomposite film that integrates turmeric cellulose nanofibers as reinforcement and turmeric essential oil as a natural additive. As a foundational step, the present work focuses specifically on the mechanical response of the films, namely tensile strength, elongation at break, and tensile modulus, to establish the distinct and complementary roles of the two turmeric-derived fractions. This study aims to clarify how integrating nanofiber reinforcement with essential-oil addition derived from a single botanical source can modulate tensile properties of PVA films, and to demonstrate the feasibility of turmeric waste as a renewable raw material for functional packaging.

Materials and Methods

Materials

PVA (MW 89,000 to 98,000 g/mol, and a DH 99%), along with Tween 80 were purchased from Sigma Aldrich. *Curcuma longa* rhizomes in fresh form were procured from a traditional market located in Padang, West Sumatra Province, Indonesia. TEO was supplied by PT. Syailendra Bumi Investama, a producer based in Karanganyar Regency, Central Java Province, Indonesia. Distilled water used throughout all experimental procedures was supplied by Andeska Laboratory, Padang, Indonesia.

Preparation of TCNF

A combination of chemical treatment and ultrasonication was employed to isolate and produce TCNF, adapted from a previously established method with several modifications [22]. Initially, turmeric was cleaned and cut into small pieces for grinding using a slow-speed juicer (Hurom H-AA-BBE17, Korea) to separate the turmeric fibre pulp from the liquid. The resulting pulp was oven-dried at 50 °C, 20 h (Memmert UN-55, Germany) and subsequently ground into fine particles using a kitchen blender. The pulverized fibres then underwent a series of chemical treatments: (1) Alkalization: fibres were immersed in a toluene-ethanol solution (2:1 ratio) and dewaxed on a hot

plate magnetic stirrer (AREC, Velp Scientifica) for 7 h at 50 °C and 500 rpm, followed by filtration through a 500-mesh sieve and repeated rinsing with distilled water until a neutral pH was reached. The suspension was subsequently spread on a Teflon plate and dried at 50 °C for 20 h. This dried fibre was then soaked in 5% NaOH and subjected to a second dewaxing step (4 h, 60 °C, 500 rpm), followed by the same rinsing, drying, and grinding procedure described above. (2) Bleaching: the fibres were treated with a $NaClO_2$ and CH_3COOH mixture (4:1 ratio) at 60 °C, 500 rpm, 2 h to remove residual lignin; this step was repeated four times until white pulp was obtained, which was then rinsed with distilled water by filtration until neutral pH was achieved. (3) Acid hydrolysis: the bleached pulp was hydrolysed in 5 M HCl at 50 °C, 12 h, then vacuum-filtered (Buchner funnel and glass flask, filter paper porosity 0.45 μm, diameter 47 mm) and rinsed with distilled water until neutral pH. (4) Ultrasonication: a 5% fibre suspension in 100 mL distilled water was sonicated for 60 min at 600 W using an ultrasonic processor (FS-1200N), with the suspension temperature kept below 60 °C throughout the process.

Film Preparation

Bionanocomposite films were fabricated via a solution casting technique, adapted from the methods reported by Abral et al. [7] and Khazaei et al. [23] with certain modifications. PVA (10 g) and TCNF suspension (20 mL, equivalent to 0.06 g dry weight) were dissolved in 100 mL of distilled water and stirred for 2 h, 500 rpm, 70 °C. TEO 1 g was then combined with Tween 80 (10% of TEO content) which served as an emulsifier to promote uniform dispersion of TEO within the film-forming solution. This mixture was subsequently homogenized for 5 min at 10,000 rpm using a homogenizer (IKA T25 Ultra Turrax, Germany), followed by sonication for 5 min at 600 W. The final solution was poured into Petri dishes and subsequently dried in an oven at 50 °C, 20 h. Three film types were prepared in triplicate for comparison: neat PVA, PVA/TCNF, and PVA/TCNF/TEO.

Mechanical Testing

Tensile properties were evaluated according to the ASTM D638 Type V standard [24], using films with an average thickness of 0.429 mm. Width and thickness of the samples were measured with a Nikon SMZ1270 stereomicroscope. Mechanical properties, including tensile strength, elongation at break, and modulus were assessed from tensile curves generated by a Com-Ten 95T testing machine at a crosshead speed of 5 mm/min under room temperature. Samples were preconditioned for three days at 25 °C, 50 ± 5% RH before testing. Tensile tests were conducted on three specimens for each formulation. It is acknowledged that ASTM D882 is the standard specifically formulated for thin plastic films; the ASTM D638 type V configuration was retained here because it is widely applied to solution-cast biopolymer and nanocomposite films in the literature [25], and because all formulations were evaluated under identical specimen geometry, crosshead speed, and conditioning, so that the comparative differences reported between samples are internally consistent and independent of the chosen standard.

Statistical Analysis

Tensile test data were statistically evaluated using SPSS 27.0 (IBM Corp, Chicago, USA). One-way ANOVA, including F-tests with corresponding p-values, was conducted to assess the effect of TCNF and TEO incorporation on the mechanical properties of bionanocomposite films. Tukey's multiple range test (95% confidence, $p < 0.05$) was employed to identify significant differences among mean values. All experiments were conducted in triplicate.

Results and Discussion

Influences of TCNF and TEO incorporation on tensile strength (TS), elongation at break (EB) and modulus (TM) across bionanocomposite specimens are presented in Fig. 1. Results obtained from mechanical testing confirm that incorporating TCNF into the PVA matrix resulted in a meaningful strengthening of the nanocomposite structure. In its unmodified state, the PVA film displayed a TS value of 23.5 MPa, an EB value of 148.9%, and a TM of 144.8 MPa. Upon inclusion of TCNF,

all three measured parameters rose to 27.3 MPa (TS), 157.8% (EB), and 190.4 MPa (TM), demonstrating a well-defined upward trend in mechanical performance attributable to nanofiber reinforcement. This corresponds to increases of +16.2% in TS, +6.0% in EB, and +31.5% in TM relative to neat PVA film. Notably, these gains were obtained at a relatively low filler loading (≈0.6 wt.% relative to PVA); achieving a simultaneous improvement in strength, stiffness, and elongation at such a low loading indicates a high specific (per-weight) reinforcement efficiency and is consistent with efficient load transfer occurring at the interfacial region between the nanofibers and the encapsulating polymeric network. This behaviour is the opposite of the strength-up/elongation-down pattern typically observed for poorly dispersed or aggregated fillers, and therefore likely reflects good nanofiber dispersion and favourable interfacial interactions, specifically, hydrogen-bond-type interactions between hydroxyl groups in the nanocellulose and the functional groups along the PVA polymer chains [13,26]. Similar results were also obtained from previous studies that incorporated CNF synthesized from agricultural or agro-industrial residues into PVA matrices, such as ginger [7], pineapple leaves [27], and rice husk [28]. For context, CNF-reinforced PVA systems at higher loadings have reported tensile strengths such as ~44 MPa for ginger nanofibers [7] and ~28 MPa for pineapple-leaf CNF at 4% [27]; the comparatively modest absolute value obtained here is therefore a direct consequence of the intentionally low filler content rather than of poor reinforcement, and the per-weight efficiency remains competitive.

Moreover, Fig. 1A indicates that the incorporation of TEO into the bionanocomposite film results in a reduction in the TS of the film to 21.6 MPa. The reduction may arise due to TEO's role as a lipid inside the film system, resulting in a heterogeneous structure characterized by discontinuities in the polymer network. Consequently, the majority of robust polymer-polymer interactions, such as hydrogen bonds between PVA and TCNF strands, are supplanted by weaker polymer-oil interactions. This mechanism diminishes the internal cohesiveness of the film network, thereby decreasing TS [17,29]. Additionally, the incorporation of TEO results in an enhancement of EB, reaching up to 161.9%. This occurs because TEO functions as a plasticizer, enhancing polymer chain mobility and diminishing matrix stiffness. TEO generates flexible domains that compromise the integrity of polymer bonds while simultaneously facilitating the mobility of polymer chains under applied tensile tension. Consequently, while TS diminishes due to reduced polymer-polymer interactions, the film exhibits increased ductility and elasticity [17,20,21]. Importantly, the strength reduction caused by TEO here is comparatively mild: the TS decreased by only about 21% relative to the reinforced film (27.3 to 21.6 MPa) and remained close to that of neat PVA. This contrasts with many EOs-modified systems in which the strength loss is severe, for example, the incorporation of black pepper essential oil into a PVA/Gum arabic/Chitosan film reduced TS from 11.81 to 7.08 MPa (a ≈40% loss) [30]. The TCNF reinforcement therefore appears to buffer the strength penalty normally imposed by essential oils, yielding a more controllable strength-ductility compromise.

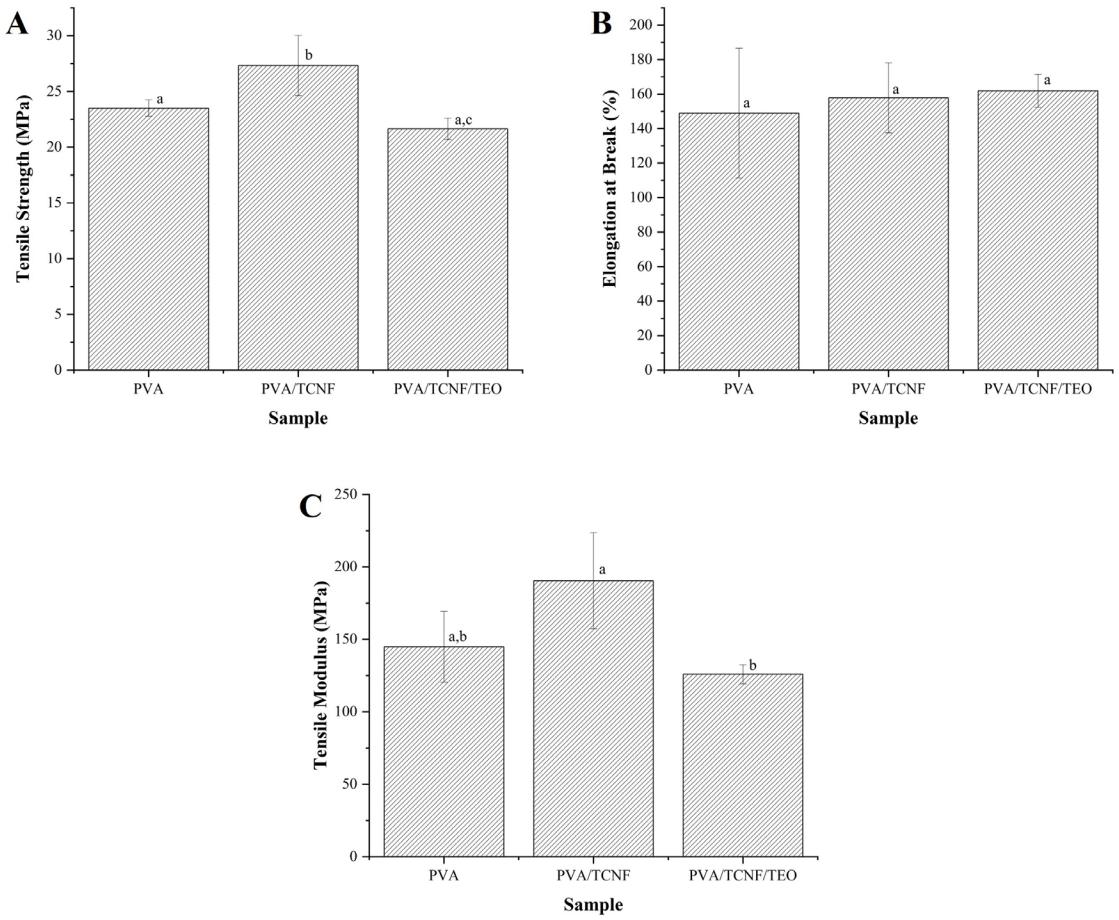


Fig. 1. Tensile performance of the bionanocomposite films, including (A) tensile strength, (B) elongation at break, and (C) elastic modulus. Each value corresponds to the mean standard deviation of three replicate measurements (n = 3); superscript letters that differ between bars reflect statistically significant distinctions as assessed by Tukey's multiple range test ($p < 0.05$).

Conclusion

In this work, PVA-based bionanocomposite films, reinforced with TCNF and incorporated with TEO, were fabricated and their mechanical properties were characterized. The addition of TCNF improved the TS, EB, and TM of the films, indicating an effective reinforcing role that is likely associated with good nanofiber dispersion and favourable interfacial interactions within the PVA matrix. Notably, these gains were obtained at a relatively low filler content (≈0.6 wt.%), and the simultaneous increase in strength, stiffness, and elongation, rather than the strength-up/elongation-down behaviour typical of poorly dispersed or aggregated fillers, is consistent with efficient stress transfer between the nanofibers and the matrix. The inclusion of TEO reduced TS while concurrently improving ductility and elasticity, behaviour characteristic of a plasticizing additive that enhances polymer-chain mobility. Among the formulations, the PVA/TCNF film achieved the best overall tensile performance, with the highest TS (27.3 MPa, +16.2% compared with neat PVA film), EB (157.8%), and TM (190.4 MPa, +31.5% compared with neat PVA film), whereas the PVA/TCNF/TEO film provided the greatest flexibility (EB of 161.9%) at the expense of TS (21.6 MPa). These findings suggest that turmeric-derived nanofibers and essential oil may be simultaneously employed to modulate the tensile characteristics of PVA-based matrices, with TCNF governing strength and stiffness and TEO governing ductility. Further studies, including

morphological, thermal, barrier, spectroscopic and antibacterial of film (e.g., SEM, TGA/DSC, WVP/OP, and FTIR) together with concentration optimization characterization, are required to confirm the proposed mechanisms and to broaden the applicability of these bionanocomposite films for functional packaging.

Acknowledgements
This study was supported by the Directorate of Research and Community Service. Directorate General of Research and Development, Ministry of Higher Education, Science, and Technology. Under the PMDSU Scheme (Contract No. 060/C3/DT.05.00/PL/2025, Fiscal Year 2025).

References

[1] Statista, Plastic waste generation worldwide from 1980 to 2019, by application., (2023). https://www.statista.com/statistics/1339124/global-plastic-waste-generation-by-application/ (accessed July 11, 2025).

[2] Y.Y. Lai, Y.M. Lee, Management strategy of plastic wastes in Taiwan, Sustain. Environ. Res. 32 (2022) 11. https://doi.org/10.1186/s42834-022-00123-0.

[3] A. Chamas, H. Moon, J. Zheng, Y. Qiu, T. Tabassum, J.H. Jang, M. Abu-Omar, S.L. Scott, S. Suh, Degradation Rates of Plastics in the Environment, ACS Sustain. Chem. Eng. 8 (2020) 3494–3511. https://doi.org/10.1021/acssuschemeng.9b06635.

[4] R. Singh, S. Gautam, B. Sharma, P. Jain, K.D. Chauhan, Biopolymers and their classifications, in: Biopolym. Their Ind. Appl., Elsevier, 2021: pp. 21–44. https://doi.org/10.1016/B978-0-12-819240-5.00003-1.

[5] WHO, Evaluation of certain food additives and contaminants (Sixty-first report of the Joint FAO/WHO expert committee on food additives), Geneva, 2004. https://doi.org/https://apps.who.int/iris/handle/10665/42849.

[6] B. Oner, R. Meral, Z. Ceylan, Determination of some quality indices of rainbow trout fillets treated with nisin-loaded polyvinylalcohol-based nanofiber and packed with polyethylene package, LWT 149 (2021) 111854. https://doi.org/10.1016/j.lwt.2021.111854.

[7] H. Abral, J. Ariksa, M. Mahardika, D. Handayani, I. Aminah, N. Sandrawati, S.M. Sapuan, R.A. Ilyas, Highly transparent and antimicrobial PVA based bionanocomposites reinforced by ginger nanofiber, Polym. Test. 81 (2020) 106186. https://doi.org/10.1016/j.polymertesting.2019.106186.

[8] H. Abral, A. Atmajaya, M. Mahardika, F. Hafizulhaq, Kadriadi, D. Handayani, S.M. Sapuan, R.A. Ilyas, Effect of ultrasonication duration of polyvinyl alcohol (PVA) gel on characterizations of PVA film, J. Mater. Res. Technol. 9 (2020) 2477–2486. https://doi.org/10.1016/j.jmrt.2019.12.078.

[9] A.A. Oun, G.H. Shin, J.-W. Rhim, J.T. Kim, Recent advances in polyvinyl alcohol-based composite films and their applications in food packaging, Food Packag. Shelf Life 34 (2022) 100991. https://doi.org/10.1016/j.fpsl.2022.100991.

[10] A. Shirdel, T. Zeinali, Polyvinyl alcohol-based films for active meat packaging: Preservation mechanisms and applications – A mini-review, Food Chem. Adv. 11 (2026) 101333. https://doi.org/10.1016/j.focha.2026.101333.

[11] N. Jain, V.K. Singh, S. Chauhan, A review on mechanical and water absorption properties of polyvinyl alcohol based composites/films, J. Mech. Behav. Mater. 26 (2017) 213–222. https://doi.org/https://doi.org/10.1515/jmbm-2017-0027.

[12] W. Ma, P. Zhang, B. Zhao, S. Wang, J. Zhong, Z. Cao, C. Liu, F. Gong, H. Matsuyama, Swelling Resistance and Mechanical Performance of Physical Crosslink-Based Poly(Vinyl Alcohol) Hydrogel Film with Various Molecular Weight, J. Polym. Sci. Part B Polym. Phys. 57 (2019) 1673–1683. https://doi.org/10.1002/polb.24902.

[13] M.C. Alvarado, Recent progress in polyvinyl alcohol (PVA)/nanocellulose composite films for packaging applications: A comprehensive review of the impact on physico-mechanical properties, Food Bioeng. 3 (2024) 189–209. https://doi.org/10.1002/fbe2.12086.

[14] S. Antony Jose, N. Cowan, M. Davidson, G. Godina, I. Smith, J. Xin, P.L. Menezes, A Comprehensive Review on Cellulose Nanofibers, Nanomaterials, and Composites: Manufacturing, Properties, and Applications, Nanomaterials 15 (2025) 356. https://doi.org/10.3390/nano15050356.

[15] M.A. Azka, F. Abdul Halim Muhammad, A. Habib, Akmal, R. Muhammad Railis, S.M. Sapuan, H. Abral,. F.M. Al-Oqla, A review of graphene, nanocellulose, and graphene/nanocellulose hybrid reinforced biopolymer composites in electronic applications, Phys. Sci. Rev. (2025) 1–27. https://doi.org/10.1515/psr-2024-0078.

[16] S. Gopi, A. Amalraj, S. Jude, K.T. Benson, P. Balakrishnan, J.T. Haponiuk, S. Thomas, Isolation and characterization of stable nanofiber from turmeric spent using chemical treatment by acid hydrolysis and its potential as antimicrobial and antioxidant activities, J. Macromol. Sci. Part A Pure Appl. Chem. 56 (2019) 327–340. https://doi.org/10.1080/10601325.2019.1578613.

[17] L. Atarés, A. Chiralt, Essential oils as additives in biodegradable films and coatings for active food packaging, Trends Food Sci. Technol. 48 (2016) 51–62. https://doi.org/10.1016/j.tifs.2015.12.001.

[18] R. Arun, R. Shruthy, R. Preetha, V. Sreejit, Biodegradable nano composite reinforced with cellulose nano fiber from coconut industry waste for replacing synthetic plastic food packaging, Chemosphere 291 (2022) 132786. https://doi.org/10.1016/j.chemosphere.2021.132786.

[19] M.D. Ibáñez, M.A. Blázquez, Curcuma longa L. Rhizome Essential Oil from Extraction to Its Agri-Food Applications. A Review, Plants 10 (2021) 44. https://doi.org/10.3390/plants10010044.

[20] Y. Zhang, L. Zhou, C. Zhang, P.L. Show, A. Du, J. Fu, V. Ashokkumar, Preparation and characterization of curdlan/polyvinyl alcohol/thyme essential oil blending film and its application to chilled meat preservation, Carbohydr. Polym. 247 (2020) 116670. https://doi.org/10.1016/j.carbpol.2020.116670.

[21] Y. Chu, T. Xu, C. Gao, X. Liu, N. Zhang, X. Feng, X. Liu, X. Shen, X. Tang, Evaluations of physicochemical and biological properties of pullulan-based films incorporated with cinnamon essential oil and Tween 80, Int. J. Biol. Macromol. 122 (2019) 388–394. https://doi.org/10.1016/j.ijbiomac.2018.10.194.

[22] H. Abral, J. Ariksa, M. Mahardika, D. Handayani, I. Aminah, N. Sandrawati, A.B. Pratama, N. Fajri, S.M. Sapuan, R.A. Ilyas, Transparent and antimicrobial cellulose film from ginger nanofiber, Food Hydrocoll. 98 (2020) 105266. https://doi.org/10.1016/j.foodhyd.2019.105266.

[23] A. Khazaei, L. Nateghi, N. Zand, A. Oromiehie, F. Garavand, Evaluation of Physical , Mechanical and Antibacterial Properties of Pinto Bean Starch-Polyvinyl Alcohol Biodegradable Films Reinforced with Cinnamon Essential Oil, Polymers (Basel). 13 (2021) 2778. https://doi.org/10.3390/polym13162778.

[24] American Society for Testing and Materials D638, Test Method for Tensile Properties of Plastics, ASTM Int. (2014) 1–17. https://doi.org/10.1520/D0638-14.

[25] A.F. Osman, L. Siah, A.A. Alrashdi, A. Ul-Hamid, I. Ibrahim, Improving the tensile and tear properties of thermoplastic starch/dolomite biocomposite film through sonication process, Polymers (Basel). 13 (2021) 1–21. https://doi.org/10.3390/polym13020274.

[26] F. Yudhanto, Jamasri, H.S.B. Rochardjo, A. Kusumaatmaja, Experimental study of polyvinyl alcohol nanocomposite film reinforced by cellulose nanofibers from agave cantala, Int. J. Eng. Trans. A Basics 34 (2021) 987–998. https://doi.org/10.5829/ije.2021.34.04a.25.

[27] M. Mahardika, N. Masruchin, D. Amelia, R.A. Ilyas, A.A. Septevani, E. Syafri, N. Hastuti, M. Karina, M.A. Khan, B.H. Jeon, N.H. Sari, Nanocellulose reinforced polyvinyl alcohol-based bio-nanocomposite films: improved mechanical, UV-light barrier, and thermal properties, RSC Adv. 14 (2024) 23232–23239. https://doi.org/10.1039/d4ra04205k.

[28] G.M. Cholant, M.W. Bosenbecker, A.A. Reichert, C.A.G. Beatrice, T.C. Freitas, N.D. Freitas, N.V.V. de Nunes, A.F. Galio, A.L. Missio, A.D. de Oliveira, Polyvinyl Alcohol Films Reinforced with Nanocellulose from Rice Husk, Macromol 5 (2025) 6. https://doi.org/10.3390/macromol5010006.

[29] A. Bahrami, R. Fattahi, Biodegradable carboxymethyl cellulose–polyvinyl alcohol composite incorporated with Glycyrrhiza Glabra L. essential oil: Physicochemical and antibacterial features, Food Sci. Nutr. 9 (2021) 4974–4985. https://doi.org/10.1002/fsn3.2449.

[30] A. Amalraj, J.T. Haponiuk, S. Thomas, S. Gopi, Preparation, characterization and antimicrobial activity of polyvinyl alcohol/gum arabic/chitosan composite films incorporated with black pepper essential oil and ginger essential oil, Int. J. Biol. Macromol. 151 (2020) 366–375. https://doi.org/10.1016/j.ijbiomac.2020.02.176.

Materials Research Proceedings 74 (2026) 109-116 https://doi.org/10.21741/9781644904473-14

Evaluating the Role of Biomass Allocation in Mango (*Mangifera indica* L.) as Predictors of Natural Fiber Yield for Sustainable Composites

Fadhilnor ABDULLAH[1,2,a *], Nurul Afidah UMORUDDIN[1,b], Mohd Khairul Rabani HASHIM[2,c], Zainal Abidin ARSAT[2,d], M.N.A. UDA[2,e] and Muhammad Firdaus ABDUL MUTTALIB[2,f]

[1]Institute of Sustainable Agrotechnology (INSAT), University Malaysia Perlis (UniMAP), Sg. Chuchuh Campus, 02100 Padang Besar, Perlis, Malaysia

[2]Faculty of Engineering & Mechanical Technology (FKTM), Universiti Malaysia Perlis (UniMAP), 02600 Arau, Perlis, Malaysia

[a]fadhilnor@unimap.edu.my, [b]nurulafidah@unimap.edu.my, [c]khairulrabani@unimap.edu.my, [d]zainalabidin@unimap.edu.my, [e]nuraiman@unimap.edu.my, [f]firdausmuttalib@unimap.edu.my

Keywords: Biomass Allocation, Biowastes, Mango, Natural Fibres, Sustainable Materials

Abstract. The growing interest in renewable resources for sustainable materials has underscored the significance of agricultural biomass as a natural fibre source for bio-composite applications. Mango (*Mangifera indica* L.) trees produce considerable amounts of vegetative biomass and bio-wastes during orchard management. This study assessed an early-stage source of lignocellulosic bio-waste from mango plants at the seedling stage. In nursery, unwanted mango seedlings planted under different shading net usually discarded and underutilised by the growers. Therefore, this study evaluated the impact of different shading treatments on biomass distribution in mango plants and investigated their implications for fibre yield and utility in composite production. The mango plants were placed under different shading regimes (0%, 50%, and 80%), and the fresh and dry weights of stems, leaves, and roots were measured, along with growth allocation characteristics such as moisture content, root-to-shoot ratio, root length, and leaf weight ratio. The findings indicated that seedlings exposed to full sunlight (0% shading) had the greatest total fresh weight and total dry weight, with notable contributions from stem and root dry matter. In contrast, heavy shading (80%) significantly decreased stem dry weight and root dry weight, while increasing moisture content and lowering the root-to-shoot ratio. Moderate shading (50%) preserved total fresh biomass similar to that under full sunlight, but exhibited reduced structural dry weight, suggesting limited advantages for fibre applications. These results highlight the important role of light availability in determining biomass quantity, quality, and distribution, which directly affects the mechanical potential of extracted fibres. Stems and roots of mango plants planted in full sunlight yield the highest levels of lignocellulosic material, making them preferable for use in natural fibre composites. Conversely, mango plants grown in shaded conditions accumulate less usable dry matter and show higher water content, which increases processing challenges and diminishes fibre performance. This research illustrates that managing environmental factors, especially light availability, is essential for optimising mango biomass for sustainable composite manufacturing. Merging biomass enhancement with materials development provides a strategy for valuing mango residues within a circular bioeconomy, decreasing agricultural waste while promoting green material innovation.

Introduction

One interesting alternative that has been drawing considerable attention is agriculture biomass or agro-biomass, which is the organic waste and by-products of agricultural operations, which

Content from this work may be used under the terms of the Creative Commons Attribution 3.0 license. Any further distribution of this work must maintain attribution to the author(s) and the title of the work, journal citation and DOI. Published under license by Materials Research Forum LLC.

constitutes a vast, untapped potential for the synthesis of bio-based products [1,2]. Agricultural waste, once regarded as bio-wastes, are now valued for its role in the creation of eco-friendly materials, thereby contributing to waste reduction and the development of a circular economy. Indeed, the agricultural biomass is a growing and increasingly significant material for the production of bio-based products, playing a significant role in the bioeconomy and contributing sustainable development. Among various crops, mango trees (*Mangifera indica* L.), one of the most cultivated tropical fruit trees, is often subjected to the regular pruning regime for canopy development, enhancing fruit production and easing pest and disease control during orchard establishment and management [3]. These cultural practices produce huge amounts of biomass waste in the form of branches, small twigs, stems and leaves, which are commonly discarded, burned, or allowed to rot under the tree canopy [3]. While the fruit is highly valued, the vegetative biomass frequently remains unutilised, notwithstanding its potential lignocellulosic constituents that are amenable to fibre extraction and material applications [4,5]. Evaluating the suitability of mango biomass for fibre production necessitates not only the quantification of total biomass yield but also a comprehensive understanding of the allocation of this biomass across various plant organs (roots, stems, and leaves), given that these tissues exhibit substantial differences in their lignin, cellulose, and hemicellulose composition [6,7].

The biomass, which refers to the total mass of organic matter in a plant [8], is often correlated with the amount and quality of fibres present. Utilisation of mango biomass waste in bio-composites not only provides an economic and environmental alternative to the use of synthetic fibres, i.e., glass or carbon fibres, but also helps alleviate the environmental impacts associated with open burning and landfilling [9]. Environmental surroundings, for example shading may influence not only the growth and physiological responses of mango trees but may also alter the dry biomass yield and structural composition of plant tissues, thereby affecting their potential use in natural fibre-reinforced bio-composites [10]. Understanding how shading impacts these traits is imperative to optimise mango biomass as a natural fibre-reinforced composite feedstock and sustainable agriculture waste management, as well as material extraction potential. Environmental factors, including light availability, directly influence plant growth and biomass accumulation, thereby influencing productivity and structural quality. In particular, shading can cause drastic changes in photosynthetic performance, moisture content, and biomass partitioning, which in turn alter the physical and mechanical characteristics of the produced fibres [10]. Environmental surroundings, for example shading may influence not only the growth and physiological responses of mango trees but may also alter the dry biomass yield and structural composition of plant tissues, thereby affecting their potential use in natural fibre-reinforced bio-composites [10]. Understanding how shading impacts these traits is imperative to optimise mango biomass as a natural fibre-reinforced composite feedstock and sustainable agriculture waste management, as well as material extraction potential. Therefore, the present investigation assesses the allocation of biomass in mango seedlings subjected to various growth conditions, with an emphasis on the quantification of both fresh and dry weights across distinct plant organs and establishing correlations between these characteristics and the potential yield of fibre.

Materials and Methods

Uniform 1-year-old mango (*Mangifera indica* L.) plants were selected and grown under controlled nursery conditions. The mango plants with comparable size were planted into 3L polyethylene bags containing a standard growing medium consisting of a soil, sand and compost at the ratio of 2:1:1. Plants were managed under consistent irrigation schedule and nutrient management to minimize variability in growth responses unrelated to light availability. In order to stimulate environmental effects (i.e. shading) on biomass allocation of mango plants, experimental mango plants were subjected under three (3) different shading regimes which are 0% shading (full sunlight, T1), treated as a control, 50% shading (moderate shading, T2) and 80% shading treatment

(heavy shading, T3). Shading was implemented utilising black polyethylene netting that have been setup previously under nursery condition. The experimental design treatments were systematically organised in a Randomized Complete Block Design (RCBD), comprising four (4) replicates for each treatment, with each replicate consisting of ten (10) plants.

The duration of the experiment was sustained for a period of 12 weeks to facilitate adequate biomass accumulation. At the end of the experimental period, all plants from each treatment were separated into three (3) parts of plant organ which are stems, leaves and roots. Immediately after harvest, the fresh weight (FW) of each organ of mango plants was weighted using an analytical balancing (BL3200HL, Shimadzu) and measured in grams (g) unit. For dry weight (DW), the plant parts were firstly oven-dried at 70 ºC for 96 hours (4 days) until constant weight and each organ of mango plants was weighted using similar analytical balancing as stated above. Total fresh and dry weight (TFW and TDW, respectively) were obtained by summing of organ weights. For moisture content (MC, %) of each mango plant organ was calculated using formula in Eq. 1. Root-to-Shoot Ratio (RSR) was calculated as the ratio of DW to the sum of stem and leaf DW. For Leaf Weight Ratio (LWR) was calculated as leaf dry weight divided by total dry weight. In addition, the length of the root organ (RL) was also measured using from the collar of stem to the root tip using flexible measurement tape (cm). Data were subjected to one-way Analysis of Variance (ANOVA) to test the effects of shading treatments on biomass and growth parameters. Where significant differences were detected ($P \leq 0.05$), means were compared using the Least Significant Difference (LSD) test. All analyses were conducted using Statistical Analysis System (SAS®).

$$MC = [\text{Fresh Weight (g)} - \text{Dry Weight (g)}] / \text{Fresh Weight (g)}] \times 100 \quad (1)$$

Results and Discussion

Table 1 presents the effects of three shading treatments 0% (T1), 50% (T2), and 80% (T3) on the fresh biomass components of mango (*Mangifera indica* L.) plants. Fresh weight (FW) distribution exhibited variation across the different shading treatments (Table 1). Mango plants exposed to full sunlight (T1) and those subjected to moderate shading (T2) demonstrated statistically comparable TFW values (136.60 g and 136.77 g, respectively), both of which were significantly greater (P=0.06) than the values recorded under heavy shading (T3, 82.18 g). A similar pattern was noted for stem fresh weight (SFW), where T1 and T2 did not present significant differences (P=0.08), yet both were superior to T3. Leaf fresh weight (LFW) did not exhibit significant differences among the treatments (P=0.32), although seedlings under T2 appeared to allocate a greater mass to leaf production. In contrast, root fresh weight (RFW) was significantly influenced by shading (P=0.01), decreasing from T1 to T3.

Table 1. Biomass allocation (i.e. fresh weight) of mango plants planted under different shading treatments.

	Total Fresh Weight (g)	Stem Fresh Weight (g)	Leaf fresh weight (g)	Root fresh weight (g)
Abbreviation[x]	TFW	SFW	LFW	RFW
T1	136.60 a	49.76 a	38.49 a	48.36 a
T2	136.77 a	50.48 a	47.97 a	38.33 a
T3	82.18 b	28.57 b	34.82 a	18.78 b
$LSD_{0.05}$	52.79	21.81	19.00	19.23
P-value	*P*=0.06	*P*=0.08	*P*=0.32	*P*=0.01

Note:
[x] The abbreviation terms used throughout this study.
[ǂ] Remarks: T1 - 0% shading treatment (Control), T2 - 50% shading treatment and T3 - 80% shading treatment.
Means sharing the same letters are not significantly different from each treatment ($P \leq 0.05$ ANOVA followed by Least Significant Difference Test).

The shading effects exhibited a greater effect in the parameters pertaining to dry weight (Table 2). The TDW recorded the highest value in treatment T1, followed by treatment T2 and treatment

T3, even though the differences did not reach statistical significance (P=0.30). An analysis of organ-specific dry weight demonstrated distinct variations (Table 2). The stem dry weight (SDW) exhibited a significant decline (P=0.05) from T1 to T3. In a similar manner, the root dry weight (RDW) was significantly greater (P=0.007) in T1 (19.07 g) and lowest in T3 (6.37 g). Conversely, the leaf dry weight (LDW) did not display significant variation among the treatments (P=0.22).

Table 2. Biomass allocation (i.e. dry weight) of mango plants planted under different shading treatments.

	Total Dry Weight (g)	Stem Dry Weight (g)	Leaf Dry weight (g)	Root Dry weight (g)
Abbreviation[x]	TDW	SDW	LDW	RDW
T1	52.19 a	17.93 a	15.19 a	19.07 a
T2	46.43 a	16.17 ab	18.86 a	11.42 b
T3	37.83 a	8.75 b	12.03 a	6.37 b
$LSD_{0.05}$	19.96	7.75	8.14	6.80
P-value	P=0.30	P=0.05	P=0.22	P=0.007

Note:
[x] The abbreviation terms used throughout this study.
[ǂ] Remarks: T1 - 0% shading treatment (Control), T2 - 50% shading treatment and T3 - 80% shading treatment.
Means sharing the same letters are not significantly different from each treatment (P≤0.05 ANOVA followed by Least Significant Difference Test).

Table 3 shows the effects of shading treatments on additional growth parameters such as Moisture Content (MC), Root-to-Shoot Ratio (RSR), Root Length (RL) and Leaf Weight Ratio (LWR). The MC exhibited a range from 51 % in T3 to 66% in T2, however, the observed differences were not statistically significant (P=0.17). The RSR was closed to significant variation (P=0.06), with the apex value registered under full sunlight conditions (T1) and diminished ratios observed under shading of T2 and T3 treatments. The RL demonstrated a declining trend in response to shading (40.25 cm in T1 versus 30.88 cm in T3), although this change did not reach statistical significance (P=0.27). The LWR exhibited an increase under moderate shading conditions (T2), in contrast to other shading treatments, yet this variation was marginally significant (P=0.12).

Table 3. Additional growth allocation parameters of mango plants planted under different shading treatments.

	Moisture content (%)	Root to shoot ratio	Root length (%)	Leaf weight ratio
Abbreviation[x]	MC	RSR	RL	LWR
T1	62.04 a	1.10 a	40.25 a	0.29 a
T2	65.85 a	0.72 b	37.50 a	0.40 ab
T3	51.00 a	0.72 b	30.88 a	0.33 b
$LSD_{0.05}$	17.07	0.37	12.58	0.11
P-value	P=0.17	P=0.06	P=0.27	P=0.12

Note:
[x] The abbreviation terms used throughout this study.
[ǂ] Remarks: T1 - 0% shading treatment (Control), T2 - 50% shading treatment and T3 - 80% shading treatment.
Means sharing the same letters are not significantly different from each treatment (P≤0.05 ANOVA followed by Least Significant Difference Test).

Biomass traits serve as essential quantitative metrics for assessing the growth and potential material yield of plants [11,12]. In agronomic and ecological research, plant biomass is generally defined by its fresh weight, the total mass of plant material including water content and dry weight, which indicates the leftover mass after moisture has been eliminated through drying methods. Various components such as leaf dry weight (LDW), stem dry weight (SDW), and root dry weight (RDW) offer more detailed evaluations of biomass distribution among plant organs, each of which can differ considerably in biochemical makeup and structural characteristics [12]. The results showed that seedlings exposed to full sunlight and moderate shading exhibited comparable total

and stem fresh weights, both of which were significantly elevated in contrast to those subjected to intense shading conditions (Table 1). The fresh weight of leaves remained unaffected by variations in shading. However, plants receiving moderate shading demonstrated a marginally increased leaf biomass. The fresh weight of roots experienced a pronounced decline under conditions of heavy shading, suggesting that root systems are particularly sensitive to diminished light availability. These results indicate that moderate shade maintained new biomass production, while dense shade significantly reduced cumulative growth, particularly root growth. From the perspective of materials science, the higher root fresh weight observed under full sunlight (T1) may indicate more developed root systems with greater cellulose-rich tissues [13], which could contribute to improved reinforcement potential in bio-composite applications [14], similar to what have been found on other plant roots such as *Acalypha indica* L. [15], *Pistia stratiotes* [16] and *Bassia indica* [17].

In this study, biomass traits or characteristics were interpreted in terms of their potential applications in natural fibre-reinforced composites. Dry weight of plants was regarded as a representative measure of usable lignocellulosic materials, while the distribution of roots and stems was highlighted as a key determinant of structural fibre yield. Meanwhile, moisture content (MC) is a critical factor in transforming plant biomass into bio-based composites [18]. In this study, the MC was assessed as a variable affecting drying efficiency and storage stability, both of which are essential for transforming plant biomass into fibres and fillers for the production of bio-based composites [19]. Results from this study indicate that implementing environmental management strategies, such as optimizing light exposure during the initial stages of plant growth, could serve as a strategic pre-processing tool to improve the quality of biomass feedstock for producing sustainable composite materials. Mango plant bio-wastes, generally underutilized in post-harvest processes, offer a valuable renewable resource for natural fibre-based composites when cultivated under ideal light conditions. This study adds to the expanding literature that supports the combination of agricultural production and material science in advancing a circular bioeconomy and innovation in green materials. Shading treatment affects not only the growth and physiological responses of mango plants but also modifies the dry biomass yield and structural makeup of plant tissues, which in turn impacts their potential application in natural fibre-reinforced bio-composites. The results confirm findings of other studies that light intensity influences the deposition of cellulose and lignin on tissues of plants, which determines the strength of the natural fibres [20-22]. For mango biomass, especially the rootstocks and the pruning residues, strategically enclosing light in the initial phases of development can improve the quantity and quality of the fibres. Such methods are in accordance with the strategies of circular bioeconomy wherein agricultural residues are transformed into renewable composites and waste and reliance on synthetic substitutes are minimized [23].

Conclusion

Overall, nursery operation and management of mango plants will generate considerable bio-wastes, including pruning materials (i.e. leaves and stems) and discarded seedlings. These bio-wastes may be rich in lignocellulosic compounds but remain largely underutilized, often contributing to waste management challenges in orchards and nurseries of mango plants. Biomass characteristics of mango seedlings and consequently the quality of potential bio-waste streams are strongly influenced by surrounding environment such as shading treatments. Mango plants grown under full sunlight accumulated greater stem and root dry biomass, potentially producing denser lignocellulosic materials with improved reinforcement properties for bio-composite applications. Conversely, moderate shading preserved fresh biomass but decreased structural dry matter, whereas heavy shading resulted in the least root and stem biomass with increased moisture levels. These results indicate that shading influences the physical and mechanical properties of mango bio-wastes; bio-wastes from shaded plants are better hydrated, less lignified, and therefore less

suitable for fibre extraction and processing. From an applied perspective, this study emphasises that mango bio-wastes are not a consistent resource and their makeup as well as appropriateness for composite applications vary with environmental conditions. Optimising light exposure in mango plants cultivation and orchard management could thus improve the yield and quality of lignocellulosic residues intended for bio-composite production. Integrating such environmental management with bio-waste utilisation strategies supports circular bioeconomy objectives, minimizing waste and generating value-added materials for sustainable industries.

Acknowledgements
The authors express their gratitude to the technical personnel from the Institute of Sustainable Agrotechnology (INSAT), Department of Agrotechnology of Faculty of Engineering & Mechanical Technology (FKTM), Universiti Malaysia Perlis (UniMAP) and Department of Agriculture Perlis State.

References

[1] S. Babu, S. S. Rathore, R. Singh, S. Kumar, V. K. Singh, S. Yadav, V. Yadav, R. Raj, D. Yadav, K. Shekhawat, Exploring agricultural waste biomass for energy, food and feed production and pollution mitigation: A review, Biores Tech 360 (2022) 127566. https://doi.org/10.1016/j.biortech.2022.127566

[2] De, S. James, B. Ji, J. Wasti, S. Zhang, S. Kore, S. Tekinalp, H. Li, Y. Ureña-Benavides, E. E. Vaidya, U. Biomass-derived composites for various applications, Advan Bioen 8 (2023) 145-196. https://doi.org/10.1016/bs.aibe.2023.01.001

[3] R. Roslim, A. A. Nordin, M. H. C. Mat, A. Zakaria, M. Jaafar, N. Evaluation of pruning waste of *Mangifera indica* var Harumanis cultivated in greenhouse. MATEC Web of Conferences, 150 (2018) 06022. https://doi.org/10.1051/matecconf/201815006022

[4] M. Patra, D. Sahu, Perspective Chapter: Environmental-Friendly Agro-Waste Management. In Solid Waste and Landfills Management-Recent Advances. Zailani, S., Sarvajayakesavalu, S. eds, IntechOpen (2022) 200. https://doi.org/10.5772/intechopen.107505

[5] L. Susmita Devi, A. Mukherjee, S. Kumar, Promising Agro-Wastes for Food Packaging. In Agro-Waste Derived Biopolymers and Biocomposites: Innovations and Sustainability in Food Packaging, Avik, M., Vimal, K., eds.; John Wiley & Sons, Inc. Beverly (2024) pp.1-31. https://doi.org/10.1002/9781394175161.ch1

[6] S. Afolalu, E. Salawu, T. Ogedengbe, O. Joseph, O. Okwilagwe, M. Emetere, O. Yusuf, A. Noiki, S. Akinlabi, Bio-agro waste valorization and its sustainability in the industry: A review. IOP Conf Series, Mat Sci Engi (2021) 012140.

https://doi.org/10.1088/1757-899X/1107/1/012140

[7] M. A. Ismail, Dubdub, I. Mousa, S. Albin, Z. A. A. Zaid, M. A. Alfaiad, Characterization, combustion behaviour, and kinetic and thermodynamic modelling of mango peel as a potential biomass feedstock, Polymers 17 (2025) 1799. https://doi.org/10.3390/polym17131799

[8] K. O. Iwuozor, V. E. Ojukwu, S. O. Eshiemogie, E. C. Emenike, A. O. Bajeh, J. O. Ighalo, A. G. Adeniyi, Plant biomass materials in composite application. In Plant Biomass Applications; Jawaid, M., Mohammed A.A., Khan A., eds.; Elsevier: Amsterdam, Netherlands, 2024 pp. 385-405. https://doi.org/10.1016/B978-0-443-15465-2.00010-0

[9] C. Santulli, Utilization of Renewable Biomass and Waste Materials for Production of Environmentally-Friendly, Bio-based Composites. In Eco-Friendly Adhesives for Wood and Natural Fiber Composites: Characterization, Fabrication and Applications; Jawaid, M., Khan,

T.A., Nasir, M., Asim, M. eds., Springer. Cham.: Springer Nature Switzerland, 2021 pp. 131-145. https://doi.org/10.1007/978-981-33-4749-6_7

[10] P. Deborah, V. Francesca, G. Giuseppe, Analysis of the environmental impact of a biomass plant for the production of bioenergy, Renew Sust Ener Rev 51 (2015) 634-647. https://doi.org/10.1016/j.rser.2015.06.048

[11] M. Kleyer, J. Trinogga, M. A. Cebrián-Piqueras, A. Trenkamp, C. Fløjgaard, R. Ejrnæs, T. J. Bouma, V. Minden, M. Maier, J. Mantilla-Contreras, Trait correlation network analysis identifies biomass allocation traits and stem specific length as hub traits in herbaceous perennial plants, J Ecol 107 (2019) 829-842. https://doi.org/10.1111/1365-2745.13066

[12] Q. Yin, T. Tian, X. Han, J. Xu, Y. Chai, J. Mo, M. Lei, L. Wang, M. Yue, The relationships between biomass allocation and plant functional trait, Ecol Indic 102 (2019) 302-308. https://doi.org/10.1016/j.ecolind.2019.02.047

[13] P. Balan, G. Priyadharshini, D. Divakaran, I. Suyambulingam, N. Sunesh, S. Rangappa, S. Siengchin, Microcrystalline cellulose extraction from comprehensive characterization of *Mangifera indica* leaf biowaste for high-performance bio-based polymer composites. J Poly Res 32 (2025), 23. https://doi.org/10.1007/s10965-024-04251-6

[14] L. M. Ana, S. Rogelio, S. Xose Carlos, M. Rosa Ana, Cell wall composition impacts structural characteristics of the stems and thereby the biomass yield, J Agric Fd Chem 70 (2022) 3136-3141. https://doi.org/10.1021/acs.jafc.1c06986

[15] V. Jeyabalaji, G. Kannan, P. Ganeshan, K. Raja, B. Nagaraja Ganesh, P. Raju, Extraction and characterization studies of cellulose derived from the roots of *Acalypha indica* L., J Nat 19 (2022) 4544-4556. https://doi.org/10.1080/15440478.2020.1867942

[16] A. J. Kings, I. Suyambulingam, S. Narayanaperumal, L. Miriam, M. Divakaran, D. Murali, A. S. S. Han, Exploring biomass derived microcrystalline cellulose from the waste aquatic plant *Pistia stratiotes*: A comprehensive characterization for polymer composite reinforcement, Inter J Biol Macromol, 300 (2025) 140217. https://doi.org/10.1016/j.ijbiomac.2025.140217

[17] D. Kouidri, M. Rokbi, Z. E. Rahmouni, Y. Kherbiche, S. Bouchareb, S. M. Rangappa, S. Siengchin, Investigation of mechanical and physico-chemical properties of new natural fiber extracted from *Bassia indica* plant for reinforcement of lightweight bio-composites, Heliyon 10 (2024) e35552. https://doi.org/10.1016/j.heliyon.2024.e35552

[18] F. G. Fonseca, A. Funke, A. Niebel, A. P. S. Dias, N. Dahmen, Moisture content as a design and operational parameter for fast pyrolysis, J Anal App Pyrol 139 (2019) 73-86.

https://doi.org/10.1016/j.jaap.2019.01.012

[19] W. A. Smith, L. M. Wendt, I. J. Bonner, J. A. Murphy, Effects of storage moisture content on corn stover biomass stability, composition, and conversion efficacy, Fron Bioeng Biotech 8 (2020) 716. https://doi.org/10.3389/fbioe.2020.00716

[20] S. Hussain, N. Iqbal, T. Rahman, T. Liu, M. Brestic, M. E. Safdar, M. A. Asghar, M. U. Farooq, I. Shafiq, A. Ali, Shade effect on carbohydrates dynamics and stem strength of soybean genotypes, Envin Exp Bot 162 (2019) 374-382. https://doi.org/10.1016/j.envexpbot.2019.03.011

[21] G. Resente, A. Crivellaro, Environmental impacts on plant cell wall lignification, J Biores Bioprod 10 (2025) 4-6. https://doi.org/10.1016/j.jobab.2024.11.001

[22] L. Wu, W. Zhang, Y. Ding, J. Zhang, E. D. Cambula, F. Weng, Z. Liu, C. Ding, S. Tang L. Chen, Shading contributes to the reduction of stem mechanical strength by decreasing cell wall synthesis in japonica rice (*Oryza sativa* L.), Front Pla Sc 8 (2017) 881.

https://doi.org/10.3389/fpls.2017.00881

[23] P. Pal, A. K. Singh, R. K. Srivastava, S. S. Rathore, U. K. Sahoo, S. Subudhi, P. K. Sarangi, P. Prus, Circular bioeconomy in action: Transforming food wastes into renewable food resources, Foods 13 (2024) 3007. https://doi.org/10.3390/foods13183007

Materials Research Proceedings 74 (2026) 117-124 https://doi.org/10.21741/9781644904473-15

Influence of Drying Heat Treatment on Physical and Mechanical Properties of Mycelium Based Composite

Zatty MINAI[1,a], M.K.R HASHIM[1,b *], Noorulnajwa Diyana YAACOB[2,c], M.N.A.UDA[1,d], Z.A. ARSAT[1,e], M. Firdaus A. MUTTALIB[1,f], F. ABDULLAH[1,g], S.M. SHAHRIL[1,h], Nur Khuzaima AZMAN[3,i] and M.A.M. AKHIR[2,j]

[1]Faculty of Mechanical Engineering & Technology (FKTM), Universiti Malaysia Perlis (UniMAP), 02600 Arau, Perlis, Malaysia

[2]Faculty of Chemical Engineering & Technology (FKTK), Universiti Malaysia Perlis (UniMAP), 02600 Arau, Perlis, Malaysia

[3]Department of Mechanical and Manufacturing Technology, Kolej Vokasional Arau, 02600, Arau, Perlis, Malaysia

[a]zatty@studentmail.unimap.edu.my, [b]khairulrabani@unimap.edu.my, [c]noorulnajwa@unimap.edu.my, [d]nuraiman@unimap.edu.my, [e]zainalabidin@unimap.edu.my, [f]firdausmuttalib@unimap.edu.my, [g]fadhilnor@unimap.edu.my, [h]mohdshahril@unimap.edu.my, [i]g-26562328@moe-dl.edu.my, [j]maisaraazad@unimap.edu.my

Keywords: Mycelium-Based Composites, Drying Temperature, Physical Properties, Compressive Strength, Morphological Analysis

Abstract. Mycelium-based composites (MBCs) were studied in context of high carbon materials as a sustainable solution and dried at 70°C, 75°C and 80°C and examined their physical, mechanical and morphological properties. One-way ANOVA confirmed that drying temperature was a statistically significant parameter, or critical factor, in the performance. Dried at 75°C, the specimens were found to have the highest density (0.3508 g/cm³), shrinkage of 24.9% and ductile failure under compression, which represented optimal structural integrity for lightweight, non-load-bearing use. The samples obtained at 70°C showed the maximum compressive strength with brittle failure and density of 0.3486g/cm³ with shrinkage of 20.22%. Morphological analysis by the SEM showed good hyphal bonding in both 70°C and 75°C groups. On the other hand, the 80°C samples showed bad bonding, lowest compressive strength, 27.8% shrinkage and porous internal structure because of over-drying. The drying condition of 75°C is the best one for sustainable building materials.

Introduction

The construction sector accounts for about 40% of carbon emissions and uses 50% of raw materials [1]. In addition, the extraction of aggregates is responsible for habitat destruction and soil erosion [3][4] and cement production contributes to 8% of global CO_2 emissions [2]. Such environmental challenges call for sustainable solutions that minimize environmental impacts while ensuring structural stability.

Innovative eco-friendly materials made from mycological mycelium growing on organic waste materials such as agricultural byproducts or sawdust became known as mycelium-based composites (MBCs) [5]. MBCs can be synthesized with significantly less energy than conventional materials and can also make use of the by-products of agriculture [6]. Previous studies have shown that MBCs have excellent thermal and acoustic insulation properties, which make them appropriate to use in non-load-bearing applications like wall panels and packaging [7]. They are naturally biodegradable, thus contributing to the circular economy by minimizing waste in landfills.

Content from this work may be used under the terms of the Creative Commons Attribution 3.0 license. Any further distribution of this work must maintain attribution to the author(s) and the title of the work, journal citation and DOI. Published under license by Materials Research Forum LLC.

Several factors affect the MBC properties, such as the selection of fungal strains, substrate composition, incubation conditions and post-growth treatments. The strength and durability of composites depend on the density of the fungal mycelial network produced by different strains of fungi [8]. The nutrient composition of the substrate affects mycelial growth, and lignin-rich material has a positive effect on the rigidity of the structure [9]. The post growth drying temperature is a critical factor that influences the performance of the material: if this is too high, moisture will evaporate very quickly, resulting in cracking and reduced compressive strength; if it is too low, microbial degradation will occur [10]. Thus, optimization of drying conditions is imperative to obtain the desired properties of the material.

Drying temperature is particularly affecting the integrity and dimensional stability of MBC. Studies have shown that a temperature of 60-80°C results in an even removal of moisture without structural distortion, which will maintain the bonding of mycelium [11]. Thermal degradation and weakening of the matrix occur at temperatures above 100°C. Comparative studies led to the selection of the optimum temperature of 70°C for compressive strength and shrinkage [12] and to the observation that controlled drying promotes mycelium–matrix interfacial bonding when analysed using SEM. These results highlight the importance of accurate temperature control for reliability in constructions.

The drying temperature examined at 70°C, 75°C and 80°C, respectively, while analysis includes drying shrinkage, moisture content, apparent density, microstructural features through scanning electron microscopy and compressive strength which are determined to find the best drying method to increase the quality of the produced composite.

Methods

The mushroom blocks were purchased as mature white oyster mycelium (Pleurotus ostreatus) blocks that were still in the pre-colonised stage, from Beseri Agrofarms Resources, Perlis, Malaysia. It was grown on a growth substrate consisting of rubberwood sawdust (90%), rice bran (9%) and calcium carbonate (1%) to which the colonised to 70–80% (Fig. 1). The colonized substrate was manually broken up and tightly pressed into sterile plastic trays (29.21 mm × 27.49 mm × 25.37 mm). The filled moulds were then covered with a perforated plastic film allowing gas exchange and placed in a temperature-controlled, dark, and sterilized chamber to allow complete colonization of the substrate during a four-week period. After incubation, they were subjected to standardized oven-drying at 70°C, 75°C and 80°C until weight was constant within 18 hours, which is sufficient to remove moisture from the specimen in a uniform way. All of physical property measurements such as density and shrinkage were made after the specimens were attained at constant weight, which is the weight loss saturation stage as seen in Figure 2. The density was determined by an Electronic Densimeter MD 300S according to ASTM D2395 [13]. The dimensional changes were used to determine the volume shrinkage. Morphological evaluation was performed using a Hitachi TM3000 Tabletop Microscope to create images of the adhesion zones between mycelium and substrate. Five specimens were tested for each drying temperature, and average values were used for analysis based on the compressive strength measurement in accordance with ASTM D3501 until the fracture at a cross-head speed of 2mm/min using the Universal Testing Machine (50 kN, AGX-V2, Shimadzu). The compression test was performed until a compression of 40% (40% strain) and the maximum stress recorded within 40% compression limit was used to determine the compressive strength, which was then analysed using One-way ANOVA to study the effect of drying temperature on the properties of the composites [14].

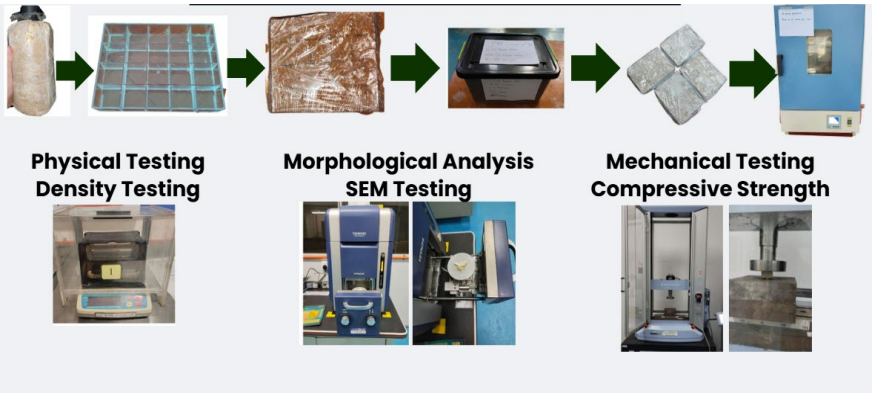


Fig. 1. The process involved in the Mycelium-Based Composites (MBCs) preparation and testing.

Results

Moisture Content

Moisture content of the mycelium-based composite (MBC) samples was determined using the gravimetric mass change method before and after a standard drying process and are presented in Table 1. The moisture content was dried according to the protocol at 70 °C for 18 hours, to obtain a stabilized moisture content of 53.42%. As the moisture content decreased it was then dried further at 75 °C for an additional 11 hours resulting in the moisture content of 47.22%. Despite the higher temperature of drying, the moisture content measured was 52.13%, which was higher than that measured at the lower temperature of 75°C (47.22%). This suggests that moisture removal was not entirely temperature dependent and could have been affected by the variability of samples and moisture distribution inside the samples. The results clearly show that the drying temperature and time are inversely related; a higher temperature will lead to a higher drying rate, but the resultant calculated moisture contents do not consistently decrease as drying temperature increases. The differences in final moisture content may have a different impact on the mechanical properties and microbial stability of MBCs during further processing and end-use applications.

Table 1. The moisture content for three different temperatures.

Temperature (°C)	Initial Weight (g)	Dry Weight (g)	Moisture Content (%)
70	307	143	53.42
75	288	152	47.22
80	282	135	52.13

Drying Test

All the samples showed maximum weight loss in the first 6 hours, indicating that moisture is being evaporated from the surface and inside the samples at a very high rate. Dried at 80°C specimens had most compressed drying time (45% moisture loss in 6–7 h), but there were concerns in regard to the structural collapse due to uneven shrinkage and formation of micro cracks. The mass loss profile of samples processed at 75°C was stabilized and resulted in 44% mass loss after 8 hours, thereby offering even temperature distribution and retaining the material architecture. In contrast, 70°C samples had significantly lower rates of moisture removal, needing 16 hours to obtain similar moisture reduction and leaving higher interstitial moisture at the end of the drying cycle. This remaining water can affect adhesion and stability of composites. The 75°C treatment was found to be providing the optimum drying balance of efficient moisture removal with good structural coherence, corresponding to good density and compressive strength performance.

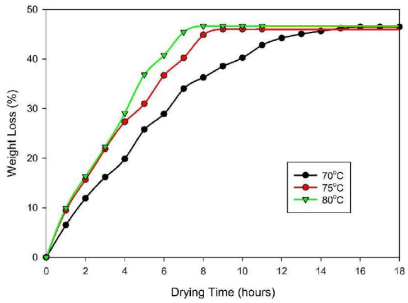


Fig. 2. Weight loss (%) - drying time (hours) curves.

Physical Testing

Mycelium-based composites were characterized for physical behaviour as density and shrinkage (Fig. 3). The highest density average value (0.3508 g/cm³) was obtained for the specimens dried at 75°C followed by the specimens dried at 80°C (0.3506 g/cm³) and the specimens dried at 70°C (0.3486 g/cm³). The coalescence and structural homogeneity were better achieved at the intermediate temperature of 75°C. The sorbed moisture content was allowed to remain at the lower temperature (70°C) and the moisture trapped as vapour as the substrate collapsed forming interstitial pores and decreasing the density. On the other hand, 80°C drying caused high heat flux and rapid water vapour movement, and micro-fractures were caused by thermal gradients and elastic modulus mismatch between mycelial filaments, which are responsible for the slight decrease in density at 80°C. Shrinkage measurements showed temperature dependent trends. The specimens heated at 80°C showed the highest average shrinkage with 75°C specimens showing more shrinkage than 70°C specimens. When temperatures were high, the moisture was quickly vaporized, and tensile responses were reduced, resulting in significant dimensional contraction. The limited shrinkage at 70°C implies diffusion limited removal of moisture, which restricted irreversible deformations and crack propagation. The one-way ANOVA data showed that the drying temperature has a significant effect on the properties of the mycelium-based composites. Here the p-value, 3.05E-14 (F-statistic = 668.71, critical value = 3.11) is well below the 0.05 value, establishing that the density differences are statistically significant as a function of temperature. This supports earlier findings that higher temperatures lead to higher internal compactness. Likewise, the shrinkage analysis (Table 3) gave an F value of 77.77, which is superior to the critical value of 3.11 at the 0.05 significance level, indicating that there was a significant difference in shrinkage between the temperature regimes. The data suggest that a higher drying temperature results in faster removal of moisture, thereby triggering a speedy shrinkage due to inner structural breakdown. These statistical results agree with the finding that the drying temperature plays a critical role in the density and dimensional stability of MBCs.

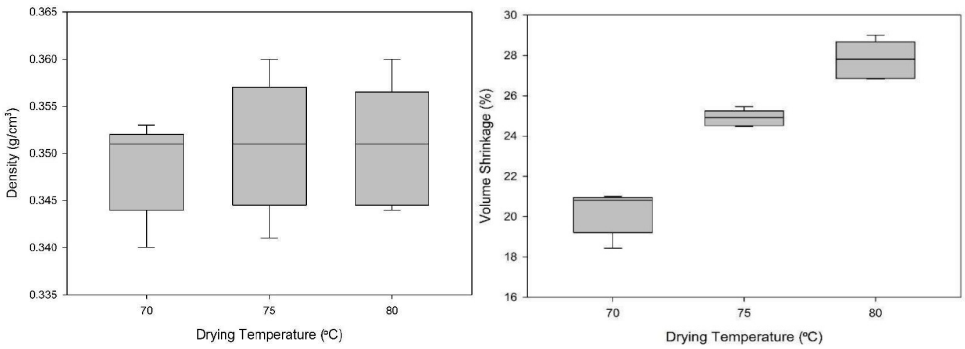


Fig. 3. The boxplot of the physical properties of (a) density, (b) shrinkage.

Table 2. One-Way ANOVA of density testing.

Source of Variation	SS	df	MS	F	P-value	F crit
Between Groups	13931.56	5	2786.311	668.7103	3.05E-14	3.105875
Within Groups	50.00033	12	4.166694			
Total	13981.56	17				

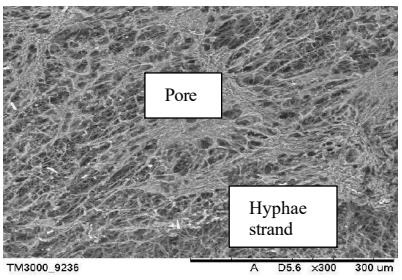
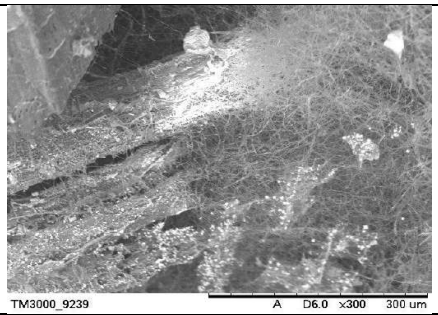
Table 3. One-Way ANOVA of shrinkage testing.

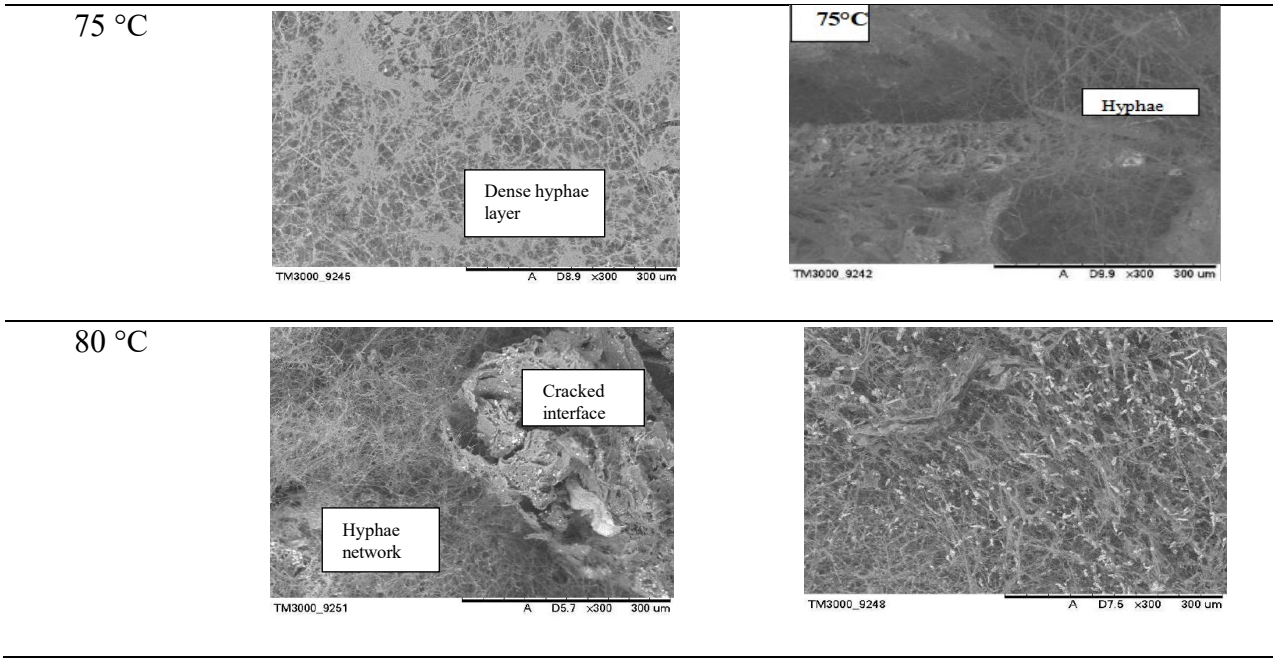
Source of Variation	SS	df	MS	F	P-value	F crit
Between Groups	6433.002	5	1286.6	77.76873	1.02E-08	3.105875
Within Groups	198.5271	12	16.54393			
Total	6631.529	17				

Morphological Analysis

The internal structure and bonding on the surface of the MBCs were investigated through scanning electron microscopy (SEM) after drying them at 70°C, 75°C and 80°C (Table 4). In this study, drying temperature directly modified the hyphal architecture and interfacial bonding with the substrate particles, as shown in the micrographs. The 70°C samples showed the particles of the rubberwood to have large interparticle spaces and lose packing, which means that moisture was still present in the samples. This prevented the mycelial colonization and adherence to the substrates, resulting in a porous lightweight structure that was susceptible to crushing under load, a similar result to that obtained by Yang et al. [16]. In contrast, at 75°C, the hyphal networks were tightly interwoven, and the hyphal surfaces were smooth and completely covering the sawdust particles, leaving very little space between the hyphae and the particles. This resulted in good bonding and mycelial growth without any degradation of the substrate and led to better mechanical performance and ductile failure, which was associated with optimal moisture removal. The 80°C micrographs showed broken filaments, cracks on the surfaces and lack of adhesion between mycelium and the substrate. Rapid drying caused uneven shrinkage, possibly causing stress concentrations, which disrupted the hyphal structure. Despite similar densities, internal cohesion was not as good, which was reflected in poor compressive strength.

Table 4. The micrographs of the three different temperatures (70°C, 75°C, and 80°C) at external surface and internal surface of the samples.

Temperature (°C)	External Surface	Internal Surface
70 °C		



Mechanical Properties

Mechanical properties of the composite materials were assessed by compressive strength testing to determine whether they would have load-bearing integrity when subjected to uniaxial loading. The specimens that were dried at 70°C had the highest peak stress values, suggesting that this temperature yielded the best microstructural cohesion and stress transfer efficiency. The marked post-peak stress decrease, however, was a sign of catastrophic low-energy brittle fracture, a very undesirable failure behaviour for an engineering application that needs to show warning behaviour before failure. Samples heated at 75°C showed a slight decrease in maximum stress but a longer softened stress curve indicating that they have more capacity for permanent strain prior to failure. This improved energy dissipation is characteristic of improved toughness which is important in the field of intermittent loading or fatigue. The 80°C specimens had very low peak stress and earliest failure, resulting in being mechanically weakest. The deteriorated behaviour has been attributed to excessive drying-induced microstructural dehydration and lack of bonding between the hyphae, which is supported by SEM micrographs showing that the interior of the hyphae is cracked and the hyphae are broken. The 75°C treatment gave optimum combination of strength and damage mitigating ductility.

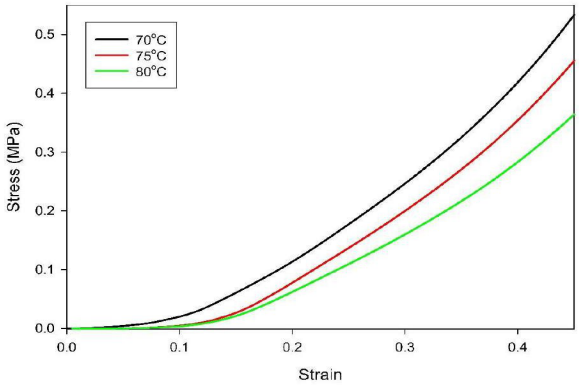


Fig. 4. Graph of the stress (MPa)- strain (%) for three different temperatures.

Conclusion

The properties of rubberwood sawdust and Pleurotus ostreatus mycelium-based composites were greatly influenced by drying temperature. The 70 °C samples had poor density and adhesion due to incomplete mycelial maturation, and the 80 °C samples had warped and microcracks due to too much moisture evaporating. The 75℃ intermediate treatments yielded the best composites, as the density was balanced and the hyphal networks were well integrated while providing a good toughness. They showed ductile behaviour prior to fracture, making them suitable for use in applications requiring flexibility and impact absorption. Results validate mycelium-based composites as an eco-efficient material for lightweight structures with optimized drying process. This work should be expanded to other industrial applications with refinement strategies to be investigated in the future.

Acknowledgement

The author would like to acknowledge the support from the Fundamental Research Grant Scheme (FRGS) under a grant number of FRGS/1/2025/TK10/UNIMAP/02/1 from the Ministry of Higher Education Malaysia.

References

[1] A. Senanu, K. Kukah, A. Victor, K. Blay, A. Opoku, International Journal of Real Estate Studies INTREST Strategies to Reduce the Impact of Resource Consumption in the Ghanaian Construction Industry (2022)

[2] Z.H. Wang, A Survey of Factors and Life Cycle Assessment in Selection of Green Construction Materials, Journal of Computational Intelligence in Materials Science 1 (2023) 23–33. https://doi.org/10.53759/832X/JCIMS202301003

[3] S. Damseth, K. Thakur, R. Kumar, S. Kumar, D. Mahajan, H. Kumari, D. Sharma, A.K. Sharma, Assessing the impacts of river bed mining on aquatic ecosystems: A critical review of effects on water quality and biodiversity, HydroResearch 7 (2024) 122–130. https://doi.org/10.1016/j.hydres.2024.01.004

[4] M.K.R. Hashim, M.S. Abdul Majid, M.R. Mohd Jamir, F.H. Kasim, H.A. Alshahrani, M.A.M. Deros, D. Hui, Effects of Ply Orientations and Stacking Sequences on Impact Response of Pineapple Leaf Fibre (PALF)/Carbon Hybrid Laminate Composites, Materials (Basel) 15 (2022) 6121. https://doi.org/10.3390/ma15176121

[5] K.K. Alaneme, J.U. Anaele, T.M. Oke, S.A. Kareem, M. Adediran, O.A. Ajibuwa, Y.O. Anabaranze, Mycelium based composites: A review of their bio-fabrication procedures, material properties and potential for green building and construction applications, Alexandria Engineering Journal 83 (2023) 234–250. https://doi.org/10.1016/j.aej.2023.10.012

[6] M.S. Soffian, F.Z. Abdul Halim, F. Aziz, M.A. Rahman, M.A. Mohamed Amin, D.N. Awang Chee, Carbon-based material derived from biomass waste for wastewater treatment, Environ. Adv., 9 (2022) 100259. https://doi.org/10.1016/j.envadv.2022.100259

[7] R. Volk, M. Schröter, N. Saeidi, S. Steffl, A. Javadian, D.E. Hebel, F. Schultmann, Life cycle assessment of mycelium-based composite materials, Resour. Conserv. Recycl. 205 (2024) 107579. https://doi.org/10.1016/j.resconrec.2024.107579

[8] C. Kohphaisansombat, Y. Jongpipitaporn, P. Laoratanakul, S. Tantipaibulvut, J. Euanorasetr, N. Rungjindamai, C. Chuaseeharonnachai, P. Kwantong, S. Somrithipol, N. Boonyuen, Fabrication of mycelium (oyster mushroom)-based composites derived from spent coffee

grounds with pineapple fibre reinforcement, Mycology 15 (2024) 665–682. https://doi.org/10.1080/21501203.2023.2273355

[9] M.E. Voutetaki and A.C. Mpalaskas, Natural Fiber-Reinforced Mycelium Composite for Innovative and Sustainable Construction Materials, Fibers 12 (2024) 57. https://doi.org/10.3390/fib12070057

[10] S. Sozcu, J. Frajova, J. Wiener, M. Venkataraman, B. Tomkova, J. Militky, Effect of Drying Methods on the Thermal and Mechanical Behavior of Bacterial Cellulose Aerogel., Gels (Basel, Switzerland) 10 (2024) 474. https://doi.org/10.3390/gels10070474

[11] A. Farrahnoor, A.D.N. Hishamuddini, H. Yusoff, M.H. Koay, N.C. Maideen, N.A.M. Fohimi, T.Z. Boey, Influence of Drying Temperature in the Oven on Physical, Morphology and Mechanical Properties of Mycelium Composite, Pertanika Journal of Science and Technology 33 (2025) 219. https://doi.org/10.47836/pjst.33.1.10

[12] W. Aiduang, J. Kumla, S. Srinuanpan, W. Thamjaree, S. Lumyong, N. Suwannarach, Mechanical, Physical, and Chemical Properties of Mycelium-Based Composites Produced from Various Lignocellulosic Residues and Fungal Species, J. fungi (Basel, Switzerland), 8 (2022) 1125. https://doi.org/10.3390/jof8111125

[13] Standard Test Method for iTeh Standards iTeh Standards, ASTM Int., vol. 1, no. October, 2022, pp. 22–25. https://doi.org/10.1520/D2395-17R22.2

[14] E. Elsacker, S. Vandelook, J. Brancart, E. Peeters, L. De Laet, Mechanical, physical and chemical characterisation of mycelium-based composites with different types of lignocellulosic substrates, PLoS One 14 (2019) 1–20. https://doi.org/10.1371/journal.pone.0213954

[15] I.S. Santos, B.L. Nascimento, R.H. Marino, E.M. Sussuchi, M.P. Matos, S. Griza, Influence of drying heat treatments on the mechanical behavior and physico-chemical properties of mycelial biocomposite, Compos. Part B Eng. 217 (2021) 108870. https://doi.org/10.1016/j.compositesb.2021.108870

[16] L. Yang, D. Park, Z. Qin, Material Function of Mycelium-Based Bio-Composite: A Review, Front. Mater. 8 (2021) 737377. https://doi.org/10.3389/fmats.2021.737377.

Materials Research Proceedings 74 (2026) 125-132 https://doi.org/10.21741/9781644904473-16

Effects of Stacking Sequence on Mode II Delamination in Hybrid Carbon/Flax Reinforced Epoxy Composites

W.K. SEE[1,a], M. JOHAR[2,b], K.J. WONG[3,c], W.W.F. CHONG[1,4,d] and A.B. CHAI[3,e *]

[1]Faculty of Mechanical Engineering, Universiti Teknologi Malaysia, 81310 UTM Skudai, Johor, Malaysia

[2]Quality Engineering Research Cluster (QEREC), Quality Engineering Section, Malaysian Institute of Industrial Technology, Universiti Kuala Lumpur, 81750 Masai, Malaysia

[3]Department of Mechanical, Materials and Manufacturing Engineering, Faculty of Science and Engineering, University of Nottingham Malaysia, Jalan Broga, 43500 Semenyih, Selangor, Malaysia

[4]Institute for Sustainable Transport (IST), Universiti Teknologi Malaysia, 81310 Johor Bahru, Malaysia

[a]seeweekeong96@gmail.com, [b]mahzan@unikl.edu.my, [c]KingJye.Wong@nottingham.edu.my, [d]william@utm.my, [e]AiBao.Chai@nottingham.edu.my

Keywords: Hybrid Composites, Carbon/Flax Epoxy, Stacking Sequence, Mode II Fracture, Delamination

Abstract. With increasing environmental awareness, natural fibres such as flax are gaining attention in polymer composite applications due to their sustainability. This study investigates the Mode II delamination behaviour of hybrid carbon/flax epoxy composites with three stacking configurations: carbon–carbon (C//C), flax–flax (F//F), and carbon–flax (C//F). Specimens were fabricated using a hand lay-up technique followed by vacuum-bagging and tested using the End Notched Flexure (ENF) method. The measured Mode II fracture toughness values (G_{IIC}) were 1416.10 ± 64.52 N/m for C//C, 1396.06 ± 95.42 N/m for F//F, and 2892.69 ± 216.35 N/m for C//F. The C//F configuration exhibited significantly higher toughness — approximately double that of the other two — suggesting enhanced resistance to delamination due to increased interfacial friction between dissimilar fibre types. These findings demonstrate that hybridisation, particularly with carbon/flax interfaces, can effectively improve the interlaminar fracture toughness of composite laminates. The results provide valuable insights for the design of sustainable, high-performance composite structures, especially in applications where delamination resistance is critical.

Introduction

Over the past few decades, the use of natural fibres in polymer composites has gained increasing popularity due to their renewable, recyclable, and biodegradable nature [1-3]. Among these, flax is considered one of the most promising candidates for mechanical performance [4]. However, delamination remains a critical failure mode in composite laminates, primarily due to low interlaminar strength [5]. It can be triggered by manufacturing defects or low-velocity impacts [5, 6], and is often difficult to detect [5]. Consequently, delamination is regarded as one of the most detrimental failure mechanisms in composites [7].

Several studies have examined the interlaminar fracture behaviour of flax fibre-reinforced polymers. For instance, Mode I fracture toughness of both unidirectional and woven flax/epoxy composites has been reported to exceed that of glass/epoxy composites [8, 9]. Bensadoun et al. [10] compared Mode I and II delamination across various fibre architectures, noting that plain

Content from this work may be used under the terms of the Creative Commons Attribution 3.0 license. Any further distribution of this work must maintain attribution to the author(s) and the title of the work, journal citation and DOI. Published under license by Materials Research Forum LLC.

weave fabrics exhibited the lowest Mode I initiation toughness but the highest Mode II toughness. Improvements in G_{IIC} have also been achieved through techniques such as carbon nanotube buckypaper interleaving [11] and through-thickness stitching [9, 12]. Rajendran et al. [13] investigated Mode I, Mode II and Mixed-mode I/II delamination of plain weave flax fabric reinforced epoxy composites. Through fitting the fracture toughness values using Benzeggagh-Kenane (BK) criterion [14], their results provide useful information on the variation of the interlaminar fracture toughness with respect to mode ratio as well. Additionally, scanning electron micrographs suggested that the major fracture mechanism in all loading modes was fibre/matrix debonding.

The hydrophilic nature of natural fibres tends to weaken the fibre-matrix interface, adversely affecting the composite's mechanical properties [15]. Hybridisation — combining natural and synthetic fibres — offers a solution by leveraging the mechanical strength of synthetic fibres and the sustainability of natural fibres. Carbon fibres, known for superior mechanical properties, are often hybridised with flax to achieve a balance between performance and sustainability. For example, it has been reported that flax/polypropylene composites outperform glass/polypropylene in specific stiffness, but they still fall short compared to carbon/polypropylene [1]. Additionally, Johar et al. [16] has reported that hybridisation of carbon and flax fibres was able to retain the specific tensile modulus and elongation at break of the composites before and after moisture attack.

This study aims to evaluate the influence of stacking sequence on Mode II delamination behaviour in hybrid carbon/flax (C/F) epoxy composites. Three configurations — C//C, F//F, and C//F — were fabricated and tested using the ENF method. Fracture toughness values were calculated and compared with existing literature.

Materials and Methods

Materials and Specimen Preparation

The hybrid composite materials used in this study consist of 200 gsm twill weave 2/2 flax fabric (average ply thickness: 0.5 mm) and 200 gsm plain weave 2/2 carbon fabric (average ply thickness: 0.25 mm). Each hybrid laminate was fabricated using 8 plies of flax and 8 plies of carbon fabric, cut to dimensions of 167 × 125 mm².

The fabrics were weighed using an electronic balance, and the epoxy resin and hardener were mixed in a 10:6 weight ratio. The mixture was stirred gently for approximately 5 minutes before being applied to the fabric layers according to the stacking sequences shown in Table 1. A 15 µm thick Teflon film, 67 mm in length, was placed between the 8th and 9th plies to initiate a pre-crack.

Table 1. Stacking sequences for hybrid carbon/flax composites with different mid-interface configurations.

Mid-Interface	Stacking Sequence
C//C	[F/C_2/F/C/F_2/C//C/F_2/C/F/C_2/F]
F//F	[C/F_2/C/F/C_2/F//F/C_2/F/C/F_2/C]
C//F	[F/C_2/F/C/F_2/C//F/C_2/F/C/F_2/C]

Note: "C" represents carbon fibre, "F" refers to flax fibre, "//" indicates Teflon location.

To cure the laminates, the vacuum-bagging method was employed. Sealant tape was used to enclose the laminate edges, preventing air leakage. A vacuum pump was then used to evacuate air from the membrane, creating a pressure differential that applied uniform clamping force across the laminate. The pump was operated for at least four hours, after which the laminates were left to cure in the mould for 24 hours. Once cured, the bleeder and vacuum bagging materials were carefully removed to avoid surface damage.

After a full cure period of ten days, each laminate was cut into five specimens measuring 150 mm × 20 mm using a precision cutting blade. Width and thickness were measured at three points

using a Vernier calliper. To facilitate crack observation during testing, the specimens were coated with white correction fluid.

Mode II Interlaminar Fracture Test

The Mode II fracture tests were conducted under quasi-static condition using the three-point End Notched Flexure (3ENF) method. All tests were performed on a SHIMADZU Universal Testing Machine equipped with a 5 kN load cell. Fig. 1 illustrates the schematic setup.

Each specimen was tested with an initial crack length of 30 mm, and the span length was set to 100 mm. Five replicates were tested for each stacking configuration to determine the average Mode II fracture toughness (G_{IIC}). Additionally, specimens with initial crack lengths of 20 mm, 25 mm, 35 mm, and 40 mm were tested to generate compliance plots, which were used to calculate G_{IIC} values. All tests were conducted at a crosshead speed of 1 mm/min under ambient conditions.

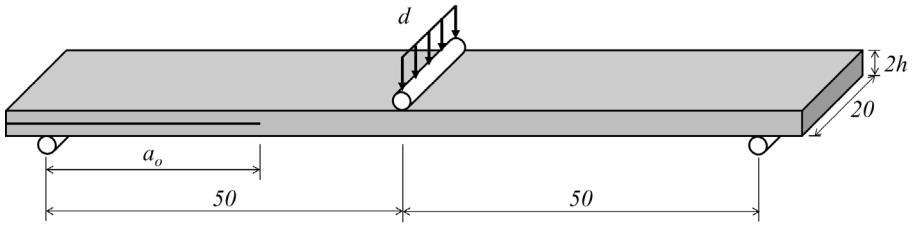


Fig. 1. Schematic diagram of the three-point End Notched Flexure (ENF) test setup. All dimensions are in mm.

Scanning Electron Micrography

To examine the fracture surfaces, delaminated specimens were sputter-coated with gold using a Bio-Rad Polaron Division coater. Scanning electron micrographs were then captured using a Philips XL40 microscope to assess fibre/matrix interfacial characteristics.

Data Reduction Scheme

The Mode II interlaminar fracture toughness was calculated using the Irwin-Kies equation [17]:

$$G_{IIC} = \frac{P_C^2}{2B}\left(\frac{dC}{da}\right) \quad \text{Eq. 1}$$

where:

- G_{IIC} is the Mode II fracture toughness,
- P_C is the peak load from the force-displacement curve
- B is the specimen width,
- C is the compliance, and
- a is the crack length.

The compliance C was modelled using a third-order polynomial fit:

$$C = C_2 a^3 + C_1 \quad \text{Eq. 2}$$

where:

- C_1 is the y-intercept,
- C_2 is the slope of the compliance vs. a^3 plot.

Substituting and differentiating the compliance equation yields:

$$G_{IIC} = \frac{P_C^2}{2B} \cdot 3C_2 a^2 \quad \text{Eq. 3}$$

This formulation allows for accurate determination of fracture toughness based on experimental data and fitted compliance curves.

Result and Discussion

Force Displacement Curves

Fig. 2 presents the experimental force–displacement curves for the hybrid flax/carbon epoxy composites under Mode II loading. The curves demonstrate good repeatability across all ENF tests. Initially, each curve exhibits a linear increase, followed by a nonlinear behaviour in force until reaching a peak load, after which a drop occurs, indicating the onset of crack propagation. This drop in load corresponds to the sliding of fibre layers at the mid-interface, which initiates crack growth. Notably, the C//F configuration exhibits the largest peak force, suggesting enhanced energy absorption and resistance to crack propagation. This behaviour suggests increased interfacial friction and mechanical interlocking between dissimilar fibres, which could contribute to higher energy release rates. Therefore, Fig. 2 demonstrates that hybridisation significantly influences crack propagation behaviour and energy dissipation mechanisms. The peak load and compliance values extracted from these curves are used to calculate the fracture toughness.

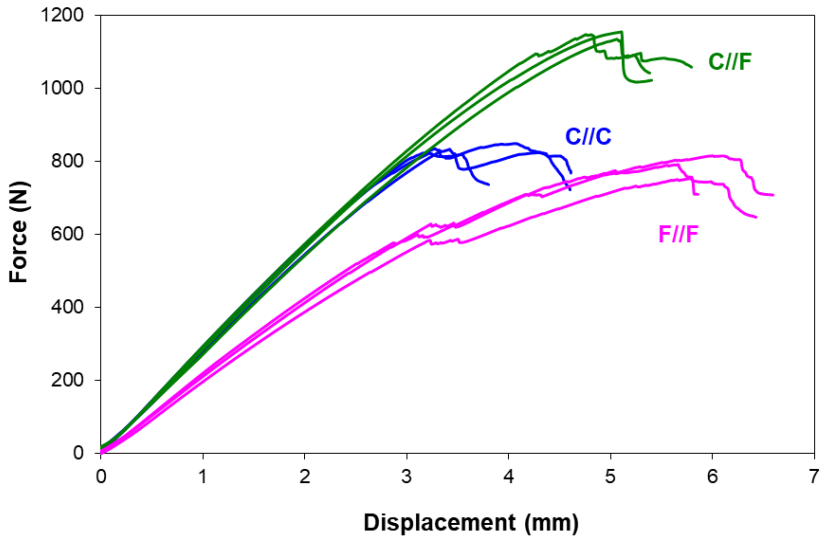


Fig. 2. Force–displacement curves for hybrid composites with mid-interface configurations: carbon–carbon (C//C), flax–flax (F//F), and carbon–flax (C//F).

Compliance Plots

Fig. 3 illustrates the compliance as a function of the cube of crack length (a_o^3) for the three stacking configurations: C//C, F//F, and C//F. The plots were generated using data from specimens with varying initial crack lengths. Each plot of C vs. a^3 was fitted with a linear line, yielding high correlation coefficients (R^2 close to unity), indicating good fit quality. The best-fit C_1 and C_2 values are as follows:

- **C//C interface**: $C_2 = 3.0897\times10^{-8}$ N·mm², $C_1 = 2.5988\times10^{-3}$ mm/N
- **F//F interface**: $C_2 = 3.2808\times10^{-8}$ N·mm², $C_1 = 4.1853\times10^{-3}$ mm/N
- **C//F interface**: $C_2 = 3.3207\times10^{-8}$ N·mm², $C_1 = 2.6073\times10^{-3}$ mm/N

It can be observed that C//C and C//F exhibit similar compliance values, suggesting comparable slopes in the force-displacement curves, as shown in Fig. 2. This indicates that both configurations possess similar elastic properties. In contrast, F//F displays higher compliance values,

corresponding to a lower force-displacement slope. Nevertheless, it is important to note that the slopes of all C vs. a^3 curves are similar, indicating a consistent trend in compliance with respect to crack length.

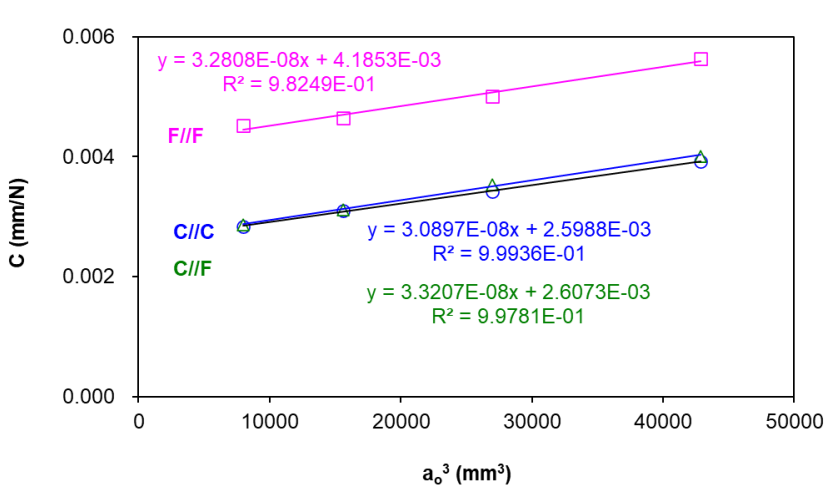


Fig. 3. Compliance plots for hybrid carbon/flax epoxy composites under Mode II loading: C//C, F//F, and C//F mid-interface configurations.

Mode II Fracture Toughness

Fig. 4 summarises the average G_{IIC} values for the three hybrid configurations:

- C//C: 1416.10±64.52 N/m
- F//F: 1396.06±95.42 N/m
- C//F: 2892.69±216.35 N/m

All test results showed good consistency, with coefficients of variation below 8% (values in the bracket in Fig. 4), confirming the reliability of the experimental procedure. The results show that the C//C and F//F interfaces exhibit comparable G_{IIC} values, indicating similar resistance to crack propagation for homogeneous interfaces. These values fall within the range reported in literature for woven carbon/epoxy [18-20] and flax/epoxy composites (Table 2).

In contrast, the C//F configuration demonstrates a significantly higher G_{IIC}, approximately twice that of the other two configurations. This substantial increase indicates superior resistance to delamination, which can be attributed to enhanced energy dissipation mechanisms at the heterogeneous interface. The mismatch in mechanical properties between carbon and flax fibres promotes additional interfacial friction which contribute to increased energy absorption during crack propagation. Similar observations have been reported in hybrid composites involving carbon and Dyneema fibres [21].

These findings suggest that hybrid interfaces play a critical role in improving fracture toughness. The results presented in Fig. 4 clearly demonstrate that strategic stacking sequence design can effectively enhance delamination resistance by modifying the underlying crack propagation and energy release mechanisms.

Materials Research Proceedings 74 (2026) 125-132 https://doi.org/10.21741/9781644904473-16

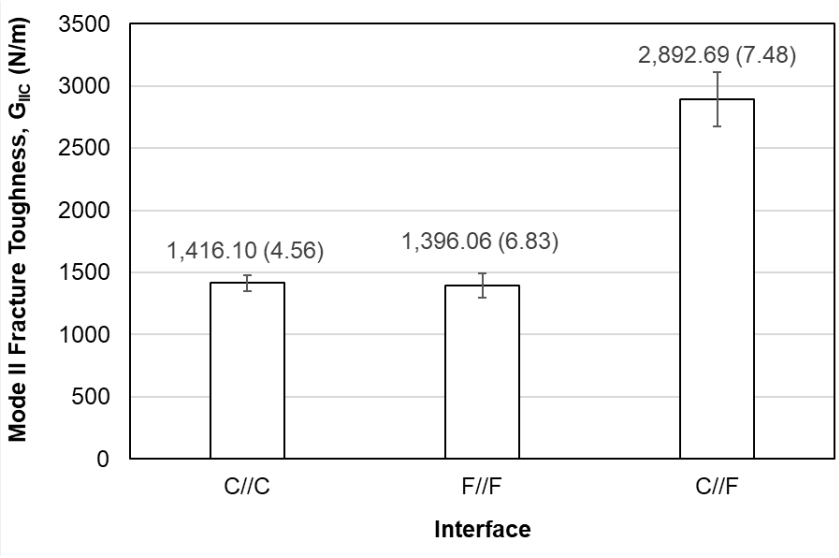


Fig. 4. Comparison of average Mode II fracture toughness for hybrid composites with C//C, F//F, and C//F mid-interface configurations.

Table 2. Summary of Mode II interlaminar fracture toughness values for flax fibre composites reported in the literature.

Resin	Fibre architecture [interface orientation]	G_{IIC} (N/m)	Ref.
Marine 820 Epoxy	200 gsm unidirectional [0//0]	378	[22]
1006 epoxy	200 gsm twill weave 2/2 [0//0]	962	[13]
Epofine 556 Epoxy	200 gsm woven 4H satin weave [0//0]	1405	[23]
Epikote 828LVEL epoxy	285 gsm plain weave [0//0]	1872	[10]
	400 gsm twill weave 2/2 [0//0]	1315	
	150 gsm twill weave 2/2 [0//0]	1588	
	300 gsm quasi-unidirectional [90//90]	1570	
	300 gsm quasi-unidirectional [0//0]	1533	
	200 gsm unidirectional [90//90]	1006	
	200 gsm unidirectional [0//0]	728	
Crystic VE676-03 vinyl ester	600 gsm woven [45//45]	266	[12]
Vinyl ester	330 gsm non-woven mat	1940	[24]

Conclusions

This study investigated the Mode II delamination behaviour of hybrid carbon/flax epoxy composites with three different mid-interface configurations: carbon–carbon (C//C), flax–flax (F//F), and carbon–flax (C//F). The laminates were successfully fabricated using a hand lay-up technique followed by vacuum-bagging for curing. The influence of stacking sequence on interlaminar fracture toughness was evaluated using the End Notched Flexure (ENF) test. The average Mode II fracture toughness values (G_{IIC}) obtained were C//C = 1416.10 N/m, F//F = 1396.06 N/m and C//F = 2892.69 N/m. The G_{IIC} values for C//C and F//F interfaces are consistent with those reported in the literature for similar composite systems. Notably, the C//F configuration exhibited significantly higher fracture toughness — approximately double that of the other two — suggesting enhanced resistance to delamination due to increased interfacial friction between dissimilar fibre types. These findings demonstrate that hybridisation, particularly with carbon/flax

interfaces, can effectively improve the delamination resistance of composite laminates. This insight is valuable for the design of sustainable, high-performance composite structures.

Acknowledgements
This work is supported by Ministry of Higher Education Malaysia through Fundamental Research Grant Scheme (FRGS) No. FRGS/1/2021/TK0/UNIM/02/4.

References

[1] L. Pil, F. Bensadoun, J. Pariset, I. Verpoest, Why are designers fascinated by flax and hemp fibre composites?, Compos. Part A-Appl. S. (2016) 83 193-205. https://doi.org/10.1016/j.compositesa.2015.11.004.

[2] M. Chandrasekar, M.R. Ishak, S.M. Sapuan, Z. Leman, M. Jawaid, A review on the characterisation of natural fibres and their composites after alkali treatment and water absorption, Plast. Rubber Compos. (2017) 46(3) 119-136. https://doi.org/10.1080/14658011.2017.1298550.

[3] K.L. Pickering, M.G.A. Efendy, T.M. Le, A review of recent developments in natural fibre composites and their mechanical performance, Compos. Part A-Appl. S. (2016) 83 98-112. https://doi.org/10.1016/j.compositesa.2015.08.038.

[4] L. Yan, N. Chouw, K. Jayaraman, Flax fibre and its composites – A review, Compos. Part B-Eng. (2014) 56 296-317. https://doi.org/10.1016/j.compositesb.2013.08.014.

[5] A. Turon, P.P. Camanho, J. Costa, C.G. Dávila, A damage model for the simulation of delamination in advanced composites under variable-mode loading, Mechanics of Materials (2006) 38(11) 1072-1089. http://dx.doi.org/10.1016/j.mechmat.2005.10.003.

[6] Y. Zhao, W. Liu, L.K. Seah, G.B. Chai, Delamination growth behavior of a woven E-glass/bismaleimide composite in seawater environment, Compos. Part B-Eng. (2016) 106 332-343. http://dx.doi.org/10.1016/j.compositesb.2016.09.045.

[7] N.J. Pagano, G.A. Schoeppner, Delamination of polymer matrix composites: problems and assessment, in: A. Kelly and C. Zweben, (Eds.), Comprehensive Composite Materials, Pergamon, Oxford, 2000. pp. 433-528. http://doi.org/10.1016/B0-08-042993-9/00073-5.

[8] M. Ravandi, W.S. Teo, M.S. Yong, T.E. Tay, Prediction of Mode I interlaminar fracture toughness of stitched flax fiber composites, J. Mater. Sci. (2018) 53(6) 4173-4188. https://doi.org/10.1007/s10853-017-1859-y.

[9] M. Ravandi, W.S. Teo, L.Q.N. Tran, M.S. Yong, T.E. Tay, The effects of through-the-thickness stitching on the Mode I interlaminar fracture toughness of flax/epoxy composite laminates, Mater. Des. (2016) 109 659-669. https://doi.org/10.1016/j.matdes.2016.07.093.

[10] F. Bensadoun, I. Verpoest, A.W. Van Vuure, Interlaminar fracture toughness of flax-epoxy composites, Journal of Reinforced Plastics and Composites (2017) 36(2) 121-136. https://doi.org/10.1177/0731684416672925.

[11] C. Chen, Y. Li, T. Yu, Interlaminar toughening in flax fiber-reinforced composites interleaved with carbon nanotube buckypaper, Journal of Reinforced Plastics and Composites (2014) 33(20) 1859-1868. https://doi.org/10.1177/0731684414548084.

[12] F.A. Almansour, H.N. Dhakal, Z.Y. Zhang, Investigation into Mode II interlaminar fracture toughness characteristics of flax/basalt reinforced vinyl ester hybrid composites, Composites Science and Technology (2018) 154 117-127. https://doi.org/10.1016/j.compscitech.2017.11.016.

[13] T.S. Rajendran, M. Johar, K.O. Low, S. Abu Hassan, K.J. Wong, Interlaminar fracture toughness of a plain weave flax/epoxy composite, Plast. Rubber Compos. (2019) 48(2) 74-81. https://doi.org/10.1080/14658011.2018.1550235.

[14] S. Benmedakhene, M. Kenane, M.L. Benzeggagh, Initiation and growth of delamination in glass/epoxy composites subjected to static and dynamic loading by acoustic emission monitoring, Compos. Sci. Technol. (1999) 59(2) 201-208. https://doi.org/10.1016/S0266-3538(98)00063-3.

[15] J. Summerscales, N.P.J. Dissanayake, A.S. Virk, W. Hall, A review of bast fibres and their composites. Part 1 – Fibres as reinforcements, Compos. Part A-Appl. S. (2010) 41(10) 1329-1335. https://doi.org/10.1016/j.compositesa.2010.06.001.

[16] M. Johar, W.W.F. Chong, K.J. Wong, Moisture absorption and tensile behaviour of hybrid carbon/flax composites, Fibers Polym. (2023) 24(5) 1799-1810. https://doi.org/10.1007/s12221-023-00157-0.

[17] G.R. Irwin, J.A. Kies, Critical energy rate analysis of fracture strength, Weld. J. Res. Suppl. (1954) 33 193-198.

[18] K. Tanaka, K. Kageyama, M. Hojo, Prestandardization study on mode II interlaminar fracture toughness test for cfrp in japan, Compos. (1995) 26(4) 257-267. https://doi.org/10.1016/0010-4361(95)93669-B.

[19] P.N.B. Reis, J.A.M. Ferreira, J.D.M. Costa, A.M. Pereira, Interlaminar fracture in woven carbon/epoxy laminates, Frat. Integrita Strutt. (2014) 30 431-437.

[20] W. Trabelsi, L. Michel, R. Othomene, Effects of stitching on delamination of satin weave carbon-epoxy laminates under mode I, mode II and mixed-mode I/II loadings, Applied Composite Materials (2010) 17(6) 575-595. https://doi.org/10.1007/s10443-010-9128-0.

[21] Y. Zhao, M. Cao, W.P. Lum, V.B.C. Tan, T.E. Tay, Interlaminar fracture toughness of hybrid woven carbon-Dyneema composites, Compos. Part A-Appl. S. (2018) 114 377-387. https://doi.org/10.1016/j.compositesa.2018.08.035.

[22] Y. Saadati, J.-F. Chatelain, G. Lebrun, Y. Beauchamp, P. Bocher, N. Vanderesse, A study of the interlaminar fracture toughness of unidirectional flax/epoxy composites, J. Compos. Sci. (2020) 4(2). https://doi.org/10.3390/jcs4020066.

[23] V. Prasad, K. Sekar, S. Varghese, M.A. Joseph, Enhancing Mode I and Mode II interlaminar fracture toughness of flax fibre reinforced epoxy composites with nano TiO2, Compos. Part A-Appl. S. (2019) 124 105505. https://doi.org/10.1016/j.compositesa.2019.105505.

[24] F.A. Almansour, H.N. Dhakal, Z.Y. Zhang, H. Ghasemnejad, Effect of hybridization on the mode II fracture toughness properties of flax/vinyl ester composites, Polym. Compos. (2017) 38(8) 1732-1740. https://doi.org/10.1002/pc.23743.

Materials Research Proceedings 74 (2026) 133-140 https://doi.org/10.21741/9781644904473-17

Statistical Evaluation of Alkali-treated Bamboo Fibre Reinforced Polyester Composites using Weibull Analysis

K.J. WONG[1,a], K.O. LOW[2,b] and A.B. CHAI[1,c *]

[1]Department of Mechanical, Materials and Manufacturing Engineering, Faculty of Science and Engineering, University of Nottingham Malaysia, Jalan Broga, 43500 Semenyih, Selangor, Malaysia

[2]Faculty of Engineering and Technology, Multimedia University, Jalan Ayer Keroh Lama, 75450, Melaka, Malaysia

[a]KingJye.Wong@nottingham.edu.my, [b]kolow@mmu.edu.my, [c]AiBao.Chai@nottingham.edu.my

Keywords: Bamboo Fibre, Polyester Resin, Alkali Treatment, Interfacial Shear Strength, Weibull Analysis

Abstract. The mechanical performance of natural fibre-reinforced composites is strongly influenced by the quality of interfacial bonding between the fibres and polymer matrices. This study investigates the effects of embedded fibre length and alkali treatment concentration on the interfacial shear strength (IFSS) of bamboo fibre bundles embedded in unsaturated polyester resin. Bamboo bundles were treated with sodium hydroxide (NaOH) at concentrations of 0, 1, 3, 5, and 7 wt%, and embedded at lengths ranging from 1 to 10 mm. Pull-out tests were conducted using a custom-designed jig to minimise premature fibre failure due to clamping stress. Statistical analysis using Weibull distribution revealed that IFSS was largely independent of embedded length beyond 3 mm, with slope values between 1.9–2.7. Alkali treatment significantly enhanced interfacial bonding, with slope values between 4.1–4.9. However, excessive alkali concentration (7 wt%) introduced surface defects, reducing interfacial performance, which can be seen from a drop of slope to 2.3. These findings underscore the importance of alkali treatment to improve the reliability and mechanical integrity of bamboo fibre reinforced polyester composites.

Introduction

Natural fibres have gained increasing attention as sustainable alternatives to synthetic reinforcements in composite materials due to their renewability, biodegradability, and low environmental impact [1]. However, a major limitation in natural fibre-reinforced composites is the inherently weak interfacial bonding between the hydrophilic fibres and hydrophobic polymer matrices [2, 3]. This poor adhesion often leads to premature fibre debonding, which is a common failure mechanism in such composites. Therefore, enhancing the fibre–matrix interfacial strength is critical to improving the overall mechanical performance of natural fibre composites.

Various surface modification techniques have been explored to improve interfacial adhesion, including alkalisation, silanation, acetylation, cyanoethylation, crystallisation, irradiation, fibrillation, and acidification. Among these, alkali treatment is one of the most widely used methods. Alkali treatment offers several advantages including simplicity, low cost, and effectiveness in modifying fibre surface roughness. Numerous studies have reported that alkali treatment enhances interfacial shear strength (IFSS) by improving fibre surface morphology and partially removing non-cellulosic components such as hemicellulose and lignin [4-18]. Reported alkali concentrations in the literature range from as low as 0.5 wt% [11] to as high as 20 wt% [15].

Despite its benefits, alkali treatment must be carefully controlled. Excessive concentrations or improper combinations with other treatments can degrade the fibre surface, leading to reduced IFSS. For instance, high-concentration NaOH (10 g/L) has been shown to damage flax fibres,

Content from this work may be used under the terms of the Creative Commons Attribution 3.0 license. Any further distribution of this work must maintain attribution to the author(s) and the title of the work, journal citation and DOI. Published under license by Materials Research Forum LLC.

weakening the interface [18]. Similarly, boiling and bleaching treatments have been reported to negatively affect interfacial bonding due to fibre degradation and increased surface polarity, respectively [11, 18].

While alkali treatment of natural fibres has been widely studied, limited work has focused on the combined effects of embedded fibre length and alkali concentration on bamboo fibre bundles using Weibull statistical analysis. This study provides a systematic evaluation of interfacial reliability by integrating pull-out test with Weibull analysis, offering insights into both average performance and variability, which are critical for engineering applications.

Materials and Methods

Materials

The matrix material used in this study was unsaturated polyester resin (Reservol P 9509), supplied by Jiashan Anserly Glass Fibre Co. Ltd., Malaysia. Bamboo stems were sourced locally from a household supplier in Sarawak, Malaysia.

Extraction of Bamboo Bundles

Bamboo bundles were manually extracted from the outer layer of the bamboo stem using a sharp blade. To maintain consistency in fibre properties, only bundles from the same stem segment were selected. These extracted elements are referred to as "bundles" rather than "fibres," as manual extraction yields multi-fibre aggregates rather than individual elementary fibres. The average diameter of untreated bundles was approximately 0.9 mm.

Alkali Treatment of Bamboo Bundles

The extracted bundles were immersed in aqueous sodium hydroxide (NaOH) solutions at concentrations of 1, 3, 5, and 7 wt% for one hour at ambient temperature. The treatment duration was selected based on prior studies [13, 19]. After soaking, the bundles were thoroughly rinsed with distilled water and air-dried under sunlight for one hour. Once dried, the bundles were trimmed to a uniform length of approximately 50 mm.

Specimen Preparation

U-shaped aluminium moulds measuring 12.7 × 12.7 × 50.0 mm^3 were used to fabricate the test specimens. The inner surfaces of the moulds were coated with a release agent to facilitate demoulding. Square rubber inserts matching the mould dimensions were placed inside to control the embedded length of the fibre bundles. A single bamboo bundle was positioned through the central hole of each rubber insert.

The polyester resin was mixed with 2 vol% methyl ethyl ketone peroxide (MEKP) as a catalyst and stirred gently to avoid air entrapment. The resin mixture was then poured into the moulds, and the specimens were cured at room temperature for 24 hours. Specimens at embedded lengths of 1, 3, 5, 7 and 10 mm were prepared. For each NaOH concentration, the specimen counts were 104, 18, 13, 15, and 7 at 0, 1, 3, 5, and 7 wt.%, respectively.

Pull-out Test

Pull-out tests were performed using Test Resources 100-250-12 universal testing machine with a load cell capacity of 1100 N at a constant crosshead speed of 1 mm/min. Fig. 1 illustrates the test setup and specimen configuration. A custom-designed jig was employed to eliminate the need for clamping the fibre ends, thereby reducing the risk of premature failure due to stress concentration. The free gauge length was maintained at 5 mm, while the fixed end was set at 20 mm — at least twice the embedded length — to ensure debonding occurred at the loaded end.

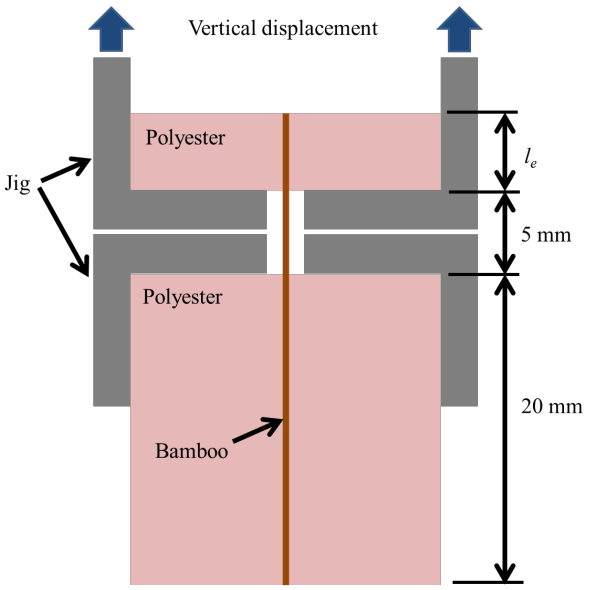


Fig. 1. Schematic of the pull-out test setup showing specimen configuration and loading arrangement using a customised jig.

Result and Discussion

Force Displacement Graphs

Fig. 2 presents a typical force–displacement curve for bamboo bundle pull-out specimens. The force increased linearly with displacement until reaching a peak, indicating elastic loading. This was followed by a sudden drop in force, signifying the onset of interfacial debonding and release of stored elastic energy. As the bundle continued to slide through the matrix, the force gradually declined due to frictional resistance. Complete fibre extraction resulted in the force returning to zero. These observations are consistent with previous studies involving pull-out and microbond tests [8, 13, 20-25]. Notably, the use of a customised jig improved test reliability, achieving a success rate exceeding 90% (without premature fibre fracture) by eliminating stress concentration at the clamping region.

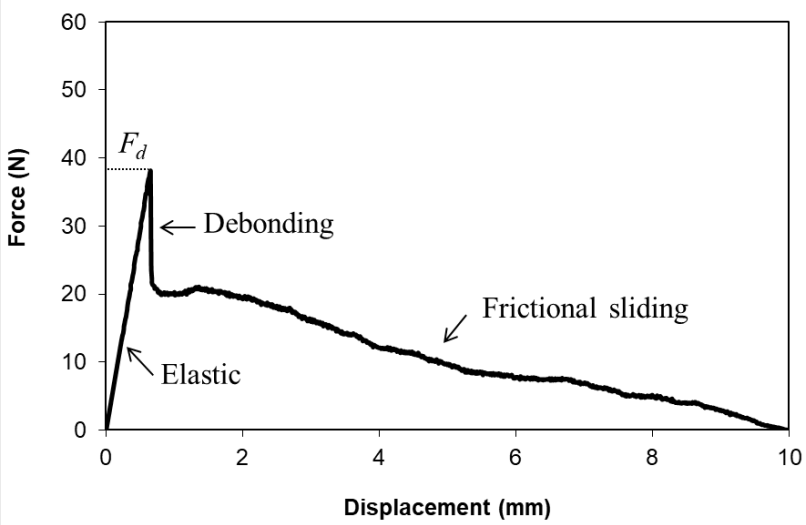


Fig. 2. Typical force–displacement curve for bamboo bundle pull-out specimens.

Apparent Interfacial Shear Strength

The apparent interfacial shear strength (τ_d) was estimated using the Kelly–Tyson model [26]:

$$\tau_d = F_d/(\pi \cdot d_f \cdot l_e) \quad \text{Eq.1}$$

where:

- F_d is the debonding force,
- d_f is the fibre bundle diameter, and
- l_e is the embedded length.

Average diameters were 0.9 mm for untreated bundles and 0.6 mm for treated ones. While the model assumes uniform shear stress and circular cross-sections, these conditions are rarely met in natural fibres, making τ_d an approximated value.

Weibull Distribution Analysis

To assess the variability and reliability of interfacial shear strength (IFSS), the Weibull distribution function was applied:

$$P_f = 1 - \exp[-(\tau_i/\tau_o)^{\alpha}] \quad \text{Eq. 2}$$

where:

- P_f is the cumulative probability of failure,
- τ_i is the IFSS of the i-th specimen,
- τ_o is the characteristic shear strength (scale parameter), and
- α is the Weibull modulus (shape parameter).

The probability of failure for each specimen was calculated using:

$$P_f = (i\text{-}0.5)n \quad \text{Eq. 3}$$

where i is the rank of the specimen in ascending order of IFSS, and n is the total number of valid tests.

By taking the double logarithm of Eq. 2, the linearised form becomes:

$$\ln[-\ln(1-P_f)] = \alpha \cdot \ln \tau_i - \alpha \cdot \ln \tau_o \quad \text{Eq. 4}$$

From the plot of $\ln[-\ln(1-P_f)]$ versus $\ln(\tau_i)$, the slope yields the Weibull modulus α, and the intercept gives $\ln(\tau_o)$. The Weibull modulus indicates the variability of interfacial strength, where higher values represent more consistent and reliable bonding. The characteristic shear strength represents the IFSS at which 63.2% of specimens fail.

Interpretation of Weibull Plots

Fig. 3 shows the Weibull probability plot for untreated bamboo bundles. Embedded lengths of 3 mm and above exhibit similar slope (Weibull modulus). This implies that they have similar interfacial behaviour, where 3 mm and above provide sufficient interfacial area for effective stress transfer between the fibre bundle and matrix. Specimens with an embedded length of 1 mm deviated significantly from the trend observed in other lengths, suggesting inefficient stress transfer at such short embedment. These data points were excluded from further analysis.

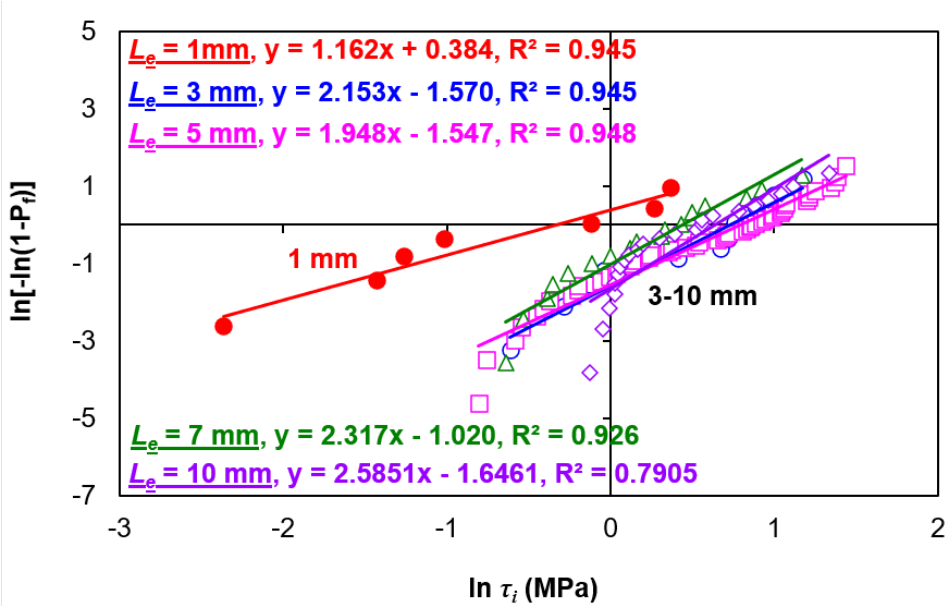


Fig. 3. Weibull probability plot for untreated bamboo bundles showing statistical distribution of interfacial shear strength across embedded lengths.

Fig. 4 presents the Weibull plots for all treatment conditions. The slopes for 1, 3, and 5 wt% treatments were similar and steeper than the untreated and 7 wt% cases, indicating lower variability and improved reliability. The reduced slope for 7 wt% treatment suggests increased surface defects, likely due to over-treatment.

These findings align with previous studies on sisal and flax fibres, where moderate alkali treatment improved surface quality and reduced flaw density, resulting in higher Weibull moduli [4, 14, 15].

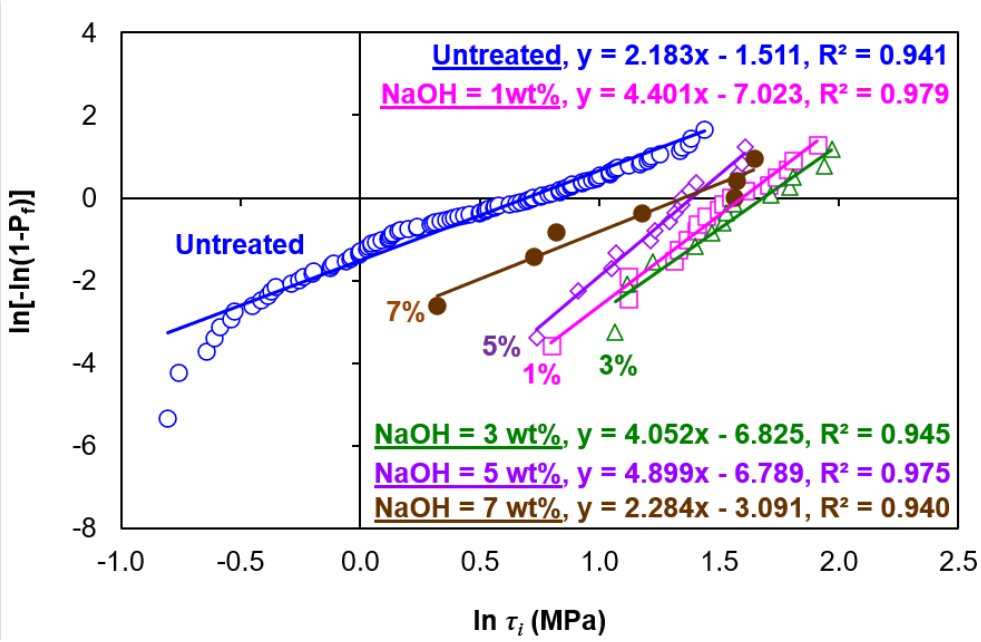


Fig. 4. Comparison of Weibull probability plots for untreated and alkali-treated bamboo bundles at different NaOH concentrations.

Conclusions

This study investigated the effects of embedded length and alkali treatment concentration on the interfacial shear strength (IFSS) of bamboo fibre bundles embedded in unsaturated polyester resin. Weibull analysis suggested that embedded length of 3 mm and above is required for effective stress transfer between the fibre and matrix. Additionally, moderate alkali treatment improved the reliability of interfacial bonding by reducing flaw sensitivity, as indicated by higher Weibull moduli. Excessive alkali concentration (7 wt%) led to surface degradation, reducing interfacial strength and increasing variability. Although the treated bamboo bundles demonstrated improved interfacial properties, their overall IFSS remains lower than that of other natural fibres reported in the literature. Future work could explore alternative fibre extraction techniques and combined surface treatments to further enhance interfacial performance.

Acknowledgements

This work is supported by Ministry of Higher Education Malaysia through Fundamental Research Grant Scheme (FRGS) No. FRGS/1/2021/TK0/UNIM/02/4.

References

[1] T.S. Rajendran, M. Johar, K.O. Low, S. Abu Hassan, K.J. Wong, Interlaminar fracture toughness of a plain weave flax/epoxy composite, Plast. Rubber Compos. (2019) 48(2) 74-81. https://doi.org/10.1080/14658011.2018.1550235.

[2] I. Elfaleh, F. Abbassi, M. Habibi, F. Ahmad, M. Guedri, M. Nasri, C. Garnier, A comprehensive review of natural fibers and their composites: An eco-friendly alternative to conventional materials, Results Eng. (2023) 19 101271. https://doi.org/10.1016/j.rineng.2023.101271.

[3] M. Mohammadi, M.R. Ishak, M.T.H. Sultan, Exploring chemical and physical advancements in surface modification techniques of natural fiber reinforced composite: A comprehensive review, J. Nat. Fibers (2024) 21(1) 2408633. https://doi.org/10.1080/15440478.2024.2408633.

[4] A. Orue, A. Jauregi, C. Peña-Rodriguez, J. Labidi, A. Eceiza, A. Arbelaiz, The effect of surface modifications on sisal fiber properties and sisal/poly (lactic acid) interface adhesion, Compos. Part B-Eng. (2015) 73(0) 132-138. http://dx.doi.org/10.1016/j.compositesb.2014.12.022.

[5] H. Kim, K. Okubo, T. Fujii, K. Takemura, Influence of fiber extraction and surface modification on mechanical properties of green composites with bamboo fiber, J. Adhes. Sci. Technol. (2012) 27(12) 1348-1358. https://doi.org/10.1080/01694243.2012.697363.

[6] M.A. Sawpan, K.L. Pickering, A. Fernyhough, Effect of fibre treatments on interfacial shear strength of hemp fibre reinforced polylactide and unsaturated polyester composites, Compos. Part A-Appl. S. (2011) 42(9) 1189-1196. http://dx.doi.org/10.1016/j.compositesa.2011.05.003.

[7] K.L. Pickering, M.A. Sawpan, J. Jayaraman, A. Fernyhough, Influence of loading rate, alkali fibre treatment and crystallinity on fracture toughness of random short hemp fibre reinforced polylactide bio-composites, Compos. Part A-Appl. S. (2011) 42(9) 1148-1156. http://dx.doi.org/10.1016/j.compositesa.2011.04.020.

[8] K.J. Wong, B.F. Yousif, K.O. Low, The effects of alkali treatment on the interfacial adhesion of bamboo fibres, P I Mech Eng L-J Mat (2010) 224(3) 139-148. https://doi.org/10.1243/14644207JMDA304.

[9] M.S. Islam, K.L. Pickering, N.J. Foreman, Influence of alkali treatment on the interfacial and physico-mechanical properties of industrial hemp fibre reinforced polylactic acid composites,

Compos. Part A-Appl. S. (2010) 41(5) 596-603. http://dx.doi.org/10.1016/j.compositesa.2010.01.006.

[10] R. Tokoro, D. Vu, K. Okubo, T. Tanaka, T. Fujii, T. Fujiura, How to improve mechanical properties of polylactic acid with bamboo fibers, J. Mater. Sci. (2008) 43(2) 775-787. https://doi.org/10.1007/s10853-007-1994-y.

[11] J.-M. Park, P.-G. Kim, J.-H. Jang, Z. Wang, B.-S. Hwang, K.L. DeVries, Interfacial evaluation and durability of modified Jute fibers/polypropylene (PP) composites using micromechanical test and acoustic emission, Compos. Part B-Eng. (2008) 39(6) 1042-1061. http://dx.doi.org/10.1016/j.compositesb.2007.11.004.

[12] C. Baley, F. Busnel, Y. Grohens, O. Sire, Influence of chemical treatments on surface properties and adhesion of flax fibre–polyester resin, Compos. Part A-Appl. S. (2006) 37(10) 1626-1637. http://dx.doi.org/10.1016/j.compositesa.2005.10.014.

[13] P.J. Herrera-Franco, A. Valadez-González, A study of the mechanical properties of short natural-fiber reinforced composites, Compos. Part B-Eng. (2005) 36(8) 597-608. http://dx.doi.org/10.1016/j.compositesb.2005.04.001.

[14] A.N. Towo, M.P. Ansell, M.-L. Pastor, D.E. Packham, Weibull analysis of microbond shear strength at sisal fibre–polyester resin interfaces, Compos. Interface. (2005) 12(1-2) 77-93. https://doi.org/10.1163/1568554053542142.

[15] A. Arbelaiz, G. Cantero, B. Fernández, I. Mondragon, P. Gañán, J.M. Kenny, Flax fiber surface modifications: Effects on fiber physico mechanical and flax/polypropylene interface properties, Polym. Compos. (2005) 26(3) 324-332. https://doi.org/10.1002/pc.20097.

[16] A. Valadez-Gonzalez, J.M. Cervantes-Uc, R. Olayo, P.J. Herrera-Franco, Effect of fiber surface treatment on the fiber–matrix bond strength of natural fiber reinforced composites, Compos. Part B-Eng. (1999) 30(3) 309-320. http://dx.doi.org/10.1016/S1359-8368(98)00054-7.

[17] J.-M. Park, S.T. Quang, B.-S. Hwang, K.L. DeVries, Interfacial evaluation of modified jute and hemp fibers/polypropylene (PP)-maleic anhydride polypropylene copolymers (PP-MAPP) composites using micromechanical technique and nondestructive acoustic emission, Compos. Sci. Technol. (2006) 66(15) 2686-2699. http://doi.org/10.1016/j.compscitech.2006.03.014.

[18] S.S. Tripathy, G. Levita, L. Di Landro, Interfacial adhesion in jute-polyolefin composites, Polym. Compos. (2001) 22(6) 815-822. https://doi.org/10.1002/pc.10583.

[19] P.J. Herrera-Franco, A. Valadez-González, Mechanical properties of continuous natural fibre-reinforced polymer composites, Compos. Part A-Appl. S. (2004) 35(3) 339-345. http://dx.doi.org/10.1016/j.compositesa.2003.09.012.

[20] R.-B. Adusumalli, M. Reifferscheid, H.K. Weber, T. Roeder, H. Sixta, W. Gindl, Shear strength of the lyocell fiber/polymer matrix interface evaluated with the microbond technique, J. Compos. Mater. (2012) 46(3) 359-367. https://doi.org/10.1177/0021998310382312.

[21] S. Luo, A.N. Netravali, Interfacial and mechanical properties of environment-friendly “green” composites made from pineapple fibers and poly(hydroxybutyrate-co-valerate) resin, J. Mater. Sci. (1999) 34(15) 3709-3719. https://doi.org/10.1023/a:1004659507231.

[22] A. Stamboulis, C. Baillie, E. Schulz, Interfacial characterisation of flax fibre-thermoplastic polymer composites by the pull-out test, Angew. Makromol. Chem. (1999) 272(1) 117-120. https://doi.org/10.1002/(sici)1522-9505(19991201)272:1<117::aid-apmc117>3.0.co;2-9.

[23] S. Wong, R.A. Shanks, A. Hodzic, Effect of additives on the interfacial strength of poly(l-lactic acid) and poly(3-hydroxy butyric acid)-flax fibre composites, Compos. Sci. Technol. (2007) 67(11–12) 2478-2484. http://dx.doi.org/10.1016/j.compscitech.2006.12.016.

[24] N. Graupner, J. Rößler, G. Ziegmann, J. Müssig, Fibre/matrix adhesion of cellulose fibres in PLA, PP and MAPP: A critical review of pull-out test, microbond test and single fibre fragmentation test results, Compos. Part A-Appl. S. (2014) 63(0) 133-148. http://dx.doi.org/10.1016/j.compositesa.2014.04.011.

[25] A. Le Duigou, P. Davies, C. Baley, Interfacial bonding of Flax fibre/Poly(l-lactide) bio-composites, Compos. Sci. Technol. (2010) 70(2) 231-239. http://dx.doi.org/10.1016/j.compscitech.2009.10.009.

[26] A. Kelly, W.R. Tyson, Tensile properties of fibre-reinforced metals: Copper/tungsten and copper/molybdenum, J. Mech. Phys. Solids (1965) 13(6) 329-350. http://dx.doi.org/10.1016/0022-5096(65)90035-9.

Materials Research Proceedings 74 (2026) 141-147 https://doi.org/10.21741/9781644904473-18

Thermal Conductivity of Ceramic Tiles Incorporating Iraqi Porcelanite Waste as a Partial Substitute for Ball Clay

Ishraq Abdalkareem Kalaf ALOGAIDI[1,2,a], Ahmed Hafedh Mohammed MOHAMMED[3,b], Khairul Anuar SHARIFF[1,c *], Hasmaliza MOHAMAD[1,d] and Muhamed Abdul Fatah Muhamed MUKHTAR[1,e]

[1]School of Materials and Mineral Resources Engineering, Engineering Campus, Universiti Sains Malaysia, Penang 14300, Malaysia

[2]Baghdad Central Laboratory, National Center for Construction Laboratories, Ministry of Construction, Housing and Public Municipalities, Baghdad 10045, Iraq

[3]Department of Materials Engineering, College of Engineering, Mustansiriyah University, Baghdad 10045, Iraq

[a]ishraqabd1971@student.usm.my, [b]ahmed.mohammed@uomustansiriyah.edu.iq, [c]biokhairul@usm.my, [d]hasmaliza@usm.my, [e]fatahmukhtar@usm.my

Keywords: Thermal Conductivity, Ceramic Tiles, Iraqi Porcelanite, Apparent Porosity

Abstract. This work investigates the effect of partial replacement of ball clay by Iraqi porcelanite waste powder on heat transport and pore related properties of ceramic tiles. Four compositions were investigated: an unmodified control and bodies containing formulations incorporating 1 wt.% (designated as A), 3 wt.% (B), and 5 wt.% (C) of porcelanite. Powder mixtures underwent 24 h milling at 60 rpm, followed by uniaxial pressing under 35 MPa for 5 min. Sintering was then performed at 1200 °C for a 6 h dwell time, using a heating rate of 5 °C/min. Thermal conductivity was interpreted together with water absorption and apparent porosity. Composition A exhibited the lowest conductivity, 1.318 W/m·K, corresponding to a 3.1% reduction relative to the control value of 1.360 W/m·K; it recorded values of 0.97% for water absorption alongside an apparent porosity of 2.44%. The conductivity response was not monotonic with porcelanite content, indicating that heat transfer depended on the combined effects of pore structure, densification, and solid-phase continuity. Within the investigated range, 1 wt.% porcelanite provided the most favourable thermal response, although the improvement was modest. The results support the controlled reuse of Iraqi porcelanite waste in ceramic production while reducing the demand for conventional raw materials.

Introduction

Porcelanite is a silica-rich rocks found widely in Iraq and suggested for use in construction and ceramic applications [1]. Iraqi porcelanite has been described as a dense fine-grained material composed principally of quartz with minor feldspar, mica and clay minerals [2]. Its durability and resistance to heat and chemical attack has made it an attractive product for technically demanding applications [3]. In fired ceramics thermal conductivity depends not only on chemical composition. Bulk density, crystalline and glassy phases and the amount, shape and connectivity of pores formed during processing and firing are also important in affecting heat flow [4,5]. Previous Iraqi studies have focused mainly on concrete and refractory products. Awadh and Fadhil [6] observed a reduction in density and thermal conductivity with the use of porcelanite as aggregate in structural lightweight concrete. Naji et al. [7] reported a reduction in thermal conductivity and diffusivity in lightweight self-compacting concrete including porcelanite. Al-Taie et al. [8] demonstrated that porcelanite-kaolinite mixtures could produce lightweight refractory bricks suitable for insulation. By comparison, limited evidence is available on the use of powdered Iraqi porcelanite waste within

Content from this work may be used under the terms of the Creative Commons Attribution 3.0 license. Any further distribution of this work must maintain attribution to the author(s) and the title of the work, journal citation and DOI. Published under license by Materials Research Forum LLC.

ceramic tile formulations, particularly regarding how its incorporation level affects pore characteristics and thermal conductivity. The present work therefore evaluates ceramic compositions containing 0, 1, 3, and 5 wt.% of fine porcelanite waste powder, and examines the relationship between their thermal conductivity, the percentage of absorbed water, and the volume fraction of open pores.

Materials and Methods

Raw material processing and sample fabrication

A commercial ceramic body containing china clay, ball clay, feldspar, bentonite, and silica was used as the reference composition. Three modified compositions were prepared by replacing an equal amount of ball clay with 1, 3 and 5 wt. % of total dry batch of Iraqi porcelanite waste powder. These compositions were labeled as A, B and C accordingly and the mixture without porcelanite served as the control. Three specimens were made and examined for each composition. The primary oxide content of the porcelanite powder was analyzed by X-ray fluorescence analysis, which was used to evaluate the impacts of the porcelanite powder on heat transport and pore features. The mixture proportions and the chemical composition findings are detailed in Tables 1 and 2.

Table 1. Batch compositions of ceramic mixtures containing different percentages of Iraqi porcelanite waste powder (wt.%).

Raw material	Reference	Samples			
		Control	A	B	C
China clay	*Commercialised ceramic tile formulation	32	32	32	32
Ball clay		22	21	19	17
Feldspar		34	34	34	34
Bentonite		6	6	6	6
Silica		6	6	6	6
Iraqi porcelanite		0	1	3	5

* *The commercial ceramic tile mixture was provided by an industrial partner who wished to remain anonymous regarding authorship and institutional details.*

Table 2. Chemical composition of Iraqi porcelanite waste powder determined by XRF analysis.

Raw material	SiO_2	P_2O_5	K_2O	CaO	TiO_2	Fe_2O_3	Cr_2O_3	MnO
Iraqi porcelanite	82.8%	2.7%	0.121%	4.607%	0.058%	0.8473%	0.022%	0.018%

The raw materials were mixed and milled at 60 rpm for 24 h to obtain a homogeneous fine powder. A 35 g portion of the milled powder was evenly placed in the mould and moistened with three sprays of distilled water. Rectangular green specimens measuring 100 mm × 40 mm × 5 mm were formed by uniaxial pressing at 35 MPa for 5 min using an Enerpac XLP756XA12GU hydraulic press. The compacted specimens were heated in a Carbolite RHF 1600 furnace to 1200 °C applying a thermal rate of 5 °C/min, held at maximum temperature for a 6 h dwell time, followed by furnace cooling down to ambient conditions (25 °C). Fig. 1 shows the prepared samples from the present study.

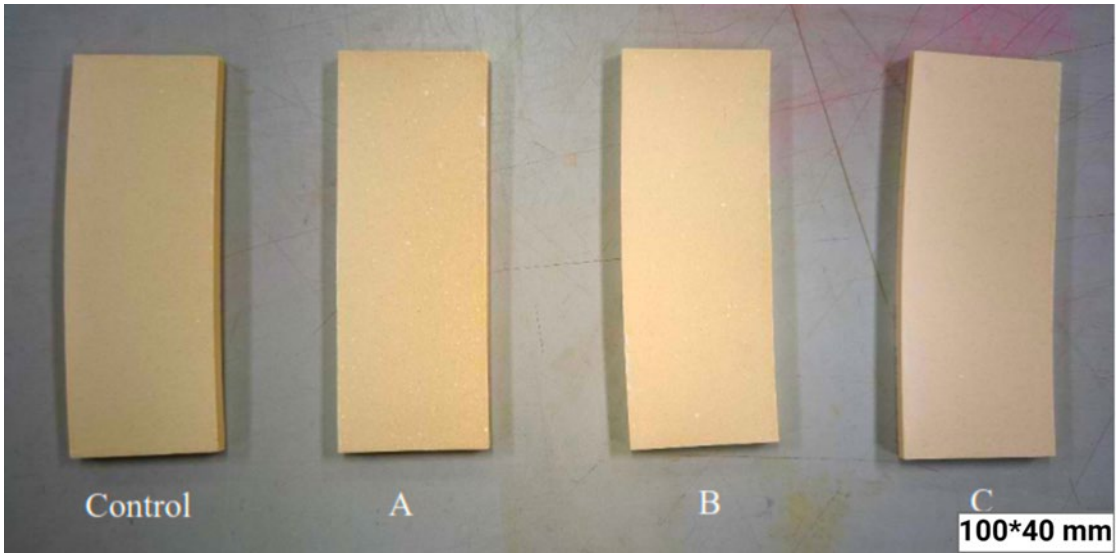


Fig. 1. The specimens formed in this work: Control (specimens with 0 wt.% Iraqi porcelanite), A (specimens with 1 wt.% Iraqi porcelanite), B (specimens with 3 wt.% Iraqi porcelanite), C (specimens with 5 wt.% Iraqi porcelanite).

Water Absorption Assessment

The water absorption of the sintered ceramic samples was determined according to ISO 10545-3. The test pieces were fully immersed in distilled water for 24 h, until they were completely saturated. Then the mass of the saturated test pieces was measured. Water absorption represents the quantity of water taken up by the accessible pores and therefore provides an indication of the open porosity of the ceramic body, which may influence its heat-transfer behaviour. Water absorption (WA) was calculated from the difference between the saturated and dry masses using Eq. (1):

$$WA(\%) = \left[\frac{(S_m - D_m)}{D_m}\right] \times 100\% \quad (1)$$

Where
$WA(\%)$ – Percentage of water absorption (%)
S_m – Soaked mass
D_m – Dry mass

Apparent Porosity Testing of Ceramic Tile Specimens

The apparent porosity of the fired ceramic bodies was carried out according to the ISO 10545-3 standard. This value is calculated as a ratio of open porosity of the tiles after firing and external bulk volume. The data was recorded during the water absorption test and the evaluation was completed. Apparent porosity was calculated with Eq. (2):

$$AP(\%) = \left[\frac{(S_m - D_m)}{V}\right] \times 100\% \quad (2)$$

Where
$AP(\%)$ – Percentage of apparent porosity (%)
V – Volume of fired ceramic

Thermal Conductivity Measurements

The thermal conductivity of the sintered ceramic samples was determined using a TPS 2500 Hot Disk Thermal Constants Analyser (Hot Disk AB, Sweden). For the measurement, each specimen was prepared with minimum dimensions of length and width of 20 mm and a flat smooth surface to provide good contact with the sensor. Each ceramic specimen was divided into two matching sections, and the planar Hot Disk sensor was positioned between their opposing surfaces. Measurements were carried out at 25 °C using an input power of 0.5 Watts for 5 seconds. Thermal conductivity was calculated based on transient temperature increase recorded by the sensor as a function of time as shown in Fig. 2.

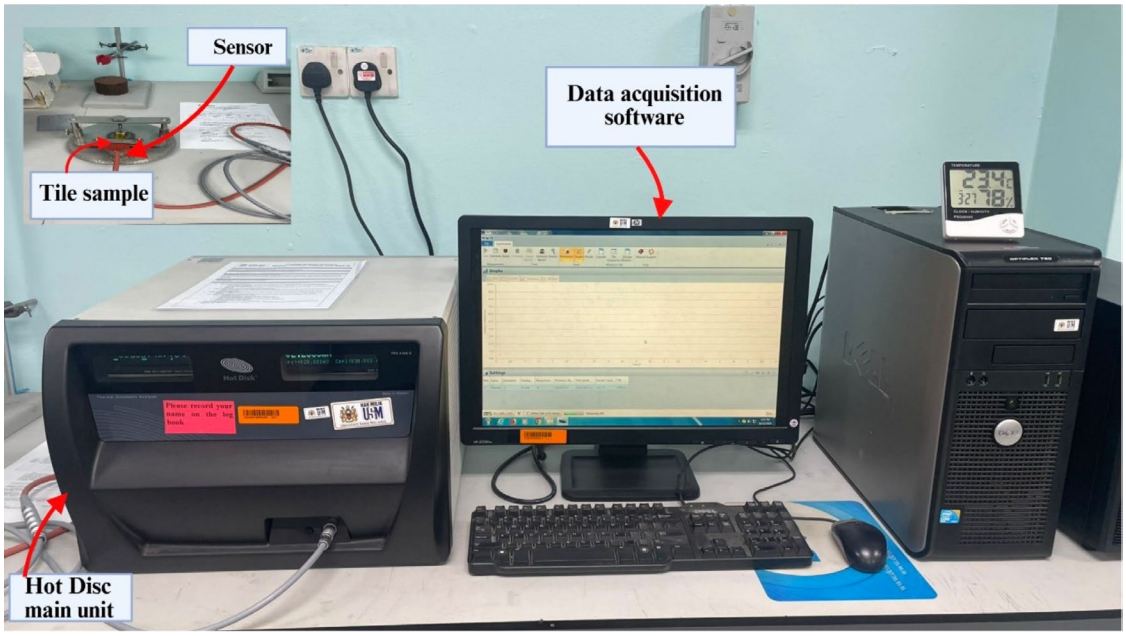


Fig. 2. Experimental configuration for measuring thermal conductivity via the Hot Disk technique.

Statistical analysis

Results are presented as mean ± standard deviation and all assays were performed in triplicate (n=3). Variance between samples in the groups was determined by Tukey's honest significant difference test following a one-way ANOVA. Differences were considered statistically significant if $p < 0.05$. *$p < 0.1$ indicates a noticeable statistical trend, $p < 0.05$ indicates a statistically significant variation, ***$p < 0.01$ indicates a highly significant variance and n.s. denotes no significant difference. These are the statistical symbols used in this study.

Result and Discussion

Assessment of Water Absorption and Apparent Porosity

Fig. 3 shows the profiles for water absorption together with the apparent porosity in the sintered ceramic bodies. The incorporation of Iraqi porcelanite powder led to a gradual decrease of both parameters from the unassigned control formulation to Sample B, which showed the lowest values of 0.76% and 1.90%, respectively. These reductions are attributed to more vitrification and densification of the body during the heat treatment. Porcelanite has a large amount of silica which, on firing, forms a molten liquid phase that seals the open channels and isolates the internal voids. Therefore, the decrease in the interconnected pore network restricts the fluid intake, correlating directly the lower apparent porosity with the lower water absorption [9]. However, In addition, as the porcelanite fraction reached 5 wt.% in Sample C, a slight rise was observed in both parameters. This behaviour can be explained by excess addition of porcelanite which may disturb the balance

between vitrification and pore elimination, leaving residual pores or creating new pores within the fired body. However, all the porcelanite-containing samples showed water absorption values below 1%, indicating high densification and confirming their applicability as low-water-absorption ceramic tiles [10]. From the statistical analysis, it was found that the water absorption and apparent porosity of Sample B were statistically significantly reduced compared to the control sample, which proved that the utilization of porcelanite improved the densification of ceramics during sintering to effectively close the pores.

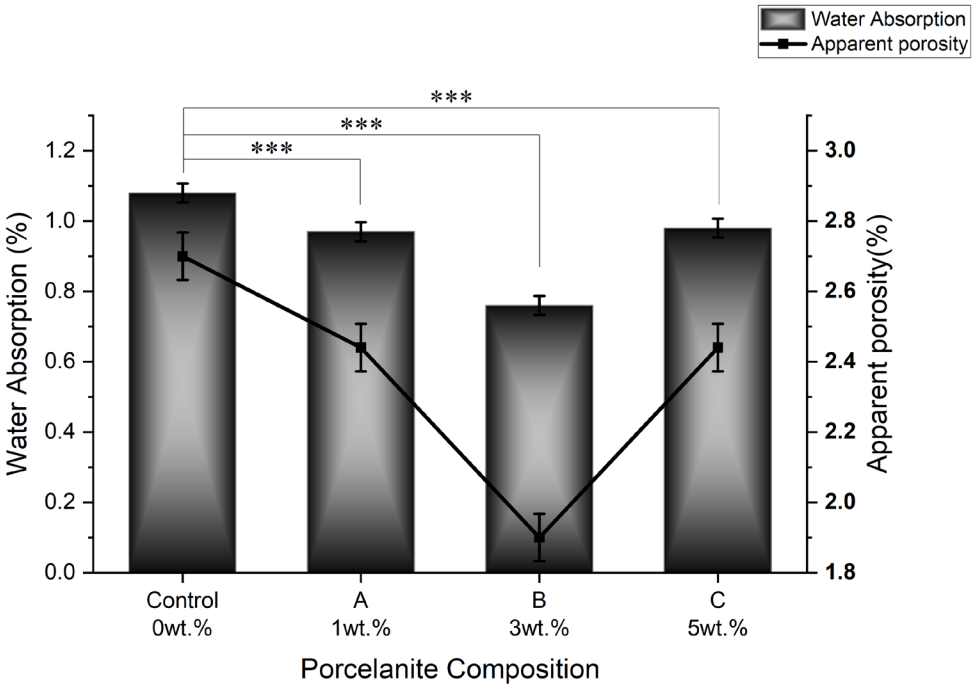


*Fig. 3. Water absorption and apparent porosity results of different compositions fired at 1200ºC (Note: *** p< 0.01).*

Thermal Conductivity Analysis

Fig. 4 presents the thermal conductivity performance of sintered ceramic bodies incorporating various proportions of Iraqi porcelanite. Thermal conductivity of the control sample recorded 1.360 W/m·K. Sample A containing 1 wt% porcelanite possessed the lowest value of 1.318 W/m·K which was 3.1% less than the control. Sample C also had a smaller value than the control (1.331 W/m·K). In contrast, the highest value of thermal conductivity was observed for Sample B with 1.389 W/m·K, which showed an enhancement of approximately 2.1% compared to the control. Although porosity is a major factor affecting heat transfer in ceramic materials, the results show that thermal conductivity was not only dependent on porosity. Sample B had the lowest apparent porosity but the highest thermal conductivity. The finding indicates that the reduced porosity enhanced the continuity of the solid phase and provided efficient heat-transfer routes through the ceramic body. Moreover, mineralogical composition, degree of vitrification, densification and the formation of thermally conductive crystalline phases may have contributed to the increase. Thus, the higher thermal conductivity of Sample B can be attributed to the combined effect of a denser microstructure, lower pore volume and more continuous solid or crystalline network after firing. By contrast, the lower thermal conductivity values of Samples A and C could be related to microstructural variations and pore distributions that obstructed heat-flow paths within the ceramic matrix [11–13]. As the reductions were small, they represent only a modest improvement in

thermal insulation. Further statistical validation and industrial-scale testing are suggested to evaluate the practical significance of these results.

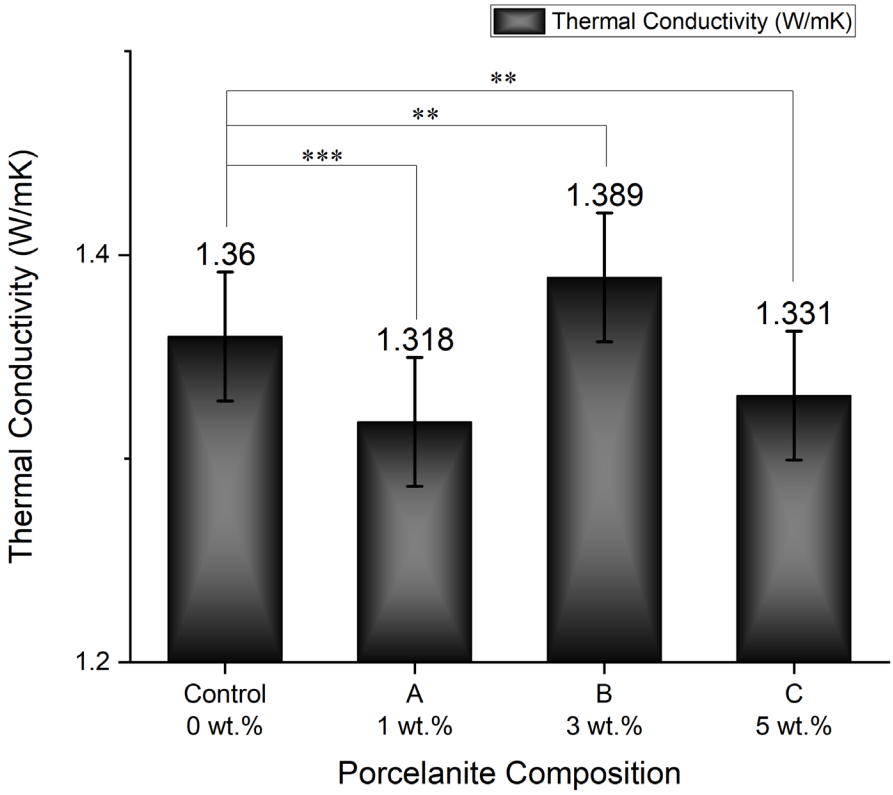


*Fig. 4. Thermal conductivity results of different compositions fired at 1200ºC (Note: *** p< 0.01, ** p<0.05).*

Summary

The obtained results indicate that the addition of Iraqi porcelanite powder exerts a marked influence on the thermal conductivity behavior of fired ceramic tiles. The lowest value of the thermal transport capability was 1.318 W/m·K in the sample of 1 wt.% porcelanite which was a reduction of approximately 3.1% compared to the control formulation. This demonstrates that minor additions of raw porcelanite can improve the thermal insulation properties of ceramic tiles. The increase in the content of porcelanite did not lead to a gradual decrease in thermal conductivity, the highest value was in sample B with 3 wt.% and the lowest in sample C with 5 wt.%, which was slightly lower than the control. Therefore, 1 wt.% Porcelanite can be considered as the most efficient composition within the range tested, but the improvement of thermal conductivity was limited. Further statistical validation and industrial scale experiments are needed to verify the practical significance of this reduction.

Acknowledgements

Heartfelt thanks are extended to the School of Materials and Mineral Resources Engineering, Universiti Sains Malaysia, for allowing full access to their research laboratories. The author gratefully recognizes Assoc. Prof. Dr. Khairul Anuar Shariff for his valuable guidance, encouragement and technical feedback. Grateful acknowledgment is also made to both the National Center for Construction Laboratories (Baghdad Center Laboratory, Ministry of Construction, Housing and Public Municipalities, Iraq) and the General Company for Geological

Survey and Mining (Ministry of Industry and Minerals, Iraq) for contributing the Iraqi porcelanite waste powder required for this investigation.

References

[1] G.A. Waheed, Assessment using of various sources of silica on the properties of porcelain, Doctoral dissertation, University of Babylon, Babylon, 2022.

[2] H.M. Saleh, Using of porcelinite as coarse aggregate in concrete, Tikrit J. Eng. Sci. 19 (2012) 33-40. https://doi.org/10.25130/tjes.19.3.04

[3] S.I. Ahmed, A.S. Al-Adili, A.M. Hameed, A short review on preparation and characterization of Iraqi porcelanite aggregate concrete, J. Appl. Sci. Nanotechnol. 2 (2022) 49-58. https://doi.org/10.53293/jasn.2021.3565.1028

[4] I. Allegretta, G. Eramo, D. Pinto, A. Hein, The effect of temper on the thermal conductivity of traditional ceramics: Nature, percentage and granulometry, Thermochim. Acta 581 (2014) 100-109. https://doi.org/10.1016/j.tca.2014.02.024

[5] J. García-Ten, M.J. Orts, A. Saburit, G. Silva, Thermal conductivity of traditional ceramics. Part I: Influence of bulk density and firing temperature, Ceram. Int. 36 (2010) 1951-1959. https://doi.org/10.1016/j.ceramint.2010.05.012

[6] S.M. Awadh, L.A. Fadhil, Assessment of porcelanites, western desert of Iraq as aggregates for structural lightweight concrete, J. Babylon Univ. Pure Appl. Sci. 23 (2015) 1636-1652.

[7] Z.H. Naji, H.M. Mubarak, A.M. Ibrahim, Thermal properties of lightweight self-compacting concrete incorporate nano silica, Ann. Chim. Sci. Matér. 48 (2024) 427-434. https://doi.org/10.18280/acsm.480315

[8] M.H. Al-Taie, A.H. Ali, A.F. Al-Attar, Study the physical properties and thermal conductivity of lightweight refractory bricks produced by adding porcelanite to kaolinite, Eng. Technol. J. 33 (2015) 51-60.

[9] Y. Dong, W. Guo, C. Jiang, Y. Shao, L. Zhang, D. Wang, X. Lu, S. Huang, X. Cheng, Using CaO as a modifier agent to optimize the pore structure of foamed ceramics from granite scrap, Ceram. Int. 49 (2023) 13443-13451. https://doi.org/10.1016/j.ceramint.2022.12.219

[10] P.O. Piccolo, A. Zaccaron, L.B. Teixeira, E.G. de Moraes, O.R.K. Montedo, A.P.N. de Oliveira, Development of translucent ceramic tiles from modified porcelain stoneware tile paste, J. Build. Eng. 45 (2022) 103543. https://doi.org/10.1016/j.jobe.2021.103543

[11] Z. Tian, Homogenization of mechanical and thermal properties of fired clay bricks: Effects of porosity, Doctoral dissertation, INSA Toulouse, Toulouse, 2018. https://theses.hal.science/tel-01897937v1

[12] J. García-Ten, M.J. Orts, A. Saburit, G. Silva, Thermal conductivity of traditional ceramics. Part II: Influence of mineralogical composition, Ceram. Int. 36 (2010) 2017-2024. https://doi.org/10.1016/j.ceramint.2010.05.013

[13] I.A. Kalaf, P.R. Nalanakumar, K.A. Shariff, A.H. Mohammed, Effect of Iraqi porcelanite composition on the properties of ceramic tiles: Experimental and simulation works, J. Phys.: Conf. Ser. 2907 (2024) 012023. https://doi.org/10.1088/1742-6596/2907/1/012023

Materials Research Proceedings 74 (2026) 148-155 https://doi.org/10.21741/9781644904473-19

Enhancing Recycled Polypropylene Composites with Rice Husk Biochar via Electron Beam Irradiation

Syahirah YUSSOFF[1,a], Noor Fauziyah ISHAK[1,b *] and Muhammad Hazim MUHAMMAD SAYUTI[2,c]

[1]Faculty of Chemical Engineering, Universiti Teknologi MARA, 40450 Shah Alam, Selangor, Malaysia

[2]Malaysian Institute for Nuclear Technology Research, 43600 Kajang, Malaysia

[a]Syahirahyussoff@gmail.com, [b]noorfauziyah@uitm.edu.my, [c]hazim@nm.gov.my

Keywords: Recycled Polypropylene, Rice Husk, Biochar, Biocomposites, Electron Beam Irradiation

Abstract. Bio-composites combining waste plastics and natural fillers are proposed as a sustainable alternative for the reduction of plastic waste and resource exhaustion. The mechanical, chemical, thermal, and morphological properties of recycled polypropylene (rPP)/rice husk (RH) and rPP/rice husk biochar (RHB) composites are investigated with a focus on the enhancement of their performances owing to electron beam irradiation (EBI). The composites were prepared with a 70:30 weight ratio of rPP to reinforcement, followed by a sequential procedure that involved RH pre-treatment, melt compounding, hot pressing, and irradiation at different doses (0, 10, 20, 30 and 40 kGy). Mechanical tests, including tensile, flexural, and impact strength were elucidated the influence of EBI. The results demonstrate that the rPP/RHB composites show improvement in tensile strength, thermal stability and fiber-matrix adhesion, mostly because of improved crosslinking and surface alteration brought on by the EBI technique. A robust network of improvement was indicated by the tensile strength which increased from 0.67 MPa of rPP/RH at 0 kGy to 0.85 MPa of rPP/RHB at 40 kGy. The best range for irradiation was found to be at 10 kGy and 20 kGy since these doses showed the most consistent and balanced improvement, without any indication of degradation. The fabrication of high-performing and eco-friendly biocomposites for the automotive, building and packaging sectors is greatly impacted by these discoveries.

Introduction

Biocomposites, combining natural fillers with polymers, have garnered increasing attention in recent years due to their potential to create sustainable materials with favorable mechanical and environmental properties [1]. These materials play a crucial role in addressing global concerns about plastic waste, resource scarcity, and the need for environmentally friendly alternatives in manufacturing. Recycled polypropylene (rPP) is a particularly attractive polymer for biocomposites because of its recyclability, cost-effectiveness, and mechanical durability. When reinforced with natural fibers like rice husk, these composites offer a promising solution for reducing environmental impact while maintaining functional performance. In addition, rice husk (RH), an agricultural by-product, is abundant, biodegradable, and cost-efficient [2]. It has been widely used as a filler in biocomposites due to its light weight, high silica content, and ability to enhance the stiffness and strength of composites [3]. Cionita et al. (2024) indicate that optimal RH loading (around 20-40 wt%) can significantly improve tensile and flexural strength, although challenges such as moisture absorption and poor fiber-matrix adhesion persist [4].

The growing demand for sustainable materials has increased interest in biocomposites made from recycled polymers and natural fillers like RH. However, hydrophobic polymers like rPP pose a challenge when integrated with hydrophilic natural fibers like RH, due to poor compatibility at

Content from this work may be used under the terms of the Creative Commons Attribution 3.0 license. Any further distribution of this work must maintain attribution to the author(s) and the title of the work, journal citation and DOI. Published under license by Materials Research Forum LLC.

the fiber-matrix interface. This incompatibility can lead to moisture absorption and compromised mechanical properties [5]. Addressing these challenges is essential for improving the performance and applicability of biocomposites in high-performance industries, ensuring they meet both functional and environmental standards. Surface treatments like alkaline and silane modifications have been explored to enhance compatibility and performance, thereby mitigating issues related to the hydrophilic nature of RH [6]. Furthermore, electron beam irradiation (EBI) is an advanced technique that significantly enhances the properties of polymer composites by inducing cross-linking and chain scission, depending on the irradiation dose applied. This clean and efficient process generates free radicals that facilitate the formation of three-dimensional network structures, improving mechanical properties such as tensile strength and thermal stability [7]. For instance, studies have shown that EBI can increase the impact strength of carbon fiber-reinforced polypropylene composites by up to 103% at optimal doses [8].

Additionally, EBI has been effectively utilized in modifying various polymeric systems, including blends and nanocomposites, resulting in improved chemical resistance and processability, which are crucial for applications in industries such as automotive and aerospace [9]. The study by Chen et al. investigates the mechanical and thermal properties of gamma-radiation-induced recycled polymer blend composites reinforced with rice husk, revealing significant enhancements in tensile strength and thermal stability. The research demonstrates that incorporating RH at optimal levels (up to 70 wt%) improves the composites' performance, with tensile strength reaching 21.2 MPa and elastic modulus at 1.6 GPa, attributed to effective fiber-matrix adhesion and cross-linking effects from gamma irradiation [10].

To address these gaps, this study proposes a novel route that incorporates rice husk biochar (RHB) into rPP matrices, in conjunction with EB). RHB has been shown to significantly enhance the mechanical, thermal, and fire-retardant properties of recycled high-density polyethylene (HDPE) composites by improving up to ~24% in tensile and flexural strength at ~30 wt% loading, along with enhanced thermal stability and flame resistance [11]. No study to date has explored its role in reinforcing rPP, especially in conjunction with EBI for interface enhancement and cross-linking. By combining RHB’s porous, high-surface-area structure with rPP’s recyclability and durability and applying EBI to foster cross-linking and interfacial bonding. This study aims to overcome the hydrophilicity-induced adhesion issues and moisture sensitivity typical of conventional rPP/RH bio-composites. Through careful optimization of irradiation dose (10 – 40 kGy), this work seeks to deliver sustainable rPP/RHB biocomposites with balanced structural and environmental performance suitable for advanced applications.

Materials

This study utilized rPP sourced from industrial recycling streams and RH obtained from a local agricultural supplier. The RH was cleaned, dried to remove moisture, and ground into a fine powder for uniformity and compatibility with the polymer matrix. The composites were prepared by using rPP, reinforced with RH and pyrolyzed RHB. The pyrolysis is conducted at 400°C for 2 hours using a Carbolite tube furnace. The preparation of biocomposites involves formulating rPP/RH and rPP/RHB in a 70:30 weight ratio. The biocomposites undergone pre-mix using 3D Mixer before being carried out using a thermal mixer at 170°C.

Methods of testing and characterization

The mechanical, chemical, thermal, and morphological properties of rPP/RH and rPP/RHB composites were systematically evaluated. Comparative analysis between RH- and RHB-based systems was performed to determine the effects of EBI, with optimal irradiation doses identified from their influence on composite performance. This methodology provides a comprehensive basis for establishing processing conditions that maximize the overall properties of the composites. The mechanical properties of the fiber-reinforced polymer were determined using tensile, flexural and impact tests. A Tinius Olsen Universal Testing Machine equipped with a load of 50 kN and

crosshead speed of 5 mm/min was used in this study to perform tensile and flexural analysis according to ASTM D638 Type IV and ASTM D790. Meanwhile, an ASTM D256 standard was used to conduct the impact test using Tinius Olsen Pendulum Impact Testing Machine.

Results and discussion

Tensile analysis

Fig. 1 illustrates the tensile strength variation of rPP/RH and rPP/RHB under different EBI dosages. For rPP/RH, the tensile strength starts at 0.67 MPa (0 kGy) and increases to 0.77 MPa (10 kGy) and 0.74 MPa (20 kGy), attributed to enhanced filler–matrix interaction and cross-linking between rPP chains [12]. At 30 kGy, tensile strength drops sharply to 0.59 MPa, indicating chain scission and oxidative degradation dominate at higher irradiation doses [13]. A slight recovery is seen at 40 kGy (0.72 MPa), which may be linked to recrystallization and structural rearrangement processes [14].

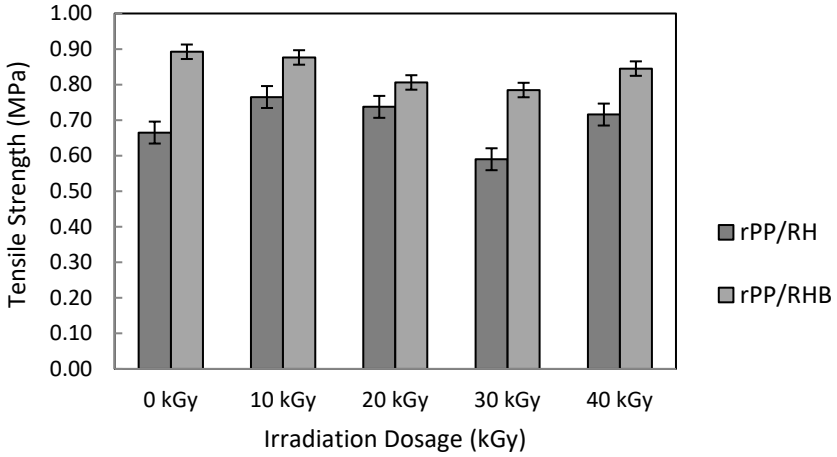


Fig. 1. Tensile strength of rPP/RH and rPP/RHB composites at different EBI dosages.

In contrast, rPP/RHB composites show consistently higher tensile strength across all doses. At 0 kGy, the composite records 0.89 MPa, which slightly decreases to 0.88 MPa (10 kGy) and 0.81 MPa (20 kGy), reflecting the stabilizing effect of biochar on filler–matrix adhesion and network cross-linking [15]. Even at higher doses, rPP/RHB maintains superior properties compared to rPP/RH, with 0.78 MPa (30 kGy) and 0.85 MPa (40 kGy). This resilience is attributed to biochar's radical scavenging capacity, thermal stability, and its ability to improve interfacial bonding and thus mitigate irradiation-induced degradation [16]. Recent studies confirm that RHB significantly improves the mechanical and thermal stability of recycled polyolefin composites compared to untreated RH fillers [17].

Overall, the optimum irradiation window lies between 10–20 kGy, where tensile properties are maximized (0.77 MPa for rPP/RH, 0.88 MPa for rPP/RHB). Beyond this range, degradation mechanisms such as chain scission dominate and reduce strength. However, rPP/RHB consistently exhibits higher tensile values across all doses, confirming that pyrolyzed rice husk (biochar) provides a reinforcing and stabilizing effect [18]. At lower doses (10–20 kGy), both systems experience tensile enhancement, attributable to improved filler-matrix bonding and controlled cross-linking. The rPP/RHB system outperforms the rPP/RH baseline across all doses, likely due to biochar's superior interfacial morphology and intrinsic mechanical reinforcement. However, at 30 kGy, tensile strengths decline in both composites, which is an outcome consistent with prevailing literature, where excessive irradiation initiates chain scission, undermining structural integrity.

Flexural analysis

Fig. 2 presents the flexural strength of rPP/RH and rPP/RHB composites under EBI at 0–40 kGy. For rPP/RH, the baseline flexural strength is 38.17 MPa at 0 kGy. A decrease to 36.67 MPa at 10 kGy suggests that early chain scission or interfacial debonding may dominate at lower doses. At 20 kGy, strength recovers to 40.17 MPa, indicating that radiation-induced crosslinking begins to outweigh degradation by reinforcing the polymer–filler interface. Beyond this, a sharp decline to 35.83 MPa at 30 kGy implies accelerated structural deterioration, although a modest rebound at 38.10 MPa (40 kGy) hints at partial molecular reorganization or localized recrystallization processes [19].

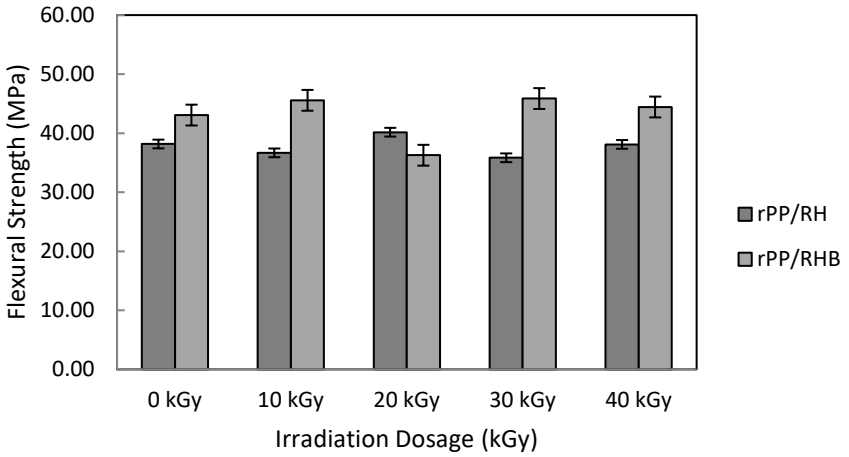


Fig. 2. Flexural strengths of rPP/RH and rPP/RHB composites at different EBI dosages.

In contrast, rPP/RHB composites consistently outperform rPP/RH across all irradiation doses. At 0 kGy, flexural strength begins at 43.07 MPa which is already superior due to biochar's higher stiffness and interfacial compatibility. Maximum strength is observed at 45.57 MPa (10 kGy) and 45.87 MPa (30 kGy), suggesting that these irradiation windows provide an optimal balance between crosslinking and enhanced filler dispersion, which promotes stronger fiber–matrix interlocking [20]. Meanwhile, at 20 kGy and 40 kGy, flexural strength at 36.27 MPa and 44.43 MPa respectively which highlights biochar's stabilizing role against chain scission by scavenging free radicals and improving stress transfer across the matrix [21].

Overall, these results confirm that biochar reinforcement (RHB) provides superior flexural performance compared to untreated RH. The enhanced surface area, rigidity, and interfacial bonding of biochar contribute to more efficient stress transmission, mechanical interlocking, and thermal stability. However, the non-linear behavior of flexural strength across radiation doses reflects the competing mechanisms of crosslinking and chain scission, with optimal properties occurring at 10 kGy and 30 kGy for rPP/RHB. For rPP/RH, improvements are more limited and inconsistent due to weaker fiber–matrix adhesion and lower thermal stability [21].

Impact strength analysis

Fig. 3 illustrates the variation in impact strength of rPP/RH and rPP/RHB composites after exposure to different irradiation doses (0–40 kGy). For rPP/RH composites, the initial impact strength at 0 kGy is 1.58 kJ/mm². A slight improvement is observed at 10 kGy (1.60 kJ/mm²) and 20 kGy (1.63 kJ/mm²), suggesting that limited crosslinking at lower doses enhances toughness. However, a significant reduction to 1.16 kJ/mm² occurs at 30 kGy, attributed to radiation-induced deterioration processes such as chain scission, polymer embrittlement, and weakened fibre–matrix adhesion [22]. At 40 kGy, a minor recovery to 1.28 kJ/mm² is noted, possibly due to restricted structural reorganization or residual crosslinking, though still below the initial strength.

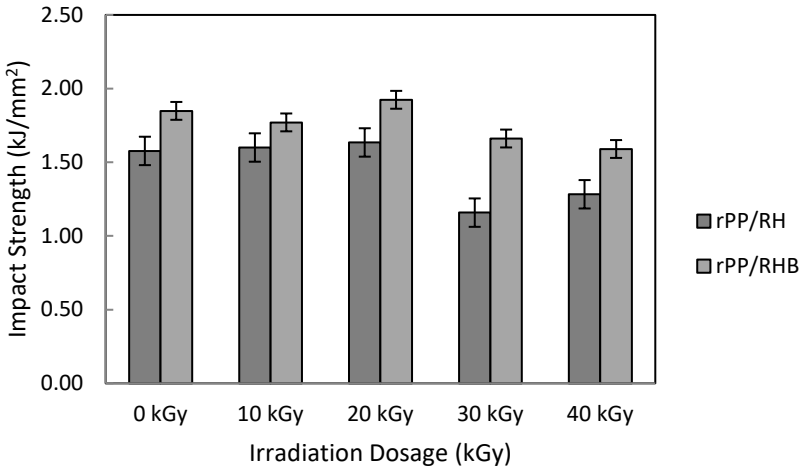


Fig. 3. Impact strength of rPP/RH and rPP/RHB composites at different EBI dosages.

In contrast, rPP/RHB composites consistently outperform rPP/RH at all irradiation doses. The initial impact strength at 0 kGy is 1.85 kJ/mm², rising to the highest value of 1.95 kJ/mm² at 20 kGy. This enhancement is linked to improved interfacial bonding and optimized crosslinking between the polymer matrix and biochar filler, which facilitates superior energy dissipation under impact [23]. At higher doses (30 kGy and 40 kGy), impact strength decreases slightly but remains higher than the equivalent rPP/RH composites, indicating greater resistance to irradiation-induced degradation. The improved performance of rPP/RHB is attributed to the rigid structure, large surface area and high stability of biochar, which promote better filler–matrix interaction, stress transfer and fracture resistance [24]. This enables the composite to absorb and release more energy upon impact compared to untreated RH fillers.

Overall, both rPP/RH and rPP/RHB composites reach their optimal impact strength at 20 kGy, indicating that this dosage maximizes toughness before degradation effects dominate. At higher doses, chain scission surpasses crosslinking effects, particularly in rPP/RH, which lacks the stabilizing and reinforcing contributions of biochar.

Comparative discussion of mechanical properties

Table 1 provides a comparative analysis of the percentage changes in tensile, flexural, and impact strengths relative to the non-irradiated control samples. The results indicate that 10 and 20 kGy irradiation dosages produce the most favorable improvements, although the optimum property varies between rPP/RH and rPP/RHB composites. For tensile strength, rPP/RH recorded the highest increase at 10 kGy (15.04%), while rPP/RHB experienced only marginal losses (–1.79%). At 20 kGy, tensile strength improved moderately for rPP/RH (10.88%) but decreased for rPP/RHB (–9.68%), suggesting that biochar-filled composites are more sensitive to over-crosslinking under prolonged irradiation. Flexural strength showed its best performance at 20 kGy for rPP/RH (5.24%) and at 30 kGy for rPP/RHB (6.50%), indicating that the addition of biochar shifts the optimum dosage towards higher radiation exposure due to its rigid reinforcement effect. Impact strength exhibited a similar trend, with rPP/RH peaking at 20 kGy (3.64%), while rPP/RHB achieved the highest improvement at 20 kGy (4.07%) compared to its negative performance at 10 kGy.

Overall, these findings reveal that rPP/RH composites benefit most consistently at 10–20 kGy, while rPP/RHB composites exhibit delayed improvements, particularly in flexural strength at 30 kGy, highlighting biochar's ability to buffer radiation-induced chain scission and sustain structural reinforcement. Importantly, excessive irradiation beyond 30 kGy resulted in performance deterioration across all properties, dominated by polymer chain scission and matrix degradation.

In conclusion, for applications requiring higher stiffness (flexural strength), 30 kGy with biochar reinforcement is optimal, but for achieving balanced overall mechanical performance across tensile, flexural, and impact properties, 20 kGy is the most effective irradiation dosage.

Table 1. Percentage performance of mechanical properties for rPP/RH and rPP/RHB composites.

Mechanical Properties	Tensile strength (%)		Flexure strength (%)		Impact strength (%)	
Dose (kGy)	rPP/RH	rPP/RHB	rPP/RH	rPP/RHB	rPP/RH	rPP/RHB
10	15.04	-1.79	-3.93	5.80	1.47	-4.23
20	10.88	-9.68	5.24	-15.79	3.64	4.07
30	-11.28	-12.07	-6.11	6.50	-26.55	-10.14
40	7.62	-5.30	-0.17	3.17	-18.65	-13.99

Conclusion

This study demonstrates the potential of rPP/RH and rPP/RHB composites as sustainable biocomposites modified through electron beam irradiation (EBI) at 0, 10, 20, 30, and 40 kGy. The results reveal that rPP/RHB consistently outperforms rPP/RH in terms of mechanical stability and resistance to irradiation-induced deterioration, owing to the stabilizing role of biochar. Moderate irradiation doses (10–20 kGy) were found to be optimal, enhancing tensile, flexural, and impact properties through effective crosslinking while minimizing chain scission. The observed patterns are further supported by structural analyses, which highlight the crosslinking tendency in RH-filled composites and the superior dimensional stability provided by RHB. Overall, these findings contribute to the development of high-performance, eco-friendly composites that align with resource efficiency and waste reduction goals. To establish a more comprehensive understanding of their behavior and long-term performance, future investigations should incorporate advanced techniques such as thermogravimetric analysis (TGA), X-ray photoelectron spectroscopy (XPS), and field emission scanning electron microscopy (FESEM). Looking ahead, the enhanced durability and thermal stability of rPP/RHB composites suggest promising applications in packaging, automotive parts, and construction materials, where sustainability and performance under demanding conditions are equally critical.

Acknowledgement

The authors wish to convey their appreciation to the Malaysian Institute for Nuclear Technology Research and Universiti Teknologi MARA (UiTM) for supporting the facilities and resources required to conduct this research.

References

[1] J. Kim, D. Cho, Effects of waste expanded polypropylene as recycled matrix on the flexural, impact, and heat deflection temperature properties of kenaf fiber polypropylene composites, Polymers 12 (2020) 2578. https://doi.org/10.3390/polym12112578.

[2] M.A. Morales, C.L. Atencio Martinez, A. Maranon, C. Hernandez, V. Michaud, A. Porras, Development and characterization of rice husk and recycled polypropylene composite filaments for 3D printing, Polymers 13 (2021) 1067. https://doi.org/10.3390/polym13071067

[3] N. Choophun et al., Natural rubber composites reinforced with green silica from rice husk: Effect of filler loading on mechanical properties, J. Compos. Sci. 6 (2022) 369. https://doi.org/10.3390/jcs6120369

[4] T. Cionita et al., Mechanical characteristics of biocomposites based on rice husk reinforced recycled polypropylene, Int. J. Integr. Eng. 16 (2024) 278–287. https://doi.org/10.30880/ijie.2024.16.02.029

[5] D.D.P. Moreno, R.V. de Camargo, D. dos Santos Luiz, L.T.P. Branco, C.C. Grillo, C. Saron, Composites of recycled polypropylene from cotton swab waste with pyrolyzed rice husk, J. Polym. Environ. 29 (2021) 350–362. https://doi.org/10.1007/s10924-020-01883-9

[6] S. Monga, M. Kadian, S. Nagoria, S. Kumar, M. Verma, A review on mechanical improvements and environmental benefits of rice husk reinforced polymer composites, Curr. World Environ. 19 (2025) 1077–1100. https://doi.org/10.12944/cwe.19.3.4

[7] T. Abou Elmaaty, S. Okubayashi, H. Elsisi, S. Abouelenin, Electron beam irradiation treatment of textiles materials: A review, J. Polym. Res. 29 (2022). https://doi.org/10.1007/s10965-022-02952-4

[8] H. Kimura et al., Strengthening process by electron beam to carbon fiber for impact strength enhancement of interlayered thermoplastic polypropylene carbon fiber composite, Materials 15 (2022) 7620. https://doi.org/10.3390/ma15217620

[9] B.K. Sharma, A. Jha, R. Agarwal, S.R. Chowdhury, S.S. Ray, Development of multi-component polymeric systems by high energy radiation, in: S.R. Chowdhury (Ed.), Applications of High Energy Radiations: Synthesis and Processing of Polymeric Materials, Springer Nature Singapore, Singapore, 2023, pp. 317–346. https://doi.org/10.1007/978-981-19-9048-9_10

[10] R.S. Chen, M.H. Ab Ghani, S. Ahmad, M.A. Tarawneh, S. Gan, Tensile thermal degradation and water diffusion behaviour of gamma radiation induced recycled polymer blend rice husk composites: Experimental and statistical analysis, Compos. Sci. Technol. 207 (2021) 108748. https://doi.org/10.1016/j.compscitech.2021.108748

[11] A. ur R. Shah, A. Imdad, A. Sadiq, R.A. Malik, H. Alrobei, I.A. Badruddin, Mechanical thermal and fire retardant properties of rice husk biochar reinforced recycled high density polyethylene composite material, Polymers 15 (2023) 1827. https://doi.org/10.3390/polym15081827

[12] R. Agarwal, S.A. Khader, S. Ray Chowdhury, Effect of electron beam irradiation on the mechanical dynamic mechanical heat shrinkable and morphological properties of linear low density polyethylene ethylene butene copolymer blends, J. Radioanal. Nucl. Chem. 334 (2025) 2997–3007. https://doi.org/10.1007/s10967-025-10054-w

[13] A.M. de Azevedo et al., Ionizing radiation and its effects on thermoplastic polymers: An overview, Polymers 17 (2025) 1110. https://doi.org/10.3390/polym17081110

[14] Q. Zhang et al., Production of high density polyethylene biocomposites from rice husk biochar: Effects of varying pyrolysis temperature, Sci. Total Environ. 738 (2020) 139910. https://doi.org/10.1016/j.scitotenv.2020.139910

[15] H. Baniasadi et al., Can biochar fillers advance the properties of composites? Early stage characterization and life cycle assessment of novel polyamide biochar biocomposites, Environ. Res. 275 (2025) 121446. https://doi.org/10.1016/j.envres.2025.121446

[16] C. Botta, C.M. Grottola, D. Amato, M.R. Acocella, Biochar as sustainable filler of recycled polylactic acid: A new generation of processable biocomposites, Polymers 16 (2024) 3347. https://doi.org/10.3390/polym16233347

[17] N. Marsi et al., Utilization of rice husk fiber blended recycled polyethylene terephthalate for manufacturing RHF/R PET polymer composites, Malays. J. Compos. Sci. Manuf. 16 (2025) 245–257. https://doi.org/10.37934/mjcsm.16.1.245257

[18] K. Papadopoulou, N.M. Ainali, O. Mašek, D.N. Bikiaris, Biochar as a UV stabilizer: Its impact on the photostability of poly(butylene succinate) biocomposites, Polymers 16 (2024) 3080. https://doi.org/10.3390/polym16213080

[19] D. Wong, G. Fabito, S. Debnath, M. Anwar, I.J. Davies, A critical review: Recent developments of natural fiber rubber reinforced polymer composites, Cleaner Mater. 13 (2024) 100261. https://doi.org/10.1016/j.clema.2024.100261

[20] O. Das, D. Bhattacharyya, A.K. Sarmah, Sustainable eco composites obtained from waste derived biochar: A consideration in performance properties, production costs, and environmental impact, J. Clean. Prod. 129 (2016) 159–168. https://doi.org/10.1016/j.jclepro.2016.04.088

[21] R.K. Dahal, B. Acharya, G. Saha, R. Bissessur, A. Dutta, A. Farooque, Biochar as a filler in glassfiber reinforced composites: Experimental study of thermal and mechanical properties, Compos. Part B Eng. 175 (2019) 107169. https://doi.org/10.1016/j.compositesb.2019.107169

[22] S.R. Allayarov, Y.N. Smirnov, G.P. Belov, L.D. Kispert, J.S. Trasher, D. Nikles, Effect of irradiation on the strength properties of polyethylene matrix glass reinforced plastics, High Energy Chem. 39 (2005) 295–298. https://doi.org/10.1007/s10733-005-0058-6

[23] A.G. Adeniyi et al., Mechanical and chemical characterization of biochar reinforced polystyrene composites, BMC Chem. 18 (2024) 246. https://doi.org/10.1186/s13065-024-01365-2

[24] U.I.A.B.M. Adnan, F.R. Wong, M.F. Morni, A.H. Abdullah, A.A. Rashid, S.K. Yong, Mechanical properties of rice husk recycled polypropylene composite, J. Mech. Eng. SI12 (2023) 45–61. https://doi.org/10.24191/JMECHE.V12I1.24637

Materials Research Proceedings 74 (2026) 156-164 https://doi.org/10.21741/9781644904473-20

Preparation and In Vitro Antibacterial Evaluation of Shrimp Shell-Derived Chitosan–Silica Formulations Against *Escherichia coli*

M.N.A. Uda[1,2,3,4,a *], Chong Siew Hong[2,b], Meor Ahmad Faris[1,c], M.K.R. Hashim[1,d], Tijjani Adam[2,e], Z.A. Arsat[1,f], Uda Hashim[4,g], M.N. Afnan Uda[4,h], F. Abdullah[1,i], Maisara A.M. Akhir[5,j], M. Firdaus A. Muttalib[1,k], N.A. Parmin[2,l], A.A.A. Halim[7,m] and N.H. Ibrahim[5,n]

[1]Faculty of Engineering & Mechanical Technology (FKTM), Universiti Malaysia Perlis (UniMAP), 02600 Arau, Perlis, Malaysia

[2]Institute of Nano Electronic Engineering, Universiti Malaysia Perlis, 01000 Kangar, Perlis, Malaysia

[3]Centre of Excellence for Biomass Utilization, Universiti Malaysia Perlis, Arau 02600, Perlis, Malaysia

[4]Center of Excellence Geopolymer & Green Technology (CEGeoGTech), Universiti Malaysia Perlis, 02600, Arau, Perlis, Malaysia

[5]Faculty of Chemical Engineering & Technology, Universiti Malaysia Perlis, 02600, Arau, Perlis, Malaysia

[6]Faculty of Engineering, Universiti Malaysia Sabah, 88400 Kota Kinabalu, Sabah, Malaysia

[7]Faculty of Electronic Engineering & Technology, Universiti Malaysia Perlis (UniMAP), 02600 Arau, Perlis, Malaysia

[a]nuraiman@unimap.edu.my, [b]s201191742@studentmail.unimap.edu.my, [c]meorfaris@unimap.edu.my, [d]khairulrabani@unimap.edu.my, [e]tijjani@unimap.edu.my, [f]zainalabidin@unimap.edu.my, [g]uda@ums.edu.my, [h]nurafnan@ums.edu.my, [i]fadhilnor@unimap.edu.my, [j]maisaraazad@unimap.edu.my, [k]firdausmuttalib@unimap.edu.my, [l]azizahparmin@unimap.edu.my, [m]ashrafhalim@unimap.edu.my, [n]hulwani@studentmail.unimap.edu.my

Keywords: Chitosan–Silica Nanoparticles, Size-Dependent Properties, Antimicrobial Activity, Green Synthesis, Biowaste Valorization

Abstract. The in vitro antibacterial activity of chitosan–silica (CS–Si) formulations prepared using commercial silica nanoparticles with nominal particle sizes of 20 nm, 50 nm, and 100–200 nm was investigated. Chitosan was extracted from shrimp shell waste and combined with silica nanoparticles to prepare the CS–Si formulations. The antibacterial activity was evaluated against Gram-negative *Escherichia coli* using the agar disc diffusion method at different concentrations. The results demonstrated variable antibacterial responses across the tested formulations and concentrations without a consistent concentration-dependent or particle-size-dependent relationship. The formulation prepared using nominally 20 nm silica exhibited the largest inhibition zone of 7.20 ± 0.20 mm at 0.25 mg/100 μL, whereas the formulations prepared using nominally 50 nm and 100–200 nm silica exhibited measurable inhibition under selected test conditions. However, the nominal particle sizes represent the starting silica materials rather than the measured sizes of the final CS–Si formulations. These findings indicate that the prepared formulations exhibited limited and variable in vitro antibacterial activity against *E. coli*. Further

Content from this work may be used under the terms of the Creative Commons Attribution 3.0 license. Any further distribution of this work must maintain attribution to the author(s) and the title of the work, journal citation and DOI. Published under license by Materials Research Forum LLC.

physicochemical characterization and quantitative antibacterial testing are necessary to establish their properties and evaluate their potential applications.

Introduction

The increasing demand for biocompatible and multi-functional nanomaterials has stimulated many researchers to investigate this type of bio-based antimicrobial materials to be applied in different fields mainly agriculture, food packaging, the environment, and biomedical areas [1], [2], [3]. Chitosan is a natural biopolymer widely used as traditional food applications due to its biological active properties with antimicrobial potentials, and chitosan–silica nanoparticles (CS–Si NPs) are exhibiting mechanical stability because they combine intrinsic antimicrobial properties of chitosan along with the structural stability, high surface area and mechanical strength of silica nanoparticles [4]. In this sense, the incorporation of these two materials is a good strategy for obtaining new hybrid nanomaterials with better physicochemical and biological properties.

Chitosan (C) is a polysaccharide obtained through the chemical conversion or deacetylation of chitin which is originated from crustaceans such as shrimps. Due to its well-known biodegradability, biocompatibility, low toxicity and renewable nature chitosan has been widely investigated as an antimicrobial, biomedical, pharmaceutical and agricultural agent [5]. The strong positive charges of the amino groups are mainly responsible for their ability to exert antibacterial action through electrostatic interactions with a negatively charged surface of bacterial membranes which led to membrane rupture, leakage of intracellular components and cessation of bacterial growth. However, chitosan is not easily reusable due to lower mechanical stability than normal polymers and because it is sensitive to a variety of environmental impacts [6].

The addition of silica nanoparticles in chitosan matrices can alleviate these disadvantages by enabling the modulus stability, thermal stability, and dispersion of the nanoparticle to be buffered. Silica nanoparticles have their specific surface area which can potentially increase interaction between antimicrobial agents and bacterial cells [7]. Chitosan–silica nanocomposites are possible materials for when employed in medical device coatings, as food packaging films, and antimicrobial wound-healing agents and agricultural control agents. Due to their intrinsic combination of biocompatible, antimicrobial activity and structural stability properties, these nanomaterials have a clear interest in fighting against gram-positive and gram-negative bacteria either for biomedical or agricultural applications [8].

Particle size is one of the most important factors for the antibacterial activity of nanomaterials. In general, smaller nanoparticles have a relatively large specific surface area and higher-level environmental mobility; they are also more likely to penetrate cell membranes than larger particles and exert significant effects on the ability of bacteria to thrive. These features allow for the improved exposure of nanoparticles to bacterial cells that contribute to a greater antibacterial effect due to the increased surface-mediated and/or cellular interactions [9]. While the effects of particle size are comparatively well established, relatively little systematic work has sought to correlate paired silica nanoparticles of commercially available sizes with the resulting physicochemical properties and antibacterial activity of chitosan–silica nanoparticles. The most previous studies only focused single silica nanoparticles or chitosan-based nanoparticles, while the size-dependent behaviour of encapsulated chitosan–silica nanocomposites are largely studied.

This study investigates the antimicrobial properties of size-selected encapsulated chitosan-silica nanoparticles (CS-Si NPs) synthesized from commercially available silica nanoparticles with nominal particle sizes spanning 20 nm, 50 nm, and 100 -200 nm against bioluminescent Gram-negative *Escherichia coli* (*E. coli)*. Brief description of the size range nominal particles was tested in small, intermediate and relatively large ranges to systematically evaluate their potential impact on the antibacterial activity of silica nanoparticles. This study used three different CS–Si nanoparticle formulations produced from silica nanoparticles of differing nominal particle sizes under identical synthesis and antimicrobial testing conditions for a direct comparison. The

information gathered in this work addresses the correlation between silica nanoparticle nominal size and antibacterial potency of respective CS–Si NPs, which will allow for the development of renewable bio-based antimicrobial nanomaterials that can be applied to agriculture, food safety or biomedicine.

Materials and Methods

Materials

Shrimp shell waste was sourced from nearby seafood restaurants and utilized as an eco-friendly biomass raw material for chitosan extraction. The chitosan–silica (CS–Si) formulations were prepared using commercially available silica nanoparticles with nominal particle sizes of 20 nm, 50 nm and 100–200 nm. The particle sizes were defined by the manufacturer and refer to the initial silica materials rather than the final experimentally determined particle size of CS–Si. Commercial analytical-grade sodium hydroxide (NaOH), hydrochloric acid (HCl), acetic acid, and ethanol were used without any purification. Institute of Nano Electronic Engineering, Universiti Malaysia Perlis (UniMAP) provided the distilled water. The Gram-negative bacterium *Escherichia coli* is isolated from the bacterial culture stock collection in the Faculty of Chemical Engineering and Technology, Universiti Malaysia Perlis (UniMAP). The records of the cultures did not document strain designation. The same bacterial culture was taken for all preliminary and subsequent experiments as test organism for the evaluation of antibacterial activity of chitosan and CS–Si formulations.

Extraction of Chitosan

Chitosan was obtained from shrimp shell waste, according to a modified previously reported method involving sequential demineralization, deproteinization and deacetylation [9]. First, 50 g of washed shrimp shells were treated with 500 mL 1 M hydrochloric acid (HCl) solution for demineralization at 35 °C by stirring the mixture continuously at a rate of 200 rpm for a period of time equal to two hours. In the next step, demineralized shells were treated with 1 M sodium hydroxide (NaOH) at a solid to liquid ratio of 1:10 (g/mL) for deproteinization. The temperature was kept at 80 °C and stirred at a rate of 250 rpm for 3 h, followed by subsequent washing with distilled water until neutral pH. Purified chitin was next obtained through treatment with 1% ethanol for 30 min, followed by overnight drying at 70 °C. Deacetylation of the obtained chitin was conducted by adding 12 M NaOH to purified chitin with a solid to liquid ratio at 1:15 (g/mL). The reaction mixture was stirred at 250 rpm and held for 4h at 115 °C. Chitosan obtained from the process, after washing with distilled water to a neutral pH, was dried overnight at 70°C before use.

Preparation of Chitosan–Silica Nanoparticles Formulations

Preparation of chitosan–silica (CS–Si) formulations were carried out according to a modified method from the literature [9]. In the first experiment, the prepared chitosan was dissolved in 1% (v/v) acetic acid and the commercial silica nanoparticles were separately dispersed in deionized water at a concentration of 0.5 g/L then mixed with chitosan and maintained at mass ratio of 1:1 (w/w). Chitosan solution was dropwise added into the silica nanoparticle suspension with vigorous magnetic stir at room temperature. At that moment, the pH of the acquired silica suspension with chitosan was modified to 9 using acetic acid and sodium hydroxide before proceeding with the rest reactions. This mixture was stirred at 200 rpm for 12 h, allowing interactions between chitosan and silica. The obtained material was then centrifuged at 6000 rpm for 15 min and washed several times with deionized water to reduce the residuals. The re-collected material was air dried for 24 h in a drying oven at 70 °C. The total mass yield of produced CS–Si formulations was experimentally calculated to be about 88%. Silica nanoparticles with nominal sizes of 20 nm, 50 nm and 100-200 nm in diameter were used to prepare three CS–Si formulations. Note that these values are manufacturer-specified cumulative sizes of the starting silica materials, not measured sizes of the final formulations. The materials are termed CS–Si formulations because the generation of a continuous chitosan coating or core–shell structure was not verified independently

Antimicrobial Activity

Chitosan and CS–Si formulations were examined for their antibacterial activity against *Escherichia coli* using the agar disc diffusion method, according to a modified standard operating protocol by other investigators [10]. Suspensions of the bacteria were performed in normal saline until a suspension comparable to the 0.5 McFarland turbidity standard was obtained before performing all tests. All the experiments were performed using sterile filter-paper discs with a diameter of 5 mm. Amoxicillin at a stock of 1 mg/100 µL was set up as the positive control and sterile distilled water served as negative control. Three independent biological replicates (n = 3) were used to evaluate each treatment, represented through separate bacterial cultures and Petri dishes. Each replicate plate provided one measurement of the inhibition zone. Zone diameters were measured in millimetres (5 mm for filter-paper disc). Scores of 0 mm indicated that no inhibition halo could be clearly seen. The results were indicated as mean ± standard deviation (SD)

Preparation of Nutrient Agar Plates

Nutrient agar medium was prepared by mixing nutrient agar powder (15 g) in 500 mL of distilled water with continuous stirring until the solution became homogeneous. Medium was sterilized by autoclaving at 121 °C for 15 min and let to cool until ~45–50 °C prior to aseptic pouring approximately 25 mL of sterile nutrient agar in each sterile Petri dish (90 mm diameter × 14 mm height) fixed inside a laminar flow cabinet. The average agar depth was 3.9 mm when the accepted volume of agar was extrapolated with a nominal diameter (150 mm) while assuming uniform distribution of the medium over an even cross-sectional area. Room temperature was then maintained to let the agar solidify. Plates were sealed to reduce cross-contamination and stored at 4 °C until used.

Agar Disk Diffusion Assay

Chitosan and CS–Si formulations were used in the agar disc diffusion assay to test the antibacterial response using *Escherichia coli.* In brief, 80 µL of 0.5 McFarland standardized bacterial suspension was spread evenly across the entire surface of nutrient agar plates with a sterile L-shaped spreader to create a bacterial lawn. After being dispersed in distilled water using vortex mixing, the chitosan and CS–Si test preparations were applied to the filter-paper discs. Discs (5mm diameter) of sterile filter-paper were aseptically placed on the inoculated agar surface. Four filter-paper discs placed on each Petri dish and 8 µL of the appropriate sample preparation pipetted onto each disc.

The test formulations were prepared as stock solutions or dispersions at concentrations of 1.00, 0.50, 0.25, 0.125, 0.063 and 0.0313 mg/100 µL (data do not indicate respective amounts applied per disc but indicate the standards indicated in separate Mg/ml). For each disc, an aliquot volume of 8 µL was loaded. Amoxicillin was used as a positive control (1 mg of amoxicillin in 100 µL, 8µL/disk = 80 µg/disc). Sterile distilled water was used as a negative control. Plates were incubated for 24 h at 37 °C, whereafter inhibition-zone diameters (mm, including the included filter-paper disc diameter of 5 mm) were measured. If no clear inhibition halo was visible, the result was recorded as 0 mm. Three independent bacterial cultures were tested for each treatment formulation, one of the Petri dishes was used to evaluate inhibition-zone in a single replicate. Results are presented as mean ± SD. Inhibition-zone sizes were interpreted as measures of apparent rather than intrinsic antibacterial activity in the conditions tested, because agar diffusion is affected by dispersion and diffusion properties of particulate material [14]. Other assays such as the minimum inhibitory concentration (MIC) and/or minimum bactericidal concentration (MBC) determination should be considered for further evaluating.

Statistical Analysis

The antibacterial assays were conducted with three independent biological replicates per treatment (n = 3) using different bacterial cultures in different Petri dish. Inhibition-zone

measurements were reported as mean ± SD. Antibacterial responses were described due to the presence of large numbers of observations with no visible inhibition, which limited the utility of standard parametric statistical comparisons. Consequently, assertions of statistically significant differences between formulations or concentrations were not attributed. We recommend further experimentation with additional independent replicates and statistical methods appropriate for the response distribution being analyzed to validate treatment differences statistically.

Results and Discussion

Antimicrobial Properties of Chitosan and Chitosan–Silica Formulations

Antibacterial activity of chitosan and chitosan–silica (CS–Si) formulations on the Gram-negative bacterium, *Escherichia coli* was determined with the agar disc diffusion assay. Commercially available silica nanoparticles were used to prepare 20 nm, 50 nm, and 100–200 nm CS–Si formulations. The results are expressed as mean ± standard deviation (SD) of the inhibition-zone diameters from three independent biological replicates (n = 3), each performed using a different bacterial culture and Petri dish, and presented in Table 4.6. Agar diffusion results for a representative extract are shown in Fig. 1. For the positive control group, amoxicillin was used, while for the negative control group sterile distilled water was utilized. Amoxicillin produced a mean inhibition-zone diameter of 11.00 ± 0.20 mm, which was the average over three replicates and used as a common positive-control reference for all tested formulations. For the distilled-water negative control (0.00 ± 0.00 mm), inhibition was not visually observed.

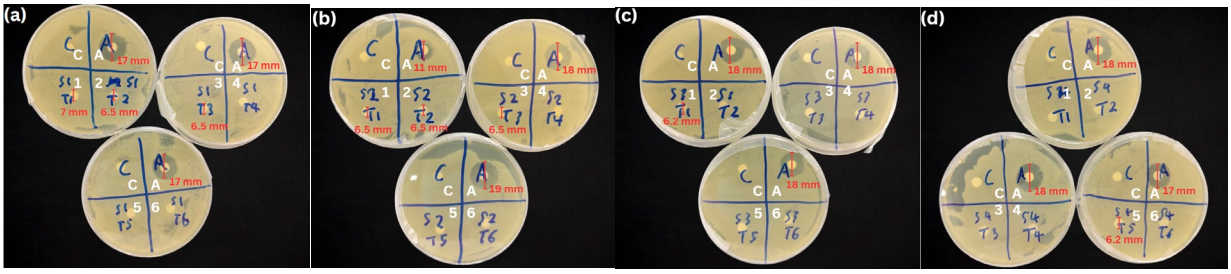


Fig. 1. Photographs of the representative agar disk diffusion assay illustrating diverse antibacterial activity against Escherichia coli of (a) chitosan, (b) 20 nm silica nanoparticles containing chitosan–silica formulation, (c) 50 nm silica nanoparticles containing chitosan–silica formulation and (d) 100–200 nm silica nanoparticles containing a chitosan–silica formulation. The sample discs correspond to 1.00, 0.50, 0.25, 0.125, 0.063 and 0.0313 mg/100 µL sample–sample volume is yet to be verified in original position. Amoxicillin (A) and distilled water (C) were used as a positive and negative control, respectively.

Antibacterial responses were formulation and concentration dependent. However, their inhibition patterns did not present a clear concentration dependency and particle sizes alone (nominal dimensions) do not allow for additional physicochemical characterization under standard conditions to confirm a direct particle-size effect. Chitosan showed inhibition at 0.50 mg/100 µL (7.00 ± 0.30 mm) and 0.25 mg/100 µL (6.00 ± 0.20 mm), but no visible inhibitions were recorded in the other concentrations. Antibacterial activity of chitosan may involve electrostatic interactions between positively charged amino groups ($–NH_3^+$) and negatively charged bacterial cell surfaces, which can disrupt membrane integrity [11]. However, the current data on agar diffusion do not corroborate against this mechanism.

The CS–Si formulation that exerted the highest mean inhibition-zone diameter (7.20 ± 0.20 mm) was prepared using a commercially available type of silica nanoparticles (high-purity nonporous silica, nominal particle size = 20 nm) at a concentration of 0.25 mg/100 µL; this same formulation yielded an inhibition-zone diameter of 6.10 ± 0.20 mm when tested at a concentration of 1.00 mg/100 µL; the measured inhibition-zone diameters estimated here are "narrow" since they

approached only approximately ±6 to 7 mm after subtracting the filter-paper discs with diameters equal to that used in our studies (i.e., discs with a diameter equal to that for standard filter-paper discs set to ≈5mm). In general, the CS–Si formulations showed minimal in vitro antibacterial activity against *Escherichia coli* at the conditions tested when compared to that of a positive control (amoxicillin 11.00 ± 0.20 mm). Silica Synthesis Systems The apparent surface area of silica nanoparticles can be affected by decreasing the particle size; smaller particles may have higher specific surface areas, which could impact their interactions with bacterial cells [12]. Nonetheless, this is only a conjectural interpretation since the final CS–Si formulations were not characterized for their actual particle sizes, dispersion behaviour and surface properties. In addition, chitosan–silica interaction may affect antibacterial activity [13], while further physicochemical characterization is needed to assess their contribution in the experimental observations.

Silica nanoparticles with a nominal particle size of 50 nm in diameter showed inhibition-zone diameters of 6.20 ± 0.20 mm (1.00 mg/100 μL) and 6.10 ± 0.20 mm (0.50 mg/100 μL) for the CS–Si formulation). At other tested concentrations, no visible inhibition was observed. Such data point to minimal antibacterial activity at chosen concentrations but do not themselves prove that differences between formulations stem from the actual silica particle size. Differences in the dispersion of particles, interactions with surfaces or diffusion through the agar medium may explain the responses observed [14].

Inhibition-zone diameter has been observed up to 6.50 ± 0.20 mm at a concentration of only 0.0313 mg/100 μL for CS–Si prepared from nominal particle sizes of 100–200 nm, which is defined as measurable inhibition [30]. No inhibition effect was recorded for the other concentrations. However, the unexpected result together with the absence of dose inhibition in several concentrations for other formulations could be considered as evidence of non-monotonic concentration–response relation. Possible reasons include nanoparticles aggregation, dispersion stability, diffusion in agar matrix and interaction with chitosan and silica surface [15]. Both of these explanations are, of course, still speculative and would need to be investigated experimentally. To clarify the antibacterial behaviour of formulations, minimum inhibitory concentration (MIC), minimum bactericidal concentration (MBC) and post-synthesis physicochemical characterisation studies should be performed subsequently.

The mean inhibition-zone diameter was highest for the CS–Si formulation prepared using silica nanoparticles whose nominal particle size is 20 nm among all formulations tested. However, despite the small inhibition zones and heterogeneous responses across concentrations, the antibacterial activity of marinating agents against *Escherichia coli* under these conditions was limited. All results are expressed as mean ± standard deviation (SD) from 3 independent biological replicates. Because the total number of observations with no visible inhibition was large and many aspects of the experimental data are limited, the results were described qualitatively without claims to statistical significance. Moreover, the lack of direct characterization on the final identities of the CS–Si formulations did not allow for confidence in their comparative impacts on anti-bacterial performance as a function of the design parameters underlying particle size. This implies that more experiments and relevant statistical analysis are needed to support the observed differences between formulations for each concentration.

Table 1. Inhibition-zone diameters of chitosan and chitosan–silica formulations against E. coli at different concentrations (mean ± SD, n = 3).

Component	Concentration (mg/100 µL)	Replicate 1 (mm)	Replicate 2 (mm)	Replicate 3 (mm)	Mean ± SD (mm)
Chitosan	1	0	0	0	0.00 ± 0.00
	0.5	6.7	7	7.3	7.00 ± 0.30
	0.25	5.8	6	6.2	6.00 ± 0.20
	0.125	0	0	0	0.00 ± 0.00
	0.063	0	0	0	0.00 ± 0.00
	0.0313	0	0	0	0.00 ± 0.00
CS–Si (nominal 20 nm)	1	5.9	6.1	6.3	6.10 ± 0.20
	0.5	0	0	0	0.00 ± 0.00
	0.25	7	7.2	7.4	7.20 ± 0.20
	0.125	0	0	0	0.00 ± 0.00
	0.063	0	0	0	0.00 ± 0.00
	0.0313	0	0	0	0.00 ± 0.00
CS–Si (nominal 50 nm)	1	6	6.2	6.4	6.20 ± 0.20
	0.5	5.9	6.1	6.3	6.10 ± 0.20
	0.25	0	0	0	0.00 ± 0.00
	0.125	0	0	0	0.00 ± 0.00
	0.063	0	0	0	0.00 ± 0.00
	0.0313	0	0	0	0.00 ± 0.00
CS–Si (nominal 100–200 nm)	1	0	0	0	0.00 ± 0.00
	0.5	0	0	0	0.00 ± 0.00
	0.25	0	0	0	0.00 ± 0.00
	0.125	0	0	0	0.00 ± 0.00
	0.063	0	0	0	0.00 ± 0.00
	0.0313	6.3	6.5	6.7	6.50 ± 0.20
Amoxicillin	1	10.8	11	11.2	11.00 ± 0.20
Distilled water	0	0	0	0	0.00 ± 0.00

Note: Values are expressed as mean ± standard deviation (SD) from three replicate measurements (n = 3). The filter-paper discs had a diameter of 5 mm. Amoxicillin served as the common positive control (11.00 ± 0.20 mm), while distilled water served as the negative control (0.00 ± 0.00 mm). A value of 0.00 mm indicates that no visible inhibition zone was recorded.

Variations in the antibacterial activity of CS–Si formulations likely arose from differences in particle aggregation, dispersion stability and surface interactions that affect their interaction with bacteria. Even so, these factors were not specifically evaluated in the current study and their potential effects are therefore speculative. The CS–Si formulations may also have diffused through the agar and this diffusion can increase or alternatively affect the inhibition-zone measurements potentially influencing these antibacterial responses. Thus, with such limitations, the results should be regarded as preliminary evidence of select in vitro antibacterial activity against *E. coli* rather than confirmation of well-defined mechanisms or clinical applications. Physicochemical characterization, quantitative antibacterial assays, and evaluations of biocompatibility and safety are required to yield better understanding regarding the antibacterial properties and potential applications for these formulations

Conclusion

In this study, the agar disc diffusion method was used to assess the in vitro antibacterial activity of chitosan extracted from shrimp shell (SH), and a mixture of chitosan–silica (CS–Si) against

Escherichia coli. CS–Si formulations were prepared using standard silica nanoparticles with calculated particle sizes of 20, 50, and 100-200 nm. The results showed differences in antibacterial activity across formulations and concentrations, but there were no concentration or particle-size-dependent trends. Of the combinations tested, CS–Si using nominally 20 nm silica nanoparticles yielded the largest mean inhibition zone diameter (7.20 ± 0.20 mm) at 0.25 mg/100 μL, but the narrow inhibition zones reflected a low antibacterial activity relative to the growth conditions employed in this study. Additionally, there was no direct physicochemical characterization conducted on the final CS–Si formulations at these time points which restricts clear conclusions to be made regarding any particle-size effects and possible antibacterial mechanisms of action. In general, these results show some preliminary information of the antibacterial behavior of CS–Si formulations against *E. coli*. To verify and value these results for possible applications, further studies with extensive physicochemical characterization, quantitative antibacterial assays or even biocompatibility and safety tests are needed.

References

[1] M.N.A. Uda, N.H.A. Jalil, M.F.A. Muttalib, F. Abdullah, U. Hashim, S.C.B. Gopinath, M.N. Afnan Uda, S.A. Shamsuddin, N.A. Karim, A.R.W. Yaakub, N.H. Ibrahim, T. Adam, N.A. Parmin, N.A. Baharum, Analysis on Silica and Graphene Nanomaterials Obtained From Rice Straw for Antimicrobial Potential, International Journal of Nanoelectronics and Materials (IJNeaM) 17 (2024) 221-228. https://doi.org/10.58915/ijneam.v17iJune.861

[2] H.M. Azwatul, M.N.A. Uda, S.C.B. Gopinath, Z.A. Arsat, F. Abdullah, M.F.A. Muttalib, M.K.R. Hashim, U. Hashim, M. Isa, M.N. Afnan Uda, A.R.W. Yaakub, N.H. Ibrahim, N.A. Parmin, T. Adam, Synthesis and characterization of silver nanoparticle using sewage algal bloom extract using visual parameter analysis, Materials Today: Proceedings (2023) https://doi.org/10.1016/j.matpr.2023.01.004

[3] H.M. Azwatul, M.N.A. Uda, S.C.B. Gopinath, Z.A. Arsat, F. Abdullah, M.F.A. Muttalib, M.K.R. Hashim, U. Hashim, M. Isa, M.N. Afnan Uda, A.R.W. Yaakub, N.H. Ibrahim, N.A. Parmin, T. Adam, Plant-based green synthesis of silver nanoparticle via chemical bonding analysis, Materials Today: Proceedings (2023) https://doi.org/10.1016/j.matpr.2023.01.005

[4] E. Akdaşçi, H. Duman, F. Eker, M. Bechelany, S. Karav. Chitosan and Its Nanoparticles: A Multifaceted Approach to Antibacterial Applications, Nanomaterials 15 (2025) 126. https://doi.org/10.3390/nano15020126

[5] H.A. Ahmed, Y.A. El-Maradny, M.A. Shalaby, H. El-Menshawy, A.E. Abd EL-Wahab, Isolation and characterization of Chitosan from shrimp shell waste and the sustainable preparation of salicylic acid-loaded Chitosan nanoparticles for antibiofilm applications, Scientific Reports 15 (2025) 19263. https://doi.org/10.1038/s41598-025-03355-3

[6] D. Mahmoudi, A.A. Kajani, M.R. Khorasgani, Synthesis, characterization, antioxidant and antimicrobial activities, and computational studies of chitosan nanoparticles loaded with vitamin E and clove essential oil, Scientific Reports 15 (2025) 32130. https://doi.org/10.1038/s41598-025-18135-2

[7] M.N.A. Uda, S.C.B. Gopinath, U. Hashim, N.H. Halim, N.A. Parmin, M.N. Afnan Uda, P. Anbu, Production and characterization of silica nanoparticles from fly ash: conversion of agro-waste into resource, Preparative biochemistry & biotechnology 51 (2021) 86-95. https://doi.org/10.1080/10826068.2020.1793174

[8] P. Bhuvaneswari, T. Shanmugavadivu, G. Sabeena, G. Annadurai, E. Sindhuja, Synthesis and Characterization of Chitosan with Silica (CS) Nanocomposite with Enhanced Antibacterial Activity, Int. J. Res. Pharm. Sci. 13 (2022) 27–34. https://doi.org/10.26452/ijrps.v13i1.16

[9] K. Pathak, M. Sarma, M. Sahariah, P. Shankarishan, J.J. Sahariah, S. Deka, A. Das, M.A. Islam, P. Pramanik, P.P. Borthakur, A.R. Bharadwaj, R. Bhaumik, Nanoparticles in the fight against antimicrobial challenges: A comprehensive review, Next Nanotechnology 9 (2026) 100420. https://doi.org/10.1016/j.nxnano.2026.100420

[10] M. Mardani, M. Pilevar, N. Behzadnia, S. Peak, M. Bavarian, S. Nejati, M. Elliott, M.D. Firouzjaei, Standardizing and Optimizing Disk Inhibition Zone Testing Against E. coli for Reproducible Evaluation of Antibacterial Polymeric Membranes, Journal of Membrane Science Letters (2026) 100123. https://doi.org/10.1016/j.memlet.2026.100123

[11] I.M. Helander, E.L. Nurmiaho-Lassila, R. Ahvenainen, J. Rhoades, S. Roller, Chitosan disrupts the barrier properties of the outer membrane of Gram-negative bacteria, Int. J. Food Microbiol. 71 (2001) 235–244. https://doi.org/10.1016/S0168-1605(01)00609-2

[12] B. Li, Y. Liao, X. Su, S. Chen, X. Wang, B. Shen, H. Song, P. Yue, Powering mesoporous silica nanoparticles into bioactive nanoplatforms for antibacterial therapies: strategies and challenges, J. Nanobiotechnol. 21 (2023) 325. https://doi.org/10.1186/s12951-023-02093-w

[13] O.D. Orbuleț, M. Grinzeanu, S. Căprărescu, C. Modrogan, An Overview of Chitosan-Based Composites Containing Silver or Zinc Oxide Nanoparticles: Antimicrobial and Antibacterial Properties, and Biomedical Perspectives, Coatings 16 (2026) 892. https://doi.org/10.3390/coatings16080892

[14] M. Nasaj, M. Chehelgerdi, B. Asghari, A. Ahmadieh-Yazdi, Factors influencing the antimicrobial mechanism of chitosan action and its derivatives: A review, Int. J. Biol. Macromol. 277 (2024) 134321. https://doi.org/10.1016/j.ijbiomac.2024.134321

[15] A.Y. Ali, A.A.K. Alani, B.O. Ahmed, L.L. Hamid, Effect of biosynthesized silver nanoparticle size on antibacterial and anti-biofilm activity against pathogenic multi-drug resistant bacteria, OpenNano 20 (2024) 100213. https://doi.org/10.1016/j.onano.2024.100213

Materials Research Proceedings 74 (2026) 165-172 https://doi.org/10.21741/9781644904473-21

Composite Material in Road Pavement: A Review of Experimental, Numerical and Machine Learning Approaches

Mazlan RAFIDAH[1,2], Mohd Khairul Afzan Mohd LAZI[2,a *], Fauzan Mohd JAKARNI[3], Yusra Aulia SARI[4], Mohamad Saifullah SAMSUDIN[5], Rosmawati MAMAT[6], Ekarizan SHAFFIE[6,7], Dylan Tay WANG AN[2], Nurul Najihah MAD ROSNI[2], and Ikhwanul IHSAN[2,8]

[1]Department of Engineering, Centre for Diploma Studies, SPACE UTM, Block T05, Universiti Teknologi Malaysia, 81310, Johor Bahru, Johor, Malaysia.

[2]Department of Geotechnics and Transportation, Faculty of Civil Engineering, Universiti Teknologi Malaysia, 81310 Johor Bahru, Johor, Malaysia

[3]Department of Civil Engineering, Faculty of Civil Engineering, 43400 Universiti Putra Malaysia, Malaysia

[4]Faculty of Civil Engineering and Planning, Universitas Internasional Batam, Indonesia

[5]Faculty of Engineering, City University Malaysia, 46100, Petaling Jaya, Selangor, Malaysia

[6]Faculty of Civil Engineering, Universiti Teknologi MARA, 40450 Shah Alam, Selangor, Malaysia

[7]Institute for Infrastructure Engineering and Sustainable Management, Universiti Teknologi MARA, 40450 Shah Alam, Selangor, Malaysia

[8]Research Center for Transportation Technology, National Reserach and Innovation Agency (BRIN), Indonesia

[a]mohdkhairulafzan@utm.my

Keywords: Composite, Pavement, Numerical, Machine Learning

Abstract. Fiber-reinforced asphalt is increasingly used to improve pavement durability and sustainability. Experimental studies show that synthetic, natural, and recycled fibers can enhance rutting resistance, cracking resistance, fatigue life, moisture durability, and binder stability. Finite element and discrete element modelling provide complementary insight into pavement-scale response and fiber-matrix mechanisms, while machine learning (ML) supports rapid performance prediction and mix optimisation. This review compares the principal fiber types and integrates experimental, numerical, and data-driven approaches. Key remaining challenges are optimum fiber selection and dosage, long-term ageing and moisture durability, natural-fiber degradation, dataset limitations, and field-scale validation. An integrated experimental-numerical-ML framework is recommended for performance-based design of durable and sustainable fiber-reinforced asphalt pavements.

Introduction

Road pavements experience rutting, fatigue and low-temperature cracking, and moisture damage, while conventional bitumen-aggregate mixtures must accommodate increasing traffic and climatic demands. Fiber-reinforced asphalt concrete (FRAC) addresses these limitations by introducing a three-dimensional reinforcing network that can bridge cracks, provide tensile reinforcement, and stabilise binder against drain-down [1]. The effectiveness of reinforcement depends on fiber type, dosage, geometry, thermal stability, dispersion, and compatibility with the asphalt matrix.

Fibers have long been used in asphalt, particularly cellulose in stone mastic asphalt (SMA). This review evaluates experimental evidence for synthetic, natural, and recycled fibers, then

Content from this work may be used under the terms of the Creative Commons Attribution 3.0 license. Any further distribution of this work must maintain attribution to the author(s) and the title of the work, journal citation and DOI. Published under license by Materials Research Forum LLC.

examines Finite Element Method (FEM), Discrete Element Method (DEM) and ML approaches used to explain reinforcement mechanisms, predict performance, and optimise fiber-asphalt composite design. The review emphasises how these approaches can be combined for performance-based pavement material selection rather than treated as separate research domains.

Fiber Reinforced Asphalt: Materials and Experimental Findings

Synthetic fibers include polypropylene, polyester, basalt, glass, aramid, and carbon fibers. Polypropylene is inexpensive, chemically stable, and has a melting point of about 165 °C, which is above typical asphalt mixing temperatures [3]. Polyester fibers, commonly PET-based, combine low density, tensile strength, elasticity, and heat resistance [4] Qabur et al. found using about 0.5-1% polyester fiber with a 6 mm length reported higher Marshall stability, tensile strength ratio (TSR), rutting resistance, and cracking performance, with the best overall response at approximately 1% fiber [5].

Basalt fibers provide high thermal stability, alkali resistance, and strong affinity with asphalt binders [6]; a dosage near 0.3% has been associated with low rut depth and high fatigue endurance relative to polyester and lignin fibers, with service-life gains reported in road and airport applications [7]. Glass fibers provide high tensile modulus and improve stiffness, strength, and moisture resistance [8]; porous asphalt containing 12 mm glass fiber at about 0.2% has shown favourable tensile and moisture performance [9]. Aramid fibers withstand high mixing temperatures and are mainly used to control fatigue and reflective cracking, while short aramid pulp can increase indirect tensile strength and toughness [10]. Carbon fibers have more specialised use, particularly where electrical conductivity is required for self-heating or self-sensing pavements. Across these materials, optimum dosage and uniform dispersion are essential because excessive fiber content can cause agglomeration, reduce workability, and offset the expected reinforcement benefit.

Natural Fibers

Natural fibers are renewable, low-cost asphalt modifiers and include cellulose, lignin, coconut coir, sisal, kenaf, bamboo, jute, and palm fibers (Fig. 1). Their main advantage is high absorbency, which allows the fibers to hold bitumen and thicken the asphalt mastic. Cellulose at about 0.3-0.5% is widely used in SMA and other gap-graded mixtures to reduce binder drain-down while maintaining cohesion [11]. Lignin fibers can improve cracking and ageing resistance because of their thermal stability; contents of approximately 0.2-0.4% have been reported to delay fatigue crack initiation and propagation [12].Bamboo fiber can enhance stiffness and Marshall stability, while kenaf and sisal can increase tensile strength and mixture stability [13]. However, some SMA studies have found only modest changes at around 0.3% sisal, showing that the benefit is highly dependent on fiber type, morphology, and dosage [14].

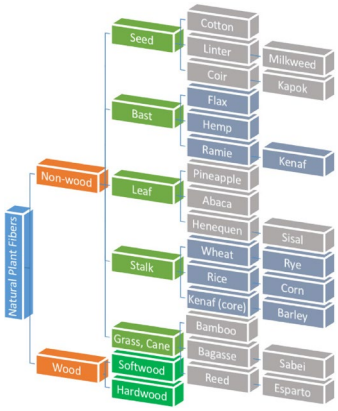


Fig. 1. Classification of natural fibers [15].

Agro-waste fibers such as coconut coir and oil-palm fibers can improve resilient modulus, tensile strength, binder stability, and rutting resistance at relatively low contents. Around 0.3-0.4% coconut or palm fiber has been reported to reduce binder drain-down and strengthen SMA mixtures, while palm-fiber modification near 0.75% can increase binder softening point and rutting resistance [16. Natural fibers can act as extra bitumen carriers, holding binder in the mix which may reduce the paths for water ingress. To date, field evidence of this is minimal, partly because fibers like cellulose have been successfully used in SMA for decades without obvious issues. Nonetheless, researchers have pointed out the need to evaluate how natural fiber decomposition might affect pavement performance in the long run. Future studies are addressing these by exploring surface-treated natural fibers to make them more hydro-stable and blending natural with synthetic fibers to get combined benefit.

Waste and Recycled Fibers

Recycled fibers provide reinforcement while diverting waste from disposal. Recycled polyethylene terephthalate (PET) from bottles can be introduced through dry mixing or binder modification [16]. Studies have shown that PET fibers significantly improve mixture strength and fatigue performance. Experimental studies report substantial gains in fatigue life, stiffness, and strength; for example, PET fibers of about 20 mm at 1% by mixture mass increased fatigue life by 148%, while PET-modified binder produced increases of up to 163% compared with conventional mixtures [17]. Even lower PET contents, around 0.6%, have improved stiffness and load-bearing capacity in SMA [18]. Tire-derived textile fibers recovered during tyre recycling, typically polyester or nylon, are another useful waste stream. Contents near 0.3% have improved flexural fatigue resistance and cracking performance in porous asphalt [19]. These fibers improve mixture durability and high-temperature stability in a manner similar to polymer modifiers.

Recycled waste fibers provide both mechanical and environmental benefits for asphalt reinforcement. Recycled PET fibers improve stiffness, fatigue life, and overall strength of asphalt mixtures. These studies demonstrate that waste fibers can significantly improve pavement performance while promoting sustainability in asphalt materials. Table 1 summarises representative studies on synthetic, natural, and recycled fiber reinforcement and their performance outcome.

Table 1. Summarized fiber reinforcement in asphalt.

Source/Examples	Typical Dosage / Length	Key Performance Improvements
Polypropylene (PP)	0.2–0.5% of mix, 10–15 mm length	Improves tensile strength ratio (TSR), enhances dynamic modulus, increases resistance to rutting, and improves durability against moisture damage and freeze–thaw cycles
Polyester (PET/PEN)	0.25–1% of mix, 6–8 mm length	Increases Marshall stability, improves rutting and fatigue resistance, and raises fracture energy at low and intermediate temperatures
Basalt	0.3–0.4% of mix, 6–12 mm length	Enhances rutting and fatigue resistance, extends pavement service life (up to 1.5 times longer)
Glass (E-glass)	0.2–0.3% of mix, 6–12 mm length	Improves stiffness, tensile strength, and resistance to binder drain-down in stone mastic asphalt
Aramid (Kevlar)	0.2–0.5% of mix, pulp or blended form	Improves fatigue life, reduces reflective cracking, and increases toughness of asphalt mixtures
Carbon	About 0.2% of mix, 5 mm length	Provides additional stiffness and imparts electrical conductivity, enabling applications such as self-heating or self-sensing pavements
Cellulose	0.3–0.5% of mix	Controls binder drain-down in stone mastic asphalt and open-graded mixes, improves mixture cohesion

Source/Examples	Typical Dosage / Length	Key Performance Improvements
Lignin	0.2–0.45% of mix	Improves rutting and cracking resistance at low temperatures, enhances ageing resistance of asphalt
Bamboo	About 0.3% of mix	Increases stiffness and Marshall stability while being biodegradable
Kenaf / Sisal	About 0.3% of mix	Provides moderate improvements in tensile strength and Marshall stability
Coconut coir / Palm	0.3–0.4% of mix	Improves resilient modulus, indirect tensile strength, and reduces binder drain-down in stone mastic asphalt
PET (waste bottles)	0.6–1% of dry mix (20 mm fibers) or 2% of binder (crumbed PET)	Substantially improves fatigue life (up to 163% longer than control), increases stiffness and strength, and strengthens stone mastic asphalt
Tire-derived textiles (TDT)	0.3% of mix, 1–2.5 mm fibers	Improves fatigue resistance, enhances resistance to cracking, and increases durability in both porous and dense mixes
Recycled steel fibers	1.5–3.5% of binder volume	Adds electrical conductivity for potential self-heating pavements and maintains good moisture durability (TSR >80%)

Recent studies also support the use of recycled polymer and composite wastes where compatibility, processing route, and dosage are controlled The reviewed evidence shows that fiber selection should be performance-based. Basalt and glass fibers are strong candidates where stiffness, rutting resistance, and fatigue endurance under high loading are priorities. Polypropylene and polyester offer lower-cost reinforcement but require dosage control to avoid agglomeration. Natural fibers are particularly attractive for binder stabilisation and sustainable SMA applications, although moisture sensitivity and biodegradation remain long-term concerns. Recycled PET and tire-derived fibers provide a useful balance between mechanical improvement and waste valorisation. Consequently, the preferred solution should consider the dominant pavement distress, mixture gradation, fiber dosage and dispersion, environmental exposure, durability, and life-cycle sustainability rather than assuming that one fiber is universally superior [20,21].

Numerical Modeling Approaches

Numerical modelling complements laboratory testing by resolving pavement responses and reinforcement mechanisms that are difficult to observe experimentally. FEM is widely used for pavement-scale stress, strain, temperature, fatigue, and vehicle-pavement interaction analyses. Zhen et al. used FEM to illustrate pavement damage mechanisms caused by temperature variations, as shown in Fig. 2 [22]. Multiscale FEM has also been applied by representing the asphalt mixture at both the microscale, including the mastic, fine aggregates, and fibers, and the macroscale, representing the overall pavement structure [23]. DEM treats aggregates and bonded mastic/fiber interactions as discrete components, allowing microscale investigation of contact, pull-out, crack bridging, and load transfer, although at higher computational cost and with greater input-data requirements. FEM is therefore more efficient for pavement-scale response, whereas DEM is more informative for local fiber-aggregate mechanisms. Their combined use is particularly valuable when model parameters are calibrated against laboratory data.

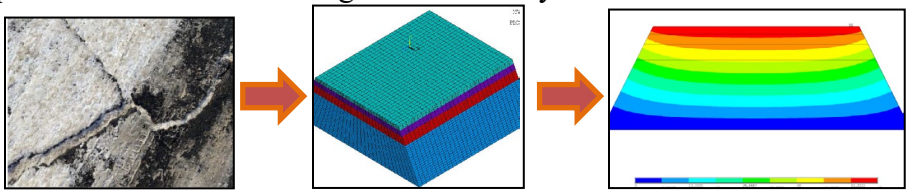


Fig. 2. Schematic workflow of road damage caused by pavement temperature. Stress analysis for FEM in asphalt pavements [22].

The strengths and limitations of the modelling approaches are complementary. FEM can represent realistic traffic and environmental loading and is well suited to pavement-scale stress distribution, temperature-induced strain, fatigue development, and vehicle-pavement interaction. Its continuum assumption, however, may oversimplify the discrete role of fibers unless fiber effects are introduced through calibrated constitutive properties, explicit reinforcement elements, or multiscale modelling. DEM captures microscale interactions more explicitly, including fiber-aggregate contact, fiber pull-out, crack bridging, aggregate interlocking, and load transfer, but it is computationally intensive and requires detailed contact and bonding parameters. Model credibility in both approaches depends on laboratory calibration and validation. Accordingly, the most robust strategy is to use experiments for measured performance, FEM for structural-scale response, and DEM for local reinforcement mechanisms rather than treating the methods as competing alternatives.

Machine Learning Approaches

Machine learning (ML) can capture nonlinear relationships between fiber type, dosage, length, binder content, aggregate gradation, air voids, temperature, ageing condition, and loading variables. Reported outputs include Marshall stability, optimum asphalt content, indirect tensile strength, dynamic modulus, rut depth, fatigue life, stiffness, and cracking resistance. ANN, SVM, random forest, decision trees, gradient boosting, Gaussian process regression, and ANFIS have all been applied to asphalt-related prediction and optimisation problems [24,25]. ANN is useful for complex nonlinear datasets, whereas SVM and tree-based models can be effective for smaller laboratory datasets and can support variable-importance analysis.

Prediction quality depends on dataset size, diversity, input quality, and validation. Many available datasets remain relatively small and laboratory-based and may not represent different binders, fiber types, climates, traffic levels, ageing states, moisture histories, or field environments. Robust assessment should therefore use clearly separated training and testing data, k-fold cross-validation, residual analysis, sensitivity analysis, and, where possible, an independent external dataset [26]. Metrics such as R2, RMSE, MAE, and MAPE provide useful measures of predictive accuracy, but they should be interpreted as predictive relevance rather than direct causality. Key limitations include overfitting, sampling bias, limited interpretability of black-box models, inconsistent reporting of input-output variables, and insufficient representation of long-term ageing, moisture damage, freeze-thaw effects, fiber degradation, and field-scale pavement behaviour. Transparent reporting of data preprocessing, model parameters, validation strategy, and uncertainty is therefore essential for reproducible ML applications.

The greatest value is obtained through an integrated material-mechanism-prediction framework. Laboratory tests establish how fiber type, dosage, length, and mixing method influence rutting, fatigue, tensile strength, moisture resistance, binder drain-down, and cracking. FEM and DEM then explain mechanisms that are difficult to observe directly, including stress redistribution, crack bridging, fiber-mastic interaction, fiber pull-out, and aggregate contact. ML can use reliable experimental and simulation-generated data to identify nonlinear relationships, rank influential variables, predict performance, and optimise mixture design [27].In this sequence, laboratory testing provides validated evidence, numerical modelling provides physical interpretation, and ML reduces trial-and-error testing and accelerates sensitivity-based decision-making. Such integration supports performance-based fiber selection and optimum dosage for specific traffic, climate, mixture, and durability requirements while reducing unnecessary experimental workload.

Conclusion

Fiber-reinforced asphalt has strong potential to improve pavement performance by enhancing resistance to rutting, fatigue cracking, moisture damage, and other common pavement distresses. Different fiber types, including synthetic, natural, and recycled fibers, offer distinct advantages

depending on their mechanical properties, compatibility with asphalt binder, environmental impact, and field application requirements. In addition, hybrid fiber systems and fiber–polymer combinations can further improve pavement functionality by combining the benefits of different reinforcement mechanisms. However, several challenges remain, particularly in selecting suitable fiber types, determining optimum fiber dosage, and achieving uniform fiber dispersion during large-scale asphalt production.

Numerical modelling and simulation have contributed significantly to understanding fiber–binder interaction, stress distribution, crack initiation, crack propagation, and fiber-bridging mechanisms. These approaches complement laboratory investigations by providing mechanistic explanations for observed performance improvements. At the same time, ML is increasingly being used to optimise mix design and predict pavement performance. Although ML offers strong potential for predicting and optimising fiber-reinforced asphalt mixtures, its future application requires larger and more diverse datasets, transparent model validation, interpretable algorithms, and integration with experimental and mechanistic modelling to ensure reliable field-scale implementation.

Despite these advances, further research is still needed on the long-term durability of fiber-reinforced asphalt under traffic loading, environmental exposure, binder ageing, moisture damage, freeze–thaw cycles, and the biodegradation of natural fibers. Future studies should also explore the combined use of fibers with other modifiers, such as polymers, reclaimed asphalt pavement (RAP), and nanomaterials, to develop more sustainable and high-performance asphalt composites. Overall, future research should adopt an integrated experimental–numerical–machine learning framework, in which laboratory testing validates material performance, numerical modelling explains fiber-reinforcement mechanisms, and ML enables rapid prediction, optimisation, and decision-making. Through this integrated approach, fiber-reinforced asphalt can be further developed as a cost-effective and sustainable composite solution for improving pavement durability and reducing common asphalt pavement distresses.

Acknowledgment
The author acknowledges the Fundamental Research Grant Scheme (FRGS), grant number FRGS/1/2023/TK02/UTM/02/4 funded by the Ministry of Higher Education Malaysia (MOHE).

References

[1] J. Li, L. Yang, L. He, R. Guo, X. Li, Y. Chen, Y. Muhammad, Y. Liu, Research progresses of fibers in asphalt and cement materials: a review, Journal of Road Engineering 3 (2023) 35-70. https://doi.org/10.1016/j.jreng.2022.09.002

[2] R. Muniandy, A. Selim, H. Omar, Laboratory Evaluation of Malaysian Cellulose Oil Palm Fiber for Use in Stone Mastic Asphalt Mixes, Int J Pavements 1 (2002) 13–21.

[3] S. Nizamuddin, Y.J. Boom, F. Giustozzi, Sustainable polymers from recycled waste plastics and their virgin counterparts as bitumen modifiers: A comprehensive review, Polymers (Basel) 13 (2021) 3242. https://doi.org/10.3390/polym13193242

[4] E. Slezák, F. Ronkay, K. Bocz, Development of an Engineering Material with Increased Impact Strength and Heat Resistance from Recycled PET, Journal of Polymers and the Environment 31 (2023) 5296–5308. https://doi.org/10.1007/s10924-023-02945-4

[5] A. Qabur, H. Baaj, M.A. El-Hakim, Laboratory Study on Enhancing Asphalt Mixture Properties through Dry Mixing with High-Dose Multilayer Plastic Packaging Pellet Additives, Journal of Materials in Civil Engineering 37 (2025) 04025049. https://doi.org/10.1061/jmcee7.mteng-19101

[6] Y. Hui, G. Men, P. Xiao, Q. Tang, F. Han, A. Kang, Z. Wu, Recent Advances in Basalt Fiber Reinforced Asphalt Mixture for Pavement Applications, Materials (Basel) 15 (2022) 6826. https://doi.org/10.3390/ma15196826

[7] M. Fahad, R. Nagy, Finite Element Modeling and Laboratory Performance Evaluation of Lignin, Basalt and Polyester Fiber-Reinforced Asphalt Mixtures, Applied Sciences 15 (2025) 3953. https://doi.org/10.3390/app15073953

[8] A.N. Aina, M.A.M. Rizal, M.F.A. Rased, R.A. Majid, D.D. Chin Vui Sheng, S.A. Hassan, Experimental investigations on performance and failure mechanisms of glass fiber-reinforced acrylonitrile butadiene styrene composites considering mesh density effect, Polymer Composites 46 (2025) 12278-12295. https://doi.org/10.1002/pc.29744

[9] R. Tanzadeh, J. Tanzadeh, M. Honarmand, S.A. Tahami, Experimental study on the effect of basalt and glass fibers on behavior of open-graded friction course asphalt modified with nano-silica, Construction and building materials 212 (2019) 467–475. https://doi.org/10.1016/j.conbuildmat.2019.04.010

[10] S.S. Saliani, P. Tavassoti, H. Baaj, A. Carter, Characterization of asphalt mixtures produced with short Pulp Aramid fiber (PAF), Construction and building materials 280 (2021) 122554. https://doi.org/10.1016/j.conbuildmat.2021.122554

[11] N.S. Aliyu Yaro, Z, Ngubane, S. Abdulrahman, A. Usman, N. Khan, A. Mohammed A, B.P. Khuzwayo, J.A. Adedeji, Scientometric and Systematic Review with SWOT Analysis of the Application and Performance of Synthetic and Composite Textile Waste-Derived Materials in Flexible Pavements, Sustainability 18 (2026) 5249. https://doi.org/10.3390/su18115249

[12] H. Yao, Y. Wang, J. Liu, M. Xu, P. Ma, J. Ji, Z. You, Review on Applications of Lignin in Pavement Engineering: A Recent Survey, Front Mater 8 (2022) 803524. https://doi.org/10.3389/fmats.2021.803524

[13] M.R.M. Asyraf, A. Syamsir, H. Bathich, Z. Itam, A.B.M. Supian, S. Norhisham, N.M. Nurazzi, T. Khan, M.Z.A. Rashid, Effect of Fibre Layering Sequences on Flexural Creep Properties of Kenaf Fibre-reinforced Unsaturated Polyester Composite for Structural Applications, Fibers Polym 23 (2022) 3232–3240. https://doi.org/10.1007/s12221-022-4386-7

[14] H. Wu, P. Xiao, Z. Fei, A. Kang, X. Wu, Evaluation of SMA-13 Asphalt Mixture Reinforced by Different Types of Fiber Additives. Materials (Basel) 17 (2024) 5468. https://doi.org/10.3390/ma17225468

[15] R.A. Ilyas, S.M. Sapuan, M.M. Harussani, M.Y.A.Y. Hakimi, M.Z.M. Haziq, M.S.N. Atikah, M.R.M. Asyraf, M.R. Ishak, M.R. Razman, N.M. Nurazzi, M.N.F. Norrrahim, Polylactic Acid (PLA) Biocomposite: Processing, Additive Manufacturing and Advanced Applications, Polymers (Basel) 12 (2021) 1326. https://doi.org/10.3390/polym13081326

[16] N. Agha, A. Hussain, A.S. Ali, Y. Qiu, Performance Evaluation of Hot Mix Asphalt (HMA) Containing Polyethylene Terephthalate (PET) Using Wet and Dry Mixing Techniques, Polymers (Basel) 15 (2023) 1211. https://doi.org/10.3390/polym15051211

[17] Z. Dehghan, A. Modarres, Evaluating the fatigue properties of hot mix asphalt reinforced by recycled PET fibers using 4-point bending test. Construction and Building Materials 139 (2017) 384–393. https://doi.org/10.1016/j.conbuildmat.2017.02.082

[18] L. Lugeiyamu, M. Kunlin, E.S.K. Mensahn, A. Faraz, Utilization of waste polyethylene terephthalate (PET) as partial replacement of bitumen in stone mastic asphalt, Construction and Building Materials 309 (2021) 125176. https://doi.org/10.1016/j.conbuildmat.2021.125176

[19] L. Kong, J. Xu, H. Yang, P. Wu, X. Li, D. Ma, Z. Wang, D. Ren, C. Ai, Enhancing crack resistance in basalt fiber asphalt mixtures: a full-field time-domain investigation of stress distribution and pore structure optimisation, Int J Pavement Eng 26 (2025) 2460746. https://doi.org/10.1080/10298436.2025.2460746

[20] S. Laib, Z. Nafa, A. Merdas, Y. Chetbani, B.A. Tayeh, Y. Tang, Experimental and Statistical Evaluations of Recycled Waste Materials and Polyester Fibers in Enhancing Asphalt Concrete Performance, Buildings 15 (2025) 2747. https://doi.org/10.3390/buildings15152747

[21] W.A. Laftah, W.A. Wan Abdul Rahman, A comprehensive review of tire recycling technologies and applications, Mater Adv 6 (2025) 4992–5010. https://doi.org/10.1039/d5ma00463b

[22] W. Zhen, Z, Li, Simulation Analysis on Temperature Field and Temperature Stress of Flexible Pavement in Cold Areas, J Appl Math Phys 9 (2021) 606–16. https://doi.org/10.4236/jamp.2021.94044

[23] C. Zhou, W. Meng, M. Cao, C. Peng, Multiscale finite element computational model and microscopic stress analysis of asphalt pavement structures, Mech Adv Mater Struct 33 (2026) 2476198. https://doi.org/10.1080/15376494.2025.2476198

[24] A. Alubeid, Z. Yousafzai, Enhancing Diagnosis of Balance Disorders Using Machine Learning: Sensor data analysis to improve diagnostic accuracy and efficiency in clinical settings (2024).

[25] M. Al-Ammari, R. Dong, M. Nasser, A. Al-Maswari, Innovative Machine Learning Approaches for Predicting the Asphalt Content During Marshall Design of Asphalt Mixtures, Materials (Basel) 18 (2025) 1474. https://doi.org/10.3390/ma18071474

[26] J.M. Gorriz, R. Martin-Clemente, F. Segovia, J. Ramirez, A. Ortiz, J. Suckling, Is K-fold cross validation the best model selection method for machine learning? Inf Fusion 135 (2026) 104404. https://doi.org/10.1016/j.inffus.2026.104404

[27] S.B. Murthy, K.P. Biligiri, V. Pandurangan, Carbon and glass fibre composite waste-modified asphalt binders: compatibility assessment, dosage optimisation, and performance evaluation, Road Mater Pavement Des 18 (2025) 1-36. https://doi.org/10.1080/14680629.2025.2599472

Materials Research Proceedings 74 (2026) 173-179 https://doi.org/10.21741/9781644904473-22

Examination of the Microstructure and Corrosion Resistance of 6063 Aluminium Alloy Reinforced with Palm Fruit Mesocarp Particles (PP) for Automobile Radiator Applications

Itopa G. AKANDE[1,a *], Oluwaseun M. DARAMOLA[2,b], Ebenezer O. AKANDE[3,c], Ezedeen A. OWOO[4,d], Abiodun D. OLORUNFEMI[5,e], Kunle M. OLUWASEGUN[6,f] and Daniel O. NASAMU[1,g]

[1]Department of Automotive Engineering, University of Ibadan, Ibadan, Nigeria

[2]Department of Mechanical Engineering, Bells University of Technology, Ota, Nigeria

[3]Department of Civil Engineering, Bells University of Technology, Ota, Nigeria

[4]Department of Agricultural Engineering, Ladoke Akintola University of Technology, Ogbomoso, Nigeria

[5]Department of Mechanical Engineering, University of Ibadan, Ibadan, Nigeria

[6]Department of Mechanical and Manufacturing Engineering, University of Manitoba, Winnipeg, Canada

[a]aigodwin2015@gmail.com, [b]maickdara@gmail.com, [c]besteben2000@yahoo.com, [d]eaowoo@lautech.edu.ng, [e]aickdara@gmail.com, [f]excetom@gmail.com, [g]nasamudanielomodafe@gmail.com

Keywords: Automobile Radiators, 6063 Aluminium Alloy, Reinforced Alloy, Agricultural Waste

Abstract. Automobile radiators are commonly built of 6063 Al alloy because of its outstanding thermal conductivity. However, radiators made from 6063 aluminium alloy have a flawed microstructure and low corrosion resistance due to the deteriorating effects of heat and high-temperature corrosion. The performance features of the reinforced alloy with PP for automobile applications were thus investigated in this work. Six specimens were used in this investigation: five reinforced specimens and one unreinforced control. Reinforced alloy specimens were fabricated and were then sectioned to 10 mm thickness and 20 mm diameter for characterisation. Corrosion resistance of the specimens was evaluated in 3.65% NaCl, in accordance with ASTM G102. Hardness was examined with a Brinell hardness machine following ASTM E10, whereas SEM/EDS and XRD were employed to study the microstructure and crystallographic phases, respectively. The unreinforced specimen displayed the minimum hardness value (104.94 kgf/mm^2) together with the maximum corrosion rate (Cr), recorded at 0.7321 mm/year. Among the specimens, the 6063 Al alloy strengthened with 10% by weight of PP achieved the minimum Cr value of 0.1092 mm/year and the maximum hardness value of 109.84 kgf/mm². These findings showed that the PP improved the selected alloy's tested properties.

Introduction

Researchers have studied strengthening aluminium alloys by incorporating agricultural residues, including unripe plantain peel, rice husk, and eggshell particles, to enhance alloy properties while improving the lightweight attributes of engineering materials [1]. This blend includes hardness, high specific strength, ductility, strong thermal resistance, impact strength, and favourable corrosion resistance. The metal matrix composites ultimately produced are frequently put forward for structural uses across a range of sectors, such as aerospace, marine, and automotive industries.

Content from this work may be used under the terms of the Creative Commons Attribution 3.0 license. Any further distribution of this work must maintain attribution to the author(s) and the title of the work, journal citation and DOI. Published under license by Materials Research Forum LLC.

Moreover, employing these agricultural residues as reinforcing agents contributes to diminishing the quantity of toxic waste present in the environment [2].

Agricultural waste materials have been adopted as reinforcements by numerous researchers. For example, Akbar et al. [3] reported that the mechanical properties of an aluminium matrix composite were enhanced through the inclusion of bean pod ash. The authors put forward the recommendation that the resulting composite might be suitable as a replacement for particular automotive components. As stated by Yekini et al. [4], the rice husk ash was dispersed uniformly throughout the aluminium alloy. The hybrid composite incorporating rice husk ash exhibited reasonably elevated mechanical properties, together with a refined microstructure adequate for the fabrication of numerous automotive components. Anwesh et al. [5] conducted an investigation into the mechanical and tribological properties of aluminium alloy reinforced with sugarcane bagasse ash, which demonstrated that an increase in the weight of bagasse ash reinforcement content was accompanied by a reduction in wear depth.

Another category of agricultural waste rich in fibre is coconut shell ash, which has been utilised for the reinforcement of composites. The density of coconut shell ash is low, at approximately 2.05 g/cm^3 [6]. Upon the addition of coconut shell ash to a composite matrix, the mechanical properties of the resultant material were enhanced. As reported by Nadimpalli [7], coconut ash is suitable for use as a reinforcement within an aluminium matrix. Composites displayed an increase in compressive strength when 6 wt.% coconut shell ash was incorporated. The plentiful availability of agricultural waste, combined with its minimal purchase cost, has rendered it an outstanding reinforcing constituent. Consequently, the current study explored the influence of PP on the microstructure, mechanical properties, and electrochemical behaviour of 6063 Al alloy.

Materials and Experiment

Raw materials and their preparations

The reinforcing material for the experiment is the palm fruit mesocarp particles, produced from the Fibres shown in Fig. 1. The fibres were dried in the sun and pulverised into particles of size 70 microns. Table 1 presents the constituent makeup of the particles comprising the palm fruit mesocarp. The 6063 aluminium alloy billets employed in this study were gotten from Tower Alloy Nigeria Ltd., Ogun State. According to the characterisation of the alloy, aluminium constituted approximately 98.9954% of its constituent elements. Table 2 provides a summary of the various trace elements identified within the alloy. In addition, emery cloth was employed to cleanse the 6063 aluminium alloy billets and to eliminate scale. In order to enable melting within the furnace, the billets were reduced into smaller fragments. The Al 6063 alloy pieces were likewise given a rapid rinse in distilled water so as to eliminate any dirt or impurities.



Fig. 1. Palm fruit mesocarp fibres.

Table 1. Composition of the Palm fruit mesocarp particles.

Component	Cellulose	Lignin	Hemicellulose
wt.%	42.64	23.5	33.86

Table 2. Composition of the Al 6063 Alloy.

Element	Mg	Cu	Mn	Cr	Ti	Ca	V	Si	Zr	S	Al
wt.%	0.56	0.028	0.223	0.028	0.018	0.0523	0.0032	0.086	0.0049	0.0012	98.9954

Casting procedure

The stir-casting technique was employed to carry out the process. A mould, a crucible, a pattern, a pit furnace (PF), and tongs constitute the equipment utilised for casting. The mould was positioned upon a level surface. Once the pattern had been positioned correctly within the mould, sand was deposited and compacted so as to produce the desired shape. Upon withdrawal of the pattern, cavities were created within the mould. Subsequently, the alloy pieces were introduced into a crucible that had been preheated in a PF. The aluminium alloy underwent melting within the crucible at a temperature of 700°C and was agitated at 300 rpm for a duration of 10 minutes. The liquid metal was poured off into a ladle at 650°C. The prescribed amount of reinforcing material was mixed with the molten product in the ladle, ensuring the composite contained the specified ratio of aluminium 6063 alloy to PP (Table 3). After the mixture had been stirred vigorously, it was cast into the cavity formed by the sand mould pattern. The solidified material was taken out of the mould, allowed to cool in the open air, and then suitably labelled. The samples were thereafter subjected to surface polishing and machining in order to eliminate surplus material.

Table 3. Percentages of alloy and PP.

Sample	wt.% of Al alloy	wt.% of PP
Control	100	0
98Al-2PP	98	2
96Al-4PP	96	4
94Al-6PP	94	6
92Al-8PP	92	8
90Al-10PP	90	10

Characterisation of samples

For the purpose of characterisation, both the reinforced and unreinforced specimens were sectioned to a thickness of 10 mm. The characterisation process comprised hardness testing, corrosion analysis, and examination of the microstructure. XRD and SEM/EDS were employed to conduct the microstructural investigations. A Brinell hardness tester was utilised to determine hardness, while corrosion behaviour was assessed through a potentiodynamic polarisation experiment in a simulated seawater environment.

Microstructural examination

The samples' grain refinement, morphology, and composition were examined using the JOEL JSM-7600F SEM fitted with EDS. A voltage of 15 kV and a magnification of 28,000× were used to get the SEM pictures. Utilising the XtaLAB mini II X-ray diffractometer (XRD), the crystallographic phases of the materials were determined. Thereafter, graphs showing intensities in a.u. against 2 degrees (2θ) were produced.

Corrosion test

At 27.7°C, the corrosion experiment was performed. Three electrodes were employed in this design: a graphite rod, a silver/silver chloride calomel electrode acting, and the test samples functioning as the working electrode. A connection was established between the AutoLab PGSTAT 101 and the three electrodes. By means of NOVA 2.1.2 software operating on a computer system linked to the AutoLab, the corrosion characteristics of the materials were examined. During the corrosion test, the electrodes were immersed in 3.65% NaCl. The potentials were established at 1.5 V and -1.5 V, respectively, with respect to the OCP, employing a scan rate of 0.005 V/s. The corrosion rate (Cr) and polarisation resistance (Pr) were derived from the anodic and cathodic slopes of the Tafel plots by means of Eq. 1 and 2. In order to establish the steady state, the OCP was plotted as a function of time. The corrosion test was performed in compliance with ASTM G102 standards for the assessment of corrosion resistance.

$$Cr = (0.00327 \times j_{corr} \times eq.w)/\rho \quad \text{Eq. 1}$$

$$Pr = 2.303^{-1} b_a b_c / j_{corr}(b_a + b_c) \quad \text{Eq. 2}$$

The sample's corrosion current density (j_{corr}), as indicated in Eq. 1 and Eq. 2, is expressed in A/cm^2; its anodic and cathodic slopes are represented by ba and bc, respectively; its density (ρ) is expressed in g/cm^3, and its equivalent weight (eq.w) is expressed in grams (g).

Hardness test

The Brinell hardness testing method was used to assess each sample's hardness. An indenter was applied to the material as part of the test. A ball indenter made from tungsten carbide with a diameter of 10 mm and a test load were used. To ensure the results were not affected, the surfaces of each sample were cleaned to remove any dust. The hardness tester is designed to accommodate loads spanning from 2 kgf to 200 kgf. A force designated as M, equal to 30 kgf, was applied to every sample for a duration of 30 seconds. Following the placement of the ball indenter on the surface of each sample, the resulting indentation depth (q) was recorded. The procedure was carried out three times in accordance with ASTM E10, and each sample was measured three times for q. The obtained values of q were used to populate Eq. 3. After collecting the three H values, the average was calculated to assess repeatability.

$$H = 2M/\pi Q[Q - \sqrt{(Q^2 - q^2)}] \quad \text{Eq. 3}$$

In this context, π equals 22/7, Q denotes the indenting ball's diameter expressed in millimetres, q represents the indentation depth in millimetres, and M stands for the applied force measured in kgf.

Results and Discussion

Microstructure of samples

The SEM (scanning electron microscope) images of 94Al-6PP and 90Al-10PP samples, as shown in Figs. 2 and 3, respectively, revealed a microstructure of exceptional refinement, a characteristic that may be ascribed to the grain-refining action exerted by the PP [8]. Furthermore, the SEM micrographs revealed that the inclusion of the particles served to lower the porosity within the composite. Figs. Figures 2 and 3 additionally demonstrated that the samples displayed a favourable distribution of PP, which was ascribed to the occurrence of whitish-grey precipitates, as observed in the SEM images. However, the precipitates of PP were more predominant in the 90Al-10PP sample, indicating the possibility of better corrosion resistance compared to the 94Al-6PP sample and other tested samples. The good dispersion of the reinforcement, as indicated by the SEM images, could also benefit the material's mechanical properties. Moreover, the EDS images in Figs. 2 and 3 indicated that the samples possess mechanical property-improving, corrosion resistance-enhancing, and grain-refining constituents such as Mg, Al, Si, Zn, Mn and C.

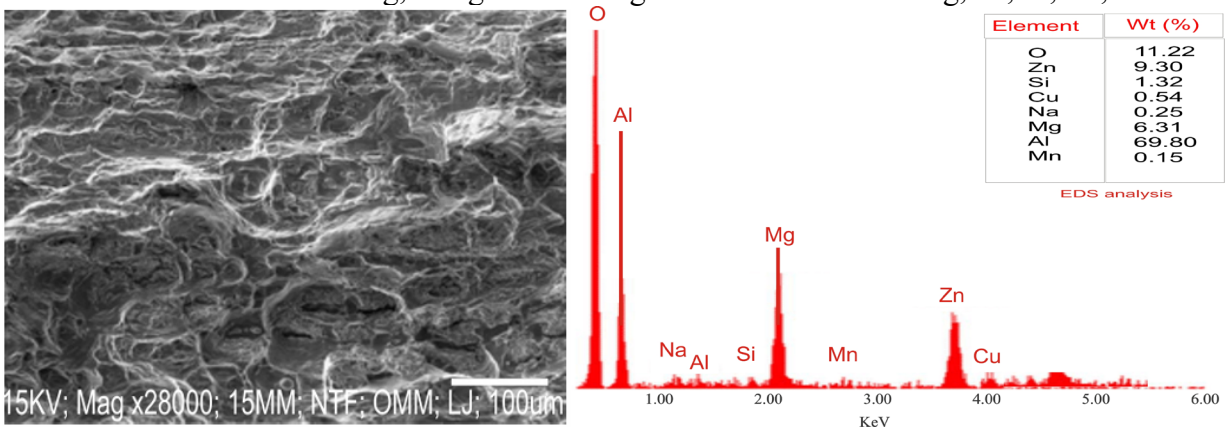


Fig. 2. SEM/EDS images of 94Al-6PP.

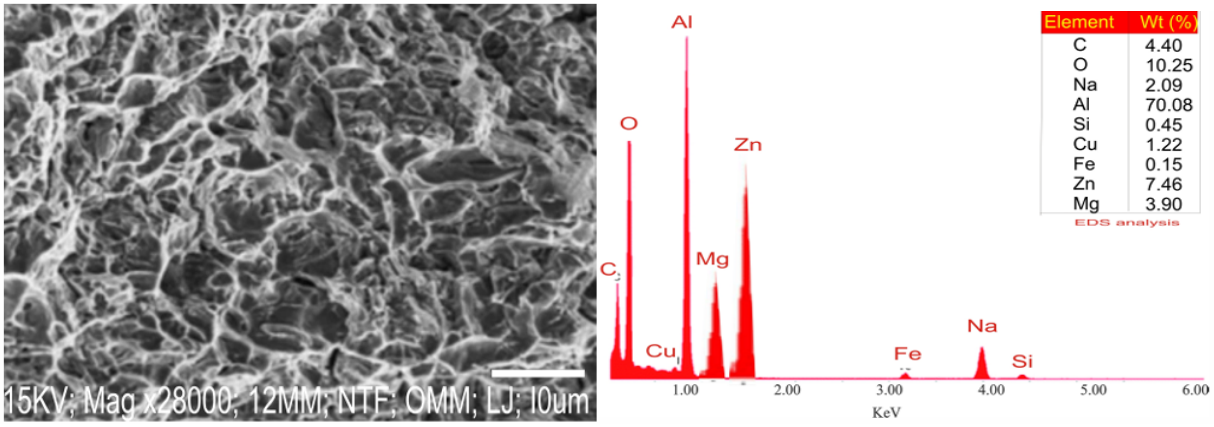


Fig. 3. SEM/EDS images of 90Al-10PP.

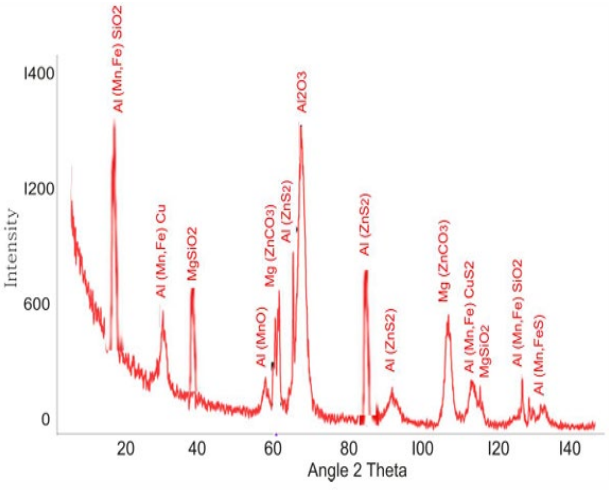


Fig. 4. XRD profile of 94Al-6PP.

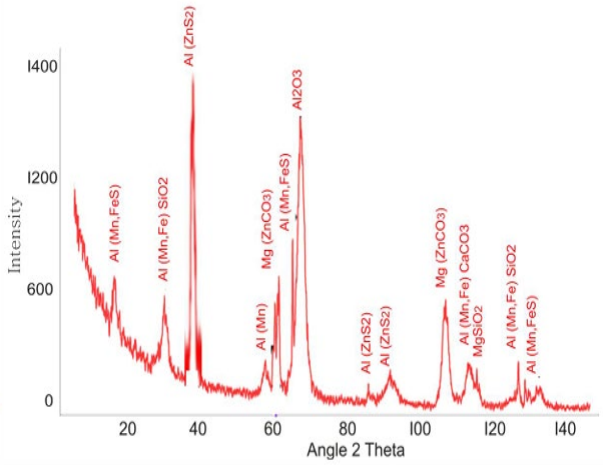


Fig. 5. XRD profile of 90Al-10PP.

Figs. 4 and 5 indicate the XRD profiles of 94Al-6PP and 90Al-10PP samples, respectively. For 94Al-6PP, at $2\theta = 18^{o}$, the (Fe,Mn)SiO_2 phase exhibits the maximum peak intensity, reaching approximately 1300 a.u., whereas the Al(ZnS_2) crystal in the 90Al-10PP sample displays its highest intensity of roughly 1400 a.u at $2\theta = 40^{o}$. The crystallographic phases identified within the XRD profiles demonstrate that the reinforced material mixture possessed microstructural homogeneity.

Corrosion properties of PP-reinforced 6063 Al alloy

Table 4, together with Figs. 6 and 7, presents the corrosion parameters for 6063 Al that has been reinforced with PP. Among the samples, 90Al-10PP demonstrates the greatest corrosion resistance, recording the least corrosion rate (Cr) at 0.1092 mm/year, the lowest corrosion current density (jcorr) at 9.40×10^{-6} A/cm^2, and the highest polarisation resistance (Pr) at 294.98 Ω. According to these corrosion parameters, the 90Al-10PP sample displayed the greatest resistance to degradation of all the reinforced samples. In contrast, the control sample exhibited the highest Cr, 0.7321 mm/year, which arose from a corrosion current density exceeding that of the other test samples. It could be affirmed that the particulate nature of the PP enabled its effective dispersion in the matrix of the composite, minimising the penetration of the chloride ions in the 3.65% NaCl into the material, and therefore enhancing the passivation of the material. Figs. 6 and 7 further revealed that PP acted as a good corrosion-protective device, indicating that it protected the steel's anodic and cathodic sites. From Fig. 7, it can be deduced that samples generally exhibited steady-state potentials within the test period. For instance, the sample 98Al-2PP exhibited a steady-state potential of -0.85 V between 40 and 120 seconds, while sample 90Al-10PP attained a stable

potential at about -0.80 V between 20 and 120 seconds. The control sample was stable at about -0.79 V from 100 to 120s.

Table 4. Polarisation data of samples.

Sample	E_{corr} (V)	j_{corr} (A/cm^2)	Cr (mm/year)	Pr (Ω)	|ba| (V/dec)	|bc| (V/dec)
Control	-1.2666	6.30×10^{-5}	0.7321	60.95	0.0138	0.0072
98Al-2PP	-1.2461	3.38×10^{-5}	0.3928	116.84	0.0075	0.0096
96Al-4PP	-1.0995	1.83×10^{-5}	0.2121	197.12	0.0165	0.0166
94Al-6PP	-1.2458	1.57×10^{-5}	0.1819	253.79	0.0431	0.2532
92Al-8PP	-1.2029	1.08×10^{-5}	0.1254	283.54	0.1721	0.0715
90Al-10PP	-1.1435	9.40×10^{-6}	0.1092	294.98	0.1384	0.1039

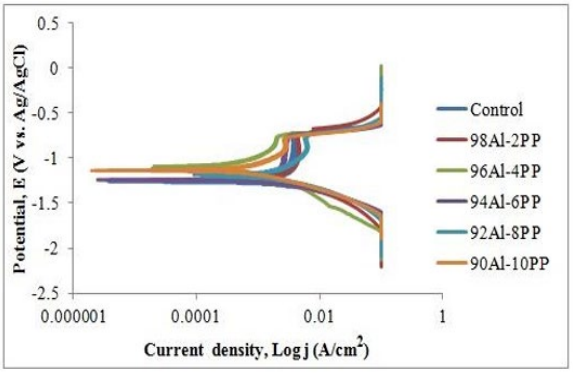


Fig. 6. Polarisation curves of samples.

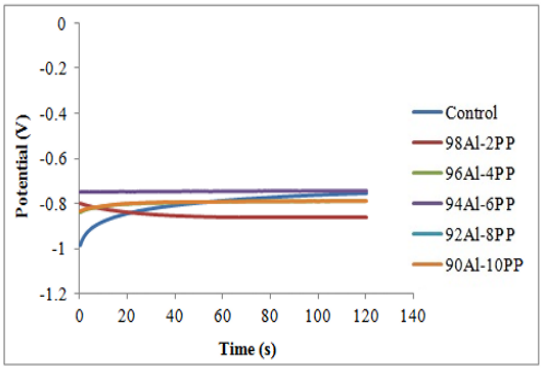


Fig. 7. OCP of samples.

Brinell hardness

The hardness values of the samples are presented in Fig. 8. Samples reinforced with PP exhibited greater hardness than those of the control or unreinforced materials. With the incorporation of 2% by weight of PP, the hardness of the alloy rose from 104.94 kgf/mm^2 to 107.52 kgf/mm^2. A correlation was demonstrated between the enhanced hardness of the alloy and the greater percentage composition of the PP. This rise in hardness could be ascribed to the binding ability of the reinforcement, which diminished plastic deformation under the indenting force and thereby improved the hardness of the material. A maximum hardness value of 109.84 kgf/mm^2 was recorded. The 6063 Al alloy containing 10% weight PP displayed greater resistance to indentation than did the remaining test samples. The superior hardness associated with the incorporation of 10% weight PP may be attributable to a favourable interface, a phenomenon likewise reported by Bhardwaj et al. [9].

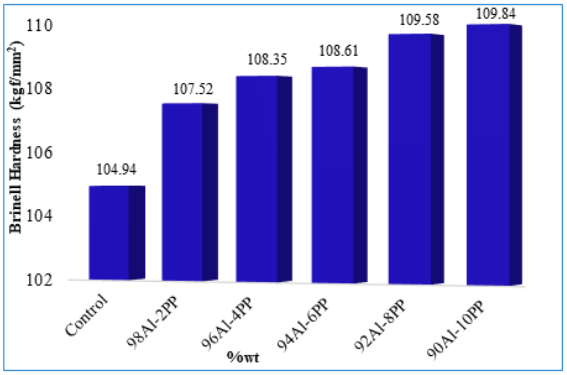


Fig. 8: Brinell hardness of samples.

Conclusions

An investigation was conducted into how PP affect the 6063 Al alloy matrix. Analyses of corrosion, hardness, and microstructure demonstrated that the unreinforced alloy specimen, which recorded the uppermost corrosion rate (Cr) of 0.7321 mm/year, also displayed the lowest hardness of 104.94 kgf/mm^2; in contrast, the sample reinforced with 10% by weight palm fruit mesocarp fibre particles (PP) recorded the lowest Cr of 0.1092 mm/year alongside the maximum hardness of 109.84 kgf/mm^2. This finding suggested that the PP improved the alloy's resistance to both indentation and corrosion. According to the SEM micrographs, the reinforced samples displayed a refined microstructure, minimal porosity, and favourable morphology. As evidenced by the EDS images, the occurrence of magnesium, silicon, copper, zinc, and manganese suggests that the PP may have refined the structure of the aluminium alloy.

Acknowledgement

The 6063 Al alloy employed in this investigation was supplied by Tower Alloy Nigeria Ltd., Ogun State, and our sincere appreciation is extended to them for this contribution.

References

[1] M.S.H. Forhad, T.M. Chowdhury, M. Rafiquzzaman, Mechanical properties evaluation of egg-shell and rice husk-based aluminium composites, Ceram Inter. 52 (2026) 33591-33610. https://doi.org/10.1016/j.ceramint.2026.05.386

[2] P. Priyadharsini, K.M. Falah, S.S. Shankari, S.S. Kumar, J.D. Rumeau, S.N. Djomo, Understanding the physicochemical, mechanical, swelling and environmental performance of cellulose nanocrystal hydrogels from agricultural residues, Poly Bullet. 83 (2026) 558. https://doi.org/10.1007/s00289-026-06597-x

[3] H.I. Akbar, E. Surojo, D. Ariawan, Investigation of industrial and agro wastes for aluminum matrix composite reinforcement, Proced Struct Integ. 27 (2020) 30-37. https://doi.org/10.1016/j.prostr.2020.07.005

[4] A.A. Yekinni, M.O. Durowoju, J.O. Agunsoye, L.O. Mudashiru, L.A. Animashaun, O.D. Sogunro, Automotive application of hybrid composites of aluminium alloy matrix: a review of rice husk ash based reinforcements, Development. 4 (2019) 12. https://doi.org/10.5923/j.cmaterials.20190902.03

[5] K. Anwesh, G. Shouvik, B. Ranjan, Study of Mechanical and Tribological Characteristics of Aluminum Alloy Reinforced with Sugarcane Bagasse Ash, Int Conf Tribol. 1 (2018) 1-6. http://dx.doi.org/10.2139/ssrn.3313510

[6] L. Mishra, S. Tandi, D. Mishra, A.K. Rout, J.K. Singh, Experimental Investigationon Physico**-** Mechanical and AbrasionWear Behavior of Walnut Shell**-**Glass Fiber Reinforced Epoxy Composites, J Harb Inst Technol. (2026). http://doi.org/10.11916/j.issn.1005-9113.2026015

[7] V.K. Nadimpalli, Fabrication and analysis of the properties of coconut shell ash reinforced aluminum 356 composite, Int J Eng Res Technol. 7 (2018) 216-221.

[8] Y. Xie, Y. Meng, Z. Li, Y. Wu, C. Ge, Y. Liu, Z. Zhu, H. Chen, Synergistic mechanism of beam oscillation and Zr micro-alloying: Achieving grain refinement and defect suppression in laser-arc hybrid welding of aluminum alloys, J Mat Proces Technol. 349 (2026) 119224. https://doi.org/10.1016/j.jmatprotec.2026.119224

[9] V. Bhardwaj, S. Akhai, H.A. Mehdi, A comprehensive review of the synergistic effects of adhesive nanoparticles and friction stir processing parameters on microstructure and mechanical properties of hybrid metal matrix composites, J Adhes Sci Technol. (2026) 1-59. https://doi.org/10.1080/01694243.2026.2699449

Materials Research Proceedings 74 (2026) 180-187 https://doi.org/10.21741/9781644904473-23

Fresh, Mechanical, and Drying Shrinkage Properties of Sustainable Self-Consolidating Lightweight Foamed Concrete Incorporating Recycled Concrete Aggregate and Waste Glass Fibre Powder

Mohd Afiq Mohd FAUZI[1,2,a*], Muhd Norhasri Muhd SIDEK[2,3,b], Nor Adlina AZWAN[3,c], Nurliza JASMI[2,d], Siti Zaidah OTHMAN[1,e], Kishen Jubli RINJA[1,f] and Khafidho ZAENAL[4,g]

[1]Faculty of Civil Engineering, Universiti Teknologi MARA Sarawak Branch, 94300 Kota Samarahan, Sarawak, Malaysia

[2]Institute for Infrastructure Engineering and Sustainable Management, Universiti Teknologi MARA, 40450 Shah Alam, Selangor, Malaysia

[3]Faculty of Civil Engineering, Universiti Teknologi MARA, 40450 Shah Alam, Selangor, Malaysia

[4]Faculty of Engineering, Diponegoro University, 50275 Semarang, Jawa Tengah, Indonesia

[a]mohdafiq3474@uitm.edu.my, [b]muhdnorhasri@uitm.edu.my, [c]adlinaazwan@gmail.com, [d]nurlizajasmi@uitm.edu.my, [e]sitizaida@uitm.edu.my, [f]kishenjubli07@gmail.com, [g]zaenalkhafidho@gmail.com

Keywords: Recycled Concrete Aggregate, Mechanical Properties, Self-Consolidating Lightweight Foamed Concrete, Sustainable Composite Materials, Waste Glass Fibre Powder

Abstract. The increasing depletion of natural aggregate resources and the accumulation of construction waste in landfills have driven interest in sustainable alternatives for concrete production. This research investigates the rheological and mechanical properties of self-consolidating lightweight foamed concrete (SCLFC) incorporating recycled concrete aggregate (RCA) and waste glass fibre powder (WGFP) as supplementary materials. SCLFC mixtures were prepared with three levels of RCA replacement (0%, 50%, and 100%) and two dosages of WGFP (0% and 2% by weight of cement). The specimens were ambient-cured, and compressive strength and drying shrinkage were evaluated at 3, 7, and 28 days. The incorporation of RCA reduced workability and compressive strength due to higher water absorption and weaker interfacial transition zones associated with adhered mortar. However, the addition of 2% WGFP improved particle packing and matrix densification, leading to enhanced compressive strength and reduced drying shrinkage. Although the control mixture achieved the highest strength, the mixture containing 50% RCA and 2% WGFP demonstrated a balanced combination of sustainability and acceptable engineering performance. These findings suggest that the combined use of RCA and WGFP can improve the performance and sustainability of lightweight concrete, offering a viable pathway for recycling construction and industrial waste in building materials.

Introduction

Self-compacting concrete (SCC), also known as "self-consolidating concrete" and "high-performance concrete", is one of the most significant breakthroughs in the building industry recently [1]. It is a form of concrete that can flow freely through reinforcement gaps and mould corners during the pouring process without the need for vibration or compaction. SCC offers several advantages, including improved concrete homogeneity and superior concrete finishes. It can be used in both precast and on-site concrete applications. According to the prior approach by Hameed et al. [2], the gravel content of the concrete mix should equal 50% of the packed density, and the sand content of the mortar should equal 50% of the packed density. SCC requires a higher

Content from this work may be used under the terms of the Creative Commons Attribution 3.0 license. Any further distribution of this work must maintain attribution to the author(s) and the title of the work, journal citation and DOI. Published under license by Materials Research Forum LLC.

powder concentration than conventional vibrated concrete to provide a uniform and cohesive mix. Additionally, lightweight concrete (LWC) requires a high proportion of cement paste to obtain the desired workability and compressive strength. The increased binder content required for LWC is comparable to that needed for SCC, allowing self-consolidating lightweight concrete (SCLC) to be produced using the same principles as conventional SCC. The workability and mechanical properties of SCLC were compared to those of conventional self-compacting concrete, and it was determined that SCLC may be utilised to repair and maintain existing concrete structures [3]. Foamed concrete, a type of cellular concrete, is lightweight, made of environmentally friendly materials, easy to use, capable of large-scale casting, and capable of structural application [4]. It has the potential to advance conventional concrete toward sustainable development. Self-consolidating lightweight foamed concrete (SCLFC) is a new type of high-performance concrete that combines the characteristics of SCC and LWC. SCC is a new type of concrete that flows and consolidates readily under its own weight in a formwork without compaction, although LWC can help reduce the structure's self-weight due to its low density. Thus, SCLFC not only has self-consolidating properties that facilitate concrete installation and result in a high-quality final product, but it is also lighter than conventional SCC, which benefits the structure's dead load and structural member size by integrating lightweight aggregates. It has been demonstrated that high-quality SCLFC may be manufactured with satisfactory mechanical properties and meet the same performance standards as SCC and LWC [5]. Various factors, including the quality and attributes of the aggregate, can influence the performance and robustness of SCC. The concrete industry continues to utilise a large amount of scarce natural resources [6], such as crushed granite, which is frequently used as coarse aggregate in the manufacture of concrete [7]. Global infrastructure development has resulted in a surge in demand for natural aggregates used in buildings [8]. However, the situation has resulted in increased aggregate mining activities, which have resulted in the destruction of natural resources and an ecological imbalance, leading to adverse effects on local ecosystems and biodiversity. With the ever-increasing usage of concrete, the fundamental natural materials that comprise it, namely fine and coarse aggregates, are rapidly decreasing. Due to environmental concerns, incorporating waste materials into concrete is one of the finest solutions, as it addresses the depletion of natural resources and promotes sustainability in construction practices [9]. Therefore, the use of recycled concrete aggregate (RCA) as a replacement for natural aggregate is advantageous to the environment because it reduces pollution and recycles waste materials [10].

Previous studies have investigated the individual effects of RCA or fibre-related additives in self-consolidating or lightweight concrete systems. However, limited studies have evaluated the combined incorporation of RCA and waste glass fibre powder (WGFP) in SCLFC. Therefore, this study aims to evaluate the combined influence of RCA and WGFP on the fresh properties, compressive strength, and drying shrinkage behaviour of SCLFC, and to assess the potential of these waste-derived materials for sustainable lightweight concrete production.

Materials selection

For SCLFC production, ordinary Portland cement (OPC) type general-purpose was utilised. The OPC to be used complies with BS EN 197-1:2000 due to its moderate rate of hardness and suitability for the majority of applications. A synthetic-based foaming agent was used to produce stable foam for the SCLFC mixtures. The foaming agent was diluted with water according to the manufacturer’s recommendation and preformed foam was generated before incorporation into the mortar matrix. The mineral admixture utilised in this research was natural ground calcium carbonate (GCC) supplied by Omya Construction. Silica Fume (SF) powder supplied by Scancem Materials Sdn. Bhd. was used for this research work. SF was applied at a rate of approximately 60 kg/m³ to concrete. It modified the rheology of the concrete and reacted with the cement hydration products, considerably increasing its strength, durability, and impermeability. WGFP

was collected from the CRT Manufacturing Sdn Bhd, in Section 16, Shah Alam. The WGFP was used with different percentages in this research, which are 0 and 2%. Sand from the river was used as fine aggregate. The sand was sieved to achieve a passing sieve size of 5 mm. Properly graded fine aggregate is essential for the successful execution of the work. Coarse normal aggregate (NA) was utilised in this research. The NA was crushed mining aggregate with a maximum size of 10 mm, which passed through a screen with a diameter of 10 mm. The aggregate sizes were determined in accordance with the specifications in BS EN 933-1:2012. Coarse RCA were produced from concrete waste obtained from Suntiga Concrete Sdn. Bhd., located at Jalan Sungai Rasau. The crushing and sieve analysis of the RCA were conducted at the concrete laboratory of UiTM Shah Alam. Before processing, the concrete waste was cleaned to remove debris and subsequently crushed using a jaw crusher. The crushed material was then graded using a grading machine to obtain aggregates with a maximum size of 10 mm. The particle size distribution complied with the grading limits for coarse aggregates specified in BS 8500-1:2006, indicating that the RCA was well graded. To ensure consistency in material properties, the RCA was sourced from normal concrete.

Experimental Methods

This research was conducted to investigate the rheological and mechanical properties of SCLFC containing different percentages of RCA as a replacement for natural aggregate (0%, 50%, and 100%) and WGFP as a partial replacement for cement (0% and 2%). The water-cement ratio was fixed at 0.3. The properties of SCLFC examined in this research include flowability in the fresh state, compressive strength, and drying shrinkage in the hardened state. The specimen dimensions for the compression test were 100 mm × 100 mm × 100 mm, and for the drying shrinkage test were 75 mm × 75 mm × 300 mm. Compressive strength tests were conducted at the curing ages of 3, 7, and 28 days.

Determination of mix proportion

For the research, the main components of SCLFC are similar to those used in normal concrete. The concrete mix for this research was designed in two stages. The first step was using the Building Research Establishment (BRE) method to develop the mix of SCLFC for this research. The first step aimed to determine the indicative quantity by weight of cement content, free water, and total aggregates (Fine Aggregate and Coarse Aggregate). Then, in the second stage, the SCLFC mix design progressed to the following stage, which determined the amount of foaming agent to use. The composition of the designed mixtures is shown in Table 1.

Table 1. Mix Proportion of SCLFC.

Batch No.	Rep. RCA (%)	Add. Waste Glass Fibre Powder (%)	Mix Proportion (kg/m³)									
			Cement	Water	Sand	Normal Aggregate	Coarse RCA	Foaming Agent	Ground Calcium Carbonate	Limestone Powder	Waste Glass Fibre Powder	Superplasticiser
M1	0	0	596	181	615	408	0	230	59.6	59.6	0	5.96
M2	50		596	181	615	204	204	230	59.6	59.6	0	5.96
M3	100		596	181	615	0	408	230	59.6	59.6	0	5.96
M4	0	2	596	181	615	408	0	230	59.6	59.6	11.92	5.96
M5	50		596	181	615	204	204	230	59.6	59.6	11.92	5.96
M6	100		596	181	615	0	408	230	59.6	59.6	11.92	5.96

Casting and curing

To ensure proper batching and achieve better SCLFC quality, the mixing process was carried out using a concrete mixer machine in accordance with BS 1881-125:2013. All materials used in the concrete mix were measured based on their specific weight as determined in the design mix.

After 24 hours of casting, the specimens were demoulded and placed in ambient conditions for curing until the testing date, following the procedure outlined in BS EN 12390-2:2009.

Test procedures

There are two categories of testing involved in this research, which are the slump flow test for the fresh concrete state, while the compressive strength and drying shrinkage need to be carried out in the hardened concrete state. A test was done on fresh concrete from each SCLFC mix to measure the slump flow using concrete slump flow test equipment. The slump flow test for the mixes was carried out according to BS EN 206- 9:2010. with a targeted slump in a range of 550 to 850 mm. Compressive strength is the primary physical property of concrete and is the one most used in design. The compressive strength test was carried out using the compressive test at the rate of 0.5 mm/sec on a Universal Testing Machine, an auto test 3000 kN compression machine, in compliance with BS EN 12390-3:2009. The specimens were cast for the determination of compressive strength at the ages of 3, 7, and 28 days. Drying shrinkage is the shrinking of concrete resulting from moisture loss during the drying process. The drying shrinkage test was conducted on a 75 x 75 x 300 mm beam in accordance with the recommended method specified in RILEM-ACC 5.2 for concrete.

Results and Discussion

Slump flow test.

Fig. 1 depicts the result of the slump flow test of 6 mix batches of SCLFC. The slump flow test for the 6 mix batches was a success. The slump flow diameter measurements for M1, M2, and M3 with no addition of WGFP are 680 mm, 672 mm, and 668 mm, respectively. While specimens of SCLFC with the addition of 2% WGFP are 578 mm, 564 mm, and 550 mm for M4, M5, and M6, respectively.

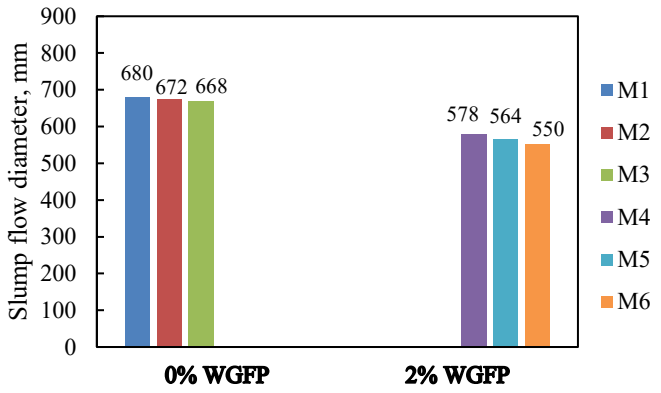


Fig. 1. Slump flow diameter of various SCLFC.

The workability value decreased as the WGFP was added to the SCLFC mixtures. The percentage difference between 0% of RCA with the addition of WGFP was a 16.22% decrease in workability compared to the control mix. As the WGFP content increases, the mix stiffens. Because of the addition of powdered waste glass fibre, the workability is reduced. Hence, the reduction in slump flow with increasing RCA and WGFP content was attributed to higher water absorption by RCA and the increased surface area introduced by WGFP particles, which reduced the amount of free water available for flow. However, adjusting the mixtures for too much water will lead to lower compressive strength. Some changes might help, such as changing physical properties or reducing the dosage, or a combination of these, to increase workability. On the other hand, the different contents of RCA, specifically 0%, 50%, and 100% of SCLFC, cause the results of slump flow diameter to vary. RCA has a lower bulk density and a higher water absorption than

natural aggregate because of the amount of adhered mortar. Therefore, a higher RCA content leads to greater absorption, which lowers the water content of cementitious materials and decreases their workability. Therefore, to produce a more workable mix, additional water needs to be added. This explains why RCA at 100% has lower workability and slump diameter than RCA at a lower concentration in SCLFC. Nevertheless, according to British Standard BS EN 206-9:2010, since all the slump flow diameters for the 6 mix batches of SCLFC are in the range of 550 to 850 mm, the slump flow test is acceptable.

Compressive strength of SCLFC.

Fig. 2 shows the result of the compressive strength of SCLFC. For each compressive strength result, three specimens were tested, and the average value was reported. Samples of size 100x100x100 mm cubes are cast, and compressive strength tests are performed at curing days of 3, 7, and 28 days in accordance with BS EN 12390-3:2009. The compressive test was done using a Universal Testing Machine at the rate of 0.5 mm/sec. Compressive strength for M1, M2, M3, M4, M5, and M6 obtained at curing day-3 is 14.77, 10.325, 5.92, 20.029, 14.89, and 9.655 N/mm², respectively. While the average compressive strength obtained on 7 days of curing is 15.854, 11.55, 6.49, 21.90, 16.488, and 10.545 N/mm^2 and lastly, the average compressive strength obtained at 28 curing days is 21.14, 16.36, 10.88, 33.383, 25.896, and 16.56 N/mm².

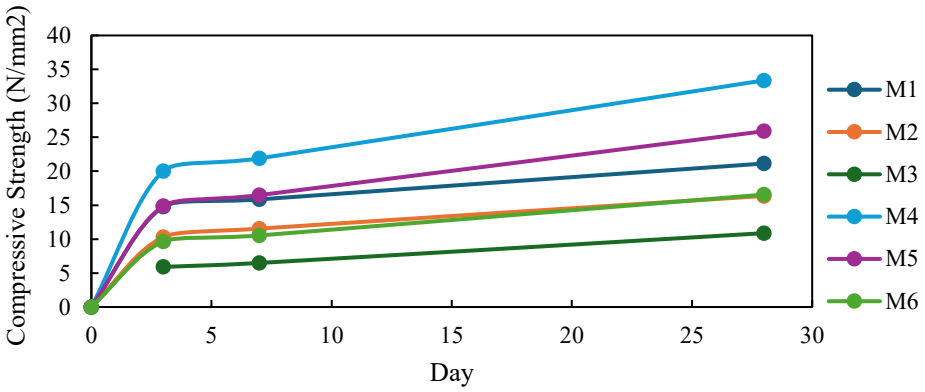


Fig. 2. Compression strength of SCLFC containing WGFP and RCA.

From Fig. 2, the compressive strength of the SCLFC increases with time of curing. Fig. 2 shows the overall compressive strength for all 6 mix batches, with M4, which contains 0% RCA and 2% fibre, being the highest for 3, 7, and 28 curing days compared to the control SCLFC. M3, with 100% RCA and 0% WGFP, has the lowest compressive strength at all curing days of 3, 7, and 28 days. When M1 is compared to M3, and M4 is compared to M6, it can be shown that the compressive strength of 0% RCA is greater than that of the control SCLFC of 100% RCA. This is due to the reduction in compressive strength with increasing RCA content, which was mainly attributed to the porous adhered mortar attached to RCA particles and the weaker interfacial transition zone between RCA and cement paste. Although RCA may provide limited internal curing effects through absorbed water release, the detrimental influence of increased porosity and weaker aggregate–paste bonding dominated the overall mechanical performance [11]. The mechanical bonding between the cement pastes and RCA became poorer at a greater level of RCA, resulting in low compressive stress [12]. From the result, the optimum RCA percentage to be used in the SCLFC that contains a 2% addition of WGFP is at 0% RCA, as it has the highest value of compressive strength compared to the control specimen M1, which contains 0% of RCA. Aggregates with high water absorption have a significant impact on the development of mechanical and durability properties in concrete. Hence, it can be concluded that 0% RCA has the

highest compressive strength compared to the replacement of 50% and 100% of RCA in SCLFC. Whilst in terms of the addition of WGFP in SCLFC, Fig. 2 depicts that the specimen containing 2% of WGFP has higher compressive strength than SCLFC that does not contain 2% WGFP. This is because powder increases the fine particle percentage in the SCLFC; thus, it makes the material more compacted. On the other hand, this situation also lessens the pores introduced in the SCLFC. As a result, less porous and more compacted SCLFC brings higher compressive strength to the specimens. It can be concluded that, with the addition of WGFP. The compressive strength is higher than that of the other SCLFC specimens that had no addition of WGFP. The incorporation of RCA and WGFP contributes to sustainable construction by reducing dependency on virgin aggregates and diverting industrial waste from landfills. Although mixtures with high RCA replacement exhibited lower compressive strength, the use of 50% RCA with WGFP demonstrated acceptable engineering performance while improving resource efficiency and waste utilization. Therefore, the proposed SCLFC mixtures have potential for non-structural and lightweight construction applications.

Drying Shrinkage of SCLFC

Fig. 3 shows the drying shrinkage of SCLFC with curing days. Drying shrinkage values are presented in terms of shrinkage strain magnitude, where higher absolute values indicate greater dimensional reduction. The drying shrinkage values of M1, M2, and M5 measured after 3, 7, and 28 days of curing gradually decreased. Furthermore, the drying shrinkage of M6 increases from the curing day of 3 days to 7 days, then decreases at 28 days. Whilst M3, which contains 100% RCA and 0% WGFP, has the highest drying shrinkage of all, at 14.673 mm/m. Lastly, M4, which contains 0% of RCA and 2% of fibre, has the lowest drying shrinkage of all, where the drying shrinkage increases about 0.205 mm/m from curing day 3 to 28 days.

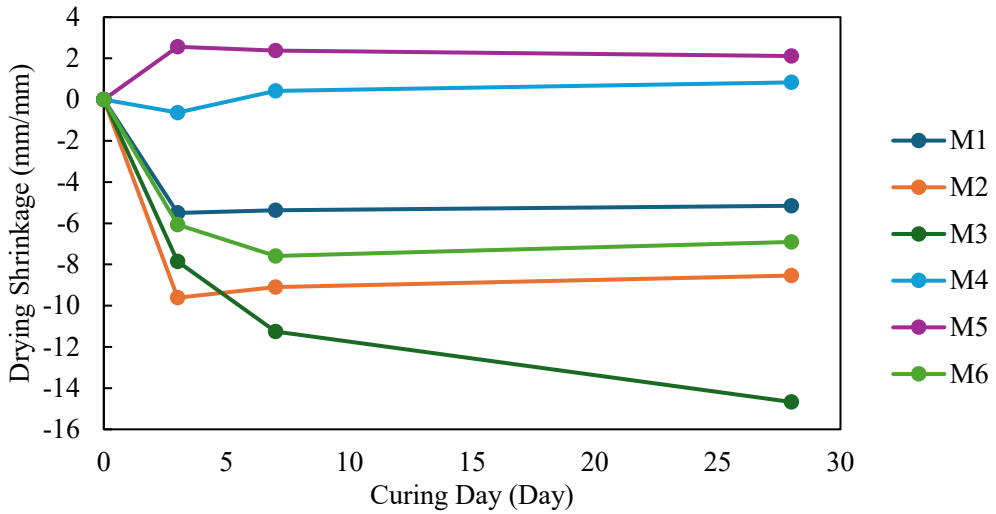


Fig. 3. Drying Shrinkage Result of SCLFC Containing WGFP and RCA.

Due to the pore-filling effect of the fibre on the structure membrane, the pore walls of the SCLFC became denser. This enabled the generation and distribution of the hydration products to become more homogeneous throughout the specimen matrix and, thereby, enhanced the resistance to shrinkage [13]. The degree of this shrinkage depends on the SCLFC's physical features, such as the type of curing and its temperature at the time of curing. According to the results, the SCLFC shrinks as a result of the hydration process that occurred. The heat that concrete generates during curing is referred to as the "heat of hydration" [14]. When cement, water, aggregate, and additives are combined, a significant heat increase brought on by hydration occurs, known as an exothermic reaction [15]. SCLFC expands as it gets hotter and contracts as it gets cooler. Hence, with the ongoing process of cementing materials hydration, the shrinkage value is increasing. There are

numerous tiny pores, fractures, and spaces between the pores on the walls of the pores in SCLFC. The addition of WGFP fills the pore walls, which improves the pore structure, decreases the occurrence of weak pores, and makes the pore wall structure denser. The layer structure created by the curing reaction can effectively fill interior pores and microcracks [13]. The filling of WGFP improves the structure of the pore wall, thus reducing water migration and improving resistance to drying shrinkage. The resistance to shrinkage was consequently improved and enhanced.

Limitation

This study is limited to slump flow, compressive strength, and drying shrinkage evaluation. Additional investigations, including rheological characterization, tensile strength, durability performance, density analysis, and microstructural evaluation, such as SEM or porosity analysis, are recommended for future work.

Conclusion

This study evaluated the influence of RCA and WGFP on the fresh and hardened properties of SCLFC. The incorporation of RCA reduced slump flow and compressive strength due to higher water absorption and weaker aggregate–paste bonding associated with adhered mortar. Conversely, the inclusion of 2% WGFP improved compressive strength and reduced drying shrinkage through filler and matrix densification effects. Among the investigated mixtures, the combination containing 50% RCA and 2% WGFP demonstrated a balanced performance in terms of sustainability and engineering properties. The findings indicate that WGFP can partially compensate for the adverse effects of RCA in lightweight foamed concrete systems. However, further studies involving durability performance, density evaluation, and microstructural characterization are recommended to strengthen the understanding of the material behaviour.

Acknowledgement

The author would like to acknowledge the Research Management Unit for providing the “Geran Penyelidikan Fundamental Penyelidik Muda” (FRGS-EC/1/2024/TK01/UITM/02/12), the Institute for Infrastructure Engineering and Sustainable Management (IIESM) and Faculty of Civil Engineering, Universiti Teknologi MARA Sarawak Branch for providing the facilities to accomplish the experimental work for this research.

References

[1] G.H. Ahmed, H. Ahmed, B. Ali, R. Alyousef, Assessment of high performance self-consolidating concrete through an experimental and analytical multi-parameter approach, Materials 14 (2021) 985. https://doi.org/10.3390/ma14040985

[2] M.S. Hameed, A.S.S. Sekar, V. Saraswathy, , Strength and permeability characteristics study of self-compacting concrete using crusher rock dust and marble sludge powder. Arabian Journal for Science and Engineering 37 (2012) 561–574. https://doi.org/10.1007/s13369-012-0201-x

[3] J.T.F. De Sousa, M.A.S. Dos Anjos, J.A.D.S. Neto, E.C. De Farias, F.G. Branco, C.M. Pederneiras, Self-compacting concrete with artificial lightweight aggregates from sugarcane ash and calcined scheelite mining waste. Applied Sciences 15 (2025) 452. https://doi.org/10.3390/app15010452

[4] S.N. Shah, K.H. Mo, S.P. Yap, J. Yang, T.-C. Ling, Lightweight foamed concrete as a promising avenue for incorporating waste materials: A review. Resources, Conservation and Recycling 164 (2021) 105103. https://doi.org/10.1016/j.resconrec.2020.105103

[5] C.-L. Hwang, V.-A. Tran, A study of the properties of foamed lightweight aggregate for self-consolidating concrete. Construction and Building Materials 87 (2015) 78–85. https://doi.org/10.1016/j.conbuildmat.2015.03.108

[6] P. Shafigh, H.B. Mahmud, M.Z.B. Jumaat, R. Ahmmad, S. Bahri, Structural lightweight aggregate concrete using two types of waste from the palm oil industry as aggregate. Journal of Cleaner Production 80 (2014) 187–196. https://doi.org/10.1016/j.jclepro.2014.05.051

[7] J.T. Wembe, L.L.M. Ngueyep, E.E.A. Moukete, J. Eslami, P. Pliya, J.-M.B. Ndjaka, A. Noumowe, Physical, mechanical properties and microstructure of concretes made with natural and crushed aggregates: Application in building construction. Cleaner Materials 7 (2023) 100173. https://doi.org/10.1016/j.clema.2023.100173

[8] D. Vijerathne, S. Wahala, C. Illankoon, Impact of crushed natural aggregate on environmental footprint of the construction industry: Enhancing sustainability in aggregate production. Buildings 14 (2024) 2770. https://doi.org/10.3390/buildings14092770

[9] F. Alsharari, Utilization of industrial, agricultural, and construction waste in cementitious composites: A comprehensive review of their impact on concrete properties and sustainable construction practices. Materials Today Sustainability 29 (2025) 101080. https://doi.org/10.1016/j.mtsust.2025.101080

[10] R.P. Neupane, N.R. Devi, T. Imjai, A. Rajput, T. Noguchi, Cutting-edge techniques and environmental insights in recycled concrete aggregate production: A comprehensive review. Resources, Conservation & Recycling Advances 25 (2025) 200241. https://doi.org/10.1016/j.rcradv.2024.200241

[11] A. Stolarska, T. Rucińska, Evaluation of Physical Characteristics and Sorption of Cement Mortars with Recycled Ceramic Aggregate. Materials 14 (2021) 7852. https://doi.org/10.3390/ma14247852

[12] A. Ayob, M.E. Razali, S. Alias, A.G. Ahmad, D.S.H. Ali, Engineering behavior of concrete with recycled aggregate. MATEC Web of Conferences 87 (2017) 01002. https://doi.org/10.1051/matecconf/20178701002

[13] J. Gong, K. Li, Minimizing drying shrinkage and enhancing impermeability of foam concrete modified with epoxy resin. Advances in Civil Engineering (2020) 897687. https://doi.org/10.1155/2020/8897687

[14] A.R.M. Ridzuan, M.A.M. Fauzi, M.F. Arshad, M.S. Harun, N. Jasmi, Effect of limestone powder in self consolidating lightweight foam concrete. Solid State Phenomena 280 (2018) 469–475. https://doi.org/10.4028/www.scientific.net/ssp.280.469

[15] J. Skibsted, R. Snellings, Reactivity of supplementary cementitious materials (SCMs) in cement blends. Cement and Concrete Research 124 (2019) 105799. https://doi.org/10.1016/j.cemconres.2019.105799

Materials Research Proceedings 74 (2026) 188-196 https://doi.org/10.21741/9781644904473-24

Compressive and Flexural Strength of Mortar with Ceramic Tile Waste Powder as Partial Cement Replacement

Samia BOUZOUAID[1,a *]

[1]Faculty of Applied Sciences, University Kasdi Merbah Ouargla, Department of Civil Engineering and Hydraulics, Laboratory of Exploitation and Valorization of Natural Resources in Arid Zones, 30000 Ouargla, Algeria

[a]samia.bouzouaid@univ-ouargla.dz

Keywords: Mechanical Properties, Ceramic Waste Powder, Cement Replacement, Compressive Strength, Flexural Strength

Abstract. This work studies the mechanical performance of mortar using ceramic tile waste powder (CWP) as a partial replacement of cement in the range from 5% to 30% of total cement weight. Although CWP has been studied in concrete systems, its effect on mortar produced with local Algerian siliceous sand has not been sufficiently investigated. Samples of mortar were made as per standard laboratory protocols and were tested for compressive strength and flexural strength after a curing period of 28 days. Flexural strength increased by 5.3% for 10% CWP replacement with respect to control mortar. In addition, the compressive strengths of MCWP20 and MCWP25 samples were 34.8 MPa and 35.2 MPa, respectively, which are similar to the strength of the control mortar (MO) of 36.2 MPa and satisfy the minimum specifications of ASTM C270 for structural mortar applications. These results indicate that CWP can be used as a partial replacement of cement and yet have the mechanical qualities needed for a structural application. In addition, the use of CWP has economic benefits, as it converts ceramic tile waste into a valuable resource and reduces the carbon footprint of the building industry by reducing Portland cement usage. Further durability tests are necessary to confirm the performance of CWP-based mortars under severe environmental conditions.

Introduction

The increased need for sustainable construction materials has prompted researchers and industry professionals to explore a range of alternatives to ordinary Portland cement. Cement production is an energy-intensive process and a major source of CO_2 emissions globally. Therefore, supplemental cementitious materials from industrial by-products and waste have been widely studied as possible substitutes [1]. The construction and demolition industries generate considerable amounts of ceramic tile trash. Such debris is problematic to dispose of and can cause severe environmental damage. Studies conducted recently have revealed that the incorporation of ceramic waste powder (CWP) into cement mortar might lead to a favorable impact on its mechanical characteristics, such as compressive and flexural strength, owing to the pozzolanic reactivity and filler effect of the waste powder in the mortar matrix [2, 3]. Generally, replacement rates up to 10–25% have been shown to improve or maintain these qualities, and greater ratios are found to lower the strength due to poor hydration and increased porosity [1, 4]. Nevertheless, the optimum CWP dosage is a function of several interrelated factors, such as the particle size distribution, chemical composition, and characteristics of the particular mortar matrix employed, with a replacement ratio of about 10% most consistently being associated with significant gains in both compressive and flexural strength, although higher ratios, while less favorable mechanically, still provide considerable economic and environmental benefits [5, 6]. Ceramic tile waste is considered an environmentally friendly material, besides its mechanical performance, because its incorporation reduces the landfill load and supports a circular economy through the recycling of

Content from this work may be used under the terms of the Creative Commons Attribution 3.0 license. Any further distribution of this work must maintain attribution to the author(s) and the title of the work, journal citation and DOI. Published under license by Materials Research Forum LLC.

industrial waste by means of current or alternative manufacturing methods [7]. Despite this body of evidence confirming the technical viability and environmental benefits of CWP in cementitious systems, a systematic investigation linking CWP's particle size distribution and chemical composition, together with the mortar's water-to-cement ratio, to its resulting mechanical performance has not been sufficiently addressed in the existing literature—particularly for mortars produced with local Algerian siliceous sand under standardized testing conditions. In particular, the combined influence of CWP fineness and pozzolanic reactivity on both compressive and flexural strength remains unclear. Therefore, the present study has been conducted to fill this gap with a systematic experimental investigation following the ASTM C348 (flexural strength) and ASTM C349 (compressive strength on broken prism halves) to find the optimum CWP replacement ratio and to correlate the physical and chemical properties of CWP with the mechanical behavior of the resulting mortar mixes.

Materials and Methods

Materials

The raw materials used in this study are shown in Fig. 1, presenting (a) Portland cement, (b) local siliceous sand, and (c) ceramic tile waste powder (CWP).



(a) (b) (c)

Fig. 1. Raw material (a) Cement (b) Sand (c) Ceramic tile waste powder (CWP).

Table 1. summarizes the physical properties of the natural sand used in this study. The specific gravity of the aggregates was determined in terms of oven-dry (OD) and saturated surface-dry (SSD) conditions in accordance with ASTM C128, and values of 2.65 and 2.70 were obtained accordingly. The sand is of medium-grade fine aggregate with a fineness modulus of 2.5 suitable for the construction of mortar.

Table 1. Physical properties of the sand.

Property	Value
Specific Gravity (oven-dry)	2.65
Bulk Density [kg/m³]	1,600
Specific Gravity (saturated surface-dry, SSD)	2.7
Water Absorption [%]	1.5
Fineness Modulus	2.5
Sand Equivalent [%]	75

The recycling procedure for producing the ceramic tile waste powder is shown in Fig. 2. Waste ceramic tiles were collected from building sites, crushed and ground in a ball mill, sieved through a 0.08 mm sieve, and dried in an oven at 100–110°C for 24 h to obtain the final CWP used in the mortar formulation. Table 2 gives a summary of the physical properties of the CWP. The cement used was ordinary Portland cement type CPA–CEM I 42.5 R, manufactured by the Lafarge cement factory in Biskra, Algeria, conforming to ASTM C150 [9]. The cement has a Blaine-specific surface area of 3700 cm²/g and a specific gravity of 3.14 g/cm³. The specific gravity of CWP is less than that of cement. This finding agrees with the values in previous studies [4, 8].

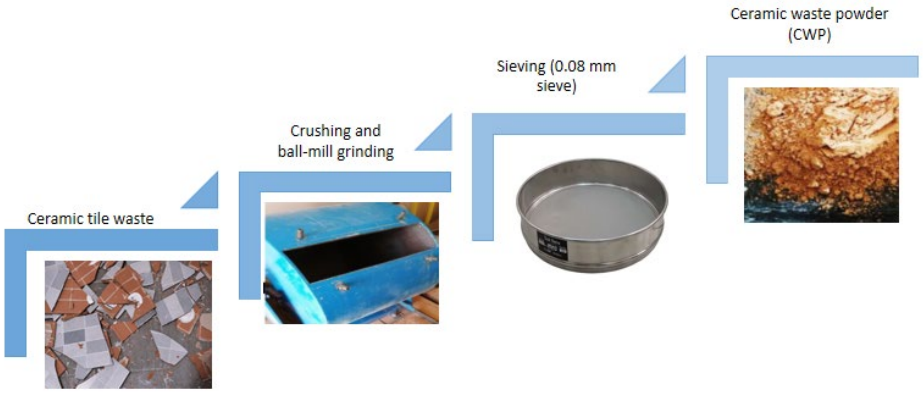


Fig. 2. Flowchart of the recycling process for ceramic tile waste.

Table 2. Physical Properties of Ceramic Tile Powder (CWP).

Property	Value
Bulk density [kg/m³]	1.125
Specific gravity	2.3
Moisture content [%]	0.10
Water absorption [%]	21.5
Fineness [µm]	~75
Color	Light brown

Mix Design

Mortar mixes were prepared in six formulations (Table 3). The reference (control) mix was prepared with only ordinary Portland cement (OPC) without ceramic tile waste powder (CWP). The other five mixes were prepared by replacing cement with CWP gradually at 5%, 10%, 20%, 25%, and 30% by weight of cement, respectively. The selected replacement levels were chosen to achieve a broad range of substitution ratios (0–30%) based on the previous literature indicating optimal mechanical performance in the 10–25% range [2, 3, 4, 5, 6, 8] and also to study the behavior at higher replacement levels. All mixes were prepared with a fixed water-to-cement ratio (w/c) of 0.5, corresponding to 225 ml of water for 450 g of cement, so that the workability and consistency were kept constant during the experimental program.

All mixtures were poured into rectangular molds of size 160 × 40 × 40 mm. The specimens were demolded after 24 h of casting and cured for 28 days under standard laboratory conditions (20 ± 2°C and 95 ± 5% relative humidity). The compressive strength was measured on the halves of the broken prisms according to ASTM C349 [10], and the flexural strength was measured according to ASTM C348 [11].

Table 3. Mixture Proportions of Prepared Mortar Specimens.

Mixture	Cement [g]	CWP [g]	Sand [g]	Water [ml]	W/C
MO-Control	450	0	1350	225	0.5
MCWP5%	427.5	22.5	1350	225	0.5
MCWP10%	405	45	1350	225	0.5
MCWP20%	360	90	1350	225	0.5
MCWP25%	337.5	112.5	1350	225	0.5
MCWP30%	315	135	1350	225	0.5

Testing

Mechanical properties of mortar specimens were determined with compressive and flexural strength tests after 28 days of curing. Flexural strength was determined using a universal testing machine with a capacity of 50 kN in a three-point bending test in accordance with ASTM C348 [11]. The test was performed at room temperature, and each result is an average of three specimens. After the flexural test, the two broken halves of each specimen were tested for compressive strength using a 2000 kN capacity machine in accordance with ASTM C349 [10] at a loading rate of 0.5 MPa/s. Three specimens were tested in each test to ensure the results were reliable and reproducible.

Results and Discussion

Fig. 3 shows the microstructure of the sand particles. The image shows irregular, angular particles with a rough surface texture, characteristic of siliceous sand from southern Algeria. This angular morphology is beneficial for mortar performance, as it promotes mechanical interlocking between particles and positively contributes to strength development. Fig. 4 shows the particle size distribution of the sand, which is continuously graded from 0.08 to 5 mm, indicating that the sand is well graded and suitable for mortar production. This well-graded distribution helps efficient particle packing and a lower void content in the mortar matrix. This explains the relatively high compressive strength reached by the control mix (36.2 MPa) and the favorable mechanical behavior reported for the CWP replaced mixtures.

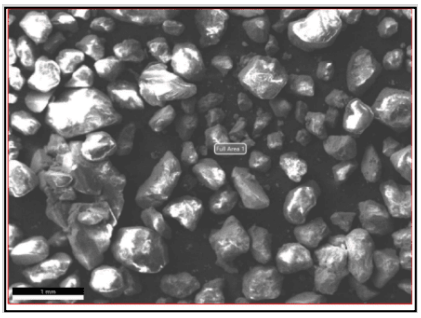


Fig. 3. SEM image of the sand particles used.

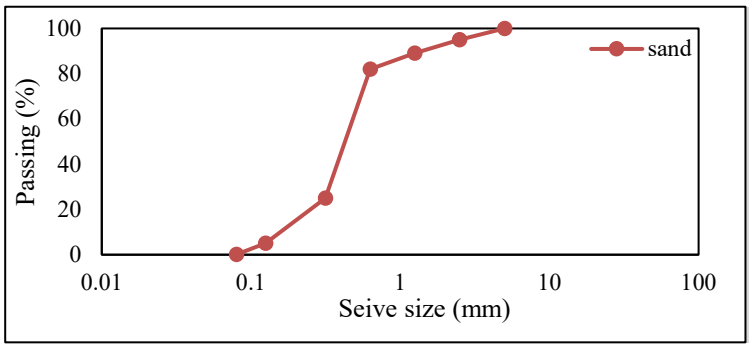


Fig. 4. Particle size analysis of the sand used.

The elemental composition and microstructural features of CWP were determined by energy dispersive X-ray (EDX) spectroscopy and scanning electron microscopy (SEM), respectively. The EDX spectrum (Fig. 5) indicated that CWP is composed of oxygen, silicon, and aluminum as the main elements, with small amounts of calcium, iron, potassium, sodium, magnesium, and carbon. The elemental profile dominated by silica and alumina is consistent with an aluminosilicate-rich composition and supports the potential pozzolanic activity of CWP, as reactive silica and alumina could combine with calcium hydroxide ($Ca(OH)_2$) released during cement hydration to form additional calcium silicate hydrate (C-S-H) gel, contributing to strength development at later ages. The SEM image (Fig. 6) shows that the CWP particles had an irregular angular morphology with a rough surface texture due to the ball mill grinding process. It is expected that this morphology would lead to better particle packing and mechanical interlocking within the mortar matrix, particularly at low replacement levels, which might be a partial reason for the observed improvement in flexural strength at 10% CWP replacement.

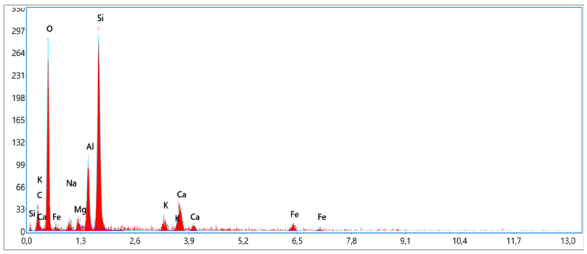


Fig. 5. EDX spectrum of the CWP.

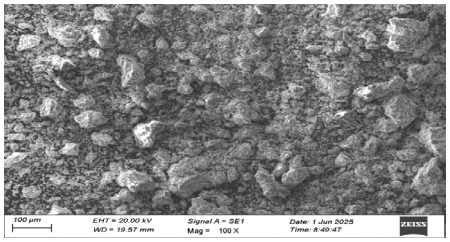


Fig. 6. SEM micrograph of ceramic tile powder (100X).

The chemical composition of the cement, as obtained from Table 4, shows that the cement conforms to the ASTM C150 requirements, with CaO (64.10%) and SiO_2 (20.54%) as the main oxides and MgO (3.01%) and SO_3 (2.22%) within the permissible limits, which confirms the suitability of this cement for use in the production of structural mortar. Table 5 summarizes the compressive and flexural strength results for all mortar mixes. Figs. 7 and 8 also present the data graphically.

Table 4. Chemical composition of the Portland cement used [%].

CaO	SiO_2	Al_2O_3	Fe_2O_3	MgO	K_2O	Na_2O	SrO	TiO_2	P_2O_5	Cl	SO_3
64.10	20.54	4.45	3.41	3.01	0.67	0.18	0.06	0.25	0.15	0.02	2.22

Table 5. Compressive and flexural strength of mortar mixes (mean ± SD, n = 3).

Mixture	Compressive Strength [MPa]	Flexural Strength [MPa]
MO-Control	36.2 ± 0.56	5.61 ± 0.16
MCWP5%	31.6 ± 0.70	5.72 ± 0.11
MCWP10%	33.1 ± 0.70	5.91 ± 0.13
MCWP20%	34.8 ± 0.89	5.60 ± 0.12
MCWP25%	35.2 ± 0.36	5.22 ± 0.12
MCWP30%	32.0 ± 0.87	4.89 ± 0.11

Compressive Strength

Fig. 7 shows the compressive strength results of all the mortar mixtures after curing for 28 days. The control mortar (MO) without CWP gave the highest compressive strength of 36.2 MPa. The compressive strength dropped to 31.6 MPa and 33.1 MPa at 5% and 10% CWP replacement. The decrease is attributed to the lower cement content at these replacement levels, which limits the amount of calcium silicate hydrate (C-S-H) gel formed during hydration, and the relatively low pozzolanic activity of CWP at early ages. These results are consistent with prior studies [2, 3, 12] that showed that moderate CWP replacement levels might not be pozzolanically sufficient to compensate for the decrease in cement content. The compressive strength was gradually restored to 34.8 MPa and 35.2 MPa at 20% and 25% CWP replacement, respectively. This improvement is attributed to the synergistic effect of the pozzolanic activity of CWP and its microfilling effect, which reduces the porosity and densifies the mortar matrix to the level of the control mix. With 30% replacement of CWP, the compressive strength decreased to 32.0 MPa. This finding is in agreement with literature [8, 13] stating that an excessive cement replacement leads to a binder content that is not enough for adequate hydration and strength development in the mortar matrix. The irregular particle morphology of CWP as seen from the SEM images (Fig. 6) influenced the packing density of the mortar matrix, which was a factor for the strength variations observed at different replacement levels.

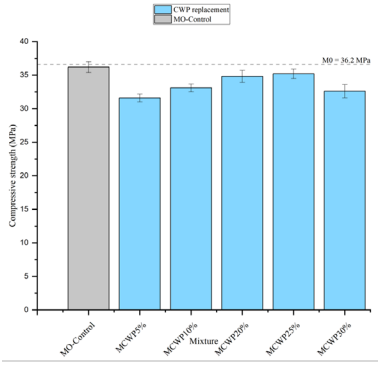


Fig. 7. Influence of CWP content on compressive strength of cementitious mortar (MPa).

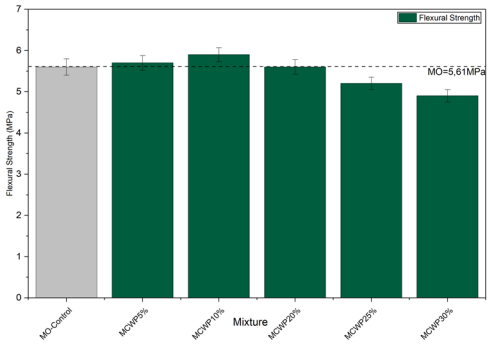


Fig. 8. Influence of CWP content on flexural strength of cementitious mortar (MPa).

Fig. 8 displays the flexural strength results. The flexural strength of control mortar (MO) was 5.61 MPa. The maximum flexural strength was achieved for 10% CWP replacement, which was 5.91 MPa, 5.3% higher than the control mix. This improvement results from the refinement and densification of the microstructure, which occurs due to better particle packing at low levels of replacement, as reported in previous studies [12, 13, 14, 15, 16]. Low-to-moderate CWP contents not only maintain the flexural resistance but can even improve it due to the combined filler effect and pozzolanic reactivity of fine ceramic particles within the mortar matrix. With an increase in replacement beyond 10%, flexural strength started decreasing. Values of flexural strength at 20%, 25%, and 30% replacement were 5.60 MPa, 5.22 MPa, and 4.89 MPa, respectively. The minimum flexural strength of 4.89 MPa was obtained at 30% CWP replacement. This means that the mortar matrix deteriorates with CWP content above this level because the cement paste is not enough to complete the hydration process. This behavior is in agreement with the results found in the literature [17], where an upper limit in strength development was observed, beyond which increasing the amount of CWP negatively affected the mechanical properties [2]. In general, replacing 10% to 25% of CWP gives the best balance between mechanical performance and environmental impact. The pozzolanic and filler effects of CWP are fully exploited in this range, but the strength values in compression and flexion still satisfy the ASTM C349 and ASTM C348 requirements for cementitious mortars. These results confirm that CWP is a feasible and sustainable supplementary cementitious material for construction applications [13].

The results indicated that the compressive and flexural strength showed different trends with increasing CWP replacement ratios. The compressive strength progressively reduced beyond 25% replacement. The flexural strength was observed to be the highest at 10% CWP content (5.91 MPa) and progressively reduced at higher replacement levels. This difference can be explained by the double role of CWP particles in the mortar matrix. At low replacement ratios (5–10%), the fine CWP particles mainly act as a physical filler, improving the packing density of the particles and refining the pore structure of the mortar. This densification effect is especially beneficial for flexural strength since it improves the interfacial transition zone (ITZ) between the cement paste and sand particles, leading to higher resistance to bending stresses. At higher replacement ratios (20–30%), the continuous reduction in cement content results in a reduction in the total amount of calcium silicate hydrate (C-S-H) gel formed during hydration. C-S-H is the main binding phase that contributes to the mechanical strength, so its reduction directly influences the compressive performance. Furthermore, the partial pozzolanic reaction of CWP at higher dosages due to insufficient calcium hydroxide ($Ca(OH)_2$) leads to unreacted CWP particles, which act as weak points in the mortar matrix, accelerating the strength reduction under compressive loading. These results are in agreement with the literature [6, 7], where similar behavior was reported for mortars

containing fine ceramic waste particles, where the filler effect dominates at low replacement rates and the dilution effect dominates at higher contents.

Conclusion

The present study investigates the possibility of using ceramic tile waste powder (CWP) as a sustainable partial replacement for cement in mortar at replacement levels of 0 to 30% by cement weight. The results demonstrate that CWP can be incorporated into mortar mixtures with acceptable mechanical performance and offer technical and environmental benefits. From the mechanical perspective, the results indicated that the compressive strength was better preserved among the treated mixes with replacement levels of 20% and 25% with values of 34.8 MPa and 35.2 MPa for MCWP20 and MCWP25, respectively. These values are close to the strength of the control mortar of 36.2 MPa and meet the minimum requirements of ASTM C270 [18] for structural mortar applications. The maximum flexural strength was achieved at 10% CWP replacement, which was 5.91 MPa (increased by 5.3% compared to the control mortar with a flexural strength of 5.61 MPa). This difference in behavior of the two strength parameters reflects the dual role of CWP in the mortar matrix: at low replacement levels, fine CWP particles improve the particle packing and reduce the interfacial transition zone, which benefits the flexural resistance; at higher levels, the reduction of cement content limits the formation of C-S-H gel, which gradually reduces the compressive performance. The flexural strength gradually decreased beyond 10% replacement, while the compressive strength decreased significantly beyond 25% replacement, which confirmed that the excessive CWP content affects the hydration process and reduces the mortar matrix strength. These results emphasize the importance of finding a replacement ratio that optimally balances mechanical performance with sustainability objectives. From the sustainability perspective, the use of CWP as a partial cement replacement is a feasible approach to address two important issues: the minimization of the ceramic waste disposed of in landfills and the reduction of the carbon footprint due to the Portland cement manufacturing. CWP substitution for up to 25% of cement produces similar mechanical performance and makes a significant contribution to sustainable construction practices. Future studies should focus on optimizing the replacement ratio of CWP in the range of 10-25% using different types of cement, water-to-cement ratios, and curing conditions. The long-term durability of CWP-based mortars should also be investigated under aggressive environments such as sulfate attack, chloride ingress, and freeze-thaw cycles. The elastic modulus should also be assessed to complete the mechanical characterization of optimized mixes. Furthermore, the present findings should be validated through field applications and case studies to promote wider use of CWP in sustainable construction. It is worth mentioning that the elastic modulus testing and X-ray diffraction (XRD)-based mineralogical characterization of CWP were not performed in the present study, which are valuable directions for future works to further understand the pozzolanic mechanisms and stiffness behavior of CWP-based mortars.

Acknowledgments

The author would like to thank the Research Centre in Analytical Chemistry and Physics (CRAPC Ouargla) in Algeria for their support in conducting advanced analyses, such as energy-dispersive X-ray (EDX) spectroscopy and scanning electron microscopy (SEM). The authors also gratefully acknowledge the Laboratory of Public Works of the South (LTPS) in Ouargla for their assistance in providing all relevant standards and overseeing the process of experimental mortar investigations.

References

[1] J. De Brito, A.S. Pereira, J.R. Correia, Mechanical behaviour of non-structural concrete made with recycled ceramic aggregates, Cement and Concrete Composites, 27 (2005) 429–433. https://doi.org/10.1016/j.cemconcomp.2004.07.005

[2] A.M. Nayana, P. Rakesh, Strength and durability study on cement mortar with ceramic waste and micro-silica, Materials Today: Proceedings, 5 (2018) 24780–24791. https://doi.org/10.1016/j.matpr.2018.10.275

[3] M. Attaelmanan, M. Elhaj Mahgoub Kambal, M.I. Mansour, Study the effect of using ceramic waste powder as partial replacement for cement on concrete properties, Journal of Karary University for Engineering Sciences (2021).https://doi.org/10.54388/jkues.v1i1.125

[4] R. Kumar Goyal, V. Agarwal, R. Gupta, K. Rathore, P. Somani, Optimum utilization of ceramic tile waste for enhancing concrete properties, Materials Today: Proceedings, 49 (2022) 1769–1775. https://doi.org/10.1016/j.matpr.2021.05.324

[5] H.M. Najm, S. Ahmad, The use of waste ceramic optimal concrete for a cleaner and sustainable environment: A case study of mechanical properties, Civil and Environmental Engineering Reports, 32 (2022) 85–115. https://doi.org/10.2478/ceer-2022-0036

[6] Y.O. Özkılıç, A. Bahrami, Y. Güzel, A.S. Soğancı, M. Karalar, E. Althaqafi, et al., Waste ceramic powder for sustainable concrete production as supplementary cementitious material, Frontiers in Materials, 11 (2025) 1450824. https://doi.org/10.3389/fmats.2024.1450824

[7] Y.O. Özkılıç, E. Althaqafi, A. Bahrami, C. Aksoylu, M. Karalar, N. Özdöner, et al., Influence of ceramic waste powder on shear performance of environmentally friendly reinforced concrete beams, Scientific Reports, 14 (2024) 10401. https://doi.org/10.1038/s41598-024-59825-7

[8] M.J. Taher, E.H. Abed, M.S. Hashim, Using ceramic waste tile powder as a sustainable and eco-friendly partial cement replacement in concrete production, Materials Today: Proceedings (2023). https://doi.org/ 10.1016/j.matpr.2023.04.060

[9] ASTM C150, Standard Specification for Portland Cement, ASTM International, West Conshohocken, PA, 2014.

[10] ASTM C349, Standard Test Method for Compressive Strength of Hydraulic-Cement Mortars (Using Portions of Prisms Broken in Flexure), ASTM International, West Conshohocken, PA, 2018.

[11] ASTM C348, Standard Test Method for Flexural Strength of Hydraulic-Cement Mortars, ASTM International, 2014.

[12] X. Chen, D. Zhang, S. Cheng, X. Xu, C. Zhao, X. Wang, et al., Sustainable reuse of ceramic waste powder as a supplementary cementitious material in recycled aggregate concrete, Journal of Building Engineering, 52 (2022) 104418. https://doi.org/10.1016/j.jobe.2022.104418

[13] M. Ebrahimi, A. Eslami, I. Hajirasouliha, M. Ramezanpour, K. Pilakoutas, Effect of ceramic waste powder as a binder replacement on the properties of cement- and lime-based mortars, Construction and Building Materials, 379 (2023) 131146. https://doi.org/10.1016/j.conbuildmat.2023.131146

[14] D. Kumar, A.R.M. Sam, S.A. Mangi, R.P. Memon, S. Bhutto, A. Waheed, Properties of mortar containing ceramic waste powder and effective micro-organisms, International Journal of Advanced Science and Technology, 29 (2020).

[15] W.E. Elemam, I.S. Agwa, A.M. Tahwia, Reusing ceramic waste as a fine aggregate and supplementary cementitious material in sustainable concrete, Buildings, 13 (2023) 2726. https://doi.org/10.3390/buildings13112726

[16] F. Erol, M.M. Al-mashhadani, Y. Aygörmez, A. Niş, Effect of ceramic waste powder content and sodium hydroxide molarity on the residual mechanical strength of alkali-activated

mortars, Materials Chemistry and Physics, 309 (2023) 128403. https://doi.org/10.1016/j.matchemphys.2023.128403

[17] O. Dehghani, A. Eslami, M.A. Mahdavipour, D. Mostofinejad, M. Ghorbani Mooselu, K. Pilakoutas, Ceramic waste powder as a cement replacement in concrete paving blocks: mechanical properties and environmental assessment, International Journal of Pavement Engineering, 25 (2024) 2370563. https://doi.org/10.1080/10298436.2024.2370563

[18] ASTM C270, Standard Specification for Mortar for Unit Masonry, ASTM International, West Conshohocken, PA, 2019.

Materials Research Proceedings 74 (2026) 197-204 https://doi.org/10.21741/9781644904473-25

Effect of Sulfuric Acid Attack on the Properties of Fiber Reinforced Geopolymer Concrete

Muhammad Affiq ABDUL JAMIL[1],
Meor Ahmad Faris MEOR AHMAD TAJUDIN[1,2,a *],
Warid Wazien AHMAD ZAILANI[3], Mohammad Firdaus ABU HASHIM[1,2],
Muhammad Fahem MOHD TAHIR[2,4], Mohd Ikram RAMLI[5],
Mohammed Izzuddeen MOHD YAZID[6] and M.N.A. UDA[1,7]

[1]Faculty of Mechanical Engineering Technology, Universiti Malaysia Perlis (UniMAP), Pauh Putra 02600 Arau, Perlis, Malaysia

[2]Center of Excellence Geopolymer and Green Technology (CEGeoGTech), Universiti Malaysia Perlis, Perlis 01000, Malaysia

[3]School of Civil Engineering, College of Engineering, Universiti Teknologi MARA (UiTM), 40450 Shah Alam, Malaysia

[4]Faculty of Chemical Engineering Technology, Universiti Malaysia Perlis (UniMAP), 01000 Kangar, Malaysia

[5]School of Engineering, Universiti of Wollongong Malaysia, Jalan Kontraktor U1/14, Seksyen U1, 40150 Shah Alam, Malaysia

[6]Faculty of Innovative Design & Technology, Universiti Sultan Zainal Abidin, 21030 Kuala Terengganu, Malaysia

[7]Institute of Nano Electronic Engineering, Universiti Malaysia Perlis, 01000 Kangar, Perlis, Malaysia

[a]meorfaris@unimap.edu.my

Keywords: Geopolymer Concrete, Fiber Reinforcement, Sulfuric Acid, Hooked Steel Fiber, Polypropylene Fiber, Durability

Abstract. This study investigates the effect of sulfuric acid attack on the physical durability of fibre-reinforced geopolymer concrete. The geopolymer concrete was prepared using fly ash as the aluminosilicate source, activated with 12 M sodium hydroxide and sodium silicate solution at a fixed sodium silicate-to-sodium hydroxide ratio of 2.5. Two types of fibres were used, namely 1% fibrillated polypropylene fibre and 1% hooked-end steel fibre, while the mixture without fibre was used as the control. Cube specimens of 100 mm × 100 mm × 100 mm were cured at room temperature for 28 days before being immersed in sulfuric acid solution at pH 1 for 7, 14, 28, and 56 days. The durability performance was evaluated through density, water absorption, and visual acid penetration using phenolphthalein indicator. The results showed that prolonged sulfuric acid exposure gradually reduced density and increased water absorption, especially after 28 and 56 days. At 56 days, the 1% hooked-end steel fibre mixture recorded the highest density and lowest water absorption compared with the control and polypropylene fibre mixtures. The phenolphthalein observation also showed that the hooked-end steel fibre mixture retained a more visible alkaline region after acid exposure. This improvement is attributed to the higher specific gravity and crack-bridging ability of steel fibre, which helped reduce pore connectivity and restrict acid ingress. The findings indicate that sulfuric acid resistance in fibre-reinforced geopolymer concrete is not governed only by the binder system, but also by the type of fibre used. Hooked-end

Content from this work may be used under the terms of the Creative Commons Attribution 3.0 license. Any further distribution of this work must maintain attribution to the author(s) and the title of the work, journal citation and DOI. Published under license by Materials Research Forum LLC.

steel fibre showed better potential than polypropylene fibre in improving the physical durability of geopolymer concrete under acidic exposure.

Introduction

Concrete is the second most widely used material on earth, with annual production exceeding 10 billion tonnes [1]. Conventional concrete is mainly composed of Portland cement, water, fine aggregate, and coarse aggregate. During hydration, cement reacts with water to form a hardened matrix that binds the aggregates together, while strength development continues through the curing process [2]. Depending on its grade and application, concrete may exhibit compressive strength ranging from 10–25 N/mm² for ordinary concrete to 60–80 N/mm² for high-strength concrete [3]. However, the production of Portland cement contributes significantly to carbon dioxide emissions, creating a need for more sustainable construction materials. Geopolymer concrete, first introduced by Davidovits in 1978, has been developed as an alternative binder system using aluminosilicate-rich industrial by-products activated with alkaline solutions such as sodium hydroxide and sodium silicate. Fly ash is commonly used as a source material in geopolymer concrete because it can reduce environmental impact while promoting the reuse of industrial waste [4].

The incorporation of fibres into concrete is one approach used to improve its performance, particularly in terms of crack control, tensile resistance, and post-cracking behaviour. Steel and polypropylene fibres are commonly used in fibre-reinforced concrete due to their different physical and mechanical characteristics. Steel fibre has high strength and stiffness, which can improve crack-bridging capacity and load resistance, although it is relatively more expensive [5]. Polypropylene fibre, on the other hand, is lightweight and can help control microcrack formation within the concrete matrix. In fibre-reinforced concrete, fibres act as reinforcement that bridges matrix cracks and enhances ductility, although they are generally used to complement rather than replace conventional reinforcement. The effectiveness of fibre reinforcement is influenced by fibre geometry, surface characteristics, and bonding between the fibre and concrete matrix [6].

Concrete structures exposed to aggressive environments may experience durability problems, especially under sulfuric acid attack. Sulfuric acid can react with cementitious materials and cause the formation of expansive products such as gypsum and ettringite, leading to matrix weakening, cracking, surface deterioration, and loss of durability [7]. Although geopolymer concrete has been reported to offer better chemical resistance than ordinary Portland cement concrete, its long-term performance under severe sulfuric acid exposure still requires further investigation, particularly when different types of fibre reinforcement are incorporated.

Therefore, this study investigates the performance of hooked steel fibre and fibrillated polypropylene fibre-reinforced geopolymer concrete exposed to sulfuric acid attack. The main focus of this study is to evaluate how different fibre types influence the physical durability and acid resistance behaviour of geopolymer concrete under pH 1 sulfuric acid exposure. The material performance was assessed through laboratory tests including density, water absorption, and visual sulfuric acid penetration using phenolphthalein indicator. These tests were used to determine the changes in the geopolymer concrete properties after different acid immersion periods and to compare the durability performance of the control, polypropylene fibre-reinforced, and hooked steel fibre-reinforced geopolymer concrete specimens.

Material and Methodology

Proper sample preparation is essential for the laboratory phase of research, as it significantly affects the accuracy and reliability of the experimental results. During this phase, all materials required for the laboratory work were precisely measured and recorded before mixing. To reduce fibre balling and material clogging, hooked steel and fibrillated polypropylene fibres were prepared and separated individually before being incorporated into the geopolymer concrete mixture. Hooked steel fibre and fibrillated polypropylene fibre were added at a fixed content of

1.0%, while the specimens without fibre were used as the control sample. The geopolymer concrete was prepared using 12 M sodium hydroxide solution, with the sodium silicate-to-sodium hydroxide ratio fixed at 2.5. Fly ash classified as Class F was used as the aluminosilicate source material. The fine aggregate used in this study was river sand passing through a 4.75 mm sieve, while the coarse aggregate had a nominal maximum size of 16 mm. Table 1 shows the mix proportion of fibre-reinforced geopolymer concrete.

Table 1. Mix proportion of fiber reinforced geopolymer concrete.

PP Fiber [%]	ST Fiber [%]	Fly Ash [kg/m^3]	Coarse Aggregate [kg/m^3]	Fine Aggregate [kg/m^3]	Na_2SiO_3 [kg/m^3]	NaOH [kg/m^3]
-	-	666.7	900	600	238.1	95.2
1.0	-	666.7	900	600	238.1	95.2
-	1.0	666.7	900	600	238.1	95.2

For the density, water absorption, and sulfuric acid resistance tests, the geopolymer concrete specimens were cast into cube moulds measuring 100 mm × 100 mm × 100 mm. After casting, the specimens were kept in the moulds for 24 hours before demoulding. All specimens were then cured at room temperature for 28 days. After the curing period, the specimens were fully immersed in sulfuric acid solution with a pH of 1 for 7, 14, 28, and 56 days. The specimens were placed separately in the acid tank to ensure complete contact between the sulfuric acid solution and all exposed concrete surfaces. After each designated immersion period, the specimens were removed from the acid solution, wiped with a clean cloth to remove excess surface solution, and left to drain for one day before testing.

The density of the hardened geopolymer concrete specimens was determined after one day of draining following sulfuric acid exposure. Each specimen was weighed to obtain its mass, while the volume was calculated based on the cube dimensions of 100 mm × 100 mm × 100 mm. The water absorption test was conducted by adapting the procedure in ASTM C642 for absorption of hardened concrete. After density measurement, the specimens were immersed in water for 24 h. The specimens were then removed from the water, and excess surface water was removed by tapping and wiping the surface using a clean cloth. The saturated surface-dry mass was recorded as (W_s). Next, the specimens were oven-dried at 110 °C for 24 h, cooled to room temperature, and weighed to obtain the oven-dry mass, (W_d). The density and water absorption were calculated using Eq. (1) and Eq. (2), respectively.

$$\rho = m/v. \quad (1)$$

$$WA\ (\%) = [(W_s - W_d)/W_{d.}] \times 100 \quad (2)$$

Where (ρ)is the density of the specimen [kg/m³], (m) is the mass of the specimen after sulfuric acid exposure and draining [kg], (v) is the volume of the specimen [m³], (WA) is the water absorption percentage [%], (W_s) is the saturated surface-dry mass of the specimen after 24 h water immersion [kg], and (W_d) is the oven-dry mass of the specimen after drying [kg].

The sulfuric acid resistance of the specimens was evaluated through visual observation using phenolphthalein spray as an indicator. After the designated sulfuric acid immersion period, the cube specimens were cut into two halves to expose the internal cross-section. A 1% phenolphthalein solution was sprayed evenly onto the freshly cut surface, and the colour change was observed and recorded. Pink colour indicated that the internal geopolymer matrix remained alkaline, while colourless regions indicated areas affected by sulfuric acid penetration. This visual assessment was used to compare the acid resistance behaviour of the control, fibrillated polypropylene fibre-reinforced, and hooked steel fibre-reinforced geopolymer concrete specimens.

Results and Discussion

Density

The density properties of fibre-reinforced geopolymer concrete after immersion in sulfuric acid for 7, 14, 28, and 56 days are presented in Fig. 1. Overall, the results show a gradual reduction in density with increasing acid exposure duration. At 7 days, the density values for 0% fibre, 1% polypropylene (PP) fibre, and 1% hooked-end steel fibre were 2445 kg/m³, 2430 kg/m³, and 2489 kg/m³, respectively. At 14 days, only slight changes were observed, with values of 2443 kg/m³, 2428 kg/m³, and 2488 kg/m³. After 28 days, the density decreased more noticeably to 2422 kg/m³, 2409 kg/m³, and 2470 kg/m³, respectively. The lowest density values were recorded at 56 days, reaching 2392 kg/m³ for 0% fibre, 2379 kg/m³ for 1% PP fibre, and 2440 kg/m³ for 1% hooked-end steel fibre.

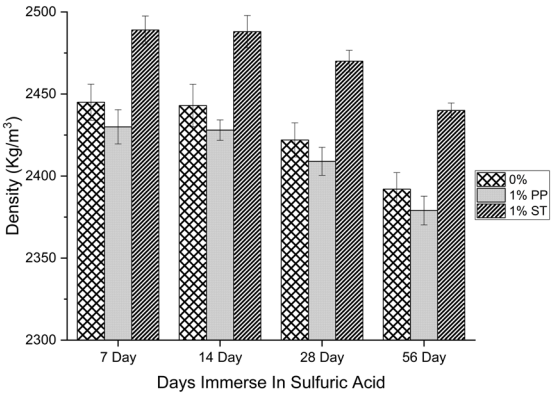


Fig. 1. Effect of sulfuric acid immersion on the density of fibre-reinforced geopolymer concrete.

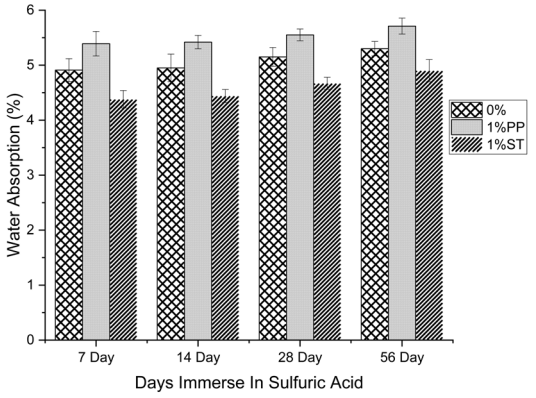


Fig. 2. Effect of sulfuric acid immersion on the water absorption of fibre-reinforced geopolymer concrete.

The small changes in density during the first 7 and 14 days indicate that the geopolymer matrix was initially able to limit rapid acid penetration. However, the clearer reduction after 28 and 56 days suggests progressive acid ingress, pore formation, and loss of matrix compactness. This behaviour is consistent with Liu et al. [8], who reported that sulfuric acid exposure can deteriorate geopolymer concrete through acid absorption and pore development. The reduction in density is also related to increased porosity and water absorption, which may weaken the geopolymer matrix and reduce durability. Mohd Azhar et al. [9] similarly reported that higher water absorption in geopolymer mixtures is associated with lower compactness and strength performance.

The density performance was also influenced by the type of fibre used. The 1% hooked-end steel fibre mixture recorded the highest density throughout the exposure period. This is mainly due to the high specific gravity of steel fibre, which is approximately 7850 kg/m³. This agrees with Harshavardhan and Bala Murugan [10], who reported that high-specific-gravity reinforcement can increase concrete density. In addition, hooked-end steel fibres may help restrict crack widening and reduce connected pathways for acid penetration, leading to better density retention. In contrast, the 1% PP fibre mixture showed the lowest density due to the lightweight nature of PP fibre. Hasan et al. [11] also reported that increasing PP fibre content reduced concrete density. Although PP fibre can assist in microcrack control, poor dispersion or weak fibre–matrix bonding may increase pore connectivity and allow easier acid ingress during prolonged exposure.

Overall, the density results show that sulfuric acid resistance in fibre-reinforced geopolymer concrete is influenced not only by the geopolymer binder, but also by the type of fibre incorporated. The binder provides chemical resistance, while the fibres affect physical deterioration by controlling crack development, pore connectivity, and acid transport pathways. Ohno and Li [12] reported that fibre-reinforced geopolymer composites can improve sulfuric acid resistance through tight crack control, while Chottemada and Kar [13] showed that different fibre reinforcements

influence the acid resistance of alkali-activated concrete. Similar durability improvements in fibre-reinforced geopolymer systems were also reported by Ganesan et al. [14] and Li et al. [15].

Water Absorption

The water absorption results of fibre-reinforced geopolymer concrete after sulfuric acid exposure are shown in Fig. 2. In general, water absorption increased with longer immersion time, especially after 28 days. At 7 days, the water absorption values for 0% fibre, 1% PP fibre, and 1% hooked-end steel fibre were 4.91%, 5.39%, and 4.38%, respectively. At 14 days, the values were 4.50%, 5.42%, and 4.44%. A clearer increase was observed at 28 days, where the values reached 5.15%, 5.55%, and 4.67%, respectively. The highest water absorption values were recorded at 56 days, with 5.30%, 5.71%, and 4.90% for 0% fibre, 1% PP fibre, and 1% hooked-end steel fibre, respectively.

The increase in water absorption indicates that prolonged sulfuric acid exposure increased the pore connectivity of the geopolymer matrix, allowing more water to enter the concrete. Liu et al. [8] similarly reported that sulfuric acid exposure can promote acid absorption, pore formation, and deterioration in geopolymer concrete. This trend is also closely related to the density reduction observed in Fig. 1. When sulfuric acid penetrates the concrete, it can dissolve reaction products, enlarge existing pores, and weaken the internal structure. As a result, the concrete becomes more permeable and absorbs more water. Mohd Azhar et al. [9] also reported that geopolymer mixtures with higher water absorption are associated with weaker internal compactness and lower strength performance. Therefore, the increase in water absorption after 28 and 56 days confirms that acid exposure progressively reduced the durability of the geopolymer concrete.

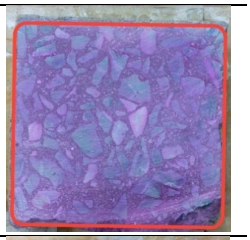
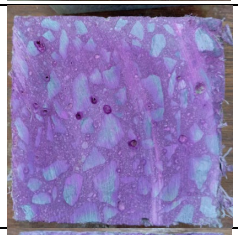
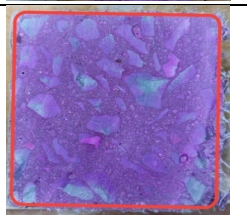
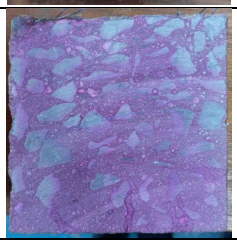
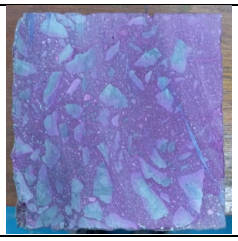
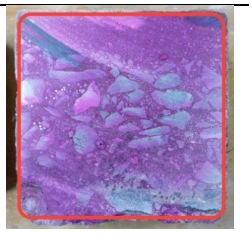
The type of fibre also influenced the water absorption behaviour. The 1% hooked-end steel fibre mixture showed the lowest water absorption throughout the exposure period. This can be related to its higher density and crack-bridging ability, which helped restrict crack widening and reduce continuous pathways for water and acid ingress. Fibre reinforcement can improve durability by limiting crack development and reducing permeability. Sathish Kumar et al. [16] reported that fibre-reinforced geopolymer concrete showed lower water absorption, reduced sorptivity, and improved acid resistance compared with plain geopolymer concrete. Gill et al. [17] also reported that fibre addition can influence the pore network and permeability behaviour of geopolymer concrete. In contrast, the 1% PP fibre mixture recorded the highest water absorption at all exposure ages. Although polypropylene fibre is chemically stable and can assist in microcrack control, its lower stiffness and possible fibre clustering may reduce compaction efficiency and create weak fibre–matrix interfacial zones. These zones can increase pore connectivity and allow easier water and acid movement during prolonged exposure. Rajak and Rai [18] reported that micro polypropylene fibre can improve acid resistance by reducing capillary porosity and controlling crack propagation; however, the effectiveness of PP fibre depends on proper dispersion and bonding with the geopolymer matrix.

Sulfuric Acid Resistance

The sulfuric acid resistance test was conducted to evaluate the extent of acid penetration in fibre-reinforced geopolymer concrete using 1% phenolphthalein solution. After spraying, the alkaline region of the geopolymer matrix appeared pink or purple, while the colourless or lighter region indicated the neutralised zone affected by sulfuric acid [8]. Table 2 presents the visual appearance of the specimens after exposure to sulfuric acid for 7, 14, 28, and 56 days. To provide a clearer observation of deterioration at prolonged exposure, close-up images of the 56-day specimens are also presented in Fig. 3. During the initial exposure period of 7 and 14 days, all specimens showed almost complete pink or purple coloration, indicating that no clear neutralised zone was visually observed. This suggests that the geopolymer matrix was still able to limit acid ingress at the early stage of exposure. At 28 days, small lighter regions began to appear near the exposed surface, indicating the onset of acid penetration. The most noticeable changes were

observed at 56 days, where distinct lighter or colourless zones became more visible around the specimen edges and corners. These features indicate that prolonged sulfuric acid exposure progressively reduced the alkalinity of the outer layer and allowed deeper acid ingress into the matrix.

Table 2. Visual appearance of fibre-reinforced geopolymer concrete exposed to sulfuric acid solution.

Days	7	14	28	56
0% Fibre				
1% PP Fibre				
1% Steel Fibre				

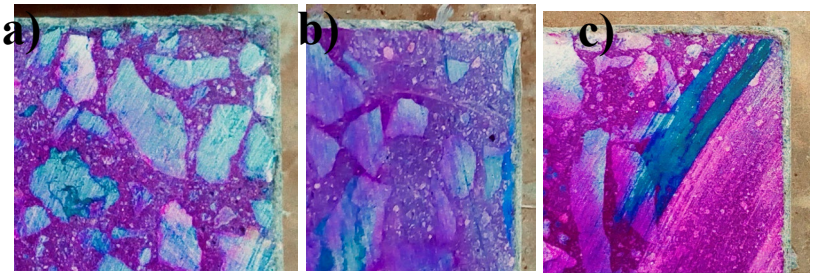


Fig. 3. Close-up view of the colourless area of fibre-reinforced geopolymer concrete after 56 days of sulfuric acid exposure: (a) 0% fibre, (b) 1% PP fibre, and (c) 1% hooked-end steel fibre.

The close-up images at 56 days provide clearer evidence of this deterioration. A lighter outer band can be observed near the specimen surface, indicating surface neutralisation caused by sulfuric acid attack. In some areas, local voids and surface irregularities are also visible, suggesting progressive matrix deterioration and loss of compactness. This observation is consistent with the density and water absorption results, where longer immersion periods led to lower density and higher water absorption, reflecting increased pore connectivity and easier acid penetration.

The fibre type also influenced the visual acid resistance behaviour. The specimen containing 1% hooked-end steel fibre appeared to retain a more continuous pink or purple internal region, indicating better resistance to acid penetration. This may be attributed to the crack-bridging ability of steel fibre, which helps reduce crack widening and limits connected pathways for acid ingress. In contrast, the 1% PP fibre specimen showed more noticeable surface neutralisation, which may be related to weaker fibre–matrix interaction and higher pore connectivity during prolonged

exposure. Therefore, the visual observations suggest that fibre addition affects sulfuric acid resistance not only through mechanical improvement, but also by influencing crack development, pore structure, and acid transport.

Overall, the phenolphthalein test confirms that sulfuric acid penetration was limited during the early exposure period but became more evident after 56 days. The close-up images further support that prolonged acid exposure caused progressive neutralisation of the surface layer, especially near the edges of the specimens. Among the mixtures, the hooked-end steel fibre specimen showed better visual resistance to acid penetration, which agrees with its higher density and lower water absorption. These findings indicate that sulfuric acid resistance in fibre-reinforced geopolymer concrete depends not only on the geopolymer binder, but also on the role of fibres in controlling cracks and restricting acid ingress.

Conclusion

Based on the results, prolonged sulfuric acid exposure caused gradual deterioration in fibre-reinforced geopolymer concrete. The density decreased with increasing immersion duration, while water absorption increased, especially after 28 and 56 days. This indicates that sulfuric acid progressively penetrated the geopolymer matrix, enlarged pores, increased pore connectivity, and reduced internal compactness. The phenolphthalein observation further confirmed this trend, where limited visual acid penetration was observed at 7 and 14 days, while clearer colourless zones appeared after 56 days. The type of fibre used significantly influenced the durability performance. The 1% hooked-end steel fibre mixture showed the highest density, lowest water absorption, and better visual resistance to acid penetration. This improvement is attributed to the higher specific gravity of steel fibre and its crack-bridging ability, which helped restrict crack widening and reduce pathways for acid ingress. In contrast, the 1% PP fibre mixture recorded lower density and higher water absorption, which may be related to its lightweight nature, possible fibre dispersion issues, and weaker fibre–matrix interfacial zones. Overall, the study shows that sulfuric acid resistance in fibre-reinforced geopolymer concrete is not controlled only by the geopolymer binder system. Fibre type also plays an important role in controlling physical deterioration, especially through crack control, pore connectivity, and acid transport resistance. Among the mixtures tested, the 1% hooked-end steel fibre mixture exhibited the best performance under sulfuric acid exposure.

References

[1] C. Meyer, Concrete Materials and Sustainable Development in the USA, Structural Engineering International 14 (2022) 203–207. https://doi.org/10.2749/101686604777963757

[2] E. Allen, J. Iano, Fundamentals of building construction: materials and methods, John Wiley & Sons, 2019.

[3] P.P. Raj, (2017). Building construction materials and techniques, Pearson Education India, 2017.

[4] K. Kishore, Geopolymer concrete and its strength influencing variables. Materials Today: Proceedings 80 (2023) 1434-1441. https://doi.org/10.1016/j.matpr.2023.01.225.

[5] N.R. Iyer, An overview of cementitious construction materials, in: P. Samui, D. Kim, N. R. Iyer, S. Chaudhary (Eds.), New Materials in Civil Engineering, Butterworth-Heinemann, 2020, pp. 1-64. https://doi.org/10.1016/B978-0- 12-818961-0.00001-6

[6] G. Plizzari, S. Mindess, Fiber-reinforced concrete, in: S. Mindess (Ed.), Developments in the Formulation and Reinforcement of Concrete (Second Edition), Woodhead Publishing, 2019, pp. 257–287. https://doi.org/10.1016/B978-0-08-102616-8.00011-3

[7] N.S.L.M. Thwin, E.M. Thwe, Investigation on the strength behaviors of ordinary and Kaolin-modified concretes severely attacked by sulfuric acid, Materials Today: Proceedings (2023). https://doi.org/10.1016/j.matpr.2023.01.114

[8] H. Liu, X. Liu, X. Wang, P. Zhu, L. Yang, X. Yan, The impact of original aggregate and attached mortar types of recycled aggregates on the sulfuric acid resistance of geopolymer recycled concrete, Journal of Building Engineering 82 (2024) 108273. https://doi.org/10.1016/j.jobe.2023.108273

[9] N.S.D. Mohd Azhar, F.F. Zainal, M.M.A.B. Abdullah, Effect of different ratio of geopolymer paste based fly ash-metakaolin on compressive strength and water absorption, IOP Conference Series: Materials Science and Engineering 701 (2019) 012010. https://doi.org/10.1088/1757-899X/701/1/012010

[10] C. Harshavardhan, S. Bala Murugan, Study on high-density concrete reinforced with steel fiber at elevated temperatures, ARPN Journal of Engineering and Applied Sciences 11 (2016) 11415–11420.

[11] A. Hasan, N. Maroof, Y. Ibrahim, Effects of polypropylene fiber content on strength and workability properties of concrete, Polytechnic Journal 9 (2019) 7–12. https://doi.org/10.25156/ptj.v9n1y2019.pp7-12

[12] M. Ohno, V.C. Li, Sulfuric acid resistance of strain-hardening fiber reinforced geopolymer composite, The Indian Concrete Journal 93 (2019) 47–53.

[13] P.G. Chottemada, A. Kar, Effect of different fibre reinforcements on the strength and acid attack resistance of alkali-activated concrete, Magazine of Concrete Research 76 (2024) 1370-1383. https://doi.org/10.1680/jmacr.24.00075

[14] N. Ganesan, P.V. Indira, R. Sahana, Strength and durability of hybrid fibre reinforced binary blend geopolymer concrete, 6th International Conference on Durability of Concrete Structures (2018) 154–159.

[15] W. Li, E.D. Shumuye, S. Tang, Z. Wang, K. Zerfu, Eco-friendly fibre reinforced geopolymer concrete: A critical review on the microstructure and long-term durability properties, Case Studies in Construction Materials 16 (2022) e00894. https://doi.org/10.1016/j.cscm.2022.e00894

[16] V. Sathish Kumar, N. Ganesan, P.V. Indira, Effect of hybrid fibres on the durability characteristics of ternary blend geopolymer concrete, Journal of Composites Science 5 (2021) 279. https://doi.org/doi: 10.3390/jcs5100279

[17] P. Gill, P. Jangra, R. Roychand, M. Saberian, J. Li, Effects of various additives on the crumb rubber integrated geopolymer concrete, Cleaner Materials 8 (2023) 100181. https://doi.org/10.1016/j.clema.2023.100181

[18] M. Rajak, B. Rai, Effect of micro polypropylene fibre on the performance of fly ash-based geopolymer concrete, Journal of Applied Engineering Sciences 9 (2019) 97–108. https://doi.org/10.2478/jaes-2019-0013

Materials Research Proceedings 74 (2026) 205-212 https://doi.org/10.21741/9781644904473-26

Effect of Sintering on the Structural, Dielectric, and Acetone Gas-Sensing Properties of Yttria-Stabilized Zirconia

Lara A. SHALAL[1,a *], Wafaa K. KHALEF[1,b] and Shihab A. ZAIDAN[1,c]

[1]Department of Applied Sciences, University of Technology-Iraq, Baghdad, Iraq

[a]lara1995hakeem@gmail.com, [b]drwafaa1980@gmial.com, [c]drshihab1969@gmail.com

Keywords: Yttria-Stabilized Zirconia (YSZ), Sintering Effect, Acetone Gas Sensor, Dielectric Constant, AC Conductivity, Surface Morphology, Crystallite Structure

Abstract. The effect of the sintering process on the structural, dielectric and acetone gas sensing properties of yttria-stabilized zirconia (YSZ) has been studied. To prevent confusion with the pure ZrO_2, the material is consistently referred as YSZ in this manuscript. Comparisons of the YSZ specimens before and after sintering at 1300°C for 5 h were made. The effects of sintering were assessed by means of x-ray diffraction (XRD), atomic force microscopy (AFM), dielectric measurements and conductometric gas-sensing tests. The results reveal that the crystalline phase and the surface topography have been changed by sintering and the behavior of the dielectric loss changes with frequency, and the behavior of the dielectric constant and AC conductivity has been improved by sintering. The unsintered, however, had a greater response at room temperature towards 500 ppm acetone. This is due to the fact that this behavior is attributed to the preservation of higher porosity and larger effective surface area which affords more sites of active adsorption where gas molecules can be adsorbed. The results suggest that, for electrical stability, it is desirable to have sintering and, for gas-sensing performance, controlled surface porosity.

Introduction

Zirconium dioxide (ZrO_2) is a versatile ceramic material with high thermal stability, chemical resistance and tuneable electrical properties, which is used in a variety of applications ranging from electronics to catalysis, biomedical devices and gas-sensors [1,2]. The ability of zirconia-based materials to change their resistance upon exposure to different gases is highly dependent on the phase composition, microstructure, porosity, surface roughness and the processing route in the case of sensor applications. Yttria is a typical stabilizer to eliminate cracking caused by the phase transformation in unstabilized zirconia and to improve the phase stability. Hence, in this work, we are interested in yttria-stabilized zirconia (YSZ) and study the influence of the sintering step on the structural, dielectric response, and acetone-sensing properties of YSZ.

Recent Studies on ZrO_2-Based Gas Sensors. It is recently found that the operating temperature, surface morphology, porosity, and composite formation of ZrO_2-based gas sensors can be controlled to improve the sensors. In room temperature and low power applications, surface modification and hybridization with catalysts/porous materials can be used to enhance the number of active adsorption sites and improve the detection of acetone [3,4]. YSZ-Co_3O_4 and In_2O_3/ZrO_2 heterojunctions-based composites have been found to have a fast and selective response at high temperature [5,6]. The present study compares different sintering strategies with the same material (YSZ), thereby isolating the effect of sintering. The comparison helps to understand the trade-off between increasing dielectric stability and decreasing gas-sensing response on the densification process [7].

Materials, Sensor Fabrication, and Characterization Methods

The sensor substrates were made of yttria-stabilized zirconia (YSZ) plates with 8 wt.% Y_2O_3. The specimens had a thickness of 2 mm and a diameter of 20 mm. The surface contamination was

Content from this work may be used under the terms of the Creative Commons Attribution 3.0 license. Any further distribution of this work must maintain attribution to the author(s) and the title of the work, journal citation and DOI. Published under license by Materials Research Forum LLC.

removed from the specimens prior to electrode deposition and testing. One group was not sintered while the other was sintered for five hours at 1300°C in an electric furnace. The material description has been created to separate and differentiate the present YSZ specimens from pure ZrO_2 without stabilization, and to make the sintering condition reproducible.

Physical vapor deposition (PVD) was used to deposit aluminum mesh electrodes on the top surface. The sensor was then installed in a sealed test chamber as illustrated in Fig. 1, with gas and air inlet pipes, a rotary pump, a heater, spring-loaded electrical contacts and a thermocouple. Base line resistance has been initially recorded in air. The sensor was then placed in the acetone with 500 ppm at room temperature and the variation of resistance was measured as a function of time. The acetone flow was then turned off and air turned on to allow resistance recovery.

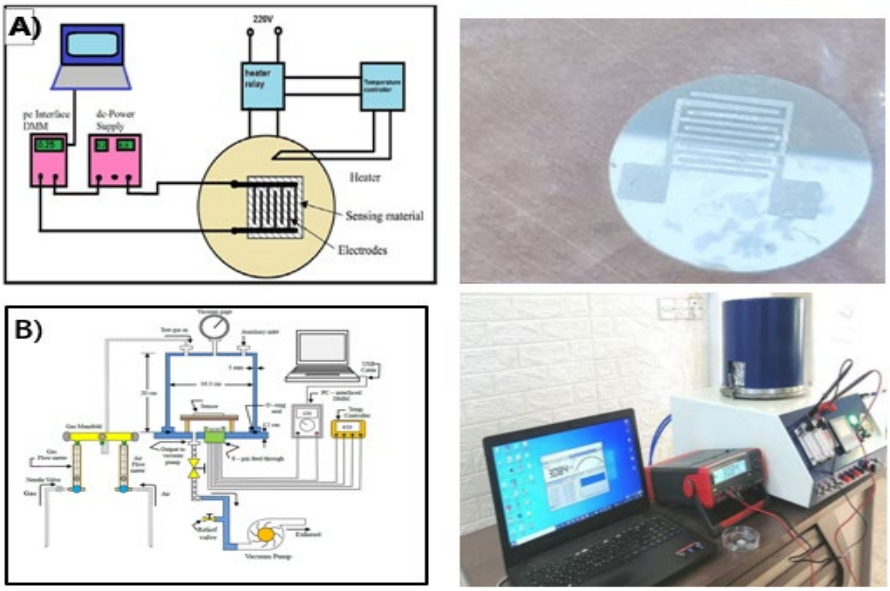


Fig. 1. (A) Photograph of the gas-sensor system and (B) schematic diagram of the sensor-testing setup.

Needle valves were used to control the gas flow, and a temperature controller was used to monitor the operating temperature. It was decided that the same measurement procedure would be followed when the unsintered and sintered YSZ specimens were measured to ensure a comparison. The definition of the response time was the time needed for the resistance to reach 90% of the total change after acetone exposure, and the definition of the recovery time needed for the resistance to return to 90% of the initial value after washing with air after the acetone exposure.

The structural characterization was done by X-ray diffraction (XRD 6000; Cu Kα radiation, λ = 1.54060 Å). The crystallite size was calculated using Debye-Scherrer equation (Eq. 1). Surface morphology and topography were analyzed with an AFM, and the dielectric properties were measured in the frequency range of 100-1000 kHz. The revised manuscript was checked and the symbols and units were unified [8].

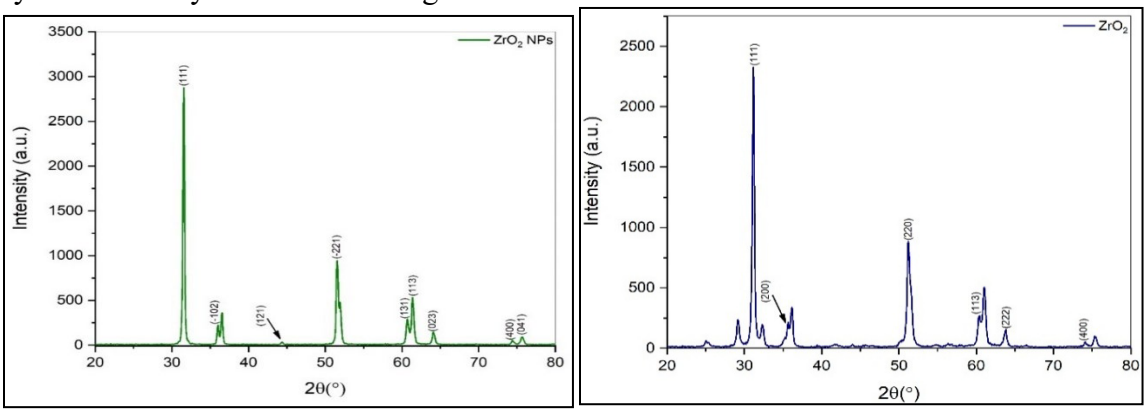
$$\boldsymbol{D = K\lambda \frac{\beta}{\cos\theta}} \tag{1}$$

where D is the crystallite size, k is the shape factor, λ = 1.54060 Å is the X-ray wavelength, β is the full width at half maximum (FWHM, in radians), and θ is the diffraction angle.

Results and Discussion

XRD Analysis of YSZ Before and After Sintering (Monoclinic and Cubic Phase Evolution)

The XRD patterns of the unsintered and sintered YSZ specimens are illustrated in Fig. 2(a,b), respectively. The diffraction peaks of the unsintered specimen show the signature peaks of the monoclinic phase, as well as a few indexed planes near 31.55°. The diffraction pattern after sintering at 1300°C indicates a higher fraction of the cubic/stabilized zirconia phase, where diffraction peaks are identified as (111), (200), (220), (113), (222) and (400). This change in structure is in accordance with the stabilising effect of yttria and the enhanced crystallinity resulting from the thermal treatment. Calculated crystallite sizes are in the nanometric range for both the unsintered sample (25.331-42.227 nm) and the sintered sample (24.768-42.385 nm). Preferred orientation is demonstrated by the presence of a strong (111) peak. These findings are consistent with the fact that the phase composition and crystallinity are changed by sintering, but not by too much crystallite coarsening.



(a) (b)

Fig. 2. XRD patterns of YSZ specimens: (a) before sintering and (b) after sintering at 1300°C.

AFM Analysis of YSZ Before and After Sintering

The surface topography, surface roughness and particle distribution of YSZ specimens were evaluated by AFM. The surface of the unsintered specimen is rough and porous, as seen in the 20 × 20 μm and 4.9 × 4.9 μm scans in Fig. 3, which also show peaks and valleys. The surface height distribution for the measured surface is approximately 171.1 nm. The particle density was found to be around 117,500 particles/mm^2 and the RMS roughness (Sq) was about 0.2137 μm. The average area of the projected particles was 4.034 μm^2 while the maximum height of the particles was 0.7712 μm. From these features it should be noted that the unsintered surface will present a relatively large surface area for gas adsorption, which is desirable for acetone sensing.

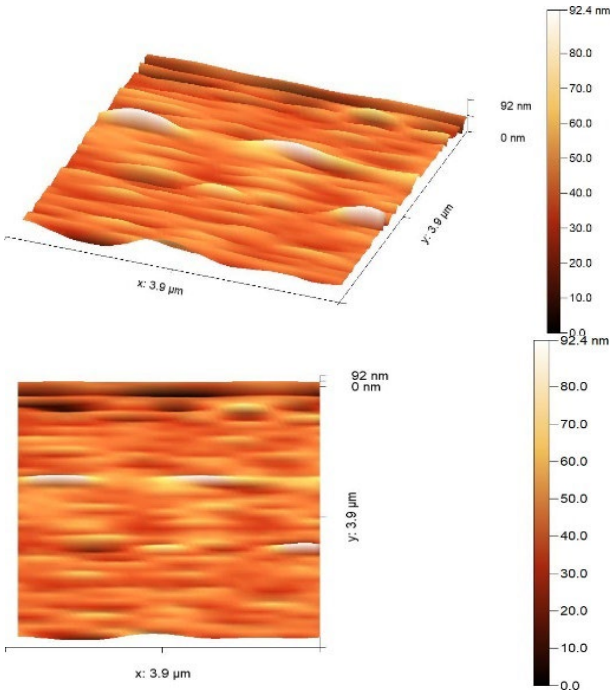


Fig. 3. AFM top-view and 3D topography of the unsintered YSZ specimen at a scan area of 4.9 × 4.9 µm.

AFM Analysis of Sintered YSZ

The results are displayed in the three-dimensional surface topography of the YSZ specimen after sintering at 1300°C (Fig. 4). The surface has a rough morphology and has distinct peaks and valleys, but the pores' structure is changed by the densification due to the sintering process and fewer available open adsorption sites are available. The RMS roughness (Sq) increases to about 0.4417 µm, the particle density decreases to approximately 12,500 particles/mm^2, and the average projected particle area increases to 34.82 µm^2. The average height is 1.407 microns. The changes suggest the coalescence and surface densification of particles following sintering. This morphology enables the material to be dielectric and to have good mechanical strength, but it can diminish the gas-sensing response due to the decrease in open porosity.

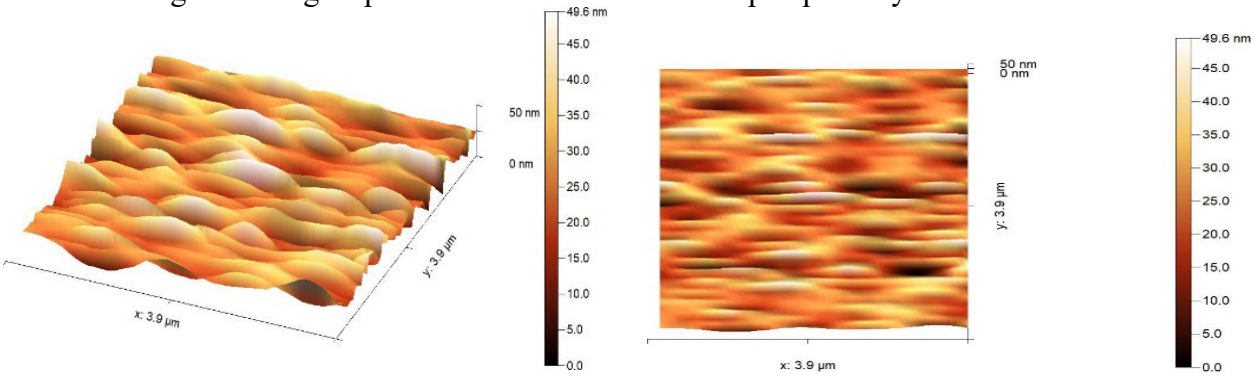


Fig. 4. AFM top-view and 3D topography of the YSZ specimen after sintering at 1300°C with a scan area of 4.9 × 4.9 µm.

Dielectric Constant Analysis

The dielectric constant of YSZ before and after sintering was listed in Table 1 for the frequency range of 100 – 1000 kHz. The general decrease of dielectric constants with increasing frequency is observed for both specimens and is a result of the decreasing ability of the dipoles and interfacial polarization to follow the alternating electric field at higher frequencies. The sintered specimen

has higher dielectric constant at all frequencies tested. The example of 100 kHz, for instance, shows that the value of dielectric constant rises from 15.43 to 33.58 after sintering. It is thought that this increase in improvement is due to improved densification, crystallinity and defect-related polarization losses following sintering. Thus, the electrical stability of YSZ for dielectric applications can be enhanced by sintering.

Table 1 Dielectric constant (εr) of YSZ before and after sintering over the frequency range of 100-1000 [kHz].

Frequency [kHz]	100	200	300	400	500	600	800	1000
After sintering	33.58	30.49	28.78	28.97	21.92	18.54	17.27	15.45
Before sintering	15.43	9.60	7.03	6.77	5.24	3.24	1.81	1.42

Dielectric Loss (tan δ) Analysis

The dielectric loss (tan δ) of the YSZ specimens, before and after sintering, is compared as a function of frequency in the range from 100 to 1000 kHz in Table 2. It is observed that the unsintered specimen has a greater dielectric loss at low frequencies such as at 100 and 200 kHz, that could be attributed to defect polarization and increase porosity. The loss decreases at low frequency after sintering but is still above that of the unsintered sample at higher frequencies. This behavior suggests that sintering affects the polarization and charge-relaxation processes but does not lead to a uniform decrease in the dielectric loss over all the frequencies. Hence, it is essential to consider the behavior of dielectric loss in conjunction with the accompanying variations of microstructure, densification, and defect distribution.

Table 2 Dielectric loss (tan δ) of YSZ before and after sintering over the frequency range of 100-1000 [kHz].

Frequency [kHz]	100	200	300	400	500	600	800	1000
After sintering	0.64	0.70	0.80	0.76	0.63	0.58	0.47	0.43
Before sintering	0.82	0.82	0.60	0.50	0.44	0.35	0.33	0.27

AC Conductivity Analysis

The AC conductivity values for YSZ are given in Table 3 before and after sintering. The conductivity of the sintered specimen is much higher than that of the investigated frequency range. The highest value appears near 400 kHz, where the sintered sample reaches 4937.386 × 10^{-7} $(\Omega.m)^{-1}$ compared with 763.0125 × 10-7 $(\Omega.m)^{-1}$ before sintering. This increase can be attributed to the improvement in crystallinity, better grain connectivity, and lower boundary resistance after sintering. These results indicate that the charge transport and the dielectric properties have been enhanced after sintering and, at the same time, the surface porosity has decreased, which can also be seen as a reason for lower gas-sensing response after sintering.

Table 3 AC conductivity ($\gamma \times 10^{-7}$ $[(\Omega.m)^{-1}]$) of YSZ before and after sintering over the frequency range of 100-1000 [kHz].

Frequency [kHz]	After sintering $\gamma \times 10^{-7}$ $[(\Omega.m)^{-1}]$	Before sintering $\gamma \times 10^{-7}$ $[(\Omega.m)^{-1}]$
100	1195.361	712.4365
200	2385.243	877.8545
300	3868.866	712.5671
400	4937.386	763.0125
500	3889.208	648.0087
600	3634.449	376.4959
800	3634.176	265.0842
1000	3698.258	215.1001

Acetone Gas-Sensing Response

The room-temperature conductometric behavior of YSZ to 500 ppm acetone is presented in Figs. 5 and 6. YSZ is an n-type metal oxide semiconductor that has a resistance change in the presence of acetone. Absorbed oxygen molecules trap electrons from the conduction band and are converted to surface-depleted, adsorbed oxygen species. The surface is provided with electrons when the acetone (a reducing gas) reaches it and reacts with the oxygen species. In this process, the resistance is reduced. The unsintered YSZ specimen has a higher porosity and a larger effective surface area than the sintered specimen, and thus has more adsorption sites, which means that the response is stronger. On the other hand, sintering increases the dielectric and structural stability, however it decreases open porosity and decreases gas-surface interaction [9,10].

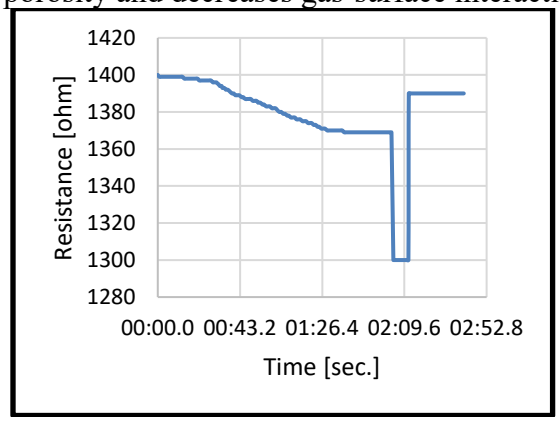


Fig. 5. Resistance–time curve of the unsintered YSZ specimen exposed to 500 ppm acetone at room temperature.

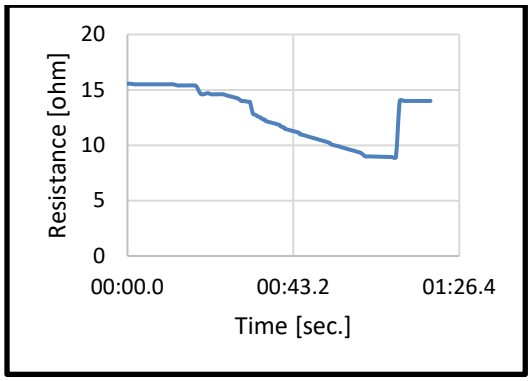


Fig. 6. Resistance–time curve of the sintered YSZ specimen exposed to 500 ppm acetone at room temperature.

$$\boldsymbol{S = \left\{\frac{(Ra-Rg)}{Rg}\right\} \times 100\%} \quad \textbf{(2)}$$

Here, Ra is the resistance in air and Rg is the resistance in acetone. The revised discussion is only about acetone to avoid having any inconsistencies with other gases. The resistance-time curves were used to assess the response and recovery behavior. The unsintered sample showed a rapid decrease in resistance when exposed to acetone; recovery was seen when air was reintroduced. The resistance variation of the sintered specimen was found to be weaker, which verified that there is less gas access to active surface sites with densification. In future, repeated gas/air exposure cycles should be used to confirm the repeatability; in the present manuscript, the repeatability is not exaggerated beyond the available resistance-time curves.

Response Time, Recovery Time, and Sensing Mechanism

Response time (RST) is the time taken for the sensor signal to recover to 90% of the maximum resistance change upon exposure to acetone. Recovery time (RCT) is the period of time needed for the signal to return 90% of its initial strength following removal of the acetone and the introduction of air. These parameters are significant as they are used to determine the speed at which the sensor can detect and release the gas. The higher response of unsintered YSZ is believed to be as a result of the higher number of adsorption sites and more open morphology, while the sintered specimen is believed to have fewer adsorption sites and being densified thus reducing the response. This compromise is the reason for the improvement in the dielectric properties and reduction in the gas-sensing response at room temperature [11,12].

$$\boldsymbol{Response\ time = t\ gas\ (on) - t\ gas\ (off) \times 0.9} \quad \textbf{(3)}$$

$$\boldsymbol{Recovery\ time = t\ gas\ (off) - t\ gas\ (on) \times 0.9} \quad \textbf{(4)}$$

Conclusion

The structural, dielectric, and acetone gas-sensitive properties of yttria-stabilized zirconia are greatly influenced by sintering at 1300°C. The AFM measurements showed that surface roughness, particle distribution and surface densification were changed after sintering, and the XRD analysis confirmed the phase modification and improved crystallinity. The sintered YSZ sample showed better dielectric properties such as higher dielectric constant and better AC conductivity and the dielectric loss was frequency dependent. However, the unsintered sample had a greater sensitivity towards 500 ppm acetone at room temperature, as a result of its higher porosity and consequently larger effective surface area, which would increase the number of available active sites for the gas absorption and surface reactions. The results show that the electric stability and dielectric properties of YSZ are improved by sintering, and that it is more beneficial to preserve the surface porosity for the use of YSZ as a room-temperature acetone sensor. Repeated exposure/recovery cycles, further acetone concentrations and long-term stability measurements should be performed in the future to further assess sensor repeatability, detection limits, and practical performance.

References

[1] N.A. Pandit, M. Shahazad, T. Ahmad, Structural characterization and gas sensing applications of ultrafine ZrO_2 nanospheres using low temperature solution route, Mater. Today Proc. 36 (2021) 724–729. https://doi.org/10.1016/j.matpr.2020.04.769

[2] A.K. Chitoria, A. Mir, M.A. Shah, A review of ZrO_2 nanoparticles applications and recent advancements, Ceram. Int. 49 (2023) 32343-32358. https://doi.org/10.1016/j.ceramint.2023.06.296

[3] V. Amiri, H. Roshan, A. Mirzaei, G. Neri, A.I. Ayesh, Nanostructured metal oxide-based acetone gas sensors: A review, Sensors 20 (2020) 3096. https://doi.org/10.3390/s20113096

[4] A. Nagare, A. Dhadage, P. Ghare, R. Naval, A. Athare, P. Gogoi, A. Datir, M. Navgire, Room temperature acetone sensing activity of β-cyclodextrin coated MoO_3–ZrO_2 nanocomposite, Surf. Interfaces 53 (2024) 105068. https://doi.org/10.1016/j.surfin.2024.105068

[5] X. Hao, T. Yu, X. Meng, C. Wei, Y. Wang, S. Sun, P. Cheng, L. Ji, Efficient mixed-potential acetone sensor with yttria-stabilized zirconia and porous Co_3O_4 nanofoam sensing electrode for hazardous gas monitoring and breath analysis, J. Hazard. Mater. 478 (2024) 135462. https://doi.org/10.1016/j.jhazmat.2024.135462

[6] G. Feng, Y. Che, S. Wang, S. Wang, J. Hu, J. Xiao, C. Song, L. Jiang, Sensitivity enhancement of In_2O_3/ZrO_2 composite based acetone gas sensor: A promising collaborative

approach of ZrO_2 as the heterojunction and dopant for in-situ grown octahedron-like particles, Sens. Actuators B Chem. 367 (2022) 132087. https://doi.org/10.1016/j.snb.2022.132087

[7] F.J. Meng, R.F. Xin, S.X. Li, Metal oxide heterostructures for improving gas sensing properties: A review, Materials 16 (2023) 263. https://doi.org/10.3390/ma16010263

[8] A. Ferlazzo, C. Espro, D. Iannazzo, K. Moulaee, G. Neri, A novel yttria-doped ZrO_2 based conductometric sensor for hydrogen leak monitoring, Int. J. Hydrog. Energy 47 (2022) 9819–9828. https://doi.org/10.1016/j.ijhydene.2022.01.036

[9] N. Kumari, S. Sareen, M. Verma, S. Sharma, A. Sharma, H.S. Sohal, V. Mutreja, Zirconia-based nanomaterials: Recent developments in synthesis and applications, Nanoscale Adv. 4 (2022) 4210–4236. https://doi.org/10.1039/D2NA00367H

[10] P.P. Fedorov, E.G. Yarotskaya, Zirconium dioxide. Review, Condens. Matter Interphases 23 (2021) 170–188.

[11] J. Wang, L. Zhao, J. Li, F. Liu, R. You, S. Lv, L. Geyu, Stabilized zirconia-based solid state electrochemical gas sensor coupled with $CdTiO_3$ for acetylene detection, Sens. Actuators B Chem. 316 (2020) 128199. https://doi.org/10.1016/j.snb.2020.128199

[12] E. Hemalatha, N. Gopalakrishnan, Effect of Cr on ZrO_2 nanostructures for gas sensing investigation, Bull. Mater. Sci. 44 (2021) 1–10. https://doi.org/10.1007/s12034-021-02585-1

Materials Research Proceedings 74 (2026) 213-221 https://doi.org/10.21741/9781644904473-27

Crashworthiness Assessment of AL6061-T4 / Composite Hybrid Tubes Subjected to Axial Loading

Ali FAROKHI NEJAD[1,2,a *], Amir Abbas REZVANFAR[1,2], Mohamad Yusuf BIN SALIM[1,2], Saleh A ALI ELHOATI[1,2], Didik NURHADIYANTO[3,4], M.Y. YAHYA[1,2,b *]

[1]Faculty of Mechanical Engineering, Universiti Teknologi Malaysia, Johor Bahru 81310, Malaysia

[2]Centre for Advanced Composite Materials, Universiti Teknologi Malaysia, 81310 Johor Bahru, Malaysia

[3]Department of Mechanical Engineering Education, Faculty of Engineering, Universitas Negeri Yogyakarta, Jl. Colombo No. 1, Yogyakarta 55281, Indonesia

[4]Center for Eco-Material Engineering and Manufacturing, Universitas Negeri Yogyakarta, Jl. Colombo No. 1, Yogyakarta 55281, Indonesia

[a]farokhi@utm.my, [b]yazidyahya@utm.my

Keywords: FRP Composite Tube, Crashworthiness, Energy Absorption, Hybrid Composites, Quasi-Static Axial Loading

Abstract. The present study experimentally investigates the axial crashworthiness of aluminium 6061-T4, carbon-fibre-reinforced polymer (CFRP), and glass/carbon fibre hybrid (FH) tubes, tested individually and in four aluminium–composite hybrid configurations with the aluminium tube placed either externally (AL/FH-S7, AL/CF-S9) or internally (FH/AL-S8, CF/AL-S10). Quasi-static axial compression tests were performed at 3 mm/min. Compared to the aluminium tubes, the hybrid configurations increased peak load by 25.32% to 37.08%, mean load by 7.43% to 31.01%, and energy absorption (EA) by 7.45% to 32.58%, with externally placed aluminium tubes outperforming internally placed ones. Hybridisation, however, increased specimen mass by approximately 45% rather than reducing it; consequently, the specific energy absorption (SEA) of the hybrid tubes was on average about 17% lower than that of the aluminium tubes, and crush force efficiency (CFE) was generally lower or unchanged. Hybridisation therefore improves the absolute load-bearing and energy-absorption capacity of these tubes but does not improve mass efficiency, and the overall crushing response is governed predominantly by the outer tube material, with the inner tube providing a supportive role.

Introduction

Improving vehicle crashworthiness remains a major engineering challenge in the automotive, aerospace, and marine sectors, particularly as structural components are increasingly required to combine high energy-absorption capacity with low mass. Thin-walled tubular structures are widely employed as sacrificial energy absorbers because their controlled collapse can dissipate substantial amounts of impact energy [1]. Conventional crash boxes are typically manufactured from metallic materials, including steel and aluminium alloys, using forming and joining processes such as stamping and spot welding. Although these approaches are well established, the associated heat-affected regions and welded joints may influence long-term structural integrity [2,3]. At the same time, increasing pressure to reduce vehicle mass and associated CO_2 emissions has accelerated the development of lightweight energy-absorbing structures [4,5]. Fibre-reinforced polymer composites are particularly attractive in this context because appropriately designed composite

Content from this work may be used under the terms of the Creative Commons Attribution 3.0 license. Any further distribution of this work must maintain attribution to the author(s) and the title of the work, journal citation and DOI. Published under license by Materials Research Forum LLC.

tubes can undergo progressive crushing and, in some cases, achieve higher specific energy absorption (SEA) than conventional metallic structures [6,7].

Fibre hybridisation combining two or more fibre types within a polymer matrix is an established route to improved toughness and overall structural performance [4,8–11]. Aramid/Kevlar offers high impact resistance but is moisture- and UV-sensitive and costly for general automotive use [4]; carbon fibre offers excellent stiffness, fatigue strength, and corrosion resistance but is costly and brittle under impact, while glass fibre is more affordable but less durable. Combining glass and carbon fibre is therefore a viable strategy for balancing properties and cost under impact loading [12–17]. Reported failure mechanisms of hybrid fibre tubes under axial loading include mode I, mode II, and mixed-mode failure, with delamination, bending, axial cracking, and fibre fracture as the dominant crash-box failure modes [8,16–18]. Trigger features such as edge chamfers are widely used to promote progressive rather than catastrophic collapse and thereby improve energy absorption [19,20]; different materials in similar geometries produce different absorption levels [21], and trigger mechanisms have been shown to shift failure behaviour from catastrophic to progressive collapse [22–24]. Tube aspect ratio length-to-diameter and thickness-to-diameter are established design variables for composite-tube crashworthiness [25,26], although fewer studies have specifically addressed hybrid composite tubes.

Recent studies have explored metal–composite hybrid tubes in which a metallic shell is combined with a composite core or in which metallic and composite layers are arranged in different sequences, with the objective of integrating the ductility of metals with the high specific strength and energy-absorption potential of composites [27–30]. The resulting performance is strongly influenced by parameters such as the relative thickness of the constituent layers, stacking or nesting sequence, and the mechanical interaction at the metal–composite interface [28,31]. Despite these potential advantages, practical challenges remain in manufacturing such structures economically and in ensuring reliable long-term behaviour of the dissimilar-material interface [30,32]. We previously investigated glass/carbon fibre hybrid composite tubes [33]; this work extends that research by introducing aluminium 6061-T4 as the metallic constituent and systematically evaluating monolithic aluminium and composite tubes alongside four aluminium–composite hybrid configurations with different aluminium tube placements. The primary objective is to quantify the influence of hybridisation and nesting sequence on peak load (P_{max}), mean crushing load (P_{ave}), energy absorption (EA), specific energy absorption (SEA), and crush force efficiency (CFE) under quasi-static axial compression, and to relate the measured load–displacement behaviour to the resulting failure mechanisms.

Materials and Methods

The materials examined were aluminium 6061-T4 tubes, carbon-fibre-reinforced polymer (CFRP, denoted CF) tubes, and glass/carbon fibre hybrid composite (denoted FH) tubes, tested individually and in four aluminum–composite hybrid arrangements. The composite tubes were made by the pultrusion process [33]. To maintain the fibre in a specific direction, the DER 331, a thermoset epoxy matrix, in combination with Jointmine 903 hardener, was injected into the pultrusion machine container with a 10:6 epoxy-to-hardener weight ratio. After the curing process, the FRP composite tube was extruded from the machine. Subsequently, during the cooling process, the composite tubes were cut by a saw machine in 2m length. The fibre volume fraction, verified by burn testing, was 60% for the CF tubes and 70% for the FH tubes. Ten specimen configurations were tested (Table 1): two aluminium tubes (AL-S1, AL-S2), two CFRP tubes (CF-S3, CF-S4), two glass/carbon hybrid tubes (FH-S5, FH-S6), and four aluminium–composite hybrid configurations (AL/FH-S7, FH/AL-S8, AL/CF-S9, CF/AL-S10). In each hybrid code, the first material listed denotes the outer tube and the second the inner tube: AL/FH-S7 and AL/CF-S9 therefore consist of an external aluminium tube surrounding an internal composite tube, while

FH/AL-S8 and CF/AL-S10 consist of an external composite tube surrounding an internal aluminium tube.

Table 1. Specimen configurations, nominal dimensions, and nesting order.

Group	Sample code	Outer dia. (mm)	Inner dia. (mm)	Wall thickness (mm)	Mass (g)
Aluminium	AL-S1	44.4	38.4	2.0 Single wall	96
Aluminium	AL-S2	38.0	31.6	2.0 Single wall	89
CFRP	CF-S3	42.6	38.8	2.0 Single wall	36
CFRP	CF-S4	38.0	34.3	2.0 Single wall	33
GF/CF hybrid	FH-S5	43.0	39.0	2.0 Single wall	45
GF/CF hybrid	FH-S6	38.0	34.0	2.0 Single wall	39
AL outer / FH inner	AL/FH-S7	44.0	34.2	4.9 hybrid	137.3
FH outer / AL inner	FH/AL-S8	43.0	31.6	5.7 hybrid	134.0
AL outer / CF inner	AL/CF-S9	44.5	34.3	5.1 hybrid	133.7
CF outer / AL inner	CF/AL-S10	42.6	31.6	5.5 hybrid	131.3

Fig. 1 shows the different types of aluminium and composite tube samples used for the compression tests. All specimens were cut to a length of 100 mm by a CNC diamond cutting saw machine. Outer diameters were 38 mm for the single-material tubes and 42 mm (outer tube) / 38 mm (inner tube) for the hybrid tubes, with a nominal wall thickness of 2 ± 0.1 mm per tube wall (Table 1). The compression test was conducted according to ASTM E9 quasi-static axial compression using an INSTRON 600DX universal testing machine, with a 500 kN load cell. For composite testing, the loading and boundary test conditions were taken from ASTM D5449 because the FRP tube in this study was filament-wound in the fabrication process. A constant quasi-static loading rate of 3 mm/min was maintained for all samples, with testing continuing until 60% of the specimen length was crushed. To ensure data reliability, three specimens were tested per configuration, and continuous load and displacement data were acquired throughout the process.

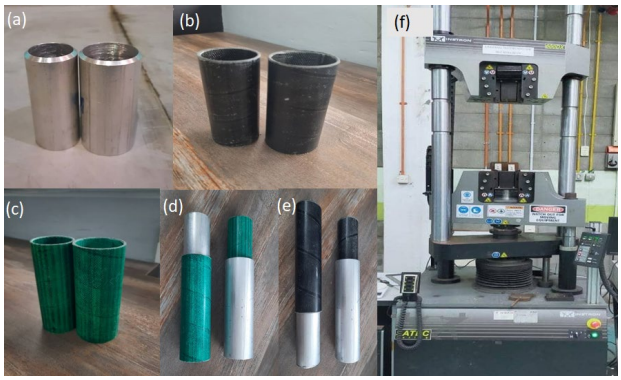


Fig. 1. Different types of aluminium and composite tube samples for compression test.

Key crashworthiness parameters, including energy absorption (EA), specific energy absorption (SEA), average stress, and crush force efficiency (CFE), were subsequently calculated from the collected data to evaluate the performance of each tube configuration quantitatively. The following crashworthiness indicators were computed from the load-displacement curve as shown in Fig. 2. EA, defined as the area under the load-displacement curve up to a crush distance δ, is

$$\mathrm{EA} = \int_0^S F\, d\delta \qquad \text{Eq. 1}$$

SEA, normalizing EA by the crushed mass m, is

$$SEA = \frac{E}{m} \quad \text{Eq. 2}$$

Average stress σ_{avr} and maximum stress σ_{max} are the mean and peak crushing loads normalized by the specimen cross-sectional area A:

$$\sigma_{avr} = \frac{\bar{P}}{A}, \quad \sigma_{max} = \frac{P_{max}}{A} \quad \text{Eq. 3}$$

CFE, the ratio of the mean crushing load to the peak load, quantifies force-displacement stability:

$$CFE = \frac{\bar{P}}{P_{max}} \quad \text{Eq. 4}$$

A higher CFE indicates a smoother crushing response with a lower peak-to-mean load ratio, which is desirable for occupant safety because it reduces the initial deceleration spike.

Result and Discussion

The experimental results presented in Fig. 2 demonstrate a clear influence of hybridisation and nesting sequence on the crushing response. Hybrid configurations incorporating an external aluminium tube produced the largest increases in mean crushing load. In particular, AL/FH-S7 and AL/CF-S9 exhibited improvements of 31.01% and 26.49%, respectively, relative to the aluminium reference tubes. Hybrid configurations with aluminium positioned internally also improved the mean load, although the increase was more limited, ranging from 7.43% to 15.90%. A consistent trend was observed for the peak crushing load: all hybrid configurations produced increases of 25.32–37.08% relative to the aluminium specimens. These results demonstrate that the relative position of the metallic and composite constituents is not merely a geometric detail but a governing factor in the global crushing response. Although hybridisation increased the applied load capacity, the corresponding stress measures were generally lower because the hybrid specimens possessed a larger effective cross-sectional area. Thus, the increase in load capacity should be interpreted together with the geometric change rather than as a direct indication of higher material-level stress resistance.

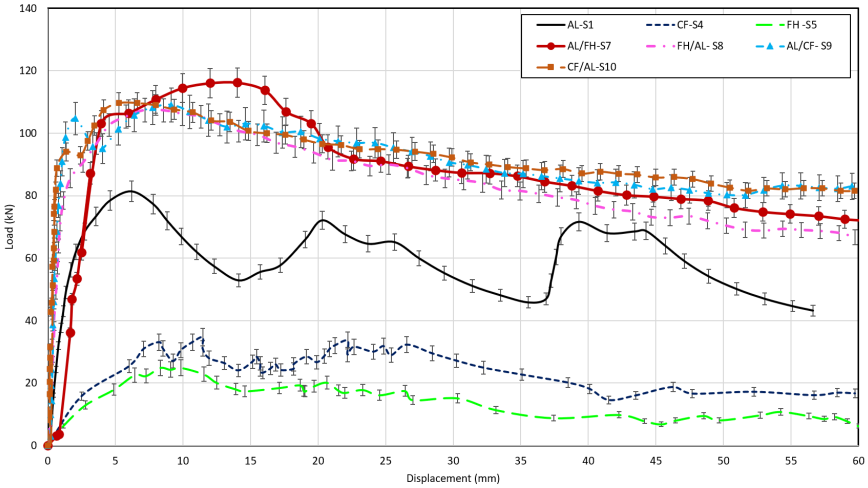


Fig. 2. Load-displacement curves for different samples: aluminium tubes, composite tubes, and hybrid tubes.

The hybrid configurations also exhibited higher absolute energy-absorption capacity, with EA increases of 7.45–32.58% relative to the aluminium references. This gain was accompanied by a substantial mass penalty: the hybrid specimens were approximately 45% heavier than the corresponding single-material aluminium specimens. As a consequence, the increase in absolute

EA did not translate into improved mass-normalised performance, with SEA decreasing by approximately 17% on average. This distinction is important when assessing crashworthiness because high load-carrying and energy-absorption capacity alone do not necessarily imply a more efficient energy absorber. The load–displacement responses nevertheless indicate that the hybrid structures dissipated more total mechanical energy, reflected by the larger area beneath the curves. CFE results further demonstrate that the hybridisation strategy does not inherently improve force-displacement stability; depending on the configuration, CFE was reduced or remained comparable to the aluminium reference. Among the investigated arrangements, specimens with an external aluminium shell provided the most favourable overall combination of load capacity, energy absorption, and progressive collapse behaviour. The superior response of these configurations is consistent with the ability of the ductile outer aluminium layer to constrain and organise the crushing process while the inner composite tube provides additional load-bearing and energy-dissipation capacity. The load–displacement results exhibited strong agreement with the experimental measurements across the evaluated parameters. The highest level of correlation was obtained for P_{max}, with an R^2 value of 0.9751, indicating that approximately 97.5% of the variation observed in the experimental results was extracted. The compressive stress also showed a strong correlation between different experimental data, yielding an R^2 value of 0.9280. Although the correlation for SEA was comparatively lower (R^2= 0.8868), it still represents a strong and acceptable agreement, particularly given the inherent variability associated with experimental measurements. Table 2 summarizes the principal crashworthiness indicators.

Table 2. Summary of crashworthiness indicators for different samples.

	Sample	Pavr (kN)	Pmax (kN)	σ_{avr} (MPa)	σ_max (MPa)	EA (J)	SEA (J/g)	CFE
Individual materials	AL-S1	59.65	85.75	152.50	219.24	3555.17	37.03	0.70
	AL-S2	65.53	83.27	187.31	238.03	3949.73	44.38	0.79
	CF-S3	20.99	27.80	82.27	108.96	1265.55	35.15	0.75
	CF-S4	25.27	33.95	120.30	161.61	1523.97	46.18	0.75
	FH-S5	18.35	22.72	71.25	88.18	1106.22	24.58	0.81
	FH-S6	23.19	28.08	101.96	123.46	1397.82	35.84	0.83
Hybrid material	AL/FH-S7	78.15	117.55	129.84	195.30	4713.56	34.32	0.66
	FH/AL-S8	70.40	109.33	105.40	163.68	4243.97	31.69	0.64
	AL/CF-S9	75.45	107.46	119.53	170.23	4549.31	34.04	0.70
	CF/AL-S10	75.95	110.71	118.49	172.70	4579.83	34.86	0.69

Failure Mode Analysis

Fig. 3 demonstrates different failure modes of hybrid samples at the end of each test. Visual examination reveals distinct failure mechanisms for each material type. Pure aluminium samples exhibit progressive failure and buckling failure modes with periodic fold formation. Fibre composite samples demonstrate two-stage failure processes: initial pre-crushing involving fibre micro-buckling and inter/intralaminar fracture, followed by post-crushing characterized by progressive failure. Hybrid samples show failure modes dominated by the external tube material, with internal tubes providing supplementary support.

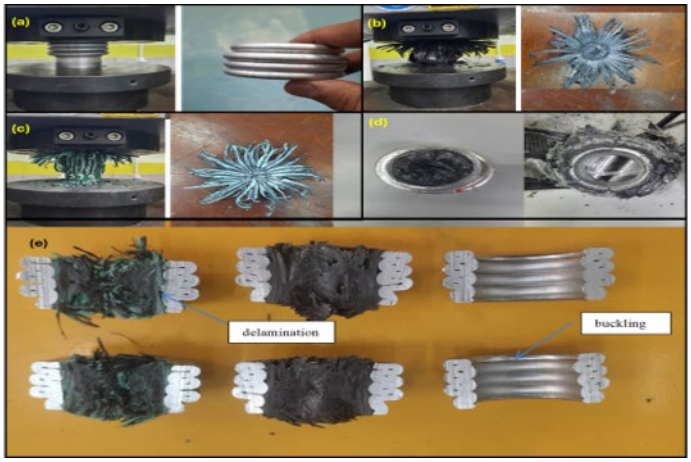


Fig. 3. Post-failure specimens subjected to compressive axial loading.

The interaction between different failure mechanisms creates observed wavelet effects in load-displacement curves, representing compromise between distinct parent material behaviours. In samples covered by outer aluminium tubes, the folding is controlled and progressive. A closer examination of the cross section shows several failure modes and mechanisms such as vertical delamination, interlaminar cracking, debonding between metallic and polymeric sections, and shear failure. On the other hand, when the aluminium tube is in the inner part, the tulip failure effect is the major failure mechanism.

Conclusions

The present investigation evaluated the quasi-static axial crushing behaviour and crashworthiness characteristics of aluminium 6061-T4, CFRP, glass/carbon fibre hybrid, and aluminium–composite hybrid tubes. Across the investigated configurations, hybridisation increased the peak crushing load by 25.32–37.08%, the mean crushing load by 7.43–31.01%, and the absorbed energy by 7.45–32.58% relative to the aluminium reference specimens. The most pronounced improvements were obtained when aluminium was used as the outer tube, demonstrating the strong influence of nesting sequence on structural response. However, the increased energy-absorption capacity was accompanied by an approximately 45% increase in specimen mass, resulting in an average SEA reduction of about 17%. CFE was likewise generally lower or comparable to that of the aluminium tubes. These findings indicate that the present hybridisation strategy enhances absolute load-carrying and energy-dissipation capacity but, for the material proportions and dimensions investigated, does not improve mass efficiency. A more mass-efficient hybrid design would therefore require a greater reduction in aluminium wall thickness or another compensating reduction in structural mass. The failure observations further indicate that the outer tube exerts the dominant influence on the macroscopic crushing mode, while the inner tube acts primarily as a secondary load-bearing and energy-dissipation component. Finally, the conclusions of this study are restricted to quasi-static axial compression. Dynamic testing and rate-dependent validation are required before the present findings can be directly extended to automotive crash-box applications.

Acknowledgements

The authors acknowledge the support of Universiti Teknologi Malaysia Fundamental Research Grant (UTMFR) through project No Q.J130000.3824.22H91.

References

[1] F. Dionisius, J. Istiyanto, D.A. Sumarsono, G. Prayogo, A.S. Baskoro, M. Malawat, Modeling of Crashworthiness criteria based on Variation of Hole as Crush Initiator in Thin-

Walled Square, Int. J. Automot. Mech. Eng. 19 (2022) 9487–9497. https://doi.org/10.15282/ijame.19.1.2022.12.0731

[2] N.K. Sever, Hybrid Steel Sheet Trends for Automotive Stampings, Int. J. Automot. Technol. 22 (2021) 1153–1158. https://doi.org/10.1007/s12239-021-0102-7

[3] T.Y. Badgujar, S.A. Bobade, Advances in Sheet Metal Stamping Technology: A Case of Design and Manufacturing of a Car Door Inner Panel Using a Tailor Welded Blank, in: Manufacturing and Industrial Engineering, CRC Press, Boca Raton, FL, USA, 2021, pp. 175–190. https://doi.org/10.1201/9781003088073-11

[4] A. Farokhi Nejad, M.Y. Bin Salim, S.S. Rahimian Koloor, S. Petrik, M.Y. Yahya, S. Abu Hassan, M.K. Mohd Shah, Hybrid and Synthetic FRP Composites under Different Strain Rates: A Review, Polymers 13 (2021) 3400. https://doi.org/10.3390/polym13193400

[5] H. Luo, D. Zhang, Z. He, X. Li, Z. Li, Experimental investigation of the quasi-static and dynamic axial crushing behavior of carbon/glass epoxy hybrid composite tubes, Mater. Today Commun. 26 (2021) 101941. https://doi.org/10.1016/j.mtcomm.2020.101941

[6] P. Zhang, Y. Wang, X. Zhang, Energy absorption and impact resistance of sandwich composite alloy structures under dynamic impact, J. Alloy. Compd. 831 (2020) 154771. https://doi.org/10.1016/j.jallcom.2020.154771

[7] C. Zhang, K. Tan, Low-velocity impact response and compression after impact behavior of tubular composite sandwich structures, Compos. Part B Eng. 193 (2020) 108026. https://doi.org/10.1016/j.compositesb.2020.108026

[8] N. Abdullah, M. Sani, M. Salwani, N. Husain, A review on crashworthiness studies of crash box structure, Thin-Walled Struct. 153 (2020) 106795. https://doi.org/10.1016/j.tws.2020.106795

[9] G. Sun, D. Chen, G. Zhu, Q. Li, Lightweight hybrid materials and structures for energy absorption: A state-of-the-art review and outlook, Thin-Walled Struct. 172 (2022) 108760. https://doi.org/10.1016/j.tws.2021.108760

[10] H. Yang, H. Lei, G. Lu, Z. Zhang, X. Li, Y. Liu, Energy absorption and failure pattern of hybrid composite tubes under quasi-static axial compression, Compos. Part B Eng. 198 (2020) 108217. https://doi.org/10.1016/j.compositesb.2020.108217

[11] D. Fernando, J. Teng, J. Gattas, M. Heitzmann, Hybrid fibre-reinforced polymer–timber thin-walled structural members, Adv. Struct. Eng. 21 (2018) 1409–1417. https://doi.org/10.1177/1369433217739709

[12] T. Liu, X. Wu, B. Sun, W. Fan, W. Han, H. Yi, Investigations of defect effect on dynamic compressive failure of 3D circular braided composite tubes with numerical simulation method, Thin-Walled Struct. 160 (2021) 107381. https://doi.org/10.1016/j.tws.2020.107381

[13] M.H. Abdallah, A. Braimah, Numerical design optimization of the fiber orientation of glass/phenolic composite tubes based on tensile and radial compression tests, Compos. Struct. 280 (2022) 114898. https://doi.org/10.1016/j.compstruct.2021.114898

[14] C. Li, X. Yin, Y. Wang, L. Zhang, Z. Zhang, Y. Liu, G. Xian, Mechanical property evolution and service life prediction of pultruded carbon/glass hybrid rod exposed in harsh oil-well condition, Compos. Struct. 246 (2020) 112418. https://doi.org/10.1016/j.compstruct.2020.112418

[15] Y. Pan, D. Yan, Study on the durability of GFRP bars and carbon/glass hybrid fiber reinforced polymer (HFRP) bars aged in alkaline solution, Compos. Struct. 261 (2021) 113285. https://doi.org/10.1016/j.compstruct.2020.113285

[16] J. Claus, R.A. Santos, L. Gorbatikh, Y. Swolfs, Effect of matrix and fibre type on the impact resistance of woven composites, Compos. Part B Eng. 183 (2020) 107736. https://doi.org/10.1016/j.compositesb.2019.107736

[17] K. Naito, Interfacial mechanical properties of carbon/glass hybrid thermoplastic epox composite rods, Compos. Struct. 257 (2021) 113129. https://doi.org/10.1016/j.compstruct.2020.113129

[18] N. San Ha, G. Lu, Thin-walled corrugated structures: A review of crashworthiness designs and energy absorption characteristics, Thin-Walled Struct. 157 (2020) 106995. https://doi.org/10.1016/j.tws.2020.106995

[19] Y. Ren, T. Ran, L. Nie, H. Jiang, Energy-absorption assessments of perforated CFRP tube induced by inward-splaying trigger with different trigger radius, Thin-Walled Struct. 167 (2021) 108236. https://doi.org/10.1016/j.tws.2021.108236

[20] Supian, S. Sapuan, M. Zuhri, E. Zainudin, H.H. Ya, Hybrid reinforced thermoset polymer composite in energy absorption tube application: A review, Def. Technol. 14 (2018) 291–305. https://doi.org/10.1016/j.dt.2018.04.004

[21] R. Sivagurunathan, S.L.T. Way, L. Sivagurunathan, M.Y. Yaakob, Effects of triggering mechanisms on the crashworthiness characteristics of square woven jute/epoxy composite tubes, J. Reinf. Plast. Compos. 38 (2018) 824–840. https://doi.org/10.1177/0731684418763218

[22] A.A. Rezvanfar, A.F. Nejad, M.N. Tamin, T. Dickhut, S.S.R. Koloor, Data-Driven Machine Learning and Finite Element-Informed Surrogate Modeling for Design Optimization and Failure Prediction of Reinforced Thermoplastic Pipes, Journal of Materials Research and Technology 42 (2026) 8557–8571. https://doi.org/10.1016/j.jmrt.2026.05.062

[23] D. Betts, P. Sadeghian, A. Fam, Experimental and analytical investigations of the flexural behavior of hollow ±55° filament wound GFRP tubes, Thin-Walled Struct. 159 (2021) 107246. https://doi.org/10.1016/j.tws.2020.107246

[24] H.R. Shalian, M.H. Alaee, J. Eskandari Jam, M. Heydari Beni, M. Eskandari Shahraki, N. Asiaban, Design and Fabrication of a Composite Energy Absorber, ADMT J. 20 (2020) 1–12.

[25] X. Gao, B. Sun, B. Gu, Damage mechanisms of 3-D rectangular braided composite under multiple impact compressions, Aerosp. Sci. Technol. 82 (2018) 46–60. https://doi.org/10.1016/j.ast.2018.08.031

[26] J.-E. Chambe, C. Bouvet, O. Dorival, J.-F. Ferrero, Energy absorption capacity of composite thin-wall circular tubes under axial crushing with different trigger initiations, J. Compos. Mater. 54 (2020) 1281–1304. https://doi.org/10.1177/0021998319877221

[27] E. Jebellat, M. Baniassadi, A. Moshki, K. Wang, M. Baghani, Numerical investigation of smart auxetic three-dimensional meta-structures based on shape memory polymers via topology optimization, J. Intell. Mater. Syst. Struct. 30 (2020) 1838–1852. https://doi.org/10.1177/1045389X20935569

[28] M. Jamshidian, N. Boddeti, D.W. Rosen, O. Weeger, Multiscale modelling of soft lattice metamaterials: Micromechanical nonlinear buckling analysis, experimental verification, and

macroscale constitutive behaviour, Int. J. Mech. Sci. 188 (2020) 105956. https://doi.org/10.1016/j.ijmecsci.2020.105956

[29] A. Farokhi Nejad, S.S. Rahimian Koloor, S.M.S.A. Syed Hamzah, M.Y. Yahya, Mechanical Behaviour of Pin-Reinforced Foam Core Sandwich Panels Subjected to Low Impact Loading, Polymers 13 (2021) 3627. https://doi.org/10.3390/polym13213627

[30] A.B. Nia, A.F. Nejad, L. Xin, A. Ayob, M.Y. Yahya, Energy absorption assessment of conical composite structures subjected to quasi-static loading through optimization-based method, Mech. Ind. 21 (2020) 113. https://doi.org/10.1051/meca/2019088

[31] R. Bhat, N. Mohan, S. Sharma, A. Pratap, A.P. Keni, D. Sodani, Mechanical testing and microstructure characterization of glass fiber reinforced isophthalic polyester composites, J. Mater. Res. Technol. 8 (2019) 3653–3661. https://doi.org/10.1016/j.jmrt.2019.06.003

[32] M. Quanjin, M. Salim, M. Rejab, O.-E. Bernhardi, A.Y. Nasution, Quasi-static crushing response of square hybrid carbon/aramid tube for automotive crash box application, Mater. Today Proc. 27 (2020) 683–690. https://doi.org/10.1016/j.matpr.2019.10.161

[33] A. Farokhi Nejad, S.S.R. Koloor, M.L.H. Arifin, A. Shafiei, S.A. Hassan, M.Y. Yahya, Crashworthiness assessment of carbon/glass epoxy hybrid composite tubes subjected to axial loads, Polymers 14 (2022) 4083. https://doi.org/10.3390/polym14194083

Materials Research Proceedings 74 (2026) 222-230 https://doi.org/10.21741/9781644904473-28

Concrete Incorporating Palm Oil Fuel Ash and Polyethylene Terephthalate for Gamma-Ray Shielding

Nurain Najwa RAMLI[1,a] and Siti Amira OTHMAN[1,b*]

[1]Faculty of Applied Sciences and Technology, Universiti Tun Hussein Onn Malaysia, 84600, Pagoh, Johor, Malaysia

[a]aw210066@student.uthm.edu.my, [b]sitiamira@uthm.edu.my

Keywords: POFA, PET, Concrete, Gamma-Ray, Shielding

Abstract. This study explores the incorporation of Palm Oil Fuel Ash (POFA) and Polyethylene Terephthalate (PET) into concrete to enhance its gamma-ray shielding capabilities while addressing environmental sustainability. POFA, a by-product of the palm oil industry, is rich in silica and exhibits excellent pozzolanic properties, strengthening the concrete matrix and improving its durability. PET, a widely available plastic waste, provides flexibility and enhances the overall mechanical properties of the concrete. The research examines various proportions of POFA and PET in concrete mixtures, focusing on their effects on density, compressive strength, water absorption, and radiation attenuation efficiency. The experimental results demonstrate significant improvements in the physical and mechanical properties of the modified concrete. The optimised mix (M3.3) achieved the highest density, compressive strength of 18.23 MPa, and a linear attenuation coefficient of 22.14, making it suitable for gamma-ray shielding. Furthermore, incorporating POFA and PET reduced porosity and improved durability, ensuring the material's long-term performance in radiation-sensitive environments. The findings indicate that POFA-PET concrete offers a sustainable, cost-effective alternative to conventional shielding materials, particularly for medical and nuclear facilities, while contributing to effective waste management by utilising industrial and plastic waste.

Introduction

Concrete is widely used as a radiation shielding material in nuclear facilities, hospitals, and research laboratories due to its high density, durability, and cost-effectiveness. Its ability to absorb and attenuate ionising radiation makes it an important material for protecting personnel and the environment from harmful radiation exposure [1–3]. It serves as a vital element in the construction of a building. This essential structural material is crafted from aggregate particles, which are hard, chemically inert particle masses cemented with Portland cement and water. Concrete is typically constructed to be both sturdy and long-lasting. The water-to-cement ratio significantly influences the appearance and quality of traditional concrete. To ensure concrete quality during production, the concrete must contain just enough water to fully enclose each aggregate particle in cement paste [4]. The research focuses on incorporating POFA and PET into concrete mixtures to enhance their shielding properties. POFA, a by-product of palm oil combustion, can enhance the strength and durability of concrete. PET, on the other hand, is a thermoplastic polymer that can improve the flexibility and impact resistance of concrete [5].

Radiation shielding is essential in many industries, including medical, industrial, and nuclear applications, to protect persons and the environment from damaging ionising radiation [6]. Gamma rays, an ionising radiation with high penetrating power, pose significant health risks because they can penetrate living tissue and induce cellular damage [7]. To reduce the intensity of these rays and ensure safety in gamma radiation-contaminated situations, effective shielding materials must be used to absorb or attenuate them. Traditional shielding materials such as lead and concrete are widely utilised but have drawbacks, including environmental problems and structural constraints

Content from this work may be used under the terms of the Creative Commons Attribution 3.0 license. Any further distribution of this work must maintain attribution to the author(s) and the title of the work, journal citation and DOI. Published under license by Materials Research Forum LLC.

[8]. As a result, developing novel materials that offer improved shielding while addressing these constraints is critical.

The global environmental crises have been driven by non-biodegradable waste and population growth. Many of them are illegally dumped into dustbins or crammed into landfills [9]. The increased usage of plastic materials has led to a rise in plastic trash in Malaysia; the country's current plastic consumption rates are as follows: PET polycarbonate (PC) 1.8 tons/day, polypropylene (PP) 12.8 tons/day, polystyrene (PS) 39.42 kg/day, acrylonitrile butadiene styrene (ABS) 13.2 tons/day, and others approximately 5 tons/day. Also, as palm oil production continues to grow, so does POFA generation. Failing to utilise this waste material poses a significant environmental challenge. In Malaysia alone, POFA production reaches approximately 10 million tonnes annually. In neighbouring countries such as Thailand, annual POFA production is currently limited to 104 tonnes, but this quantity is increasing [10]. So, to tackle all of these issues, using sustainable resources is the best way to mitigate the environmental problems arising globally from waste disposal. Although numerous studies have investigated the use of POFA as a supplementary cementitious material and PET as a recycled aggregate replacement, limited studies have evaluated their combined effect on gamma-ray shielding performance. This study contributes new knowledge by systematically investigating the synergistic influence of POFA and PET on radiation attenuation, density, compressive strength, and water absorption characteristics of concrete. The findings provide insight into the development of sustainable radiation-shielding materials using plastic waste.

Methodology

This study utilised ordinary Portland cement (OPC), fine and coarse aggregates, and a POFA–PET composite as a supplementary concrete addition. The study's purpose is to assess the effectiveness of gamma-ray shielding by embedding POFA and PET into concrete and analysing its density and water absorption. New concrete was cured and evaluated for density, water absorption, and gamma-ray shielding performance. The first step involves preparing the sample using aggregates, water, PET, OPC, and POFA. The process began with drying palm ash to remove any moisture that could affect subsequent steps. This was done to ensure the ash was completely dry and ready for further processing. Once dried, the ash was allowed to cool, then ground to a fine powder using a ball mill. The grinding process was carried out continuously for 7 days to achieve a uniform, consistent particle size. After the grinding process, the fine powder was sieved through a 0.075 mm mesh to retain only particles of the desired size. This sieving step was crucial to eliminate any larger particles that could compromise the quality of the final material. Finally, the ground POFA was carefully stored in airtight containers to prevent exposure to moisture and contamination, as both factors could affect its properties and performance in subsequent applications. PET was gathered in the Pagoh region, chopped into pieces, and then blended to achieve fine flakes (<10mm). The specimens employed varying percentages of PET by weight (1%, 2%, and 3%) based on the overall volume of the combination. In the investigation, M30 grade concrete was used (Table 1 and 2).

Table 1. Amount of PET percentages in concrete mix.

Concrete batch	Percentages of [%]	Weight of PET flakes [kg]
Control	0	0.0000
PE1	1	0.0021
PE2	2	0.0042
PE3	3	0.0062

Table 2. Number of concrete materials in the concrete mix.

Mix	OPC [kg]	PET [%]	POFA [kg]	Sand [kg]	Gravel [kg]	Water to cement ratio [kg]
M0	0.021	-	-	0.5	1.0	0.5
M1.1	0.020	1	0.01	0.5	1.0	0.5
M1.2	0.020	2	0.01	0.5	1.0	0.5
M1.3	0.020	3	0.01	0.5	1.0	0.5
M2.2	0.019	1	0.02	0.5	1.0	0.5
M2.2	0.019	2	0.02	0.5	1.0	0.5
M2.3	0.019	3	0.02	0.5	1.0	0.5
M3.1	0.018	1	0.03	0.5	1.0	0.5
M3.2	0.018	2	0.03	0.5	1.0	0.5
M3.3	0.018	3	0.03	0.5	1.0	0.5

The specimen, which is cube-shaped (3 cm × 3 cm × 4 cm), is placed between two plates and compressed. The batch-controlled (M0) sample is designed to withstand this force and deform accordingly. The deformation is measured to determine mechanical properties, such as compressive strength. The expected compressive strength, σ, of the M0 sample is 30 MPa, representing its maximum stress tolerance. The density of a concrete sample may be calculated by dividing its weight by its volume.

Water Absorption of Concrete

The concrete's water absorption percentage was determined by conducting a water absorption test (Fig. 1). Initially, the samples are allowed to harden for 24 hours and then placed in a drying oven at 105°C for 5 hours. This process is repeated until the samples reach a consistent mass, at which point they are weighed again. A minimum separation distance of 25mm is maintained between the samples to avoid interference. Once removed from the drying oven, the samples are weighed at their dry weight (W_1) and placed in a water tank. Within 30 minutes, all samples are fully immersed in the water tank. Subsequently, the damp samples are carefully wiped with a towel and immediately weighed as their dry weight (W_2). The water absorption of the concrete is then calculated using the Eq. 1.

$$\boldsymbol{Water\ absorption} = \frac{\boldsymbol{W_2 - W_1}}{\boldsymbol{W_1}} \quad (1)$$



(a) (b)

Fig. 1. (a) Specimens after the 5 hours of drying process; and (b) specimens immersed in water for 30 minutes.

Results and Discussion

The linear attenuation coefficient (μ) for concrete samples ranging from the control sample (M0) to the modified samples (M1.1 to M3.3) is shown in Table 3. The control sample (M0) exhibits an attenuation coefficient, μ ≈ 18, indicating a significant amount of radiation passes through. The ability of a substance to attenuate gamma radiation as it passes through it is known as its shielding capability. In radiation-sensitive settings, such as nuclear and medical facilities, where efficient protection is necessary to guarantee safety, this feature is crucial. The linear attenuation coefficient, which indicates the percentage of gamma rays absorbed or scattered per unit thickness of the shielding material, is the primary tool used to determine capability. Furthermore, the rate of gamma radiation reaching the substance relative to the original intensity is measured by the transmission ratio (T). The composition, thickness, and structural homogeneity of the material are some of the variables that affect shielding efficiency. In general, materials with larger atomic

numbers and densities are better at attenuating gamma rays. In contrast, the modified samples (M1, M2, and M3 groups) show progressive increases in μ, demonstrating the effectiveness of incorporating POFA and PET in enhancing gamma-ray attenuation.

Table 3. Linear attenuation coefficient [μ].

Sample	Transmission ratio	Linear attenuation coefficient [μ]
M0 (Control)	0.600	18.01
M1.1	0.830	7.45
M1.2	0.830	7.45
M1.3	0.830	7.45
M2.1	0.680	15.43
M2.2	0.670	16.02
M2.3	0.670	16.02
M3.1	0.680	15.43
M3.2	0.670	16.02
M3.3	0.575	22.14

The M1 group exhibits a lower linear attenuation coefficient (7.45 cm^{-1}) than the control sample (18.01 cm^{-1}), indicating that the initial incorporation of POFA and PET did not immediately enhance gamma-ray attenuation performance. This reduction may be attributed to the relatively low POFA content and the introduction of PET particles, which may have increased interfacial voids and reduced matrix compactness. Although the pozzolanic reaction of POFA can contribute to microstructural refinement and matrix densification by forming additional calcium silicate hydrate (C-S-H) gel, these beneficial effects were insufficient at this incorporation level to improve shielding performance. Consequently, the M1 group exhibited lower gamma-ray attenuation and shielding effectiveness than the control sample [12]. POFA undergoes a pozzolanic reaction with calcium hydroxide, producing additional C-S-H gel that improves matrix densification, reduces porosity, and enhances durability. However, at the POFA content used in the M1 group, these benefits were insufficient to compensate for the increased voids associated with PET incorporation [11]. The higher transmission ratio observed in the M1 group (0.83) confirms that a larger fraction of gamma radiation passed through the specimen, which is consistent with the lower attenuation coefficient values obtained. This observation validates the attenuation measurements and suggests that low levels of POFA-PET incorporation were insufficient to improve shielding performance.

The M2 group demonstrates a substantial recovery in attenuation performance, with μ values increasing to 15.43–16.02 cm^{-1}. The increased POFA content likely enhanced the pozzolanic reaction, reduced porosity, and improved particle packing, resulting in a denser matrix and improved radiation attenuation. The additional POFA reduces porosity, densifies the matrix, and enhances particle packing, thereby increasing gamma-ray attenuation [13]. The consistent μ values across M2.1 to M2.3 suggest that this group achieves a balance between shielding effectiveness and structural integrity. Structural integrity and shielding effectiveness must be balanced to ensure a material is both strong and effective at blocking gamma radiation. Structural integrity ensures the material can handle loads and maintain stability, while shielding effectiveness focuses on its ability to attenuate radiation. High-density materials often provide better radiation shielding but may become brittle, reducing structural strength. On the other hand, lightweight materials with high structural integrity may lack the density needed for effective shielding [11].

POFA-PET concrete achieves this balance by combining the strengths of both materials. POFA enhances structural integrity through pozzolanic reactions that strengthen the concrete matrix, while PET improves flexibility and reduces voids, thereby contributing to both strength and radiation shielding. The combination results in a dense, durable material that effectively blocks gamma radiation while maintaining load-bearing capacity [14]. The highest attenuation coefficient was observed for M3.3 (22.14 cm^{-1}), exceeding those of the control sample and all other modified

mixtures. This result suggests that the combination of 3% PET and 0.03 kg POFA achieved the optimal balance between matrix densification and particle distribution, resulting in the most effective gamma-ray shielding performance among all samples tested [15].

Time, Distance, and Thickness-Dependent Shielding Effectiveness

Figs. 2 to 4 present the radiation shielding performance of the POFA-PET-incorporated concrete under different measurement conditions: time-dependent, distance-dependent, and thickness-dependent evaluations. In all cases, the control sample (M0) recorded the highest radiation readings, indicating the lowest shielding capability. The incorporation of POFA and PET progressively reduced the radiation intensity from M1 to M3 mixes, demonstrating enhanced attenuation performance.

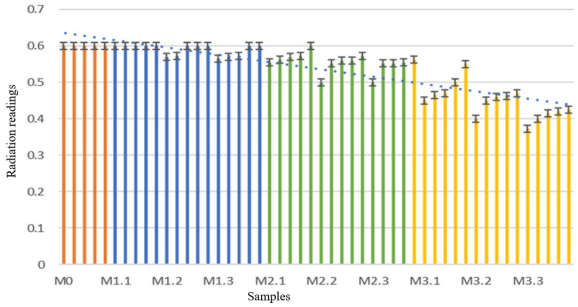


Fig. 2. Time-dependent shielding effectiveness.

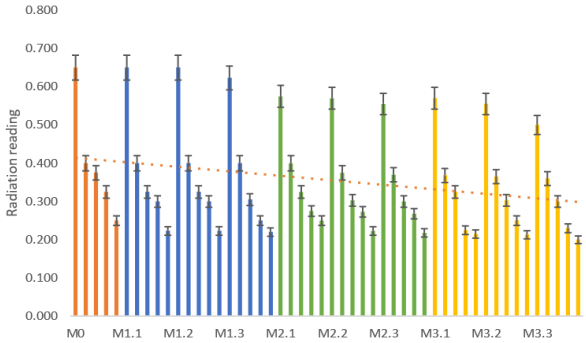


Fig. 3. Distance-dependent shielding effectiveness.

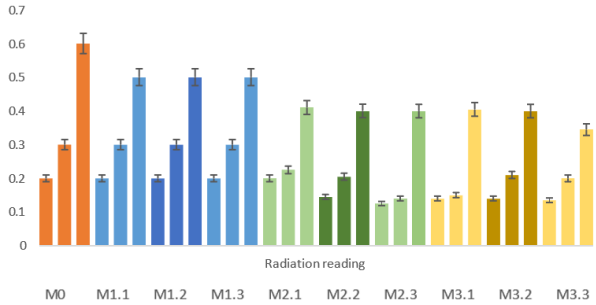


Fig. 4. Thickness-dependent shielding effectiveness.

The improvement is mainly attributed to the pozzolanic reaction of POFA, which refines the pore structure and increases matrix density. At the same time, PET improves particle distribution and reduces void formation. The M2 and M3 series exhibited significantly lower radiation readings than the control mix, indicating improved gamma-ray attenuation. Among all samples, M3.3 consistently demonstrated the best shielding performance, which corresponded to its highest density and lowest water absorption. The enhanced compactness of the concrete matrix reduced radiation transmission and increased the linear attenuation coefficient. These findings confirm that the synergistic effect of POFA and PET improves the shielding effectiveness of concrete while maintaining adequate structural properties, making the material suitable for radiation protection applications such as medical imaging facilities and nuclear-related structures [17].

Compressive Strength Test

A compressive strength test was carried out on cube specimens (30 mm × 30 mm × 20 mm). A total of 10 cube specimens were tested, and an ultimate load was applied to each specimen until failure, as shown in Fig. 5. The average compressive strength at 14 days is then calculated.

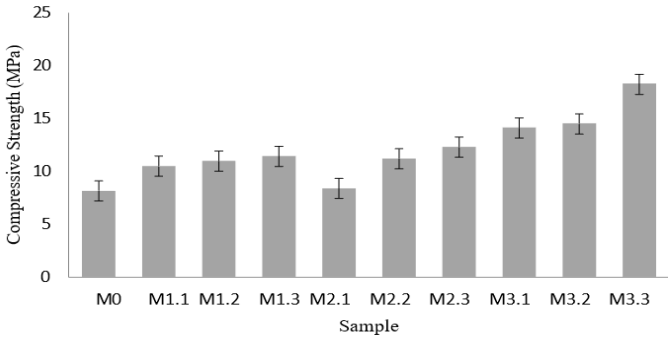


Fig. 5. Compressive strength.

The results show that the compressive strength of the concrete samples increases significantly with different mix designs. The baseline mix, M0, has the lowest compressive strength at 8.1 MPa, while the modified mixes show consistent improvement. In the M1 group (M1.1 to M1.3), the strength ranges from 10.45 MPa to 11.38 MPa, indicating a positive effect of the modifications. For the M2 group, the strength starts at 8.34 MPa (M2.1) and increases to 12.26 MPa (M2.3), showing further improvements due to enhanced material distribution and microstructural densification [11].

The M3 group achieves the highest values, increasing from 14.08 MPa (M3.1) to 18.23 MPa (M3.3), more than doubling the baseline strength. This trend highlights the effectiveness of the mix modifications, likely due to materials such as POFA or PET improving concrete hydration, filling voids, and enhancing structural integrity. The results suggest that the optimised mix in M3.3 provides the best performance, making it suitable for applications requiring higher strength while potentially promoting sustainable construction practices [13].

Density of the concrete

The addition of POFA and PET results in a steady upward trend, suggesting that modifications to the mix designs enhance the material's ability to retain or densify water content (Table 4). Higher water density may indicate a denser microstructure, improving concrete quality and reducing porosity [11]. The incorporation of supplementary materials such as POFA and PET has been shown to refine the pore structure, resulting in reduced porosity and improved overall durability [18-19]. These enhancements significantly improve concrete's long-term performance, particularly in environments exposed to aggressive conditions.

Table 4. Density of the sample.

Sample	Weight [kg]	Density [kg/m^3]
M0 (control)	0.0321	0.1789
M1.1	0.0324	0.1800
M1.2	0.0341	0.1894
M1.3	0.0363	0.2017
M2.1	0.0349	0.1939
M2.2	0.0360	0.200
M2.3	0.0370	0.2056
M3.1	0.0349	0.1994
M3.2	0.0367	0.2039
M3.3	0.0372	0.2067

The results, shown in Table 4, show a gradual increase in water density across the different mix designs. The baseline mix, M0, has the lowest water density at 0.1789 kg/m³. In the M1 group, the density ranges from 0.18 kg/m³ (M1.1) to 0.2017 kg/m³ (M1.3), showing a noticeable improvement [11]. For the M2 group, the water density increases consistently from 0.1939 kg/m³ (M2.1) to 0.2056 kg/m³ (M2.3), reflecting a further positive trend [14]. The M3 group shows the

highest values, with water density increasing from 0.1994 kg/m³ (M3.1) to a peak of 0.2067 kg/m³ (M3.3). This indicates that the M3 mix design provides the most optimised concrete mix, achieving the highest water density among all tested samples [19]. A higher water density in concrete indicates reduced porosity and enhanced compaction, leading to improved mechanical properties and durability [18].

Water Absorption of Concrete

The reduction in water absorption across the samples (M1.1 to M3.3) directly reflects the changes in the material's porosity, as shown in Fig. 6. Porosity, the volume of voids or air gaps within the concrete structure, significantly influences the material's ability to absorb water. The control sample, M0, with the highest water absorption value (13.26%), suggests higher porosity and greater void content. In contrast, the modified samples (M1, M2, and M3 groups) exhibit lower water absorption, indicating reduced porosity [11].

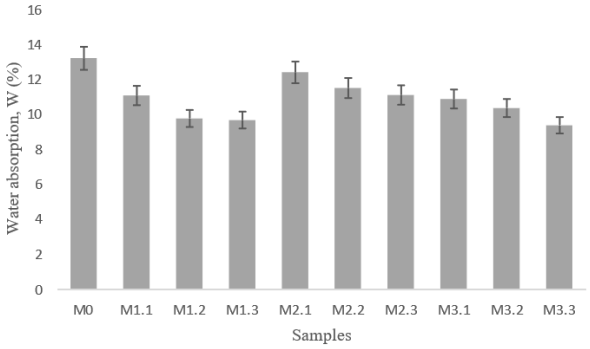


Fig. 6. Water absorption of concrete for all samples.

The M1 group (M1.1, M1.2, and M1.3) shows noticeable improvements, with absorption values ranging between 9.71% and 11.12%. This reduction suggests that the modifications applied to this group successfully reduced voids, resulting in a denser concrete structure [18]. Similarly, the M2 group (M2.1, M2.2, and M2.3) exhibits slightly higher water absorption values (11.15% to 12.45%) compared to the M1 group, implying that while porosity has been reduced compared to M0, some voids remain in this group.

The most significant improvement is observed in the M3 group (M3.1, M3.2, and M3.3), with water absorption values ranging from 9.41% to 10.92%, indicating the lowest porosity among all tested samples. This suggests that the M3 modifications were the most effective in minimising voids and air gaps, resulting in a denser, less permeable concrete structure [19]. Lower porosity is highly beneficial for concrete performance, as it reduces moisture ingress, enhances durability, and improves resistance to long-term environmental effects such as freeze-thaw cycles, chemical attacks, and material degradation [14].

Overall, the consistent decrease in water absorption from M0 to M3.3 suggests a progressive reduction in porosity, demonstrating that the applied modifications successfully enhanced the material's density and quality [18]. Lower porosity not only reduces water absorption capacity but also contributes to the long-term durability and mechanical strength of concrete [19]. Enhanced durability due to reduced porosity improves resistance to environmental factors, such as freeze-thaw cycles, sulfate attack, and chloride penetration, which are critical to the long-term performance of concrete structures.

Conclusion

This study aimed to achieve three main objectives: assess the physical properties of POFA-PET-incorporated concrete for gamma-ray shielding, evaluate the durability and mechanical strength of the modified concrete mix, and analyse the radiation attenuation effectiveness of the POFA-PET concrete. The incorporation of POFA and PET significantly enhanced the physical properties of

the concrete. The M3.3 mix displayed the highest density, minimising porosity and improving overall durability. Reduced water absorption was observed across all modified samples, with the optimised mix exhibiting the lowest, indicating better resistance to environmental degradation. These improvements align with the material's suitability for long-term applications in challenging conditions. Concrete samples containing POFA and PET exhibited higher compressive strength than the baseline mix. The M3.3 mix demonstrated the highest compressive strength of 18.23 MPa, meeting structural integrity requirements for potential applications. This result underscores the effectiveness of the additives in improving interfacial bonding and structural compaction, essential for durability and load-bearing capabilities. The study revealed a significant improvement in gamma-ray shielding properties with the addition of POFA and PET. The optimised M3.3 mix achieved the highest linear attenuation coefficient (22.14), demonstrating superior gamma-ray attenuation performance. This effectiveness was attributed to increased density, optimised particle packing, and the synergistic effects of the additives, making the mix viable for use in medical and nuclear facilities. The novelty of this work lies in the combined utilisation of POFA and PET as sustainable additives for radiation-shielding concrete. The study demonstrates that an optimised combination of both materials can simultaneously improve mechanical performance and radiation attenuation while promoting waste valorisation. These findings contribute to the growing body of knowledge on eco-friendly shielding materials for medical and nuclear applications.

Acknowledgement
This research was supported by Universiti Tun Hussein Onn Malaysia (UTHM) through Tier 1 (vot Q510). The authors would like to thank the Faculty of Applied Sciences and Technology for the facilities provided that enabled the research.

References

[1] G. S. Anunike, M. Tarabin, O. A. Hisseine, Assessment of the mechanical, radiation shielding, and durability of ultra-high-performance concrete for radiation shielding: A review, Construction and Building Materials 474 (2005) 140896. https://doi.org/10.1016/j.conbuildmat.2025.140896

[2] S. Barbhuiya, B.B. Das, P. Norman, T. Qureshi, A Comprehension review of radiation shielding concrete: Properties, design, evaluation and applications, Structural Concrete 26 (2024) 1809-1855. https://doi.org/10.1002/suco.202400519

[3] D. A. Aloraini, M. Y. Hanfi, M. I. Sayyed, K. A. Naseer, A. H. Almuqrin, P. Tamayo, O. L. Tashlykov, K. A. Mahmoud, Design and Gamma-Ray Attenuation Features of New Concrete Materials for Low- and Moderate-Photons Energy Protection Applications, Materials (Basel, Switzerland) 15 (2022) 4947. https://doi.org/10.3390/ma15144947

[4] M. E. Kangavar, W. Lokuge, A. Manalo, W. Karunasena, T. Ozbakkaloglu, Development of sustainable concrete using recycled polyethylene terephthalate (PET) grabules as fine aggregate, Developments in the Built Environment 15 (2023) 100192. https://doi.org/10.1016/j.dibe.2023.100192

[5] M. K. Askar, Y.S.S. Al-Kamaki, A. Hassan, Utilizing Polyethylene Terephthalate PET in Concrete: A Review, Polymers 15 (2023) 3320. https://doi.org/10.3390/polym15153320

[6] G.F. Knoll, Radiation Detection and Measurement, 4th ed., Wiley, United State, 2010.

[7] L. Sylisomchanh, A. Wongsa, C. Yenchai, J. Ekprasert, U. Rattanasak, V. Sata, C. Jaturapitakkul, P. Chindaprasirt, Novel heavyweight geopolymer concrete with mill scale and barite aggregates for sustainable radiation shielding applications, Construction and Building Materials 503 (2025) 1444453. https://doi.org/10.1016/j.conbuildmat.2025.144453

[8] Q. Xu, Q. Ding, P. Zhou, S. Huang, D. Chen, Characterization of the microstructure for hydration products of various cements and the mechanism of radiation shielding effectiveness, Journal of Building Engineering 114 (2025) 114322. https://doi.org/10.1016/j.jobe.2025.114322

[9] G.S. Anunike, O.A. Hisseine, A novel two-phase mixture optimization framework for radiation shielding UHPC: Advancing ultra-high-performance shielding materials for improved nuclear safety and security, Construction and Building Materials 496 (2015) 143659. https://doi.org/10.1016/j.conbuildmat.2025.143659

[10] ASTM International. ASTM C642-21: Standard Test Method for Density, Absorption, and Voids in Hardened Concrete. West Conshohocken, PA: ASTM International (2021).

[11] P. Smarzewski, A. Stolarski, Properties and Performance of Concrete Materials and Structures, MDPI Books (2022). https://doi.org/10.3390/books978-3-0365-5602-4.

[12] J. Zapała-Sławeta, G. Mazurek, J. Woś, Analysis of the Influence of PET and Glass Packaging Waste Materials on the Physical and Mechanical Properties of Cementitious Composites, Applied Sciences 13 (2023) 12409. https://doi.org/10.3390/app132212409

[13] S. Khasanov, J. Temirov, M. Tashmetov, Bismuth oxide-based lead-free radiation shielding materials: a cross-matrix review, Radiation Physics and Chemistry 248 (2026) 114122. https://doi.org/10.1016/j.radphyschem.2026.114122

[14] J. Xiao, Z. Lv, Z. Duan, C. Zhang, Pore structure characteristics, modulation and its effect on concrete properties: A Review, Construction and Building Materials 397 (2026) 132430. https://doi.org/10.1016/j.conbuildmat.2023.132430

[15] M. Olivia, W.R. Putri, S. Supit, G. Wibisono, P.S. Utama, Compressive Strength and Pororsity of POFA Blended Concrete Admixed with Micro Silica, E3S Web of Conferences 445 (2023) 01034. https://doi.org/10.1051/e3sconf/202344501034

[16] T.K. Bui, T.T. Dat, L.G. Huy, D.Q. Minh, Material and processing design strategies for enhancing gamma-radiation shielding of geopolymer concrete as an emerging shielding material: A review, Radiation Physics and Chemistry 246 (2026) 113937. https://doi.org/10.1016/j.radphyschem.2026.113937

[17] D. Jóźwiak-Niedźwiedzka, M.A. Glinicki, K. Gibas, T. Baran, Alkali-Silica Reactivity of High Density Aggregates for Radiation Shielding Concrete, Materials (Basel, Switzerland) 11 (2018) 2284. https://doi.org/10.3390/ma11112284

[18] M. Alexander, A. Bentur, S. Mindess, Durability of Concrete: Design and Construction, CRC Press, 2017. https://doi.org/10.1201/9781315118413

[19] Z. Zhang, H. Luo, J. Liu, Incorporation of knowledge and data-driven models applied in shield tunneling: A review, Reliability Engineering & System Safety 264 (2025) 111379. https://doi.org/10.1016/j.ress.2025.111379

Materials Research Proceedings 74 (2026) 231-240 https://doi.org/10.21741/9781644904473-29

Polymer Graphene Nanocomposites: A Historical Preliminary Review

Zaid G. MOHAMMADSALIH[1,a *]

[1]Applied Science Research Unit, College of Applied Science, University of Technology, Iraq

[a]Zaid.G.Mohammadsalih@uotechnology.edu.iq

Keywords: Polymer, Graphene, Nanocomposites, Preparation, Properties, Applications

Abstract. The history of polymer composite materials can be traced back to the period of 1930s-1940s with the development of glass fibre reinforced composites. Since then several generations of this technology have evolved, each one marked by increasingly smaller scales of the reinforcement materials. Polymer nanocomposites, PNCs, are the most recent class, which- by virtue of their remarkable thermal and mechanical properties- have attracted worldwide attention. These properties are ascribed to the presence of graphene as a reinforcing agent, which has exceptional thermal conductivity, high electron mobility, and superior mechanical properties. Although the modulus of graphene oxide, GO, is only about 25% of that of a monolayer of graphene, it remains the preferred material for polymer reinforcement. This is due to the abundance of oxygenated functional groups in its basal plane and peripheries, which enables easier coupling interactions between the nanofillers and different polymer matrices. Furthermore, GO is the initial material that can be considered as an introductory stage of graphene production. The structure of the polymer matrix and the low loadings of the nanofillers are the main attributes leading to an improved nanocomposite performance. The purpose of this work is to highlight the challenges associated with the production of scalable amount of graphene, other challenges related to preparation and performance of PNC's, and identifying some gabs of knowledge adhered to this unique class of materials.

Introduction

The concepts that seeded the word of ‘Nanotechnology’ which is tiny in scale but infinitely immense in possibility were first discussed in December 29, 1959 by the renowned physicist Richard Feynman in his talk at the California Institute of Technology entitled ‘’There is plenty of room at the bottom’’ where he discussed the ability to manipulate matter [1]. The term ‘’Nanotechnology’’ represents a revolution in materials science that started over thirty years ago and has expanded the scientific horizons of several fields in engineering, chemistry, and medicine with the development of new technological applications, new materials, and new knowledge on the properties of materials. A new sub-discipline that emerged from these advances in nanotechnology is polymer based matrix nanocomposites PMCs or polymer nanocomposites PNCs that refers to heterogeneous solid materials that are composed from a polymer matrix with nanoscale reinforcements to reinforce that matrix. These nanocomposites can be classified according to the material of the host matrix, and includes metal matrix nanocomposites MMNs, ceramic matrix nanocomposites CMNs, and the aforementioned PMCs. In 2004, two researchers, Andre Geim and Konstantin Novoselov at the University of Manchester conducted some groundbreaking work in which they produced and characterized one atom thick, two dimensional nano material of carbon called graphene, for which they received the Nobel Prize in 2010. Graphene can be identified as a carbon crystal in which the carbon atoms are packed in a hexagonal lattice similar to a honeycomb. This material has unique properties such as high strength, high transparency, a large surface area, good thermal and electrical conductivity as well as excellent electronic properties.

Content from this work may be used under the terms of the Creative Commons Attribution 3.0 license. Any further distribution of this work must maintain attribution to the author(s) and the title of the work, journal citation and DOI. Published under license by Materials Research Forum LLC.

Since its first discovery in 2004, graphene and graphene-based nanocomposites has been the focus of worldwide research in many laboratories in industry and academia, with the aim of harnessing its potential for the myriad applications in which these materials could be used. These applications include flammability resistance, barrier properties, different kinds of sensors (electrochemical sensors, biosensors, etc..), and supercapacitors [2, 3]. However, before the unique benefits of these materials can be realized in practical applications, and compete with existing technologies, several challenges need to be met. The most important of these is in developing bulk production techniques for graphene. Several approaches to meet this challenge, amongst them is graphene reflux adopted by some collaborators [4] at Texas A&M University, USA. A second challenge is in finding the best polymer material that can be used in practical applications, and the research described in this thesis focusses on this challenge in PNCs. The research on PNCs has been aimed at finding ways of incorporating graphene into various polymer matrices such as nylon-6, polypropylene PP, and different epoxies and polyesters [2]. However, as pristine graphene has a poor dispersion in polymers, alternative forms of modified graphene have been explored such as graphene oxide GO as these are easier to disperse. The extensive oxidation of graphite results in graphite oxide, which has different oxygenated functionalities in the basal plane and peripheries and this offers an indirect route to creating GO. This is achieved by using sonication as part of the processing [5, 6]. Nanocomposites refer to ultrafine phase dimension fillers reinforcing many types of matrices [7]. Amongst these is the polymer matrix and polymer nanocomposites PNCs can be defined as including filling agents that have at least one dimension at the nano-scale in the polymer matrix. The reinforcements may be one dimensional such as nano-fibers or carbon nano tubes CNTs, two-dimensional 2D additives such as graphene sheets, or 3-dimensional 3D additives such as spherical particles [8]. The nano-scale covers the range of (1-100) nano-meters (nm) (1.0 nm = 10^{-9} m) for the size of the incorporated fillers in the matrix [9]. Some co-authors [8] reported that the earliest study on nanocomposites was in 1950 when the effect of exfoliated layered silicate was studied on latex based elastomers. However, significant industrial and academic interest in nanocomposites began with the work of Japanese researchers [10] who were based at the Toyota central research and development laboratories in Japan. They highlighted and explained the considerable mechanical improvement obtained by reinforcing Nylon-6 with a type of clay known as montmorillonite MMT with which they successfully prepared a polymer clay nanocomposite. The property enhancement of PNCs can be achieved by incorporating low loadings of nanofillers in the matrix (typically at a 1-10 % volume fraction) which contribute to weight reduction facilitation of the processing [11]. A research group [12] described the improvement in (Young's modulus and tensile strength) for epoxy reinforced with 0.1 wt. % of graphene. Two other reinforcements along with graphene platelets were investigated, namely single walled carbon nanotube SWCNT and multi walled carbon nanotube MWCNT and the results showed that epoxy reinforced with graphene nano-platelets GNPs performed considerably better than epoxy reinforced with SWCNT and MWCNT in terms of enhancing a variety of mechanical properties including Young's modulus, tensile strength, fracture energy, fracture toughness and resistance to fatigue crack growth. For example, Young's modulus and tensile strength for the epoxy reinforced with 0.1 wt. % of GNPs were improved by (31and 40) % respectively compared to same weight fraction of SWCNT that reinforced the same polymer as the improvement showed (3 and 14) % only. PNCs are important because they offer a range of promising applications in the automotive, aerospace, marine, military and building industries, see table 1 [13, 14, 9]. A research group [15] demonstrated an efficient anti-corrosion application for PS reinforced with 2.0 wt.% modified GO. Another potential application as a membrane (gas barrier) was reported by another research group [16] based on a polysulfone PSF matrix with very low loadings of GO (0.25, 0.5 and 1.0) wt.%.

In spite of the impressive potential for PNCs, there are many challenges that need to be solved before these applications can represent viable alternatives to existing technologies. The main challenges include: (1) the preparation of homogenous polymer nanocomposites represents a major challenge in the field. For example, fabricating a homogenous dispersion of NPs or nanofillers in the matrix is a significant challenge in its own right [17]; (2) the addition of nanofillers to the matrix, for example clay, lead to improve the Young's modulus as well as the strength. The study published by a research group [18] supported the aforementioned approach. In some cases, the opposite might happen and this is another challenge needs to be investigated. Another research group [19] showed that the addition of 3.2% of MMT to SAN led to decrease in the values of strength and strain at break compared to the neat polymer; (3) the interfacial adhesion between the matrix and nanofillers. This is a significant gap in the field of PNCs because there are no specific techniques measuring the degree of adhesion of the nanofillers to the polymer matrices [9]; and (4) the property- morphology correlation in PNCs refer to any possible change in mechanical, thermal and electrical properties generated from the change in morphology of polymer associated with the addition of the nanofillers. The understanding of this correlation is still in its early stages though some progress that has been recently achieved. This requires a comprehensive understanding of the interface properties, the nanofillers distribution, and identification of correlations between the nanofillers and nanofillers-matrix interactions and the way they influence the various properties of the fabricated material [11].

Table 1. Commercial applications for some of PNCs [9].

Polymer matrix	Nano-Particle	Property improvement	Application	Company
PA 6	Exfoliated clay	Stiffness	Timing belt cover, automotive	Toyota / Ube
TPO (Thermoplastic Polyolefin)	Exfoliated clay	Stiffness / Strength	Exterior step assist	General motors
Epoxy	CNT	Strength / stiffness	Tennis rackets	Babolat
Polyisobutylene PBI	Exfoliated clay	Permeability barrier	Tennis balls, tyres, soccer balls	InMalt LLC
SBR rubber	Not disclosed	Improved tyre performance I winter	Winter tires	Pirelli

The novelty of this work is emphasizing the substantial improvement of physical performance of polymer matrices by incorporating low loadings of graphene. On the other hand, highlighting the importance of this topic, explaining its main classifications, and the most significant challenges (gabs of knowledge) can be considered as the main objectives of the work.

Preparation of graphene and Graphene Oxide

Graphene can be prepared according to two general approaches: (1) the TOP-DOWN approach, which involves a decomposition of bulk materials, such as CNT and graphite, to a graphene nano-structure; and (2) the BOTTOM-UP approach, which refers to synthesizing graphene using hydrocarbon gases. Both approaches entail a number of physical and chemical methods [20].

The five most important of these are listed below [21]: (1) mechanical exfoliation of a single sheet of graphene from bulk graphite by applying Scotch tape over a silicon substrate and then removing it. This approach is regarded as an inefficient with a low yield of a single layer sheet of graphene having acceptable quality. Nevertheless, it was the first successful method for producing a single layer or few layers of graphene; (2) epitaxial growth of graphene films on a silicon carbide substrate SiC which is a promising method for obtaining a uniform wafer size of graphene layers. The single crystal of SiC is heated up to 1400 oC in vacuum and graphene is growing epitaxially

on the substrate. A research group [22] used this method and achieved a large area of homogenously stacked bilayer epitaxial graphene SiC (0001) substrate; (3) chemical vapour deposition CVD of the graphene monolayer. Transition metal surfaces are employed in this technique with the assistance of hydrocarbon gases. The deposition temperature is 1000 ºC, and some co-authors [23] used a copper substrate with a flow of H_2 and CH_4 and controllably synthesized 1 and 7 layers of graphene; (4) longitudinal unzipping of CNT describes several methods in which a large-scale production of graphene nanoribbons GNRs is produced with a controllable width. Two unzipping methods include oxidative treatment of CNTs and plasma etching with nanoparticles of transition metals (Co or Ni) and high burning current. These techniques have been effectively developed in order to efficiently unzip CNTs to produce GNRs that have applications in electron devices. A research group [24] demonstrated the unzipping of CNTs to ultra-narrow GNRs with smoother edges upon oxidation; and (5) the reduction of GO where the oxidative exfoliation of graphite took place followed by thermal or chemical reduction. Low-cost graphene with relatively large-scale production can be achieved using this method with potential for applications in photovoltaic cells and electrochemical devices.

Graphene is a flat 2D sheet of carbon atoms with a Van der Waals thickness of 0.34 nm. A CNT on the other hand is a rolled-up monolayer of carbon atoms. Graphene has a high thermal and electrical conductivity of (5.1×10^{3}) W m^{-1} K^{-1}, and (6×10^{5}) S m^{-1}; respectively. The width of graphene sheets is dependent on the method of production and can be from a few nano-meters to many centimeters [20, 25]. The structure of graphene is still a subject of discussion because; in one respect, it appears as a 2D material with high crystal quality, which enables the electrons to travel for some distance (submicron) without scattering. Some theories and experiments however show that perfect 2D crystals cannot be found in the Free State.

On the other hand, the graphene structure studies so far are an integral part of a 3D structure, either embedded in a 3D matrix or supported by a bulk substrate [26]. GO is a relatively new nanoscale material that can provide an alternative path to the production of graphene. The structure of GO can be simplistically described as different oxygenated functionalities surrounded the graphene sheet. These oxygenated functionalities are carboxylic (__COOH) and carbonyls in the periphery of the graphene sheet.

The hydroxyls (-OH) and epoxies are located in the basal plane, and the thickness of a monolayer sheet of GO is about (1.0-1.4) nm. This is thicker than a monolayer of graphene due to the oxygenated functionalities in the periphery and basal plane of the GO nano-sheet and, adsorbed molecules and water - trapped molecules due to the hydrophilic nature of GO [27, 28].

Properties of graphene, Graphene Oxide, and reduced Graphene Oxide

Table 2 shows the most important characteristics of the carbonaceous derivatives of graphene, GO, and rGO [29].

Polymer graphene/Graphene Oxide nanocomposites

The impressive properties of graphene paved the way for researchers to prepare, characterize, and investigate its properties and possible applications for PGNs. One specific area of interest with regard to graphene is its incorporation into different polymers in order to gain mechanical, thermal, thermos-mechanical, and electrical enhancements and this has been achieved at very low loadings of graphene, GO and its reduced form [30, 31]. A research group [32] confirmed that adding only 1.0 wt. % of GO to polyethylene oxide PEO led to a 260% improvement in thermo-mechanical stability for the polymer that was used in lithium-ion battery applications. This result was achieved according to the superior properties of GO and the strong interfacial interaction between GO and the surrounding PEO.

Table 2. Some properties of graphene, GO and rGO [29].

Property	Single layer graphene	GO	rGO
Young's modulus	1000 GPa	220 GPa	Not available
Fracture strength	130 GPa	120 MPa	Not available
Optical transmittance	97.7%	Not available (expected has a lower value due to defects in the functional groups	60-90% depending on the agent of reduction and fabrication method
Room temperature mobility	~ 200.000 $cm^2 V^{-1} S^{-1}$	Not available (expected to be a lower value due to disruption in mobility)	Not available (due to less defects it is expected to be intermediate)
Thermal conductivity	~ 5000 W/m K	2000 W/m K for pure	0.14-0.87 W/m K
Electrical conductivity	10^4 S/cm	10^{-1} S/cm	200-35.000 S/cm
Charge carrier concentration	1.4* 10^{13} cm^{-2}	Not available (expected to be lower due to defects in functional groups)	Not available

Another reported study [33] concluded that the toughness increased by 50% for polyurethane, which is commonly used in diverse industrial applications such as automotive, by adding 1.0 wt. % of GO without losing elasticity. In order to make a stable suspension, it is important to have a good understanding of the solubility parameters of the various solvents. To this end, Hansen solubility parameters are used to investigate the dispersion mechanism in the organic solvents for GO and rGO. Pristine graphene is aggregated according to the intrinsic Van der Waals force. This represents a real challenge to exfoliation, and for the incorporation of pristine graphene in polymer matrices with a homogenous dispersion. A research group [34] described different types of interaction between the polymer matrix and graphene. These interactions can be covalent functionalization, non-covalent functionalization such as Π-Π interactions, electrostatic interactions, or polymer blending. Non-covalent interactions consolidate the attachment of organic molecules on the surface of graphene. Π-Π stacking, electrostatic or hydrophobic interactions are techniques for non-covalent interactions of polymers and surfactants with graphene surfaces. Beneficial modifications to graphene's surfaces can be achieved by adopting the non-covalent interactions and this will consequently help facilitate the preparation of PGNs. However, the functionalization of graphene in polymer matrices is in its infancy, and significant efforts are required to improve the present strategies and to find novel ones for promoting the utility of PGNs from the laboratory curiosities to practical components that have various technological applications. Most importantly, the toughest challenge with these new materials is in achieving a comprehensive understanding the surrounding interphase (The intermediate region between two or more materials in equilibrium, which will joint to form the nanocomposite). The characteristics of the interphase region, the reliance of this vital region on graphene's surface chemistry, and the apparent arrangement of the constituents and their relationship to different properties of PGNs are also challenges submerged within the over-arching challenge of engineering the interphase. There is a vigorous competitive scientific endeavor in various disciplines of materials science, chemistry, and materials engineering to meet these challenges, and to successfully prepare advanced graphene based nanocomposites [35].

Preparation of Polymer Graphene Nanocomposites

There are a number of factors playing a crucial role in the preparation of PGNs. These include the molecular weight, the polarity, reactive groups, and hydrophobicity. The most widely applied methods for preparing polymer graphene/GO nanocomposites are: in-situ polymerization, melt

compounding and solution mixing or solution blending [36]. In-situ polymerization, melt compounding, and solution blending are the most prominent methods employed to prepare PGN's. Table 3 shows the benefits and drawbacks for these methods [37]. Solution mixing is employed pervasively although a huge number of organic solvents used for this approach. According to a personal perspective, Tetrahydrofuran (THF) was used as a co-solvent to obtain a suspension of GO of different concentrations together with a polymeric solution obtained from the dissolving of PS pellets. It was an efficient approach for preparing polymer graphene nanocomposites films in spite of the remaining traces of the solvent within the structure of the prepared material. It is highly recommended to use water as a non-toxic agent for preparing stable suspensions of nanomaterials. The extensive employment of organic solvents has detrimental influences on the heuristic environment of laboratories as well as the general health of the researchers who are working in these laboratories [38].

Table 3. Scale, advantages and disadvantages of PNCs preparation methods [37].

Preparation method	Scale	Advantages	Disadvantages
In-situ polymerization	Bulk	Highly effective, high level dispersion	Loss of polymerization rate at later stage
Melt compounding	Mass production	Eco-friendly, cost effective	Poor dispersion of nanoparticles
Solution mixing	Bulk	Versatile, good dispersion	Extensive use of organic solvents

In-situ polymerization is a common way for synthesizing polymer graphene /GO nanocomposites and the result is a uniformly dispersed graphene/GO in the polymer matrices. In this method, the graphene or its precursors and the monomer are dissolved using a co-solvent and then ultra-sonicated to obtain a uniform dispersion. Next, an initiator such as metallocene catalyst solution is added to the mixture to form the polymer. In-situ polymerization has a number of benefits such as simplicity, scalability, ease of manipulation, low cost, and lower environmental concerns. Melt compounding refers to the direct inclusion in the graphene or any of its precursors of the melted polymer matrices by using a twin-screw extruder. The key variables of the screw that need to be optimized are time to complete the operation, the temperature, and the speed. The major drawback with this method is the poor dispersion of graphene sheets in polymer matrices, and this has a negative impact on the mechanical properties. Another drawback is the low bulk density of the thermally exfoliated graphene. Solution mixing has the appeal of simplicity and its proven capability for achieving a homogenous dispersion of graphene or GO in casted-polymer films. In this method, graphene is dispersed in a solvent via sonication, which is the act of applying sound energy to agitate particles in a sample. Then, the suspension is added to the polymer solution obtained from dissolving polymer pellets in the same solvent. The solution is then evaporated at ambient or an elevated temperature. For a rapid solvent evaporation, a highly volatile co-solvent should be carefully selected. However, there is a significant challenge with this method in terms of the removal of the organic solvent from the obtained nanocomposites. Any remaining traces of the organic solvents have detrimental effects on the mechanical, electrical and thermal properties of the nanocomposites [36, 37]. To sum up, polymer graphene nanocomposites have become very popular and common in our daily lives. They made an upheaval revolution for various industries and applications. These unique materials have paved the way towards the improvement of functional items as well as tackling urgent environmental concerns [39].

Summary

PGN's are unique class of materials due to their low cost, easiness of processibility, and their inclusiveness for wide range of applications. Beside graphene and its counterparts, many kinds of nano-scale reinforcements can be embedded in different polymer matrices in order to improve the

overall mechanical, thermal, and the overall performance of these materials that can be prepared using different protocols. Incorporating fillers into a matrix however is not without its challenges and these are listed below: (1) for a modest enhancement in polymer properties, a high loading (high weight or volume fraction) is required for traditional fillers, which are mostly have a micron size; (2) the high density of traditional fillers represents a trade-off for achieving lightweight composites; and (3) the poor interfacial interaction between traditional fillers and the matrix leads to poor interfacial adhesion between the different components of the composite material and this can lead to failure. One of the challenges for the production of graphite oxide is the ethical requirement to develop a preparation technique that is Eco-friendly or green approach. The chemical components used to prepare graphite oxide are highly reactive and hazardous materials and some of them are explosive materials or highly toxic. In addition, there are so many gaps of knowledge associated with reduction of GO as rGO is considered as an efficient reinforcing agent. Some of these are listed below: (1) the extent of the elimination of functional groups is still uncertain and it is not certain that the entire elimination of GO functional groups is achievable; (2) the restoration of lattice defects that were formed during oxidation is another area of uncertainty. In other words, reduction of GO is a process that aims to produce a graphene-like material similar to pristine graphene. However, significant efforts have been done to achieve this target, but it is still a dream. Defects in the lattice, which are intimately associated with oxidation process, are altering the structure and the extent of restoration or healing of these defects through reduction process is still uncertain; and (3) there is no clear measure of the defect density of graphene sheets, and whether it is increased or decreased with the reduction process. These gaps of knowledge are required to be filled through more detailed experimental investigations and characterization complement by better computer models of these materials. In most cases, computer simulations are used to elucidate the obvious chemical mechanisms as no direct observations of the reduction process have been developed. The current targeted objectives related to this topic, and investigated by different counterparts around the globe are how to prepare GO using an eco-friendly approach without using extensive hazardous oxidants, green reduction of GO in order to obtain graphene without structural defects, and the efficient employment of other carbonaceous derivatives to prepared PGN's such as fullerenes, nanotubes, and clays. The professional employment of these nano-additives to prepare PGN's would pave the way towards manufacturing promising applications related to medical sector, infrastructure, and daily life applications.

Acknowledgments

Zaid G. Mohammadsalih would like to acknowledge Dr. Ahmad Ilyas Rushdan, the senior lecturer at Faculty of Chemical and Energy Engineering- Universiti Teknologi Mara (UTM) - Johor Bahru, and his respected colleagues for their kind support to publish this work, and for their valuable guidance that made the contribution in the annual conference of the Faculty possible and effective.

References

[1] Earl and Nancy Boysen, Nanotechnology for dummies 2nd ed.,USA: Wiley Publishing, Inc.2011

[2] J. Silvestre, N. Silvestre, J. De Brito, Polymer nanocomposites for structural applications: Recent trends and new perspectives, Mech. Adv. Mater. Struct. 23 (2015) 1263-1277. https://doi.org/10.1080/15376494.2015.1068406

[3] J. Xu, Y. Wang, S. Hu, Nanocomposites of graphene and graphene oxides: synthesis, molecular functionalization and application in electrochemical sensors and biosensors. A review, Microchim. Acta 184 (2017) 1-44. https://doi.org/10.1007/s00604-016-2007-0

[4] K.S. Rountree, S.A. Shah, C.B. Sweeney, F. Irin, M.J. Green, Graphene reflux: improving the yield of liquid-exfoliated nanosheets through repeated separation techniques, Nanotech. 27 (2016) 505601. https://doi.org/10.1088/0957-4484/27/50/505601

[5] R. Shah, A. Kausar, B. Muhammad, S. Shah, Progression from graphene and graphene oxide to high performance polymer-based nanocomposite: a review, Polym-Plast Technol Eng. 54 (2015) 173-183. https://doi.org/10.1080/03602559.2014.955202

[6] K.P. Loh, Q. Bao, P.K. Ang, J. Yang, The chemistry of graphene, J. Mater. Chem. 20 (2010) 2277-2289. https://doi.org/10.1039/B920539J

[7] E.P. Giannelis, Polymer layered silicate nanocomposites, Adv. Mater. 8 (1996) 29-35. https://doi.org/10.1002/adma.19960080104

[8] H.J. Salavagione, G. Martínez, G. Ellis, Graphene-based polymer nanocomposites, Physics and applications of graphene—experiments (2011) 169-192

[9] D.R. Paul, L.M. Robeson, Polymer Nanotechnology: nanocomposites, Polym. 49 (2008) 3187-3204. https://doi.org/10.1016/j.polymer.2008.04.017

[10] A. Okada, A. Usuki, The chemistry of polymer-clay hybrids, Mater Sci Eng: C 3 (1995) 109-115. https://doi.org/10.1016/0928-4931(95)00110-7

[11] R.A. Vaia, J.F. Maguire, Polymer nanocomposites with prescribed morphology: going beyond nanoparticle-filled polymers, Chem Mater. 19 (2007) 2736-2751. https://doi.org/10.1021/cm062693+

[12] J. Reif, J. Rafiee, Z. Wang, H. Song, Z.Z. Yu, N. Koratkar, Enhanced mechanical properties of nanocomposites at low graphene content, ACS nano 3 (2009) 3884-3890. https://doi.org/10.1021/nn9010472

[13] J.K. Pandey, K.R. Reddy, A.P. Kumar, R.P. Singh, An overview on the degradability of polymer nanocomposites, Polym. Degrad. Stab. 88 (2005) 234-250. https://doi.org/10.1016/j.polymdegradstab.2004.09.013

[14] Q.H. Zeng, A.B. Yu, G.Q. Lu, Multiscale modeling and simulation of polymer nanocomposites, Progress in polymer science 33 (2008) 191-269. 10.1016/j.progpolymsci.2007.09.002

[15] Y.H. Yu, Y.Y. Lin, C.H. Lin, C.C. Chan, Y.C. Huang, High-performance polystyrene/graphene-based nanocomposites with excellent anti-corrosion properties, Polym. Chem. 5 (2014) 535-550. https://doi.org/10.1039/C3PY00825H

[16] M. Ionita, A.M. Pandele, L. Crica, L. Pilan, Improving the thermal and mechanical properties of polysulfone by incorporation of graphene oxide, Compos. B: Eng. 59 (2014) 133-139. https://doi.org/10.1016/j.compositesb.2013.11.018

[17] S.C. Tjong, Structural and mechanical properties of polymer nanocomposites, Mater. Sci. Eng.: R: Rep. 53 (2006) 173-197. https://doi.org/10.1016/j.mser.2006.06.001

[18] T.D. Fornes, P.J. Yoon, H. Keskkula, D.R. Paul, Nylon 6 nanocomposites: the effect of matrix molecular weight, Polym. 42 (2001) 09929-09940. https://doi.org/10.1016/S0032-3861(01)00552-3

[19] H.A. Stretz, D.R. Paul, P.E. Cassidy, Poly (styrene-co-acrylonitrile)/montmorillonite organoclay mixtures: a model system for ABS nanocomposites, Polym. 46 (2005) 3818-3830. https:/doi.org/10.1016/j.polymer.2005.03.043

[20] M. Pumera, Graphene-based nanomaterials and their electrochemistry, Chem. Soc. Rev. 39 (2010) 4146-4157. https://doi.org/10.1039/C002690P

[21] S. Guo, S. Dong, Graphene nanosheet: synthesis, molecular engineering, thin film, hybrids, and energy and analytical applications, Chem. Soc. Rev. 40 (2011) 2644-2672. https://doi.org/10.1039/C0CS00079E

[22] P. Dharmaraj, K. Jeganathan, S. Parthiban, J.Y. Kwon, S. Gautam, K.H. Chae, K. Asokan, Selective area growth of Bernal bilayer epitaxial graphene on 4H-SiC (0001) substrate by electron-beam irradiation, Appl. Phys. Lett. 105 (2014). https://doi.org/10.1063/1.4901074

[23] Z. Tu, Z. Liu, Y. Li, F.Yang, L. Zhang, Z. Zhao, C. Xu, S. Wu, H. Liu, H. Yang, P. Richard, Controllable growth of 1–7 layers of graphene by chemical vapour deposition, Carbon 73 (2014) 252-258. https://doi.org/10.1016/j.carbon.2014.02.061

[24] C. Chen, W. Kong, H. Duan, J. Zhang, Theoretical simulation of the reduction of graphene oxide by lithium naphthalenide, Phys. Chem. 17 (2015) 13654-13658. https://doi.org/10.1039/C5CP00357A

[25] X. Sun, H. Sun, H. Li, H. Peng, Developing polymer composite materials: carbon nanotubes or graphene?, Adv. Mater. 25 (2013) 5153-5176. https://doi.org/10.1002/adma.201301926

[26] J.C. Meyer, A.K. Geim, M.I. Katsnelson, K.S. Novoselov, T.J. Booth, S. Roth, The structure of suspended graphene sheets, Nature 446 (2007) 60-63. https://doi.org/10.1038/nature05545

[27] K.A. Mkhoyan, A.W. Contryman, J. Silcox, D.A. Stewart, G. Eda, C. Mattevi, S. Miller, M. Chhowalla, Atomic and electronic structure of graphene-oxide, Nano lett. 9 (2009) 1058-1063. https://doi.org/10.1021/nl8034256

[28] Y. Si, E.T. Samulski, Synthesis of water soluble graphene, Nano lett. 8 (2008) 1679-1682. https://doi.org/10.1021/nl080604h

[29] G. Mittal, V. Dhand, K.Y. Rhee, S.J. Park, W.R. Lee, A review on carbon nanotubes and graphene as fillers in reinforced polymer nanocomposites, J. Ind. Eng. Chem. 21 (2015) 11-25. https://doi.org/10.1016/j.jiec.2014.03.022

[30] T. Kuila, A.K. Mishra, P. Khanra, N.H. Kim, J.H. Lee, Recent advances in the efficient reduction of graphene oxide and its application as energy storage electrode materials, Nanoscale 5 (2013) 52-71. https://doi.org/10.1039/C2NR32703A

[31] R.J. Young, I.A. Kinloch, L. Gong, K.S. Novoselov, The mechanics of graphene nanocomposites: A review, Compos. Sci. Technol. 72 (2012) 1459-1476. https://doi.org/10.1016/j.compscitech.2012.05.005

[32] M. Yuan, J. Erdman, C. Tang, H. Ardebili, High performance solid polymer electrolyte with graphene oxide nanosheets, RSC. Adv. 4 (2014) 59637-59642. https://doi.org/10.1039/C4RA07919A

[33] D. Cai, J. Jin, K. Yusoh, R. Rafiq, M. Song, High performance polyurethane/functionalized graphene nanocomposites with improved mechanical and thermal properties, Compos. Sci. Technol. 72 (2012) 702-707. https://doi.org/10.1016/j.compscitech.2012.01.020

[34] M. Terrones, O. Martín, M. González, J. Pozuelo, B. Serrano, J.C. Cabanelas, S.M. Vega-Díaz, J. Baselga, Interphases in graphene polymer-based nanocomposites: achievements and challenges, Adv. Mater. 23 (2011) 5302-5310. https://doi.org/10.1002/adma.201102036

[35] H. Chang, H. Wu, Graphene-based nanocomposites: preparation, functionalization, and energy and environmental applications, Energy Environ. Sci. 6 (2013) 3483-3507. https://doi.org/10.1039/C3EE42518E

[36] T.K. Das, S. Prusty, Graphene-based polymer composites and their applications, Polym-Plast. Technol. Eng. 52 (2013) 319-331. https://doi.org/10.1080/03602559.2012.751410

[37] L. Androvič, J. Bartáček, M. Sedlák, Recent advances in the synthesis and applications of azo initiators, Res. Chem. Intermed. 42 (2016) 5133-5145. https://doi.org/10.1007/s11164-015-2351-4

[38] Z.G. Mohammadsalih, B.J. Inkson, B. Chen, The effect of dispersion condition on the structure and properties of polystyrene/graphene oxide nanocomposites, Polym. Compos. 42 (2021) 320-328. https://doi.org/10.1002/pc.25827

[39] S.M. Sapuan, V.U. Siddiqui, Z.G. Mohammadsalih, Nanocomposites: Preparation, Characterization and Applications, Royal Society of Chemistry, 2026.

Materials Research Proceedings 74 (2026) 241-248 https://doi.org/10.21741/9781644904473-30

Cadmium Oxide Nanostructures Prepared by Oblique Angle Physical Vapour Deposition

Wafaa K. KHALEF[1,a *], Nibras S. HAMEED[2,b], Raghad H. HILAL[1,c], Rafah A. NASSIF[1,d], Dhufigar S. MUTASHAR[1,e], Zinah S. SHAKIR[1,f] and Sura R. MOHAMMED[3,g]

[1]Applied Science Research Unit, Applied Science College - University of Technology- Baghdad-Iraq

[2]Ministry of Higher Education and Scientific Research, Baghdad, Iraq

[3]Ministry of Science and Technology, Iraq

[a]drwafaa1980@gmail.com, [b]nibras.alabayachy@gmail.com, [c]Raghad.H.Hilal@uotechnology.edu.iq, [d]Rafah.A.Nasif@uotechnology.edu.iq, [e]dhulfiqar.s.mutashar@uotechnology.edu.iq, [f]zinah.s.shakir@uotechnology.edu.iq, [g]suraraad98@yahoo.com

Keywords: Oblique Deposition, Cadmium Oxide Nanostructure CdO, Oblique Angle Deposition (OAD) Technique

Abstract. Nanostructures of cadmium oxide (CdO) were deposited on silicon and quartz substrates using oblique angle deposition (OAD). High-purity cadmium was thermally evaporated at incidence angles of 0°, 50° and 70°, and the as-deposited films were oxidized in a typical furnace at 573 K for 1.5 h. X-ray diffraction revealed a polycrystalline cubic CdO phase with a (111) preferred orientation that sharpened and increased in intensity as the angle increased. The (200) and (222) reflections under normal incidence disappeared at 70°, and an almost single-orientation texture emerged. The self-shadowed columnar growth first refines the (111) crystallites at moderate obliquity before coarsening at the highest angle: the grain size varies non-monotonically from 49.71 nm at 0° to 44.48 nm at 50° and 57.51 nm at 70°, the full width at half maximum follows the corresponding inverse trend (0.174° to 0.195° to 0.151°), the lattice constant decreases from 4.662 Å to 4.646 Å and the microstrain increases monotonically while remaining tensile throughout, from 0.57% at 0° to 0.90% at 70°. About the optical properties, the films demonstrated high transmittance in the visible-near-infrared region (approximately 75% at 0°). The roughening of the surface resulted in a decrease to roughly 70% at 70°, whereas the direct permissible optical band gap increased with the angle (from 2.4 eV at 0° to 2.5 eV at 50° and 2.6 eV at 70°). Rectifying behaviour was evidently noticed from the current–voltage measurements of Al/CdO/p-Si/Al heterojunctions. The dark current was found to decrease with deposition angle, but the reverse photocurrent under illumination was found to be much larger for the oblique device in comparison to the conventionally deposited one, indicating that OAD-grown CdO can be a potential absorber for silicon-based photodetectors.

Introduction

Cadmium oxide (CdO) is an n-type semiconductor with a rock-salt cubic structure. Its low electrical resistivity and great visible and near-infrared transparency make it ideal for transparent conducting electrodes, gas sensors, solar cells, and photodetectors [1–3]. Because stoichiometry and microstructure can substantially alter carrier concentration and optical band gap, CdO film growth is as critical as the material [4,5]. CdO nanostructures can be synthesized using the sol–gel technique [6], chemical vapour deposition (CVD) [7], hydrothermal and solvothermal synthesis [8], template-assisted growth [9], and physical vapour deposition (PVD) [10,11], each with

Content from this work may be used under the terms of the Creative Commons Attribution 3.0 license. Any further distribution of this work must maintain attribution to the author(s) and the title of the work, journal citation and DOI. Published under license by Materials Research Forum LLC.

different control, cost, and scalability implications. In PVD, atoms are delivered to the substrate in a vacuum to precisely control deposition geometry, film thickness, crystallinity, and shape [5]. PVD outperforms wet-chemical and gas-phase methods. Unlike the sol-gel process, it does not require precursor chemistry, solvent or post-deposition organic combustion, and it yields clean films. It operates at near-ambient temperatures, nucleates faster than hydrothermal synthesis, and ensures uniform thickness over large areas while avoiding the high substrate temperatures and toxic metal-organic precursors of CVD. PVD with an oblique vapour incidence, known as oblique angle deposition (OAD), produces tilted columnar nanostructures using atomic self-shadowing. The incidence angle directly controls porosity, surface area, and texture in these structures, a unique morphological control impossible by any other method in one step [12,13]. These findings are contextualized by previous system studies. Khalef and Ibrahim observed that evaporating cadmium at 0°, 50°, and 70° produced polycrystalline films with a preferential (002) orientation and increased grain size and faceting as the deposition angle increased [11]. A further study oxidized comparable films at 500°C and found a (111)-dominant CdO microstructure, a band gap increase from 4.2 to 4.9 eV between normal and oblique deposition, and a lower dark current at higher angles [10]. Cadmium obliquely put over quartz and oxidized at 773 K had a constant band gap, refractive index, dielectric function, and extinction coefficient that altered with incidence [1]. Oblique-deposited chevron- and columnar-TiO_2 photodetectors on p-Si are UV-sensitive with 3.31 eV band gaps. CdO photodetectors made by laser ablation are wideband. Pulsed laser deposition of CdTe/Si heterojunctions is worse than sheets [14,15]. In 2025, columnar form affected spectrum absorption, reflection, and transmission in OAD photodetectors [16,17]. This study linked device responsiveness to the organic additive deposition (OAD) angle for both a single material and a heterojunction. Oxidation took 1.5 h at 573 K for incidence angles of 0°, 50°, and 70°. Columnar shadowing structural refinement affects optical band gap, dark current, and photocurrent in Al/CdO/p-Si/Al heterojunctions made from films with different FWHM, lattice constant, and microstrain. This paper reports simply the deposition angle as a tuning knob for a CdO photodetector, not structure, optics, or electrical performance.

Materials and Methods

Cadmium thin films were deposited on glass and quartz substrates via thermal evaporation using a Thermionic Laboratory Inc. (Germany) coating unit at incidence angles of 0°, 50°, and 70°. High-purity cadmium was placed in a tungsten boat and evaporated at a base pressure of 7×10^{-5} Torr, with the source-to-substrate distance set to 15 cm for each run to ensure homogeneous film deposition across the substrate. The substrates (2×2 cm²) were subjected to ultrasonic cleaning for 15 minutes (Transistor/UL T-7) in acetone and ethanol, subsequently rinsed in deionized water, and dried under a nitrogen stream. Following deposition, each sample was converted to cadmium oxide by annealing in a KSL-1100X furnace at 300°C (573 K) for 1.5 hours under atmospheric conditions. Structural parameters were recovered from the X-ray diffraction patterns: the average grain size (D) of the polycrystalline CdO films was determined from the full width at half maximum (FWHM) of the most intense peaks using the Scherrer equation, Eq. 1 [18,19].

$$\boldsymbol{D = \frac{A\,\lambda}{\beta \cos\theta}} \tag{1}$$

Formula: β = integral XRD peak breadth at θ diffraction angle, λ = X-ray wavelength, and A = form factor (0.94) determined by crystallite morphology. Microstrain (δ), the lattice strain during film growth, was calculated using Eq. 2 to compare measured spacing to the standard value [18].

$$\boldsymbol{\delta = \frac{|a_{ASTM} - a_{XRD}|}{a_{ASTM}}} \tag{2}$$

where a is the lattice constant. The interplanar spacing d was found from the Bragg condition, Eq. 3, in which n is a positive integer, λ the X-ray wavelength, and θ the diffraction angle; the lattice

constant a of the cubic CdO phase then followed from the plane spacings and Miller indices (h, k, l) through Eq. 4 [15,18].

$$n\lambda = 2d\sin\theta \tag{3}$$

$$a = d\sqrt{(h^2 \times k^2 \times l^2)} \tag{4}$$

The texture coefficient Tc, which quantifies the strength of the preferred orientation, was calculated from the measured and reference intensities using Eq. 5 [18].

$$T_{c\,(h,k,l)} = \frac{I\,(h,k,l)/I_{\circ}\,(h,k,l)}{N_r^{-1}\,\Sigma\, I(h,k,l)/\,I_{\circ}(h,k,l)} \tag{5}$$

I represents the measured intensity, I_0 the ASTM reference intensity, Nr the reflection count, and (h, k, l) the Miller indices. Eq. 6 yielded the number of deposited layers, NL, as film thickness divided by mean grain size [20].

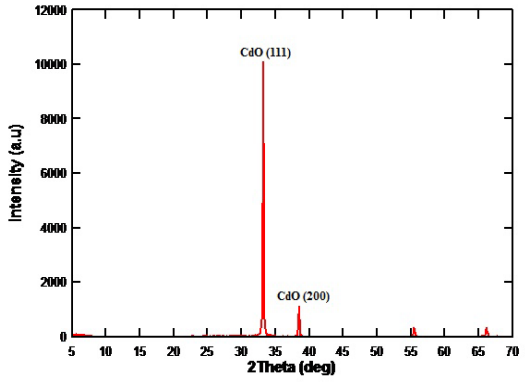
$$N_l = \frac{t}{G.S} \tag{6}$$

where t is the film thickness, and G.S is the average grain size.

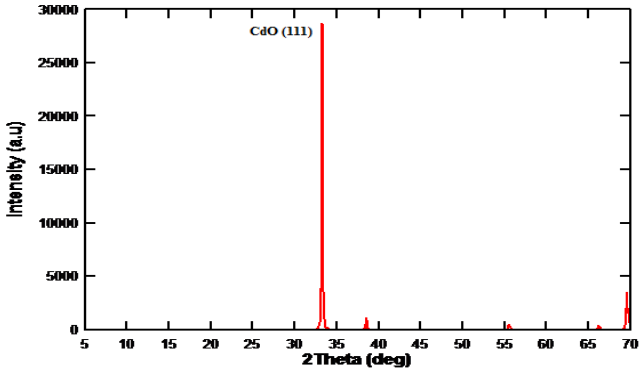
Result and Discussion

XDR Analysis

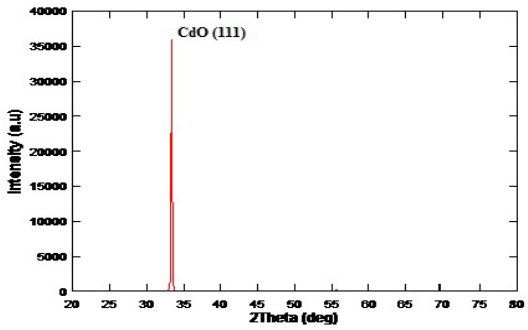
Fig.1 depicts the XRD patterns of CdO films that were deposited at 0°, 50°, and 70° and then oxidized at 573 K. Each film is composed of polycrystalline cubic CdO, yet the pattern varies dramatically with angle. With a normal incidence, as shown in Fig. 1(a), the (111) peak, which is located close to 2θ = 33°, is the most prominent. The weaker (200) and (222) reflections are located at roughly 38° and 69°, respectively. As the angle increases (as shown in Figs. 1(b) and 1(c), the (111) peak becomes more concentrated and narrows, while the secondary reflections become less noticeable. This results in the 70° film being essentially single-oriented along the (111) direction. This sharpening arises from the OAD geometry: at oblique incidence, the incident flux is intercepted by the tallest nuclei, and the resulting self-shadowing drives growth into slanted columns aligned with the low-energy (111) direction, thereby reducing competing orientations [21,22]. It has been determined that the peak positions agree with the reference data for cubic CdO (JCPDF 05-0640) [23].



(a)



(b)



(c)

Fig. 1. XRD patterns of CdO thin films oxidized at 573 K for 1.5 h: (a) normal deposition (0°), (b) oblique deposition 0at 50°, and (c) oblique deposition at 70°.

Table 1. XRD-derived structural parameters of CdO nanostructures deposited at 0°, 50°, and 70° and oxidized at 573 K.

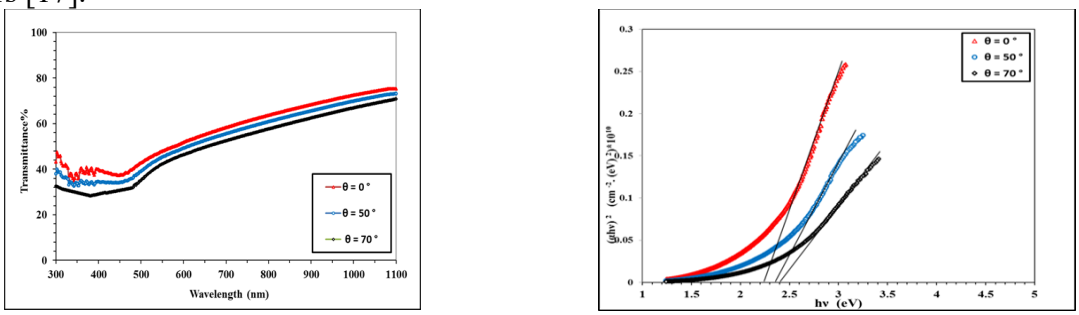
θ_d [°]	2θ [°]	hkl	FWHM [°]	dASTM [A˚]	dXRD [A˚]	Δd [A˚]	aXRD [Aº]	G.s [nm]	Tc	NL	δ [%]
0	33.257	111	0.1742	2.7000	2.6917	0.0083	4.662	49.71	1.6	12	0.57
	38.518	200	0.1763	2.3400	2.3353	0.0047	4.670	49.85	0.4	12	0.39
50	33.307	111	0.1947	2.7000	2.6878	0.0122	4.655	44.48	1	13	0.71
70	33.371	111	0.1506	2.7000	2.6828	0.0172	4.646	57.51	1	10	0.90

The structural parameters are listed in Table 1. The lattice constant (111) is lower than the ASTM value of cubic CdO (a = 4.695 Å) from all directions, indicating that the films are under tensile residual stress [24]. The FWHM of the (111) peak varies non-monotonically with deposition angle, rising from 0.174° at 0° to 0.195° at 50° before falling to 0.151° at 70°, while the corresponding grain size from Eq. (1) follows the inverse trend, dipping from 49.71 nm to 44.48 nm before rising to 57.51 nm. The two parameters remain inversely related at every angle: oblique flux and self-shadowing limit the breadth to which each column can expand, refining the crystallites and broadening the peak at 50°, whereas the sparser, more isolated columns at 70° allow individual grains to coalesce and coarsen even as the film becomes more porous [25]. As the surface progresses to isolated tilted columns, the texture coefficient of the (111) orientation decreases with angle, from 1.6 at 0° to 1 at 50° and 70°. The micro strain from Eq. (2) increases monotonically with angle and remains tensile throughout the full range, from 0.57 % at 0° to 0.71 % at 50° and 0.90 % at 70°, reflecting dislocations and stacking faults that accumulate progressively in the more porous, shadowed structure at high angles [12,14,17]. At 70°, the lattice constant decreases further to 4.646 Å and the interplanar spacing deviates most from the standard value, consistent with a more strained, defect-rich structure under high oblique incidence.

Optical Properties Result for Normal and Oblique CdO Films

Fig. 2(a) shows the optical transmittance of the CdO films as a function of the wavelength. All films are quite transparent in the visible and near-infrared with a window effect which increases with wavelength. The transmittance for the usual deposited film is close to 75%. As the films become thinner, the deposition angle is increased to reduce transmittance because the surface becomes rougher due to oblique growth. The columnar needle and rod-like structures formed at 50° and 70° scatter more of the incident light, and the 70° film transmits only about 70% of the incident light over the same range [1,11]. The direct allowable optical band gap obtained from the Tauc plot (Fig. 2(b)) increases with the deposition angle (2.4 eV at 0°, 2.5 eV at 50°, and 2.6 eV at 70°). This monotonic widening does not track the grain size in Table 1, which dips at 50° before coarsening at 70°; instead, it is more consistent with the progressively decreasing film thickness, which introduces a quantum-size contribution, together with the increasing microstrain and defect

density reflected in the (111) texture coefficient and lattice constant. The consequent spreading makes oblique films valuable for optical devices, e.g., memory elements and short-wavelength detectors [17].



(a) (b)

Fig. 2. (a) Optical transmittance as a function of wavelength for CdO thin films deposited at different angles and oxidized at 573 K, and (b) Tauc plot showing the direct allowed optical band gap at these deposition angles.

Electrical Measurement I-V Characteristics Under Dark Conditions and Illumination

The dark current density–voltage (J–V) of normal and oblique Al/CdO/p-Si/Al heterojunctions under forward and reverse bias is shown in Fig. 3. We can divide forward bias curves into two halves. At low voltage, recombination dominates current. This occurs when the product of the created carriers exceeds the inherent level (n*p> n_i^2). At higher voltages, diffusion limits current. The reverse branch also separates, where electron-hole production increases gradually at low bias, followed by minority-carrier diffusion across the junction at higher reverse voltage. At constant bias, dark current increases linearly with voltage but decreases with deposition angle. Result of columnar morphology. Oblique growth increases sheet resistance and column gaps. This causes anisotropic, well-separated columns at high angles to carry less current than thick films at normal incidence [26,27]. Fig. 4(a), 4(b), and 4(c) show the reverse bias J–V response of the normal and oblique heterojunctions under three light intensities by using a 100W halogen lamp. The depletion region under reverse bias broadens with illumination, absorbs more photons, and generates more electron–hole pairs; consequently, the reverse photocurrent increases. The diode resistance lowers under light. At a given bias, the oblique device yields a larger photocurrent than the standard device, a gain associated with the rougher, more porous surface of the obliquely deposited CdO, which traps and absorbs more incident light. The photocurrent continues to increase across the three intensities without saturation, demonstrating the excellent linearity of the manufactured photodetectors and their compatibility with silicon-based optoelectronic sensing.

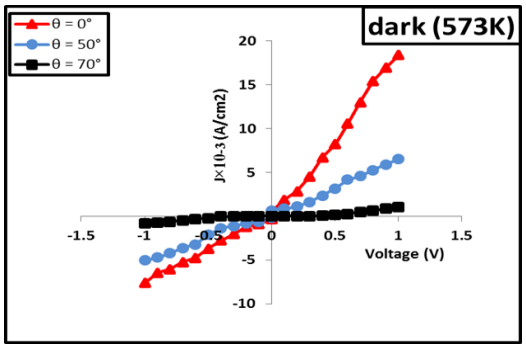


Fig. 3. J–V characteristics under dark conditions and forward bias for normal and oblique deposition of Al/CdO/p-Si/Al thin films prepared at an oxidation temperature of 573 K.

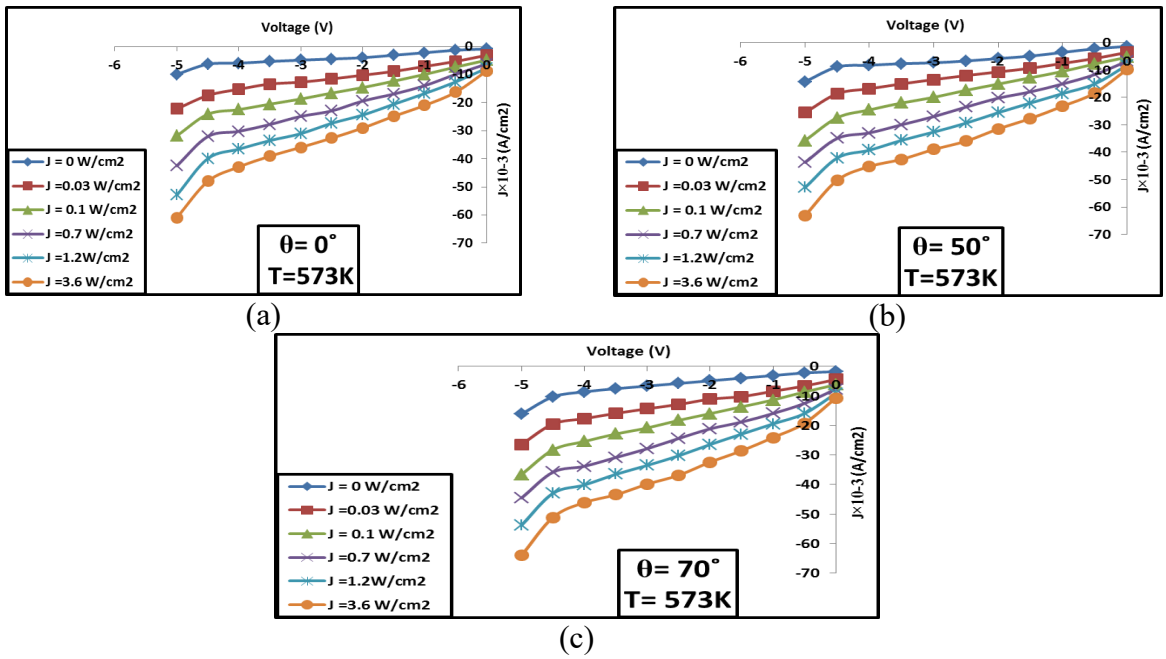


Fig. 4. J–V characteristics under reverse bias and illumination for normal (a) and oblique deposition Al/CdO/p-Si/Al thin films (b and c) at 573 K oxidation with varying light intensities.

Conclusion

Oblique-angle deposition simplifies the incidence angles, optics, and electrical responsiveness of the CdO layer and heterojunction structure. Higher angles (0° to 70°) resulted in a stronger (111) texture, a non-monotonic grain size and FWHM with an extremum at 50°, a lattice constant that decreased to 4.646 Å, and a microstrain that increased monotonically while remaining tensile (0.57% to 0.90%). Columnar and self-shadowed growth decreased visible–near-infrared transmittance from 75% to 70% and increased the direct optical band gap. Rectification happens in Al/CdO/p-Si/Al heterojunctions. Increased deposition angle decreased dark current. Lighting increased the reverse photocurrent in oblique devices, and the increase was linear with light intensity. They found that CdO is a silicon-compatible 70° OAD optical detector. Future research should measure the responsivity, detectivity, and response time of these heterojunctions, determine the optimum at intermediate and steeper angles, extend the spectral response to the ultraviolet, and test the long-term stability of the columnar films under sustained illumination and thermal cycling.

References

[1] W.K. Khalef, S.R. Mohammed, A.A. Salman, N.J. Shukur, B.A. Yousif, S.B. Al-Baghdadi, A.D. Faisal, Oblique angle deposition of cadmium oxide film on quartz substrate, Int. J. Nanoelectron. Mater. 11 (2018) 23–30.

[2] S. Sharma, S. Chaudhary, A. Kapoor, Structural and optical properties of thermally treated CdO thin films deposited on ITO coated glass substrates for photovoltaic applications, J. Sol-Gel Sci. Technol. 82 (2017) 315–321. https://doi.org/10.1007/s10971-016-4301-z

[3] B. Amudhavalli, R. Mariappan, M. Prasath, R.N. Jayaprakash, Fabrication and characterization of thin film CdO nanoparticles for gas sensing applications, J. Mater. Sci.: Mater. Electron. 35 (2024) 547. https://doi.org/10.1007/s10854-024-12240-0

[4] R.H. Hilal, Using Taguchi experimental design to calculate and analyze thermal conductivity for (polyacrylamide–kaolin) composite, Kuwait J. Sci. 50 (2023). https://doi.org/10.48129/kjs.21061

[5] P. Sakthivel, S. Asaithambi, M. Karuppaiah, S. Sheikfareed, R. Yuvakkumar, G. Ravi, Different rare earth (Sm, La, Nd) doped magnetron sputtered CdO thin films for optoelectronic applications, J. Mater. Sci.: Mater. Electron. 30 (2019) 9999–10012. https://doi.org/10.1007/s10854-019-01342-9

[6] S. Singh, P. Singh, D.Y. Kim, I.H. Lee, Physical vapor deposition synthesis of CdO nanostructures: A review, Mater. Today Proc. 17 (2019) 1067–1072. https://doi.org/10.1016/j.matpr.2019.06.107

[7] D.M. Carballeda-Galicia, R. Castanedo-Pérez, O. Jiménez-Sandoval, S. Jiménez-Sandoval, G. Torres-Delgado, C.I. Zúñiga-Romero, High transmittance CdO thin films obtained by the sol-gel method, Thin Solid Films 371 (2000) 105–108. https://doi.org/10.1016/S0040-6090(00)00987-1

[8] K. Kaviyarasu, E. Manikandan, P. Paulraj, S.B. Mohamed, J. Kennedy, One-dimensional well-aligned CdO nanocrystal by solvothermal method, J. Alloys Compd. 593 (2014) 67–70. https://doi.org/10.1016/j.jallcom.2014.01.019

[9] R. Henríquez, P. Grez, E. Muñoz, E.A. Dalchiele, R.E. Marotti, H. Gómez, Template-free non-aqueous electrochemical growth of CdO nanorods, Thin Solid Films 520 (2011) 41–46. https://doi.org/10.1016/j.tsf.2011.06.027

[10] W.K. Khalef, Preparation and characterization of CdO thin films obtained by oxidation of obliquely evaporated Cd thin films, J. Al-Nahrain Univ. Sci. 17 (2017) 103–110. https://doi.org/10.22401/jnus.17.4.14

[11] W.K. Khalef, W.N. Ibrahim, Study the effect of oblique deposition on surface characterization and microstructure of evaporated cadmium thin films, Eng. Technol. J. 31 (2013) 130–141.

[12] M.M. Hawkeye, M.J. Brett, Glancing angle deposition: Fabrication, properties, and applications of micro- and nanostructured thin films, J. Vac. Sci. Technol. A 25 (2007) 1317–1335. https://doi.org/10.1116/1.2764082

[13] K. Robbie, J.C. Sit, M.J. Brett, Advanced techniques for glancing angle deposition, J. Vac. Sci. Technol. B 16 (1998) 1115–1122. https://doi.org/10.1116/1.590073

[14] A. Tuna, S.Y. Gezgin, B. Mercimek, H.Ş. Kılıç, Photodetector properties of CdTe thin films and CdTe/Si heterojunctions produced by pulsed laser ablation, Opt. Quantum Electron. 58 (2026) 126. https://doi.org/10.1007/s11082-026-08708-4

[15] H.H. Abbas, N.A. Yousif, T.H. Ali, S.M.H. AL-Jawad, Efficient CdO photodetector prepared via laser ablation in propanol medium, J. Opt. (2025). https://doi.org/10.1007/s12596-025-02912-3

[16] G. Lee, R. Ko, S. Kang, Y.J. Kim, Y.-J. Kim, H. Yoo, Nanostructure engineering by oblique angle deposition for photodetectors and other applications, Micromachines 16 (2025) 865. https://doi.org/10.3390/mi16080865

[17] S. Kumar, V. Dhiman, R. Kumar, S. Kaur, P. Sharma, K. Singh, Unveiling the photocatalytic properties of cadmium oxide for a sustainable approach towards water remediation: A review, Coord. Chem. Rev. 539 (2025) 216713. https://doi.org/10.1016/j.ccr.2025.216713

[18] W.K. Khalef, S.D. Al-Algawi, S.R. Mohammed, Structure and morphological properties of cadmium oxide nanostructure prepared by oblique angle deposition method, Eng. Technol. J. 33 (2015) 1741–1752

[19] P. Khundrakpam, B. Shougaijam, A. Ranjan, Development of a highly sensitive UV photodetector based on chevronic TiO_2 thin film using a simple oblique angle deposition technique, J. Mater. Sci.: Mater. Electron. 35 (2024) 2137. https://doi.org/10.1007/s10854-024-13913-6

[20] A.A. Aljubouri, A.D. Faisal, W.K. Khalef, Fabrication of temperature sensor based on copper oxide nanowires grown on titanium coated glass substrate, Mater. Sci. Pol. 36 (2018) 460–468. https://doi.org/10.2478/msp-2018-0064

[21] A.I. Mohmad, A.A. Aldabagh, T.A. Zaker, M.M. Uonis, T.J. Polus, Effect of substrate temperature on the structural and optical properties of CdO thin films prepared using spray pyrolysis, J. Opt. (2025). https://doi.org/10.1007/s12596-025-02475-3

[22] S.G. Ilkal, A.V. Kasture, Effect of indium doping on structural properties of spray pyrolysed cadmium oxide thin films, Int. J. Multidiscip. Res. 5 (2023).

[23] M. Aronniemi, J. Saino, J. Lahtinen, Structure and gas-sensing behavior of an iron oxide thin film prepared by atomic layer deposition, Thin Solid Films 516 (2008) 6110–6115. https://doi.org/10.1016/j.tsf.2007.10.066

[24] F.C. Eze, Optical characterisation of thin film cadmium oxide prepared by a modified reactive thermal evaporation process, Glob. J. Pure Appl. Sci. 9 (2004) 567–574. https://doi.org/10.4314/gjpas.v9i4.16066

[25] R.H. Hilal, Removal of precious metals from electronic-waste by using composite material, IOP Conf. Ser. Mater. Sci. Eng. 881 (2020) 012089. https://doi.org/10.1088/1757-899X/881/1/012089

[26] N. Hassan, Fabrication of n-CdO NPs/PS heterojunction by laser ablation in ethanol, Polytech. J. 8 (2018) 299–308. https://doi.org/10.25156/ptj.2018.8.2.165

[27] K. Shimakawa, Meherun-Nessa, H. Ishida, A. Ganjoo, Quantum efficiency of light-induced defect creation in hydrogenated amorphous silicon and amorphous As_2Se_3, Philos. Mag. 84 (2004) 81–89. https://doi.org/10.1080/14786430310001614782

Keyword Index

6063 Aluminium Alloy 173

AC Conductivity 205
Acetone Gas Sensor 205
Acrylonitrile Butadiene Styrene 9
Adsorption 32
Agricultural Waste 173
Alkali Treatment 1, 133
ALOHA Modeling 40
Antimicrobial Activity 156
Apparent Porosity 141
Applications 231
Artificial Intelligence 76
Artificial Neural Networks 93
Automobile Radiators 173

Bamboo Fibre 133
Biochar 148
Biocomposites 148
Biomass Allocation 109
Biowaste Valorization 156
Biowastes 109

Cadmium Oxide Nanostructure CdO 241
Carbon/epoxy Composite 24
Carbon/Flax Epoxy 125
Cellulose 1
Cement Replacement 188
Ceramic Tiles 141
Ceramic Waste Powder 188
Cetyltrimethylammonium Bromide 32
Chitosan Silica Nanoparticles 156
Clinoptilolite 32
Composite Material 76
Composites 101, 165
Compressive Strength 117
Compressive Strength 188
Concrete 222
Congo Red 32
Consequence Assessment 40
Crashworthiness 213

Deep Learning 76
Delamination 125
Dielectric Constant 205
Dissolved Cellulose 55
Drying Temperature 117
Durability Prediction 93
Durability 197
Dynamic Mechanical Analysis 24

Electromagnetic Interference 63
Electron Beam Irradiation 148
Elongation at Break 101
Energy Absorption 213
Ethylene Leakage 40

Fiber Reinforcement 197
Field Emission Scanning Electron Micrograph 24
Flexural Strength 188
FRP Composite Tube 213
Functionally Graded Structure (FGMs) 48

Gamma-Ray 222
Geopolymer Concrete 197
Geopolymer Concrete 93
Glass Fibre 9
Graphene 9, 231
Green Synthesis 55, 156

Hardness 16
High-Pressure Tubular Reactor 40
Hooked Steel Fiber 197
Hybrid Composites 125, 213
Hybrid Systematicâ€“Bibliometric Review 93
Interfacial Shear Strength 133
Iraqi Porcelanite 141
Machine Learning 76, 93, 165
Mango 109
Mechanical Properties 180, 188
Mechanical-Chemical Treatment 1
Mesh 9
Microwave Absorber 63
Mode II Fracture 125
Modification 32
Morphological Analysis 117
Morphological Characteristics 16

Multilayer 63
Mycelium-Based Composites 117

Nanocellulose Fiber 101
Nanocomposites 231
Nanoparticles 84
Napier Grass 1
Natural Fibres 109
Nickel Oxide 55
Non-Fickian 24
Numerical 165

Oblique Angle Deposition (OAD) Technique 241
Oblique Deposition 241

Pavement 165
PET 222
Physical Properties 117
Plant Extract Synthesis 84
POFA 222
Polyester Resin 133
Polymer Reinforced Composite 48
Polymer 231
Polypropylene Fiber 197
Precipitation 55
Preparation 231
Primary Compressor Feed Line 40
Properties 231

Quasi-Static Axial Loading 213

Rainwater Immersion 24
Recycled Concrete Aggregate 180
Recycled Polypropylene 16, 148
Reflection Loss 63
Reinforced Alloy 173
Renewable Resources 84
Rice Husk 148

Self-Consolidating Lightweight Foamed Concrete 180
Shielding 222
Single Layer 63
Sintering Effect 205
Size-Dependent Properties 156
Stacking Sequence 125
Sulfuric Acid 197
Surface Morphology 205
Sustainable Composite Materials 180
Sustainable Construction Materials 93
Sustainable Materials 109
Sustainable Nanomaterials 84

Thermal Conductivity 141
Turmeric Residue 101

Ultrasonic Attenuation 48
Ultrasonic Transducer 48

Waste Glass Fibre Powder 180
Weibull Analysis 133
Wood Plastic Composite 16
Woven 9
Yttria-Stabilized Zirconia (YSZ) 205

About the Editors

Norhayani Othman is an Associate Professor in the Faculty of Chemical and Energy Engineering at Universiti Teknologi Malaysia (UTM). She is also a researcher in the Enhanced Polymer Research Group (EnPro), an associate member of the Centre for Advanced Composite Materials (CACM), and a member of the Materials and Manufacturing Research Alliance (MMRA). She holds bachelor's and master's degrees in Polymer Engineering from UTM and received her PhD in Chemical and Biological Engineering from the University of British Columbia, Canada, in 2012. She has nearly 20 years of experience in research, teaching, and academic publication in chemical and polymer engineering. Her current research interests include plastic-waste management, the crystallization and degradation behavior of recycled plastics and biopolymers, melt rheology, and polymer processing. She is registered as a Professional Engineer with the Board of Engineers Malaysia and is a certified trainer. She also conducts training programmes and short courses in polymer science and technology.

Mohd Nor Faiz Norrrahim is a distinguished researcher with a profound passion for nanotechnology, composites, and polymers. His remarkable expertise in these fields is underscored by his extensive body of high-impact publications. To date, he has authored or co-authored over 246 scholarly publications, including 6 books, 170 journal papers, and 70 book chapters published by esteemed publishers and in esteemed journals. His exceptional work has not gone unnoticed; he has been honored with several local and international innovation awards. His remarkable scholarly influence is reflected in his current h-index, which stands at 56 on Google Scholar and 49 on Scopus, solidifying his place as a leading authority in his field. His dedication and contributions have led to his inclusion in the prestigious list of the world's top 2% of scientists compiled by Stanford University, USA.

Munirah Onn has been a Senior Lecturer at Universiti Teknologi MARA (UiTM), Pasir Gudang Campus, since 2014. She holds a Science degree from UiTM and a master's degree in Polymer Engineering from UTM, where she also earned her PhD in Polymer Engineering. Her doctoral research focused on developing an ultraviolet light-emitting diode-curable polymer from acrylated waste palm cooking oil. During her studies, she received the Best Degree Student, Best Thesis Writing, and Vice-Chancellor's Awards from UiTM, as well as the Best Student Award for the Master's Programme from UTM. She brings industrial experience from her roles as a Production Engineer at Universal Cable, a Research Officer at the Malaysian Nuclear Agency, and an Executive Chemist at Multisquare Sdn. Bhd. Her current research interests lie in renewable and advanced materials.

Pui San Khoo is a Postdoctoral Researcher in the Department of Mechanical and Aerospace Engineering at Tokyo University of Science, Japan. She received her PhD in Bio-composite Technology and Design from Universiti Putra Malaysia, where her doctoral research focused on the mechanical behavior, interfacial bonding, and delamination of rubberwood laminated veneer lumber. She subsequently conducted postdoctoral research at the Centre for Advanced Composite Materials, Universiti Teknologi Malaysia, focusing on natural-fibre and thermoplastic composites. Her current research encompasses composite materials, interface engineering,

experimental mechanics, damage characterization, and finite element modelling, with particular emphasis on the mechanical behavior, delamination, and interlaminar reinforcement of carbon fiber-reinforced polymer laminates. She has authored or co-authored more than 40 peer-reviewed journal articles. She also has university teaching experience and has contributed to academic publishing, peer review, journal editing, conference organization, and international research collaboration.